UNIVERSITY OF Southampton

University of Southampton Research Repository
ePrints Soton

Copyright © and Moral Rights for this thesis are retained by the author and/or other copyright owners. A copy can be downloaded for personal non-commercial research or study, without prior permission or charge. This thesis cannot be reproduced or quoted extensively from without first obtaining permission in writing from the copyright holder/s. The content must not be changed in any way or sold commercially in any format or medium without the formal permission of the copyright holders.

When referring to this work, full bibliographic details including the author, title, awarding institution and date of the thesis must be given e.g.

AUTHOR (year of submission) "Full thesis title", University of Southampton, name of the University School or Department, PhD Thesis, pagination

http://eprints.soton.ac.uk

UNIVERSITY OF SOUTHAMPTON

Comprehensive Characterisation of Turbulence Dynamics with Emphasis on Wall-Bounded Flows

by

Patrick Bechlars

A thesis submitted in partial fulfillment for the degree of Doctor of Philosophy

in the

Faculty of Engineering and the Environment

Aerodynamics and Flight Mechanics Group

November 2015

Acknowledgements

This work would not be to what it finally developed without the support and the help that I received from some truly amazing people.

Firstly and most importantly there is the support from my loved family: My parents Wolfgang and Jutta who always shower me with their love and support. Both taught me to question statements and to not take things as set in stone even though they seem so - a trait of great importance in science. My sisters Susi and Betti who always have an open ear, open arms and an open door. Their support, not only on the psychological level, is priceless. I could not think of better sisters. My brothers-in-law Chris and Jeff who are not less important to me than my sisters are. And additionally to the psychological support they are always up for discussing things over a beer. My lovely nieces Mimi Lotte, Ella Marley, Maggie Lynn and Hanna Bailey who where all born during the time of my studies for this work. They have the incredible power to make you happy no matter how stressed you are. They already developed to remarkable little ladies and I cannot wait spending more time with them. My Oma Hilde who always makes me laugh and taught me that whenever you land with your face on a piece of bread, then it will be on the side with the jam - pure physics! My girl-friend Sonia who was there every day during the long process of writing this thesis. She finds nice words to cheer you up even after the longest working day. Thank you for going with me through all this. I cannot find the right words to express the importance of my entire family to my life and to this work. I am sorry for all the unanswered messages and calls in the last few years.

The main supporter of this work was my supervisor Richard Sandberg with his invaluable input and long discussions. He guided me in the right moments, but also gave me the freedom, time and resources to be creative and built up this work in a way that I am very happy with it. Also the few discussion with my co-supervisor Bharath Ganapathisubramani were of great value. He gave me the right push in the right direction when I was looking for the path that I wanted to go with my thesis.

As a Mathematician and rookie in the field of turbulence, I pretty much had no clue about the work I would go through in during this studies. I have to thank Toni Alomar, Yusik Kim and Richard Pichler for all the nice discussions and great fights about what is turbulence and what we actually need to know about it.

My friends Andrea, Nico and many more in Southampton were amazing in supporting, helping , distracting and celebrating with me. I will miss you all a lot. But as well my old friends Fabian, Aline and many many more that I left behind when starting this study where always there for visits, on the phone or just keeping there arms open whenever I came home for a visit.

Thank you all for this amazing support. This work is for you!

UNIVERSITY OF SOUTHAMPTON

ABSTRACT

FACULTY OF ENGINEERING AND THE ENVIRONMENT
AERODYNAMICS AND FLIGHT MECHANICS GROUP

Doctor of Philosophy

by Patrick Bechlars

This report describes the work carried out in 'universality' aspects of the dynamics of turbulence in compressible flows. Direct numerical simulations (DNSs) are carried out in different inhomogeneous and anisotropic flows. All discussed flows show regions of strong imbalance of turbulent production and turbulent dissipation. This distinguishes this work from most studies in the literature about the fundamentals of turbulent dynamics. A characteristic decomposition in addition to temporal and spatial filtering are applied as tools to compare differences in the turbulent dynamics across different flow topologies. The work includes a discussion about universal aspects of the velocity gradient and related quantities in a turbulent boundary layer, in a jet flow as well as in a wake flow. Invariant features are highlighted and quantified and the differences are pointed out. The velocity gradient and the enstrophy production, as one of the key quantities in the turbulent energy cascading process, are discussed in great detail in the turbulent boundary layer flow. Focus hereby is on the wall-normal development of the structure of the enstrophy production. This is followed by a comprehensive overview of a turbulent boundary layer. This includes the presentation and discussion of global energy redistributing mechanisms from different perspectives. The key role of turbulence in these processes is made clear. The energy cascade is dissected at different locations which reveals three different transfer processes. Two of which are transferring energy from larger scales of motion towards smaller scales of motion. In addition a backscatter mechanism was discovered that transfers energy from smaller scales towards larger scales of motion. Besides this some specific and potentially universal features of turbulence within the turbulent boundary layer results are discussed.

Contents

List of Figures

List of Tables

Chapter 1

Introduction

1.1 Motivation

Once we have got up in the morning, had breakfast and driven to work, we have been affected more or less directly by fluid dynamics. When we wake up our metabolism becomes more active and our blood flow is changing its dynamic. The milk and the coffee we have for breakfast are mixing. The petrol we use to run our car is transported on tanker ships over the ocean or pumped through pipelines before being refined via chemical processing. Even sometimes we are annoyed that we drive through a rainstorm although the forecast said: Sunny! The common point is that every step involves dynamical flow problems. Curiosity and the need for sustainability drive us to understand these processes. We want to understand the world around us and we want it to stay as clean as possible. As we do not want to miss out on luxury, it leads us to permanently try to increase the efficiency of the way we are using resources. To achieve this in processes that involve flows of fluids, it is necessary to understand the dynamics of the flow problems. But a fact most fluid flow problems share is that they are not fully understood, which poses a barrier in appropriately designing processes and reaching the best performance in various applications. This is the reason why fluid dynamics is a very active research topic.

The biggest issue in fluid dynamics is that flows in particular circumstances become turbulent (further description in section 1.2) and as such they are difficult to describe in detail. On the other hand manipulation and improvement of most applications do not directly need this detailed information about the flow. Nevertheless, flows are highly coupled systems so that we need a certain knowledge about the fine details of a flow to be able to predict quantities which are needed to manipulate applications for our needs. Various ways of describing the impact of turbulence on the quantities of interest (e.g. mean velocity, drag, dissipation,...) exist. They form turbulence models which are based on what we can assume or hypothesize about turbulence and its underlying mechanisms. In order for there to be a fully general turbulence model, that is applicable

to all turbulent flows, we would require turbulence to have some sort of universal character. Limited universality of turbulent flows was already hypothesized by Kolmogorov (1941) more than 70 years ago. Although we know that his hypotheses are not fully applicable in all kinds of flow, the majority of today's turbulence models are based on them. In this work we want to investigate some of the boundaries of the hypothesized universality and find whether different approaches of universality in fluid dynamics can be stated. Therefore we first have to get a better picture of what the characteristics of turbulence are and how it is driven. Further we need to obtain a better knowledge of how universality is hypothesized so far.

1.2 What is turbulence?

Flows or flow regions can commonly be classified into laminar, transitional and turbulent. The definition of this classification is slightly nebulous. The dimensionless Reynolds number, which is a result of the non-dimensionalization of the flow equations (chapter 2), is an important parameter characterising of a flow and its value indicates if a flow stays laminar or undergoes transition and becomes turbulent. It can be seen as ratio between amplification and damping of pertubations in the flow field. The Reynolds number $Re_\infty = \frac{\rho_\infty u_\infty L}{\mu_\infty}$ is calculated as function of a reference density ρ_∞, a reference velocity u_∞, a reference length L and a reference dynamic viscosity μ_∞ that are characteristic for the flow, the fluid and the size of the observed problem. If the Reynolds number of a flow is small enough the flow will maintain laminar behaviour. Laminar flow describes flows whose flow field is ordered and only a few flow structures are distinct. The flow field in laminar flows can be steady in time or have a regular time dependent behaviour. Figure 1.1 shows laminar flows around a circular cylinder at three different low Reynolds numbers. Vortical structures are developing in the wake of the cylinder.

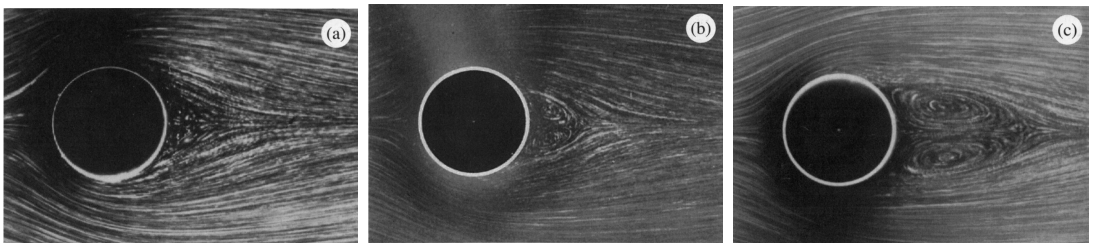

Figure 1.1: Flow around a circular cylinder at $Re = 9.6$ (a), $Re = 13.1$ (b), $Re = 26$ (c) (Van Dyke, 1982).

With increasing Reynolds number it can be observed that these structures are growing. But the important fact to mention is that the structures are part of a steady flow field. These flows are described as laminar. If the Reynolds number is increased the amplification of irregularities in the flow field is increasing with respect to their damping. This allows the vortical structures to detach from the cylinder so that they develop a so called

Kármán vortex street in the wake of the cylinder (fig. 1.2). These flow fields are time dependent but in a periodic manner and therefore still have some sort of regularity and are defined as laminar. If the Reynolds number is increased further, the transitional

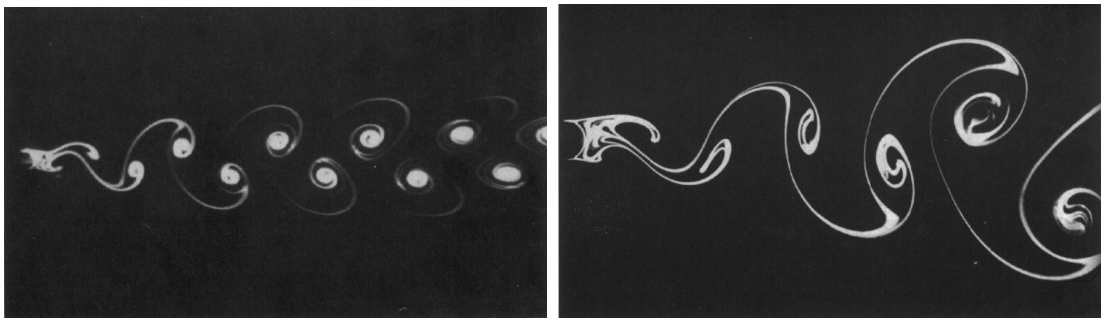

Figure 1.2: Flow around a circular cylinder at $Re = 105$ (left), $Re = 140$ (right) (Van Dyke, 1982).

regime will be reached. Figure 1.3 shows the flow behind two cylinders at a Reynolds number that allows the flow to become transitional. If we look at the region in the close wake behind the upper cylinder a similar flow field to the low Reynolds number case is observable. But the further we go downstream the more the regularity of the structures is vanishing. The structures of the Kármán vortex street are still present but become more and more overlaid with smaller structures. The larger vortices are breaking down, feeding smaller structures and allow them to gain energy. This is what is called transition. A part of the earlier mentioned coupling of the flow can be observed here as the larger structures produce smaller structures. If we take the next step and increase the

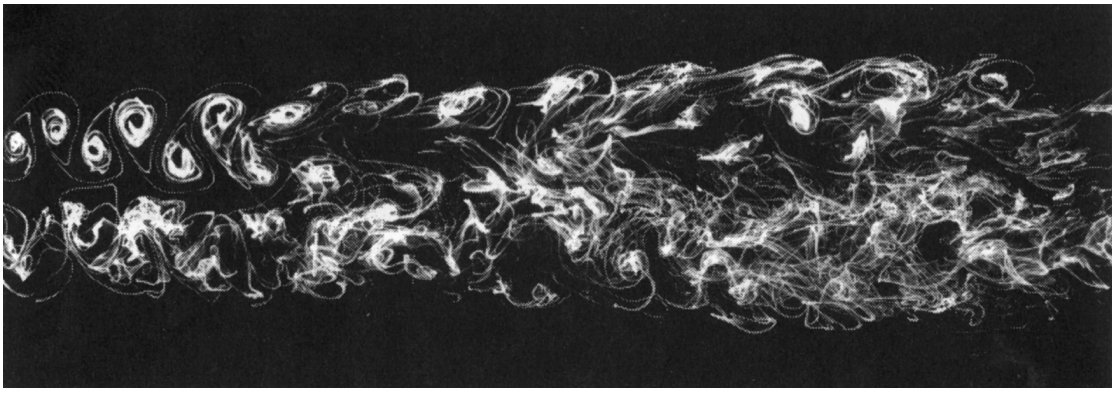

Figure 1.3: Wake behind two identical cylinders at $Re = 240$ (Frisch, 1995).

Reynolds number even more we reach a flow that is described as turbulent. Figure 1.4 shows the wake of two cylinders at a reasonably high Reynolds number. If we focus on the near wake region, the regularity of the large-structured Kármán vortex street is still present, but completely overlaid with smaller structures. If we look further downstream the flow field becomes very blurry and it is very difficult to pick out some sort of structure. The flow has become 'chaotic'. This process of larger structures that are breaking

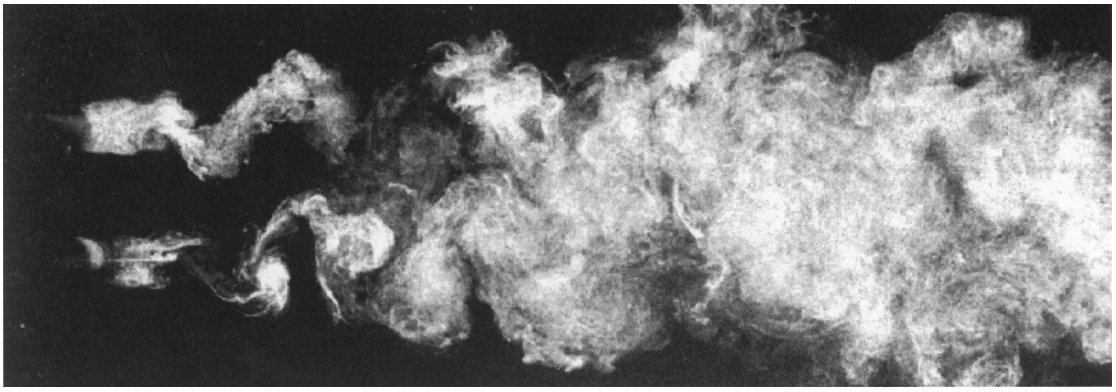

Figure 1.4: Wake behind two identical cylinders at $Re = 1800$ (Frisch, 1995).

down and letting smaller structures develop, was mentioned by Richardson (1925). He introduced the idea of a turbulent energy cascade. This cascade shall illustrate that flow structures permanently break down into smaller ones. The process is then stopped in the smallest scales as viscous friction is dissipating all the kinetic energy in the smallest scales. Richardson summarized this process as

> Big whorls have little whorls,
> Which feed on their velocity;
> And little whorls have lesser whorls,
> And so on to viscosity
> (in the molecular sense).

As one might assume it is extremely difficult to define turbulence in a quantitative way (Doering & D.Gibbon, 2004), but we are able to outline certain features turbulence has. Any object in a flow, whether it is a wing of an aircraft, a moving car or a wind turbine, will develop a similar or at least related kind of turbulent wake, if the Reynolds number is comparable. When it comes to calculating the drag and/or efficiency of such an object it is important to know what is happening to the kinetic energy in the wake. How much energy is dissipated and how much will this wake spread? This leads to the conclusion, that we have to understand the behaviour of the wake including all its details such as the smallest 'whorls'. We need to understand the way the smallest whorls gain and dissipate energy, but we need to understand as well the effect the smaller whorls have on the larger ones and vice versa. This is roughly what turbulence research is about.
Richard Feynman[1] stated that turbulence remains "the most important unsolved problem of classical physics". The problem with turbulence is that it includes structures from large size to a very small size and everything in between. All these structures are coupled in a complex way what makes it difficult to understand their interaction. Turbulence is

[1] Nobel Prize winning physicist

often described as a 'random' behaviour of the fluid quantities, which is not true. We say that we are able to describe a fluid as a continuum and its movement is modelled with the Navier-Stokes equations (equation 2.9). This system is of deterministic nature and cannot produce solutions with random character. The Navier-Stokes equations can be transformed to a dynamical system (Doering & D.Gibbon, 2004). In this form it can be shown how strongly the actual state of the system is dependent on previous states (e.g. initial conditions). Its behaviour is described as deterministic chaos. That, roughly speaking, means that if we set the systems to the same state, it will always follow the same behaviour. But if we change the initial state only a bit, this difference will grow strongly and the system follows a completely different path from the unchanged one. For turbulence that means that it is very difficult to predict in detail and this is the reason for why it is often described as having 'random behaviour'. In order to describe this apparent random behaviour, the use of statistics has become a standard approach in turbulence research.

1.2.1 The Kolmogorov Energy Cascade

Kolmogorov (1941) quantified the behaviour of turbulence in a mean sense. He described the behaviour of fully developed homogeneous isotropic turbulence (HIT) in a periodic box. The idea is that a turbulent flow is composed of structures with different size and frequencies. For a structure of given characteristic size l, we can find a characteristic velocity $u(l)$ and time-scale $\tau = \frac{l}{u(l)}$. There can be (and mostly are) structures of different sizes on top of each other, so that the instantaneous energy at each point of a turbulent flow is distributed over many scales and frequencies.
The size of the largest structures l_0 is comparable to the length scale of the flow $\mathcal{L}$ and equivalently their characteristic velocity $u_0 = u(l_0)$ is comparable to the global velocity scale u_∞. This implies that the Reynolds number of these structures, Re_0, is high and comparable to Re_∞ and the effects of viscosity are small. The scales of these large structures are the ones into which energy enters the process due to initial and boundary conditions (here: size of the box). These structures then start to transfer energy to smaller structures. This transfer process is not only found in the largest scales, it is active in every scale. This system forms an energy cascade (figure 1.5) in which energy is transferred successively to smaller and smaller structures. If we go downwards (in the sense of structure size) the cascade, the corresponding Reynolds number of the structures $Re = \frac{u(l)l}{\nu}$ decreases (Kolmogorov, 1941). This shows that the viscous effects are becoming stronger and at some point the transfer of energy downwards the cascade is balanced by dissipation that dissipates kinetic energy and converts it to internal energy. Since the total kinetic energy in a fully developed turbulent flow is constant on average, the rate of dissipation ε must be the same as the rate of kinetic energy that is put into the system, i.e. the transfer rate of energy into the largest scales $\frac{u_0^3}{l_0}$. The equation $\varepsilon = \frac{u_0^3}{l_0}$ shows that the dissipation is independent of the viscosity and the Reynolds

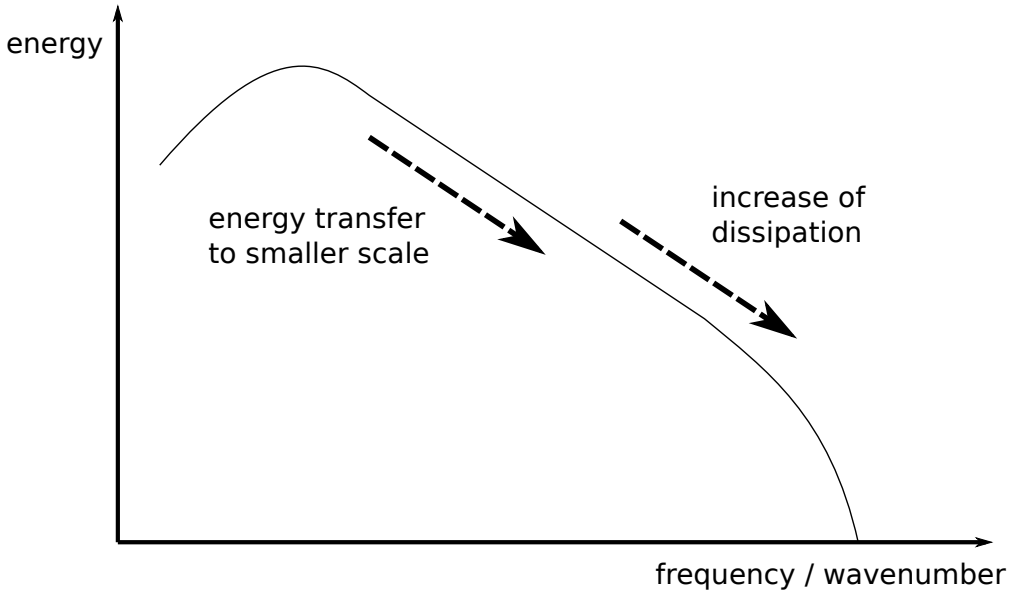

Figure 1.5: schematic illustration of the energy cascade in an statistically isotropic, turbulent flow

number only describes how dissipation is distributed over the different scales.
Almost two decades after Richardson (1925) invented the idea of the cascade, Kolmogorov (1941) quantified it and stated three hypotheses about HIT flows in equilibrium. As consequence of his theory the velocity scale and time-scale $u(l)$ and $\tau(l)$ of the structures decrease with the size l of a structure. This is the reason for the decreasing Reynolds number on the way down the cascade, stated before.
Kolmogorov's first hypothesis is based on the argument that the directional information of the large scale structures enforced by initial and boundary conditions is lost in the chaotic scale reduction along the cascade. This has the effect that anisotropy of the larger structures will not reach the small-scale structures, which then can be regarded as isotropic. Kolmogorov (approximately) stated the hypothese by Taylor (1935) as:

Kolmogorov's hypothesis of local isotropy.
At sufficiently high Reynolds number, the small-scale turbulent motions ($l \ll l_0$) are statistically isotropic.

As weak demarcation between anisotropic large scales ($l > l_{\mathrm{EI}}$) and isotropic small scales ($l < l_{\mathrm{EI}}$) we introduce the length scale l_{EI} with the approximation $l_{\mathrm{EI}} \approx \frac{1}{6} l_0$.
Investigating the dependencies of this statistically isotropic state, Kolmogorov pointed out the energy transfer to successively smaller scales and the viscous dissipation as the two dominant processes in the range below l_{EI}. Fourier analysis (Doering & D.Gibbon, 2004) shows that under the assumptions of 'local isotropy', equilibrium and that energy

is mainly dissipated in the smallest scales, the rate $\mathcal{T}_{\mathrm{EI}}$ at which small scales are receiving energy from larger scales can be approximated by $\mathcal{T}_{\mathrm{EI}} \approx \varepsilon$. With ν denoting the kinematic viscosity the first similarity hypothesis can be stated as:

Kolmogorov's first similarity hypothesis.
In every turbulent flow at sufficiently high Reynolds number, the statistics of the small-scale motions ($l < l_{\mathrm{EI}}$) have a universal form that is uniquely determined by ν and ε.

The range of structures with the size $l < l_{\mathrm{EI}}$ is referred to as the *universal equilibrium range*, as the time-scales are small compared to the global time-scale and the structures can adapt quickly to maintain a dynamic equilibrium with the energy-transfer rate $\mathcal{T}_{\mathrm{EI}}$ imposed by the larger structures.
With the two parameters ν and ε determining the statistics of the small-scales and the assumption that energy transfer from larger scales and dissipation are balanced at a Reynolds number equal to unity, we can form unique length, velocity and time scales using dimensional analysis. These are the resulting Kolmogorov scales:

$$\eta := \left(\frac{\nu^3}{\varepsilon}\right)^{\frac{1}{4}}, \tag{1.1}$$

$$u_\eta := (\varepsilon\nu)^{\frac{1}{4}}, \tag{1.2}$$

$$\tau_\eta := \left(\frac{\nu}{\varepsilon}\right)^{\frac{1}{2}}. \tag{1.3}$$

Defining a Reynolds number with these quantities we find it to be unity $\frac{\eta u_\eta}{\nu} = 1$. Using the Kolmogorov scales to non-dimensionalise a high-Reynolds-number turbulent flow, we find the flow field does not depend on ε and ν (Pope, 2000). This shows: *On the small scales, all high-Reynolds number turbulent velocity fields are statistically similar; that is, they are statistically identical when they are scaled by the Kolmogorov scales* (Pope, 2000).
Further we can provide the scaling of the ratio between the smallest and largest scales with the scaling $\varepsilon \sim \frac{u_0^3}{l_0}$ (Pope, 2000):

$$\frac{\eta}{l_0} \sim Re^{-\frac{3}{4}}, \tag{1.4}$$

$$\frac{u_\eta}{u_0} \sim Re^{-\frac{1}{4}}, \tag{1.5}$$

$$\frac{\tau_\eta}{\tau_0} \sim Re^{-\frac{1}{2}}. \tag{1.6}$$

This tells us that at high Reynolds number velocity and time-scales of the smallest structures are small compared with those of the large ones.
As the ratios are increasing with Reynolds number there must be structures with length

scale l very small compared to the largest energy-containing length scales and very large compared to the Kolmogorov length scale. Hence, the structures with length scale l in the range $l_0 \gg l \gg \eta$ have a sufficiently large Reynolds number $\frac{lu(l)}{\nu}$ to be only insignificantly affected by viscosity. Further, they are small enough to be statistically isotropic as stated in Kolmogorov's first hypothesis. This led Kolmogorov to his second similarity hypothesis:

Kolmogorov's second similarity hypothesis.
In every turbulent flow at sufficiently high Reynolds number, the statistics of the motions of scale l in the range $(l_0 \gg l \gg \eta)$ have a universal form that is uniquely determined by ε, independent of ν.

Defining the length scale $l_{\mathrm{DI}}(\approx 60\eta)$ (Pope, 2000) as weak demarcation between the range where dissipation is strong and the range where dissipation is too small to have a significant impact on the flow, the scale condition in the last hypothesis can be written as $l_{\mathrm{EI}} > l > l_{\mathrm{DI}}$. That means l_{DI} then splits the universal equilibrium range $(l < l_{\mathrm{EI}})$ into two subranges: the *inertial subrange* $(l_{\mathrm{EI}} > l > l_{\mathrm{DI}})$ and the *dissipation range* $(l < l_{\mathrm{DI}})$. The upper part of the spectrum $(l > l_{\mathrm{EI}})$ is then called *energy-containing range* as all the energy of the system is introduced in these scales. The decomposition of the spectrum is shown graphically in figure 1.6.

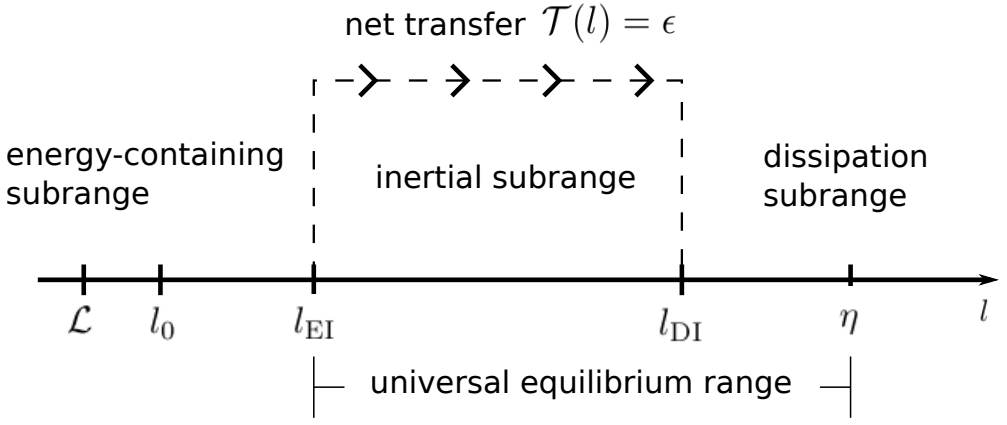

Figure 1.6: Decomposition of the energy spectrum.

1.2.1.1 The Structure Functions

Structure functions are a tool to describe the statistical behaviour of a vector field. Consider a turbulent flow in the domain Ω (fig. 1.7). If we want to obtain information about the larger flow structures (black) in the domain without detailed knowledge about the small structures (red), then we have to describe the small structures and especially

their impact on the larger ones in another way. Structure functions $H(\vec{r})$ are handling this task in an average sense. They are utilized to describe the mean quantities of the smaller structures in sub-domains (green circle in figure 1.7) and their size l is characteristic for the decomposition between what we define as large scales and small scales. The second-order structure function tensor H is defined as the covariance tensor

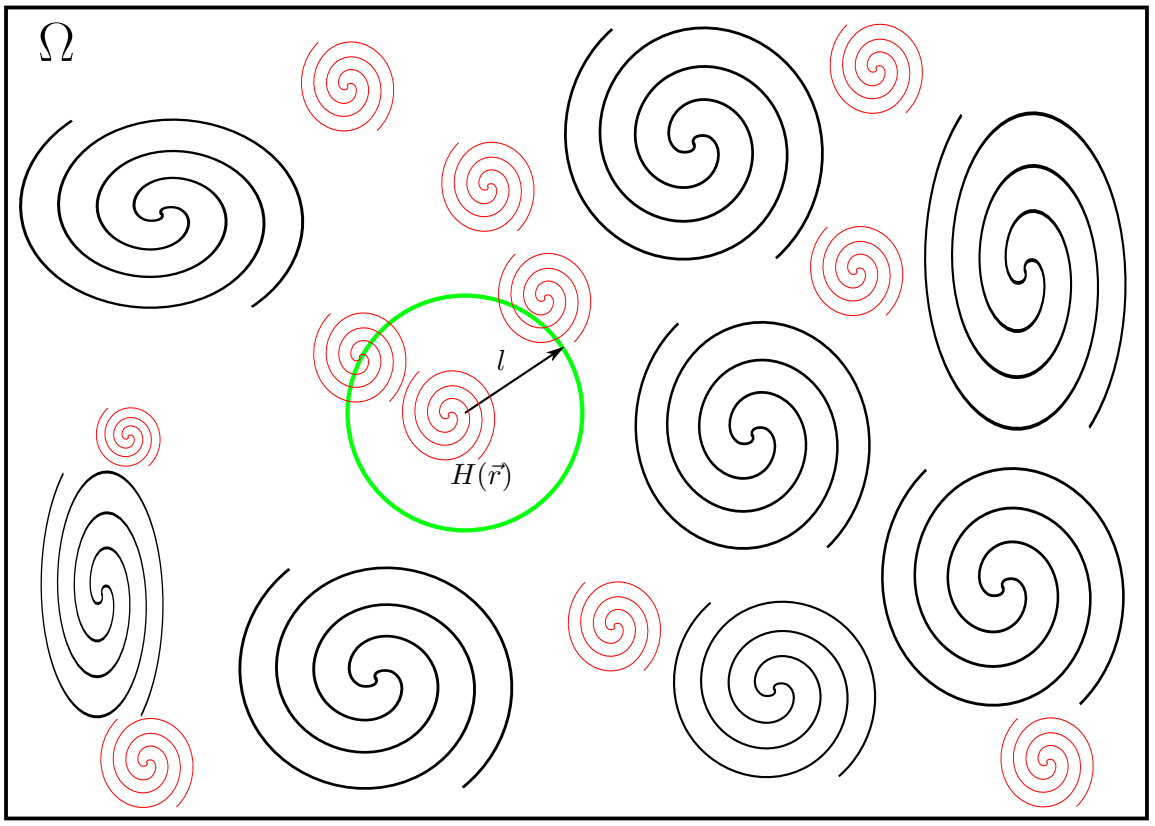

Figure 1.7: Schematic description of structure functions in a turbulent flow in the domain Ω. Black circles indicate large structures, red circles indicate small structures. The green circle shows the sub-domain in which we want to obtain knowledge about the small structures via the structure function.

of the difference in velocity between two points $\vec{x}+\vec{r}$ and $\vec{x}$.

Definition 1.1. Second Order Structure Function
The second-order tensor $H(\vec{r},\vec{x})$ defined as

$$H(\vec{r},\vec{x}) := \langle(\vec{u}(\vec{x}+\vec{r})-\vec{u}(\vec{x}))\otimes(\vec{u}(\vec{x}+\vec{r})-\vec{u}(\vec{x}))\rangle$$

is called the *second-order structure function* of the velocity field $\vec{u}$. Here $\langle\cdot\rangle$ denotes the ensemble average and $\otimes$ defines the outer product or dyadic product of two vectors (see 2.1).

If Kolmogorov's hypothesis of local isotropy holds and we choose the sub-domain to be sufficiently small so that $\|\vec{r}\| \leq l \ll \mathcal{L}$, then the structure function is not dependent on

the location $\vec{x}$ of the sub-domain as local homogeneity is implied. With local rotational invariance of the statistics and incompressibility arguments it can be shown (Pope, 2000) that the structure function is only dependent on a scalar function $H_{LL}(r)$ (with $r := \|\vec{r}\|$) and the orientation of the vector $\vec{r}$. H_{LL} is called the longitudinal structure function.

$$H(\vec{r}) = \left(H_{LL}(r) + \frac{r}{2}\frac{\partial H_{LL}(r)}{\partial r}\right) I - \left(\frac{r}{2}\frac{\partial H_{LL}(r)}{\partial r}\right) \frac{\vec{r} \otimes \vec{r}}{r^2}, \tag{1.7}$$

where I is the unity matrix.

1.2.1.2 The Energy Spectrum

Before we start to introduce the spectral distribution of the energy in the spatial Fourier space we need to define some useful statistical tools that allow us to analyse the scales of a flow.

Definition 1.2. Two-Point Correlation
The simplest statistic containing information on spatial structure of the velocity field is the two-point, one-time auto-covariance tensor (often referred to as **two-point correlation**) $R(\vec{r}, \vec{x}, t)$

$$R(\vec{r}, \vec{x}, t) := \langle \vec{u}(\vec{x} + \vec{r}, t) \otimes \vec{u}(\vec{x}, t) \rangle$$

where $\langle \cdot \rangle$ defines the mean value (see Pope, 2000, as reference) and $\otimes$ defines an outer product (2.1).

This statistic is a tool to measure how strong the flow field is coupled in two points on average. This definition can be used to, e.g., derive integral length scales (Pope, 2000). The dynamic behaviour of this statistic is describe by Batchelor (1959)

$$\frac{\partial R(\vec{r}, t)}{\partial t} = T(\vec{r}, t) + P(\vec{r}, t) + 2\nu \Delta R(\vec{r}, t), \tag{1.8}$$

where T is the divergence of the triple velocity correlation tensor and P is the pressure-velocity correlation tensor. By applying the Fourier transform we obtain the corresponding spectrum.

Definition 1.3. Velocity Spectrum Tensor
For homogeneous turbulence the correlation $R(\vec{r}, \vec{x}, t) = R(\vec{r}, t)$ is independent of the location $\vec{x}$ and its Fourier transform $\mathcal{F}(\cdot)$ is the **velocity spectrum tensor** $\Phi(\vec{k}, t)$

$$\Phi(\vec{k}, t) := \mathcal{F}\left(R(\vec{r}, t)\right) := \frac{1}{(2\pi)^3} \iiint_{-\infty}^{\infty} R(\vec{r}, t) e^{-i\vec{x}\cdot\vec{r}} d\vec{r}.$$

The inverse Fourier transform of the velocity spectrum tensor $\Phi(\vec{k}, t)$ then is

$$R(\vec{r}, t) := \mathcal{F}^{-1}\left(\Phi(\vec{k}, t)\right) := \iiint_{-\infty}^{\infty} \Phi(\vec{k}, t) e^{i\vec{x}\cdot\vec{r}} d\vec{k}.$$

The dynamics of the velocity spectrum tensor then reads (Batchelor, 1959)

$$\frac{\partial \Phi(\vec{k},t)}{\partial t} = \Gamma(\vec{k},t) + \Pi(\vec{k},t) - 2\nu\vec{k}^2\Phi(\vec{k},t). \tag{1.9}$$

with $\Gamma := \mathcal{F}(T)$ and $\Pi := \mathcal{F}(P)$ being the Fourier transforms of the triple velocity correlation tensor and the pressure-velocity correlation tensor respectively. In the incompressible case the trace of the pressure-velocity correlation tensor $\text{trace}(P) = 0$ and the trace of its Fourier transform $\text{trace}(\Pi) = 0$ are zero. For the kinetic energy $\frac{1}{2}\ \text{trace}(\Phi(\vec{k},t))$ we then obtain the identity

$$\frac{\partial \frac{1}{2}\ \text{trace}(\Phi(\vec{k},t))}{\partial t} = \frac{1}{2}\ \text{trace}(\Gamma(\vec{k},t)) - 2\nu\vec{k}^2\frac{1}{2}\ \text{trace}(\Phi(\vec{k},t)). \tag{1.10}$$

In case of HIT the energy spectrum is not depending on the spatial direction and it is useful to define an energy spectrum function that is only dependent on the absolute value $\kappa := \|\vec{k}\|$ of the wavenumber vector.

Definition 1.4. Energy Spectrum Function
The **energy spectrum function** $E(\vec{k},t)$ is defined as the integral of the trace of the velocity spectrum tensor over the sphere with radius κ

$$E(\kappa,t) := \iiint_{-\infty}^{\infty} \frac{1}{2}\text{trace}(\Phi(\vec{k},t))\delta(\|\vec{k}\| - \kappa)d\vec{k},$$

where $\delta(\cdot)$ is the Dirac delta function.

The energy spectrum function is the integral of the kinetic energy over all directions for each scalar wave number (for more details see Pope, 2000). The energy spectrum function is not only useful for HIT as we will see later. In fact it can be used in all intervals of the spectrum that are statistically isotropic.
For statistically stationary (we drop time dependence of the statistics) homogeneous turbulence we then write the turbulent kinetic energy e_k and the dissipation rate ε as integrals over the energy spectrum function:

$$e_k = \int_0^{\infty} E(\kappa)d\kappa. \tag{1.11}$$

The dissipation rate for the incompressible case is $\varepsilon := \langle\langle 2\nu S, S\rangle_F\rangle$, where S is the strain rate tensor (see 2.2 for the definition of the Hilbert-Schmidt inner product $\langle\cdot,\cdot\rangle_F$), and it can be written as

$$\varepsilon = \int_0^{\infty} 2\nu\kappa^2 E(\kappa)d\kappa. \tag{1.12}$$

Applying Kolmogorov's second similarity hypothesis to these two equations we can derive for the inertial subrange, using dimensional analysis, that the energy spectrum function

is a function of wavenumber and dissipation, including a universal constant C (see Pope, 2000). The famous Kolmogorov's $(-\frac{5}{3})$-law emerges as

$$E(\kappa) = C\varepsilon^{\frac{2}{3}}\kappa^{-\frac{5}{3}}. \tag{1.13}$$

With the fact that dissipation becomes very active in the dissipation subrange and adding the empirical shape of energy distribution in the energy-containing range observed in experiments and simulations, we can give a qualitative plot of the energy distribution in figure 1.8. The top graph shows how the Reynolds number affects the energy distribution scaled with outer variables, while the bottom graph shows the same for the energy and wave length scaled with inner variables.
Kolmogorov's $(-\frac{5}{3})$-law is well established for HIT in equilibrium. For these type of flows it can be seen as a sort of universal law. However, most engineering flows such as, e.g., wall-bounded flows or flows involving a mean shear are non homogeneous, strongly anisotropic and not in equilibrium. To describe these kinds of turbulent flows we need to find out to what extent we are able to apply what Kolmogorov hypothesized and find different approaches where the hypotheses fail.

1.2.1.3 Universal aspects related to K41

Before we address universal aspects of flow related to and derived from Kolmogorov (1941) (K41), we shall outline what we want to know about a flow. It is useful to introduce a schematic equation of the kinematic energy in a flow

$$\frac{\partial E_{\text{kin}}}{\partial t} = P_{\text{kin}} - T_{\text{kin}} - D_{\text{kin}}, \tag{1.14}$$

where E_{kin} describes the kinetic energy of the whole system, P_{kin} stands for the production of kinetic energy, T_{kin} covers the convection of kinetic energy as well as describing the inter-scale transfer of energy that drives the cascading process, and D_{kin} is the rate at which kinetic energy is dissipated into internal energy. Similar equations can be stated for the moments but they will cover more or less the same mechanisms.
A universal law for the behaviour of the instantaneous kinetic energy is essentially a global analytical solution for the Navier Stokes equations and will not be discussed in the present work. Furthermore we focus on the right hand side of equation (1.14). The production term is implied by initial and/or boundary conditions and/or external forcing of the flow, all of which are defined by the setup of the flow problem we are investigating. In other words, this term is not governed by the Navier-Stokes equations specific to a certain flow. Therefore this term will be non-universal in general and will not be investigated in the present work. But the essential fact about the production term is that it starts the whole process of forming a flow - it provides the flow with energy. As mentioned before the way it does this is specific to the flow problem and in general flows this mechanism is neither homogeneous nor isotropic. The transport term

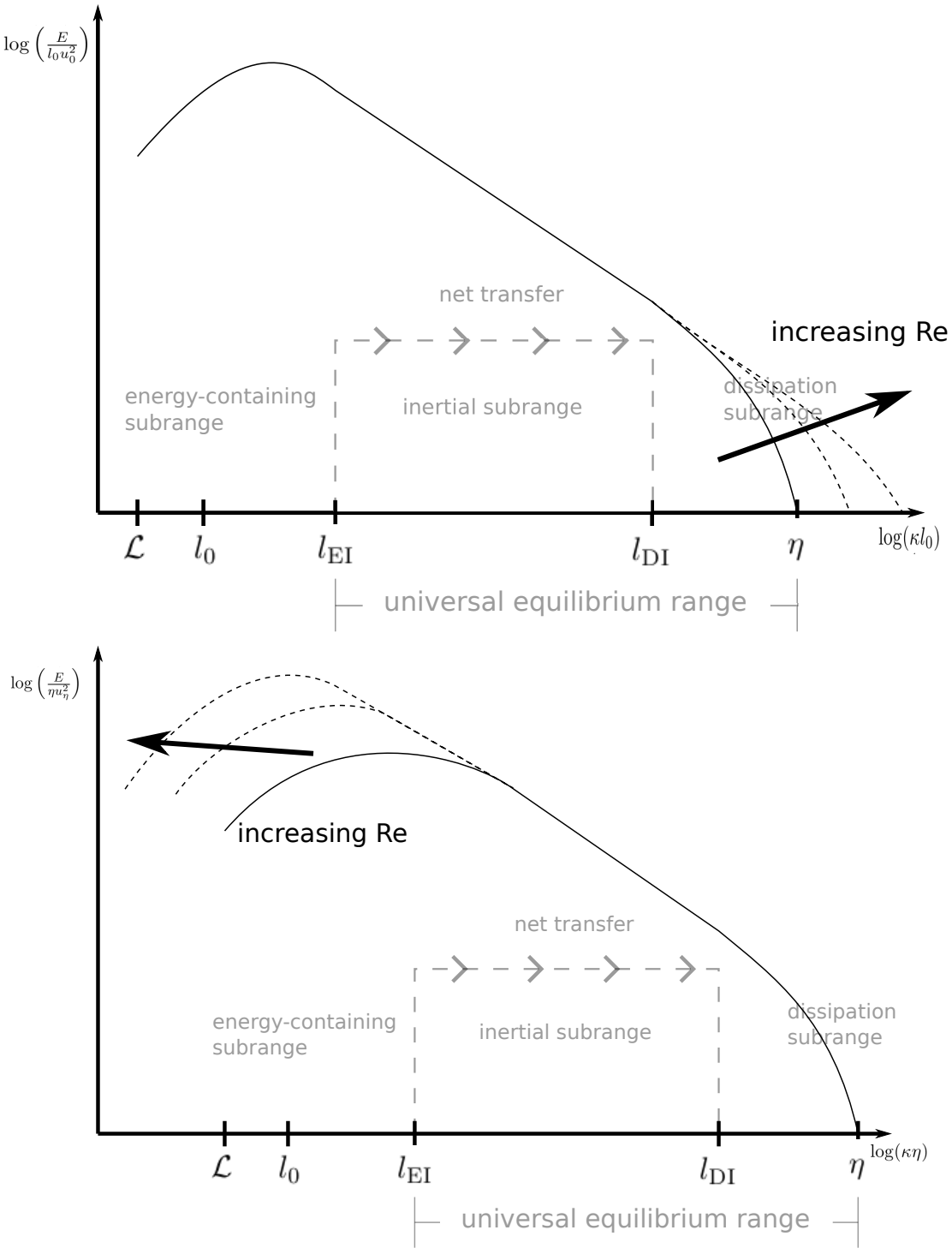

Figure 1.8: top: Energy cascade with outer scaling; bottom: Energy cascade with inner scaling.

T_{kin} governs two mechanisms. It convects flow patterns by space translation and its non-linear nature leads to the fact that it is changing the flow patterns in a manner that energy is transferred between different scales of motion. This transfer is reflected in the

energy cascade described above. The hope is that this term blurs the non-homogeneity and the anisotropy brought in by the production term towards smaller scales. An important nature of this term is that it just redistributes kinetic energy in the system. Redistribution in this case has to be understood in physical (convection) as well as in a spectral (scale transfer) sense. The dissipation term describes the energy dissipation of kinetic energy. It is almost not active at relatively large scales, but becomes stronger the smaller the scales are. Knowledge of this term is important as it tells us how much kinetic energy stays in the system. We limit the research in this work to statically steady flow problems which implies that the mean of quantities derived with respect to time vanish. This and the fact that the transport is neither a source nor a sink of kinetic energy leads to the identity

$$\langle P_{\text{kin}} \rangle = \langle D_{\text{kin}} \rangle, \tag{1.15}$$

where $\langle \cdot \rangle$ denotes a time averaged mean quantity. In other words, the energy brought in by the production is taken out by the dissipation after the transport cascaded it into the range were the dissipation becomes more active. Certainly, the underlying mechanisms of all these processes are universal - they are based on the deterministic Navier-Stokes equations. The issue in finding universality of flows is not finding universality in the mechanisms, it is (loosely speaking) finding universality in the data streamed into the mechanism. By just looking at different flows as, e.g., a subsonic turbulent boundary layer and a supersonic wake (figure 1.9) we observe very different flow fields. That implies that the data streamed into the mechanism cannot be universal in different flows at the largest scales. The idea following Kolmogorov's hypotheses is that flows are losing more and more of these differences in the cascading process governed by T_{kin}. For high enough Reynolds numbers the cascading process might then be long enough, in a spatial scale range sense, to take out most of the differences of the flow patterns so that the smaller scales show only minor differences or even no differences over a variety of flows. This state would the be described as 'quasi-universal' or universal small-scale structure. Figure 1.10 shows a zoom in the flow field of the subsonic turbulent boundary layer and the supersonic wake. It seems that the large scale differences vanish if we zoom into the small scales. Therefore it is useful to split the velocity field into a large scale $\vec{u}^{\mathcal{L}}$ and a small scale part $\vec{u}^{\mathcal{S}}$ (Kerr *et al.*, 1996)

$$\vec{u}(\vec{x}, t) = \vec{u}^{\mathcal{L}}(\vec{x}, t) + \vec{u}^{\mathcal{S}}(\vec{x}, t).$$

The goal in utilizing this is that the velocity field is split up in such a way that the large scale part covers all the complexity that is introduced by initial and boundary conditions down to a scale that can be regarded as 'quasi-independent' from initial and boundary conditions. The complex structure of the turbulence in smaller scales is then covered by the small scale part. If such a splitting is possible and if some universality arguments can be found for the small scales depends on the rate on which the cascading process is taking out homogeneity and anisotropy from the larger scales and how long,

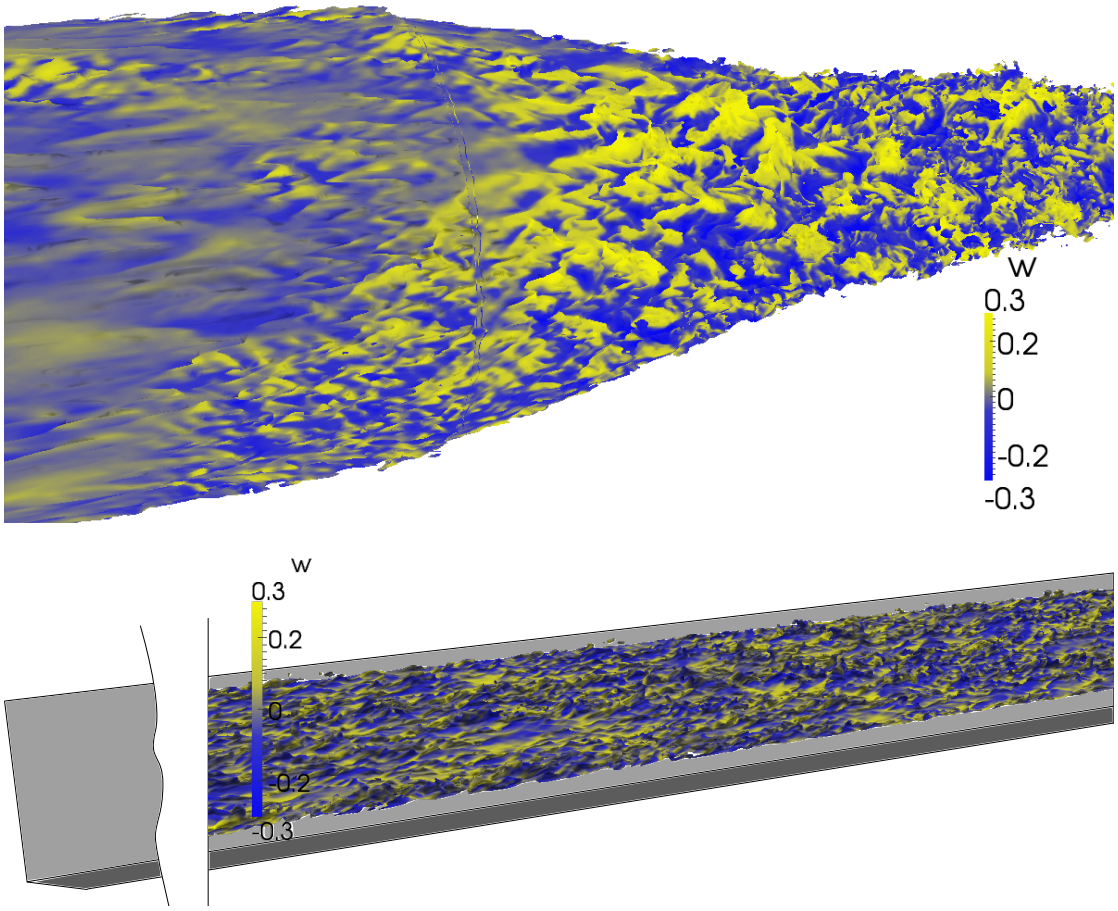

Figure 1.9: This figure shows iso-surfaces of streamwise velocity coloured with the azimuthal or spanwise velocity component w for two different flows respectively. Top: Supersonic ($M = 2.48$) wake behind a circular cylinder with cylinder axis in flow direction (Sandberg, 2012*a*). Bottom: Subsonic ($M = 0.5$) turbulent boundary layer over a flat plate with zero pressure-gradient.

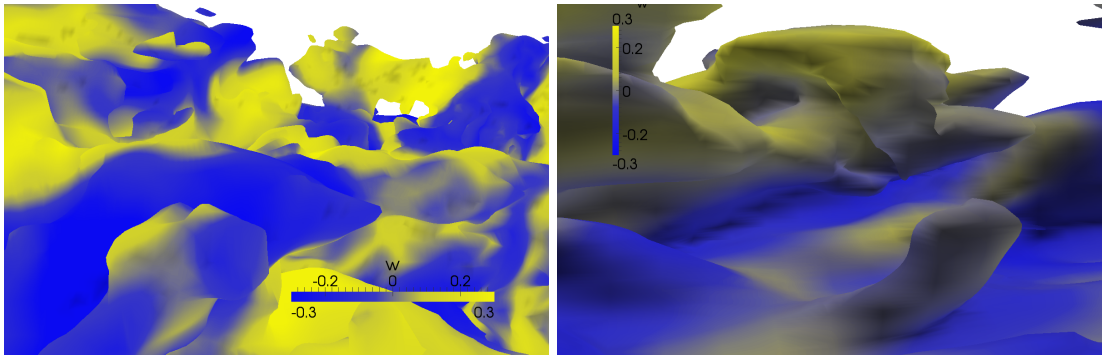

Figure 1.10: Zoom in the two flows of fig. 1.9. Left: Supersonic wake. Right: Subsonic turbulent boundary layer.

in a spatial scale range sense, the cascading process to the small scales is. The latter is defined by the Reynolds number and increases for increasing Reynolds number. In the present work we want to rely on relatively high Reynolds number flows enlarging the cascading process and making a distinction between large scale structures and small

scale structures easier.

As mentioned before and as can be seen in the figures that are presented above, turbulence has a very complex structure. It shows a strong unsteady behaviour in space and time that is often described as random-like behaviour. To find universality in this will be difficult. In turbulence research it is common to approach this task via finding universality in the statistics of this complex, random-like behaviour. For a definition of statistics and an introduction on how this concept is used in fluid dynamics we suggest to study the respective chapters in Pope (2000).

Although the theory Kolmogorov (1941) introduced is only explained for HIT in equilibrium (Pope, 2000) we can already learn a lot about how turbulence is behaving and developing in this type of flow. As most flows are not in equilibrium and are neither isotropic nor homogeneous, Kolmogorov's theory can not be applied directly. What turbulence researchers are trying to find is a theory that covers all kinds of turbulent flows. This theory would be significantly less complex if we find universality in turbulence. Universality in this sense means that we are able to describe a certain behaviour of the flow, that is unchanged over all kinds of turbulent flows. For the velocity field as a whole, this will be impossible.

But assuming Kolmogorov's first similarity hypothesis is true, dimensional analysis (Pope, 2000) leads to the conclusion that the longitudinal structure function is given by the identity

$$H_{LL}(r) = (\varepsilon r)^{\frac{2}{3}} \hat{H}_{LL}\left(\frac{r}{\eta}\right), \tag{1.16}$$

where $\hat{H}_{LL}$ is a universal function depending on $\frac{r}{\eta} = \frac{r\varepsilon^{\frac{1}{2}}}{\nu^{\frac{3}{4}}}$. For r lying in the ISR ($\eta \ll r \ll \mathcal{L}$) Kolmogorov's second similarity hypothesis states the H_{LL} independence of ν so that $\hat{H}_{LL}$ becomes a constant $\hat{H}_{LL} = C_2$, which leads to

$$H(\vec{r}) = C_2(\varepsilon r)^{\frac{2}{3}}\left(\frac{4}{3}I - \frac{1}{3}\frac{\vec{r}\otimes\vec{r}}{r^2}\right) \tag{1.17}$$

Similar approaches using the *Kármán-Howarth equation* (Pope, 2000) lead to Kolmogorov's famous $\frac{4}{5}$-law. It describes the universality of the third order longitudinal structure function $H_{LLL} := \left\langle (u_1(\vec{x}+\vec{e}_1 r) - u_1(\vec{x}))^3 \right\rangle$ in the ISR where $\vec{e}_1$ describes the unit vector in the first direction.

The Kolmogorov $\frac{4}{5}$-law

$$H_{LLL}(r) = -\frac{4}{5}\varepsilon r \tag{1.18}$$

The importance of this law is that the third order moments are unidirectional. These third order moments drive the energy transfer between large scales and small scales (Monin & Yaglom, 1975). If we can state isotropy and universality for the inter-scale transport, then we would have a strong basis for a turbulence theory and turbulence models. In fact most of the common sub-grid scale models used in large eddy simulations are based on the isotropy and universality of the third order moments. Several research groups have investigated which other information can be obtained from this law (e.g.

Kailasnath *et al.* (1992),Novikov (1971),Chorin (1994) and Vainshtein & Sreenivasan (1994)).
Similar universal laws can be derived for moments of all orders by assuming local isotropy and that Kolmogorov's hypotheses hold (Sreenivasan & Antonia, 1997). So for the nth-order moment of the longitudinal velocity increment it can be seen that

$$\langle (u_1(\vec{x} + \vec{e}_1 r) - u_1(\vec{x}))^n \rangle = C_n \, (\varepsilon r)^{\frac{n}{3}} \, , \tag{1.19}$$

where C_n are universal constants.
In general turbulent flows, global isotropy and global homogeneity are not given. However, since the structure functions only involve velocity difference instead of velocity itself it is often thought that the findings for HIT can be transferred to non HIT flows assuming local homogeneity and local isotropy holds (Sreenivasan & Antonia, 1997). But on the other hand, Zubair (1993) states that even for high Reynolds numbers the large scale contribution to the third order moments may be non-trivial.
To investigate this further it is useful to investigate the spectral footprint of turbulence. The velocity spectrum tensor (eq. 1.3) and the energy spectrum function (eq. 1.4) are the right tools to do that. Based on Kolmogorov's theory, Pope (2000) introduced a model for the energy spectrum function (figure 1.11)

$$E(\kappa) = C\varepsilon^{\frac{2}{3}}\kappa^{-\frac{5}{3}} f_{l_0}(\kappa l_0) f_\eta(\kappa\eta), \tag{1.20}$$

where f_{l_0} and f_η are 'universal functions' (Pope, 2000) to be defined. f_{l_0} describes the behaviour of the model spectrum in the energy containing region and will not be universal in general. It will tend to unity for larger wave numbers, so that in the inertial subrange it will allow the $-\frac{5}{3}$-law to be active. The second universal function f_η describes the behaviour of the spectrum in the dissipation range. Opposite to f_{l_0} it tends to unity for approaching the ISR from higher wave numbers. For general flows the energy containing

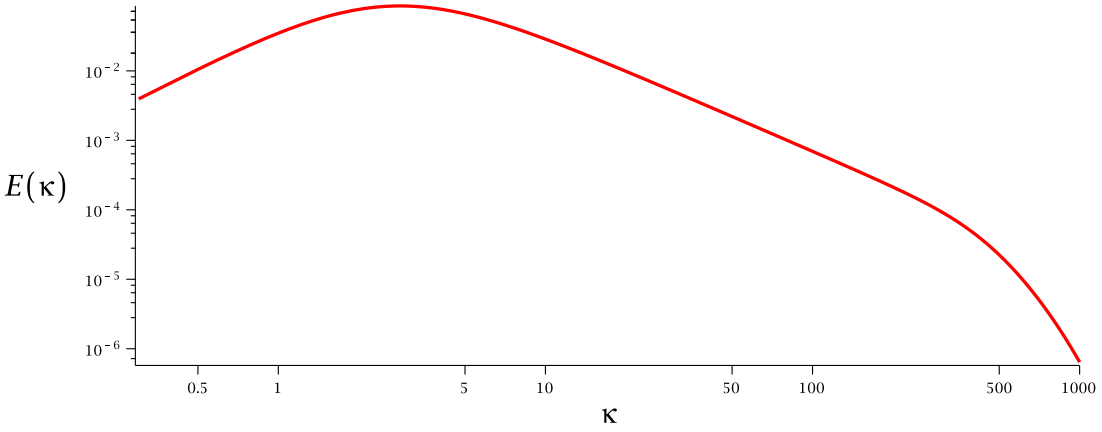

Figure 1.11: A model spectrum 1.20 with universal functions suggested by Pope (2000) p.233 at $Re = 10000$.

part will not be universal as in Kolmogorov's example of HIT. But in the present work

we will focus on small scales which are distributed in the spectrum starting in the ISR up to the end of the dissipation range. Therefore the function f_{l_0} describing the change of the spectrum in the energy containing range will not be taken into account. The spectrum of the small scale motion with high enough wave numbers $\kappa \gg \frac{1}{l_0}$ then will be

$$E(\kappa) = C\varepsilon^{\frac{2}{3}}\kappa^{-\frac{5}{3}} f_\eta(\kappa\eta). \tag{1.21}$$

Much research has been done in investigating the behaviour of $f_\eta(K)$ ($K := \kappa\eta$). What seems to be consistent across previous studies is that the function approaches C for small K, the behaviour for large κ is still discussed and the universality can not be taken for granted. A summary of non-exponential approaches are summarized by Monin & Yaglom (1975), but have now been superseded by exponential estimates. Foias *et al.* (1990) proposed via empirical and theoretical investigations of the Stokes eigenfunctions that the universal function has the form $f_\eta(K) = e^{-gK}$ with $g \geq 1$ under certain smoothness assumptions. Another approach states that $f_\eta(K) = K^\alpha e^{-gK}$, where the HIT turbulence simulations of Kerr (1990) and Sanada (1992) lead to approximations of $g \approx 5.2$ and $\alpha \approx 3.3$. On the other hand, Chen *et al.* (1993) suggested $g \approx 7.1$ based on their observations for low Reynolds number ($Re_\lambda \approx 15$) HIT. Sirovich *et al.* (1994) even observed Reynolds number dependence of g in their simulations of HIT. A comparison of dissipation ranges of many flows of various different types was done by Saddoughi & Veeravalli (1994). They showed a good (although not fully satisfactory (Sreenivasan & Antonia, 1997)) collapse of the dissipation spectra of all flows. A more detailed discussion on this topic can be found in Sreenivasan & Antonia (1997), who summarized this overview as: *"On the whole, it is not possible to assert that K41* (authors comment: K41 = Kolmogorov (1941)) *works exactly, even for second order statistics,..."*. A reason for the failure is given by Oboukhov (1962) who mentioned that the strong variability of the energy dissipation rate causes strong *"change of the large scale processes"*. Further he suggested replacing the time averaged dissipation by a locally averaged dissipation.
Two important points of this part of the literature review will be addressed in this work. One is that, following Kolmogorov's $\frac{4}{5}$th-law, third order moments are universal in the small scales of high Reynolds number flows. This will be discussed in the context of spatially filtered Navier-Stokes equations. Filtering the Navier-Stokes equations allows to separate different scales and decrypt the energy transfer between large scales and small scales. Universality arguments for this transfer will be discussed. The second important point is the universality of the dissipation range. It is rarely discussed for non-equilibrium flows. This will be addressed in this work by comparing dissipation range spectra of different flows.

1.2.2 Lagrangian Dynamics

The last section introduces on the mean distribution of energy across the scales of motion as well as the transfer rates within the cascading process and the dissipation range. But what remains unknown is how this transfer physically happens. In this regard it is useful to know about the character of turbulent structures, their evolution, and how they are distributed in a turbulent flow. Lagrangian dynamics offer a possibility to investigate that. Lagrangian dynamics in contrast to Eulerian dynamics describe a flow in a reference system that is fixed to a fluid particle instead of an inertial system which is fixed to the flow domain. This allows a different perspective on the flow and exposes other ways of describing turbulence. Regarding turbulence as an ensemble of structures of different size there is need to describe the character of these structures as well as their dynamics. From the previous section we know about the presence of a cascading process that drives the kinetic energy to smaller and smaller scales until it reaches a scale where it dissipates to internal energy. What is missing from our understanding is how this process works in physical space and how structures affect each other. To describe this interaction Lagrangian dynamics appear to be a suitable tool.
The velocity gradient tensor contains a huge amount of information about a flow and its dynamics. In their review about 'critical-point' concepts, Perry & Chong (1987) summarized how local flow patterns can be characterized by just regarding the velocity gradient tensor at the location of interest. The idea behind this approach is applying a Taylor series expansion to describe the velocity field in a local area around an arbitrary location $\vec{x}_0$ ('critical point') in the domain via the velocity gradient tensor $A := \nabla\vec{u}$. The second order Taylor series expansion around this critical point has the form

$$\vec{u}(\vec{x},t) = \vec{u}(\vec{x_0},t) + A(\vec{x_0},t)\cdot(\vec{x}-\vec{x_0}) + \left(\frac{\nabla A(\vec{\xi})}{2}\cdot(\vec{x}-\vec{x_0})\right)\cdot(\vec{x}-\vec{x_0})\,, \tag{1.22}$$

where the last term is the truncation error with $\vec{\xi}$ being a point in the neighbourhood of $\vec{x}_0$, $B_\varepsilon(\vec{x}_0) = \{\vec{x}\in \mathrm{R}^3 |\, \|\vec{x}_0-\vec{x}\| < \varepsilon\}$. Assuming that the truncation error is negligible we obtain the system

$$\vec{u}(\vec{x},t) - \vec{u}(\vec{x_0},t) = \dot{\vec{x}} - \dot{\vec{x_0}} + A(\vec{x_0},t)\cdot(\vec{x}-\vec{x_0})\,. \tag{1.23}$$

By assuming A is constant for small time increments we obtain a system of linear ordinary differential equations (ODEs) of the form

$$\dot{\vec{y}} = A\cdot\vec{y}. \tag{1.24}$$

Systems of first order linear ODEs can be characterized by the eigenvalues and eigenvectors of the matrix A. The eigenvalues describe the character of the solution of 1.24 and therefore the flow topology at the critical point. The eigenvectors add the directivity.

The characteristic polynomial $p_{\text{char}}(\alpha)$ of A is defined as

$$p_{\text{char}}(\alpha) := \det(A - \alpha I) = \alpha^3 + P\alpha^2 + Q\alpha + R. \tag{1.25}$$

Eigenvalues of A are obtained as the solutions for $p_{\text{char}}(\alpha) = 0$. P denotes the first invariant of the velocity gradient tensor and is defined as the additive inverse divergence of the velocity field

$$P := -\nabla \cdot \vec{u}. \tag{1.26}$$

For simplicity reasons we will consider an incompressible flow in this introduction and therefore the divergence is zero. Q is the second invariant and is half the sum of all sub determinants of A and can be written as

$$Q := -\frac{1}{2}\left\langle A, A^T\right\rangle_F. \tag{1.27}$$

$\langle\cdot,\cdot\rangle_F$ denotes the Hilbert-Schmidt inner product defined in 2.2. The third invariant R is defined via the determinant of A which is the volume of the parallelepiped spanned by the columns of A

$$R := -\frac{1}{3}\left\langle AA, A^T\right\rangle_F = -\det A. \tag{1.28}$$

More invariants of the velocity gradient can be found in Meneveau (2011).
The discriminant of 1.25

$$\Delta = \frac{27}{4}R^2 + Q^3 \tag{1.29}$$

is a significant quantity as its sign divides the eigenvalue into being purely real or being combinations of real and complex values. The subset of all (Q, R) with $\Delta = 0$ is the same subset of all (Q, R) that fulfil

$$R = \pm\frac{2\sqrt{3}}{9}(-Q)^{\frac{3}{2}}.$$

The velocity gradient tensor has either purely real eigenvalues ($\Delta \leq 0$) or one real and two complex eigenvalues which form a complex conjugate pair ($\Delta > 0$). The local pattern describing the flow can then be characterized with the eigenvalues and eigenvectors. Figure 1.12 sketches the different flow topologies that can be determined from the values of Q and R. If (Q, R) falls into the lower right sector (S III), then Δ is negative and we find purely real eigenvalues and therefore the corresponding flow structure is a pure straining structure. When R is positive two eigenvalues are positive and one is negative, which leads to an unstable node/saddle/saddle topology. In other words the structure has an expanding character in two spatial directions while having a contracting character in the third direction. The lower left sector (S IV) covers, like S III, a pure strain regime as Δ is negative and the eigenvalues are purely real. But as R has opposite sign compared to S III, the corresponding structure is contracting in two directions while expanding in the third one. Therefore it is described as stable node/saddle/saddle topology. If (Q, R) falls into the upper left sector (S I) the discriminant is positive and therefore the

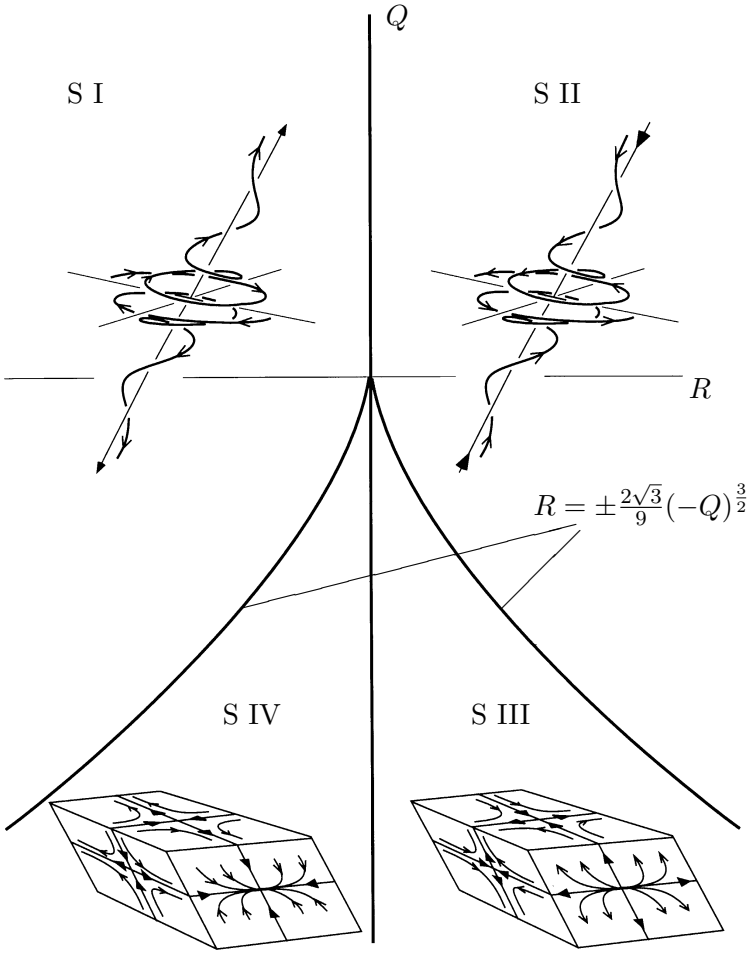

Figure 1.12: Incompressible (Q, R) phase-space, together with sketches of the local flow topology prevalent in each sector. Figure adapted from Ooi *et al.* (1999).

corresponding eigenvalues are not purely real any more. One eigenvalue remains real while the other two form a complex conjugate pair. This indicates a rotational flow with the eigenvector corresponding to the real eigenvalue being the rotation axis. The structure is described as stable focus/stretching. The real eigenvalue is positive while the real part of the complex conjugate pair is negative. This leads to a stretching character along the rotation axis of the structure while the structure is contracting towards the axis. Finally, the upper right sector (S II) contains rotational structures as well, but unlike S I these structures are contracting along their rotation axis while expanding away from the axis. This leads to an unstable focus/stretching structure. The interpretation of these structures has to be conducted with care. The analysis description of the character of a structure is purely local, therefore it does not necessarily describe the actual shape of the structure in the flow field. In other words, the characteristic analysis describes the tendency of the development of a structure at a given point in space and time. To obtain the actual shape of flow structures a non-local approach is needed. This could be carried out via Minkowski functionals as a tool to classify shapes of structures (Leung *et al.*, 2012). At this stage, however, we have enough information about the character

of the development of a given structure for the purpose of the current study, and will also pursue more involved analysis techniques.
The dynamics of Q and R in the incompressible case can be stated as (Cantwell, 1992):

$$\begin{aligned} \frac{dQ}{dt} &= -3R - \langle A, H^t \rangle_F \\ \frac{dR}{dt} &= \frac{2}{3}Q^2 - \langle AA, H^t \rangle_F, \end{aligned} \tag{1.30}$$

where H contains the anisotropic part of the pressure Hessian as well as the viscous diffusion

$$H := -\frac{1}{\rho}\left(\nabla(\nabla p) - \frac{1}{3}\text{trace}\left(\nabla(\nabla p)\right) I\right) + \nu\Delta A.$$

This system of equations fully describes the evolution of Q and R and therefore the change of flow topologies characterized by the critical point analysis in incompressible flows. To give a first impression of what this evolution can look like, the restricted Euler equations can be investigated. We can obtain the restricted Euler system by neglecting non-local diffusion terms and non-local pressure terms in the evolution equations. For further detail, read Meneveau (2011). In this restricted system Vieillefosse (1982, 1984), the dynamical system for Q and R simplifies to

$$\begin{aligned} \frac{dQ}{dt} &= -3R \\ \frac{dR}{dt} &= \frac{2}{3}Q^2. \end{aligned} \tag{1.31}$$

The discriminant $\Delta(t) = \frac{27}{4}R(t)^2 + Q(t)^3$ is a time invariant (Meneveau, 2011) and

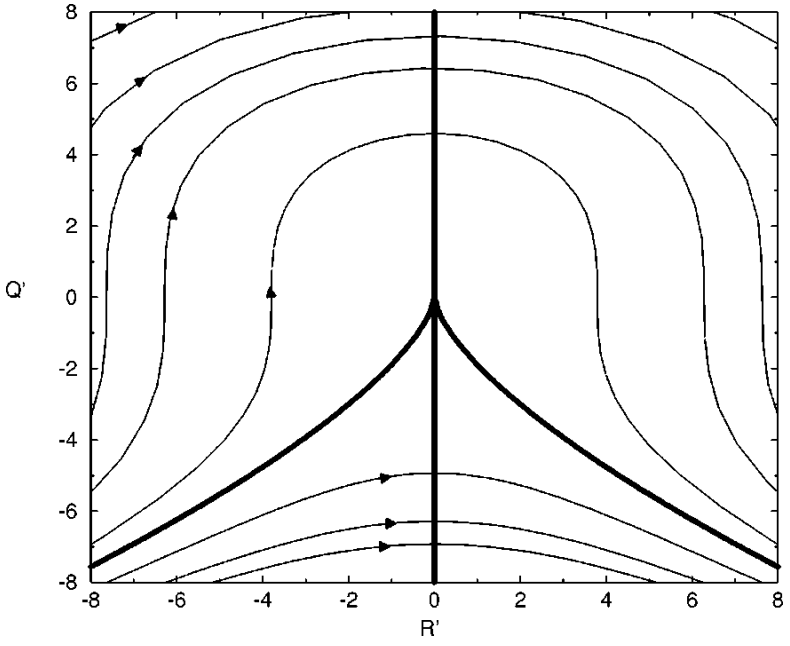

Figure 1.13: Incompressible (Q, R) phase-space, showing trajectories for the restricted Euler system 1.31 (Martin *et al.*, 1998).

the phase-space flow is shown in figure 1.13. We can observe how a certain (Q, R)-state is developing in time when only the non-linear terms of the Navier-Stokes equations are active. It should be mentioned that for time marching towards infinity the third invariant is unbounded

$$R(t) \xrightarrow{t\to\infty} \infty.$$

The second invariant shows asymptotic behaviour

$$Q(t) \xrightarrow{t\to\infty} -\frac{3}{2^{\frac{2}{3}}} R^{\frac{2}{3}}.$$

The diffusion, which is set to zero in this restricted Euler system, will certainly work against R approaching infinity as diffusion grows with growing velocity Hessian magnitude. Martin *et al.* (1998) carried out DNS of homogeneous isotropic turbulence at $Re_\lambda = 71$ and showed separately the effect of the first order terms (restricted Euler system) and the effect of the pressure Hessian and diffusion on the dynamics of Q and R (1.14). At first glance the plots seem to be a mirror-image of the respective other

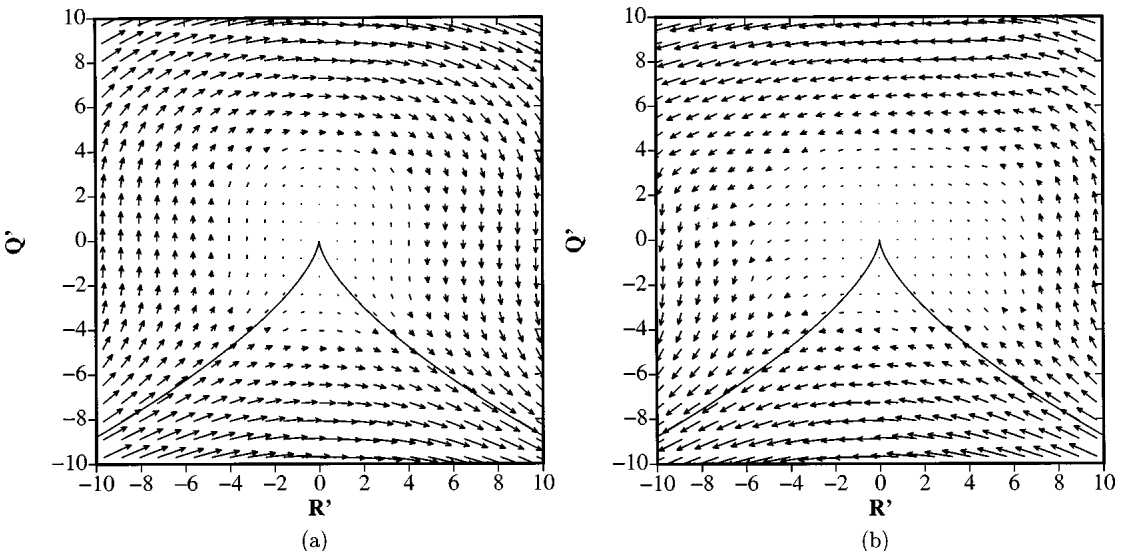

Figure 1.14: The effect of the different forcing mechanisms on $\overline{\frac{dQ}{dt}}$ and $\overline{\frac{dR}{dt}}$ as vector plots. (a) shows the vector field resulting from the restricted Euler system and (b) illustrates the mean evolution of R and Q due to terms involving H.(Martin *et al.*, 1998)

one. While the source terms in the restricted Euler flow (1.31) let structures tend to develop from patterns with one unstable and two stable directions to patterns with two unstable and one stable directions, the pressure Hessian and diffusion have the reverse effect. But the effects do not exactly cancel each other out. This would lead to a steady state of flow structures, which is not what we observe in turbulent flows. Indeed there is a significant difference between both plots. This becomes more obvious if the total mean evolution of Q and R is plotted (1.15). In this plot of Martin *et al.* (1998)'s DNS data the mean evolution of a flow structure is clearly presented. The plot states that flow

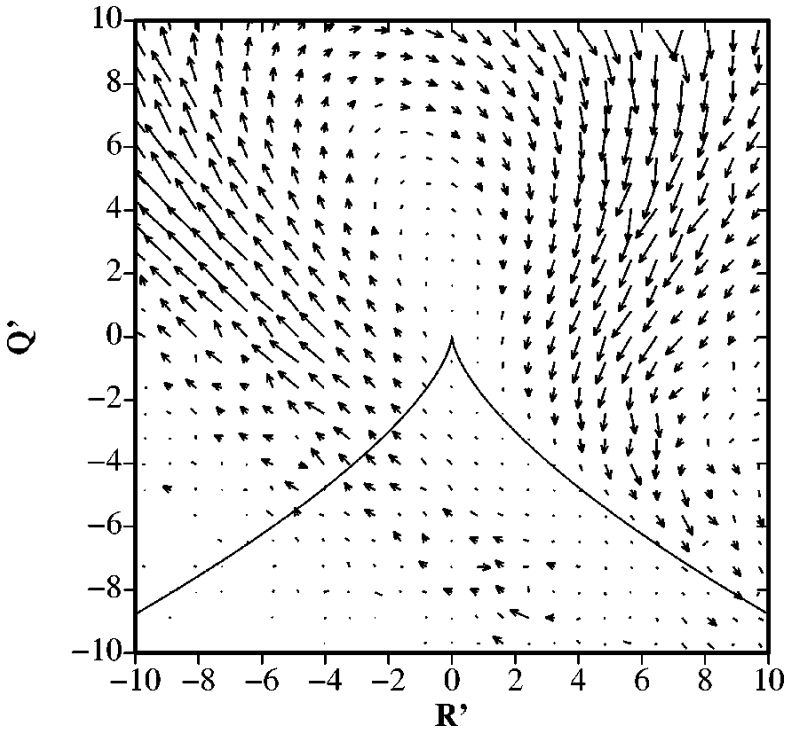

Figure 1.15: $\overline{\frac{dQ}{dt}}$ and $\overline{\frac{dR}{dt}}$ as vector plots multiplied by a factor 5. (a) shows the vector field resulting from the restricted Euler system and (b) illustrates the mean evolution of R and Q due to terms involving H.(Martin *et al.*, 1998)

structures start off as unstable node/saddle/saddle structures which are pure staining structures. Then they develop from one to two contracting directions and from two to one expanding direction at the same time. While these processes seem to be slow the development of the structures, in a (Q, R)-sense, accelerates as they develop to rotational structures. First they become stretching foci and as such the structures increase the magnitude of the velocity gradient tensor. At some point the structures seem to become unstable enough to flip over to a positive value of R and become contracting foci. In this state they first decrease the magnitude of the velocity gradient until the final increase sets in and the structures dissipate.

It is well established that vortex stretching is a major mechanism of the cascading process towards smaller scales. In the (Q, R) phase space this mechanism is located in sector I. Vortex stretching has received great attention in turbulence research. In the stretching process the radius of a vortex is decreasing and as angular momentum has to be conserved, vorticity magnitude has to increase. In this context enstrophy, which is the vorticity magnitude squared, $\|\vec{\omega}\|^2$, is a suitable quantity to investigate the cascading process. Especially the production of enstrophy, $\vec{\omega}^t S\vec{\omega}$ (S denotes the strain rate tensor), has a significant role in the process of vortex stretching. It can be rewritten as $\|\vec{\omega}\|^2 \sum_{i=1}^{3} \lambda_i \left(\hat{\vec{e}}_i \cdot \hat{\vec{\omega}}\right)^2$ where $\lambda_1 \geq \lambda_2 \geq \lambda_3$ are the eigenvalues and $\hat{\vec{e}}_i$ the corresponding normalized eigenvectors of the strain rate tensor. Further, $\hat{\vec{\omega}}$ is the normalized vorticity

vector with $\|\hat{\vec{\omega}}\| = 1$. In this form of the enstrophy production it can be seen that the alignment between principal strain axes (i.e. the normalized eigenvectors) and vorticity are essential for the composition of the production itself. As the strain rate tensor is symmetric its eigenvalues are purely real and incompressibility leads to λ_1 being positive and λ_3 being negative. λ_2 can vary in sign. The average ratio of magnitudes in homogeneous isotropic turbulence was found to be $(\lambda_1 : \lambda_2 : \lambda_3) = (3 : 1 : -4)$ (Ashurst *et al.*, 1987) and was more recently confirmed by other researchers for flows close to equilibrium (e.g. Ganapathisubramani *et al.*, 2008).
Considering vortex stretching to be the dominant process in turbulent flows one would intuitively think that vorticity is most likely to be aligned with the strongest extensive strain direction $\vec{e}_1$ so that the strongest strain is acting in the direction of the vortex axis. But Ashurst *et al.* (1987) found vorticity most likely to be aligned with the intermediate strain direction $\vec{e}_2$ (figure 1.16). This finding was confirmed by other researchers conducting experimental (e.g. Ganapathisubramani *et al.*, 2008) as well as numerical (e.g. Hamlington *et al.*, 2008; Leung *et al.*, 2012) studies and is part of Meneveau (2011)'s review on the topic of Lagrangian dynamics. At first glance this is a surprising finding,

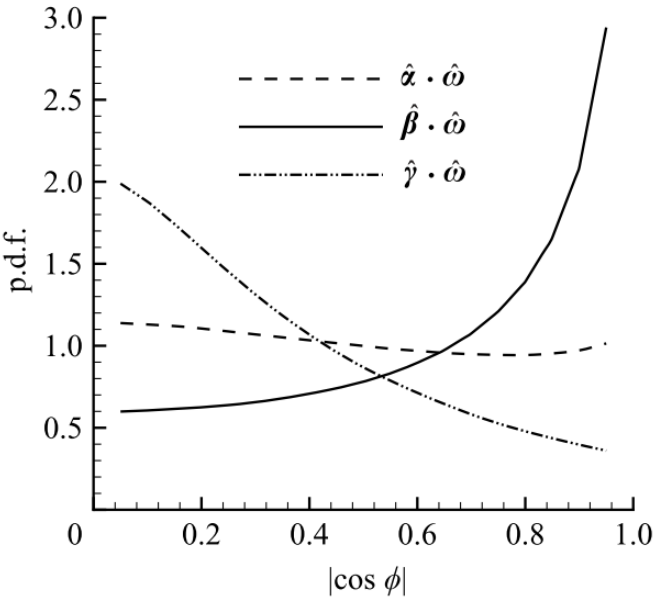

Figure 1.16: Probability density functions of the orientation of vorticity vector with eigenvectors of the strain-rate tensor ($\vec{e}_1 = \hat{\alpha}; \vec{e}_2 = \hat{\beta}; \vec{e}_3 = \hat{\gamma}$) (Ganapathisubramani *et al.*, 2008).

but in their vortex model Ashurst *et al.* (1987) already presented the idea that this finding simply shows the alignment of a vortex with its own strain field. This strain field is created by the shear stress the vortex is producing due to viscous effects in the plane normal to its rotation axis. Hamlington *et al.* (2008) then decomposed the strain rate tensor in the surrounding area of a vortex into a part that contains the self-produced strain and a part that contains the background strain. Although it was not possible to decompose the strain exactly, their results show that the likeliness of vorticity to align

with the intermediate strain direction is decreasing the more of the self-produced strain is removed. In Leung *et al.* (2012)'s work on geometry and interaction of turbulent structures they bandpass filtered DNS data of decaying homogeneous isotropic turbulence at a Taylor Reynolds number $Re_\lambda = 141$. Figure 1.17 indicates that the vorticity

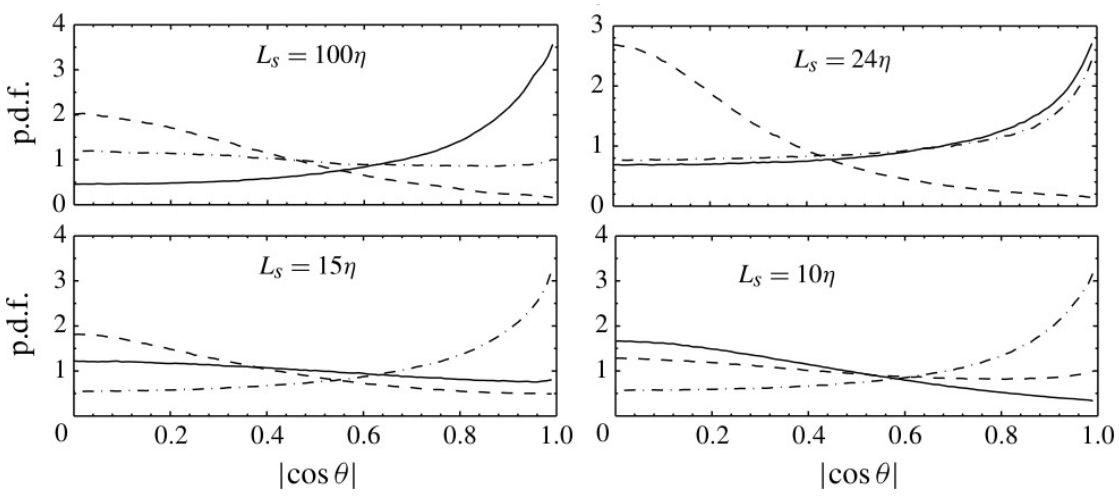

Figure 1.17: Probability density functions of the orientation of vorticity vector bandpass filtered at 15η with eigenvectors of the strain-rate tensor filtered at $100\eta, 24\eta, 15\eta$ and 10η respectively. The continuous lines show $pdf(\hat{\vec{e}}_1 \cdot \hat{\vec{\omega}})$, the chain lines show $pdf(\hat{\vec{e}}_2 \cdot \hat{\vec{\omega}})$ and the dashed lines show $pdf(\hat{\vec{e}}_3 \cdot \hat{\vec{\omega}})$. (Leung *et al.*, 2012).

is aligned with the intermediate strain direction of its own strain field but is aligned with the extensive strain direction of structures that are larger than itself. They showed this for vorticity filtered at 15η as well as 10η and the results show the same trend. Further their work shows that if the ratio of filter length for the strain field and filter length for the vorticity become too large then the vorticity looses any tendency to align with a specific strain direction. This 'random' alignment of structures with large differences in size can be seen as loss of directivity during the cascading process. This could underline Kolmogorov's hypothesis of local isotropy which states that for sufficiently large Reynolds numbers the small scales are locally isotropic. Further this picture fits well into the 'cascading via vortex stretching idea'. Larger structures feed smaller structure via the strain field they are producing. The smaller structures are aligning with the larger structures in a way that they get stretched in the larger structures' strain field. But this only happens in a fixed band of scale ratios of the two structures. This fact underlines the Reynolds number invariant decaying exponent of kinetic energy with respect to wavenumber (i.e. Kolmogorov's $-\frac{5}{3}$-law). Besides the stretching of vortices by larger structures the tendency of a vortex to contract due to its own strain field is underlined with these results as well. These opposite effects can at some point lead to an unstable state where we might find the change from stretching to contracting structures.
Another approach to explain the, in the context of vortex stretching 'unexpected', preferred parallel alignment of vorticity and intermediate strain direction was shown by

Buxton & Ganapathisubramani (2010). In their experimental work on the far field of an axisymmetric turbulent jet they stated a global alignment of the vorticity vector with the principal strain axis that is consistent with literature. Further, they put the significant imbalance of mean enstrophy production over the different (Q, R)-sectors in focus. They showed that the lion's share of the enstrophy is produced in S II (see table

(Q, R)-sector (S)	$\frac{\langle \vec{\omega}^t S \vec{\omega} \rangle \vert \mathbf{s}}{\langle \vec{\omega}^t S \vec{\omega} \rangle}$	Proportion of total volume
S I	2.44	37%
S II	−0.40	29%
S III	0.69	24%
S IV	0.54	10%

Table 1.1: Ratios of the mean enstrophy production conditioned to appear in the different (Q, R)-sectors and the global mean production (second column). Ratios of the probability of a structure to be in the respective sector (third column). Data taken from Buxton & Ganapathisubramani (2010).

1.1), which underlines that the main part of the scale transfer via vortex stretching is located in this sector. Based on this fact they conditioned the probability density functions of the alignment to be located in the respective (Q, R)-sectors (figure 1.18). Their results show that while the alignment of vorticity and intermediate strain direc-

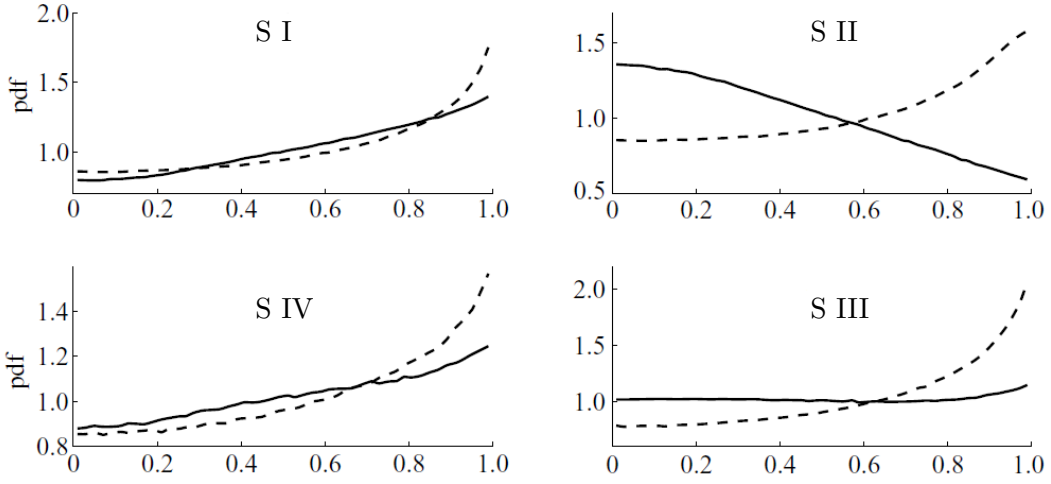

Figure 1.18: Probability density functions of the alignment between vorticity vector with extensive strain direction (solid lines) and intermediate strain direction (dashed lines) conditioned to be located in the different (Q, R)-sectors respectively (Buxton & Ganapathisubramani, 2010).

tion is widely unaffected, the probability density function of the alignment of vorticity with the extensive strain direction is dependent on the condition. This finding reveals that the globally arbitrary alignment of vorticity with the extensive strain direction is a superposition of non-arbitrary alignments for structures of different character. While

for S III the alignment remains arbitrary, in S II the two vectors prefer to align perpendicularly. But in S IV and especially S I, where vortex stretching is supposed to be the most active mechanism, vorticity is likely to be aligned with the extensive strain direction. As mentioned before, this type of alignment is favouring the idea of vortex stretching. This work was extended on experimental data of a planar mixing layer (Buxton *et al.*, 2011), where the data was additionally filtered to expose the behaviour of different spatial scales. The data was filtered at four different scales ($2.5\eta, 5\eta, 7.5\eta$ and 25η) and is shown in figure 1.19. While for unstable foci (S II) the different scales show

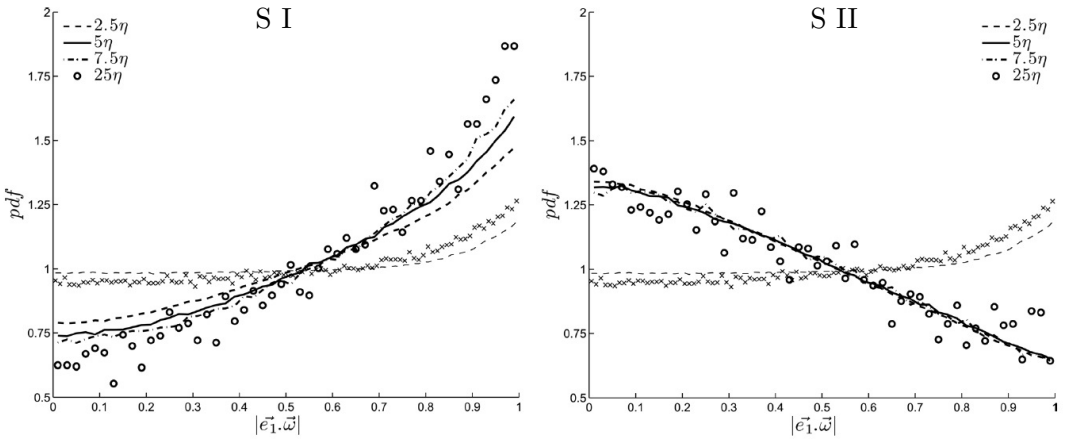

Figure 1.19: Probability density functions (PDFs) of the alignment between filtered vorticity vector with filtered extensive strain direction conditioned to be located in S I (left) and S II (right). The dashed line and the crosses are global PDFs across all four sectors, for the filtered data at 2.5η and 7.5η, respectively. (Buxton *et al.*, 2011).

similar behaviour, the alignment in the regime of stable foci (S I) shows a dependency on the size of the structures. The fact that the tendency of parallel alignment is given for all filtered scales and is magnified for larger scales, Buxton *et al.* (2011) interpret in the way that enstrophy amplification is a process that takes place over a wide range of scales. But it is more pronounced in the inertial sub-range than in the dissipation range and therefore predominantly driven by larger scale structures. This coincides with the previously presented filtered results from Leung *et al.* (2012).

Now that we have an overview of the evolution of flow structures the rates at which these structures appear in a turbulent flow still needs to be shown. A well known plot stating this is the 'teardrop' which the joint probability density function of Q and R shows (figure 1.20). The proportions of the different sectors are stated in table 1.1. The sector with the highest probability of Q, R having values fitting to it is S I and if this sector represents stretching vortical structures, then indeed this is the dominant mechanism in turbulence. The sector with the second highest probability is S II where we find contracting vortical structures. The remaining 34% of the probability is distributed over sectors S IV and S III which represent pure straining, with a larger proportion in S III. SII and S III show a tail of the joint PDF towards large values of R around $\Delta = 0$.

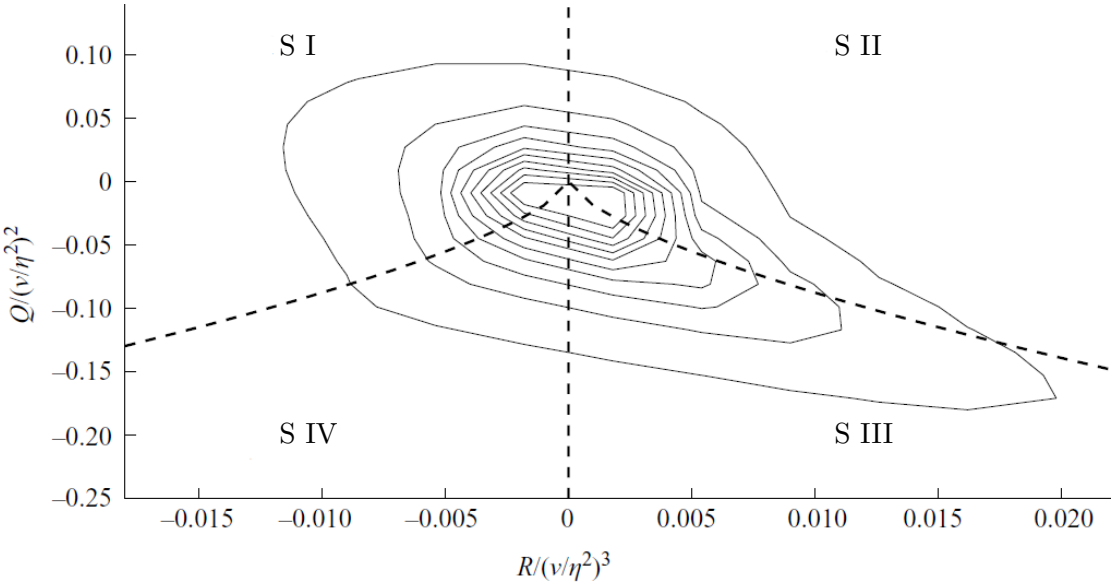

Figure 1.20: Joint probability density functions (PDFs) between Q and R normalized by the second and third powers of $\frac{\nu}{\eta^2}$, respectively. The outer contour is at level 70 and the inner contour is at level 700. The spacing between adjacent contour levels is 70. The dashed lines mark $R = 0$ and $\Delta = 0$ (Buxton & Ganapathisubramani, 2010).

The largest magnitudes of R in this distribution are found in this tail. This can be an indication that the main dissipation is taking place for structures that are characteristic for the region where this tail is located.
This literature review provides an overview of turbulence that is sufficient for the start of this work. Further and more detailed literature reviews will be provided where needed.

1.3 Outline of the Report

In the following chapter 2 the Navier-Stokes equations that are used to model and as well to analyse the flows are outlined. Some key facts are discussed and complexity issues are highlighted. For the further analysis the Navier-Stokes equations are split into large-scales and small-scale parts (sec. 2.2) and some dynamics of turbulence are outline and others are newly derived (sec. 2.3). After this basis is provided the numerical methods to approximate and analyse the flows are described in chapter 3. This chapter includes a full description, and validation where needed, of the later analysed flows (sec. 3.3). In chapter 4 results about universal features of the velocity gradient and related quantities are discussed. Results of several location in three different flows are analysed and compared. Part of this study is then extended to great detail on the data of a turbulent boundary layer flow in chapter 5. This includes a decomposition of the enstrophy production and a discussion about the development of the respective pieces in the turbulent boundary layer. A full and comprehensive discussion of energy

redistribution mechanisms in a turbulent boundary layer is presented in chapter 6. Besides the presentation and analysis of the global mechanisms many important features of turbulence in wall-bounded flows are discovered, analysed and described. Finally all the previous is summarized in chapter 7. At this stage recommendation for future work, that is directly related to this work, is provided.

Chapter 2

Governing Equations for Compressible Fluids

2.1 Compressible Navier-Stokes Equations

Fluid flow problems are omnipresent in our life. We encounter fluid flows in nature, e.g. blood flow, airflow in our lungs or driving the global weather, as well as in technical applications like oil pipelines, ships or aircrafts. To understand and describe them and to be able to make improvements, we need to model the underlying physics and express them in an abstract way. Mathematics then will help to classify, analyse and solve the problems for the different applications. A few different ways of modelling fluid flow problems exist, e.g. the Euler equations, Boltzmann's equations of motion, Jindřich Nečas'[1] higher order viscosity model, etc. Commonly, solutions for these abstract models are approximated numerically. Depending on the temporal and spatial scales present in the flow, and the character of the problem, some models are more and some of them are less suitable to solve the given physical problems. We can even find models that are only suitable for analytical investigation as the effort to solve the resulting system of equations is immense and not reasonable with today's knowledge, techniques and computational resources (e.g. Boltzmann equations). If we accept Moore's Law about the sustained increase of computational power, there is an upper bound (although high) of the available computational resources. Hence, a promising way is to extend our understanding of flow systems and use it to improve the techniques we use to treat and solve them.

In the present work, we will concentrate on the Navier-Stokes (NS) equations to describe a fluid flow problem. They are the result of the most common model of macro scale fluid flows and can be derived with additional assumptions from more complex models. We

[1] Czech mathematician (1929 - 2002)

will consider a single phase, compressible fluid being a continuum, fulfilling the Newtonian conditions and the properties of a perfect caloric gas. Applying the conservation of mass, Newton's conservation of momentum and the conservation of energy, we end up with a system of five coupled non-linear, partial differential equations (PDEs) for density ρ (2.1), the velocity vector $\vec{u}$ (2.2) and the total energy $E := e + \frac{1}{2}\vec{u}^2$ (2.3). The algebraic equation of state (2.4) governing the relation between pressure p, temperature T, internal energy e, and ρ completes the system. To simplify the notation we define the so-called outer product on vector spaces.

Definition 2.1. Outer product
Let $V \subseteq \mathbb{R}^n$ be a n-dimensional vector space over $\mathbb{R}$ and $\vec{x}, \vec{y} \in V$ elements of this vector space. Further let $\mathrm{Mat}_n(\mathbb{R})$ be the set of all $n \times n$ square matrices over $\mathbb{R}$. Then the operation

$$\otimes(\cdot,\cdot) : V \times V \to \mathrm{Mat}_n(\mathbb{R}); \quad \otimes(\vec{x},\vec{y}) \mapsto (x_i y_j)_{i,j=1}^{3}$$

is called *outer product* or *dyadic product*. For simplification the notation

$$\vec{x} \otimes \vec{y} := \otimes(\vec{x},\vec{y})$$

will be used.

The flow describing equations in conservative form can be stated as follows.

Continuity-Equation

$$\frac{\partial \rho}{\partial t} + \nabla \cdot (\rho \vec{u}) = 0 \tag{2.1}$$

Momentum-Equation

$$\frac{\partial \rho \vec{u}}{\partial t} + \nabla \cdot (\rho \vec{u} \otimes \vec{u}) = -\nabla p + \nabla \cdot \tau + \rho \vec{f} \tag{2.2}$$

Energy-Equation

$$\frac{\partial \rho E}{\partial t} + \nabla \cdot (\rho E \vec{u}) = -\nabla \cdot (\vec{u} p) + \nabla \cdot (\tau \cdot \vec{u}) + \nabla \cdot \vec{q} + \rho \vec{u} \cdot \vec{f} \tag{2.3}$$

Equation of State

$$p = \frac{\rho T}{\gamma M_\infty^2} = (\gamma - 1)\rho e \tag{2.4}$$

In this system $\vec{f}$ describes external forces. The viscous stress tensor τ is the source of molecular diffusion due to friction in the fluid and defined as

$$\tau := \frac{\mu}{Re_\infty} \left(\underbrace{\left(\nabla \vec{u} + \nabla \vec{u}^T\right)}_{=:2S} - \left(\frac{2}{3} \underbrace{\nabla \cdot \vec{u}}_{=\mathrm{trace}(S)} \right) I \right) \tag{2.5}$$

$$= 2\frac{\mu}{Re_\infty} \underbrace{\left(S - \frac{1}{3}\mathrm{trace}(S) I \right)}_{=:S^*} \tag{2.6}$$

where μ is the dynamic viscosity that follows the Sutherland's law (here in dimensionless form)

$$\mu = T^{\frac{3}{2}} \frac{1 + T_{\mathrm{Su}}}{T + T_{\mathrm{Su}}}, \tag{2.7}$$

where T_{Su} denotes the Sutherland's temperature. I denotes the 3×3 unity matrix. The velocity gradient $\nabla \vec{u} = S + \Omega$ can be decomposed into a symmetric part $S := \frac{1}{2}\left(\nabla \vec{u} + \nabla \vec{u}^T\right)$ and a skew-symmetric part $\Omega := \frac{1}{2}\left(\nabla \vec{u} - \nabla \vec{u}^T\right)$. The symmetric part S is called strain rate tensor and the skew-symmetric part Ω is called rotation tensor. In the energy equation the heat flux vector $\vec{q}$ is defined as

$$\vec{q} := \frac{\mu}{Re_\infty (\gamma - 1) M_\infty^2 Pr_\infty} \nabla T, \tag{2.8}$$

so that the thermal conduction satisfies Fourier's law. Therefore, γ is the isentropic coefficient of the fluid. It is to mention that this system is non-dimensionalised to reduce truncation errors and for generalization as well as for comparison reasons. The non-dimensionalisation results in the dimensionless Reynolds (Re_∞), Mach (M_∞) and Prandtl number (Pr_∞), which are functions of the dimensional reference values of the non-dimensionalisation: $Re_\infty := \frac{\rho_\infty u_\infty L}{\mu_\infty}$, $M_\infty := \frac{u_\infty}{\sqrt{\gamma \mathcal{R} T_\infty}}$ and $Pr_\infty := \frac{\mu_\infty c_{p,\infty}}{\kappa_\infty}$. In the following all the variables are dimensionless unless stated otherwise.

To fully define the abstract problem of a turbulent flow the domain on which the system of PDEs is defined needs to be specified. As flows in general are three dimensional, we define the space-domain Ω as an open or closed subset of $\mathbb{R}^3$ ($\Omega \subseteq \mathbb{R}^3$). The time is marching forward and so we define the space-time domain Ω_T as $\Omega_T := \mathbb{R}_+ \times \Omega$. The flow then is defined on Ω_T as $(\rho, \vec{u}, T) : \Omega_T \to \mathbb{R}^5$. The boundary conditions will be enforced by the differential operator $BC(\rho, \vec{u}, T)$ defined as $BC : \left(\partial\Omega_T \to \mathbb{R}^5\right) \to \left(\partial\Omega_T \to \mathbb{R}^5\right)$, where $\partial\Omega_T$ is defined as $\partial\Omega_T := \mathbb{R}_+ \times \partial\Omega$, the spatial boundary of Ω_T. The initial condition at $t = 0$ is given as $\rho_0 := \rho(0, \cdot), \vec{u}_0 := \vec{u}(0, \cdot), T_0 := T(0, \cdot) \in C^2(\overline{\Omega})$ where $\overline{\Omega}$ is the closure of the space-domain. With these definitions we can state the formal definition of the flow problem:

Find $\quad (\rho, \vec{u}, T) : \Omega_T \to \mathbb{R}^5$

$$\begin{aligned}
\tfrac{\partial \rho}{\partial t} + \nabla \cdot (\rho \vec{u}) &= 0 && \left(\forall (t, \vec{x}) \in \Omega_T\right) \\
\tfrac{\partial \rho \vec{u}}{\partial t} + \nabla \cdot (\rho \vec{u} \otimes \vec{u}) &= -\nabla p + \nabla \cdot \tau + \rho \vec{f} && \left(\forall (t, \vec{x}) \in \Omega_T\right) \\
\tfrac{\partial \rho E}{\partial t} + \nabla \cdot (\rho E \vec{u}) &= -\nabla \cdot (\vec{u} p) + \nabla \cdot (\tau \cdot \vec{u}) + \nabla \cdot \vec{q} + \rho \vec{u} \cdot \vec{f} && \left(\forall (t, \vec{x}) \in \Omega_T\right) \\
p &= \tfrac{\rho T}{\gamma M_\infty^2} = (\gamma - 1) \rho e && \left(\forall (t, \vec{x}) \in \overline{\Omega_T}\right)
\end{aligned}$$

with

$$BC(\rho, \vec{u}, T) = 0 \qquad \left(\forall (t, \vec{x}) \in \partial\Omega_T\right)$$

and

$$(\rho, \vec{u}, T)(0, \cdot) = (\rho_0, \vec{u}_0, T_0) \qquad \left(\forall t = 0, \vec{x} \in \overline{\Omega}\right)$$

(2.9)

Although this system of PDEs, at least in a comparable form, has been known for more

than 150 years, it is still unsolved in its general form. Even the existence and the uniqueness of solutions is still not proven. The root of all the trouble lies in the equations' non-linearity. As effect of the non-linearity, the solutions (if they exist) seem to have a wide range of temporal and spatial scales, that we know as 'turbulence' and that will be the focus of the present work. Even if we know only little about the analytical solution, it is possible to approximate a solution in a numerical way. The method of approaching a solution to the Navier-Stokes equations without using any further model to describe turbulence and therefore resolving all the scales of motion is called direct numerical simulation (DNS), and will be explained in more detail in chapter 3. These approximated solutions provide an opportunity to get an idea about the underlying character of the system (2.9) for different applications and will help in two ways. One is the improved understanding of this system and the role of its individual terms. The second is the general understanding of the behaviour of possible solutions in different turbulent flows. The latter is one of the basic research topics in computational fluid dynamics as for most practical flows a direct approximation of the system (2.9) is simply not achievable in a reasonable time as current computational resources are insufficient. In these cases the NS equations will be modified, in a way that not all the flow structures of the solution need to be captured by the equations (e.g. RANS, URANS, LES, DES,...). But the effect of these structures need to be modelled instead. To reduce complexity of the solution without losing too much information is the challenge in these turbulence modelling approaches. To discuss some existing models and bring up guidelines for new models will be one of the goals of the present work. For simplicity, we will assume that no body forces are acting on the fluid and therefore neglect the forcing terms $\rho\vec{f}$ in the following. For the understanding of the equations and improving or developing turbulence models, it is indispensable to take a closer look at the different terms of the PDE system (2.9). Applying the chain-rule to the continuity equation (2.1), we end up with the non-conservative form of the continuity equation

$$\frac{\partial \rho}{\partial t} + \vec{u} \cdot \nabla \rho + \rho \left(\nabla \cdot \vec{u} \right) = 0. \tag{2.10}$$

In (2.10) the first term describes the change of mass in time of an infinitesimally small cube in the flow field, which is from now on referred to as 'fluid particle'. The second term transports the fluid particle's mass with the flow. The last term is the dilatation (divergence of velocity $\nabla \cdot \vec{u}$) weighted with the density and shows the compression of a fluid particle due to velocity gradients acting on it.
With definition (2.1) and applying the chain-rule, $\nabla \cdot (\rho\vec{u} \otimes \vec{u})$ can be rewritten as $\vec{u} \cdot \nabla \rho\vec{u} + \rho\vec{u} \left(\nabla \cdot \vec{u} \right)$. Substituting this into (2.2) and applying the chain-rule to the time derivative we get

$$\frac{\partial \rho\vec{u}}{\partial t} + \vec{u} \cdot \nabla \rho\vec{u} + \rho\vec{u} \left(\nabla \cdot \vec{u} \right) = -\nabla p + \nabla \cdot \tau. \tag{2.11}$$

Here the first term of the LHS describes the change of velocity while the second is the non-linear transport term, in which a source of turbulence is hidden. The third term is

conserving mass and will drop out if the equation is transformed into primitive form. The first term on the RHS shows the forces due to pressure differences in the flow field. Momentum diffusion is represented by $\nabla \cdot \tau$, which includes all the second derivatives and acts as a smoothing operator on the velocity field.
As mentioned earlier (1.2), two main characteristics of turbulence are the transfer of kinetic energy between different scales of motion and the dissipation of kinetic energy to internal energy. Therefore it is essential to get a clear image of the energy distribution in the flow. To highlight this the equations of internal and kinetic energy will be introduced in the following. But first there is a need for two definitions and a useful theorem and a lemma to simplify the notation.

Definition 2.2. Hilbert-Schmidt inner product
Let $\mathrm{Mat}_n(\mathbb{C})$ denote the space of all $n \times n$ square matrices with the usual operations and $A, B \in \mathrm{Mat}_n(\mathbb{C})$. We define the mapping

$$\langle \cdot, \cdot \rangle_F : \mathrm{Mat}_n(\mathbb{C}) \times \mathrm{Mat}_n(\mathbb{C}) \to \mathbb{C}$$

by

$$\langle A, B \rangle_F := \mathrm{trace}(AB^*),$$

where A^* is the conjugate transpose (i.e. if $A = (a_{i,j})$ then $A^* = (b_{i,j})$ where $b_{i,j} = \overline{a_{j,i}}$). This is called the **Hilbert-Schmidt inner product** on $\mathrm{Mat}_n(\mathbb{C})$.

That mapping is an inner product with the properties of linearity, conjugate symmetry and that it is positive definite is given by the following theorem:

Theorem 2.3. *The Hilbert-Schmidt inner product* $\langle A, B \rangle_F := \mathrm{trace}(AB^*)$ *is an inner product on* $Mat_n(\mathbb{C})$.

Proof: See Horn & Johnson (2006).
Further we want to state the following property of this product.

Lemma 2.4. *Let* $Mat_n(\mathbb{R})$ *denote the space of all* $n \times n$ *square matrices with the usual operations and* $A, B \in Mat_n(\mathbb{R})$. *Then the Hilbert-Schmidt inner product* $\langle A, B \rangle_F := \mathrm{trace}(AB^*)$ *can be written as*

$$\langle A, B \rangle_F = \sum_{i=1}^{n} \sum_{j=1}^{n} a_{i,j} b_{i,j}$$

.

See Horn & Johnson (2006).
Based on the Hilbert-Schmidt inner product we now can define a norm on $\mathrm{Mat}_n(\mathbb{C})$:

Definition 2.5. Frobenius norm
Let $\mathrm{Mat}_n(\mathbb{C})$ denote the space of all $n \times n$ square matrices with the usual operations and $A \in \mathrm{Mat}_n(\mathbb{C})$. The mapping

$$\|\cdot\|_F : \mathrm{Mat}_n(\mathbb{C}) \to \mathbb{C}$$

defined by

$$\|A\|_F := \sqrt{\langle A, A\rangle_F} = \sqrt{\mathrm{trace}(AA^*)} = \left(\sum_{i=1}^{n}\sum_{j=1}^{n} |a_{ij}|^2\right)^{1/2}$$

is called the **Frobenius norm** on $\mathrm{Mat}_n(\mathbb{C})$.

Equipped with these tools we can take a first look at the internal energy equation. It is derived from the total energy equation (2.3) and the momentum equation (2.2). The complete derivation can be found in the appendix (A.1.2)

$$\frac{\partial \rho e}{\partial t} + \nabla \cdot (\vec{u}\rho h) = \nabla \cdot \vec{q} + \vec{u} \cdot \nabla p + \langle \tau, \nabla \vec{u}\rangle_F . \tag{2.12}$$

The last term (dissipation) can be further simplified. As the stress tensor τ is a symmetric tensor it is worth splitting up the velocity gradient into the symmetric shear stress tensor S and the skew-symmetric rotation tensor Ω:

$$\begin{aligned} \langle \tau, \nabla \vec{u}\rangle_F &= \langle \tau, S + \Omega\rangle_F \\ &= \langle \tau, S\rangle_F + \underbrace{\langle \tau, \Omega\rangle_F}_{=0\ (\tau \text{ sym.}, \Omega \text{ skew-sym.})} \\ &= \langle \tau, S\rangle_F . \end{aligned} \tag{2.13}$$

Further the definition of τ (2.5) can be substituted to obtain the following equality

$$\begin{aligned} \langle \tau, S\rangle_F &= 2\frac{\mu}{Re_\infty}\langle S^*, S\rangle_F \\ &= 2\frac{\mu}{Re_\infty}\langle S, S\rangle_F - \frac{2}{3}\frac{\mu}{Re_\infty}\mathrm{trace}(S)^2 \\ &= 2\frac{\mu}{Re_\infty}\langle S, S\rangle_F - \frac{2}{3}\frac{\mu}{Re_\infty}\langle S, I\rangle_F^2 . \end{aligned} \tag{2.14}$$

Using the *Cauchy-Schwarz inequality* (see Horn & Johnson, 2006) ($\langle x, y\rangle^2 \le \langle x, x\rangle \cdot \langle y, y\rangle$) we can show

$$\begin{aligned} \langle S, I\rangle_F^2 &\le \langle S, S\rangle_F \underbrace{\langle I, I\rangle_F}_{=3} \\ &\Leftrightarrow \\ \frac{1}{3}\langle S, I\rangle_F^2 &\le \langle S, S\rangle_F . \end{aligned} \tag{2.15}$$

Substituting this into (2.14) leads to

$$\begin{aligned}\langle \tau, S\rangle_F &\geq 2\frac{\mu}{Re_\infty}\langle S, S\rangle_F - \frac{2}{3}\frac{\mu}{Re_\infty}3\langle S, S\rangle_F \\ &= 0. \end{aligned} \tag{2.16}$$

Thus the dissipation term is positive definite, which is very useful to know for the transfer of energy. Substituting 2.13 into 2.12 we obtain the final conservative form of the **internal energy equation**:

$$\frac{\partial \rho e}{\partial t} + \nabla \cdot (\vec{u}\rho h) = \nabla \cdot \vec{q} + \vec{u} \cdot \nabla p + \langle \tau, S\rangle_F . \tag{2.17}$$

Before we discuss this equation any further, let us introduce the transport equation for the kinetic energy $e_{\text{kin}} := \frac{1}{2}\vec{u}^2$. This now can be obtained by either subtracting the internal energy equation (eq. 2.17) from the total energy equation (eq. 2.3) or by multiplying the velocity vector onto the momentum equation (eq. 2.2) and subtracting the continuity equation (eq. 2.1) pre-multiplied with the kinetic energy from the product. Which way is more convenient is the readers choice. After some transformations (see A.1.1) and applying equation (2.13), the **kinetic energy equation** in conservative form becomes

$$\frac{\partial \rho e_{\text{kin}}}{\partial t} + \nabla \cdot (\rho \vec{u} e_{\text{kin}}) = -\vec{u} \cdot \nabla p + \nabla \cdot (\tau \cdot \vec{u}) - \langle \tau, S\rangle_F . \tag{2.18}$$

Now that we have introduced the equation for internal and kinetic energy the distribution process of energy and the difficulties it introduces will be stated. This will guide the further course of this work. The first law of thermodynamics states that total energy E of a fluid particle is conserved if no sources and sinks of energy are given, as is the case in this work. Following this all terms in the total energy equation (2.3) can only redistribute energy. To understand these redistribution processes it is helpful to split up the total energy. The total energy $E = e + e_{\text{kin}}$ can be decomposed (fig. 2.1) into internal energy e, which represents the kinetic and potential energies of the molecules of the fluid (Pai & Luo, 1991) , and kinetic energy e_{kin} which is the energy described by the movement of the fluid.

To analyse the transfer and redistribution process in the Navier-Stokes equations it is important to have a global picture to categorize the processes and understand their connection. For this reason figure (fig. 2.1) allows a schematic overview on the processes that govern the energy in a system that is described by the Navier-Stokes equation. This type of figure will be used to explain the filtered equations as well and is of great importance to display the focus of this work. For this reason it will be described in more detail at this stage. The total energy at one location in the domain is described by the transport equation of the total energy density ρE (eq. 2.3). This equation can be reordered to an equation with the time derivative on the left hand side (LHS) and the redistribution terms on the right hand side (RHS). In this way the time derivative (purple node) and therefore the variation in time at one point of space if governed by all

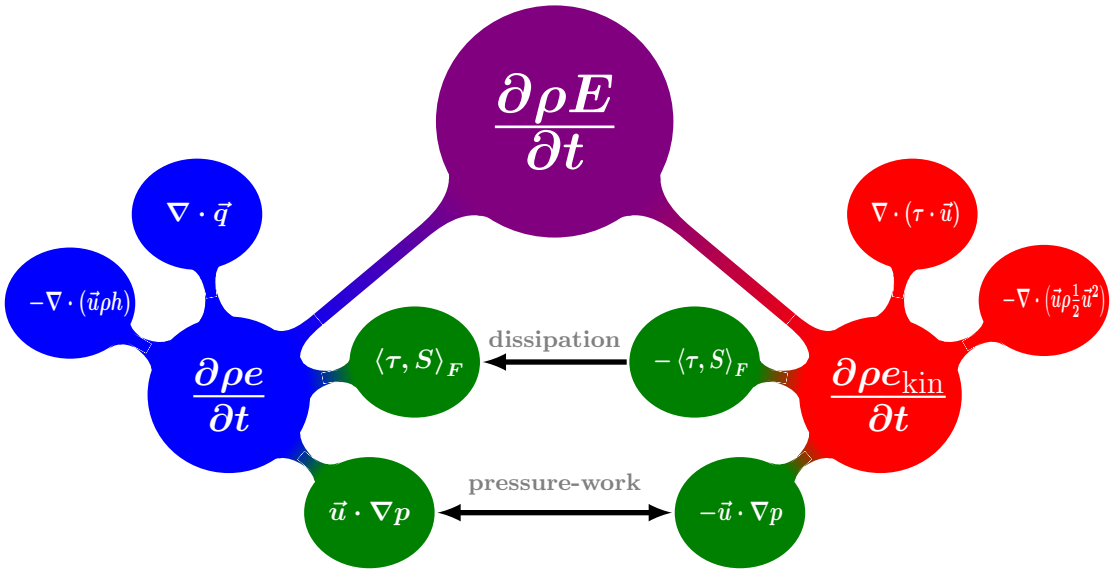

Figure 2.1: Schematic decomposition of the governing equation of total energy E (2.3) into the governing equations for internal energy e (2.17) and kinetic energy e_{kin} (2.18). Signs are chosen such that only the time-derivative is on the LHS and all other terms are found on the RHS.

the terms (small red and blue nodes) on the RHS. By splitting the total energy variation into internal energy variation (large blue node) and kinetic energy variation (large red node) it is possible to distinguish between terms that govern the respective parts of the energy. We find terms that govern the internal energy only (small blue nodes) and terms that govern the kinetic energy only (small red nodes). But more interestingly the splitting reveals terms that are responsible for the transfer between the kinetic energy and the internal energy (green nodes). These terms are not visible in the total energy transport equation. Here the decomposition is based on the physical quantities e and e_{kin}. The same idea is used in the next paragraph to reveal the transfer of energy between different scales of motion. But firstly we discuss the unfiltered energy balance.
Focusing on the internal energy equation (2.17) we see that the divergence of the heat flux vector $\nabla \cdot \vec{q}$ is redistributing the internal energy only. It acts as thermal diffusion. Further, this equation contains the part $-\nabla \cdot \vec{u}\rho h$ of the total energy transport term that transports the enthalpy only. This term is linear in each variable and therefore purely transporting the internal energy with the flow velocity. As mentioned before, additional to the terms that are already part of the total energy equations, the decomposition exposes two more terms that appear with different sign in the equations for internal and kinetic energy respectively. These terms maintain the transfer of energy from kinetic to internal energy and vice versa. $\pm \vec{u} \cdot \nabla p$ is the pressure-momentum-work and denoted as pressure-work in the following. It describes the force that balances pressure and momentum. For instances a slow-down of the flow in an adverse pressure gradient is reflected. In such a case the velocity vector and the pressure gradient are aligned and the term transfers energy from kinetic to internal. On the other hand, in a vortex the

velocity vector is more likely to be perpendicular to the pressure gradient and this term remains small. Dissipation $\langle \tau, S \rangle_F$ is always positive as shown in equation (2.16). In the kinetic energy equation is appears to have a negative sign (sink) whereas in the internal energy equation the sign is positive (source). This states that dissipation is draining energy from the kinetic energy equations and adds it to the internal energy equation, so that this process does not affect the total energy. A further term in the kinetic energy is the molecular diffusion, $\nabla \cdot (\tau \cdot \vec{u})$, which is only redistributing the kinetic energy. The non-linear transport term of the kinetic energy $-\nabla \cdot \left(\rho \vec{u} \frac{1}{2} \vec{u}^2\right)$ contains the spatial transport of kinetic energy as well as transport of kinetic energy across different scales of motion. This term is the energetic counterpart of the non-linear transport term for the momentum (2.2). This redistribution of kinetic energy in between different scales of motion is achieved via a spectral convolution process (Doering & D.Gibbon, 2004) that can be elucidated by Fourier transforming the Navier-Stokes equations. This term is the cause of the phenomenon that we call turbulence and is studied in detail in the following. As Fourier transformations are not a feasible tool to decompose the Navier-Stokes equations in a general flow, we choose a different way to highlight the scale transfer of energy in this work. The applied filtering approach is described in the next paragraph.

2.2 Filtered Navier Stokes Equations

In the last section (2.1) the Navier-Stokes equations and the corresponding energy equations were introduced. We highlighted the transfer of energy between kinetic and internal energy, but the inter-scale transfer due to turbulence, settled in the non-linear transport term, is still overlayed by the pure transport of kinetic energy or momentum. The focus of this work is on this inter-scale transfer of kinetic energy. Investigations on this inter-scale transfer requires to expose the cascading (1.2.1) process which is hidden in the non-linear terms of momentum and energy in the current form of the equations (eq. 2.9). There are more possibilities to proceed some of which are covered in books like, e.g., Frisch (1995); Doering & D.Gibbon (2004). An interesting method is studied by Brasseur & Yeung (1991). They transform the Navier-Stokes equation to Fourier space and reveal the triad mechanism. One of their conclusions is that the scale transfer is a mechanism that couples 3 different scales in spectral space. When energy transfer is happening between two structures with scales of similar order, a third structure of significantly different size might control this process. This might be interpreted as that in the surroundings of large scale vortices there are regions of strong, small scale shear that produce small scale vortices. This is a theory that we will support with results of a turbulent boundary layer at a later stage.
However, considering more complex geometries and strongly inhomogeneous mean flows, the approach of Fourier transforming the entire system of equation is not an option. But

spatial and/or temporal filtering turns out to be a suitable tool to study the cascading process in complex geometries. To decouple this cascading process from the spatial momentum/kinetic energy transport filter operators will be applied to the flow field and its governing equations. The idea behind filtering and decomposing the equations is to obtain a 'cut' at an arbitrary location of the energy cascade (1.2.1). In general this leads to a decomposition of the flow quantities into a part containing scales larger than the scales at the cut location and a part containing scales smaller than those at the cut location. In the governing equation for the large-scale (LS) quantities, the non-linear terms can then be decomposed into terms that contain LS information, terms that contain small-scale (SS) information, and mixed terms that contain mixed LS-SS information. The latter two are maintaining the transfer across the cut in the cascade. This kind of transfer terms will be studied extensively in this work. Secondly these equations are the governing equations for Large-Eddy Simulation (LES) and Reynolds averaged Navier-Stokes (RANS) simulations. Studying these equations on experimental data or DNS data allows us to understand the model contributions of the turbulence models applied in LES and RANS. To obtain the filtered equations (2.2.2) we first have to introduce an appropriate filter operator.

2.2.1 Filter

It is convenient to describe the filter operator that decomposes the flow field into a small-scale contribution and a large-scale contribution in a general form. This allows to have one system of equations that describes RANS, LES and other filtered equations in the same form. The only difference between the system is then the choice of the filter operator. For this reason we define the filter operator noted with a bar that transforms a function f into its filtered counterpart $\bar{f}$. The filter operation is a convolution of the function f with a filter kernel H combined with a normalization and has the compact form

$$\overline{f}(\vec{x},t) := \frac{f * H[\vec{x},t]}{1 * H[\vec{x},t]}. \tag{2.19}$$

The explicit form of the filter operation is

$$\overline{f}(\vec{x},t) := \frac{\int_{\bar{\Omega}_T} f(\vec{\xi},\tau) H(\vec{x},t,\vec{x}-\vec{\xi},t-\tau) d\vec{\xi} d\tau}{\int_{\bar{\Omega}_T} H(\vec{x},t,\vec{x}-\vec{\xi},t-\tau) d\vec{\xi} d\tau}. \tag{2.20}$$

The filter kernel H has to be a piecewise integrable function on the space-time domain $\bar{\Omega}_T$ where the filter is applied. To obtain the RANS equation the filter kernel has to be chosen to be a purely temporal kernel that is constant for all times

$$H(\vec{x},t,\vec{y},s) = \delta(\vec{y}). \tag{2.21}$$

This kernel leads to a filter operation that is equivalent to the well known Reynolds averaging (Reynolds, 1895). On the other hand, LES is defined as a purely spatially filtered approach and the filter kernel takes the form

$$H(\vec{x}, t, \vec{y}, s) = \delta(s) G(\vec{x}, \vec{y}). \tag{2.22}$$

G is a spatial filter kernel and in this work we mostly use a Gaussian kernel with variable filter width

$$G(\vec{x}, \vec{y}) = e^{-\frac{1}{2}\frac{\|\vec{y}\|^2}{(\sigma(\vec{x}))^2}}. \tag{2.23}$$

In case of implicitly filtered LES this filter kernel results from the respective discretisation of the PDE system.
Depending on the choice of the filter kernel we do separate the flow-field into a large scale contribution represented by filtered quantities and a small-scale contribution that is represented by the difference of the actual flow field and the large-scale contribution. Formally this decomposition reads

$$f' := f - \overline{f} \quad \Leftrightarrow \quad f = \overline{f} + f' \tag{2.24}$$

for f being an arbitrary function. For compressible flows it is useful to introduce a so called Favre filtering. It was first introduced by A. (1965) and normalizes the filtered conservative values with the filtered density

$$\tilde{f} := \frac{\overline{\rho f}}{\overline{\rho}}. \tag{2.25}$$

Let f be any primitive variable while ρ stands for density and ρf is the respective conservative variable. This leads to the Favre decomposition

$$f'' := f - \tilde{f} \quad \Leftrightarrow \quad f = \tilde{f} + f'', \tag{2.26}$$

where $\tilde{f}$ denotes a Favre-filtered quantity and f'' denotes the fluctuations with respect to the Favre filtering.

2.2.1.1 Filter Properties

There are four key properties that filters can have and that need to be outlined. This helps to understand the derivation and possible applications of the filtered equations that will be derived in the following section.

1. Conservation of Constants Constants are invariant under the filter operation

$$\bar{c} = c, \tag{2.27}$$

with c being an arbitrary constant. This property is fulfilled by any filter operator discussed in this work.

2. Linearity with Respect to Summation The filter operator is commuting with the summation operator

$$\overline{f + g} = \bar{f} + \bar{g}, \tag{2.28}$$

with f and g being arbitrary piecewise integrable functions on the considered domain. This property is fulfilled by any filter operator discussed in this work.

3. Commutation with Differential Operators This describes the property of the filter operator to commute with differential operators

$$\overline{\frac{\partial f}{\partial s}} = \frac{\partial \bar{f}}{\partial s}, \tag{2.29}$$

with f being an arbitrary piecewise integrable function on the considered domain and s being an arbitrary direction (x_1, x_2, x_3, t) in the space-time domain. This condition is only fulfilled if the filter operator is homogeneous in the respective direction i.e.

$$\frac{\partial H}{\partial s} = 0. \tag{2.30}$$

This for example is given for the Reynolds filter operator as well as for spatial filters that are identical in the whole domain. But many spatial filters (as the spatial filters used in this work) violate this condition due to varying filter width and/or varying filter operators at domain boundaries e.g. walls. For this reason we introduce filter residua that cover the contributions due to inhomogeneous filters.

Definition 2.6. These residua are noted as $[\cdot]_R$ and defined as

$$[\nabla f]_R := \overline{\nabla f} - \nabla \bar{f} \tag{2.31}$$

or

$$[\nabla \cdot \vec{f}]_R := \overline{\nabla \cdot \vec{f}} - \nabla \cdot \bar{\vec{f}} \tag{2.32}$$

4. Reynolds Operator This property describes the invariance under multiple applications of the filter operator

$$\bar{\bar{f}}\bar{g} = \bar{f}\bar{g} \tag{2.33}$$

and

$$\overline{\bar{f}} = \bar{f}. \tag{2.34}$$

This property is in general not fulfilled by the filter operators. However, the Reynolds averaging fulfils this condition.

2.2.2 Filtered Equations

Equipped with the introduced general filter operator we can derive the filtered counterpart of the compressible Navier-Stokes equations (eq. 2.9). The resulting new system of equations are the governing equations for the filtered flow field. Therefore they can be applied in RANS simulations or LES with the respective choice of the filter operator. Further, the newly derived system allows to study the coupling of large-scales and small-scales in form of transfer terms that link both sides of the decomposition. This will then be illustrated with diagrams, that give an overview of the energy distribution in the filtered system. But first the basic governing equations are derived.

Filtered Continuity Equation To obtain the filtered continuity equation the filter operator (eq. 2.19) is applied on the continuity equation (eq. 2.1). The resulting equation

$$\frac{\partial \bar{\rho}}{\partial t} + \nabla \cdot \left(\bar{\rho} \tilde{\vec{u}} \right) = -[\nabla \cdot (\rho \vec{u})]_R \tag{2.35}$$

governs the filtered density $\bar{\rho}$. The full derivation can be found in the appendix (eq. A.6). Note that the filter residuum $[\nabla \cdot (\rho \vec{u})]_R$ is a fragment of a spatially inhomogeneous filter operator.

Filtered Momentum Equation To obtain the filtered momentum equations the filter operator (eq. 2.19) is applied to the momentum equations (eq. 2.2). The resulting equations

$$\frac{\partial \bar{\rho} \tilde{\vec{u}}}{\partial t} + \nabla \cdot \left(\overline{\rho \vec{u} \otimes \vec{u}} \right) = -\nabla \bar{p} + \nabla \cdot \bar{\tau} - [\nabla \cdot (\rho \vec{u} \otimes \vec{u})]_R - [\nabla p]_R + [\nabla \cdot \tau]_R, \tag{2.36}$$

govern the filtered momentum $\bar{\rho} \tilde{\vec{u}}$. The full derivation can be found in the appendix (eq. A.7). The filtered viscous stress tensor $\bar{\tau}$ in the latter equations reads

$$\bar{\tau} := \overline{\frac{\mu}{Re_\infty} \left((\nabla \vec{u} + \nabla \vec{u}^T) - \left(\frac{2}{3} \nabla \cdot \vec{u} \right) I \right)}. \tag{2.37}$$

For RANS and LES a frequently made assumption is that dynamic viscosity fluctuations/residuum and velocity gradient fluctuations/residuum are uncorrelated under

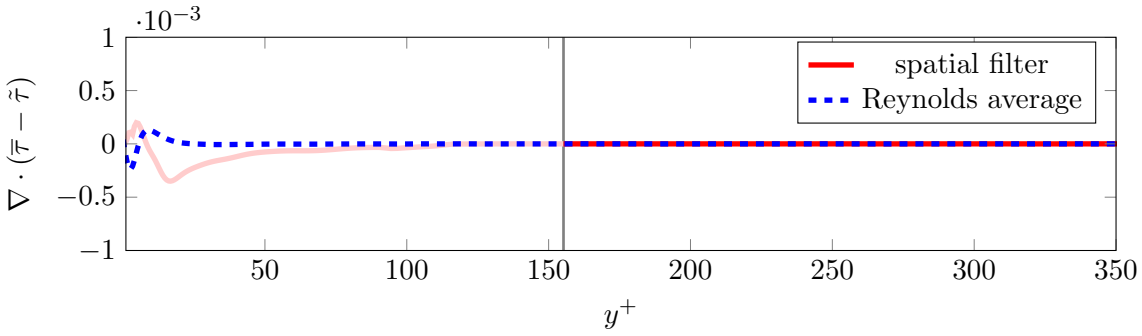

Figure 2.2: Error function for the filtered diffusion term in a TBL. The spatial filter results below $y^+ \lesssim 155$ (marked by the vertical grey line) are superimposed by the remaining terms of the filter residuum that rise due to inhomogeneous filter operations in this region.

application of the respective filter. Following this we assume for this work that the identity

$$\bar{\tau} = \frac{\bar{\mu}}{Re_\infty} \left(\underbrace{\left(\nabla \widetilde{\vec{u}} + \nabla \widetilde{\vec{u}}^T \right)}_{=2\bar{S}} - \left(\frac{2}{3} \underbrace{\nabla \cdot \widetilde{\vec{u}}}_{=\mathrm{trace}(\bar{S})} \right) I \right) \tag{2.38}$$

holds. Here we define the filtered strain rate tensor as

$$\bar{S} := \frac{1}{2} \left(\nabla \widetilde{\vec{u}} + \nabla \widetilde{\vec{u}}^T \right). \tag{2.39}$$

As $\overline{\nabla \cdot \tau} - \nabla \cdot \bar{\tau}$ is captured in the filter residuum $[\nabla \cdot \tau]_R$ we can test the validity of this assumption on the boundary layer data that will be introduced later (sec. 3.3). Figure (2.2) shows that the error made by this assumption is small for both, spatial filtering as well as Reynold averaging. Besides the filter residua the filtered momentum equation (eq. 2.36) includes the filtered transport term that we would like to decompose into a part that is dependent on large-scale quantities only and in a part that describes the coupling with the small-scales. For this reason we define the Favre stress/sub-grid stress tensor σ as difference between the transport of the large-scale quantities and the filtered transport of the unfiltered quantities

$$\sigma := -\left(\overline{\rho \vec{u} \otimes \vec{u}} - \bar{\rho} \widetilde{\vec{u}} \otimes \widetilde{\vec{u}} \right) \tag{2.40}$$

For filters that fulfil the properties of Reynolds operators (as in case of RANS) this stress tenor can be written as

$$\sigma = -\overline{\rho \vec{u}'' \otimes \vec{u}''}. \tag{2.41}$$

Substituting this into the filtered momentum equation (eq. 2.36) we obtain the final form for these governing equations

$$\frac{\partial \bar{\rho}\widetilde{\vec{u}}}{\partial t} + \nabla \cdot \left(\bar{\rho}\widetilde{\vec{u}} \otimes \widetilde{\vec{u}}\right) = -\nabla \bar{p} + \nabla \cdot \bar{\tau} + \nabla \cdot \sigma - [\nabla \cdot (\rho \vec{u} \otimes \vec{u})]_R - [\nabla p]_R + [\nabla \cdot \tau]_R. \quad (2.42)$$

Besides the filter residua, we find terms that are only dependent on large-scales and one term that governs the coupling of large scales and small scales, $\nabla \cdot \sigma$.

Filtered Total Energy Equation The filtered total energy equation is obtained by applying the filter operator (eq. 2.19) to the total energy equation (eq. 2.3). The full derivation can be found in the appendix (eq. A.8). The resulting equation

$$\begin{aligned}\frac{\partial \bar{\rho}\tilde{E}}{\partial t} + \nabla \cdot \left(\overline{\vec{u}\rho E}\right) = \nabla \cdot \bar{\vec{q}} + \nabla \cdot \left(\overline{\tau \cdot \vec{u}}\right) - \nabla \cdot \left(\overline{\vec{u}p}\right) \\ - \underbrace{[\nabla \cdot (\vec{u}\rho E)]_R}_{=:\mathbb{D}_R^{E-\text{trans}}} + \underbrace{[\nabla \cdot \vec{q}]_R}_{=:\mathbb{D}_R^{\text{heat}}} + \underbrace{[\nabla \cdot (\tau \cdot \vec{u})]_R}_{=:\mathbb{D}_R^{\text{diff}}} - \underbrace{[\nabla \cdot (\vec{u}p)]_R}_{=:\mathbb{D}_R^{\text{press}}} \quad (2.43)\end{aligned}$$

describes the filtered part of the full energy distribution in the domain. The terms $\mathbb{D}_R^{E-\text{trans}}$, $\mathbb{D}_R^{\text{heat}}$, $\mathbb{D}_R^{\text{diff}}$ and $\mathbb{D}_R^{\text{press}}$ note the diffusively acting filter residua rising from the respective terms. They are described as diffusively acting as the do only reorder the respective part of the energy, but do not transfer energy between different types of energy as we will see later. Similar to the assumption for the filtered viscous stress tensor in the filtered momentum equations, an assumption can be made for the filtered heat flux

$$\bar{\vec{q}} := \overline{\frac{\mu}{Re_\infty(\gamma-1)M_\infty^2 Pr_\infty}\nabla T}. \quad (2.44)$$

For RANS and LES an often made assumption is that dynamic viscosity fluctuations/residuum and temperature gradient fluctuations/residuum are uncorrelated under application of the respective filter. For this assumption the identity

$$\bar{\vec{q}} = \frac{\bar{\mu}}{Re_\infty(\gamma-1)M_\infty^2 Pr_\infty}\nabla \tilde{T} \quad (2.45)$$

holds. Here as well the full contribution is captured in the filter residuum term $\mathbb{D}_R^{\text{heat}}$ and possible violations of this assumption on the boundary layer data that will be introduced later (sec. 3.3). Figure (2.3) shows that the error made by this assumption is small for both, spatial filtering as well as Reynold averaging. In this form we can see which terms are governing the development of the filtered total energy. Figure (fig. 2.4) shows an influence diagram of the total energy. Here it is illustrated that additionally to the filtered physical terms, that are a logical result from the unfiltered total energy equation, we find the filter residua that influence the filtered total energy. As mentioned before, they are a result of inhomogeneous filter operators and represent the imbalance that arises from the fact that the different locations of the domain are filtered differently.

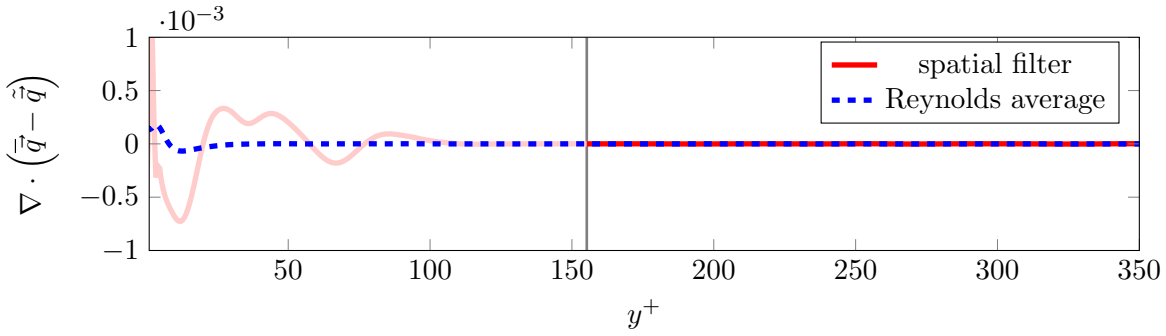

Figure 2.3: Error function for the filtered heat flux term in a TBL. The spatial filter results below $y^+ \lesssim 155$ (marked by the vertical grey line) are superimposed by the remaining terms of the filter residuum that rise due to inhomogeneous filter operations in this region.

For example, the filter residuum of the filtered transport $\mathbb{D}_R^{E\text{-trans}}$ covers the transport of energy in an inhomogeneous filter direction.
To give an impression of these filter residua, consider the following scenario: In a region where the spatial filter width is relatively small we consider a given decomposition into large-scales and small-scales based on the local filter width. When this energy is transported into a region with a larger filter width then the decomposition of scales is changing as it is still based on the local filter width. This results in that a part of the energy that was considered as large scale at the previous location is now considered to be part of the small scales. That means that the respective transfer between the scales has to be covered in the equation. As this transfer is not natural, but an artefact of the inhomogeneous filter, it has to be separated from the natural scale transfer. This and all other artificial filter effects will be covered by the filter residua. In the illustrations these contributions will be shown as grey nodes.

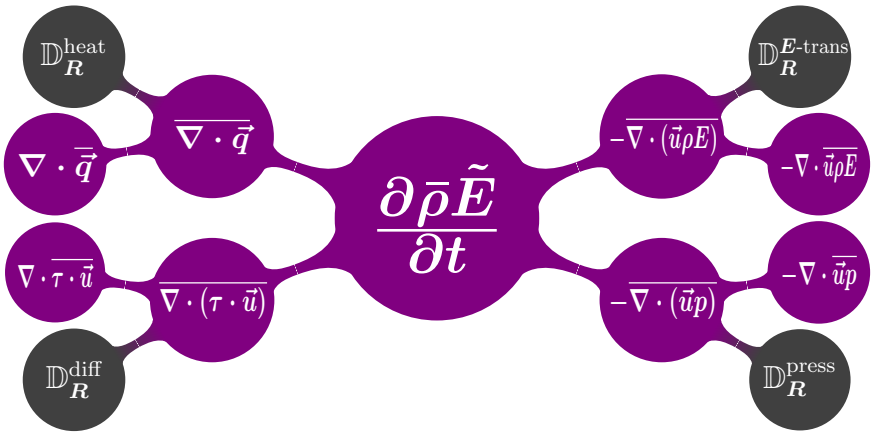

Figure 2.4: Schematic representation of the filtered total energy equation in its raw form and with the differentiation between physical influence (small purple nodes) and influence of inhomogeneous filter operators (small grey nodes).

Before we go on to derive the split filtered energy equations the filtered analogue of the equation of state is stated.

Filtered Equation of State Equations By applying the filter operator (eq. 2.19) to the equation of state (eq. 2.4) the filtered equation of state

$$\bar{p} = \frac{\bar{\rho}\tilde{T}}{\gamma M_\infty^2} = (\gamma - 1)\bar{\rho}\tilde{e} \tag{2.46}$$

is obtained.

2.2.3 Filtered Energy Distribution in the Navier-Stokes Equations

The filtered energy is the large scale part of the energy of the system. What exactly the *large-scale* part is, is defined by the filter operator. However, these large scales are not only governed by large scales only. There is still a significant contribution coming from the small scales in the flow. But the beneficial feature of the filtered equations is that we can distinguish between large-scale and small-scale contributions. Exactly this is the reason why we introduced the filtering in the first place. To arrive at a form where we can distinguish between inter-scale transfer and pure spatial reordering terms we need to decompose the energy equation step by step. So we make our way from the filtered total energy $\tilde{E}$ to the decomposition into filtered internal energy $\tilde{e}$ and filtered kinetic energy $\widetilde{e_{\text{kin}}}$ to the final decomposition. This then splits the filtered total energy into the filtered internal energy $\tilde{e}$, the kinetic energy of the filtered moments e_f and the filtered kinetic energy of the small scales k.

2.2.3.1 Split into Filtered Internal Energy and Filtered Kinetic Energy in Raw Form

In this section we split the filtered total energy into the part that represents the contributions of the internal energy and a second part that represents the contributions of the kinetic energy.

$$\bar{\rho}\tilde{E} = \bar{\rho}\tilde{e} + \bar{\rho}\widetilde{e_{\text{kin}}} \tag{2.47}$$

Filtered Internal Energy Applying the filter operator (eq. 2.19) to the internal energy equation (eq. 2.17) leads to the transport equation for the filtered internal energy (see appendix A.9)

$$\frac{\partial \bar{\rho}\tilde{e}}{\partial t} + \nabla \cdot \left(\overline{\vec{u}\rho h}\right) = \nabla \cdot \bar{\vec{q}} + \overline{\overline{\vec{u}} \cdot \nabla p} + \overline{\langle \tau, S \rangle_F} - \underbrace{[\nabla \cdot (\vec{u}\rho h)]_R}_{=:\mathbb{D}_R^{h\text{-trans}}} + \underbrace{[\nabla \cdot \vec{q}]_R}_{=\mathbb{D}_R^{\text{heat}}}. \tag{2.48}$$

The filter residual diffusions $\mathbb{D}_R^{h\text{-trans}}$ and $\mathbb{D}_R^{\text{heat}}$ can be combined into one single diffusion of the internal energy

$$\mathbb{D}_R^{e} := -\mathbb{D}_R^{h\text{-trans}} + \mathbb{D}_R^{\text{heat}}. \tag{2.49}$$

Substituting this definition into the filtered internal equation leads to

$$\frac{\partial \bar{\rho}\tilde{e}}{\partial t} + \nabla \cdot \left(\overline{\vec{u}\rho h}\right) = \nabla \cdot \bar{\vec{q}} + \overline{\vec{u} \cdot \nabla p} + \overline{\langle \tau, S \rangle_F} + \mathbb{D}_R^{\text{e}}. \tag{2.50}$$

Filtered Kinetic Energy Equation The filtered kinetic energy

$$\widetilde{e_{\text{kin}}} := \frac{1}{2}\widetilde{\vec{u}^2} \tag{2.51}$$

is the large-scale part of the kinetic energy, not to be mistaken with the kinetic energy of the filtered velocities e_f which will be introduced in the next section. The transport equation for the filtered kinetic energy is obtained by applying the filter operator (eq. 2.19) to the kinetic energy equation (eq. 2.18)

$$\begin{aligned}\frac{\partial \bar{\rho}\widetilde{e_{\text{kin}}}}{\partial t} + \nabla \cdot \left(\overline{\vec{u}\rho\frac{1}{2}\vec{u}^2}\right) = &-\overline{\vec{u} \cdot \nabla p} + \nabla \cdot \left(\overline{\tau \cdot \vec{u}}\right) - \overline{\langle \tau, S \rangle_F} \\ &- \underbrace{\left[\nabla \cdot \left(\vec{u}\rho\frac{1}{2}\vec{u}^2\right)\right]_R}_{=:\mathbb{D}_R^{e_{\text{kin}}\text{-trans}}} + \underbrace{[\nabla \cdot (\tau \cdot \vec{u})]_R}_{=\mathbb{D}_R^{\text{diff}}}.\end{aligned} \tag{2.52}$$

Details for this derivation can be found in the appendix (A.10). Like for the filtered internal energy equations the filter residua can be combined to a filter residuum for the filtered kinetic energy

$$\mathbb{D}_R^{e_{\text{kin}}} := -\mathbb{D}_R^{e_{\text{kin}}\text{-trans}} + \mathbb{D}_R^{\text{diff}}. \tag{2.53}$$

Substituting this into the above equation leads to

$$\frac{\partial \bar{\rho}\widetilde{e_{\text{kin}}}}{\partial t} + \nabla \cdot \left(\overline{\vec{u}\rho\frac{1}{2}\vec{u}^2}\right) = -\overline{\vec{u} \cdot \nabla p} + \nabla \cdot \left(\overline{\tau \cdot \vec{u}}\right) - \overline{\langle \tau, S \rangle_F} + \mathbb{D}_R^{e_{\text{kin}}}. \tag{2.54}$$

Filtered Total Energy With the derived filtered versions of the respective equations and the identity

$$\mathbb{D}_R^{E\text{-trans}} = \mathbb{D}_R^{e\text{-trans}} + \mathbb{D}_R^{e_{\text{kin}}\text{-trans}} \tag{2.55}$$

the filtered total energy equation (eq. 2.43) can be split up into a contribution of the filtered internal energy and a contribution of the filtered kinetic energy

$$\begin{aligned}\frac{\partial \bar{\rho}\tilde{e}}{\partial t} + \nabla \cdot \overline{\vec{u}\rho h} + \frac{\partial \bar{\rho}\widetilde{e_{\text{kin}}}}{\partial t} + \nabla \cdot \overline{\vec{u}\rho\frac{1}{2}\vec{u}^2} = \\ \nabla \cdot \bar{\vec{q}} + \overline{\vec{u} \cdot \nabla p} + \overline{\langle \tau, S \rangle_F} + \mathbb{D}_R^{e} + \nabla \cdot \overline{\tau \cdot \vec{u}} - \overline{\vec{u} \cdot \nabla p} - \overline{\langle \tau, S \rangle_F} + \mathbb{D}_R^{e_{\text{kin}}}.\end{aligned} \tag{2.56}$$

The color scheme represents the related energy. Blue indicates filtered internal energy, red indicates filtered kinetic energy and the green terms are the transfer terms between both energies.

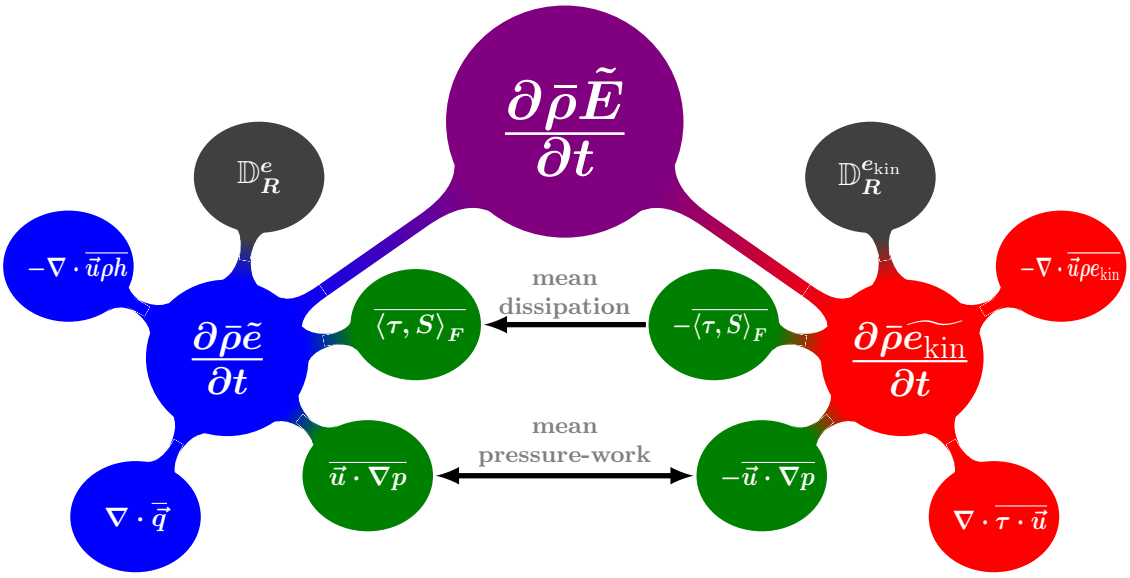

Figure 2.5: Illustration of the transport equation for the filtered total energy $\bar{\rho}\tilde{E}$ split into a filtered internal energy $\bar{\rho}\tilde{e}$ contribution and a filtered kinetic energy $\bar{\rho}\widetilde{e_{\text{kin}}}$ contribution.

Figure (2.5) illustrates the process that governs the filtered total energy decomposed into internal energy and kinetic energy just like for the unfiltered counterpart (fig. 2.1). There are not many different terms in the filtered equations. Besides the filter residua, we find the expected filtered versions of the redistribution terms and the filtered analogues for the dissipation and the pressure-work. The important fact that we gain from this form of the equation is that, besides the filter residua, there are no characteristically new terms added to the energy budget due to the filtering. This helps to interpret terms what will be obtained by further decomposition of the energy.

2.2.3.2 Split into Filtered Internal Energy and Filtered Kinetic Energy Mean and Fluctuation Form

The filtered total energy equation is just a sum of the transport equations for filtered internal energy and filtered kinetic energy which describe the filtered total energy as system of equations

$$\frac{\partial \overline{\rho}\widetilde{e}}{\partial t} + \nabla \cdot \overline{\vec{u}\rho h} = \nabla \cdot \vec{\bar{q}} + \overline{\vec{u} \cdot \nabla p} + \overline{\langle \tau, S \rangle_F} + \mathbb{D}_R^e \tag{2.57}$$

$$\frac{\partial \bar{\rho}\widetilde{e_{\text{kin}}}}{\partial t} + \nabla \cdot \overline{\vec{u}\rho\frac{1}{2}\vec{u}^2} = +\nabla \cdot \overline{\tau \cdot \vec{u}} - \overline{\vec{u} \cdot \nabla p} - \overline{\langle \tau, S \rangle_F} + \mathbb{D}_R^{e_{\text{kin}}}. \tag{2.58}$$

In the following, the terms on the RHS of this system are split into terms that contain large-scale contributions only and terms that couple the large scales with the small scales.

Filtered Internal Energy By adding and subtracting the respective large scale terms on the RHS of the filtered internal energy equation (eq. 2.50) we obtain the decomposed form

$$\frac{\partial \overline{\rho}\widetilde{e}}{\partial t} + \nabla \cdot \left(\widetilde{\vec{u}}\,\overline{\rho}\widetilde{h}\right) = \nabla \cdot \overline{\vec{q}} + \widetilde{\vec{u}} \cdot \nabla \overline{p} + \left\langle \overline{\tau}, \overline{S} \right\rangle_F - \nabla \cdot \underbrace{\left(\overline{\vec{u}\rho h} - \widetilde{\vec{u}}\,\overline{\rho}\widetilde{h}\right)}_{=:-c_{\text{h-u}}} + \underbrace{\left(\overline{\vec{u} \cdot \nabla p} - \widetilde{\vec{u}} \cdot \nabla \overline{p}\right)}_{=:\vartheta} + \underbrace{\left(\overline{\langle \tau, S \rangle_F} - \left\langle \overline{\tau}, \overline{S} \right\rangle_F\right)}_{=:\varepsilon} + \mathbb{D}^e_R. \quad (2.59)$$

The pure large-scale terms are fully described by the large-scale flow field and, in case of RANS simulation or LES, these terms do not need any modelling. The more interesting terms are the coupling terms that link large scales and small scales. The first one is $\nabla \cdot c_{\text{h-u}}$ with

$$c_{\text{h-u}} := -\left(\overline{\vec{u}\rho h} - \widetilde{\vec{u}}\,\overline{\rho}\widetilde{h}\right), \quad (2.60)$$

which is some sort of turbulent transport of internal energy. The other two linking terms are the small-scale/large-scale pressure-work

$$\vartheta := \left(\overline{\vec{u} \cdot \nabla p} - \widetilde{\vec{u}} \cdot \nabla \overline{p}\right), \quad (2.61)$$

and the small-scale/large-scale dissipation

$$\varepsilon := \left(\overline{\langle \tau, \nabla \vec{u} \rangle_F} - \left\langle \overline{\tau}, \nabla \widetilde{\vec{u}} \right\rangle_F\right). \quad (2.62)$$

Both terms represent the large-scale exchange of energy between kinetic energy and internal energy that is maintained by a combination of small-scales and large-scales. This might sound a bit confusing, but it is simply one case of the triadic energy transfer described by Brasseur & Yeung (1991). The actual transfer is happening at a large scale, but it has its origin and control in a combination of small scales and large scales. Substituting this into the latter equation we obtain the final equation for the filtered internal energy

$$\frac{\partial \overline{\rho}\widetilde{e}}{\partial t} + \nabla \cdot \left(\widetilde{\vec{u}}\,\overline{\rho}\widetilde{h}\right) = \nabla \cdot \overline{\vec{q}} + \widetilde{\vec{u}} \cdot \nabla \overline{p} + \left\langle \overline{\tau}, \overline{S} \right\rangle_F + \nabla \cdot c_{\text{h-u}} + \vartheta + \varepsilon + \mathbb{D}^e_R. \quad (2.63)$$

Filtered Kinetic Energy Equation The analogous procedure is applied to the transport term of the filtered kinetic energy equation (eq. 2.54) which leads to

$$\begin{aligned}\frac{\partial \frac{1}{2}\overline{\rho\vec{u}^2}}{\partial t} + \nabla\cdot\left(\tilde{\vec{u}}\frac{1}{2}\overline{\rho\vec{u}^2}\right) &= -\overline{\vec{u}\cdot\nabla p} + \nabla\cdot\left(\overline{\tau\cdot\vec{u}}\right) - \overline{\langle\tau, S\rangle_F} \\ &\quad - \nabla\cdot\underbrace{\left(\frac{1}{2}\overline{\rho\vec{u}\vec{u}^2} - \overline{\rho\vec{u}\otimes\vec{u}\vec{u}}\tilde{\vec{u}} + \bar{\rho}\tilde{\vec{u}}\otimes\tilde{\vec{u}}\tilde{\vec{u}} - \frac{1}{2}\tilde{\vec{u}}\overline{\rho\vec{u}^2}\right)}_{=:\chi} \\ &\quad - \nabla\cdot\left(\underbrace{\left(\overline{\rho\vec{u}\otimes\vec{u}} - \bar{\rho}\tilde{\vec{u}}\otimes\tilde{\vec{u}}\right)}_{=-\sigma}\cdot\tilde{\vec{u}}\right) + \mathbb{D}_R^{e_{\text{kin}}}. \end{aligned} \tag{2.64}$$

The filtered transport of the kinetic energy is now decomposed into a large-scale transport of the filtered kinetic energy $\nabla\cdot\left(\tilde{\vec{u}}\frac{1}{2}\overline{\rho\vec{u}^2}\right) = \nabla\cdot\left(\tilde{\vec{u}}\widetilde{e_{\text{kin}}}\right)$ and two terms that couple large scales with small scales just like we found for the internal energy. The first of both is known as the turbulent transport $\nabla\cdot\chi$ with

$$\chi := \frac{1}{2}\underbrace{\overline{\rho\vec{u}\otimes\vec{u}\vec{u}}}_{=\overline{\rho\vec{u}\vec{u}^2}} - \overline{\rho\vec{u}\otimes\vec{u}}\tilde{\vec{u}} + \bar{\rho}\tilde{\vec{u}}\otimes\tilde{\vec{u}}\tilde{\vec{u}} - \frac{1}{2}\tilde{\vec{u}}\overline{\rho\vec{u}^2}. \tag{2.65}$$

For filter operators that are Reynolds operators, this turbulent transport can be written in a potentially more familiar form

$$\chi = \frac{1}{2}\overline{\rho\vec{u}''\otimes\vec{u}''\vec{u}''} \tag{2.66}$$

$$= \frac{1}{2}\overline{\rho\vec{u}\otimes\vec{u}\vec{u}} - \overline{\rho\vec{u}''\otimes\vec{u}''}\tilde{\vec{u}} - \frac{1}{2}\bar{\rho}\tilde{\vec{u}}\otimes\tilde{\vec{u}}\tilde{\vec{u}} - \frac{1}{2}\tilde{\vec{u}}\overline{\rho\vec{u}''^2}. \tag{2.67}$$

The turbulent redistribution of large scale motion is governed by the term $\nabla\cdot\left(\sigma\cdot\tilde{\vec{u}}\right)$ that involves the small-scale stress tensor σ. When these terms are substituted and the remaining mixed terms are decomposed into their pure large-scale part and into their large-scale small-scale coupling part the latter equation takes the form

$$\begin{aligned}\frac{\partial\bar{\rho}\widetilde{e_{\text{kin}}}}{\partial t} + \nabla\cdot\left(\tilde{\vec{u}}\bar{\rho}\widetilde{e_{\text{kin}}}\right) &= \nabla\cdot\left(\sigma\cdot\tilde{\vec{u}}\right) + \nabla\cdot\left(\overline{\tau}\cdot\tilde{\vec{u}}\right) - \widetilde{\vec{u}}\cdot\nabla\bar{p} \\ &\quad - \left\langle\overline{\tau}, \nabla\tilde{\vec{u}}\right\rangle_F - \nabla\cdot\chi + \nabla\cdot\underbrace{\left(\overline{\tau\cdot\vec{u}} - \overline{\tau}\cdot\tilde{\vec{u}}\right)}_{=:c_{\tau\text{-u}}} \\ &\quad - \underbrace{\left(\overline{\vec{u}\cdot\nabla p} - \widetilde{\vec{u}}\cdot\nabla\bar{p}\right)}_{=:\vartheta} - \underbrace{\left(\overline{\langle\tau, \nabla\vec{u}\rangle_F} - \left\langle\overline{\tau}, \nabla\tilde{\vec{u}}\right\rangle_F\right)}_{=:\varepsilon} + \mathbb{D}_R^{e_{\text{kin}}}. \end{aligned} \tag{2.68}$$

Besides the turbulent dissipation ε and the turbulent pressure-work ϑ that are part of the filtered internal energy equation as well, there are two more large-scale small-scale coupling terms. The turbulent kinetic energy diffusion $\nabla\cdot c_{\tau-u}$ with

$$c_{\tau-u} := \overline{\tau\cdot\vec{u}} - \overline{\tau}\cdot\tilde{\vec{u}} \tag{2.69}$$

is contributing to the development of the filtered kinetic energy.

Filtered Total Energy Split into $\tilde{e}$ and $\widetilde{e_{\mathbf{kin}}}$ with LS and SS Contributions
Substituting the latter definitions into the previous form of the filtered kinetic energy equation allows to write the system (eq. 2.57 ,2.58) in the form

$$\begin{aligned}
\frac{\partial \bar{\rho}\widetilde{e}}{\partial t} + \nabla\cdot\left(\tilde{\vec{u}}\,\bar{\rho}\tilde{h}\right) =& \nabla\cdot\bar{\vec{q}} + \nabla\cdot c_{\text{h-u}} + \widetilde{\vec{u}}\cdot\nabla\bar{p} + \left\langle\bar{\tau},\nabla\tilde{\vec{u}}\right\rangle_F + \vartheta + \varepsilon + \mathbb{D}_R^e \\
\frac{\partial \bar{\rho}\widetilde{e_{\text{kin}}}}{\partial t} + \nabla\cdot\left(\tilde{\vec{u}}\bar{\rho}\widetilde{e_{\text{kin}}}\right) =& \nabla\cdot\left(\bar{\tau}\cdot\tilde{\vec{u}}\right) + \nabla\cdot c_{\tau\text{-u}} - \nabla\cdot\chi + \nabla\cdot\left(\sigma\cdot\tilde{\vec{u}}\right) \\
& - \widetilde{\vec{u}}\cdot\nabla\bar{p} - \left\langle\bar{\tau},\nabla\tilde{\vec{u}}\right\rangle_F - \vartheta - \varepsilon + \mathbb{D}_R^{e_{\text{kin}}}.
\end{aligned} \tag{2.70}$$

This form of the filtered total energy can be used in RANS simulations and LES when no additional transport equation for the small scales should be used. The terms containing large-scale information only are the ones LES and RANS simulations are solving for and are therefore known. But the remaining terms need to be modelled to close the system. For filter operators that are not commuting with differential operators the filter residua are covering the respective additional contributions and may have significant impact on the development of the energies as well as on the momentum and density development. Vasilyev *et al.* (1998) derived commuting filter operators to avoid these residua in LES. But if non-commutative filter operators are used it is essential to take their residua into account when simulating the large-scale flow. However, to the author's best knowledge, this form of large scale equations including the filter residual terms is novel. We suggest that this system of equations should be used for LES with inhomogeneous explicit or implicit filter operators.
Figure (fig. 2.6) illustrates the energy distribution process in this split system of equations. Besides the use for RANS simulations and LES we can use this form of the energy equation to understand the energy redistribution processes that happen in a flow. Whereas the brighter coloured terms in the system represent the processes governed by large scales only, the darker coloured terms are the terms that couple large scales with small scales. For example it is now obvious that the transfer between the filtered kinetic energy and the filtered internal energy is not only governed by large scales. Although (due to the filter operation applied on the whole system) only the large scale energy transfers are in this system, it is obvious that turbulent dissipation as well as turbulent pressure-work are contributing to this process. However, these quantities are large-scale small-scale combinations. Here we can see that the small scales are interacting with the large scales. On the other hand the actual cascading process which builds the core of turbulence is still hidden in the transport term for the filtered kinetic energy. To unveil this process is the aim of the next and last decomposition that we apply to energy.

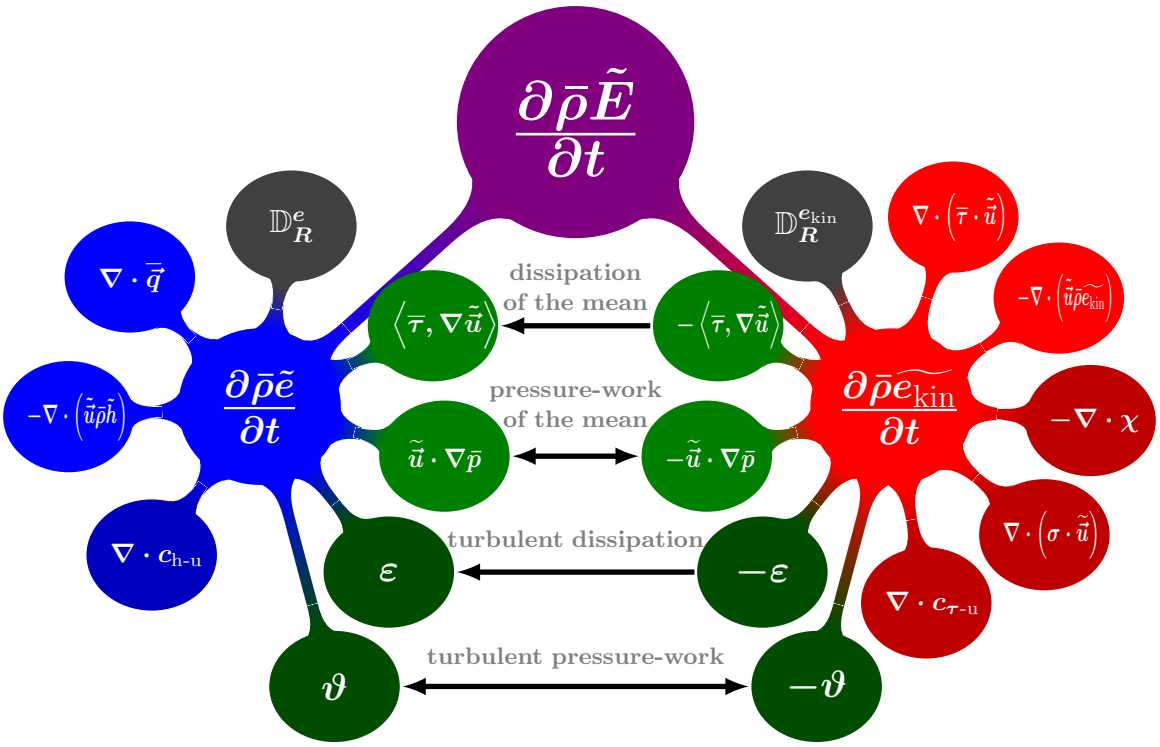

Figure 2.6: Illustration of the transport equation for the filtered total energy $\bar{\rho}\tilde{E}$ split into a filtered internal energy $\bar{\rho}\tilde{e}$ contribution and a filtered kinetic energy $\bar{\rho}\widetilde{e_{\text{kin}}}$ contribution. All terms are split into pure large-scale contribution and their remainders.

2.2.3.3 Split into Filtered Internal Energy, Kinetic Energy of Filtered Velocity and Filtered Fluctuation Energy

This is the final and most important step of the decomposition of the filtered energy equation. In this step a part of the cascading process is exposed and decoupled from the transport of kinetic energy. The filtered total energy was split into the filtered internal energy and the filtered kinetic energy in the previous section. The filtered kinetic energy is now further decomposed into the kinetic energy that is related to the motion of the filtered flow field

$$e_f := \frac{1}{2}\tilde{\vec{u}}^2 \tag{2.71}$$

and the filtered kinetic fluctuation energy

$$k := \frac{1}{2}\left(\widetilde{\vec{u}^2} - \tilde{\vec{u}}^2\right). \tag{2.72}$$

The decomposition then reads

$$\begin{aligned}\bar{\rho}\tilde{E} &= \bar{\rho}\tilde{e} + \bar{\rho}\widetilde{e_{\text{kin}}} \\ &= \bar{\rho}\tilde{e} + \bar{\rho}\frac{1}{2}\widetilde{\vec{u}^2} \\ &= \bar{\rho}\tilde{e} + \bar{\rho}\underbrace{\frac{1}{2}\tilde{\vec{u}}^2}_{=e_f} + \bar{\rho}\left(\underbrace{\frac{1}{2}\widetilde{\vec{u}^2} - \frac{1}{2}\tilde{\vec{u}}^2}_{=k}\right) \\ &= \bar{\rho}\tilde{e} + \bar{\rho}e_f + \bar{\rho}k.\end{aligned} \tag{2.73}$$

To derive the transport equations for the newly defined quantities e_f and k we have to start from the filtered flow field.

Kinetic Energy Equation of the Filtered Velocity To obtain the governing equation for the kinetic energy of the filtered velocity we need to multiply the filtered transport equation (eq. 2.42) by the filtered velocity $\tilde{\vec{u}}$ and subtract the filtered continuity equation (eq. 2.35) multiplied by half the filtered velocity squared $\frac{1}{2}\tilde{\vec{u}}^2$ multiplied

$$\text{Transport-Eq}(\bar{\rho}\frac{1}{2}\tilde{\vec{u}}^2) = \tilde{\vec{u}} \cdot \text{Transport-Eq}(\bar{\rho}\tilde{\vec{u}}) - \frac{1}{2}\tilde{\vec{u}}^2\text{Transport-Eq}(\bar{\rho}). \tag{2.74}$$

With some transformations which can be found in the appendix (A.17) this leads to the transport equation for the kinetic energy of the filtered motions of the flow

$$\begin{aligned}&\frac{\partial\bar{\rho}\frac{1}{2}\tilde{\vec{u}}^2}{\partial t} + \nabla\cdot\left(\bar{\rho}\tilde{\vec{u}}\frac{1}{2}\tilde{\vec{u}}^2\right) = \nabla\cdot\left(\sigma\cdot\tilde{\vec{u}}\right) - \tilde{\vec{u}}\cdot\nabla\bar{p} + \nabla\cdot\left(\bar{\tau}\cdot\tilde{\vec{u}}\right) - \left\langle\bar{\tau},\nabla\tilde{\vec{u}}\right\rangle_F \\ &- \left\langle\sigma,\nabla\tilde{\vec{u}}\right\rangle_F - \underbrace{\tilde{\vec{u}}\cdot[\nabla\cdot(\rho\vec{u}\otimes\vec{u})]_R}_{=:\mathbb{T}_R^{\text{mom}}} + \underbrace{\frac{1}{2}\tilde{\vec{u}}^2[\nabla\cdot(\rho\vec{u})]_R}_{=:\mathbb{T}_R^{\rho}} - \underbrace{\tilde{\vec{u}}\cdot[\nabla p]_R}_{=:\mathbb{T}_R^{\text{press}}} + \underbrace{\tilde{\vec{u}}\cdot[\nabla\cdot\tau]_R}_{=:\mathbb{T}_R^{\text{diff}}}.\end{aligned} \tag{2.75}$$

Unlike in the previous equations the filtered residua $\mathbb{T}_R^{\text{mom}}$, $\mathbb{T}_R^{\rho}$, $\mathbb{T}_R^{\text{press}}$ and $\mathbb{T}_R^{\text{diff}}$ in this equation do not have a diffusive character. As we see later, they will contribute to the inter-scale transfer of energy and are therefore noted with a $\mathbb{T}$. To simplify the notation they are all combined into a transfer filter residuum for the filtered kinetic energy

$$\mathbb{T}_R^{e_{\text{kin}}} := -\mathbb{T}_R^{\text{mom}} + \mathbb{T}_R^{\rho} - \mathbb{T}_R^{\text{press}} + \mathbb{T}_R^{\text{diff}}. \tag{2.76}$$

Substituting this into equation (2.75) we obtain the final form of the transport equation governing e_f

$$\begin{aligned}&\frac{\partial\bar{\rho}\frac{1}{2}\tilde{\vec{u}}^2}{\partial t} + \nabla\cdot\left(\bar{\rho}\tilde{\vec{u}}\frac{1}{2}\tilde{\vec{u}}^2\right) = \\ &\qquad\nabla\cdot\left(\sigma\cdot\tilde{\vec{u}}\right) - \tilde{\vec{u}}\cdot\nabla\bar{p} + \nabla\cdot\left(\bar{\tau}\cdot\tilde{\vec{u}}\right) - \left\langle\bar{\tau},\nabla\tilde{\vec{u}}\right\rangle_F - \left\langle\sigma,\nabla\tilde{\vec{u}}\right\rangle_F + \mathbb{T}_R^{e_{\text{kin}}}.\end{aligned} \tag{2.77}$$

Filtered Fluctuation Energy The filtered fluctuation energy equation is obtained by subtracting the equation for the kinetic energy of the filtered velocity (eq. 2.77) from the filtered kinetic energy equation (eq. 2.68)

$$\text{Transport-Eq}(\bar{\rho}k) = \text{Transport-Eq}(\frac{1}{2}\overline{\rho\vec{u}^2}) - \text{Transport-Eq}(\frac{1}{2}\bar{\rho}\tilde{\vec{u}}^2). \tag{2.78}$$

This equation takes the form

$$\frac{\partial \bar{\rho}k}{\partial t} + \nabla\cdot\left(\tilde{\vec{u}}\bar{\rho}k\right) = \nabla\cdot c_{\tau\text{-u}} - \nabla\cdot\chi + \left\langle\sigma, \nabla\tilde{\vec{u}}\right\rangle_F - \vartheta - \varepsilon - \mathbb{T}_R^{e_{\text{kin}}} + \mathbb{D}_R^{e_{\text{kin}}}. \tag{2.79}$$

For the cases when the filter operator fulfils the properties of a Reynolds operator, as is the case for the RANS equations, the equation for the filtered kinetic fluctuation energy can be written as

$$\begin{aligned}\frac{\partial \bar{\rho}k}{\partial t} + \nabla\cdot\left(\tilde{\vec{u}}\bar{\rho}k\right) = \nabla\cdot\left(\overline{\tau\cdot\vec{u}''}\right) - \nabla\cdot\chi \\ + \left\langle\sigma, \nabla\tilde{\vec{u}}\right\rangle_F + \overline{\vec{u}''\cdot\nabla p'} - \overline{\vec{u}''}\cdot\nabla\bar{p} - \overline{\langle\tau, \nabla\vec{u}''\rangle_F}.\end{aligned} \tag{2.80}$$

(please consider that τ is going in as instantaneous value)

Filtered Total Energy split into $\tilde{e}$, e_f and k Considering the previous derivations it can be seen that the development of the filtered total energy can be decomposed into a system of three coupled equations. These equations describe the development of the filtered internal energy $\bar{\rho}\tilde{e}$, the development of the kinetic energy of the large-scale motions $\bar{\rho}e_f$ and the filtered kinetic energy of the small scale motions k. This is the final form of the equations that will be used of investigations of the cascading process in this work.

$$\begin{aligned}\frac{\partial \bar{\rho}\widetilde{e}}{\partial t} + \nabla\cdot\left(\tilde{\vec{u}}\bar{\rho}\tilde{h}\right) =& \nabla\cdot\bar{\vec{q}} + \nabla\cdot c_{\text{h-u}} + \tilde{\vec{u}}\cdot\nabla\bar{p} + \left\langle\bar{\tau}, \nabla\tilde{\vec{u}}\right\rangle_F + \vartheta + \varepsilon + \mathbb{D}_R^e \\ \frac{\partial \bar{\rho}e_{\text{f}}}{\partial t} + \nabla\cdot\left(\bar{\rho}\tilde{\vec{u}}e_{\text{f}}\right) =& \nabla\cdot\left(\sigma\cdot\tilde{\vec{u}}\right) + \nabla\cdot\left(\bar{\tau}\cdot\tilde{\vec{u}}\right) \\ & - \tilde{\vec{u}}\cdot\nabla\bar{p} - \left\langle\bar{\tau}, \nabla\tilde{\vec{u}}\right\rangle_F - \left\langle\sigma, \nabla\tilde{\vec{u}}\right\rangle_F + \mathbb{T}_R^{e_{\text{kin}}} \\ \frac{\partial \bar{\rho}k}{\partial t} + \nabla\cdot\left(\tilde{\vec{u}}\bar{\rho}k\right) =& \nabla\cdot c_{\tau\text{-u}} - \nabla\cdot\chi + \left\langle\sigma, \nabla\tilde{\vec{u}}\right\rangle_F - \vartheta - \varepsilon - \mathbb{T}_R^{e_{\text{kin}}} + \mathbb{D}_R^{e_{\text{kin}}}\end{aligned} \tag{2.81}$$

The system of the filtered energy equations (eq. 2.81) together with the filtered equations to conserve continuity (eq. 2.35) and momentum (eq. 2.42) and the filtered equation of state (eq. 2.46) describes the development of the filtered flow field governed by the Navier-Stokes equations. With the respective turbulence models it can be used to conduct RANS simulations and LES and even hybrid simulations. The presented description of the filtered equations allows inhomogeneous filter operators and is as such a novelty to the best of the author's knowledge.

In contrast, the system of filtered energies split into internal and kinetic contribution

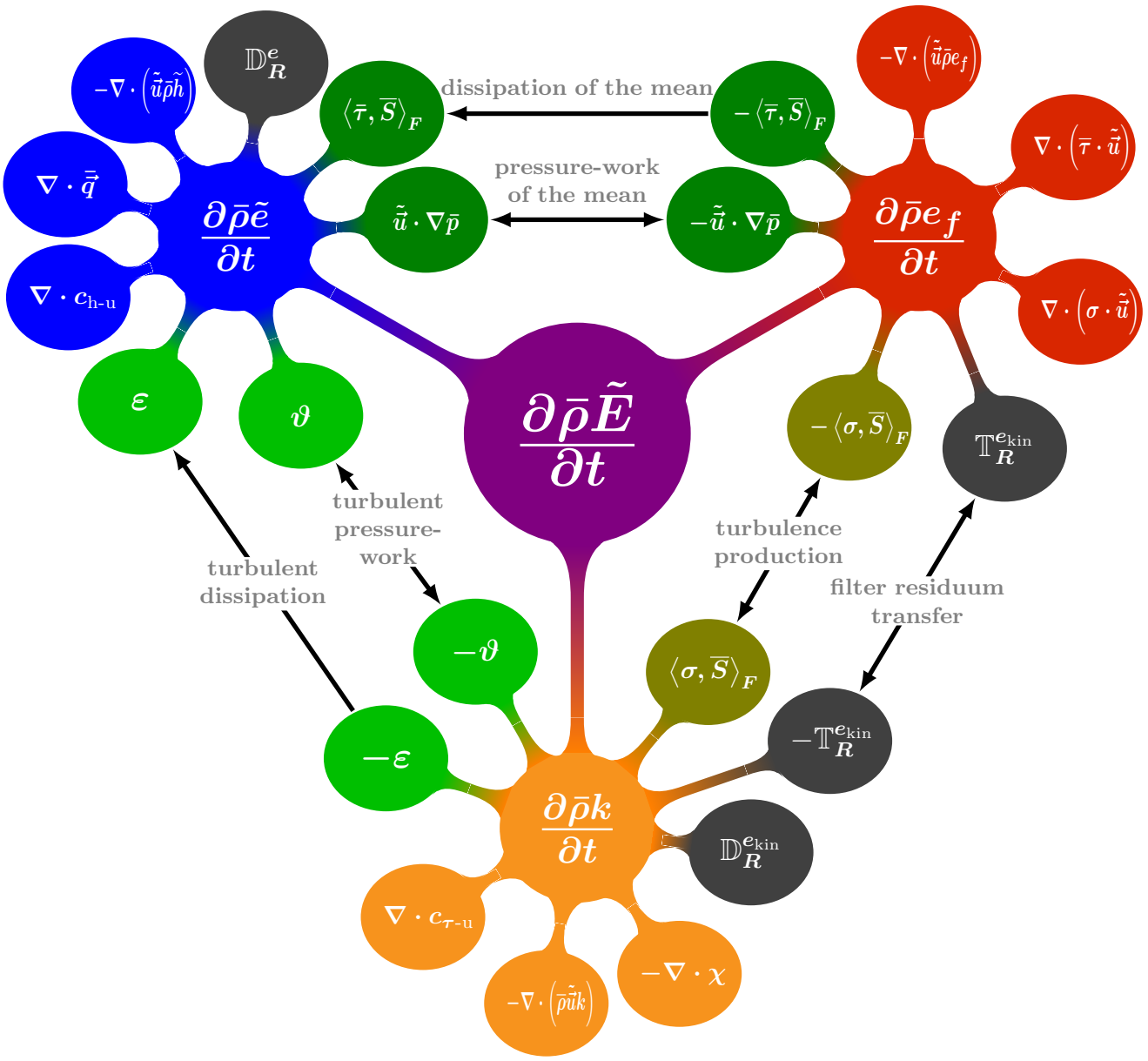

Figure 2.7: Illustration of the transport equation for the filtered total energy $\bar{\rho}\tilde{E}$ split into a filtered internal energy $\bar{\rho}\tilde{e}$ contribution, a contribution of the kinetic energy of the large-scale motions $\bar{\rho}e_f$ and a contribution of the filtered kinetic energy of the small scale motions k. It represents the system of equations (eq. 2.81).

(eq. 2.70) contained $\widetilde{e_{\text{kin}}}$ as term that contains pure large-scale as well mixed large-scale small-scale terms. This system is now fully decomposed. The terms that govern the large scales of motion are clustered in the transport equation for e_f and the terms that govern the small scale motions that interact with the large scales are clustered in the transport equation for k. Now we can see that the exchange of energy between internal and kinetic energy can be split into two parts. A large-scale part with the *dissipation of the mean* and *pressure-work of the mean* and a small-scale part with the *turbulent dissipation* and the *turbulent pressure-work*. Both parts are playing an important role

for turbulence in that these terms regulate how much of the kinetic energy decays and therefore how much kinetic energy remains in the turbulence. Besides the inter-scale kinetic energy process we investigate the dissipation mechanism in this work.

The main reason for the decomposition presented in the last pages was to be able to expose part of the cascading process (1.2.1) that drives the turbulence. This cascade is now dissected at the point were the large scales of motion, defined by the filter operator, are interacting with the small scales of motion in the flow. This term is called the *turbulent production* and reads as $\langle \sigma, \nabla \tilde{\vec{u}} \rangle_F$. On the one hand the production involves the Favre stress/sub-grid stress tensor σ that is a small scale feature; on the other hand it involves the gradient of the filtered velocities $\nabla \tilde{\vec{u}}$ which is a large-scale feature. The Favre stress/sub-grid stress tensor by itself is already a product of two velocities, which implies that it potentially covers two scales. With the third scale added by the large-scale gradient we have a hint that this could be the physical analogue to the triadic cascading process that Brasseur & Yeung (1991) discussed in their work. The large-scale gradient could be interpreted as a kind of control parameter, that controls the scale transfer between small scales and large scales. Such interpretations would direct towards conclusions about large-scale modulation of small scale fluctuation as shown, e.g., by Ganapathisubramani *et al.* (2012). This cascading process will be studied in great detail in this work.

Additional to the natural transfer of kinetic energy across different scales this system of equations reveals the transfer due to inhomogeneous non-commutating filter operators. How significant this artificial transfer is, will be investigated for different filter operators.

2.3 Compressible Velocity Gradient Dynamics

In this section the focus lies on the dynamics of the velocity gradient. This gradient is an important quantity in several aspects.
As already mentioned in the previous section the velocity gradient takes an important role in the cascading process that drives turbulence. It is a direct part of the non-linear kinetic energy transport

$$\frac{1}{2}\nabla\cdot(\rho\vec{u}\otimes\vec{u}\cdot\vec{u}) = \langle\rho\vec{u}\otimes\vec{u},\nabla\vec{u}\rangle_F + \frac{1}{2}\vec{u}^2\nabla\cdot(\rho\vec{u}) \tag{2.82}$$

which drives the energy cascade. Further its large-scale part $\nabla\tilde{\vec{u}}$ is, via the turbulent production $\langle\sigma,\nabla\tilde{\vec{u}}\rangle_F$, possibly involved in the large-scale small-scale modulation process presented by Ganapathisubramani *et al.* (2012).
As it was discussed in the introduction (1.2.2), the velocity gradient invariants and their dynamics are useful tool to study the character and development of turbulence. In the next chapter these dynamics will be derived for compressible flows. The velocity gradient dynamics, derived and outlined in this chapter, will build the basis for that derivation. Further, the velocity gradient is the basis for dissipation and enstrophy which are subject of this study. Dissipation needs to be investigated in several aspects as outlined in the previous section. Enstrophy is a measure of vortical motions and as such an important quantity of turbulence. In the context of vortex stretching we want to study the enstrophy production which is part of the enstrophy dynamics and will we outlined in this chapter.
For these reasons it is necessary to derive and present the dynamics for the velocity gradient and related quantities in this section.

2.3.1 Velocity Gradient Dynamics

The dynamics for the velocity gradient $A := \nabla\vec{u}$ are obtained by the following schematic formula

$$\text{Transport}(\nabla\vec{u}) = \nabla\left(\frac{\text{Transport}(\rho\vec{u}) - \vec{u}\,\text{Transport}(\rho)}{\rho}\right). \tag{2.83}$$

The continuity equation (2.1) multiplied by the velocity vector is subtracted from the momentum equation (2.2). The result is divided by the density and finally the gradient is taken of the entire equation. This leads to the dynamics for the velocity gradient

$$\frac{dA}{dt} := \frac{\partial A}{\partial t} + (\vec{u}\cdot\nabla)A = -AA + H. \tag{2.84}$$

The source term H

$$H := \Gamma - \Sigma \tag{2.85}$$

combines the viscous effects Γ acting on the velocity gradient

$$\Gamma = \nabla(\frac{1}{\rho}\nabla \cdot \tau), \tag{2.86}$$

with the pressure-density term Σ

$$\Sigma = \nabla(\frac{1}{\rho}\nabla p). \tag{2.87}$$

An equivalent form of the matrix Σ is

$$\Sigma = \frac{1}{\rho}C - \frac{1}{\rho^2}B, \tag{2.88}$$

where C is the symmetric pressure-Hessian

$$C = \nabla(\nabla p) \tag{2.89}$$

and B is the baroclinic matrix

$$B = \nabla p \otimes \nabla \rho. \tag{2.90}$$

For the derivation of the velocity gradient invariants we need to derive the evolution of the second and third power of the velocity gradient tensor. The evolution of the second power is

$$\begin{aligned} \frac{dA^2}{dt} &= -2\ A^3 - A\Sigma - \Sigma A + A\Gamma + \Gamma A \\ &= -2\ A^3 + AH + HA. \end{aligned} \tag{2.91}$$

The evolution of the third power is

$$\begin{aligned} \frac{dA^3}{dt} &= -3\ A^4 - A^2\Sigma - A\Sigma A - \Sigma A^2 + \Gamma A^2 + A^2\Gamma + A\Gamma A \\ &= -3\ A^4 + A^2H + AHA + HA^2. \end{aligned} \tag{2.92}$$

Defining the magnitude of the velocity gradient A as its Frobenius norm $||A||_F$ we can define the evolution of this magnitude squared $||A||_F^2$ by piecewise multiplying A to (eq. 2.84) (i.e. applying the Hilbert-Schmidt inner product $\langle A, \cdot \rangle_F$ to (eq. 2.84))

$$\begin{aligned} \frac{1}{2}\frac{d||A||_F^2}{dt} &= \frac{1}{2}\frac{d\langle A, A\rangle_F}{dt} \\ &= \langle A, \frac{dA}{dt}\rangle_F \\ &= -\langle A, A^2\rangle_F + \langle A, H\rangle_F, \end{aligned} \tag{2.93}$$

2.3.2 Strain Rate Dynamics

The strain rate tensor S is defined as the symmetric part of the velocity gradient tensor, $S := \frac{1}{2}(A + A^t)$. With the identity $AA + (AA)^t = 2SS + 2\Omega\Omega$ we obtain the evolution

equation for the strain rate tensor S from equation (2.84):

$$\frac{dS}{dt} = -SS - \Omega\Omega + \frac{1}{2}\left(H + H^t\right). \tag{2.94}$$

Applying the Hilbert-Schmidt inner product $\langle S, \cdot \rangle_F$ to equation (2.94), knowing that $\langle S, \Omega\Omega \rangle_F = \frac{1}{4}\vec{\omega}^t S \vec{\omega}$ and $\langle M, N^t \rangle_F = \langle M^t, N \rangle_F$, leads to the evolution of the strain rate magnitude squared:

$$\begin{aligned}
\frac{d||S||_F^2}{dt} &= \frac{d\langle S, S\rangle_F}{dt} \\
&= 2\langle S, \frac{dS}{dt}\rangle_F \\
&= -2\langle S, SS\rangle_F - 2\langle S, \Omega\Omega\rangle_F - \langle S, H + H^t\rangle_F \\
&= -2\langle S, SS\rangle_F - 2\langle S, \Omega\Omega\rangle_F - 2\langle S, H\rangle_F \\
&= -2\langle S, SS\rangle_F - \frac{1}{2}\vec{\omega}^t S \vec{\omega} - 2\langle S, H\rangle_F,
\end{aligned} \tag{2.95}$$

where $\vec{\omega}$ is the vorticity vector which is defined as

$$\vec{\omega} := \nabla \times \vec{u} = \begin{pmatrix} \frac{\partial u_3}{\partial x_2} - \frac{\partial u_2}{\partial x_3} \\ \frac{\partial u_1}{\partial x_3} - \frac{\partial u_3}{\partial x_1} \\ \frac{\partial u_2}{\partial x_1} - \frac{\partial u_1}{\partial x_2} \end{pmatrix}.$$

2.3.3 Rotation Rate Dynamics

The rotation rate tensor is defined as the skew-symmetric part of the velocity gradient tensor, $\Omega := \frac{1}{2}(A - A^t)$. With the identity $AA - (AA)^t = 2S\Omega + 2\Omega S$ we obtain the evolution equation for the rotation rate tensor from equation (2.84):

$$\frac{d\Omega}{dt} = -S\Omega - \Omega S + \frac{1}{2}\left(H - H^t\right). \tag{2.96}$$

With the identity for vorticity vector and rotation rate tensor

$$\Omega = \frac{1}{2}\begin{pmatrix} 0 & -\omega_3 & \omega_2 \\ \omega_3 & 0 & -\omega_1 \\ -\omega_2 & \omega_1 & 0 \end{pmatrix}$$

we obtain the **dynamics of the vorticity** vector from equation (2.96)

$$\frac{d\vec{\omega}}{dt} = \frac{\partial \vec{\omega}}{\partial t} + (\vec{u}\cdot\nabla)\vec{\omega} = (\vec{\omega}\cdot\nabla)\vec{u} - \vec{\omega}(\nabla\cdot\vec{u}) + \frac{1}{\rho^2}\nabla\rho\times\nabla p + \nabla\times\left(\frac{\nabla\cdot\tau}{\rho}\right). \tag{2.97}$$

Applying the Hilbert-Schmidt inner product $\langle \Omega, \cdot \rangle_F$ to this equation (2.96), knowing that $\langle \Omega, S\Omega \rangle_F = -\langle \Omega\Omega, S \rangle_F$, leads to the evolution of the enstrophy, which is the magnitude

of vorticity squared:

$$\begin{aligned}\frac{d\|\Omega\|_F^2}{dt} &= \frac{d\langle\Omega,\Omega\rangle_F}{dt}\\ &= 2\langle\Omega,\frac{d\Omega}{dt}\rangle_F\\ &= -2\langle\Omega,S\Omega\rangle_F - 2\underbrace{\langle\Omega,\Omega S\rangle_F}_{=\langle\Omega,S\Omega\rangle_F} + \langle\Omega,H\rangle_F - \underbrace{\langle\Omega,H^t\rangle_F}_{=-\langle\Omega,H\rangle_F}\\ &= -4\langle\Omega,S\Omega\rangle_F + 2\langle\Omega,H\rangle_F\\ &= 4\langle\Omega\Omega,S\rangle_F + 2\langle\Omega,H\rangle_F.\end{aligned} \tag{2.98}$$

Substituting the identity $\langle\Omega\Omega,S\rangle_F = \frac{1}{4}\vec{\omega}^t S\vec{\omega}$ and the enstrophy $\frac{1}{2}\vec{\omega}^2 = \langle\Omega,\Omega\rangle_F$ this equation can also be written in a different notation in form of the **enstrophy equation**

$$\frac{1}{2}\frac{d\vec{\omega}^2}{dt} = \vec{\omega}^t S\vec{\omega} + \langle\Omega,H\rangle_F. \tag{2.99}$$

2.4 Compressible Velocity Gradient Invariant Dynamics

In chapter (1.2.2) the critical point analysis (Perry & Chong, 1987) was outlined and its importance as a tool to investigate the character and development of turbulence was shown. To summarize very roughly what Meneveau (2011) discusses in a review about the Lagrangian dynamics and the velocity gradient: the velocity gradient invariants allow us to classify turbulent structures in distinct characteristic groups. The dynamics of the velocity gradient then allows us to understand the characteristic development of the turbulent structures. Understanding these dynamics and their meaning in the context of turbulent scale transfer can lead to significant improvement in understanding turbulence and lead to improvements in turbulence models. Even though the invariants of the velocity gradient are known for general compressible flows, the dynamics of the same are only developed for incompressible flows, as outlined in the introduction (eq. 1.30). To the author's best knowledge, the fully compressible velocity gradient invariant dynamics is a novel contribution to fluid dynamics research. The derivation of these dynamics is the subject of this chapter.

2.4.1 Velocity Gradient Invariants

The first three invariants P, Q and R of 3×3 matrix A are defined via the characteristic polynomial of the matrix A

$$p_{\text{char}}(\alpha) := \det(A-\alpha I) = \alpha^3 + P\alpha^2 + Q\alpha + R \tag{2.100}$$

and can be calculated as

$$\begin{aligned} P =& -\operatorname{trace}(A) \\ Q =& \frac{1}{2}\left((\operatorname{trace}(A))^2 - \operatorname{trace}(AA)\right) \\ R =& -\det(A). \end{aligned} \tag{2.101}$$

For the application of the velocity gradient of a flow field following the Navier-Stokes equations the invariant are then interpreted as follows.
The first invariant P is defined as the additive inverse of the dilatation, which is the additive inverse of the divergence of the velocity vector

$$\begin{aligned} P :=& -\operatorname{trace}(A) \\ =& -\nabla \cdot \vec{u}. \end{aligned} \tag{2.102}$$

This invariant is a measure for the rate of compression as we can find the dilatation as part of a source term in the continuity equation governing the density.
The second invariant Q

$$\begin{aligned} Q :=& \frac{1}{2}\left(\operatorname{trace}(A)^2 - \operatorname{trace}(A^2)\right) \\ =& \frac{1}{2}\left(P^2 - \operatorname{trace}(A^2)\right) \end{aligned} \tag{2.103}$$

can be rewritten by substituting the definition for the Hilbert-Schmidt inner product (def. 2.2) for $\operatorname{trace}(A^2)$

$$\begin{aligned} Q =& \frac{1}{2}\left(P^2 - \langle A, A^T\rangle_F\right) \\ =& \frac{1}{2}\left(P^2 - \langle S, S\rangle_F + \langle \Omega, \Omega\rangle_F\right). \end{aligned} \tag{2.104}$$

In this form it becomes obvious that, besides the compression term P^2, the second invariant Q is a measure for the absolute imbalance of rotation rate and strain rate. For small compression effects, positive values of Q state an overshoot of rotation rate over stain rate whereas negative values indicate the opposite.
The third invariant R is the additive inverse of the determinant of the velocity gradient tensor

$$\begin{aligned} R :=& -\det(A) \\ =& -\frac{1}{6}\left(\underbrace{\operatorname{trace}(A)^3}_{=-P^3} - 3\ \underbrace{\operatorname{trace}(A)}_{=-P}\underbrace{\operatorname{trace}(A^2)}_{=P^2-2Q} + 2\ \operatorname{trace}(A^3)\right) \\ =& -\frac{1}{3}\left(P^3 - 3PQ + \operatorname{trace}(A^3)\right). \end{aligned} \tag{2.105}$$

This equation can be transformed by substituting the definition for the Hilbert-Schmidt inner product (def. 2.2) for $\text{trace}(A^3) = \text{trace}(A^2 A)$

$$\begin{aligned} R &= -\frac{1}{3}\left(P^3 - 3PQ + \langle A^2, A^T\rangle_F\right) \\ &= -\frac{1}{3}\left(P^3 - 3PQ + \langle (S+\Omega)^2, (S+\Omega)^T\rangle_F\right) \end{aligned} \tag{2.106}$$

For further transformation of the third invariant, the following identity is useful

$$\begin{aligned} \langle (S+\Omega)^2, (S+\Omega)^T\rangle_F =& \langle SS, S\rangle_F + \langle S\Omega, S\rangle_F + \langle \Omega S, S\rangle_F + \langle \Omega\Omega, S\rangle_F \\ &+ \langle SS, \Omega^T\rangle_F + \langle S\Omega, \Omega^T\rangle_F + \langle \Omega S, \Omega^T\rangle_F + \langle \Omega\Omega, \Omega^T\rangle_F \\ =& \langle SS, S\rangle_F + \langle S\Omega, S\rangle_F + \langle \Omega S, S\rangle_F + \langle \Omega\Omega, S\rangle_F \\ &- \langle SS, \Omega\rangle_F - \langle S\Omega, \Omega\rangle_F - \langle \Omega S, \Omega\rangle_F - \underbrace{\langle \Omega\Omega, \Omega\rangle_F}_{=0} \\ =& \langle SS, S\rangle_F + \underbrace{\langle \Omega, SS\rangle_F}_{=0} + \underbrace{\langle \Omega, SS\rangle_F}_{=0} + \langle \Omega\Omega, S\rangle_F \\ &\underbrace{-\langle SS, \Omega\rangle_F}_{=0} - \langle S, \Omega^T\Omega\rangle_F - \langle S, \Omega\Omega^T\rangle_F \\ =& \langle SS, S\rangle_F + \langle \Omega\Omega, S\rangle_F + \langle S, \Omega\Omega\rangle_F + \langle S, \Omega\Omega\rangle_F \\ =& \langle SS, S\rangle_F + 3\langle \Omega\Omega, S\rangle_F. \end{aligned} \tag{2.107}$$

Applying this to the previous expression of the third invariant R leads to the form

$$\begin{aligned} R &= -\frac{1}{3}\left(P^3 - 3PQ + \langle S^2, S\rangle_F + 3\langle \Omega^2, S\rangle_F\right) \\ &= -\frac{1}{3}\left(P^3 - 3PQ + \underbrace{\langle S^2, S\rangle_F + \langle \Omega^2, S\rangle_F}_{=-2\mathcal{P}_{\|S\|_F^2}} + \underbrace{2\langle \Omega^2, S\rangle_F}_{=2\mathcal{P}_{\|\Omega\|_F^2}}\right), \end{aligned} \tag{2.108}$$

where $\mathcal{P}_{\|S\|_F^2}$ and $\mathcal{P}_{\|\Omega\|_F^2}$ are the production of the strain rate squared and the rotation rate squared respectively. For low compressible effects this means that whereas Q is the balance of strain rate and rotation rate, R is the balance of their respective productions. Another invariant of the velocity gradient is the discriminant of the characteristic polynomial

$$\Delta := -\frac{1}{4}P^2Q^2 + Q^3 + P^3R + \frac{27}{4}R^2 - \frac{18}{4}PQR. \tag{2.109}$$

2.4.2 First Invariant Dynamics

With the definition of the first invariant of the velocity gradient tensor (2.102) we obtain its evolution by taking the trace of the velocity gradient tensor evolution (2.84) and

multiplying it by -1

$$\begin{aligned}\frac{dP}{dt} =& -\operatorname{trace}(\frac{dA}{dt})\\ =&\operatorname{trace}(AA) - \operatorname{trace}(H)\\ =&P^2 - 2\ Q - \operatorname{trace}(H).\end{aligned} \tag{2.110}$$

2.4.3 Second Invariant Dynamics

We can simplify the following derivations if we split the pressure and viscous stress matrix H into a traceless part $H*$ and a diagonal matrix containing the trace information

$$H = H^* + \frac{1}{3}\operatorname{trace}(H)I. \tag{2.111}$$

This decomposition will be used for all terms that involve H. The following identity will be used to simplify the dynamics for the second invariant

$$\begin{aligned}\operatorname{trace}(AH) =&\operatorname{trace}\left(A\left(H^* + \frac{1}{3}\operatorname{trace}(H)I\right)\right)\\ =&\operatorname{trace}(AH^*) + \operatorname{trace}\left(A\frac{1}{3}\operatorname{trace}(H)I\right)\\ =&\operatorname{trace}(AH^*) + \frac{1}{3}\operatorname{trace}(H)\operatorname{trace}(A).\end{aligned} \tag{2.112}$$

With the definition of the second invariant of the velocity gradient tensor (2.103) we obtain its evolution by subtracting the trace of the second velocity gradient tensor evolution (2.91) from the evolution of P (2.110) squared

$$\begin{aligned}\frac{dQ}{dt} =&\frac{1}{2}\left(2\ P\frac{dP}{dt} - \operatorname{trace}(\frac{dA^2}{dt})\right)\\ =&\underbrace{P^3 - 2\ QP + \operatorname{trace}(A^3)}_{=QP-3\ R} - P\ \operatorname{trace}(H) - \frac{1}{2}\operatorname{trace}(AH) - \frac{1}{2}\underbrace{\operatorname{trace}(HA)}_{=\operatorname{trace}(AH)}\\ =&QP - 3\ R - P\ \operatorname{trace}(H) - \operatorname{trace}(AH)\\ =&QP - 3\ R - P\ \operatorname{trace}(H) - \operatorname{trace}(AH^*) - \frac{1}{3}\operatorname{trace}(H)\underbrace{\operatorname{trace}(A)}_{=-P}\\ =&QP - \frac{2}{3}P\ \operatorname{trace}(H) - 3\ R - \operatorname{trace}(AH^*).\end{aligned} \tag{2.113}$$

2.4.4 Third Invariant Dynamics

First let us apply the decomposition (eq. 2.111) to $\text{trace}(A^2H)$ which will help to simplify the dynamics of the third invariant

$$\begin{aligned}\text{trace}(A^2H) =& \text{trace}\left(A^2\left(H^* + \frac{1}{3}\text{trace}(H)I\right)\right)\\ =& \text{trace}(A^2H^*) + \text{trace}\left(A^2\frac{1}{3}\text{trace}(H)I\right)\\ =& \text{trace}(A^2H^*) + \frac{1}{3}\text{trace}(H)\text{trace}(A^2).\end{aligned} \tag{2.114}$$

Further we will make use of the *Cayley-Hamilton Theorem* which states that *'Every square matrix satisfies its own characteristic equation'*. It directly leads to the equation

$$A^3 + PA^2 + QA + RI = 0. \tag{2.115}$$

Multiplying this equation with A and taking the trace of the product leads to

$$\begin{gathered}\text{trace}(A^4) + P\,\text{trace}(A^3) + Q\,\text{trace}(A^2) + R\,\text{trace}(A) = 0\\ \Longleftrightarrow\\ \text{trace}(A^4) + P\left(3PQ - P^3 - 3R\right) + Q\left(P^2 - 2Q\right) - PR = 0\\ \Longleftrightarrow\\ \text{trace}(A^4) = -3P^2Q + P^4 + 3PR - P^2Q + 2Q^2 + PR\\ \Longleftrightarrow\\ \text{trace}(A^4) = P^4 - 4P^2Q + 2Q^2 + 4PR.\end{gathered} \tag{2.116}$$

With the definition of the third invariant of the velocity gradient tensor (2.105) we obtain its evolution as

$$\begin{aligned}
\frac{dR}{dt} =& -\frac{1}{3}\left(3\ (P^2-Q)\frac{dP}{dt} - 3P\frac{dQ}{dt} + \mathrm{trace}(\frac{dA^3}{dt})\right)\\
=& -\ (P^2-Q)\left(P^2-2\ Q-\mathrm{trace}(H)\right)\\
&+P\left(QP-\frac{2}{3}P\ \mathrm{trace}(H)-3\ R-\mathrm{trace}(AH^*)\right)\\
&+\mathrm{trace}(A^4)-\frac{1}{3}\mathrm{trace}(A^2H)-\frac{1}{3}\underbrace{\mathrm{trace}(AHA)}_{=\mathrm{trace}(A^2H)}-\frac{1}{3}\underbrace{\mathrm{trace}(HA^2)}_{=\mathrm{trace}(A^2H)}\\
=& -P^4+2\ P^2Q+P^2\mathrm{trace}(H)+P^2Q-2\ Q^2-Q\mathrm{trace}(H)\\
&+P^2Q-\frac{2}{3}P^2\ \mathrm{trace}(H)-3\ PR-P\,\mathrm{trace}(AH^*)\\
&+P^4-4P^2Q+2Q^2+4PR\\
&-\mathrm{trace}(A^2H)\\
=& -P^4+2\ P^2Q+P^2\mathrm{trace}(H)+P^2Q-2\ Q^2-Q\mathrm{trace}(H)\\
&+P^2Q-\frac{2}{3}P^2\ \mathrm{trace}(H)-3\ PR-P\,\mathrm{trace}(AH^*)\\
&+P^4-4P^2Q+2Q^2+4PR-\mathrm{trace}(A^2H^*)-\frac{1}{3}\mathrm{trace}(H)\underbrace{\mathrm{trace}(A^2)}_{=P^2-2Q}\\
=& -P^4+2\ P^2Q+P^2\mathrm{trace}(H)+P^2Q-2\ Q^2-Q\mathrm{trace}(H)\\
&+P^2Q-\frac{2}{3}P^2\ \mathrm{trace}(H)-3\ PR-P\,\mathrm{trace}(AH^*)\\
&+P^4-4P^2Q+2Q^2+4PR\\
&-\mathrm{trace}(A^2H^*)-\frac{1}{3}P^2\mathrm{trace}(H)+\frac{2}{3}Q\mathrm{trace}(H)\\
=& -\frac{1}{3}Q\,\mathrm{trace}(H)+PR-P\,\mathrm{trace}(AH^*)-\mathrm{trace}(A^2H^*).
\end{aligned} \tag{2.117}$$

2.4.5 Invariant System Dynamics

The velocity gradient dynamics in compressible form were derived in the latter section and can be summarized as

$$\begin{aligned}
\frac{dP}{dt} =& P^2-2\,Q-\mathrm{trace}(H)\\
\frac{dQ}{dt} =& QP-\frac{2}{3}P\,\mathrm{trace}(H)-3\ R-\mathrm{trace}(AH^*)\\
\frac{dR}{dt} =& -\frac{1}{3}Q\,\mathrm{trace}(H)+PR-P\,\mathrm{trace}(AH^*)-\mathrm{trace}(A^2H^*).
\end{aligned} \tag{2.118}$$

This system in its compressible form is novel to the author's best knowledge. It will be extensively studied in this work.

Chapter 3

Direct Numerical Simulation and Post-Processing

As stated in the previous chapter there is no known general solution for the Navier-Stokes equations (2.9). For this reason almost all practical and research work in fluid dynamics has to resort to numerical methods to approximate solutions and/or carry out physical experiments to study the respective problems. Numerical simulations and laboratory experiments in fluid dynamics are strongly coupled. Either approach can be used for firstly validating the other, and secondly for extending the results as both approaches have limits. In the project 'Is fine-scale turbulence universal?' which funded this PhD study experiments were carried out as well, but the current work focuses on a numerical approach.

Depending on the flow problem, the results needed, the time and resources available, we choose numerical methods with smaller or larger levels of turbulence modelling. If we are only interested in mean flow quantities it may be suitable to use methods based on solving the Reynolds Averaged Navier-Stokes Equations (RANS) or solving only the larger spatial scales with Large Eddy Simulations (LES). There are additional numerical approaches, but they all have in common that they include turbulence models that try to predict the unresolved turbulent structures in some or all parts of the domain and scales of motion. These models are based on theories combined with empirical experience and are often only suitable for very few flow cases. In the project "Is fine-scale turbulence universal?" and in the work described in this report, we want to validate some of these theories and models and create a basis for future theories as mentioned in chapter 1. To achieve this, we have to understand how turbulence is behaving in different flows and figure out if there is anything in common (universal) we can create a theory out of. For this reason in this project it is not suitable to model any of the scales of motion, as we could neglect important characteristics of turbulence. Thus, we use direct numerical simulation (DNS) of the Navier-Stokes equations (2.9). This implies that we have to resolve all the scales in the flow, from the largest scales introduced by the

initial- and boundary conditions down to the smallest scales where all the kinetic energy is transferred into internal energy (see section 1.2.1).
This is achieved by a discretisation of the original system of PDEs (2.9). In this process the PDE-system is replaced by an algebraic system which can be solved or approximated with known numerical methods and algorithms. To solve the algebraic system we have to replace the flow domain with a grid that achieves the mentioned scale resolution.
The code we use to approximate the solution of the Navier-Stokes equations (2.9) is called HiPSTAR (High-Performance Solver for Turbulence and Aeroacoustics Research) and its main objective is efficiency and accuracy. It is designed for parallel computing, with a state-of-the-art scaling in performance (Sandberg, 2009).
The obtained flow data need to be further processed to extract the information that we are interested in for our investigations. Part of this post-processing is done on the fly while calculating the flow fields in HiPSTAR. But many investigations are too complex to carry them out alongside the DNS. For this reason detailed time-resolved datasets were stored of the different flows. A Flow Analysis Tool (FAT) was developed to run on HPC clusters and aims to post-process the large data produced by DNS efficiently containing a large variety of quantities.

3.1 Simulation (HiPSTAR)

3.1.1 Discretisation

For large-scale DNS of turbulent flow problems, the amount of memory used for the simulation exceeds the available cache of the CPUs and the slower RAM has to be accessed, which is a bottle neck from a performance point of view. To keep this performance-degrading way of accessing large amounts of data from RAM at a minimum and increase the performance, one should try to reduce the needed memory the algorithm is using. To achieve this an ultra low storage Runge-Kutta scheme is chosen for the discretization in time. This five-step fourth-order Runge-Kutta scheme was developed by Kennedy *et al.* (2000) and achieves fourth-order accuracy with only two registers of memory.
In two spatial direction (streamwise and lateral), three options are available for the spatial discretization. A five-point stencil standard central finite difference scheme (STD-FD), which is an explicit spatial difference scheme, and two compact finite difference schemes. For the latter two the difference stensils include the first derivatives on neighbouring points as part of the stencil and thus they are implicit schemes (COMP-FD) and (COMP-FD-NF). All the schemes have an accuracy of order four, but the implicit schemes have lower numerical dispersion and dissipation error for a given wavelength of the function. Although the calculation time per grid point is higher for implicit schemes, it is possible to decrease the number of grid points to reach the same numerical error. This leads to an overall benefit in performance for the more complex schemes. The

boundary scheme (Carpenter *et al.*, 1999) used with the STD-FD is explicit and has rge same order of accuracy as the interior scheme. The parallelization is comparatively simple as both temporal and spatial discretizations are explicit. So there is only need to fill halo cells at the subdomain boundaries with the values of the neighboring subdomain. The boundaries in COMP-FD and COMP-FD-NF are treated with an optimized compact boundary scheme (Kim & Lee, 1996; Kim, 2007) of the same order of accuracy as the interior scheme. As both schemes are implicit the parallelization is more difficult than in the explicit case. Therefore a novel approach (Kim & Sandberg, 2011) for compact finite differences is applied. This parallelization method also works with halo cells. The third direction (spanwise) is assumed to be periodic and is discretized with Fourier transformations. Therefore the FFTW library (Frigo & Johnson, 2005) is applied.
In order to increase stability of the numerical scheme a stabilizing method of the system (2.9) according to Kennedy & Gruber (2008) is applied. This method employs skew-symmetric splitting of the non-linear terms.

3.1.2 Initial and Boundary Conditions

Once the PDEs are discretized (see section 3.1.1), the domain is chosen and a grid has been generated, we have to impose an initial condition at the grid points in $\overline{\Omega}$ and boundary conditions at the points on $\partial\Omega_T$.
The ideal initial condition would be an instantaneous field of the expected flow, which in general we do not know before hand. If such an instantaneous field is not available, then it is useful to use an approximated theoretical or empirical solution or take a solution of similar problems, if any of them exist. All initial conditions will be case specific and will be stated when the setup of the cases are outlined.
The boundary conditions should reflect the physics at the location of the respective boundary in the real flow. Mostly this is not possible in an exact way as we already made assumptions about the flow when we obtained the Navier-Stokes equations from a model of the flow physics. These assumptions make it difficult to create reality-like boundary conditions. In some cases we are able to find conditions that are quite close to reality, in some not. In the latter we have to improvise. One common possibility is extending the domain Ω with buffer zones to reduce the effect of non-physical boundary conditions on the area of interest. Like the initial condition, the boundary conditions are specific to the chosen flow problem. Even if they are classifiable, it is more useful to explain them when the cases are outlined (see chapter 3.3.1). Here we will give a brief outline about the background of characteristic boundary conditions (see section 3.1.2.1) and turbulent inflow conditions (see section 3.1.2.2) used in the work discussed in this report.

3.1.2.1 Characteristic Conditions

The benefit of characteristic boundary conditions is that we are able to reduce reflections at artificial boundaries as they often appear in CFD. In those cases, buffer zones are often used to damp these artificial reflections. Reducing the reflections then implies a reduction of domain size as no or at least smaller buffer zones are needed. This is particularly important in aeroacoustics where buffer zones to reduce reflections at artificial boundaries cause an immense increase of domain sizes, which implies more expense to calculate the cases. But these boundary conditions are of great interest in compressible turbulence research as well, as turbulence is a noise source and we end up with the same problems as in aeroacoustics.

Characteristic boundary conditions were originally developed for hyperbolic systems (Thompson, 1987, 1990), but can be used for Navier-Stokes equations as well, if we assume that the flow at the boundaries is locally one-dimensional and inviscid (Poinsot & Lele, 1992). Kim & Lee (2000) then made these conditions applicable to Navier-Stokes equations in generalized coordinates. The same theory, underlying characteristic boundary conditions, works well as a basis for characteristic interface conditions (Kim & Lee, 2003; Peers *et al.*, 2009), and will be used in later work following the boundary layer case (see chapter 3.3.1).

In the following we will give a brief overview about the background of these conditions. For a clearer notation, we combine the conservative flow variables to a vector $\vec{Q} :=^t (\rho, \rho\vec{u}, \rho E)$ and add the pressure gradient in (2.9) to the LHS. The RHS is of less interest and will be referred to as R. If we define adequate flux vectors $\vec{F}_1, \vec{F}_3, \vec{F}_3$ for the transport terms, then the system (2.9) can be rewritten as

$$\frac{\partial \vec{Q}}{\partial t} + \frac{\partial \vec{F}_1}{\partial x_1} + \frac{\partial \vec{F}_2}{\partial x_2} + \frac{\partial \vec{F}_3}{\partial x_3} = R. \tag{3.1}$$

With the formal Jacobi matrices $A_k := \frac{\partial \vec{F}_k}{\partial \vec{Q}}$ (Thompson, 1987) this can be transformed to quasi linear form

$$\frac{\partial \vec{Q}}{\partial t} + A_1 \frac{\partial \vec{Q}}{\partial x_1} + A_2 \frac{\partial \vec{Q}}{\partial x_2} + A_3 \frac{\partial \vec{Q}}{\partial x_3} = R. \tag{3.2}$$

Considering we have a boundary with its normal vector in direction x_1 (more general cases are described in Kim & Lee (2000)) then the derivatives in the x_2 and x_3 directions are parallel to the observed boundary and need only information from the inside of the computational domain. As these derivatives can be treated as normal, they are of no interest for the further procedure and are swapped to the modified LHS R^*. Which information is needed to calculate the boundary-normal derivatives is unclear at this point. Looking closer at the system

$$\frac{\partial \vec{Q}}{\partial t} + A_1 \frac{\partial \vec{Q}}{\partial x_1} = R^* \tag{3.3}$$

we are able to transform it to a one-dimensional transport equation. This will be conducted in two steps. First we have to find the matrix P_1 to diagonalize $A_1 = P_1 \Lambda_1 P_1^{-1}$, where Λ_1 is a diagonal matrix. Substituting that into (eq. 3.3), we get the expression

$$\frac{\partial \vec{Q}}{\partial t} + P_1 \Lambda_1 P_1^{-1} \frac{\partial \vec{Q}}{\partial x_1} = R^*. \tag{3.4}$$

Now multiplying with P_1^{-1} from the left and defining $\delta\vec{C} := P_1^{-1}\delta\vec{Q}$ (Thompson, 1987), we get the mentioned one-dimensional transport equation

$$\frac{\partial \vec{C}}{\partial t} + \Lambda_1 \frac{\partial \vec{C}}{\partial x_1} = R^{**}, \tag{3.5}$$

where $R^{**} := P_1^{-1} R^*$. This is called the characteristic form of the system. Assuming a local one-dimensional inviscid (LODI) system (Poinsot & Lele, 1992) and neglecting the LHS

$$\frac{\partial \vec{C}}{\partial t} + \Lambda_1 \frac{\partial \vec{C}}{\partial x_1} = 0, \tag{3.6}$$

we can identify the propagation direction of the information travelling across the boundary from the sign of the respective entry of Λ_1 (Thompson, 1987). If information is traveling out of the domain, we keep stability of the discretized system even if we calculate the derivative with a one-sided interior difference scheme (Thompson, 1987). If the information is entering the domain, we need to find an interpretation for the physics at this location. Various ways of these boundary conditions can be found in Thompson (1987, 1990); Poinsot & Lele (1992); Kim & Lee (2000). The exact boundary conditions we use in our simulations is explained where the cases are outlined.

3.1.2.2 Turbulent Inflow Conditions

We use a turbulent inflow instead of starting the domain upstream of the location where transition takes place. This reduces the domain size and makes it possible to simulate turbulent flows up to higher Reynolds numbers with given computational resources. The turbulent inflow method we are using was first developed by Klein *et al.* (2003), who introduced a three dimensional digital filtering method for incompressible flows. This method is working in two steps:

1. First a provisional three-dimensional signal $\mathcal{U}_i$ is generated for each velocity component which possesses a prescribed two point statistic (length scale, energy spectrum). If there was only the need to obtain homogeneous turbulence, the procedure could stop here.

2. If cross correlations between the different velocity components have to be taken into account, a method proposed by Lund *et al.* (1998) can be used. First define

$\mathcal{U}_i$ so that $\overline{\mathcal{U}_i} = 0, \overline{\mathcal{U}_i \mathcal{U}_j} = \delta_{ij}$, and then perform the following transformation: $u_i = \overline{u_i} + a_{ij}\mathcal{U}_j$ where a_{ij} is the solution of an algebraic system which impose the given correlations, R_{ij}, which may be known from experimental data. u_i is the desired velocity signal.

This method is quite expensive as it is working in an additional three-dimensional box upstream of the inlet boundary. Xie & Castro (2008) improved the method and managed to generate a turbulent inlet condition using only a two-dimensional slice of the computational domain. The correlation in the streamwise direction is covered with correlations in time according to the streamwise mean velocity. As this improved method was only developed for incompressible flows, Touber & Sandham (2009) extended the method for compressible flow. This is the method we are using in this work.

3.2 Post-Processing (FAT)

The DNS code HiPSTAR described above provides statistical moments for many quantities. For this work there was need to extend those statistics as well as sampling raw DNS data for further processing. The sampling is restricted to the areas of interest and includes density, the velocity vector and temperature. To handle the large time series in order to calculate gradients, spectra and probability density functions, a new Flow Analysis Tool (FAT) was devoloped. To achieve high performance in handling large data sets the tool needed to be parallizable and efficient. The bottle-neck was found to be the reading of the raw DNS data. For this part the MPI IO-library was put in place. A post-processing tool, that has a modular structure to enable an easy updating and upgrading procedure, was implemented. A selection of FAT's capabilities is outlined in this section.

3.2.1 Spatial Filter

Besides temporal averaging, FAT is equipped with several filter options. The filter used for this work has a Gaussian kernel and variable filter width $\Delta(\vec{x})$. A Gaussian filter in three spatial dimensions is defined as

$$\bar{f}(\vec{x}) := \frac{\iiint_{-\infty}^{\infty} f(\vec{r})\ G(\vec{x},\vec{r})d\vec{r}}{\iiint_{-\infty}^{\infty} G(\vec{x},\vec{r})d\vec{r}} \tag{3.7}$$

with the filter kernel

$$G(\vec{x},\vec{r}) := e^{-\frac{(\vec{x}-\vec{r})^2}{2(\sigma(\vec{x}))^2}}. \tag{3.8}$$

The filter parameter $\sigma(\vec{x})$ is a function of the filter width Δ

$$\sigma(\vec{x}) := \frac{\Delta(\vec{x})}{\sqrt{8\ln(2)}} \approx \frac{\Delta(\vec{x})}{2.3548}. \tag{3.9}$$

It scales the Gaussian kernel so that the *full width at half maximum* of the kernel function is considered to be the filter width $\Delta(\vec{x})$. The integral on the whole domain can be truncated and the trunction error Σ can be estimated as

$$\Sigma := \operatorname{erf}\left(\frac{s}{\sqrt{2}}\right) \tag{3.10}$$

for the integral range of $\pm s\sigma$.

$$\bar{f}(\vec{x}) = \frac{\iiint_{-s\sigma}^{s\sigma} f(\vec{r})\ G(\vec{x},\vec{r})d\vec{r}\Sigma^n}{\iiint_{-s\sigma}^{s\sigma} G(\vec{x},\vec{r})d\vec{r}\Sigma^n} \tag{3.11}$$

An overview of the approximate error:

s	$\Sigma \approx$
1	0.682689492137086
1.5	0.866385597462284
2	0.954499736103642
2.5	0.987580669348448
3	0.997300203936740
3.5	0.999534741841929
4	0.999936657516334
4.5	0.999993204653751
5	0.999999426696856

Just like the numerical scheme for the DNS, that was described in the last chapter, the filter needs to be discretized as well. Therefore the filtered integral needs to be described on the computational grid with the coordinate system $\vec{\xi}$. For this reason we apply *integration by substitition* to the actual filtering

$$\bar{f}(\vec{x}) = \frac{\iiint_{-\infty}^{\infty} f(\vec{r}(\vec{\xi}))\ G(\vec{x},\vec{r}(\vec{\xi}))d\vec{r}(\vec{\xi})}{\iiint_{-\infty}^{\infty} G(\vec{x},\vec{r}(\vec{\xi}))d\vec{r}(\vec{\xi})} \tag{3.12}$$

$$= \frac{\iiint_{-\infty}^{\infty} f(\vec{r}(\vec{\xi}))\ G(\vec{x},\vec{r}(\vec{\xi}))|\det(D_{\vec{\xi}}\vec{r})(\vec{\xi})|d\vec{\xi}}{\iiint_{-\infty}^{\infty} G(\vec{x},\vec{r}(\vec{\xi}))|\det(D_{\vec{\xi}}\vec{r})(\vec{\xi})|d\vec{\xi}} \tag{3.13}$$

with the Jacobian

$$D_{\vec{\xi}}\vec{r} := \begin{pmatrix} \frac{\partial x_1}{\partial \xi_1} & \frac{\partial x_1}{\partial \xi_2} & \frac{\partial x_1}{\partial \xi_3} \\ \frac{\partial x_2}{\partial \xi_1} & \frac{\partial x_2}{\partial \xi_2} & \frac{\partial x_2}{\partial \xi_3} \\ \frac{\partial x_3}{\partial \xi_1} & \frac{\partial x_3}{\partial \xi_2} & \frac{\partial x_3}{\partial \xi_3} \end{pmatrix} \tag{3.14}$$

3.2.2 Budgets

The aim of this work is to obtain a better understanding of the complex coupling of the Navier-Stokes equations that results in turbulence. For this reason we calculate and sample various statistics. An important aspect is how the coupling is changing at different locations a flow as well as across different flows. To investigate this we sample the budgets of all equations that we outlined in chapter (2). This allows to compare the energy distribution and the energy transfer for different flow topologies.

3.2.3 Propability Density Functions and Conditional Averages

For the detailed study of the dynamics of turbulence it is not sufficient to extract ordinary mean quantities only. It is often beneficial to sample more detailed statistics of quantities to understand the underlying character and driving mechanisms. For this reason a dynamic probability density function (pdf) sampling similar to the one described by Jain & Chlamtac (1985) was implemented and parallelized. Further, this was extended to joint-pdf sampling as well as conditional averaging procedures, that allow to investigate complex couplings between different quantities.

3.3 Outline of Investigated Flows

To investigate the universality arguments that were outlined in the introduction, DNS is carried out for flows that provide a variety of different characteristics. Universality in wall parallel flows and trailing edges are investigated in a flat-plate turbulent boundary layer flow (3.3.1) as well as in a pipe flow exiting into a co-flow and thus creating a jet (3.3.2). Another flow topology that are examined is a free shear layer. To that end the shear layer of the mentioned jet are studied at different streamwise locations. In addition, DNS data of a supersonic axisymmetric wake (3.3.3) are explored in the context of free shear layers. Besides the shear layer provided by this wake the flow also provides a region with a strong pressure gradient that could be studied. Furthermore, in the near wake region the flow develops a stagnation point and a recirculation region that impinges at the end-wall of the cylinder. These are two more topologies that received attention in this work. In this section the important characterisics of the respective topologies are discussed and the cases studied are outlined.

3.3.1 Compressible Zero-Pressure-Gradient Flat-Plate Boundary Layers

In the context of the project 'Is fine-scale turbulence universal?' (see section 1.2.1.3) the behaviour of the smallest turbulent motions and their interaction with larger scale structures in different flows was investigated. One category is wall-bounded flows. We study a subsonic flow of a compressible fluid over a flat plate in absence of a global pressure-gradient and external forces. This flow forms a thin boundary layer (BL) (Schlichting, 1979) on the plate in which viscous effects are important. As many engineering applications include wall-bounded flows it is a very active research area. One is interested, for example, in lift and drag of bodies or the noise emitted by the flow. Both applications and many more have in common that the turbulent boundary layer (TBL) needs to be better understood to be able to make improvements. We will focus on the turbulent part of this BL (see section 3.3.1.1), study the structural composition and therefore the interaction between the different scales of motion. DNS (see chapter 3) will be used as tool for this research as it is, next to experimental studies, the only way to represent all characteristics of a flow.
Section 3.3.1.1 will give an overview about the past and current work done in this field. Afterwards results of the DNS are presented and some characteristics are selected for later investigations.

3.3.1.1 State-of-the-art

Having a closer look at the boundary layer one can coarsely divide it into three streamwise regions (figure 3.1). The first region is the *laminar boundary layer* which is widely

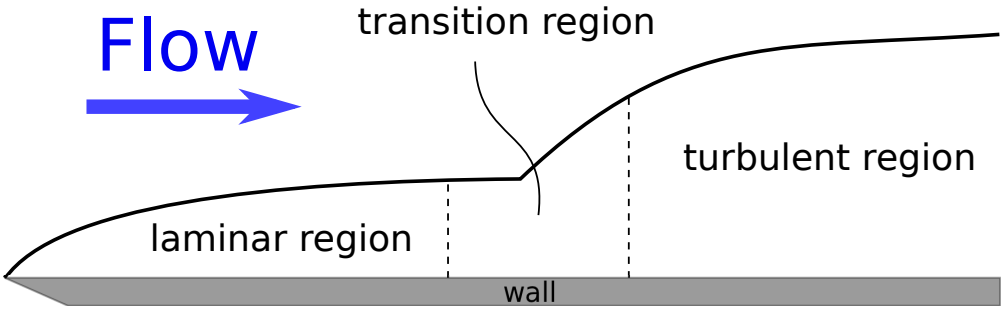

Figure 3.1: Schematic exposition of a developing boundary layer on a flat-plate

understood (Schlichting, 1979). This laminar part is followed by a *transition region* where disturbances break down an fill the boundary layer with structures of different scales. When the breakdown has advances enough to fill the boundary layer with all the scales from the largest turbulent scales with size of the boundary layer thickness down to the smallest where dissipation is dominant we are in the *turbulent region* and we speak of a *fully developed turbulent boundary layer*. This turbulent region is what we

are interested in.

Prandtl introduced the idea of a boundary layer more than 100 years ago (Anderson, 2005), but still a rational theory for TBLs is exists neither for wall-bounded turbulent flows nor for general turbulent flows (Schlichting, 1979). It has not been possible to fully understand even the simplest quantity, the streamwise mean velocity (Schlatter & Örlü, R., 2010). We can find a common description of the streamwise mean velocity profile in the wall-normal direction $\overline{u}(y)$ where $\overline{u}$ is the averaged streamwise velocity and y is the wall-normal position with the wall at $y = 0$. Although the validity of this description for higher Reynolds numbers and the universality of relevant model constants has more recently been questioned (discussed in the following), it is acceptable to get an overview about the structure of a fully turbulent boundary layer. Further it is the best description we have so far. It is a presumably universal mean streamwise velocity distribution in wall-bounded flows scaled with the wall shear stress τ_{wall} and is known as the *law of the wall* (figure 3.2). The turbulent boundary layer is decomposed into four region *viscous sublayer*, *buffer layer*, *logarithmic layer* and *outer layer* in order of increasing distance from the wall. The first three layers are often combined to the *inner layer*. In the following, the subscript '+' marks dimensionless variables scaled with the wall shear stress. The **viscous sublayer** starts at the wall and lasts up to $y^+ \approx 5$. The velocity is

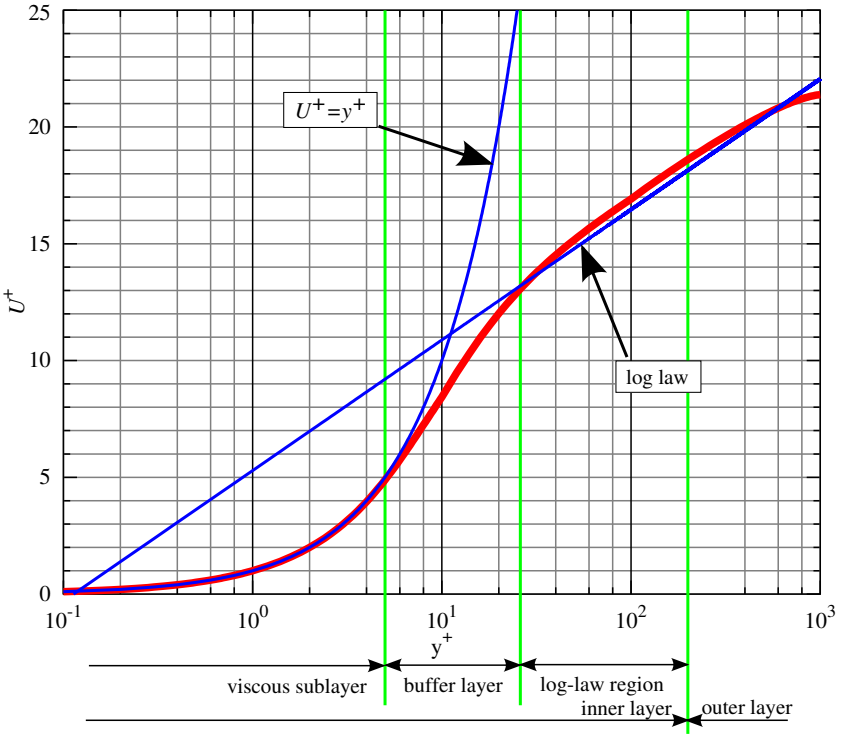

Figure 3.2: Mean streamwise velocity (red) scaled with u_τ and plotted in logarithmic scale over wall-distance y^+; functions $f(y^+) := y^+$ and $g(y^+) := \frac{1}{\kappa} \log y^+ + C$ are plotted in blue; the green lines show the approximate limits of the different sub-layers

linearly dependent on the wall-distance and we can state the equation

$$u^+ = y^+. \tag{3.15}$$

On top of the viscous sublayer there is the **buffer layer** which usually is considered to have the extent of $5 \lesssim y^+ \lesssim 30$. The value of the upper bound is questioned, though, as for high Reynolds numbers it has been found to extend to $y^+ \approx 200$ or even higher (discussed in the following). This shows that it may be a function of Reynolds number. We cannot state an equation for this layer, but one can say that the profile function slowly crosses over from the linear function to the logarithmic law of the wall.
The next layer is the **logarithmic layer** that is found for $30 \lesssim y^+ \lesssim 0.2\delta_{99}^+$ and the profile follows the logarithmic behaviour (log law)

$$u^+ = \frac{1}{\kappa} \log y^+ + C. \tag{3.16}$$

κ is the von Kármán constant and has been found in experiments to be universal and independent of Reynolds number and flow geometry, $\kappa \approx 0.4$. However, recent studies question this value and its universality (discussed in the following). The same is true for the constant C which has been stated as $C \approx 5$ for a smooth wall.
As last layer we find the **outer layer** where the profile adapts to the free-stream velocity.

Wall-Bounded Flows Pipe flows, channel flows and boundary layer flows are treated in the same way as wall-bounded flows. Even if pipe and channel are internal flows and the boundary layer is an external flow, they are comparable qualitatively. Hence, it is possible to use easier experimental setups and cheaper simulations (Sillero, 2011) of internal flow to find conclusions which are valid for boundary layers as well. With Reynolds numbers around $Re_\theta \approx 3000$ the inner scaled mean profiles are matching well in all three flows for the distance from the wall $y < \frac{1}{4}\delta_{99}$ and higher order moments match even at least up to $y = \frac{1}{2}\delta_{99}$ (Monty *et al.*, 2009). On the other hand Monty *et al.* (2009) found, that the energy spectra show differences that cannot be explained by scaling arguments. With higher Reynolds number the similarities in the statistics decrease. Marusic *et al.* (2010) found that for different and higher Reynolds numbers the streamwise turbulent intensity and the intensities of other components of the Reynolds stress tensor may scale in a different way. They showed this even down to the viscous buffer region. The law of the wall seems to depend on the flow geometry as well. It was shown by Marusic *et al.* (2010) that the 'universal' constants κ and C, valid in the log-region, are not universal and vary from pipe over channel to the boundary layer flow. Next to the clear differences in the outer region, the large structures behave differently , too (Monty *et al.*, 2009; Marusic *et al.*, 2010). Monty *et al.* (2009) observed a difference with increasing distance to the wall: In internal flow the kinetic energy is moving to longer wavelength, while in the external flow the structures decrease in size rapidly beyond the log-layer. But due to the lack of reliable turbulent boundary layer data it was

important to accept the similarity between the flows in understanding the structure of the near wall flow (Monty *et al.*, 2009). This still could be helpful in understanding how coherent structures in turbulent flows are behaving, how they are created, transported and how they break down.

Turbulent Boundary Layer Even though the zero-pressure-gradient flat-plate boundary layer (ZPGFPBL) is a very important case for theoretical, numerical and experimental studies in understanding wall bounded turbulence, only very few DNS for high Reynolds number exist (Wu & Moin, 2009; Schlatter & Örlü, R., 2010). On the other hand there have been a large number of experimental studies carried out on this topic. What is missing in most cases on the experimental side are direct or indirect measurements of the skin friction and another issue is that it is difficult to accurately achieve a zero-pressure gradient in the streamwise direction (Schlatter & Örlü, R., 2010). In the time before the recently (in the 1990s) developed experimental technique of particle image velocimetry (PIV) was available, it was impossible to get two dimensional planes or three dimensional volumes of flow field data from experiments. To fill this gap and, more generally, to make a vice-versa validation between experimental and numerical data possible, DNS is needed.
Almost all DNS performed on this topic are incompressible, and only few compressible DNS studies on a ZPGFPBL have been conducted and it seems these all are in the area of aero-acoustics and focus on different characteristics than we do in our study. Hence, the focus in this literature review is on incompressible ZPGFPBL with the assumption that the structure of a boundary layer does not differ significantly due to compressibility effects in the subsonic case. The impact of compressibility on the turbulent flow will be investigated later.

Mean Profiles In general it is remarkable that mostly only profiles of the mean streamwise velocity in the wall-normal direction are discussed. Especially the profiles of the mean steamwise velocity component in the streamwise direction and the mean wall-normal velocity component in the wall-normal direction are of great interest, as their gradients appear in the non-linear terms of the Navier-Stokes equations (eq. 2.9), which are considered to be one root of turbulence.
Getting an overview about the wall-normal profile of the streamwise component of the mean velocity we notice that every experimental or numerical dataset collapses almost perfectly with the law of the wall in the viscous sublayer. For the logarithmic region things are different. Even in the first highly cited DNS of a turbulent boundary layer, carried out by Spalart (1988), at quite low Reynolds number, issues were arising. While Spalart matched the log law quite well for Reynolds numbers of $Re_\theta = 670$ and 1410, his results in the log region for $Re_\theta = 300$ were slightly higher than suggested from the log law. Using $\Xi = y^+ \frac{\partial u^+}{\partial y^+}$ as an indicator for a log region (the graph should show a plateau

with Ξ = const. as indication for the log-region), he stated that in the low-Reynolds number case the possibility for an infinitely small log region is given.
Nevertheless, for higher Reynolds numbers the log law seems to be valid. Österlund *et al.* (2000) show a good collapse with the log law with coefficients set to $\kappa = 0.41$ and $C = 5.2$ of their experimental data at $Re_\theta = 2532, 3651$ and 4312.
Schlatter *et al.* (2009) obtain a good match of DNS data with $\kappa = 0.41$ and $C = 5.2$ at $Re_\theta = 670$ and 1410 and one year later they used LES to reach higher Reynolds numbers (Schlatter *et al.*, 2010) and compared the results to the experiments of Österlund *et al.* (2000). With Reynolds numbers of $Re_\theta = 685, 1433, 2560, 3660$ and 4307 they matched the experimental results and the log law with the same coefficients as Österlund *et al.* (2000). However, their mean profile at $Re_\theta = 1433$ shows discrepancies further away from the wall when compared to the DNS of Spalart (1988).
The (so far) highest Reynolds number $Re_\theta = 6650$ (Sillero, 2011) achieved in DNS of turbulent boundary layer simulations collapsed with the log law with coefficients $\kappa = 0.4$ and $C = 5$.
Regarding these results the log law seems to be proven, with small discrepancies in the coefficients, for at least Reynolds numbers $Re_\theta \gtrsim 650$. However, Marusic *et al.* (2010) compared different channel, pipe and turbulent boundary layer flows at higher Reynolds numbers. In the case of mean profiles of TBLs they compared experiments with Reynolds numbers from $Re_\theta = 14000$ to 23000 and found values for the van Kármán constant between 0.38 and 0.39. In addition the logarithmic regions started at $y^+ \gtrsim 200$ and seemed to be Reynolds number dependent. Even replacing the log law with a power law was discussed. Johnstone & Coleman (2012) discussed the 'right' value of κ in their work as well. Experiments and simulations showed that a sufficiently high Reynolds number is needed to get a clear log layer. Monkewitz *et al.* (2007) suggested $Re_{\delta^*} \gtrsim 10^4$. All this shows that the discussion about the log law and the streamwise mean velocity profile in general are far from being closed.

Reynolds Stresses Marusic *et al.* (2010) mentioned that the Reynolds stresses do not receive enough attention compared to the mean values. They are the source of turbulence and drive the transfer of mass, heat and momentum and, due to this, they are important quantities.
Spalart (1988) investigated the production of turbulent kinetic energy $-\overline{u'v'}\frac{du^+}{dy^+}$ and achieved with his DNS a striking match between the results of the two Reynolds numbers $Re_\theta = 670$ and 1410. The Reynolds stress $-\overline{u'v'}$ instead differed in both simulations, which could not be explained by traditional arguments.
Sillero (2011) showed excellent agreement of their DNS data with experimental results of De Graaff & Eaton (2000); Österlund *et al.* (2000) and simulations by Schlatter & Örlü, R. (2010) for u^+_{rms}, v^+_{rms} and w^+_{rms}. The plots, scaled with inner variables, showed Reynolds dependence in the outer region (figure 3.3).
The same behaviour was stated by Schlatter *et al.* (2010) with LES data up to $Re_\theta =$

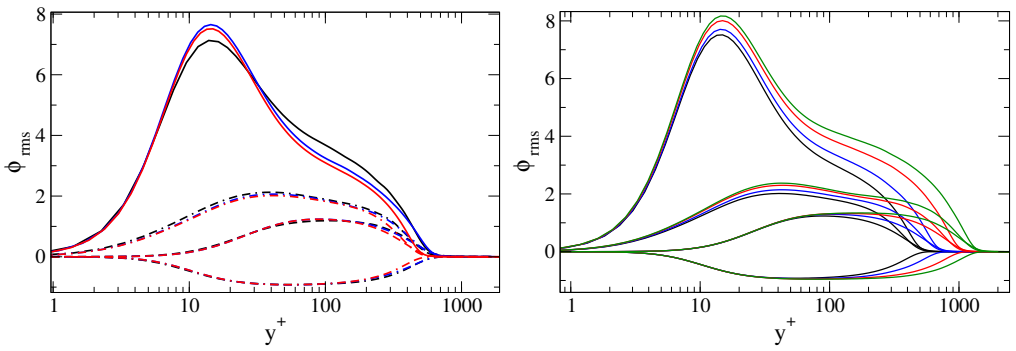

Figure 3.3: the plots show Reynolds stresses: left: $\overline{u'u'}$ $(- - -)$, $\overline{v'v'}$ $(- - -)$, $\overline{w'w'}$ $(\cdot - \cdot - \cdot)$, $-\overline{u'v'}$ $(\cdot - -)$, different DNS datasets are plotted: at $Re_\theta = 1410$ (Spalart, 1988) (black), at $Re_\theta = 1551$ (Jimenez *et al.*, 2010) (blue) and at $Re_\theta = 1410$ (Schlatter & Örlü, R., 2010) (red); right: Reynolds stresses of (Schlatter & Örlü, R., 2010)'s DNS at different Reynolds numbers $Re_\theta = 1410, 2000, 3030$ and 4060 (black,blue,red and green)

4300. They extended the argument for $-\overline{u'v'}$. Further, they mentioned a good agreement between DNS and LES data.

The comparison of wall-bounded flows (Marusic *et al.*, 2010) included experimental data of pipes ($Re_\tau = 4000, 30000$), channels ($Re_\tau = 4000, 4800$) and boundary layers ($Re_\tau = 14000, 22000, 23000, \mathcal{O}(10^6)$). They showed that a secondary peak in $\overline{u'u'}$ arises in the outer region once the Reynolds number is high enough. Even though the Reynolds numbers in figure (3.3) are not high enough, the trend to a secondary peak for $\overline{u'u'}$ in the outer region can already be seen. It was mentioned that the first peak in the $\overline{u'u'}$-profile located at $y^+ \approx 15$ shows a weak Reynolds number dependency in contrast to the classical point of view, i.e. that its location is fixed in inner scaled wall distance.

Correlations and Spectra Spalart (1988) investigated the spectra for the simulation of a turbulent boundary layer at $Re_\theta = 1410$ at the wall distances $y^+ = 100$ and 200. He found a significant inertial range in the x-direction for the streamwise kinetic energy distribution. Jimenéz, J. (2012) shows in a review about cascades in wall-bounded flows clear inertial ranges in streamwise length scale spectra for $\overline{u'u'}$ and $-\overline{u'v'}$ in a channel flow (fig. 3.4). It can be seen that the size of the inertial range is increasing with the distance to the wall.

Schlatter *et al.* (2010) showed clear evidence of large structures in the outer region with increasing Reynolds number (figure 3.5). These structures are known as 'superstructures' or 'very large scale motions' (VLSMs). They mention that the VLSMs received considerable interest in the last years from the experimental side (Kim & Adrian, 1999; Guala *et al.*, 2006; Hutchins & Marusic, 2007*a*; Ganapathisubramani, B., 2007; Hutchins *et al.*, 2011) as well as from the numerical side (del Álamo, J.C. and Jimenéz, J., 2003; Schlatter *et al.*, 2009). The origin and regeneration of these structures are open questions and discussed by Hutchins & Marusic (2007*b*); Mathis *et al.* (2009).

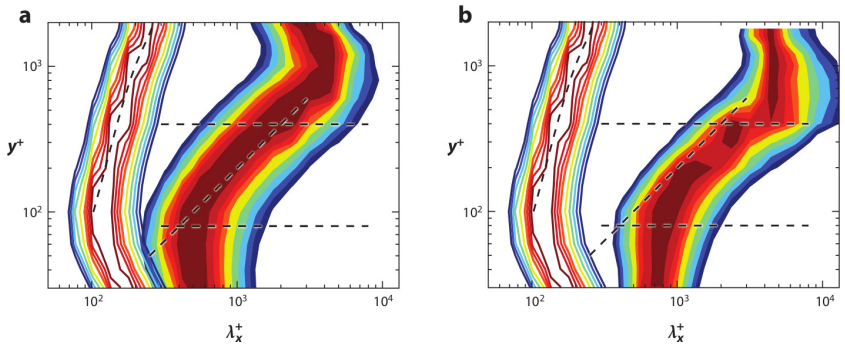

Figure 3.4: Spectral densities in a numerical simulation of a turbulent channel at $\delta^+ = 2000$, as functions of the streamwise wavelength λ_x and of the wall distance y. The shaded contours in panel a are the kinetic energy of the velocity fluctuations, $k_x E_{uu}(k_x)$, and those in panel b are co-spectra of the tangential Reynolds stress, $-k_x E_{uv}(k_x)$. In both panels, the line contours are spectra of the surrogate dissipation, $\nu k_x E_{\omega\omega}(k_x)$, where ω is the vorticity magnitude. At each y, the lowest contour is 0.86 times the local maximum. The horizontal lines, $y^+ = 80$ and $y/\delta = 0.2$, are the approximate limits in which the energy length scale grows linearly with y. The diagonal lines through the two shaded spectra are $\lambda_x = 5y$. Those through the dissipation spectra are $\lambda_x = 40$.(reproduced from Jimenéz, J., 2012)

Jimenéz, J. (2012) compared the spatial extent of these structures at different Reynolds numbers as well. He mentioned their footprint on the near wall region. Remarkable is that this footprint is only located very close to the wall $y^+ \approx 6$ and vanishes very quickly further away from the wall ($y^+ \lesssim 10$).
Even larger structures with the same consequences for higher Reynolds numbers were shown by Sillero (2011) (figure 3.6).
We will describe the VLSMs in more detail in section 3.3.1.1.

Coherent Structures A turbulent flow is characterized by the interaction of fluctuations and eddies of various sizes, shapes and energy. It is the ensemble of these eddies that eventually leads to, e.g., the characteristic law of the wall or well known profiles of the rms values (Schlatter *et al.*, 2010). Marusic *et al.* (2010) describe coherent structures as organized motions that are persistent in time and space and contribute significantly to the transport of heat, mass and momentum. They need to be understood to understand wall-turbulence. Following Townsend (1961, 1976) the eddies in a wall bounded flow can be generally categorized due to their distance from the wall y: One of the categories combines all *detached eddies* with a smaller size than y and the ones with size larger than y are described by the category of *attached eddies*. The detached eddies are roughly isotropic and form a classical Kolmogorov cascade (Jimenéz, J., 2012). On the other hand the attached eddies cannot contain wall-normal velocity or tangential Reynolds stress as they are connected to the wall and must fulfil the no-slip condition imposed by the wall. Therefore the only force acting on them is the pressure gradient, which implies that they are irrotational. The idea of attached eddies has been extensively studied

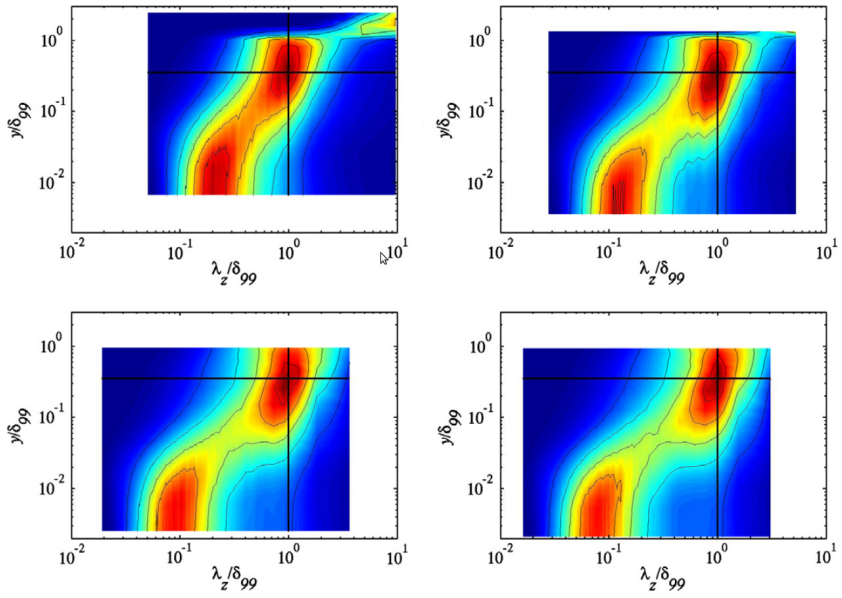

Figure 3.5: Pre-multiplied spanwise spectra $k_z\Phi_{uu}(\lambda_z)/u^2_{\rm rms}$ of the streamwise velocity fluctuation u'. The vertical lines indicate $\lambda_z = \delta_{99}$, the horizontal lines $y = 0,35\delta_{99}$; contour lines have a spacing of 0.1. From left to right and top to bottom: $Re_\theta = 1433, 2560, 3660, 4307$. (reproduced from Schlatter *et al.*, 2010)

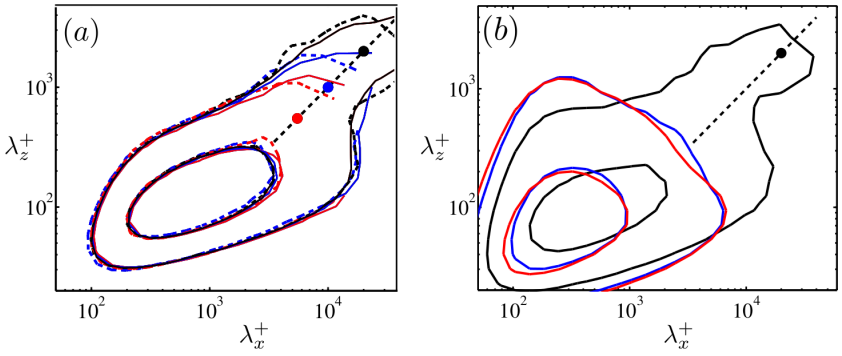

Figure 3.6: (a) Solid lines are two-dimensional spectral densities Φ^+_{uu} from channels at $Re_\tau = 550 - 2000$ (Hoyas & Jiménez, 2006), and dashed ones those of boundary layers at $Re_\tau = 550$ (Jimenez *et al.*, 2010), and 1000 and 2000 from the present case at the buffer layer, $y^+ = 15$, in red, blue, and black respectively. (b) Large scales boundary layer footprint in the vorticity spectral densities $\Phi^+_{\omega\omega}$ at the viscous sublayer $y^+ = 5$ (black) and for the buffer layer at $y^+ = 10 - 15$ (red, blue) at $Re_\tau \approx 2000$. In both cases, the straight dashed line is $\lambda_x = 10\lambda_z$ and dots are $\lambda_z = Re_\tau$.(reproduced from Sillero, 2011)

to model wall turbulence and is behind elementary arguments for the mean streamwise velocity profile in the log region. These eddies can be single vortices or coherent vortex clusters.

If we want to describe how structures are distributed in a wall-bounded flow, we have to take into account that structural models mean something different close to the wall than further away. The local Reynolds number increases with the wall distance and the

structure must be treated in a more and more inertial regime compared to the near-wall region.

Streaks in the viscous sublayer were first identified by Kline *et al.* (1967). The dynamics of these streak then were studied by Kim *et al.* (1971). They are like a layer of counter rotating streamwise vortices constantly present in the viscous sublayer. Two of these sublayer streaks form either a *sweep* ($u > 0, v < 0$) or an *ejection* ($u < 0, v > 0$) at the location where their surfaces are touching. The ejections reach at least up to the buffer region and are therefore called buffer-layer ejections. Experimental results showed that they can be linked to ramp-like, low-momentum regions surrounded by shear layers populated by intense transverse vortices (see Jimenéz, J., 2012). Another interpretation presented these ramps as packets of self-propelled hairpin vortices, each of which includes an ejection arising from the viscous sublayer (Adrian, 2007). It is unclear how far from the wall this mechanism extends (Robinson, 1991; Ganapathisubramani *et al.*, 2003; Tomkins & Adrian, 2003; Wu & Christensen, 2005; Carlier & Stanislas, 2005; Herpin, 2010).

Further away from the wall del Alamo & Jiménez (2006) detected similar ejections extending from the near-wall region into the outer region. They located the surfaces of large attached vortex clusters extending above $y^+ = 100$. In this early log region most of the structures we find are streaks with medium streamwise extent 1000^+ and medium diameter 100^+ (Schlatter *et al.*, 2010). They are known as large scale motions (LSMs) and Marusic *et al.* (2010) characterize them as motions with length scale $\mathcal{O}(\delta)$. Further they are part of the hairpin vortex paradigm and consist of streamwise aligned individual eddies (Adrian, 2007).

A recent finding for high-Reynolds number wall-bounded flows are very large structures in the outer region as shown in the spectra before. Marusic *et al.* (2010) called them *superstructure* and characterized them with a length scale of $\mathcal{O}(10\delta)$. They are also known as *very large scale motions* (VLSMs) and are similar in internal and external wall-bounded flows. In the case of internal flows the VLSMs are further away from the wall and have larger wavelength than in external flows (Marusic *et al.*, 2010). It was shown in several studies including Hutchins & Marusic (2007*a*); Jiménez *et al.* (1999); Mathis *et al.* (2009) that outer-scale influence on the near-wall region becomes increasingly noticeable with high Reynolds number. It is likely that this leads to the increase of the streamwise turbulence intensity (Marusic *et al.*, 2010).

3.3.1.2 Turbulent Boundary Layer DNS - Outline and Validation

A turbulent boundary layer flow along a flat plate without streamwise mean pressure gradient (TBL) was chosen in the context of wall-bounded flows. Wall-bounded flows are fundamental from an engineering point of view and find large attention in research. They develop a particular kind of turbulence that is a subcategory in fluid mechanics

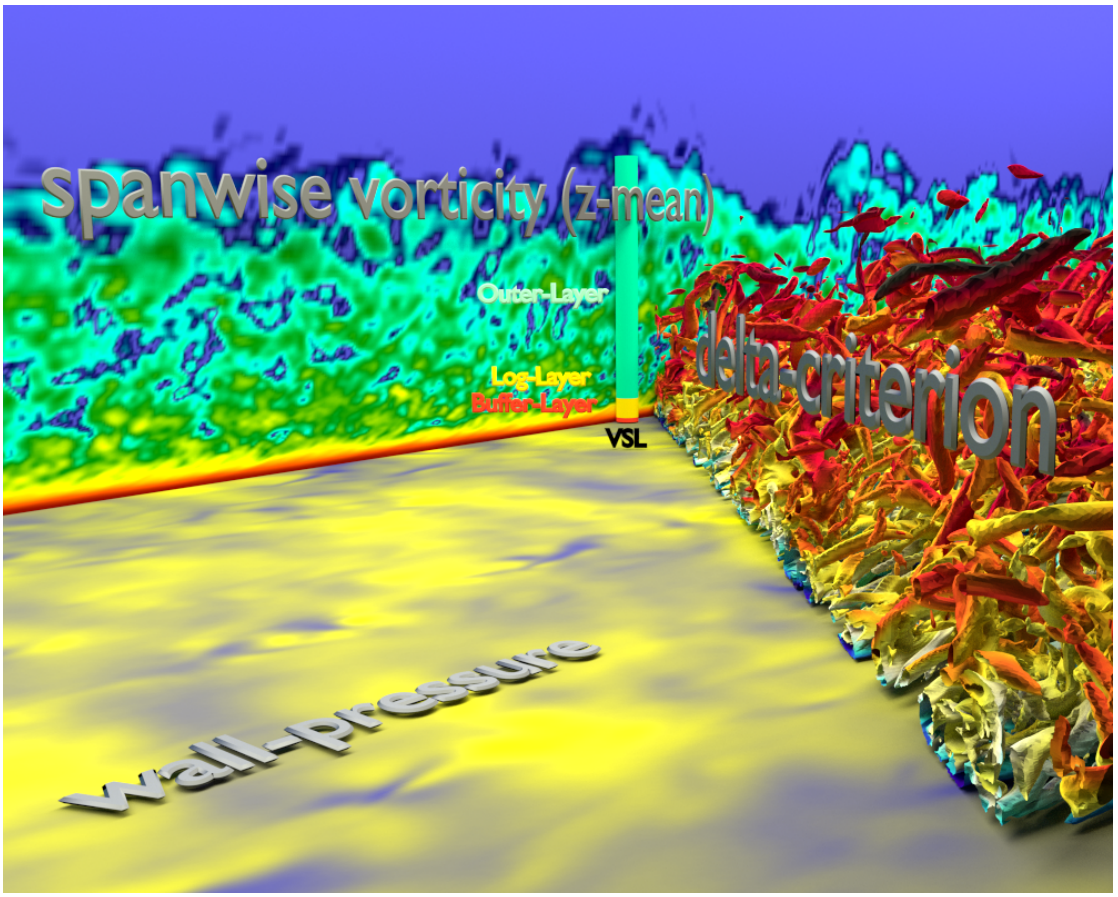

Figure 3.7: Overview of the turbulent boundary layer flow that is used in this work. Besides the extent of the respective sublayer, the image shows a snapshot of the turbulent structures as iso-surfaces of the delta criterion. Further the wall is coloured with the wall-pressure levels and the back plane shows the spanwise zero mode of the spanwise vorticity component.

(3.3.1.1) of which figure (fig. 3.7) gives a first impression. A DNS of such a flow was carried out to investigate the features that will be outlined in the following. The Cartesian domain for the simulation covers a volume with a streamwise extent $L_x \approx 165\,\delta_{99,\text{in}}$. In the wall-normal direction if covers $L_y \approx 16.7\,\delta_{99,\text{in}}$ and in the spanwise direction $L_z = 7\,\delta_{99,\text{in}}$. $\delta_{99,\text{in}}$ denotes the inflow boundary layer thickness which is the reference length scale for all the following if not specified differently. The Reynold number range is $Re_\theta \approx 670 - 2330$ ($Re_\tau \approx 220 - 830$) and therefore in the fully developed turbulent regime of the boundary layer. The Mach number in the free stream is $M_\infty = 0.5$ and the Prandtl number $Pr_\infty = 0.72$. The wall is set to be isothermal at the adiabatic temperature of the freestream $T_{\text{wall}} \approx 1.05$. In order to obtain a turbulent boundary layer an artificial turbulent inflow condition (Touber & Sandham, 2009) was applied . This method is described in more detail in section (3.1.2.2). The outflow is a characteristic outflow condition (Poinsot & Lele, 1992) to minimize artificial reflections from this boundary (see sec. 3.1.2.1 for details). The freestream is an ordinary non-reflective

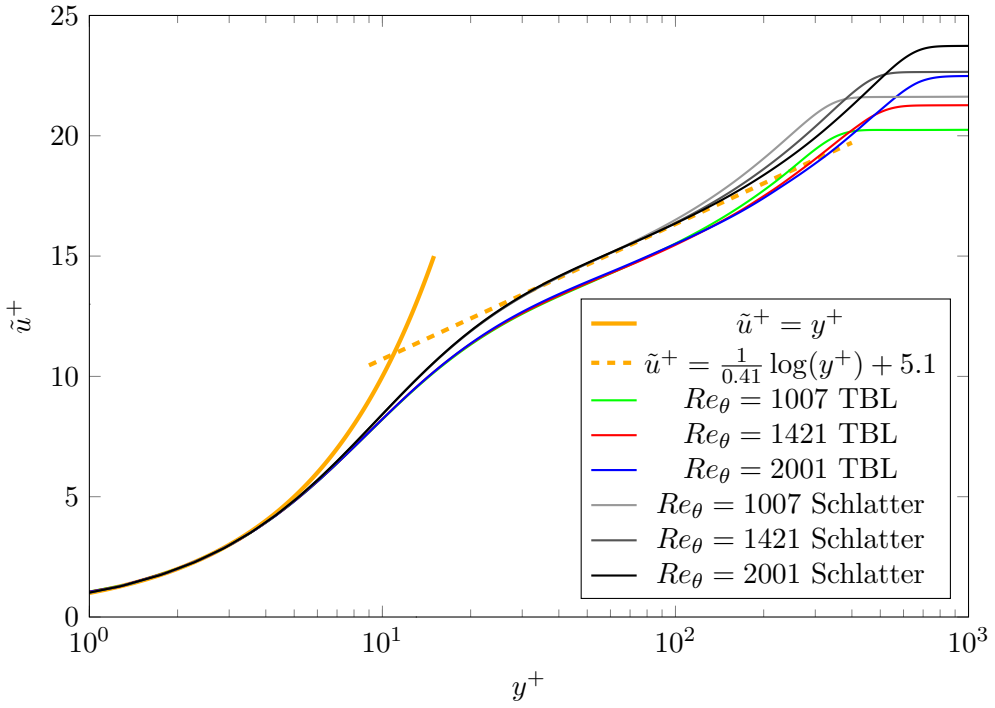

Figure 3.8: Mean velocity profiles in wall-scaling. As references, the yellow lines indicate the *law of the wall* and the gray profiles show incompressible DNS results from Schlatter & Örlü (2010). The coloured profiles show the present TBL data.

characteristic boundary condition (Thompson, 1990) that is described in more detail in section (3.1.2.1).

The spatial discretisation is done using standard differences in the streamwise and wall normal directions, whereas the spanwise direction is discretised using Fourier decomposition. For the discretisation of time a 4^{th}-order accurate 5-step Runge-Kutta method was chosen. Further details of the methods are outlined in section 3.1.1. The grid for the decomposition is a structured Cartesian mesh and counts 7200×260 points in the streamwise and wall-normal directions. 193 spanwise Fourier modes were used to discretise the spanwise direction. This leads to a total of about 723 million collocation points in the domain. The grid is stretched in the streamwise direction to keep the wall-scaled spacing relatively constant. The streamwise spacing has an upper bound of $\Delta x^+ < 5.12$ throughout the entire domain. The wall-normal location of the first point of the wall ($y = 0$) is located at $y^+|_1 \approx 0.600 - 0.712$ and the 10^{th} grid point is located at $y^+|_{10} \approx 5.43 - 6.40$. The collocation points in the spanwise direction have a spacing of $\Delta z^+ \approx 3.72 - 4.38$. After an initial transient of the simulation the flow reaches a statistically steady state. All presented data are sampled in the statistically steady regime. The statistics presented here are sampled over a non-dimensional time period of $\Delta T \approx 575$. The profiles of the mean streamwise velocity scaled with the friction velocity u_τ are presented in figure (3.8). The plot shows the incompressible *law of the wall* (in orange) as reference. Further results of an incompressible DNS of a turbulent

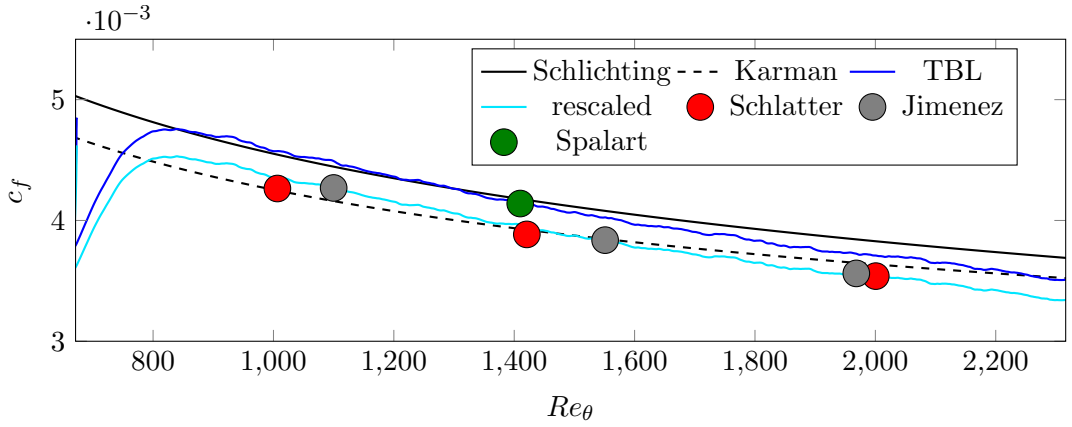

Figure 3.9: The skin friction comparison shows the two incompressible empirical formulas of Schlichting (continuous) and Karman-Schoenherr (dashed). The dots mark the values obtain by incompressible DNS from Schlatter & Örlü (2010) (red), Jimenez *et al.* (2010) (gray) and Spalart (1988) (green). The blue line shows the actual data of the present work, whereas the cyan line shows the present data after rescaling with the local wall viscosity.

boundary layer (Schlatter & Örlü, 2010) are added. The linear behaviour in the viscous sublayer as well as the slope of the log layer are captured well in the DNS of the present work. This is as first indication that the typical dynamics of a TBL are recovered in this simulation. The slight shift of the log-layer and the wall-scaled maximum velocity reflect a deviation in skin friction. This can have two reasons. On the one hand, we compare a compressible to an incompressible flow. The wall temperature in the present case is 1.05 compared to the freestream. This leads to an increase of viscosity ($\mu_{\text{wall}} = 1.05$) towards the wall which is directly affecting the skin-friction at the wall. Figure (3.9) shows the development of the skin friction in the present DNS in blue compared to different incompressible references. The skin-friction of Spalart (1988) matches well, whereas the DNSs of Jimenez *et al.* (2010) and Schlatter & Örlü (2010) are significantly lower. However it can be shown by a simple scaling with the viscosity, that this is a pure temperature effect. The cyan coloured line shows the skin friction divided by the local viscosity at the wall. The rescaled viscosity shows a perfect match with results of Jimenez *et al.* (2010). This reveals that the actual velocity gradient at the wall matches whereas the viscosity is different which results in a difference of skin-friction and, as we will see later, lower intensities of turbulence.

On the other hand, the turbulent inflow condition creates artificial disturbances that decay initially before they start growing again in amplitude and start to develop physical turbulence. This causes an imbalance of turbulent momentum that reflects in a stagnation of momentum thickness θ growth. Figure (3.10,top left) shows that the displacement thickness δ^* does not experience the same stagnation. Therefore the initial decay of the turbulence strength causes a shift of large scale quantities which is shown in the shape factor $H_{23} = \frac{\delta^*}{\theta}$ (fig. 3.10, top right). Further, figure (3.10,bottom) shows

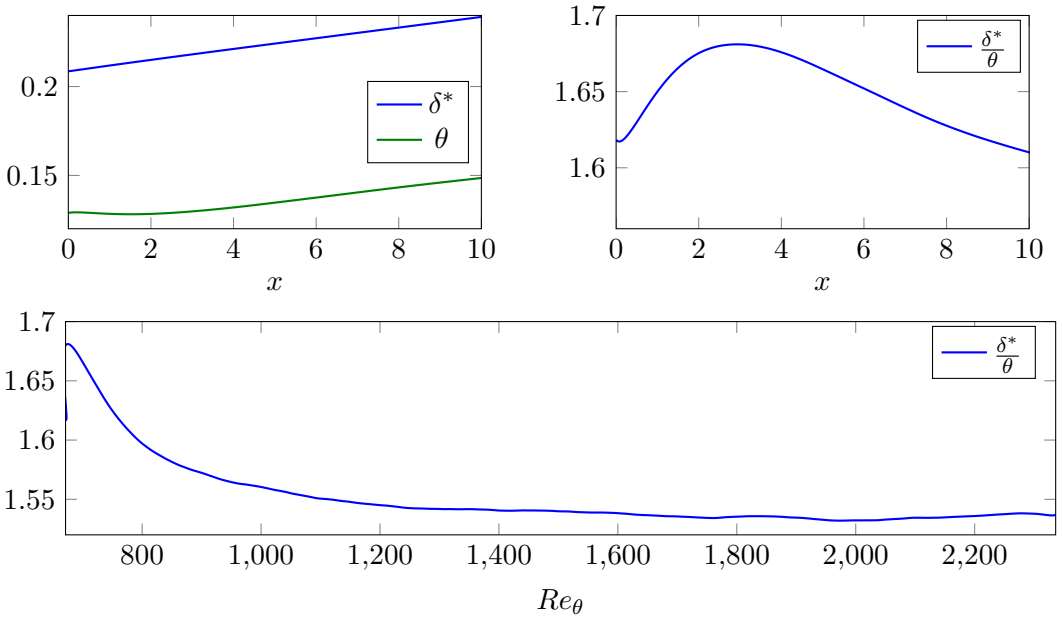

Figure 3.10: Boundary layer thicknesses and shape factor are plotted at the inflow region (top) and the development of the shape factor in the full domain is shown (bottom).

that this initial shift does not recover within the simulated domain length. Whereas a shape factor of $H_{23} \approx 1.3 - 1.4$ is expected for zero pressure gradient flat plate turbulent boundary layers, the present flow does stay above $H_{23} = 1.5$.
However, this shift will not affect the focus of the present work. We are focusing on the effects of a wall on turbulence. Whether this turbulence is studied in a canonical zero pressure gradient flat plate turbulent boundary layer or in a boundary layer flow that is close to the canonical case is not important. What we need to ensure is that the wall dynamics of turbulence are recovered. Therefore figure (3.11) shows the distribution of turbulence in the boundary layer. The components of the Favre stress tensor σ are shown in wall-scaling and plotted against the DNS data of Schlatter & Örlü (2010). The development of the profiles match and the amplitudes are well in the range of differences seen in literature (see fig. 3.3). The streamwise normal component $-\sigma_{11}$ shows a perfect match in the viscous sublayer, but the data of the present work does not recover the full intensity of the streamwise fluctuations in the buffer layer. This might well be caused by the difference in skin friction mentioned before. The mismatch of the buffer layer decays in the logarithmic sublayer so that there is a perfect match in the outer layer. On the other hand, all other components of the Favre stress tensor $-\sigma$ show a perfect match with the reference data throughout the entire wall-normal direction. Besides the wall-normal distribution, the streamwise development is recovered as well. It can be seen that both, present data as well as reference data, show the same trend with increased Reynolds number.
The energy distribution (fig. 2.7) in the flow was derived and described in section (2.2). This distribution is the driving force for turbulence in this TBL and one focus of the

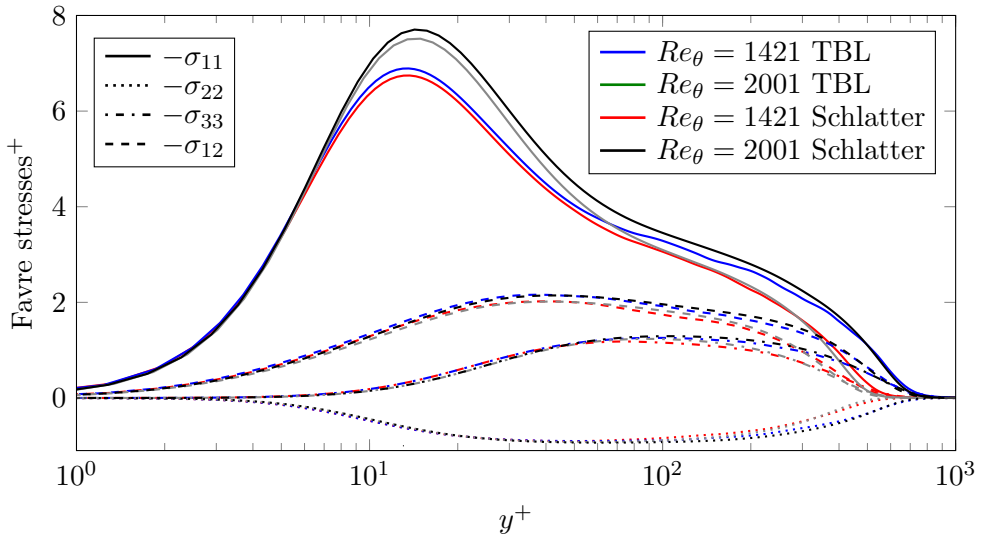

Figure 3.11: Comparison of the Favre stress tensor of the present work with the DNS results of Schlatter & Örlü (2010).

present work. Figure (3.12) shows the budget of the turbulent kinetic energy k in case of the filter operation being the Reynolds average operator. The figure compares the budget sampled from the data of the present work compared to the DNS data of Schlatter & Örlü (2010). A very good agreement can be seen over the entire wall-normal direction. All amplitudes are matching almost perfectly and the differences are mainly due to shifts of the respective profiles in the wall-normal direction. The peak of turbulent production, for instance, is closer to the wall in the present data set than it is for the incompressible DNS data of Schlatter & Örlü (2010). On the other hand, the magnitude of dissipation and diffusion at the wall are slightly increased. However, all differences are well within an acceptable range and the data is therefore well suited for a detailed study of the near wall dynamics of turbulence and its characteristic distribution.

The budget of the turbulent kinetic energy (fig. 3.12) reveals the forces that keep the turbulent kinetic energy statistically constant at every point in the boundary layer. The strong variation of governing forces in the wall-normal direction indicates that the properties of the turbulence itself might vary equally strongly in the wall-normal direction. This is a fact that is reflected by the varying composition of turbulence that can be seen in figure (fig. 3.11). To understand this better, we can take a walk through the static turbulence cycle in the near wall region. As we can see in figure (2.7) it takes two things to produce turbulent kinetic energy. One is turbulent motion itself, represented by σ ($k = -\frac{1}{2}\text{trace}(\sigma)$), and the second part is a mean strain rate $\bar{S}$.

Figure (3.13) shows the main ingredients of wall bounded turbulence. The presence of a strongly varying streamwise mean velocity profile $\tilde{u}$ results in a strong wall normal velocity gradient $\frac{\partial \tilde{u}}{\partial y}$ i.e. a strong strain rate. Intuitively one might think that the location of the highest strain rate, the wall, would cause the strongest production. But the wall itself bounds the kinetic energy in the near wall region. The strong potential that is

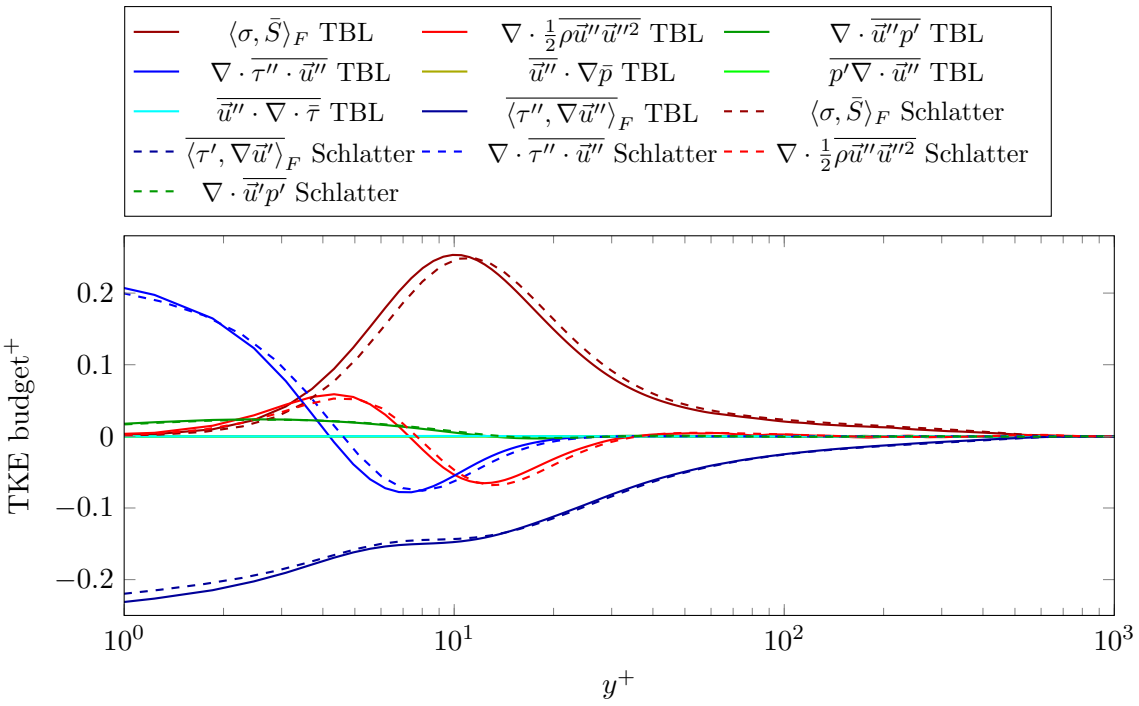

Figure 3.12: Turbulent kinetic energy budget at $Re_\theta = 2001$. Results of the present work are shown as continuous lines and compared with results of Schlatter & Örlü (2010) (dashed lines).

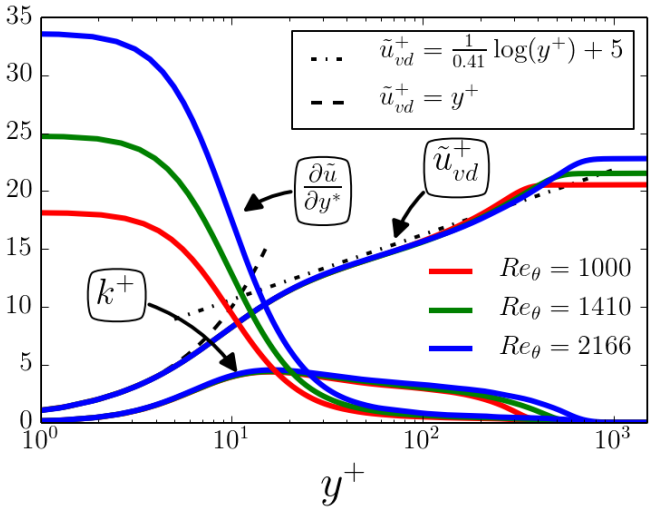

Figure 3.13: Plot of the main ingredients of wall turbulence from a static point of view.

provided by the velocity gradient cannot be exploited very close to the wall. Therefore the production is shifted in the buffer layer as we can see in figure (3.12). The relatively local production peak causes an imbalance of turbulent kinetic energy which will be redistributed by other mechanisms. The two strongest forces that redistribute this initial imbalance of produced turbulence are turbulent transport and turbulent diffusion.

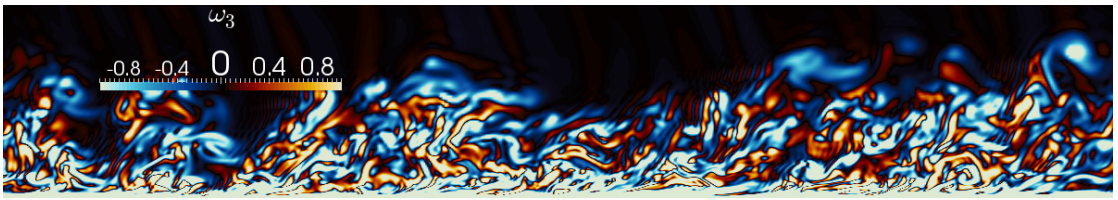

Figure 3.14: Instantaneous snapshot of spanwise vorticity in the turbulent boundary layer. The image shows as constant z-plane. The flow direction is left to right.

The first of the two redistributes kinetic energy via turbulent mixing and can only act strongly where turbulence itself is strong. It mixes turbulent kinetic energy by transporting it on larger structures in different regions. For instance, a small vortex travelling within a larger vortex. On the other hand, turbulent diffusion results from friction and can redistribute turbulent kinetic energy toward regions were only little kinetic energy is present. As figure (3.12) shows, it is the main contributor that brings turbulence into the viscous sublayer. This already shows that the main part of turbulence in the viscous sublayer is neither produced there nor is it transported there via turbulent mixing. It is to a large extent caused by viscous effects that find their origin further away from the wall - i.e. it is a footprint of turbulent structures in higher layers that reaches down to the wall. At the end of the cycle the produced and redistributed turbulent kinetic energy is finally dissipated into heat. This process is most active at the wall and is monotonously decaying towards the freestream.
Following these static observations we can discuss the same mechanism from a dynamic point of view by studying instantaneous snapshots of the turbulent boundary layer. Here as well the strongest alternation of quantities in TBLs is found in the wall-normal direction. An impression of this is given by figure (3.14) which shows contours of the spanwise vorticity component (ω_3). The wall is located at the bottom of the figure. Besides some weak sound waves the freestream is in a laminar regime. The laminar-turbulent interface is indicated by the slightly blurred border between the region of mainly zero vorticity (black) and the region with varying vorticity (strongly coloured). This interface has a strongly irregular shape and contains steep canyons reaching close to the wall as well as peaks reaching far in the laminar region. On a closer look one might be able to argue that the interface has a fractal like character. On the turbulent side of the laminar-turbulent interface a variety of turbulent structures across a wide range of spatial (and temporal) scales are present. At a larger distance to the wall more bulky structures are found and a variety of directivities can be observed. Approaching the wall the structures become stronger and the relative variation is higher. Structures are thinner but not necessarily much shorter. The preferred space for the elongation of thin structures appears to be the wall parallel plane with a slight lift in the streamwise direction. In the near wall region we find an apparently continuous layer of the most extreme values of spanwise vorticity.
Another perspective on the dynamics, that form the skeleton for the presented statistics,

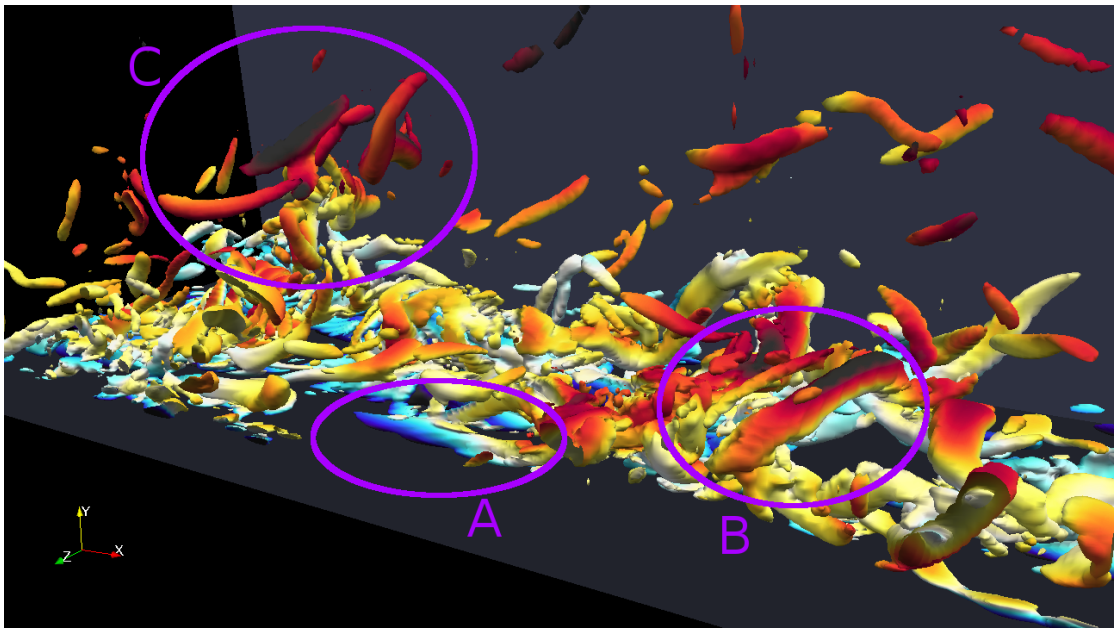

Figure 3.15: Turbulent structures in a TBL visualized as iso-surfaces of the discriminant of the velocity gradient tensor and coloured with streamwise velocity. The flow direction is left to right.

is given in figure (fig. 3.15). This figure provides an overview of the spatial composition of a turbulent boundary layer. The wall is at the bottom and the flow direction is x. The visualization of turbulence with a vortex identification criterion helps to obtain an impression of the variety of the different structures and structure formations that can be found in wall-bounded flows. In the direct periphery of the wall the majority of structures are relatively straight tubes that are predominantly elongated in the streamwise direction (region 'A'). Moving further away from the wall a three dimensional structure shape can be developed. In region 'B' an arc-shaped vortex followed by an aligned smaller vortex can be seen. In the outer regions of the boundary layer the structures seem to be free from any boundaries and develop seemingly random alignments. Region 'C' highlights a cluster in the outer region. Besides the alignment it can be seen that the structure density is rapidly decreasing towards the outer regions of the boundary layer. To get an impression from a different perspective figure (3.16) shows the view on the wall from above while the flow direction in the image is bottom to top. The flow structures are shown at a more sensitive level and therefore more structures are shown. The TBL is sliced at the different levels in the wall-normal direction. On the left the cut is in the near wall region. As mentioned before, the majority of structures in this layer is elongated in streamwise direction. The colours are an indication of the instantaneous streamwise velocity, the with dark blue being slow and dark red being fast. Most of the structures close to that wall are relatively slow but clusters of structures with higher velocity can be found in between (region 'A'). In literature these structures are referred to as high speed streaks. These clusters of smaller structures can form very long

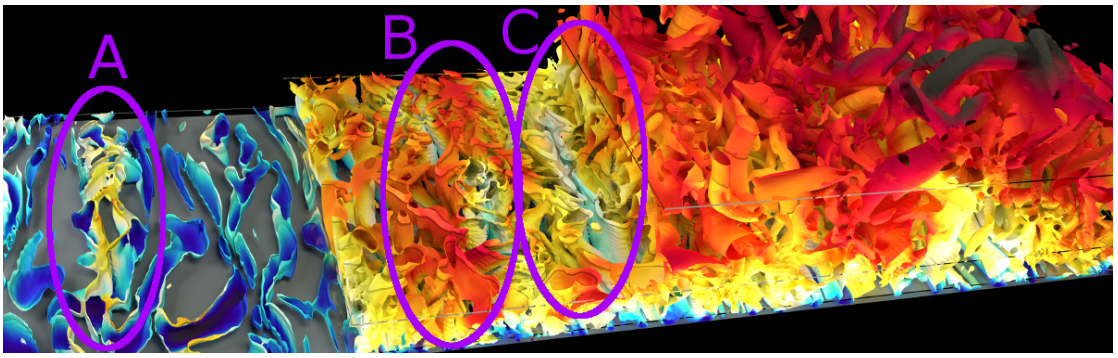

Figure 3.16: Turbulent structures in a TBL visualized as iso-surfaces of the discriminant of the velocity gradient tensor and coloured with streamwise velocity. The flow direction is bottom to top.

streamwise elongate super structures. Focusing on the center of the image, a slice further elevated from the wall is shown. Structures at this height are packed more densely, but show a higher variation in their directivity than the ones closer to the wall. Like in the area closer to the wall streamwise elongated clusters of higher velocity (region 'B') can be seen. Besides that also their low velocity counterparts (region 'C') are present. In literature these spots of lower velocity in higher layers are called ejections. On the outer region of the TBL can be seen that like in the middle section the structures show a high variation of directivity and a broad range of shapes. More than that the structure density is decreasing towards the outer region.
Overall, we have seen that from a static point of view as well as from a dynamic point a view, a turbulent boundary layer flow is bearing complex turbulent mechanism. On the other hand boundary layers are present in the majority of engineering flows. These are the two driving reasons why this flow will be the focus of the present work.

3.3.2 Jet

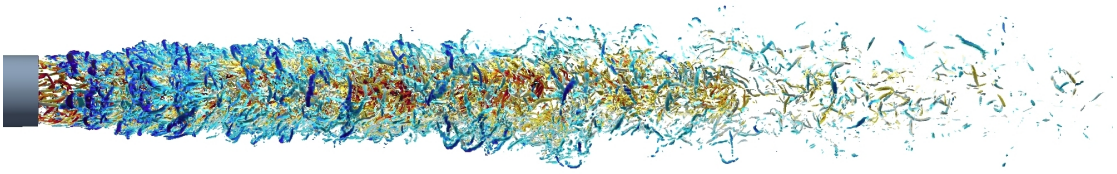

Figure 3.17: Iso-surfaces of the Q-criterion at a level of $Q = 3$ coloured with streamwise velocity (see fig. 3.18 for color levels).

In the context of wall-bounded flows and free shear flows a compressible turbulent pipe flow exiting in a laminar co-flow was investigated. A detailed description of this flow and the setup can be found in Sandberg *et al.* (2012). In this report we outline the general setup and the important features of the flow in the context of investigations on universality arguments.

The coordinate system for this case is cylindrical with its axis at the center of the pipe. The Reynolds number was chosen to be $Re_R = 3350$ based on radius and bulk velocity, the Mach number and Prandtl number were set to be $M_\infty = 0.46$ and $Pr_\infty = 0.72$ respectively. The streamwise and radial direction were discretised with a standard finite difference method (3.1.1). The wall-scaled streamwise resolution has a maximum at the inflow $\Delta x^+ \approx 16$ and becomes finer towards the nozzle exit, where $\Delta x^+ \approx 1.8$. In the radial direction 68 points were used and the location of the first grid point off the

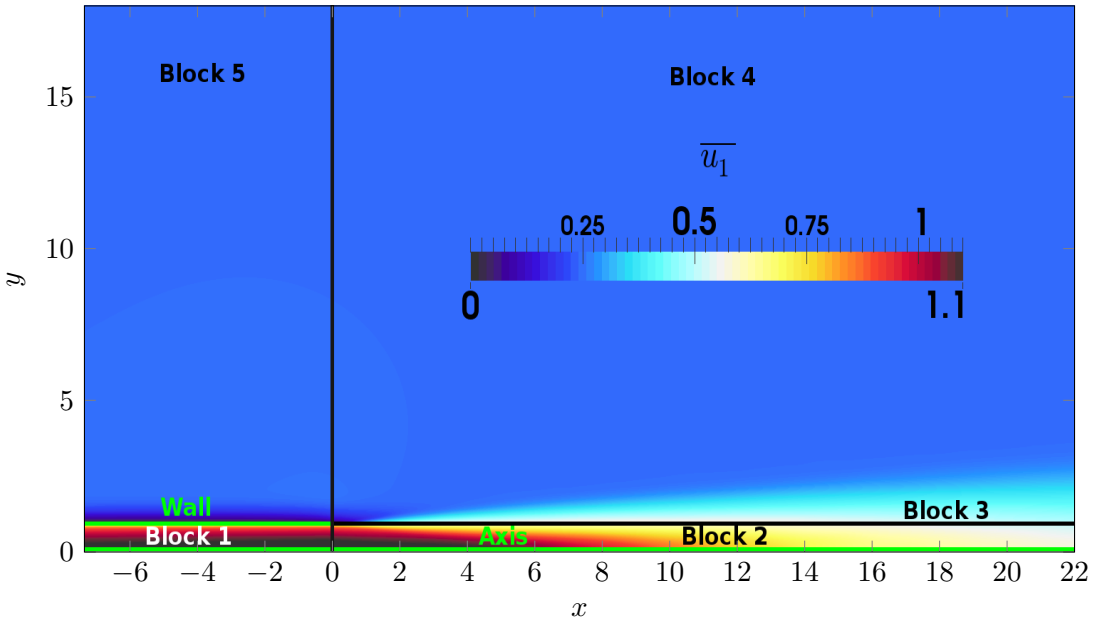

Figure 3.18: Streamwise mean velocity contours at the exit location of the pipe and schematic setup of the flow domain.

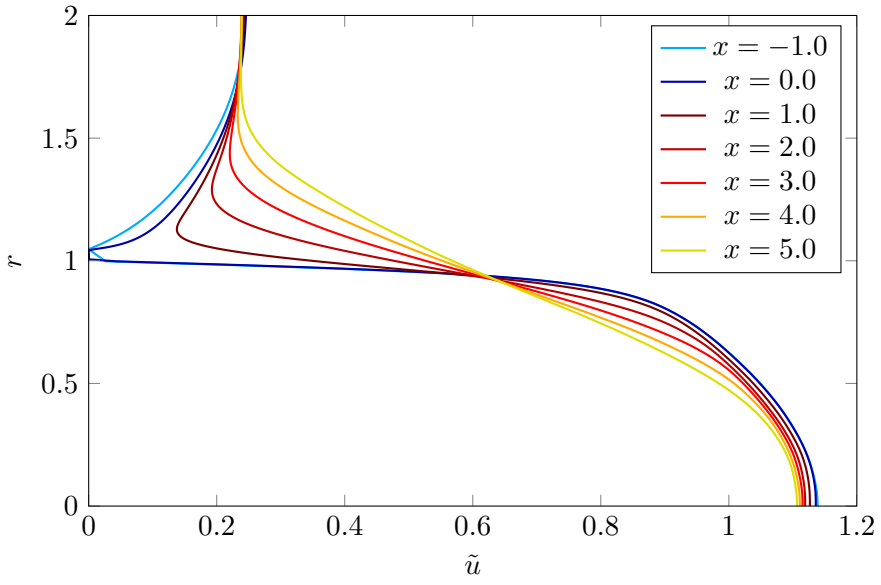

Figure 3.19: Streamwise mean velocity over radial direction at different streamwise locations. The pipe wall is located at $r = 1$, the axis at $r = 0$, and the pipe exit at $x = 0$.

wall is at $y^+ \approx 0.91$ with the wall being at 1. The grid in the wall-normal direction is stretched towards the axis. In the azimuthal direction the Navier-Stokes equations are discretised with a Fourier method as periodicity is given in this direction. For the present case a total of 64 Fourier modes were chosen, which leads to a spacing of $\Delta z^+ \approx 16$ at the wall. Due to the cylindrical coordinate system, this value tends to 0 towards the axis. To avoid the CFL number to go to infinity for a given timestep, a mode-clipping and an axis-treatment (Sandberg, 2011) is applied close to the axis. The pipe inflow is an artificial turbulent inflow condition (3.1.2.2) whereas the inflow at the co-flow is a laminar boundary layer profile with a freestream velocity of 0.2. The outflow is a zonal characteristic outflow condition (Sandberg & Sandham, 2006) to minimize artificial reflections from this boundary (see sec. 3.1.2.1 for details). The freestream is an ordinary non-reflective characteristic boundary condition (Thompson, 1990) that is described in more detail in section (3.1.2.1). The general setup of the computational domain is shown in figure (3.18).

When the flow in the pipe reaches the nozzle the velocity profiles vary and the flow changes its characteristics from a wall-bounded turbulent flow to a free shear flow. This transition region will be studied in the present work into context of universality aspects. Therefore a more detailed description of the flow around the nozzle is needed. Figure Figure (3.19) shows the development of the streamwise mean velocity profile dependent on the radial location in the streamwise direction. The velocity profile in the pipe does not significantly change once turbulence has fully developed. This is true until the flow comes close to the nozzle. Approximately at $x = -1$, the profile starts adjusting from a typical profile for wall-bounded flows towards a free shear flow profile. Five radii ($x = 5$)

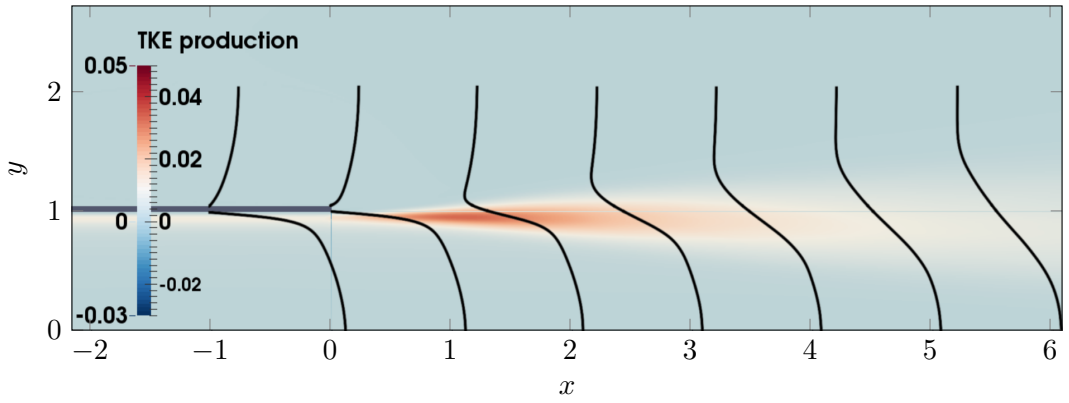

Figure 3.20: Contour plot of TKE production around the pipe exit. The black curves show the streamwise mean velocity profile at the locations $x = -1, 0, 1, 2, 3, 4$ and 5. Compare with figure 3.19 for quantitative information.

downstream of the nozzle, the velocity profile shows the typical characteristics of a free shear flow profile. The change of the mean velocity profile causes a change in the TKE production and therefore changes the source of turbulence (fig. 3.20).
Downstream of the nozzle we can see a strong increase of the TKE production magnitude as well as a widening of the area where turbulence is produced. Whereas the area of the main production in the pipe was limited to a small area in the buffer layer, already 5 radii downstream of the nozzle the area has spread over almost one radius in the radial direction. The TKE production is a product of Favre stresses and the mean strain rate tensor

$$\langle \sigma, \bar{S} \rangle_F, \tag{3.17}$$

where σ is the Favre stress tensor and $\bar{S}$ is the Favre averaged strain rate tensor. To understand the roots and character of the production and its development in the streamwise direction we will take a closer look at its components.
Figure (3.21) shows that the strain rate tensor develops strong anisotropy in its normal components once the flow reaches the nozzle exit as well as downstream of the nozzle. This leads to a change in the composition of the turbulence production. While at locations towards the outer end of the buffer layer (at $r = 0.882$) and at the end of the logarithmic layer (at $r = 0.674$) the wall-normal strain component is increasing, in the viscous sublayer (at $r = 0.977$) the streamwise strain component is increasing. Due to low mean compression and a two-dimensional mean flow, the two presented normal strain components are almost additive inverses of each other. The behaviour of the profiles show that the logarithmic layer of the boundary layer at the pipe wall is entirely contained within the jet core whereas the viscous sublayer is merged into the shear layer of the jet. What the present plots do not show is that the lion share of the buffer layer and therefore the peak of the streamwise normal component of the Favre stress tensor is merged into the shear layer. In this region the high amplitude streamwise Favre stress component and the high amplitude streamwise strain component are amplifying each

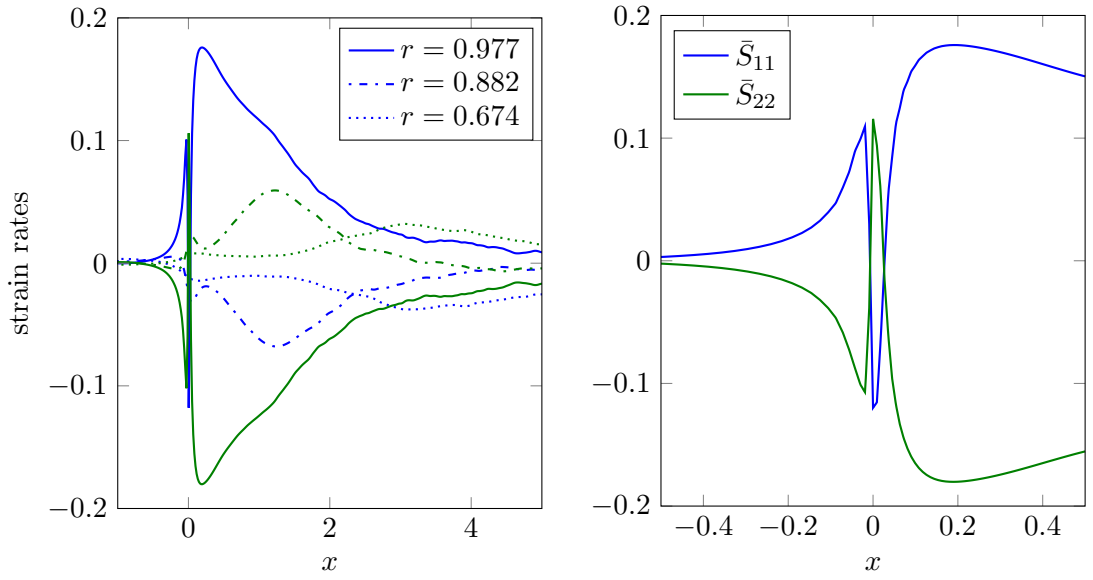

Figure 3.21: Mean values of the normal strain rate components plotted over streamwise direction at three different radial locations (left). The plots on the right are zooms into the near nozzle region for the radial location $r = 0.977$.

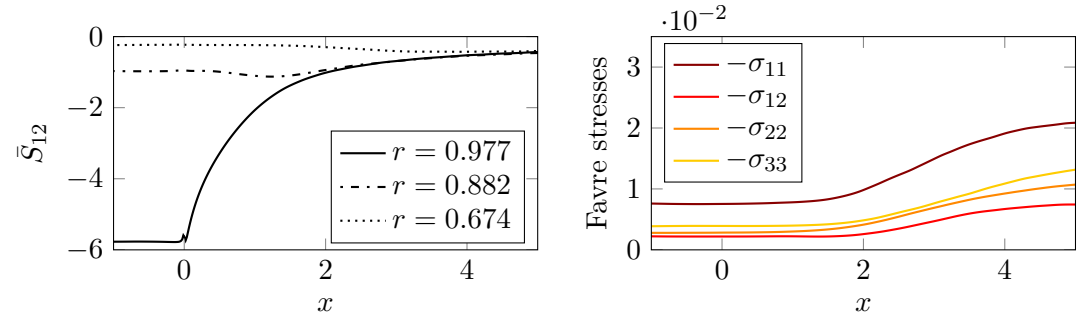

Figure 3.22: Left: Mean shear stress plotted over the streamwise direction. Right: Favre stresses plotted over streamwise direction at radial location $r = 0.674$.

other and become the strongest contributor to the TKE production. The mean shear (3.22 left), which is the strongest component of the strain rate tensor in wall-bounded flows, is rapidly decreasing its magnitude at $r = 0.977$ after exiting the pipe. This leads to the fact that the anisotropy of the strain rate tensor is changing from the transverse terms to the normal terms which changes the character of this tensor. For $r = 0.882$ the effect is similar but less intense. However, at the end of the logarithmic layer (at $r = 0.674$) the shear component is slightly increasing, so that the shear has the same magnitude for all three locations from 5 radii downstream of the nozzle onwards.
Figure 3.22 (right) shows the development of the Favre stresses at the end of the logarithmic layer ($r = 0.674$). It shows an increase in all components, but no significant change in their ratios. On the other hand, figure (3.23) shows that the components in the viscous sublayer (left) and at the end of the buffer layer (right) change their ratios. Whereas

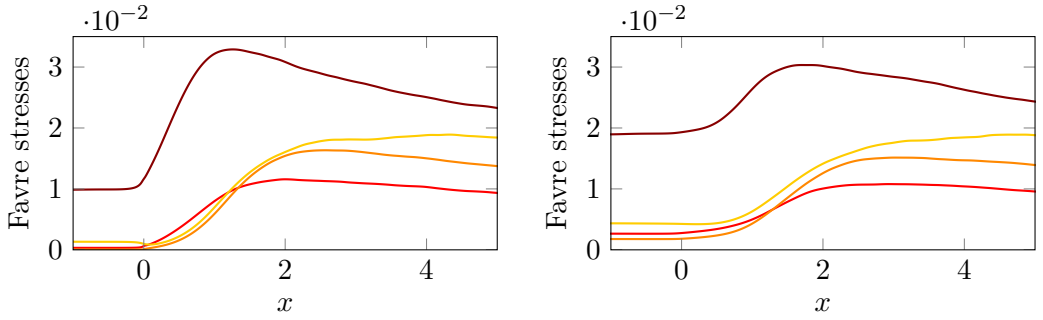

Figure 3.23: Favre stresses plotted over the streamwise direction at $r = 0.977$ (left) and $r = 0.882$ (right). Legend see figure (3.22).

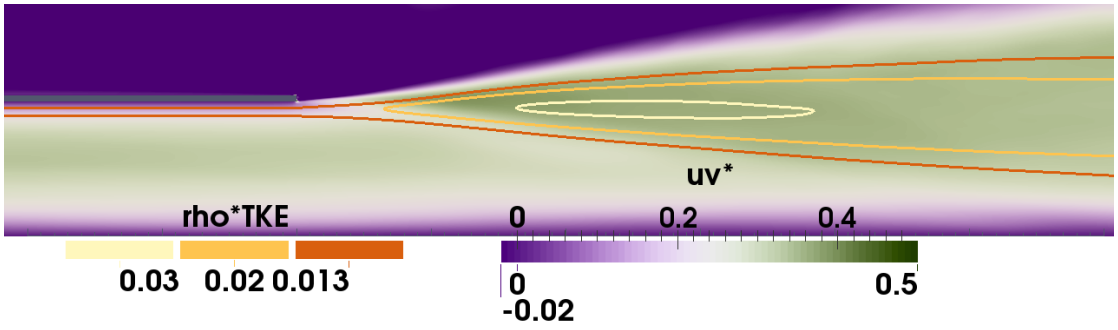

Figure 3.24: Contours of the Favre shear stress component normalized with local TKE ($uv^* := \frac{\widetilde{\overline{\rho} u'' v''}}{\overline{\rho}\mathrm{TKE}}$). The iso-lines show $\overline{\rho}$ TKE at three different levels.

the streamwise and wall-normal components show a slow decrease after a sharp increase downstream of the nozzle, the normal component in the azimuthal direction shows a longer and relatively higher increase. Although the streamwise normal component remains the dominant quantity of the Favre stress tensor, the overall characteristics are changing due to its normal components. Further there is a recognizably steeper increase of the shear stress component close to the nozzle. This is more clearly shown in figure (3.24) where the shear stress is normalized by the product of density and TKE. It shows the stronger increase of the shear stress in the whole area around the global maximum of TKE which balances again a few radii downstream of the peak. A last characteristic that should be emphasised at this stage is the development of the non-equilibrium state. In the last section (3.3.1.2), the non-equilibrium state in a boundary layer was outlined. The pipe flow develops a flow very similar to the described one. Once the effect of the wall is lost and the jet starts to spread, the balance changes rapidly. The TKE production is increasing much more than the dissipation which leads to an axial imbalance of production and dissipation. This is not the case inside the pipe.
Overall it can be said that turbulence itself as well as its sources and sinks are strongly changing their character downstream of the nozzle, what makes this case interesting in the context of universality aspects of turbulence.

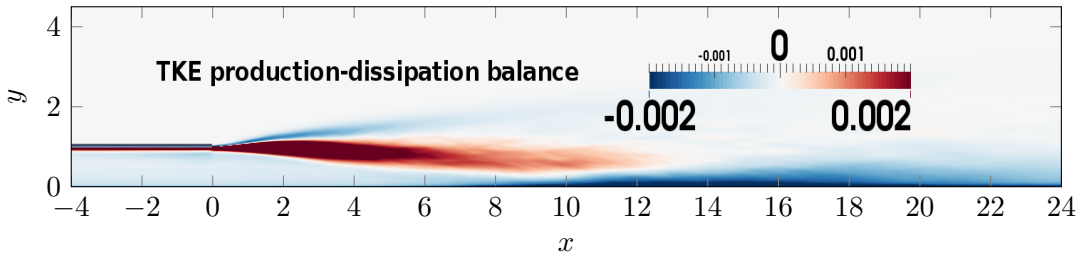

Figure 3.25: Contours show the sum of TKE production and dissipation rate.

3.3.3 Supersonic Wake

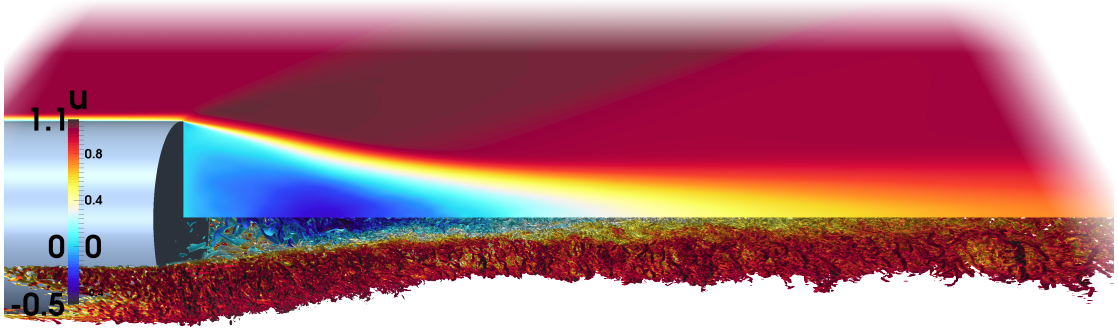

Figure 3.26: Supersonic wake behind an axisymmetric cylinder shown as iso-surfaces of the Q-criterion at a level of $Q = 5$ coloured with streamwise velocity.

In this section a supersonic turbulent flow around an axisymmetric cylinder is outlined. The focus will be on the shear layer, the recirculation region and the wake the flow is developing downstream of the cylinder. A more detailed description of the setup and the DNS of this case can be found in Sandberg (2012*b*). A schematic setup of the computational domain as well as the streamwise mean radial pressure gradient is shown in figure 3.27. The Reynolds number based on cylinder radius and freestream velocity is $Re_R = 50000$. At the inflow an artificial turbulence condition (3.1.2.2), that creates a thin turbulent boundary layer on the surface of the cylinder, is set as inlet. The boundary layer thickness at the trailing edge is $\delta_{99} \approx 0.12$. The freesteam Mach number at the inflow is $M_\infty = 2.46$, which leads to an expansion fan forming at the trailing edge of

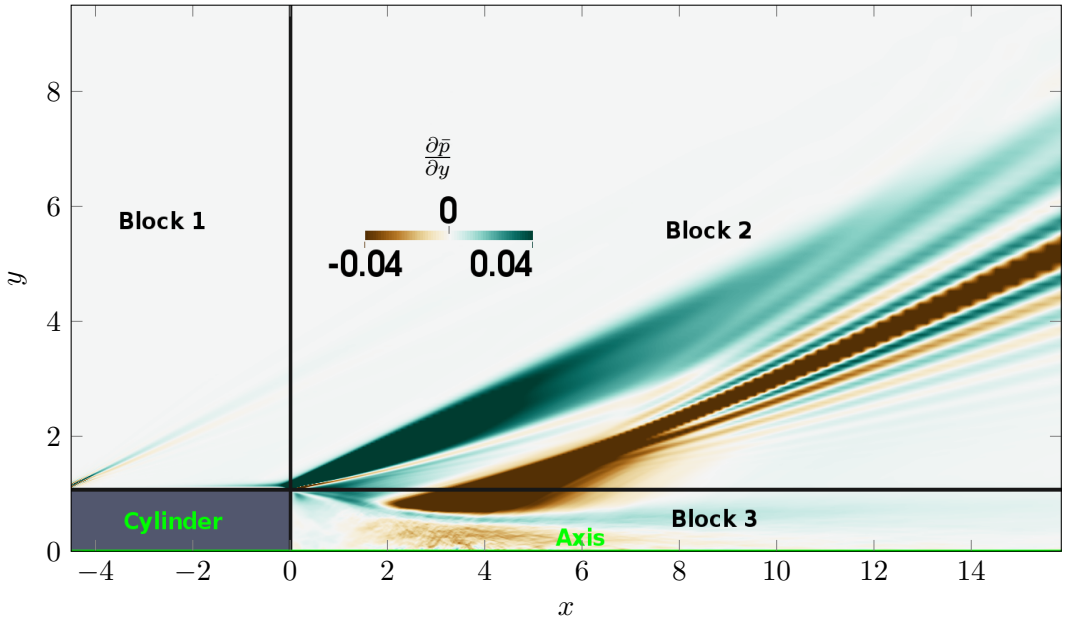

Figure 3.27: Streamwise mean velocity contours at the exit location of the pipe and schematic setup of the flow domain.

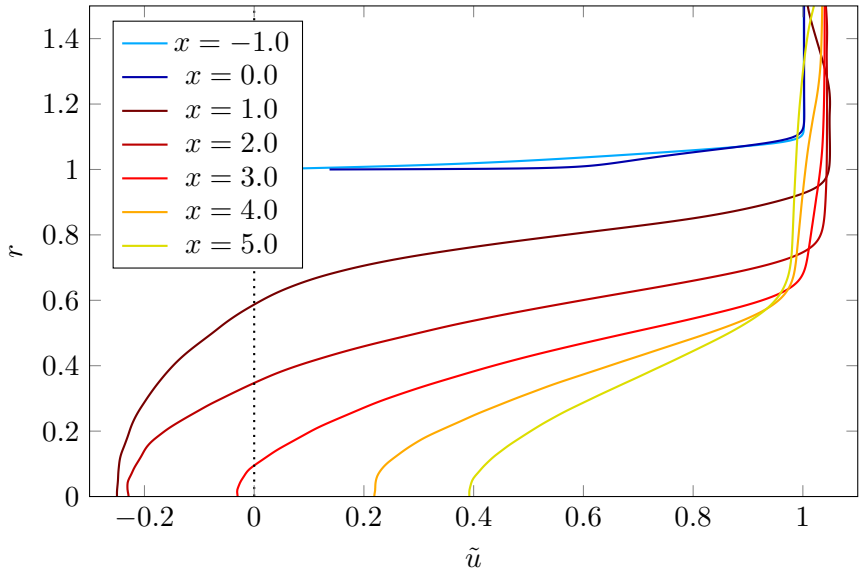

Figure 3.28: Streamwise mean velocity over the radial direction at different streamwise locations. The cylinder wall is located at $r = 1$, the axis at $r = 0$, and the end wall of the cylinder at $x = 0$.

the cylinder and a recompression shock system in the wake of the cylinder. The Prandtl number is set to be $Pr_\infty = 0.72$. The discretization scheme and axis-treatment are the same as in the case of the jet (3.3.3).

Figure 3.28 shows the development of the streamwise mean velocity profile along the streamwise direction. The light blue profile shows the turbulent boundary layer on the cylinder at $x = -1$ and the blue profile shows mean velocity at the trailing edge ($x = 0$). The sharp trailing edge forms a singularity on the domain boundaries. Therefore it demands a special numerical treatment which leads to the velocity not being exactly zero at this point. Marching further downstream the development of a recirculation region

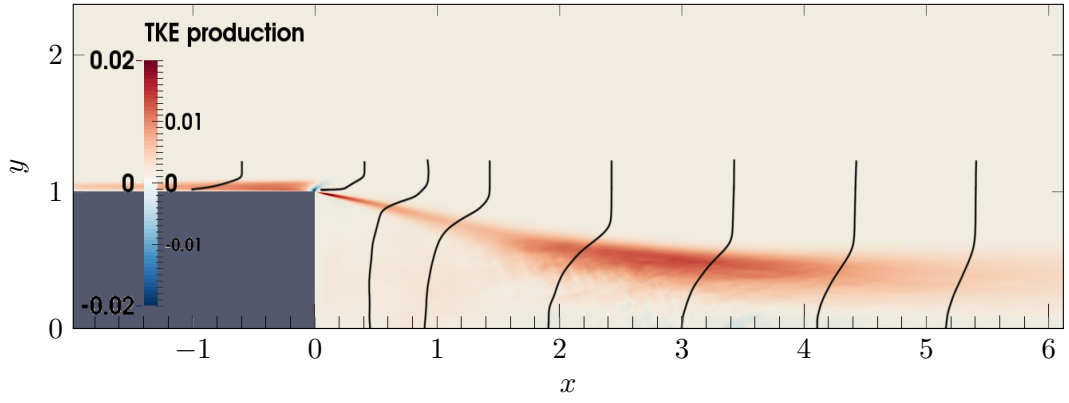

Figure 3.29: The contours show the production of turbulent kinetic energy at and behind the cylinder (grey). The black lines show streamwise mean velocity profiles at the locations $x = -1, 0, 0.5, 1, 2, 3, 4$ and 5 (see fig. 3.28 for a quantitative impression).

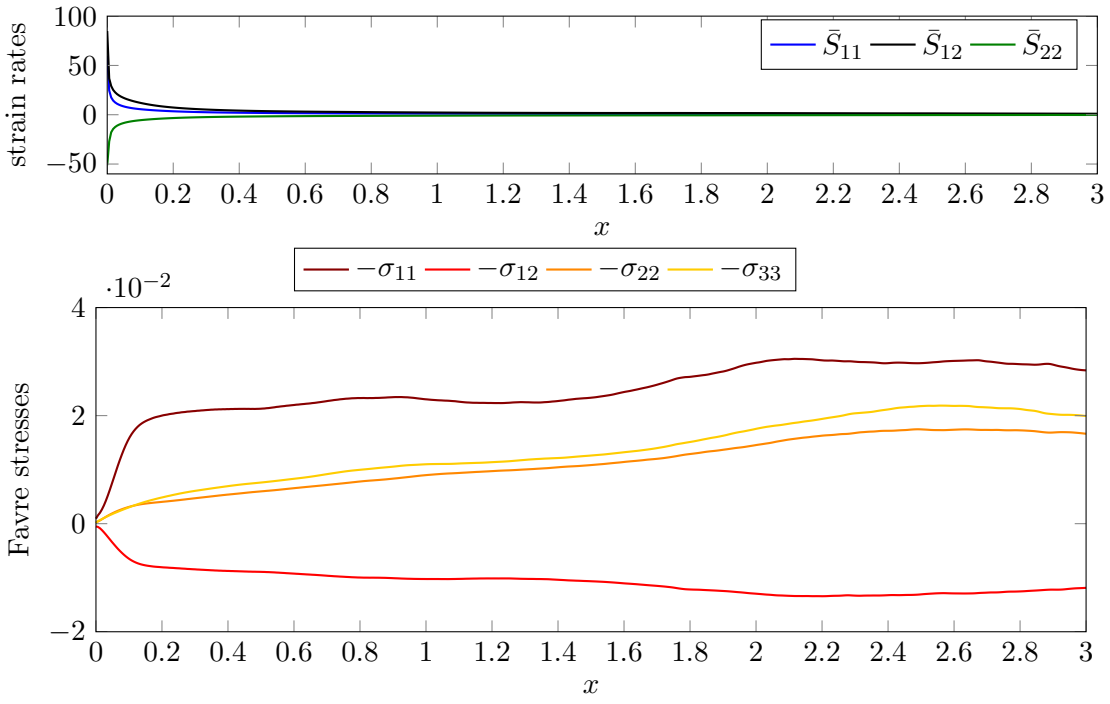

Figure 3.30: Data for these plots is taken along the centerline of the shear layer $((0.00, 1.00) - (3.00, 0.38))$. The top graph shows the development of the mean strain rate tensor components and the bottom graph shows the development of the Favre stress components.

can be seen at $x = 1, 2$. This region ends in a statistical stagnation point around $x = 3$. From there onwards, a wake profile is developing. The TKE production caused by the boundary and shear layer is shown in figure 3.29. Around the trailing edge expansion fan negative production can be found. Downstream of this location a remarkable increase of production is taking place, which is caused by the loss of the wall-effect and the strongest part of the shear layer which is found at this location. This behaviour is similar to what we have found in the jet case (3.3.2). If we follow the centerline of the shear layer downstream the TKE production is slightly decreasing until it starts again to increase towards a second peak at about $x = 3$. This second peak did not exist in the jet case and cannot be explained by the streamwise mean velocity profile. Further, we take a look at the components of TKE production (eq. 3.17) (figure 3.30). Here we can see that all strain components are strictly monotonically decreasing in the shear layer whereas the Favre stress components show a sharp increase at the start of the shear layer which fades into a slower increase. At $x \approx 1.5$ a second stronger increase is initiated. The development of the strain rates clearly states that the second peak of production is not caused by the shear layer itself, but by the increase of turbulent quantities which are amplified just before the second peak of TKE production. To find a possible explanation for the increase of the Favre stresses figure 3.31 is helpful. It shows the distribution of the streamwise pressure gradient in the flow. The recompression shock system (red) is

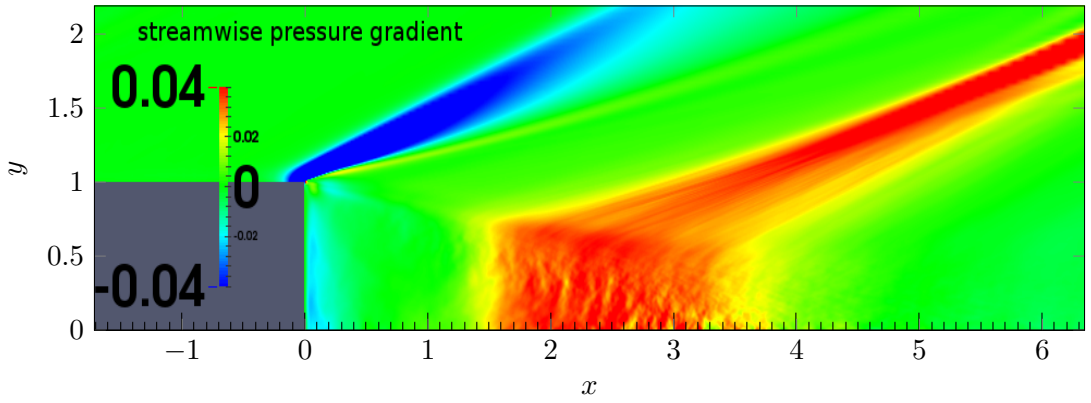

Figure 3.31: Contour plot of the mean streamwise pressure gradient. The strongest negative gradient (blue) is found where the expansion shock is located and the strongest positive gradient (red) is found around the recompression shock system.

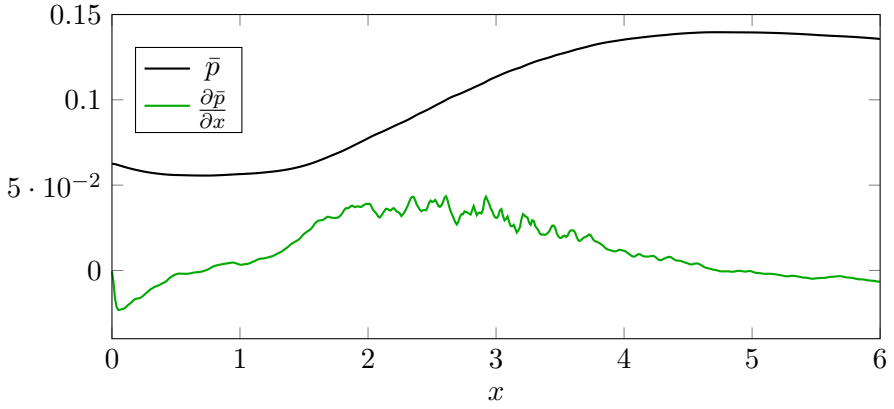

Figure 3.32: Streamwise development of the mean pressure (blue) and its streamwise gradient (green). Data is taken along a line parallel to the axis at $r = 0.1$.

affecting the shear layer exactly at the location where we find the second increase of TKE which is causing its own production to rise. Figure 3.32 allows a more quantitative impression of the pressure and streamwise pressure gradient development. It states the steepest increase of the streamwise pressure gradient to be located at $x \approx 1.5$, which is the same location were we can find the increase of the Favre stresses.

This development of the TKE production then leads to the distribution of TKE that we can find in figure 3.33. Here we can see that the peak of TKE is far downstream of the highest strain magnitude of the shear layer and can be found between $x = 3.2$ and $x = 3.6$. This is just downstream of the peak of the streamwise derivative of the mean pressure. These characteristics of the presented wake flow makes it interesting to investigate this region separatly in terms of effect of the pressure gradient on turbulence.

A last feature that is outlined in this introduction of the wake is the balance of TKE production rate and TKE dissipation rate (figure 3.34).

The distribution in the early shear layer region ($x < 1$) is similar to what we have seen

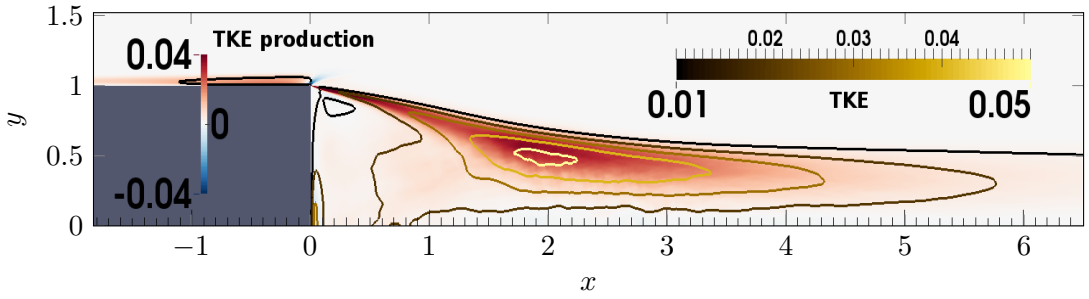

Figure 3.33: The contours show the production of turbulent kinetic energy at and behind the cylinder (grey). The superimposed lines make isolines of $\overline{\rho}$ TKE at five different levels.

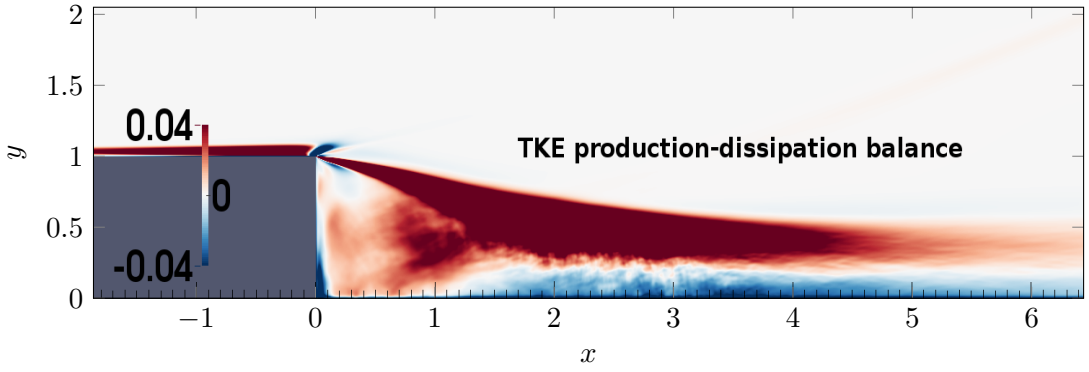

Figure 3.34: Contours show the sum of TKE production and dissipation rate.

in the jet case (figure 3.25). Downstream of this point the wake is clearly divided into an outer part where production exceeds dissipation and a core where dissipation exceeds production. This shows the non-equilibriums state of this wake.

Chapter 4

Universal and Non-Universal Features of the Velocity Gradient in Non-Equilibrium Flows

The universality of properties of the velocity gradient is investigated in flow-data obtained from direct numerical simulations. The analysis compares a turbulent boundary layer flow with the shear layer of a turbulent jet and the recirculation region of a supersonic wake flow behind an axisymmetric, streamwise elongated cylinder. For most of the investigated flow regions the production and dissipation of turbulent kinetic energy are in a rather strong imbalance i.e. the flow takes locally a non-equilibrium state. To span a wide variety of flow topologies some of the chosen regions are exposed to a strong mean shear whereas others are located in regions with nearly zero mean gradients. As first universal feature the invariant log-normal distribution of the velocity gradient magnitude is shown. Further, the coupling of the mean shear strength with the variations of the correlation between strain rate magnitude and the rotation rate magnitude and the variations of the strain-rotation-alignment is discussed and potential universal aspects are proposed. Lastly, the characteristic distribution of turbulence, that is reflected in QR-plots, is shown to be not an universal feature of turbulence.

4.1 Introduction

Turbulence models are used to reduce the complexity of a turbulent flow to allow a simpler description of the aforesaid. This allows a quicker and cheaper work-flow for design processes that involve complex turbulent flow. But, the development of such models in general is slow as different (specific) models are needed for different flows (Blackburn *et al.*, 1996). The large scales of motion in a flow depend on and vary with the respective geometries and boundary conditions that are imposed on the flow. In other words,

the large scales will always be case dependent. However, the part of turbulence that should be covered by the models often reduces to the small scales in the respective flow. Kolmogorov (1941) hypothesized that for *large enough* Reynolds numbers *small enough* scales of motion are statistically universal across different flows. This means that the small scales become independent from geometries and boundary conditions and it should be possible to apply universal turbulence models with the same accuracy across all flows that fulfil the condition set by Kolmogorov (1941). Unfortunately the thresholds when a Reynolds number is large enough and when a scale of motion is small enough are not found yet.

It is important to study different flows to investigate the potential limits of models in order to push them to as universal a state as possible. Therefore key quantities for turbulence need to be identified and decomposed into their essential pieces. The behaviour of those pieces need to be studied in many different flow topologies to identify potential universal features. If universal mechanisms are found they need to be described mathematically and put together with the remaining pieces. The recomposed flow quantity now contains the respective universal model. So far the theory.

In this chapter we focus on the velocity gradient $A := \nabla\vec{u}$ in the flow. Chong *et al.* (1990) have shown that the velocity gradient is an important quantity to study turbulence as it determines the local flow topology. Further, it decomposes ($A = S + \Omega$) into the strain rate tensor S and the rotation rate tensor Ω. Both are of inherent importance for turbulence as the strain rate is associate with the dissipation of kinetic energy to heat and the strain coupled with rotation governs the vortex stretching process (Tsinober, 2000; Hamlington *et al.*, 2008) that is important for the cascading process that drives turbulence.

Buxton & Ganapathisubramani (2010) have shown that the sign of enstrophy production, and therefore the decision if enstrophy is produced or destoyed, is coupled with the alignment between the vorticity vector $\vec{\omega}$ and the extensive strain direction $\vec{r}_1$. This shows one significant property of the alignment of vorticity with the principal strain directions. It is seen as a universal feature in turbulent flows (e.g. Elsinga & Marusic, 2010) that the vorticity shows the tendency to align parallel with the intermediate strain direction $\vec{r}_1$. This was stated and supported for many different flows including homogeneous isotropic turbulence (HIT), free shear layers, turbulent boundary layers and atmospheric turbulence as well as a variety of Reynolds numbers (e.g. Ashurst *et al.*, 1987; Tsinober *et al.*, 1992; Vincent & Meneguzzi, 1994; Blackburn *et al.*, 1996; Kholmyansky *et al.*, 2001; Lüthi *et al.*, 2005; Ganapathisubramani *et al.*, 2008, amongst others). Further, many of them stated that on average vorticity shows an arbitrary alignment with the extensive strain direction. However, Blackburn *et al.* (1996) have shown that this does not hold for the near-wall region in turbulent boundary layers.

The characteristic decomposition applied by Chong *et al.* (1990) goes back to the work of Perry & Chong (1987) that allows to characterise the current flow topology, that a certain fluid particle is part of, according to the invariants Q and R of the velocity

gradient tensor at the location of the fluid particle. The decomposition distinguishes between stable/stretching vortices, unstable/contracting vortices, unstable node/saddle structures and stable node/saddle structures. Here the first two structure types have a rotational character whereas the latter two have a purely straining character. The QR-space, spanned by the velocity gradient invariants, can be divided into four sectors where each sector represents one characteristic structure type. Meneveau (2011) summarizes this decomposition in the review on the topic of Lagrangian dynamics. Chen *et al.* (1990) found in a turbulent mixing layer a specific shape for the iso-lines of the joint probability density function (pdf) of R and Q. The iso-lines have the shape of a horizontally-flipped and sheared drop. The tail extends in positive R direction and negative Q direction. This shape of the joint-pdf of Q and R was confirmed for different turbulent flows (e.g. Soria *et al.*, 1994; Chong *et al.*, 1998; Ooi *et al.*, 1999; Ganapathisubramani *et al.*, 2008; Elsinga & Marusic, 2010). Therefore the particular shape is often referred as *universal teardrop* of turbulence. From their DNS results of a turbulent channel flow, Blackburn *et al.* (1996) could confirm the teardrop shape in the outer regions of the boundary layer. They found a reduced extent of the tail when approaching the wall. However, above the buffer layer they describe the joint-pdf of Q and R as apparent self-similar, but do not quantify these results. As a main feature when moving from the buffer layer to the VSL they describe the decrease of the maximum value of Q. They reason this fact with the strong coupling of S and Ω in the near-wall region that we discussed before.
In this chapter the velocity gradient in general is discussed together with the outlined features. The joint-pdfs of Q and R as well as the alignment of vorticity with the eigenvectors of the strain rate tensor are discussed on three different non-equilibrium flows.

4.2 Flow Outline and Methodology

The flow regions that are discussed in this chapter are outlined briefly in this section. The general flow details are presented in the previous chapter (3.3). The flows and especially the flow regions are chosen to have a great variety of flow topologies to investigate the features of the velocity gradient regarding their universality aspects. As first flow we have chosen a flat-plate zero pressure-gradient turbulent boundary layer (sec. 3.3.1) at a free stream Mach number of $M = 0.5$ - from now on *TBL* for brevity. The streamwise location of the sampling regions is between $Re_\theta \approx 1224 - 1248$ ($Re_\tau \approx 481 - 491$). The second flow is a turbulent pipe flow exiting in a laminar co-flow (sec. 3.3.2) - from now on *Jet* for brevity. The Reynolds number based on the pipe radius and the bulk velocity is $Re_R \approx 3350$ and the Mach number based on the bulk velocity is $M \approx 0.48$. Particular interest exists here on the turbulent flow exiting the pipe. The last flow is a supersonic wake behind an axisymmetric cylinder (sec. 3.3.3) at a Reynolds number base on the radius of $Re_R = 50,000$ and a free stream Mach number of $M = 2.48$ - from

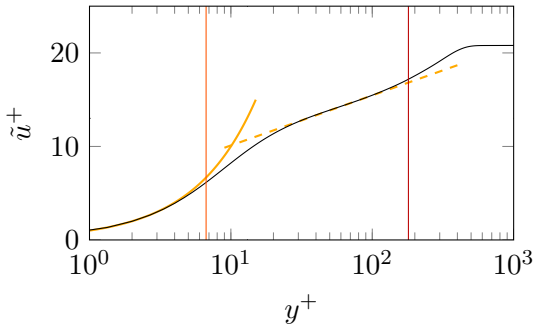

(a) TBL: Streamwise mean velocity profile (black) over wall-normal direction scaled with friction velocity. Continuous yellow line shows linear behaviour of the VSL and the dashed yellow line follows a log-law.

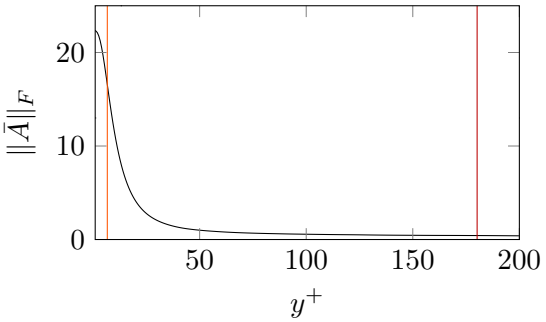

(b) TBL: Wall-normal profile of the magnitude of the Favre average velocity gradient normalized with the ratio of freestream velocity and boundary layer thickness $\frac{U_e}{\delta_{99}}$.

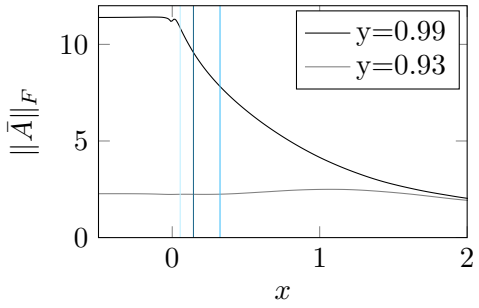

(c) Jet: Streamwise profile of the magnitude of the Favre average velocity gradient at two different radii y. The nozzle is at $x = 0$.

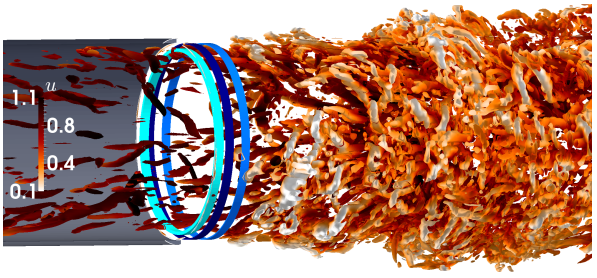

(d) Jet flow at nozzle (grey) exit. Turbulent structures as iso-surfaces at $Q = 2$ coloured with streamwise velocity component. The three blue rings behind the nozzle indicate the sampling regions.

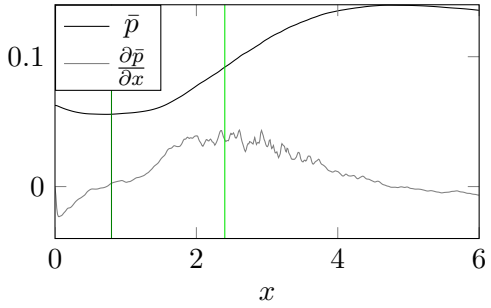

(e) Wake: Streamwise profile of the pressure and the streamwise pressure gradient at radius $y = 0.1$. The end-wall of the cylinder is at $x = 0$.

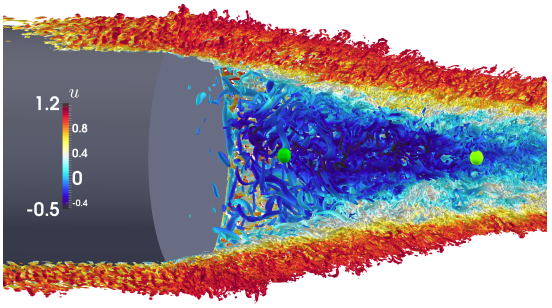

(f) Supersonic wake flow behind cylinder (grey) exit. Turbulent structures as iso-surfaces at $Q = 10$ coloured with streamwise velocity component. The two green balls at the flow axis indicate the sampling regions.

Figure 4.1: Outline of the flows and sampling regions of the data discussed in this chapter. The coloured lines in the plots mark the respective sampling location. The colour code will be maintained during the entire chapter.

now on *Wake* for brevity. Particular interest exists on the recirculation region behind the cylinder which is exposed to a mean pressure gradient.

In this work we will compare results of strong shear layer regions, weak (almost vanishing) shear layer regions as well as wall-attached regions and free turbulence regions. All regions are shown and highlighted in figure (4.1) by coloured markers. The colour code used to identify the sampling locations will be kept for the entire chapter. The sampling regions in the boundary layer are marked in reddish colours. We discuss data close to the wall at $y^+ \approx 6.7$ (orange, TBL 2 for brevity) and a region between the outer end of the logarithmic layer and the start of the wake region $y^+ \approx 180$ (dark red, TBL 1). For the Jet case we discuss three different locations in the near-nozzle region which are coloured in blueish colours. Two locations are at a radius $y = 0.99$ that coincides with the viscous sublayer of the turbulent boundary layer that developed inside of the pipe. The first one is 0.14 radii downstream of the nozzle (dark blue, Jet 1) and the second one is 0.32 radii downstream of the nozzle (cyan, Jet 2). A third sampling location is found at a radius of $y = 0.93$ which coincides with the buffer layer of the turbulent boundary layer in the pipe and is 0.05 radii downstream of the nozzle (light blue, Jet 3). For the Wake we have two sampling regions that are exposed to almost no mean shear highlighted in greenish colours. The first location is at a radius of $y = 0.1$ close to the axis and 0.8 radii downstream of the end-wall in the center of the recirculation region of the wake of the cylinder (dark green, Wake 1). The second location is at the same radius but 2.4 radii downstream of the end-wall, towards the end of the recirculation region (light green, Wake 2).

Summarizing, we cover strong shear layers (TBL 2, Jet 1, Jet 2 and Jet 3), weak shear layers with nearly no mean shear (TBL 1, Wake 1 and Wake 2) and turbulence exposed to a mean pressure gradient (Wake 2). Furthermore, we can compare turbulence in the direct surrounding of a wall (TBL 2) against turbulence that just lost its wall-bounded restrictions (Jet 1, Jet 2 and Jet 3).

With the focus of this work on production of turbulent motions and enstrophy $\frac{1}{2}\vec{\omega}^2 = \|\Omega\|_F^2$ being a measure of vortex intensity we will concentrate on the enstrophy production term $\vec{\omega}^t S\vec{\omega}$. Applying an eigenvalue decomposition on the strain rate tensor can be particularly helpful for investigations on the enstrophy production. The production terms decomposes to

$$\vec{\omega}^t S\vec{\omega} = 2\|\Omega\|_F^2\|S\|_F \sum_{i=1}^{3} \mathring{\lambda}_i \left(\mathring{\vec{\omega}} \cdot \vec{r}_i\right)^2 \tag{4.1}$$

where $\mathring{\vec{\omega}} := \frac{\vec{\omega}}{\sqrt{\vec{\omega}^2}}$ is the normalized vorticity vector and $\mathring{\lambda}_i$ and $\vec{r}_i$ are the normalized eigenvalue and eigenvectors of the strain rate tensor S, respectively. The Frobenius norm of a matrix/tensor is denoted by $\| \bullet \|_F$. The vectors are scaled to unit length whereas the eigenvalues are normalized by the strain rate magnitude $\mathring{\lambda}_i = \frac{\lambda_i}{\sqrt{\sum \lambda_j^2}} = \frac{\lambda_i}{\|S\|_F}$. The eigenvectors are purely real (as S is symmetric) and in decreasing order: $\lambda_1 \geq \lambda_2 \geq \lambda_3$. Further, the relation $\nabla \cdot \vec{u} = \lambda_1 + \lambda_2 + \lambda_3$ holds and for incompressible flows this leads to $\lambda_1 \geq 0$ and $\lambda_3 \leq 0$. With this decomposition it can be seen that enstrophy production

scales with enstrophy itself as well as with the magnitude of the strain rate tensor. The mechanism of composing the production term is solely governed by

$$\mathring{\lambda}_i \left(\mathring{\vec{\omega}} \cdot \vec{r}_i\right)^2. \tag{4.2}$$

The alignment between the vorticity vector and principal strain axis (eigenvectors of the strain rate tensor) weights the contribution of the respective normalized eigenvalue to the enstrophy production. $\left(\mathring{\vec{\omega}} \cdot \vec{r}_i\right)^2$ takes values between 0 and 1. It is equal to 1 if vorticity is parallel to $\vec{r}_i$ and equal to 0 if they are perpendicular to each other.
The earlier mentioned characteristic decomposition is based on the *critical point concept*, first introduced by Perry & Chong (1987), which decomposes a flow according to the form of the eigenvalues of the local velocity gradient. Therefore this analysis is purely local and describes the character of a structure at the location of the current fluid particle only. It does not describe the character of a structure as a whole. To obtain a better overview of the method we suggest to read the original publication Perry & Chong (1987) or a summary about Lagrangian dynamics by Meneveau (2011). However, we will introduce the method with its key points for our analysis in a brief manner.
Picking a fluid particle at a particular location, the character of the velocity gradient $A := \nabla\vec{u}$ reflects the shape that the flow has in the infinitesimal surrounding of the particle. This can be shown by a Taylor's expansion for the particle movement (sec. 1.2.2 or Perry & Chong (1987)). The character of the velocity gradient, on the other hand, is reflected by its eigenvalues $(\alpha_1, \alpha_2, \alpha_3)$, that are obtained as the roots of the characteristic polynomial of the velocity gradient

$$p_{\text{char}}(\alpha) := \det\left(A - \alpha I\right) = \alpha^3 + P\alpha^2 + Q\alpha + R. \tag{4.3}$$

Here P,Q and R are invariants of the velocity gradient, the definition of which can be found in section (2.4) and in Perry & Chong (1987). These invariants span a state space, PQR-space, in which we find certain regions defining certain properties of the eigenvalues, and therefore certain properties of the local flow topology at the fluid particle. P, which is the additive inverse of the dilatation $-\nabla \cdot \vec{u}$, is zero for incompressible flows. All flow regions discussed in this chapter show only small compressibility effects and the first invariant P is insignificantly small. For this reason we map the results of the PQR-space onto its subset with $P = 0$, which we call the QR-space. This does not mean that the flow is considered to be incompressible. The analysis still takes compressibility into account, but it is not distinguished between different values of the first invariant of the velocity gradient $P = -\nabla \cdot \vec{u}$. The results were validated against a fully compressible analysis in the (PQR)-space, but no significant differences were found. The QR-space, is spanned by the second and third invariant, Q and R, of the velocity gradient. From the point of view of a fluid particle located on a structure, this analysis allows to distinguish between four different states of the structure. Figure (4.2) shows the QR-space and the four structure types. The discriminant of the velocity gradient

$\Delta = -\frac{1}{4}P^2Q^2 + Q^3 + P^3R + \frac{27}{4}R^2 - \frac{18}{4}PQR$ has an important role in this decomposition. For positive value of $\Delta > 0$ the velocity gradient has one purely real eigenvalue and a complex conjugate pair of complex eigenvalues. Therefore the fluid particle sits on a part of a structure that has a rotational character. On the other hand, if $\Delta \leq 0$ all eigenvalues of the velocity gradient are purely real and the supporting structure is purely straining at the location of the fluid particle. Further, for negative third invariant $R \leq 0$ we find two contracting directions and one stretching direction, whereas if $R > 0$ is positive we find two stretching direction and one contraction direction of the structure at the location of the fluid particle. So four characteristic structure types can be described:

I : vortical structure with stretching character / $\Delta > 0$; $R \leq 0$ / $\Im(\alpha_2) = 0$; $\Im(\alpha_1) = -\Im(\alpha_3) \neq 0$; $\Re(\alpha_1) = \Re(\alpha_3) \leq 0$; $\alpha_2 \geq 0$

II : vortical structure with contracting character / $\Delta > 0$; $R > 0$ / $\Im(\alpha_2) = 0$; $\Im(\alpha_1) = -\Im(\alpha_3) \neq 0$; $\Re(\alpha_1) = \Re(\alpha_3) \geq 0$; $\alpha_2 \leq 0$

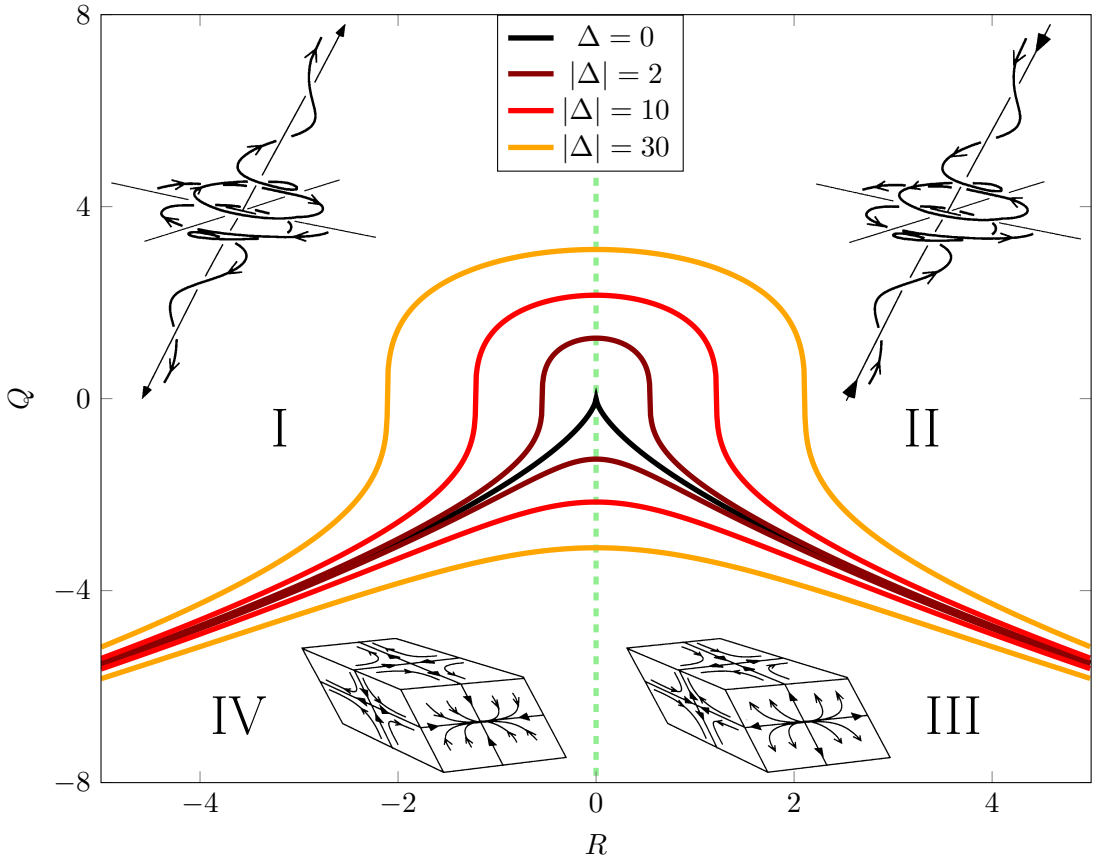

Figure 4.2: Introduction to the invariant space of the velocity gradient. The continuous lines show different values for the discriminant Δ of the velocity gradient and the dashed green line marks $R = 0$. The pictures and numbers show schematically the characteristic structure in the respective area of the QR-space. Subfigures adapted from Ooi *et al.* (1999).

III : pure straining structure with flattening character / $\Delta \leq 0$; $R > 0$ / $\Im(\alpha_1) = \Im(\alpha_2) = \Im(\alpha_3) = 0$; $\alpha_1 \geq \alpha_2 \geq 0 \geq \alpha_3$

IV : pure straining structure with elongating character /$\Delta \leq 0$; $R \leq 0$ / $\Im(\alpha_1) = \Im(\alpha_2) = \Im(\alpha_3) = 0$; $\alpha_1 \geq 0 \geq \alpha_2 \geq \alpha_3$

4.3 Results

To obtain an overview about the flow at the specific sampling locations, figure (4.3) summarizes some key facts. The probability distributions of the streamwise velocity component reveals differences in the character of this quantity. As reference the respective pdfs of normal (or Gaussian) distributions are plotted in the same plot. A normal distributed random variable X has the pdf f of the form

$$f(x;\mu,\sigma) = \frac{1}{\sigma\sqrt{2\pi}} e^{-\frac{(x-\mu)^2}{2\sigma^2}}, \tag{4.4}$$

where μ denotes the mean (or expectation) of the random variable and σ^2 denotes the variance of the random variable. We find that streamwise velocity at TBL 1, Wake 1 (although noisy due to convergence issues) and Wake 2 can be stated as nearly normal distributed variables. On the other hand, the pdfs of the streamwise velocity at TBL 2, Jet 1 and Jet 2 are skewed towards small values compared to the ones of a normal distributed variable. At location Jet 3 the pdf shows a flattened peak as well as a slight skewness towards larger values. Overall, the character of the distribution of the streamwise velocity component shows different character when we compare locations with a strong mean shear to locations with a low mean shear.

The energy spectra, on the other hand, do not show significant differences in their character. For all locations we find a wide range of scales that contain energy, without distinct dominant peaks or valleys. The overall energy content as well as the scale sizes do vary between the different locations, but this is expected as the locations represent strongly differing flow topologies. The emphasis here is to show that all locations show the spectrum of a fully developed turbulent flow.

To quantify the isotropy in the different flows the alignment between the gradient of the second invariant of the velocity gradient ∇Q and the respective coordinate system is shown. Whereas we find an arbitrary alignment with all directions for the weak shear layers (TBL 1, Wake 1 and Wake 2), we find preferred alignments for the stronger shear layers. The Q gradients for all strong shear layers (TBL 2, Jet 1, Jet 2 and Jet 3) show a preferred orthogonal alignment with the streamwise direction and a preferred parallel alignment with the y-direction. This direction is the wall-normal direction in the TBL case but the radial direction (that points towards the wall in the pipe boundary layer) in the Jet case. In the cylindrical cases (Jet) a positive parallel alignment with y is slightly preferred over a negative one, whereas this is the opposite in the Cartesian case

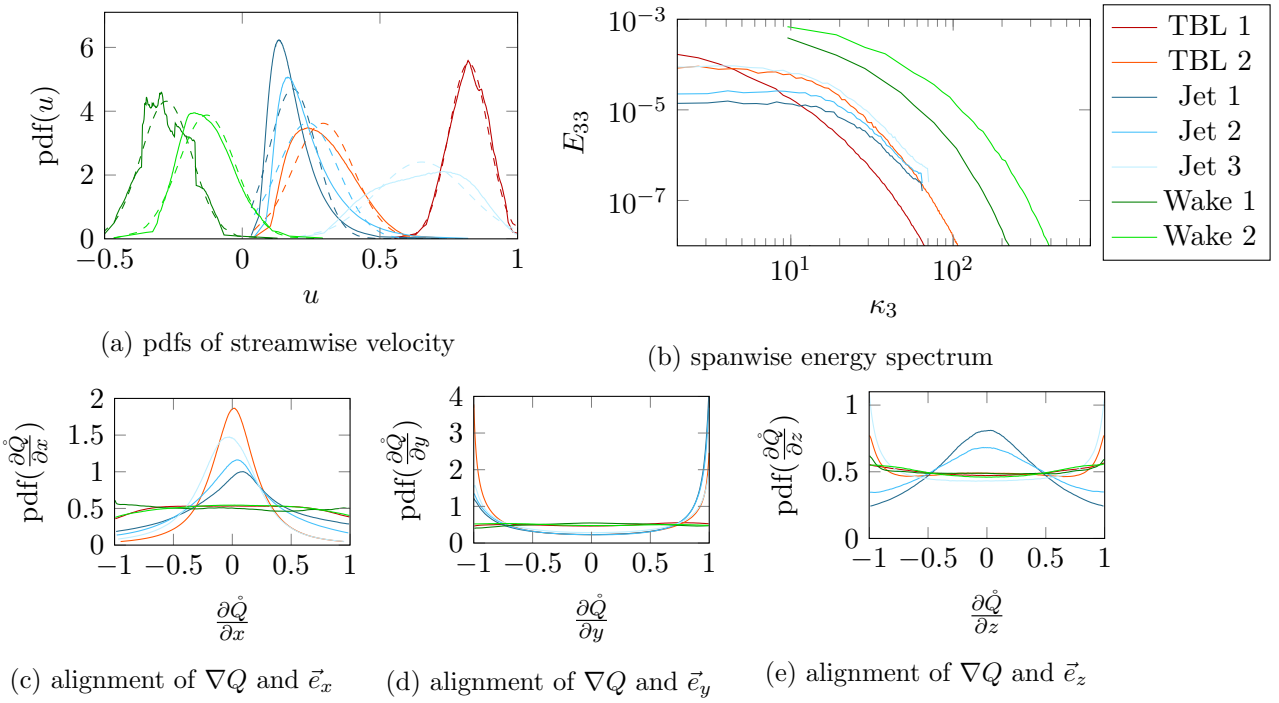

(a) pdfs of streamwise velocity

(b) spanwise energy spectrum

(c) alignment of ∇Q and $\vec{e}_x$

(d) alignment of ∇Q and $\vec{e}_y$

(e) alignment of ∇Q and $\vec{e}_z$

Figure 4.3: Characterisation of the sampling regions. The different colours represent the respective flow sampling region. a: Probability density functions of the streamwise velocity component (continuous lines) and the respective Gaussian distributions (dashed lines). b: Spanwise kinetic energy spectrum E_{33} of the spanwise velocity component w over spanwise wavenumber κ_3. c-e: Probability density functions of the alignment of the gradient of the second invariant of the velocity gradient with the respective coordinate system. c: Alignment with the streamwise direction; d: Alignment with the wall-normal (TBL) or the radial (Jet and Wake) direction; e: Alignment with the spanwise (TBL) or azimuthal (Jet and Wake) direction.

(TBL). This indicates that a part of the alignment shows the general alignment of the respective mean shear layer. However, a large portion still represents the alignment of the turbulent structures. For the statistically homogeneous z-direction we find a preferred perpendicular alignment for Jet 1 and Jet 2, whereas for Jet 3 and TBL 2 we find a preferred parallel alignment. Summarizing, we find strong variations in the alignment of turbulence and, judging from the strong peaks in the pdfs, partially some sort of spatially ordered turbulence.

An important invariant of the velocity gradient is its magnitude. The probability density functions of this magnitude are shown in figure (4.4). Contrasting the variations that we found for the velocity distribution and for the alignment of turbulent structures, this quantity appears to have a invariant character across all analysed flow topologies. The plot in figure (4.4) superimposes the actual distributions (continuous lines) with the associate log-normal distributions (dashed lines). A random variable X is log-normal distributed, if there exists a normal distributed random variable Z, so that $X = e^Z$

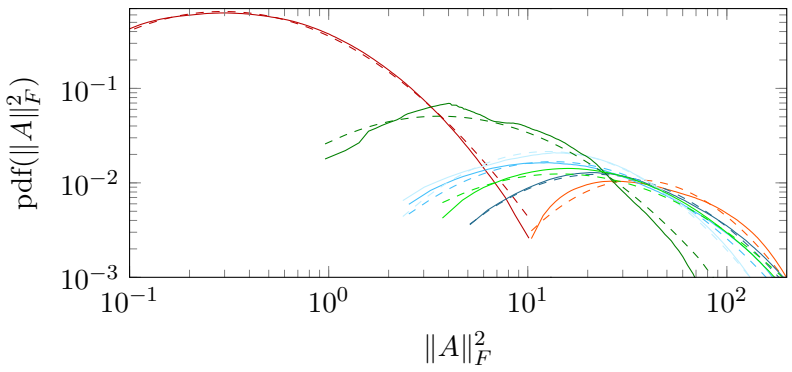

Figure 4.4: Probability density functions of the velocity gradient magnitude. The different colours represent the respective flow sampling region. Continuous line are the sampled distributions. Dashed lines are the respective log-normal distributions.

holds. For given log-normal distributed variable X we then get

$$X = e^{\mu(X)+\sigma(X)Z}, \tag{4.5}$$

where Z is a standard normal distributed random variable ($\mu(Z) = 0$ and $\sigma(Z) = 1$) and $\mu(X)$,$\sigma^2(X)$ are the mean and the variance of X respectively. The pdf of this log-normal distribution then has the form

$$f(x;\mu(X),\sigma(X)) = \begin{cases} \frac{1}{x\sigma(X)\sqrt{2\pi}} e^{-\frac{(\log x-\mu(X))^2}{2\sigma(X)^2}} & x > 0 \\ 0 & x = 0. \end{cases} \tag{4.6}$$

It appears that the sampled distributions at all locations match their respective log-normal distributions well. This holds for flows exposed to strong mean gradients, nearly no gradient and turbulent flows close to a wall, as well as flows free from any restrictive boundary. Therfore it suggests that the log-normal distribution is a universal feature of the velocity gradient.

As a next step the velocity gradient A is split into its symmetric part, the strain rate tensor S, and its skew-symmetric part, the rotation rate tensor Ω. For this decomposition it can be shown that

$$\|A\|_F^2 = \|S\|_F^2 + \|\Omega\|_F^2 \tag{4.7}$$

and therefore the magnitude of the velocity gradient can be composed by the magnitudes of the strain rate tensor and the rotation rate tensor. The pdfs of both respectively (not plotted here) show that, just like for $\|A\|_F^2$, both magnitudes are log-normal distributed at all investigated locations. Figure (4.5) shows the joint probability density function (joint-pdf) of the normalized strain rate magnitude squared and the normalized rotation rate magnitude squared. For this plot and for the following we introduce a scaling based on the local variance of the velocity gradient magnitude

$$\mathrm{var}(A) := \langle\langle A - \tilde{A}, A - \tilde{A}\rangle_F\rangle. \tag{4.8}$$

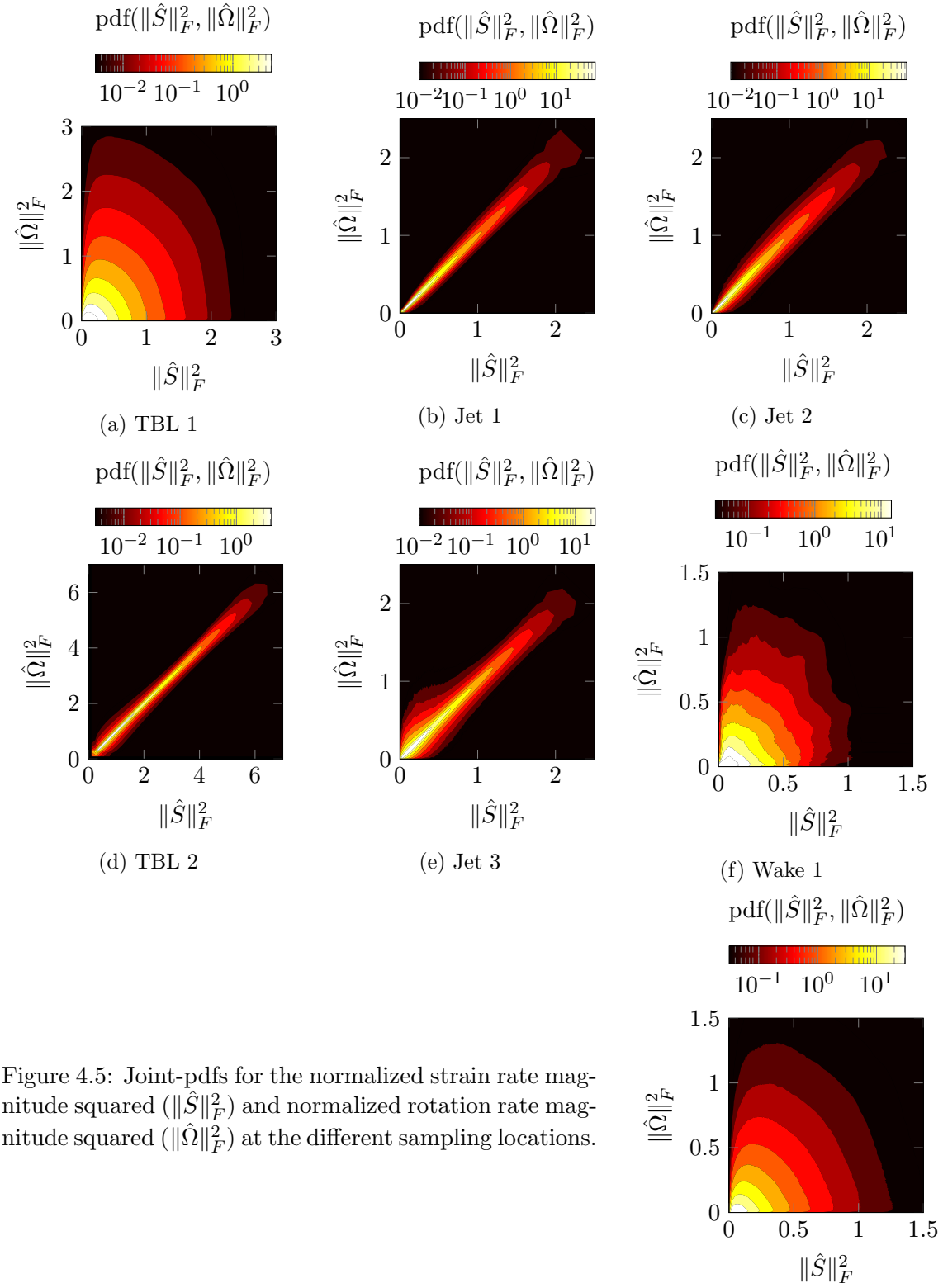

(a) TBL 1 (b) Jet 1 (c) Jet 2

(d) TBL 2 (e) Jet 3 (f) Wake 1

(a) Wake 2

Figure 4.5: Joint-pdfs for the normalized strain rate magnitude squared ($\|\hat{S}\|_F^2$) and normalized rotation rate magnitude squared ($\|\hat{\Omega}\|_F^2$) at the different sampling locations.

The velocity gradient related quantities are then scaled as

$$\hat{A} := \frac{A}{\sqrt{\mathrm{var}(A)}}, \hat{S} := \frac{S}{\sqrt{\mathrm{var}(A)}}, \hat{\Omega} := \frac{\Omega}{\sqrt{\mathrm{var}(A)}}, \hat{Q} := \frac{Q}{\mathrm{var}(A)}, \hat{R} := \frac{R}{\mathrm{var}(A)^{\frac{3}{2}}}. \quad (4.9)$$

The variation in these plots is conspicuous. Whereas for some location we find wide spread joint-pdfs, we see restricted ones for other locations. In fact we find the same grouping as for the previous results that have revealed differences across the various sampling locations. The weak shear locations (TBL 1, Wake 1 and Wake 2) show a relatively weak correlation between strain rate and rotation rate. This includes the locations with no mean pressure gradient (TBL 1 and Wake 1) as well as the region that is exposed to a mean pressure gradient (Wake 2). On the other hand, there are the locations in strong mean shear regions (TBL 2, Jet 1, Jet 2 and Jet 3). They all show strongly coupled strain and rotation magnitudes. Jet 3, which is the location with the weakest mean shear in-between the as *strong mean shear* declared regions, is the only location where we find a slightly relaxed coupling of strain and rotation magnitude for low velocity gradient magnitudes. Nevertheless, all strong shear location reveal a very strong linear coupling between both parts of the velocity gradient magnitude. The interesting fact is that the strain rate magnitude as well as the rotation rate magnitude show a universal behaviour respectively, but their coupling is strongly dependent on the flow topology and not invariant. However, a positive fact from a complexity reducing point of view is that the coupling is changing in the same way for all strong shear regions. This might eventually lead to a universal coupling mechanism of strain and rotation that scales with the strength of the local mean shear.

The next step is investigating the coupling of the strain rate and the rotation rate in form of the enstrophy production (eq. 4.1). As we have seen before for this production not only the magnitudes, but as well the alignment between vorticity and the principal strain directions (eq. 4.2) is of importance. The probability density function of the normalized enstrophy production (fig. 4.6, g) shows the relative variation of the entire production term within the selected sampling locations. The strongest differences to all the other pdfs is shown by TBL 2 which is the location between VSL and buffer layer in the TBL. The fact that no other production term shows similar behaviour indicates that the wall has a strong influence on the production term. The pdf shows a peak shifted towards a negative production, whereas the pdfs of all other locations show a peak at zero. Further, the legs in positive as well as in negative direction are spread further than for any other location. This indicates that the wall causes extreme production events with extremely high or extremely low relative enstrophy production. The pdfs of the locations in the weak shear regions (TBL 1, Wake 1 and Wake 2) are all similar and the only difference seems to be the scaling. On the other hand, the pdfs of the remaining strong shear regions (Jet 1, Jet 2 and Jet 3) vary stronger and the fatness of the negative leg is changing depending on the location. An interpretation of this is not given at this stage, however, it is believed to be related with transport effects that find their origin

in the turbulent boundary layer inside the pipe.
As outlined before (eq. 4.1), the enstrophy production decomposes to a scaling by rotation rate magnitude and strain rate magnitude and a weighting which is a term that couples the principal strain rate ratios with the alignment between the vorticity vector and the principal strain directions (eq. 4.2). Pdfs of this alignment are shown in figure (4.6, a-f, h). Here again the two groups, strong mean shear versus weak mean shear, become obvious. The alignment for the low mean shear location (TBL 1, Wake 1 and Wake 2) all show nearly the same trends for the alignment that coincides with what we discussed in the introduction and agrees with many flows that where discussed in literature. The vorticity vector shows an arbitrary alignment with the extensive strain direction, a weak tendency to align perpendicular with the compressive strain direction and a strong tendency to align parallel with the intermediate strain rate. This as well does not seem to be effected by the mean pressure gradient that is imposed on Wake 2. On the other hand, for all strong shear locations (TBL 2, Jet 1, Jet 2 and Jet 3) these alignments change strongly, but show the same trends. The tendency of the vorticity

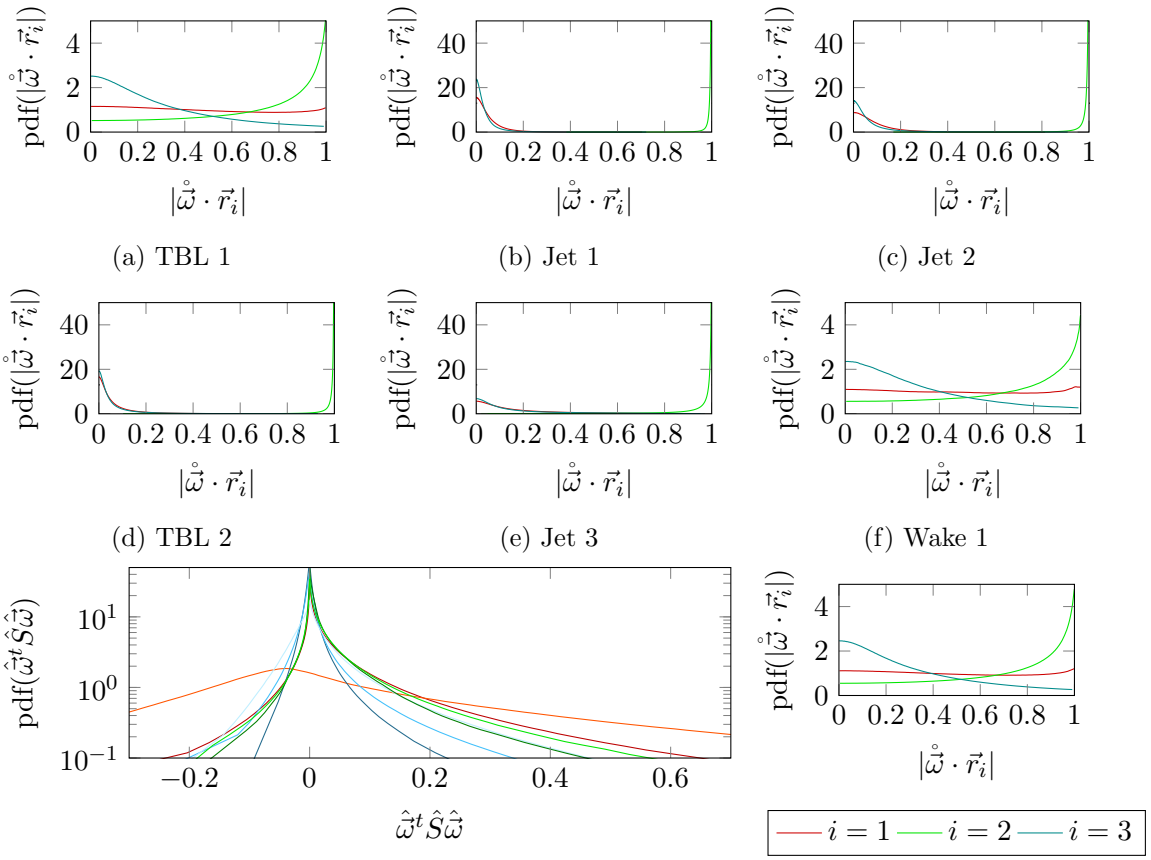

(a) TBL 1 (b) Jet 1 (c) Jet 2

(d) TBL 2 (e) Jet 3 (f) Wake 1

(g) pdf of enstrophy production (h) Wake 2

Figure 4.6: (a-f,h) Probability density functions of the alignment between the vorticity vector and the principal strain directions. Colour scheme shown at the bottom right. (g): Probability density functions of the enstrophy production. The different colours represent the respective flow sampling region.

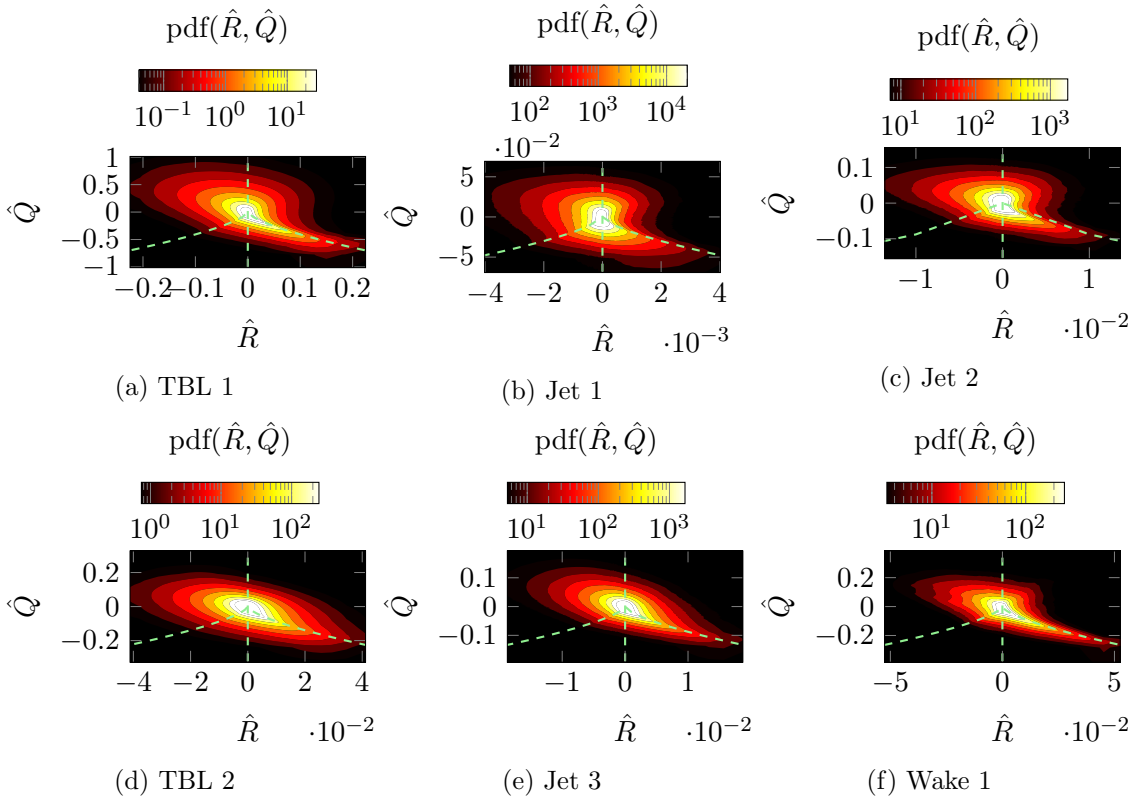

(a) TBL 1 (b) Jet 1 (c) Jet 2

(d) TBL 2 (e) Jet 3 (f) Wake 1

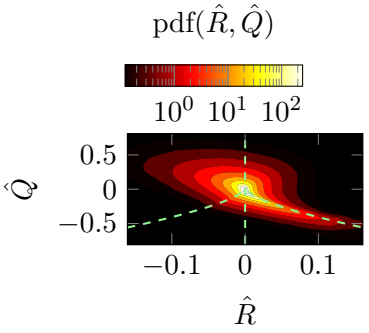

(a) Wake 2

Figure 4.7: Joint-pdfs for the normalized second ($\hat{Q}$) and third ($\hat{R}$) invariant of the velocity gradient at the different sampling locations. The dashed green lines indicate the limits of the sectors defined by the characteristic decomposition.

vector to align parallel with the intermediate strain direction increases strongly. As a consequence of this vorticity tends to align perpendicular with the remaining two principal strain directions. Just like for the coupling of the strain rate magnitude and rotation rate magnitude it appears that the change of the alignment is less pronounced in Jet 3 than it is in TBL 1, Jet 1 and Jet 2. Following this, there could be a link between mean shear, strain-rotation-magnitude correlation and vorticity-strain alignment. The strongly similar trends that we have seen in the results suggest that this link exists. However, further investigations on this will be part of the future work.

The remaining feature that we discussed in the introduction and which is said to be potentially universal in the joint-pdf of R and Q, often referred to as QR-plot. The joint-pdfs for the respective sampling locations are shown in figure (4.7) normalized with the variance of the velocity gradient magnitude (eq. 4.9). Visually we find clear similarities between the plots of all locations, but as well some distinctive differences for

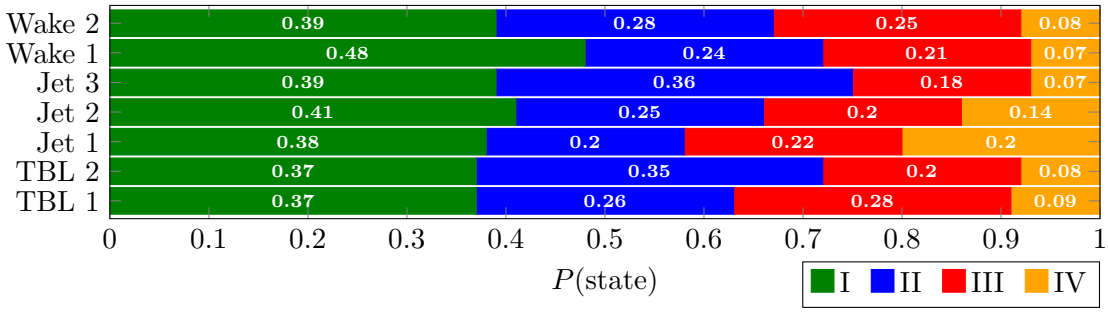

Figure 4.8: Distribution of the characteristic flow topologies defined by the characteristic decomposition for the different sampling locations.

the different location. All plots show a tilting towards the upper left and lower right which indicates a slight negative correlation coefficient $\mathrm{corr}(R, Q)$. Further, all iso-lines show a rounded bulky shape for large values of R and small values of Q but a spiky and relatively thin shape for small values of R and large values of Q. This property is the reason why this joint-pdf is often referred to as *teardrop*. However, on a closer look the joint-pdf reveal differences. Some of them have a more oval shape (TBL 2 and Jet 3) while others develop longer tail towards negative Q and positive R (Wake 1). Some have a flatter top and therefore a relatively small extend towards positive Q (TBL 2 and Wake 1). On the other hand, the joint-pdfs for TBL 1, Jet 2 and Wake 2 visually agree well with what we have discussed is a potentially universal shape.

To obtain a more quantitative impression the joint-pdf was integrated over the respective characteristic regions to calculate the probabilities at which we find a certain structure type in the flow at the respective location. This frequency of occurrence is shown in figure (4.8) for all sampling locations. The different colours represent the respective characteristic types that were introduced earlier (sec. 4.2). The ratios indeed vary significantly between the different locations. The clear grouping into low mean shear and high mean shear location, as it was possible for all presented results so far, is here not possible. The QR-plot and the shown ratios describe a statistical state of turbulence which is not only influenced by the local flow topology or production and dissipation mechanisms, but as well dependent on the character of turbulence transported in the respective sampling region.

There is a number of potential reasons for the differences of the QR-plots, but they will not be discussed at this stage. Here we want to emphasize two things. Firstly, a visual investigation on the joint-pdfs of R and Q might only reveal half of the truth. The visually dominant shapes are the large shapes which have a relatively low frequency of occurrence. This means they are not dominant in the representation of the characteristic distribution of turbulence. The QR-states become more dominant the higher their frequency of occurrence is. The higher the frequency of occurrence of a certain QR-state is, the closer it moves towards the origin. In this way it becomes difficult to see potential differences of the characteristic distribution as big parts of potentially

important features of turbulence are represented by a relatively small region in the QR-plot. We suggest to always apply both, a visual study of the QR-plot together with the quantitative analysis of the frequencies of occurrence of the certain structure types. In this way one can make sure not to misinterpret QR-plots like for Wake 1 (fig 4.7, f) for instance. Due to the flat hat and the long tail it conveys the impression that structure types II and III might have become more dominant over structure types I and IV at this location. The ratios in figure (4.8), however, reveal that instead type I develops a strong dominance. Secondly, both, the visual impression as well as the ratios, state that the characteristic distribution and therefore the QR-plot is not a universal feature of turbulent flows.

4.4 Conclusions

The velocity gradient was analysed in several regions of three different flows in order to identify universal and non-universal features. The studied regions have a strongly varying character, are all in a non-equilibrium state and spread over a wide range of different properties in general.

We found that with strong shear layers turbulent structures show preferred alignment with the orientation of the shear layer and the velocity pdfs are skewed, whereas when there is no strong mean shear present, then structures are randomly aligned and the velocity shows similar characteristics to a normal distributed random variable.

As a first universal feature the magnitudes of the velocity gradient were shown to have the character of log-normal distributed random variables. This holds for any of the studied locations. Although not shown in this work, the same was stated for the strain rate magnitude as well as the rotation rate magnitude. Contrasting this, the coupling of strain rate magnitude was shown to vary with the strength of the mean shear layer. Moreover, the coupling was shown to change in the same manner for all stronger mean shear regions.

Next, the enstrophy production was studied. The overall probability density function of the production varies for the different location, but no clear trends were found. However, it seems that the presence of a wall close to the location of interest has a strong impact on the distribution of the enstrophy production. As part of the overall production, the alignment between the vorticity vector and the principal strain directions was analysed. Here as well, the group of locations in a weak mean shear region has shown different tendencies for the alignments to the group of locations in strong mean shear regions. Furthermore, the trends for the alignment was the same within the groups, respectively. Within weak shear regions the vorticity vector tends to align parallel with the intermediate strain direction, orthogonal with the extensive strain direction and shows an arbitrary alignment with the extensive strain direction. On the other hand, in strong mean shear regions the tendency of a parallel alignment between the vorticity vector

and the intermediate strain direction increases and at the same time the vorticity vector tends to align perpendicular with the remaining principal strain directions.
Although the alignment of vorticity and the principal strain directions as well as the correlation between strain rate magnitude and rotation rate magnitude are not universal, the results suggest that there is a link between both features that couples the variations with the strength of the respective mean shear or related values. This coupling mechanism has a good potential to be universal across different flow topologies.
Additionally, the characteristic distribution of turbulence was analysed via QR-plots and a comparison of the ratios of the frequencies of occurrence of the certain structure types was done. It was shown that a visual inspection of the QR-plots do only reveal half of the truth and that they should always be studied together with the frequencies of occurrence integrated for the respective characteristic structure types. Both do vary across different flow topologies and cannot be stated as universal features of the velocity gradient.
Finally it is to mention that no effects of the mean pressure gradient could be identified for the one particular location that was exposed to a mean pressure gradient. However, this was a fairly specific case and cannot draw a general conclusion about turbulence passing through (or being exposed to) a mean pressure gradient.

Chapter 5

Variation of Strain-Rotation Relation and Enstrophy Production in a Turbulent Boundary Layer

Enstrophy production is strongly coupled to the vortex stretching process that is of inherent importance to the cascading process that drives turbulence in a flow. In this chapter this production mechanism is investigated to identify its variation in the wall-normal direction for the case of a turbulent boundary layer. Production is decomposed into its core quantities including the ratio of the principal strains and the alignment of vorticity with the eigenvectors of the strain rate tensor. The strong variations of these quantities with the wall distance is presented and explained. Further, we propose a modification to an existing *vortex stretch model* in order to cover the mechanisms in a boundary layer and gain a more universal character. A characteristic decomposition is applied on the turbulence and the production mechanism is studied for certain structure types separately. This reveals a potential backscatter mechanism that transfers kinetic energy from smaller scales towards larger ones, for a structure type described as unstable vortices.

5.1 Introduction

The velocity gradient tensor $A := \nabla \vec{u}$ can be decomposed into its symmetric part and its skew-symmetric part $A = S + \Omega$ which forms the strain rate tensor S and the rotation rate tensor Ω. Whereas the strain rate tensor is governing the dissipation of kinetic energy, the coupling of both, strain rate tensor and rotation rate tensor, is governing the

process of vortex stretching and vortex compression (Tsinober, 2000; Hamlington *et al.*, 2008). These vortex dynamics are considered as key quantity in the turbulent cascade that drives the scale transfer of kinetic energy. The development of both, S and Ω, are strongly coupled as we can see in eqs. (2.95) and (2.99). They form the system

$$\frac{1}{2}\frac{d||S||_F^2}{dt} = -\langle S, SS\rangle_F - \frac{1}{4}\vec{\omega}^t S\vec{\omega} - \langle S, H\rangle_F, \tag{5.1}$$

$$\frac{1}{2}\frac{d\vec{\omega}^2}{dt} = \vec{\omega}^t S\vec{\omega} + \langle \Omega, H\rangle_F, \tag{5.2}$$

where $\vec{\omega} = \nabla \times \vec{u}$ is the vorticity vector and $\| \bullet \|_F$ denotes the Frobenius norm. Further, H is the pressure-viscous diffusion term

$$H := \nabla\left(\frac{1}{\rho}\nabla\cdot\tau - \frac{1}{\rho}\nabla p\right) \tag{5.3}$$

with the density ρ, the pressure p and the viscous stress tensor τ. With the focus of this work on production of turbulent motions and enstrophy $\frac{1}{2}\vec{\omega}^2 = \|\Omega\|_F$ being a measure of vortex intensity we will concentrate on the enstrophy production term $\vec{\omega}^t S\vec{\omega}$. The net enstrophy production is known to be positive as suggested by (Taylor, 1938) and confirmed numerically (Betchov, 1975) as well as experimentally (Tsinober *et al.*, 1992). Applying an eigenvalue decomposition on the strain rate tensor can be particularly helpful for investigations on the enstrophy production. The production term decomposes to

$$\vec{\omega}^t S\vec{\omega} = 2\|\Omega\|_F^2\|S\|_F \sum_{i=1}^{3} \mathring{\lambda}_i \left(\mathring{\vec{\omega}}\cdot\vec{r}_i\right)^2 \tag{5.4}$$

where $\mathring{\vec{\omega}} := \frac{\vec{\omega}}{\sqrt{\vec{\omega}^2}}$ is the normalized vorticity vector and $\mathring{\lambda}_i$ and $\vec{r}_i$ are the normalized eigenvalue and eigenvectors of the strain rate tensor S, respectively. The eigenvectors are scaled to unit length whereas the eigenvalues are normalized by the strain rate magnitude $\mathring{\lambda}_i = \frac{\lambda_i}{\sqrt{\sum \lambda_j^2}} = \frac{\lambda_i}{\|S\|_F}$. The eigenvectors are purely real (as S is symmetric) and in decreasing order: $\lambda_1 \geq \lambda_2 \geq \lambda_3$. Further, the relation $\nabla\cdot\vec{u} = \lambda_1 + \lambda_2 + \lambda_3$ holds and for incompressible flows this leads to $\lambda_1 \geq 0$ and $\lambda_3 \leq 0$. Through this decomposition it can be seen that enstrophy production scales with enstrophy itself as well as with the magnitude of the strain rate tensor. The structural composition of the production term is solely governed by

$$\mathring{\lambda}_i \left(\mathring{\vec{\omega}}\cdot\vec{r}_i\right)^2. \tag{5.5}$$

The alignment between the vorticity vector and principal strain axis (eigenvectors of the strain rate tensor) weights the contribution of the respective normalized eigenvalue to the enstrophy production. $\left(\mathring{\vec{\omega}}\cdot\vec{r}_i\right)^2$ takes values between 0 and 1. It is equal to 1 if vorticity is parallel to $\vec{r}_i$ and equal to 0 if both are perpendicular to each other.

Summing up, to understand the enstrophy production, that is recognized as core of

the vortex stretching mechanism and therefore of inherent importance for the cascading process of turbulence, four quantities as well as their coupling have to be understood. The magnitudes of the strain rate tensor $\|S\|_F$ and the rotation rate tensor $\|\Omega\|_F$, together with the weighting character of the normalized principal strain rates $\mathring{\lambda}_i$ and the alignment of vorticity with the principal strain directions $\left(\mathring{\vec{\omega}} \cdot \vec{r}_i\right)^2$. In literature it was discussed that the mechanism of vortex stretching (rotation production) and the production of strain (and therefore dissipation) may only be weakly correlated (Tsinober, 2000). However, Blackburn *et al.* (1996) have shown that the strain rate and the rotation rate are strongly coupled in the near-wall region of in wall-bounded turbulence in the data of a direct numerical simulation (DNS) of a channel flow. This was further discussed on the same data set by Chong *et al.* (1998). They interpreted the strong coupling of strain and rotation at the wall as the preferred appearance of vortex sheets in the viscous sublayer. Moving away from the wall this coupling loosens and the tendency of the flow developing vortex sheets only gets lost. The structure types are more mixed in the regions further away from the wall. This interpretation was based on the description of the $\|S\|_F - \|\Omega\|_F$-space by Perry & Chong (1994). They linked structure types to certain states of $\|S\|_F$ and $\|\Omega\|_F$ in the $\|S\|_F - \|\Omega\|_F$-space: The $\|S\|_F$-axis indicates the presence of irrotational strain, whereas the $\|\Omega\|_F$-axis indicates the presence of vortex tubes. Accordingly the line $\|S\|_F = \|\Omega\|_F$ when strain rate balances the rotation rate indicates the presence of vortex sheets.

The average ratio of the principal strain rates in a DNS of incompressible homogeneous isotropic turbulence was found to be $(\lambda_1 : \lambda_2 : \lambda_3) = (3 : 1 : -4)$ (Ashurst *et al.*, 1987). This was confirmed numerically by Lund & Rogers (1994) and experimentally, based on hot-wire measurements by Tsinober *et al.* (1992) as well as through stereoscopic particle image velocimetry of the far-field of a turbulent jet-flow (Ganapathisubramani *et al.*, 2008). With the jet data they went further and investigated on the coupling of the intermediate relative strain rate $\mathring{\lambda}_2$. For high strain rates the intermediate strain rate was found to be $\mathring{\lambda}_2 \approx 0.2$, which again agrees with the results of Ashurst *et al.* (1987). This fact was interpreted that regions of high strain rate tend to be sheet-forming.

The remaining piece of the decomposed enstrophy production (eq. 5.4) is the alignment between the vorticity vector and the principal strain directions. Considering vortex stretching to be the dominant process in turbulent flows one would intuitively think that vorticity is most likely to be aligned with the strongest extensive strain direction $\vec{r}_1$ so that the strongest strain is acting in the direction of the vortex axis. But Ashurst *et al.* (1987) found vorticity most likely to be aligned with the intermediate strain direction $\vec{r}_2$. This finding was confirmed by other researchers conducting experimental (e.g. Ganapathisubramani *et al.*, 2008) as well as numerical (e.g. Hamlington *et al.*, 2008; Leung *et al.*, 2012) studies and is part of Meneveau (2011)'s review on the topic of Lagrangian dynamics. At first glance this is a surprising finding, but in their vortex model Ashurst *et al.* (1987) presented already the idea that this finding simply shows the alignment of a vortex with its own strain field. This strain field is created by the

shear stress the vortex produces due to viscous effects in the plane normal to its rotation axis. Hamlington *et al.* (2008) then decomposed the strain rate tensor in the surrounding area of a vortex into a part that contains the self-produced strain and a part that contains the background strain. Although it was not possible to decompose the strain exactly, their results show that the likeliness of vorticity to align with the intermediate strain direction is decreasing the more of the self-produced strain is removed. In Leung *et al.* (2012)'s work on geometry and interaction of turbulent structures they bandpass filtered DNS data of decaying homogeneous isotropic turbulence at a Taylor Reynolds number $Re_\lambda = 141$. The vorticity is aligned with the intermediate strain direction of its own strain field but is aligned with the extensive strain direction of structures that are larger than itself. They showed this for vorticity filtered at 15η as well as 10η and the results show the same trend. Further, their work shows that if the ratio of filter length for the strain field and filter length for the vorticity become too large then the vorticity looses any tendency to align with specific strain direction. This 'random' alignment of structures with large differences in size can be seen as loss of directivity during the cascading process. This could underline the hypothesis of local isotropy (Taylor, 1935; Kolmogorov, 1941) which states that for sufficiently large Reynolds numbers the small scales are locally isotropic. Further, this picture fits well into the cascading via vortex stretching idea. Larger structures feed smaller structure via the strain field they are producing. The smaller structures are aligning with the larger structures in a way that they get stretched in the larger structures' strain field. But this only happens in a fixed band of scale ratios of the two structures. This fact underlines the Reynolds number invariant decaying exponent of kinetic energy with respect to wave number (i.e. Kolmogorov's $-\frac{5}{3}$-law). Besides the stretching of vortices by larger structures the tendency of a vortex to contract due to its own strain field is underlined with these results as well. These opposite effects can at some point lead to an unstable state where we might find the change from stretching to contracting structures.

Another approach to explain the, in the context of vortex stretching 'unexpected', preferred parallel alignment of vorticity and intermediate strain direction was shown by Buxton & Ganapathisubramani (2010). In their experimental work on the far field of an axisymmetric turbulent jet they stated a global alignment of the vorticity vector with the principal strain axis that is consistent with literature. Moreover, they apply a characteristic decomposition on the flow. This characteristic decomposition goes back to the work of Perry & Chong (1987) that allows to characterize the current flow topology, a certain fluid particle is part of, according to the invariants Q and R of the velocity gradient tensor at the location of the fluid particle. The decomposition distinguishes between stable/stretching vortices, unstable/contracting vortices, unstable node/saddle structures and stable node/saddle structures. Here the first two structure types have a rotational character whereas the latter two have a purely straining character. The QR-space can be divided into four sectors whereas each sector represents one characteristic structure type respectively. Meneveau (2011) summarizes this decomposition

in the review on the topic of Lagrangian dynamics. Buxton & Ganapathisubramani (2010) put the significant imbalance of mean enstrophy production over the different QR-sectors that they found in focus of their work. They showed that the lion's share of the enstrophy is produced by stable/stretching vortices. Based on this fact they conditioned the probability density functions of the alignments to be located in the respective QR-sectors. Their results show that while the alignment of vorticity and intermediate strain direction is widely unaffected, the probability density function of the alignment of vorticity with the extensive strain direction is dependent on this condition. This finding reveals that the globally arbitrary alignment of vorticity with the extensive strain direction is a superposition of non-arbitrary alignments for structures of different character. While for unstable node/saddle topologies the alignment remains arbitrary, for unstable/contracting vortices the two vectors prefer to align perpendicularly. But for stable node/saddle topologies and especially for stable/stretching vortices vorticity is likely to be aligned with the extensive strain direction. As mentioned before, this type of alignment is favouring the idea of vortex stretching.

For the unconditioned alignment of the vorticity vector with the principal strain directions Blackburn *et al.* (1996) confirmed results for HIT and weak shear layers in the outer region of a channel flow obtained by DNS. However, they have shown that the alignment is changing strongly in the near-wall region. When approaching the wall, the tendency of vorticity to align parallel with the intermediate strain direction becomes stronger. At the same time it becomes more likely for vorticity to align orthogonal with the extensive strain direction as well as with the compressive strain direction.

As the enstrophy production strongly varies for the different sectors of the QR-space (Buxton & Ganapathisubramani, 2010) it is necessary to know about the distribution of the respective structures in a turbulent flow. Depending on their frequency of occurrence the structure-specific production weights more or less in the flow. Chen *et al.* (1990) found a specific shape for the iso-lines of the joint probability density function (pdf) of R and Q in a turbulent mixing layer. They report the iso-lines to have the shape of a horizontally flipped, sheared drop. The tail is extending in positive R direction and negative Q direction. This shape of the joint-pdf of Q and R was confirmed for different turbulent flows (e.g. Soria *et al.*, 1994; Ganapathisubramani *et al.*, 2008). Therefore the particular shape is often referred as *universal teardrop* of turbulence. From their DNS results of a turbulent channel flow Blackburn *et al.* (1996) could confirm the teardrop shape in the outer regions of the boundary layer. They find a reduced extent of the tail when approaching the wall. However, above the buffer layer they describe the joint-pdf of Q and R as apparent self-similar, but do not quantify these results. As a main feature when moving from the buffer layer to the VSL they describe the decrease of the maximum value of Q. They reason this fact with the strong coupling of S and Ω in the near-wall region that we discussed before.

The approach we chose for the present work to describe the development of enstrophy production in the boundary layer is done in two steps. As a first step we quantify

the components of the enstrophy production (eq. 5.4) and their development in wall-normal direction (sec. 5.3). For the outer layer results we find agreement with all off the previously introduced flows. The regions closer to the wall agree with what was discussed by Blackburn *et al.* (1996). However, we extend this about the development of the principal strain rate and the overall developments of the respective quantities. As a second step we discuss the decomposition of the production with respect to the characteristic structure types that we just introduced (sec. 5.4). We show agreement of the outer layer results with the results of the far-field of turbulent jet flow (Buxton & Ganapathisubramani, 2010). Further we quantify the variation of the joint-pdf of Q and R with the wall-normal location. Further, we investigate on the effects caused by the wall on the decomposed enstrophy production.

5.2 Turbulent Boundary Layer Data

The data for this investigations were obtained by carrying out a DNS of a compressible zero pressure-gradient flat plate turbulent boundary layer as outlined and validated in section (3.3.1). Figure (5.1) marks the streamwise location that was chosen for the present work. The selected data spans over a spanwise range of $Re_\theta \approx 1224 - 1248$ ($Re_\tau \approx 481 - 491$). The volume is short enough that statistical homogeneity is assumed over its streamwise extent.

The wall-normal profiles of the mean streamwise velocity component as well as of the energy budget of turbulent kinetic energy for the selected streamwise location are shown in figure (5.2). The plots are scaled with a wall-scaling based on the friction velocity $u_\tau = \sqrt{\frac{\mu_{\text{wall}}}{Re\,\rho_{\text{wall}}}\frac{\partial \tilde{u}}{\partial y}}$ at the particular streamwise location. For the a length l this means $l^+ = l\frac{Re\,\rho_{\text{wall}} u_\tau}{\mu_{\text{wall}}}$ whereas velocities v scale as $v^+ = \frac{v}{u_\tau}$. The terms b of the energy budget are scaled as $b^+ = b\frac{T}{Re\,\rho^2 u_\tau^4}$. In both plots the vertical lines mark the location that are chosen when data are plotted for certain wall-normal locations only. This becomes clear in the following. Overall is to say that the wall-normal gradient of the mean streamwise velocity component is varying strongly over the wall-normal location. The rate of change is more extreme in the near-wall region than it is in the regions further away from the wall. This gradient is the driving force of turbulence in this particular flow. The strong

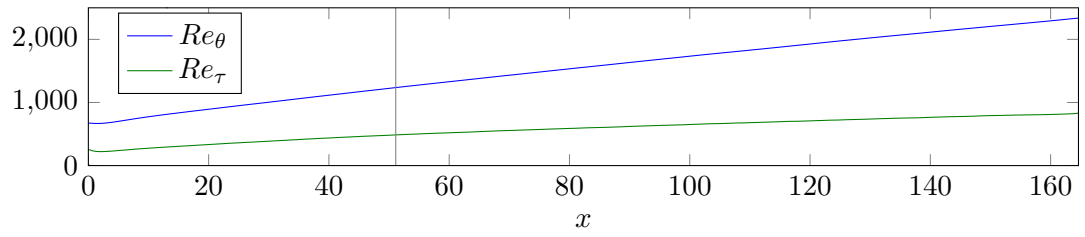

Figure 5.1: Streamwise development of the momentum thickness based Reynolds number Re_θ and the friction Reynolds number Re_τ. The grey line indicates the streamwise location where the analysis of this chapter is carried out.

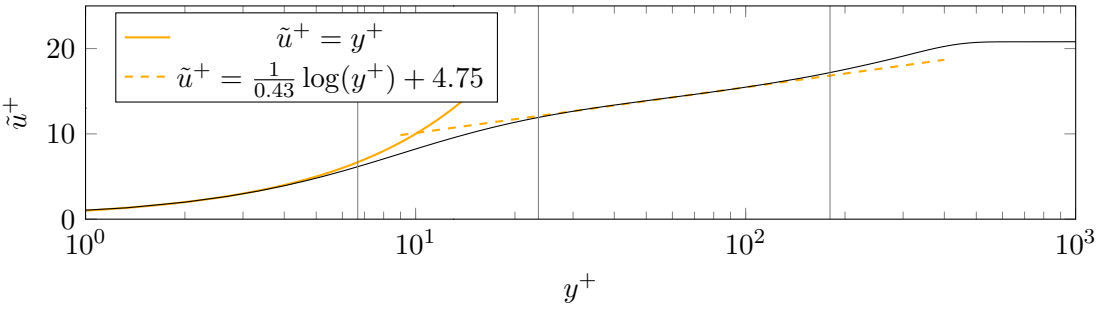

(a) streamwise mean velocity profile

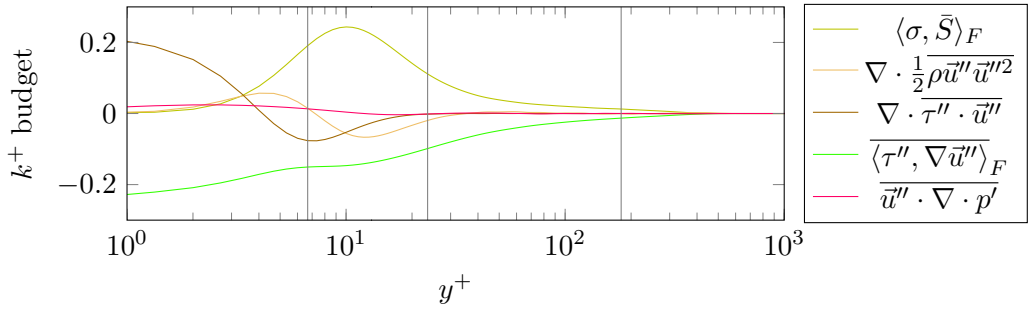

(b) turbulent kinetic energy budget

Figure 5.2: (a):Profile of the streamwise mean velocity in wall-scaling over the distance to the wall in wall-scaling. The continuous and dashed yellow lines indicate the linear behaviour in the VSL and a logarithmic law for the development of the velocity, respectively. (b): Profile of the turbulent kinetic energy budget in wall-scaling over the distance to the wall in wall-scaling. (a,b):The vertical, grey lines indicate locations at which data is plotted in the results section.

variation of the gradient cause therefore a strong variation of turbulence especially in the near-wall region. For more details about the simulation and the flow itself we refer to section (3.3.1).

5.3 Wall-Normal Development of Enstrophy Production

As a reflection of vortex stretching and vortex contraction and therefore a representation of the cascading mechanism of kinetic energy in a turbulent flow the highest values of enstrophy production are expected in the near-wall region. Figure (5.3, a) shows the development of the mean production in the wall-normal direction of the turbulent boundary layer. The components of the velocity gradient A are therefore scaled with the freestream velocity U_e and the boundary layer thickness δ_{99} to $\breve{A} = \frac{A\delta_{99}}{U_e}$. Unlike the production of turbulent kinetic energy (fig. 5.2), the enstrophy production does not peak at $y^+ \approx 10$. Moreover, it reaches its maximum value much closer to the wall. Potentially it is even reached at the wall, but in the current dataset we do not have information about enstrophy production directly at the wall. Above $y^+ \geq 6.7$ the mean enstrophy production develops an exponential decay with the increasing distance to the

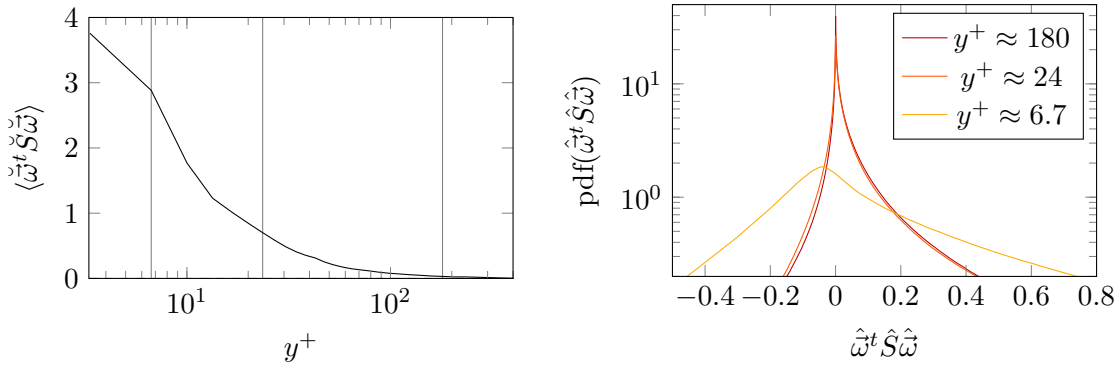

(a) wall-normal development

(b) pdf of enstrophy production

Figure 5.3: Overview of enstrophy production in the turbulent boundary layer flow. (a): Wall-normal development of the mean enstrophy production scaled with outer scaling ($\breve{f} = f\frac{\delta_{99}}{U_e}$). Grey vertical lines indicate the location at which the pdfs (b) are taken. (b): Pdf of the scaled enstrophy production at three different wall-normal location.

wall and remains positive throughout the entire boundary layer.

Contrasting the strictly positive net production the pdfs (fig. 5.3, b) reveal that the instantaneous production has significant negative contributions. For this plot and for the following we introduce a scaling based on the local variance of the velocity gradient magnitude

$$\mathrm{var}(A) := \langle \langle A - \tilde{A}, A - \tilde{A} \rangle_F \rangle, \tag{5.6}$$

where $\langle \bullet \rangle$ denotes the temporal mean and $\langle \bullet, \bullet \rangle_F$ denotes the Hilbert-Schmidt inner product. The velocity gradient quantities are then scaled as

$$\hat{A} := \frac{A}{\sqrt{\mathrm{var}(A)}}, \quad \hat{S} := \frac{S}{\sqrt{\mathrm{var}(A)}} \quad \text{or} \quad \hat{\Omega} := \frac{\Omega}{\sqrt{\mathrm{var}(A)}}. \tag{5.7}$$

For $y^+ \approx 24$ and $y^+ \approx 180$ a significant peak can be seen at zero while an asymmetric shape of the pdf is developed. The legs towards positive production reach to significantly higher magnitudes and are fatter than the ones on the negative side. This underlines the general consensus in the literature (e.g. Taylor, 1938; Tennekes & Lumley, 1972) that vortex stretching (positive enstrophy production) is favoured over vortex compression (negative enstrophy production) which is reflected in the previously discussed net production. Further, the shape of the pdfs agree well with experimental results of turbulent shear flow and a turbulent jet results from Mullin & Dahm (2006); Buxton & Ganapathisubramani (2010), respectively. Above $y^+ \approx 24$ the enstrophy production does not change its character as far as represented by the pdf. Further, the most likely value stays as zero and its variance scales well with the variance of the velocity gradient $\mathrm{var}(\vec{\omega}^t S \vec{\omega}) \sim \mathrm{var}(A)^3$. However, closer to the wall the properties of the pdf changes. Although we have seen that the mean value of the production increases towards the wall, we find that the most likely value of the production moves towards negative values. Further, the variance of the production no longer scales with the velocity gradient

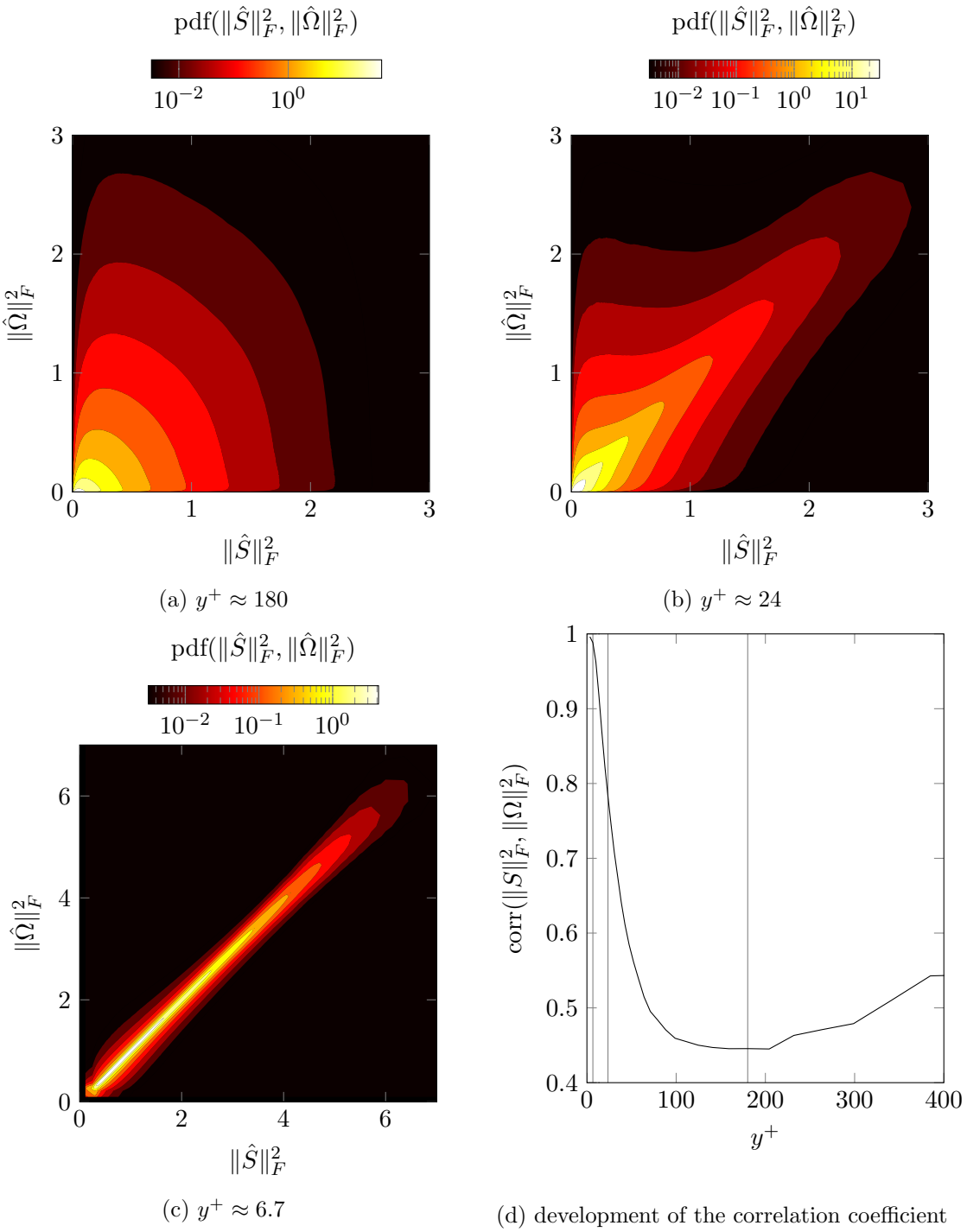

(a) $y^+ \approx 180$

(b) $y^+ \approx 24$

(c) $y^+ \approx 6.7$

(d) development of the correlation coefficient

Figure 5.4: Joint-pdf of normalized strain rate magnitude squared and normalized rotation magnitude squared at three different wall-normal locations (a-c) and the development of the correlation between strain rate and rotation rate on wall-normal direction (d).

variance and is much higher than at the higher locations in a relative sense. Both, the negative and positive tail of the pdf are enlarging, however, additional to the shift of the peak, the negative tail is growing proportionally more than the positive one.
To understand these changes in the near-wall region the enstrophy production is decomposed according to the introduced decomposition base on the eigen-decomposition of the strain rate tensor (eq. 5.4). In this identity we see that the scaling term for the production is $\|\Omega\|_F^2\|S\|_F$. For the magnitude of this term the correlation of the strain rate and the rotation rate is an essential quantity. A strong correlation increases the potential for relatively high values of this term

$$\langle\|S\|_F\|\Omega\|_F^2\rangle = \mathrm{corr}(\|S\|_F, \|\Omega\|_F^2)\sqrt{\mathrm{var}(\|S\|_F)}\sqrt{\mathrm{var}(\|\Omega\|_F^2)} + \langle\|S\|_F\rangle\langle\|\Omega\|_F^2\rangle. \quad (5.8)$$

We did not consider the exact correlation $\mathrm{corr}(\|S\|_F, \|\Omega\|_F^2)$ that is demanded by this equation, however, there is a close relation to the correlation of $\|S\|_F^2$ and $\|\Omega\|_F^2$ which is studied in figure (5.4). The results shown in the joint-pdfs strongly agree with results presented by Blackburn *et al.* (1996). Perry & Chong (1994) introduce the interpretation for these plots in a way that vortex tubes are found close to the $\|\Omega\|_F^2$-axis pure straining structures are found close to $\|S\|_F^2$-axis and in the line at an angle of 45 degrees we find vortex sheets. According to this interpretation the predominant structure type in the near-wall region are vortex sheets. Whatever a *vortex sheet* is left to the inspiration of the reader. Either way, the important fact that we take on from these plots is that vorticity is strongly coupled to the strain rate which implies (Tsinober, 2000) that vortices in this region of the boundary layer have a relatively strong dissipative character. However, this dominance of vortex sheets is replaced by a mix of vortex sheets, vortex tubes and irrotational straining structures which agrees with the interpretation of Chong *et al.* (1998). Further the strong coupling of rotational structures with dissipation is lost. The correlation coefficient is plotted as summary over the wall-normal location (fig. 5.4). According to the previous interpretation this plot can be seen as how strong the dissipation of a vortex is in relation to its rotation rate. The fact that the correlation is increasing in the near-wall region could be caused by the fact that vortices are packed more densely at the wall. This causes an increased interaction of their strain fields which acts in addition to the interaction of the strain fields with the wall itself. This enhanced interaction then amplifies the correlation between strain and rotation.
The magnitudes, imposed by the the strain rate and the rotation rate, are scaled by the term (eq. 5.5) which is a combination of the relative principal strain rates and the alignments between the vorticity vector and the respective principal strain direction. The mean development of the principal strain rates are is shown in figure (5.5). In the outer layer as well as in the logarithmic layer we find a slightly positive value for in mean of the intermediate strain. This, qualitatively, agrees with literature about HIT (Ashurst *et al.*, 1987) and weak shear layers (e.g. Ganapathisubramani *et al.*, 2008). However, a quantitative comparison reveals a disagreement with the ratio of $(\lambda_1 : \lambda_2 : \lambda_3) \approx (3 : 1 : -4)$ that was found uniformly found in literature. In case of the present TBL we obtain the

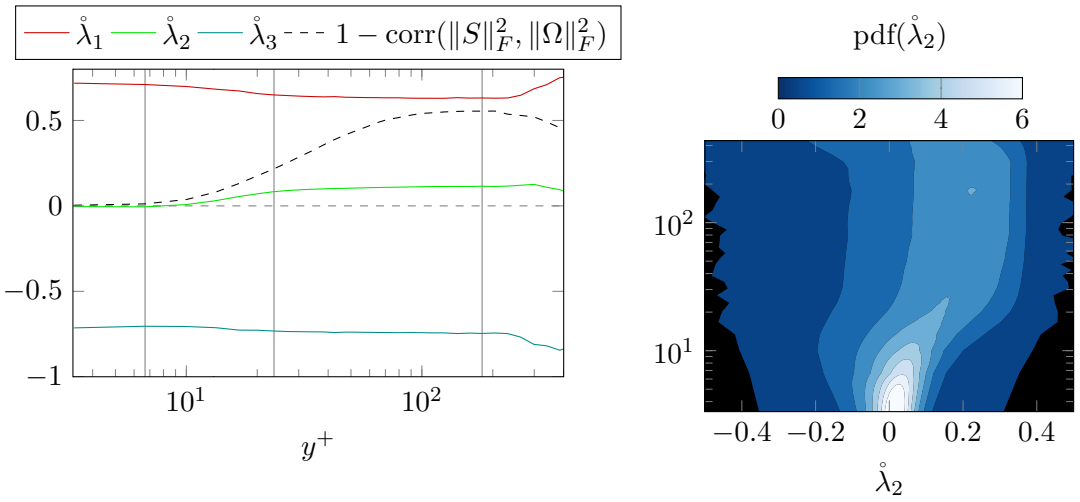

(a) Mean development of the principal strain rates. The dashed black line shows the correlation of $\|S\|_F^2$ and $\|\Omega\|_F^2$. The dashed grey line marks zero.

(b) Development of the pdf of the intermediate strain rate as single pdfs for each location plotted as one contour plot.

Figure 5.5: Wall-normal development of the normalized strain rates in the turbulent boundary layer.

ratios $(5.5 : 1 : -6.5)$ for $y^+ \approx 180$, $(7.8 : 1 : -8.8)$ for $y^+ \approx 24$ and $(128 : -1 : -127)$ for $y^+ \approx 6.7$. Therefore the plots show that when approaching the wall, the relative intermediate strain tends to zero. It is slightly negative in the near-wall region, but its magnitude is small enough that the sign does not play a significant role. The pdfs in figure (5.5, b) shows that the fluctuations around this zero mean are relatively small compared to the fluctuations that can be found in the outer layer. Further, the pdf is skewed towards positive values in the higher regions of the boundary layer which does not hold for the near-wall region. In the near-wall region we find a nearly symmetric pdf.

The joint-pdfs between $\mathring{\lambda}_2$ and the strain rate magnitude and the rotation rate magnitude, respectively, are shown in figure (5.6, c and d). Comparing the present results to the experimental results of the far-field of a turbulent jet (Ganapathisubramani *et al.*, 2008), there are two things to mention. Firstly, the joint-pdf of $\mathring{\lambda}_2$ and $\|S\|_F^2$ shows great similarities for both cases. This indicates that the strain magnitude - strain composition coupling is not changing significantly across both cases. Secondly, we find that the joint-pdf of $\mathring{\lambda}_2$ and $\|\Omega\|_F^2$ reveals significant differences of both flows. Whereas for high rotation magnitudes the behaviour appears to be similar in both flows (agrees as well with Ashurst *et al.* (1987)), the pdfs diverge for low rotation rates. In the jet case it is unlikely to find spots without rotation. However, in the logarithmic layer and in the outer layer of the TBL these events seem to be very likely. Moreover, for low values of rotation magnitude the pdf is less skewed towards positive $\mathring{\lambda}_2$. Putting both together we reason that, in a relative sense, lower intermediate strain rate in the higher layers of the TBL are caused by the higher frequency of occurrence of straining structures with zero or very little rotation.

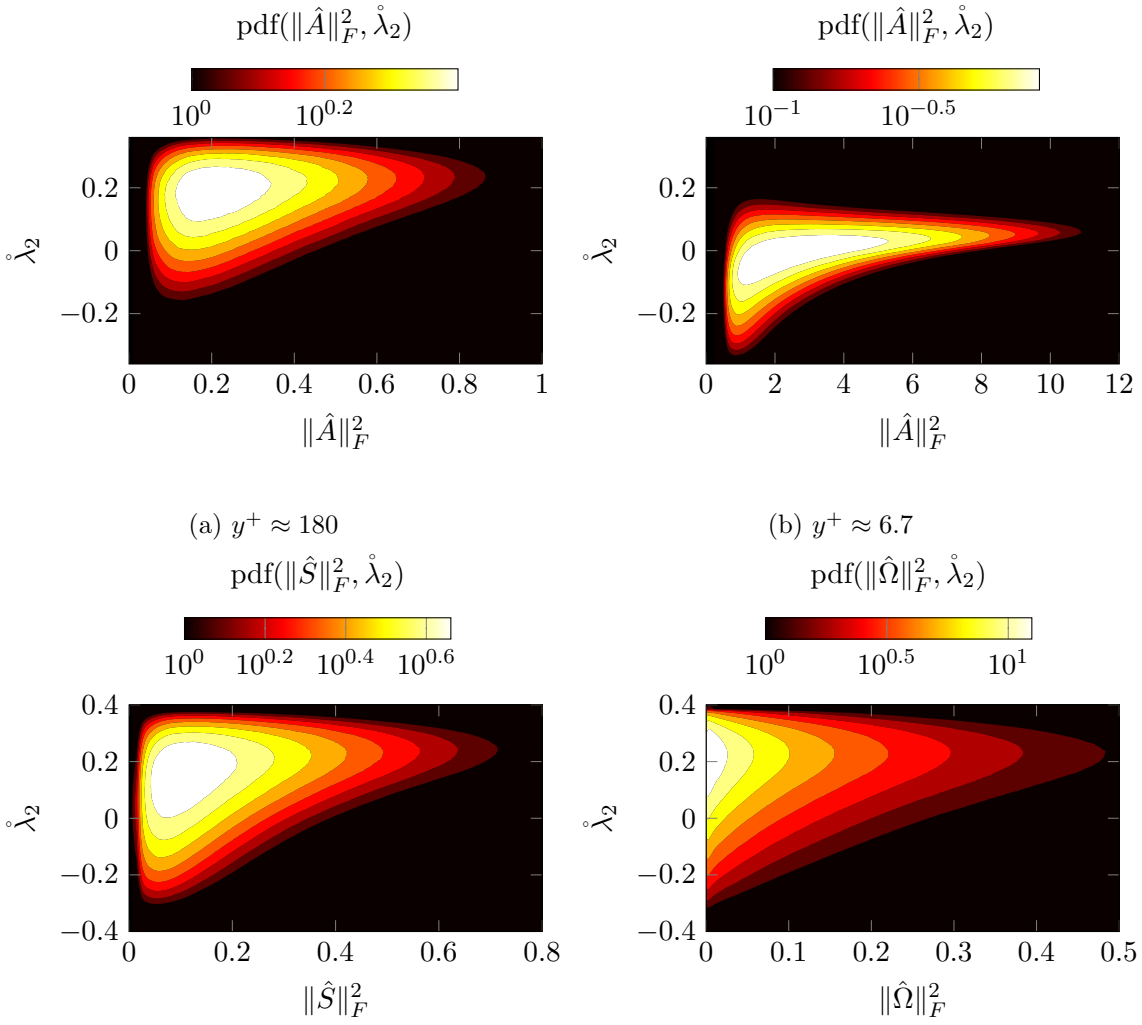

(a) $y^+ \approx 180$ (b) $y^+ \approx 6.7$

(c) $y^+ \approx 180$ (d) $y^+ \approx 180$

Figure 5.6: Joint-pdfs of the normalized intermediate strain rate $\mathring{\lambda}_2$ and the normalized velocity gradient magnitude squared at two different wall-normal locations (a,b). Joint-pdf of the normalized intermediate strain rate and the normalized strain rate magnitude squared (c) and the normalized rotation rate magnitude squared (d),respectively, at $y^+ \approx 180$.

Figure (5.6, a and b) show the joint-pdfs of the relative intermediate strain rate with the velocity gradient magnitude squared in the logarithmic layer (a) as well as between VSL and buffer layer (b). A clear shift of the pdf towards negative $\mathring{\lambda}_2$ is seen when going from the higher layer towards the wall. Further, the relative skewness for strong gradients is larger in the near-wall region, than it is in the logarithmic layer. The plots show that for high velocity gradients at the wall it is more likely to find $\mathring{\lambda}_2 > 0$ whereas for low velocity gradients it is slightly more likely to find $\mathring{\lambda}_2 < 0$.

The *vortex stretch model* introduced by Ashurst *et al.* (1987) still suits well to interpret the development of the principal strains in the boundary layer. In the model a

vortex is described as a line vortex that stretches along its axis. The stretching mechanism itself creates a strain field with the according principal strain ratio described by $R_{\text{stretch}} := (-1 : 2 : -1)$. However, the vortex own strain field, caused by the rotation that decays with increasing distance to the axis, causes a shear that results in a principal strain ratio described by $R_{\text{shear}} := (1 : 0 : -1)$. Depending on the ratio of the strength of the stretching to the strength of the shearing due to the vortex rotation $(\gamma_{\text{stretch}} : \gamma_{\text{shear}})$ this composes to the final ratio $\gamma_{\text{stretch}} R_{\text{stretch}} + \gamma_{\text{shear}} R_{\text{shear}}$. Ashurst *et al.* (1987) found that a ratio $(\gamma_{\text{stretch}} : \gamma_{\text{shear}}) = (1 : 7)$ leads to the ratio $(\lambda_1 : \lambda_2 : \lambda_3) = (3 : 1 : -4)$ that fits well to the ratio of principal strains found for HIT and weak shear layers as mentioned before. However, in agreement with Blackburn *et al.* (1996) we have found a strong increase of correlation between strain rate and rotation rate when approaching the wall. We believe that this variation strongly influences the ratio $(\gamma_{\text{stretch}} : \gamma_{\text{shear}}) = (1 : 7)$ and drives it an even more extreme value than it is in HIT. In our case we get the correct principal strain ratios for $(\gamma_{\text{stretch}} : \gamma_{\text{shear}}) = (1 : 12)$ at $y^+ \approx 180$, $(\gamma_{\text{stretch}} : \gamma_{\text{shear}}) = (1 : 16.6)$ at $y^+ \approx 24$ and $(\gamma_{\text{stretch}} : \gamma_{\text{shear}}) = (1 : -255)$ at $y^+ \approx 6.7$. The coupling between the strain-rotation-correlation and the strain composition should be emphasized as well in figure (5.5, a) where the black dashed line shows the development of $1 - \text{corr}(\|S\|_F, \|\Omega\|_F^2)$ which shows similar trends as the intermediate principal strain in the widest sense. Obviously, this does not clearly state the coupling, however, it shows that it is worth to spend more time on this in the future.
Overall its seems that at the wall, according to their strain field, turbulent structures develop a strong variation in two direction whereas the third directions is nearly homogeneous as stated by the nearly vanishing relative intermediate strain. This suits well to the fact that we find relatively long streamwise elongated, densely packed structures in

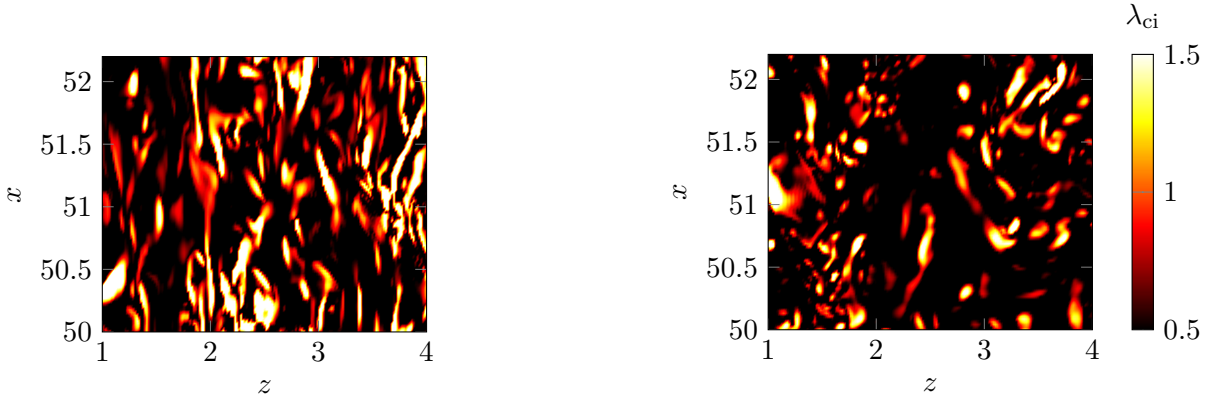

(a) $y^+ \approx 11$ (b) $y^+ \approx 114$

Figure 5.7: Top view onto a boundary layer. The instantaneous snapshots of the λ_{ci}-criterion are taken at the same instance of time at two different heights in the boundary layer. The right is a location within the logarithmic layer ($y^+ \approx 114$,b) and the left shows a location at the lower part of the buffer layer ($y^+ \approx 11$, a). The flow direction is bottom to top.

the near-wall region whereas the structures at higher layers are more randomly aligned and less densely packed (fig. 5.7). The strongest strain of vortical structures is found in the plane normal to its rotation axis is discussed by Ashurst *et al.* (1987). When the structures are densely packed at the wall, then their strain fields amplify each other. Further the streamwise orientation of the structures leads to the fact that the strongest strain fields of all structures are in the plane normal to the streamwise direction. Alignments of the rotation axis of smaller structures the extensive strain direction of larger structures, as stated by Leung *et al.* (2012), is suppressed by the wall. This leads to a missing stretching force and enforces the 2d character of the strain fields that we observe in the results.

Further, it seems that outside of the main production region of the turbulent boundary around $y^+ \approx 10$ we find large amounts of decaying turbulence which results in a higher frequency of occurrence of pure straining structures without rotational contribution. This will be further supported later as we will see that the ratio of rotational structures to pure straining structures decreases towards higher layers.

Besides the principal strains, the other piece of the term (eq. 5.5) that weights the strain rate magnitude and the rotation magnitude in the enstrophy production (eq. 5.4) is the alignment of the vorticity vector with the principal strain directions. In figure (5.8) these alignments are shown for different wall-normal locations in the TBL. For the outer most location ($y^+ \approx 180$) the alignments agree well with the ones stated for HIT and weak shear layers in literature (e.g. Ashurst *et al.*, 1987; Ganapathisubramani *et al.*,

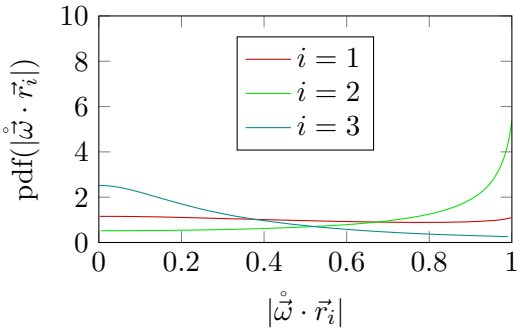

(a) $y^+ \approx 180$

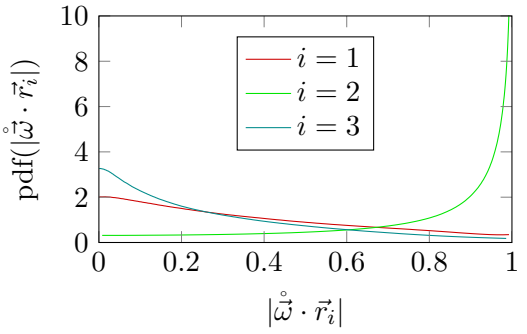

(b) $y^+ \approx 24$

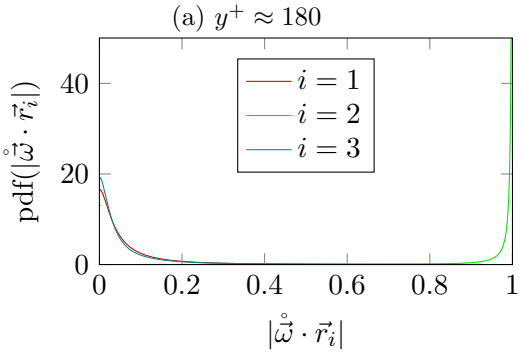

(a) $y^+ \approx 6.7$

Figure 5.8: Pdfs of the alignment between the vorticity vector and the principal strain directions at three different wall-normal locations.

2008; Hamlington *et al.*, 2008; Meneveau, 2011; Leung *et al.*, 2012). Vorticity shows an arbitrary alignment with the extensive strain direction ($i = 1$), but tends to align parallel with the intermediate strain direction ($i = 2$). The tendency to an orthogonal alignment between the vorticity vector and the compressive strain direction ($i = 3$) is stated. Ashurst *et al.* (1987) proposed with their previously described vortex stretch model that this alignment reflects the alignment of the vorticity vector with the vortex induced strain field rather then the alignment of a vortex with imposed strain field of other structures and/or boundary conditions. This is supported by the work of Hamlington *et al.* (2008) in which the total strain is split into a local strain and a non-local background strain to study the alignment of vorticity with the so obtained vortex own strain field. Further, Leung *et al.* (2012) supported the hypothesis of Ashurst *et al.* (1987) by investigations on the alignment of vorticity with the strain field filtered at several different spatial filter widths.

The change of the alignments with the wall-normal location stated in figure (5.8) agrees well with the variations that where found by Blackburn *et al.* (1996). The parallel alignment of vorticity with the intermediate strain direction becomes more likely when approaching the wall. At the same time the orthogonal alignment with the compressive strain direction further increases its frequency of occurrence. Further, the arbitrary alignment of vorticity and the extensive strain direction does not hold anymore when approaching the wall. Already at $y^+ \approx 24$ we find a slight trend towards an orthogonal alignment between both vectors. At $y^+ \approx 6.7$ the tendency of an orthogonal alignment of $\vec{\omega}$ and $\vec{r}_1$ became strong enough to show the same pdf as $|\vec{\omega} \cdot \vec{r}_3|$.

As we have seen when discussing the principal strains, the strain field of the vortices is dominated by strain field that is induced by the vortex own shear rather than the stretching strain. However, the vortex' rotation axis is aligned with the stretching strain direction and therefore we find $|\vec{\omega} \cdot \vec{r}_2| \to 1$. On the other hand, the surrounding strain field develops aligned with the axis normal plane which leads to $|\vec{\omega} \cdot \vec{r}_1| \to 0$ and $|\vec{\omega} \cdot \vec{r}_3| \to 0$.

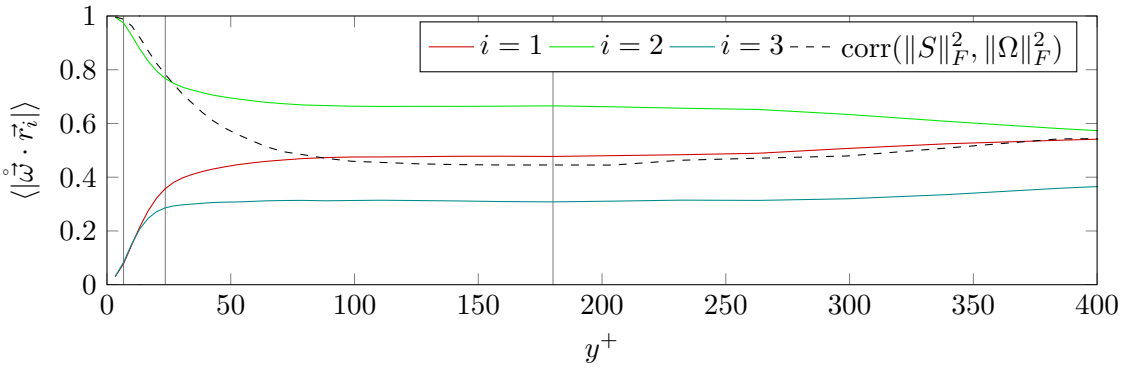

Figure 5.9: Mean alignment of vorticity with the three principal strain directions, respectively (continuous lines). Correlation coefficient between the strain rate magnitude squared and the rotation rate magnitude squared. All is plotted over the distance to the wall.

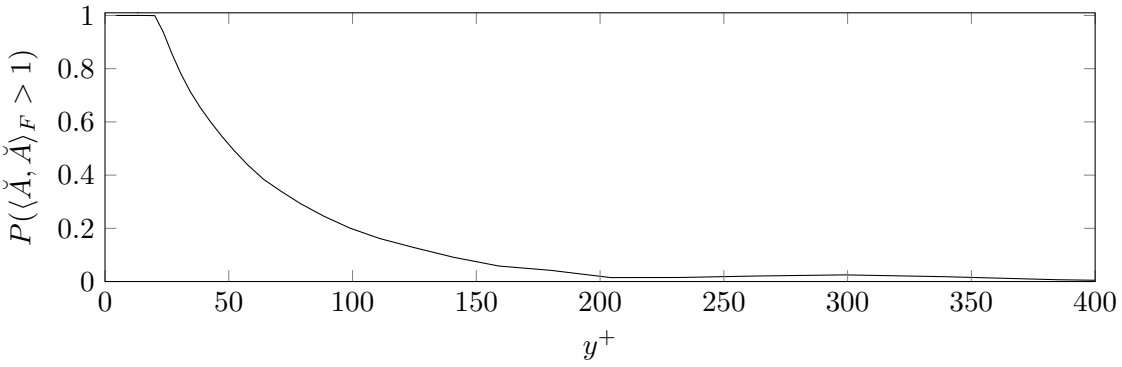

Figure 5.10: The probability of the magnitude of the normalized velocity gradient squared being larger than unity as a measure of intermittency is plotted over the distance to the wall. The velocity gradient is normalized by the ratio of freesteam velocity and boundary layer thickness $\breve{A} = A\frac{\delta_{99}}{U_e}$.

In figure (5.9) the development of the mean alignment of the vorticity vector with the principal strain direction is shown over the distance to the wall. In wide part of the boundary layer we find a relatively constant mean alignment which coincides with the previously discussed results from literature about HIT and weak shear layers. We find a slight variation towards the far outer region which is believed to be caused by the strongly decaying turbulence in this region. Therefore a measure of intermittency is shown in figure (5.10). This the high proportion of strong gradients in the near-wall region indicates that the flow is nearly always turbulent. On the other hand, in the outer regions weak velocity gradients are present more often. This indicates that turbulence occures as rare events in the outer layer. This affects the outer region results in terms of alignment and strain composition. However, the stronger change of the aligments can be seen in the near-wall region as discussed in the previous paragraph. The mean alignment of vorticity with the intermediate strain direction becomes parallel whereas vorticity align perpendicular with the remaining two principal strain directions. The alignments start to change below $y^+ \lesssim 110$ which is roughly the region where the correlation of strain rate magnitude and rotation rate magnitude starts to vary. This supports the previously mentioned link between the be-said correlation, the ratio of the principal strain rates and the alignment of vorticity and the principal strain directions. Overall the great importance of the strain-rotation-magnitude correlation is discovered to be a good indication of how the enstrophy production is composed.

5.4 Characteristic Decomposition of Enstrophy Production

In the previous section the enstrophy production was decomposed by the eigenvalue decomposition of the strain rate tensor (eq. 5.4). We have seen how the certain parts of the

production vary with the distance to the wall and how they are coupled. In their work on the experimental data of the far-field of a turbulent jet Buxton & Ganapathisubramani (2010) have shown that the sign of the production, i.e. whether enstrophy is produced or destructed, is dictated by the alignment of vorticity with the extensive strain direction. Applying a characteristic decomposition the to turbulent flow, the dominant enstrophy destructing structures where found within the unstable/contracting vortical structures. In this section we discuss to what extend this holds in a turbulent boundary layer. As part of this there is need to discuss the distribution of the characteristic structure types in the turbulent boundary layer.

The applied characteristic decomposition is based on the *critical point concept* first introduced by Perry & Chong (1987) which decomposes a flow according to the form of the eigenvalues of the local velocity gradient. Therefore this analysis is purely local and describes the character of a structure at the location of the current fluid particle only. It does not describe the character of a structure as a whole. To obtain a better overview of the method we suggest to read the original publication Perry & Chong (1987) or a summary about Lagrangian dynamics by Meneveau (2011). However, we will introduce the method with its key point for our analysis in a brief manner.

Picking a fluid particle at a particular location, the character of the velocity gradient $A := \nabla\vec{u}$ reflects the shape the flow has in the infinitesimal surrounding of the particle. This can be shown by a Taylor's expansion for the particle movement (sec. 1.2.2 or Perry & Chong (1987)). The character of the velocity gradient, on the other hand, is reflected by its eigenvalues $(\alpha_1, \alpha_2, \alpha_3)$, that are obtained as roots of the characteristic polynomial of the velocity gradient

$$p_{\text{char}}(\alpha) := \det(A - \alpha I) = \alpha^3 + P\alpha^2 + Q\alpha + R. \tag{5.9}$$

Here P,Q and R are invariants of the velocity gradient, the definition of which can be found in section (2.4). These invariants span a state space, PQR-space, in which we find certain regions defining certain properties of the eigenvalues, and therefore certain properties of the local flow topology at the fluid particle. P, which is the additive inverse of the dilatation $-\nabla \cdot \vec{u}$, is zero for incompressible flows. In the present compressible turbulent boundary layer we have a freestream Mach number of $M_\infty = 0.5$ which leads to little compressibility effects only and the first invariant P is insignificantly small. For this reason we map the results of the PQR-space onto its subset with $P = 0$, which we call the QR-space. This does not mean that the flow is considered to be incompressible. The analysis still takes compressibility into account, but it is not distinguished between different values of the first invariant of the velocity gradient $P = -\nabla \cdot \vec{u}$. The results were validated against a fully compressible analysis in the PQR-space, but no significant differences were found. The QR-space, is spanned by the second and third invariant, Q and R, of the velocity gradient. From the point of view of a fluid particle located on a structure, it allows to distinguish between four different states of the structure at the location of the particle. Figure (5.11) shows the QR-space and the four structure types.

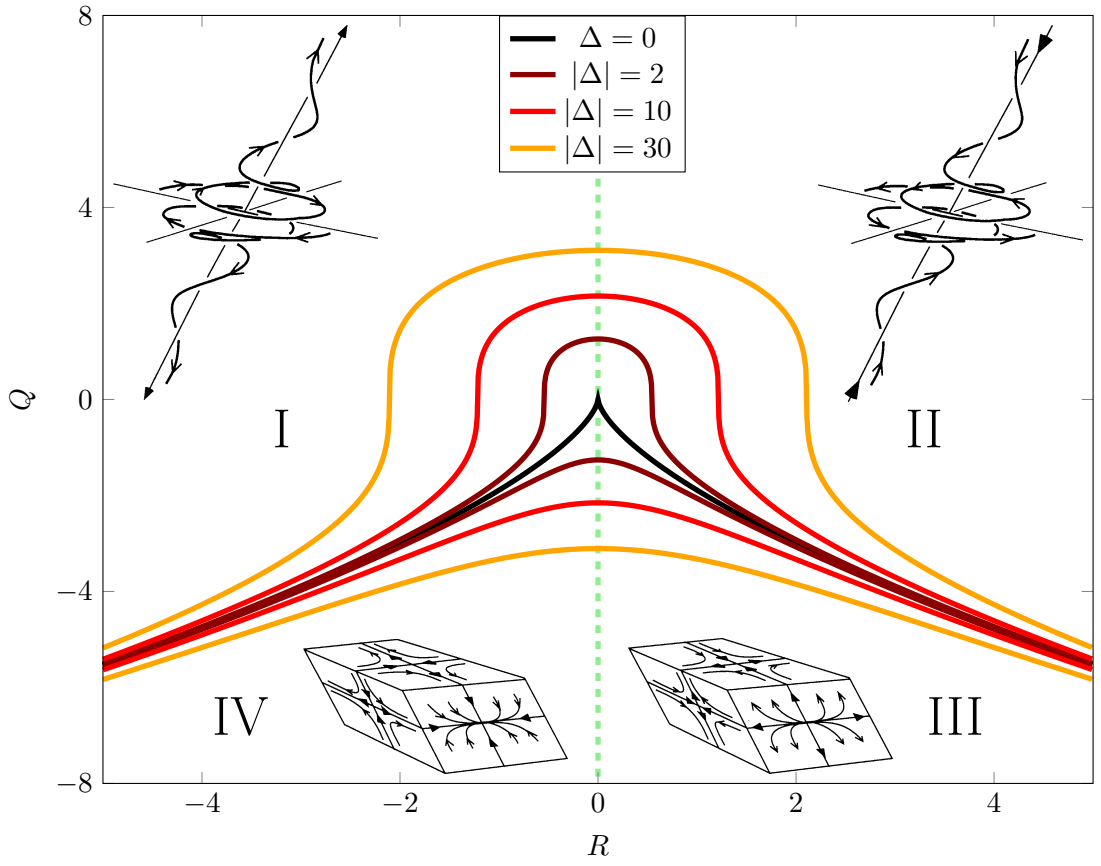

Figure 5.11: Introduction to the invariant space of the velocity gradient. The continuous lines show different values for the discriminant Δ of the velocity gradient and the dashed green line marks $R = 0$. The pictures and numbers show schematically the characteristic structure in the respective area of the QR-space. Subfigures adapted from Ooi *et al.* (1999).

The discriminant of the velocity gradient $\Delta = -\frac{1}{4}P^2Q^2 + Q^3 + P^3R + \frac{27}{4}R^2 - \frac{18}{4}PQR$ has an important role in this decomposition. For positive value of $\Delta > 0$ the velocity gradient has one purely real eigenvalue and a complex conjugate pair of complex eigenvalues and therefore the fluid particle sits on a part of a structure that has a rotational character. On the other hand, if $\Delta \leq 0$ is negative all eigenvalues of the velocity gradient are purely real and the supporting structure is purely straining at the location of the fluid particle. Further, for negative third invariant $R \leq 0$ we find two contracting directions and one stretching direction, whereas if $R > 0$ is positive we find two stretching direction and one contraction direction of the structure at the location of the fluid particle. So four characteristic structure types can be described:

I : vortical structure with stretching character / $\Delta > 0$; $R \leq 0$ / $\Im(\alpha_2) = 0$; $\Im(\alpha_1) = -\Im(\alpha_3) \neq 0$; $\Re(\alpha_1) = \Re(\alpha_3) \leq 0$; $\alpha_2 \geq 0$

II : vortical structure with contracting character / $\Delta > 0$; $R > 0$ / $\Im(\alpha_2) = 0$; $\Im(\alpha_1) = -\Im(\alpha_3) \neq 0$; $\Re(\alpha_1) = \Re(\alpha_3) \geq 0$; $\alpha_2 \leq 0$

III : pure straining structure with flattening character / $\Delta \leq 0$; $R > 0$ / $\Im(\alpha_1) = \Im(\alpha_2) = \Im(\alpha_3) = 0$; $\alpha_1 \geq \alpha_2 \geq 0 \geq \alpha_3$

IV : pure straining structure with elongating character /$\Delta \leq 0$; $R \leq 0$ / $\Im(\alpha_1) = \Im(\alpha_2) = \Im(\alpha_3) = 0$; $\alpha_1 \geq 0 \geq \alpha_2 \geq \alpha_3$

The result of the characteristic decomposition branching from the critical point analysis is visualized in figure (5.12). The same hairpin structure is shown with different techniques. For the bottom picture the λ_{ci}-criterion was used to create the iso-surface. It is coloured with streamwise velocity from blue (slow) to red (fast). The legs as well as the arc are seen clearly. The top pictures use iso-surfaces based on the magnitude of the discriminant of the velocity gradient. Differently to the λ_{ci}-criterion, this criterion visualized not only rotational structures, but also purely straining structures. This allows that the overall structure (top right) can be decomposed into the respective structure types of the characteristic decomposition. It becomes obvious that a clear distinction by the characteristic structure types is now possible. The decomposition can be used to describe e.g. which parts of the structure are stretching, which parts are purely straining, etc.

According to the previous normalization of the different parts of the velocity gradient

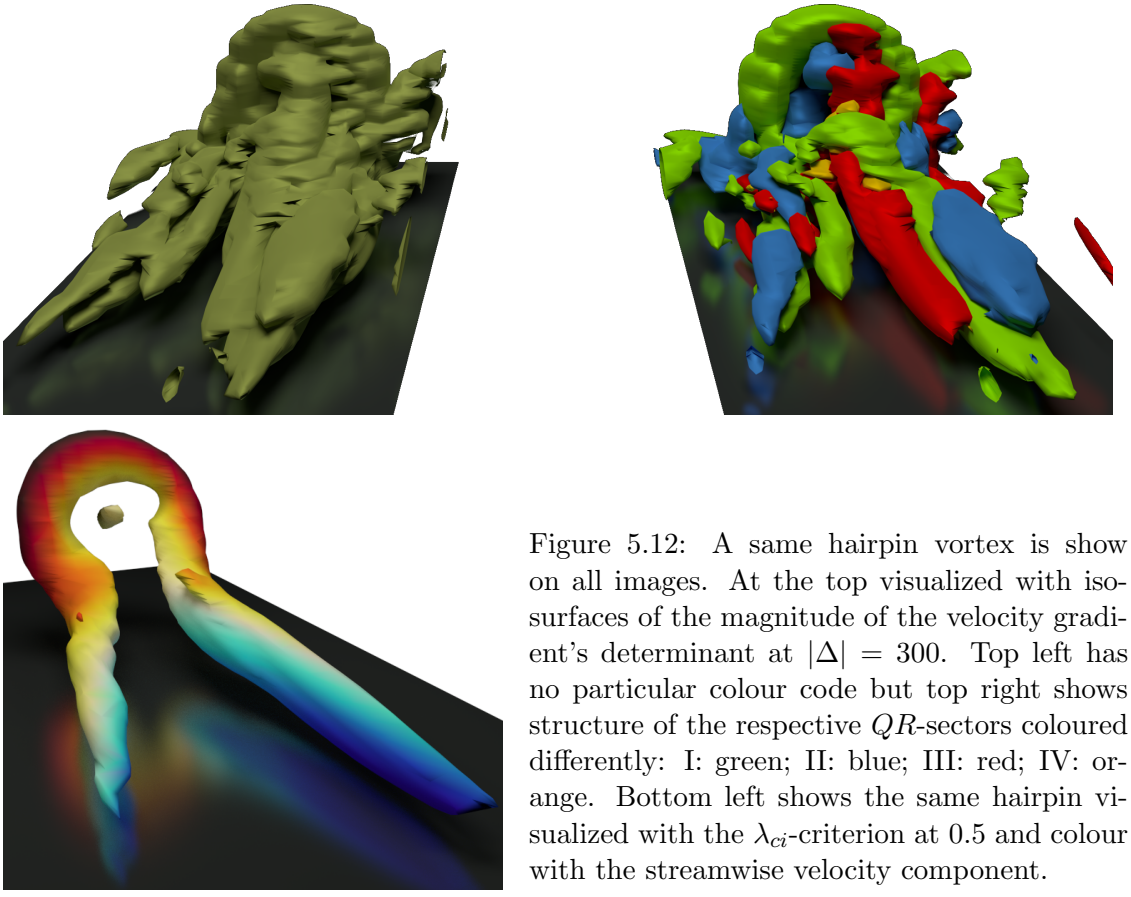

Figure 5.12: A same hairpin vortex is show on all images. At the top visualized with iso-surfaces of the magnitude of the velocity gradient's determinant at $|\Delta| = 300$. Top left has no particular colour code but top right shows structure of the respective QR-sectors coloured differently: I: green; II: blue; III: red; IV: orange. Bottom left shows the same hairpin visualized with the λ_{ci}-criterion at 0.5 and colour with the streamwise velocity component.

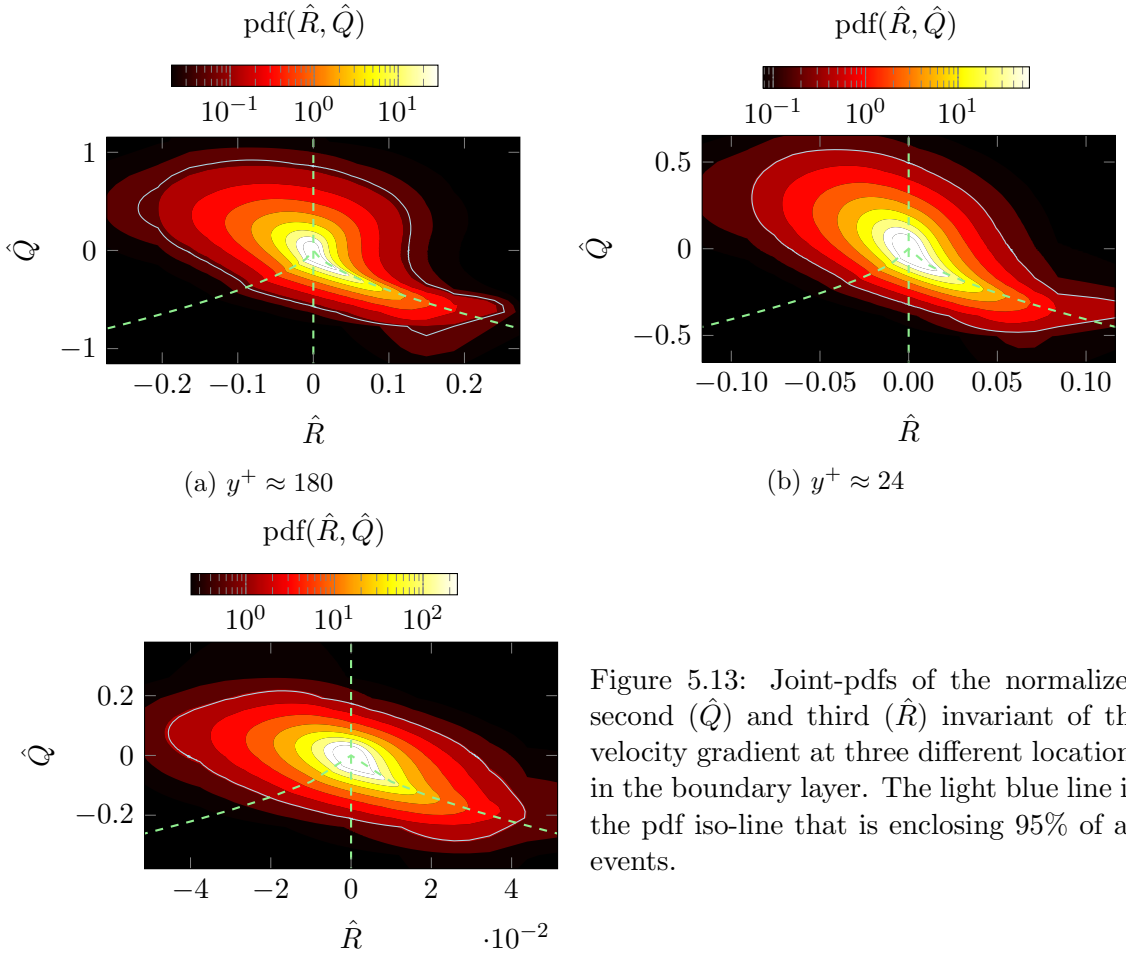

(a) $y^+ \approx 180$ (b) $y^+ \approx 24$

(a) $y^+ \approx 6.7$

Figure 5.13: Joint-pdfs of the normalized second ($\hat{Q}$) and third ($\hat{R}$) invariant of the velocity gradient at three different locations in the boundary layer. The light blue line in the pdf iso-line that is enclosing 95% of all events.

(eq. 5.6) the second and third invariant of the velocity gradient are normalized using the variance of the velocity gradient (eq. 5.7)

$$\hat{Q} := \frac{Q}{\mathrm{var}(A)}, \quad \hat{R} := \frac{R}{\mathrm{var}(A)^{\frac{3}{2}}}. \tag{5.10}$$

The frequency of occurrence of the characteristic structures in a flow can now be measured by sampling joint-pdfs of R and Q in the flow. The resulting plots are commonly known as QR-plots and are shown for the present turbulent boundary layer in figure (5.13). All shown QR-plot agrees with literature. The shape of the plot of the outermost location at $y^+ \approx 180$ agrees in a wider sense with literature about HIT (Martin *et al.*, 1998), the far-field of a turbulent jet (Ganapathisubramani *et al.*, 2008) and experimental results of the outer layer of a turbulent boundary layer (Elsinga & Marusic, 2010). Further, the results agree with the result Blackburn *et al.* (1996); Chong *et al.* (1998) show for different wall-normal locations in a turbulent boundary layer flow. Against the widely established opinion that these QR-plots are a universal feature of turbulence Chong *et al.* (1998) already stated that the shape of the iso-lines of the plot are varying

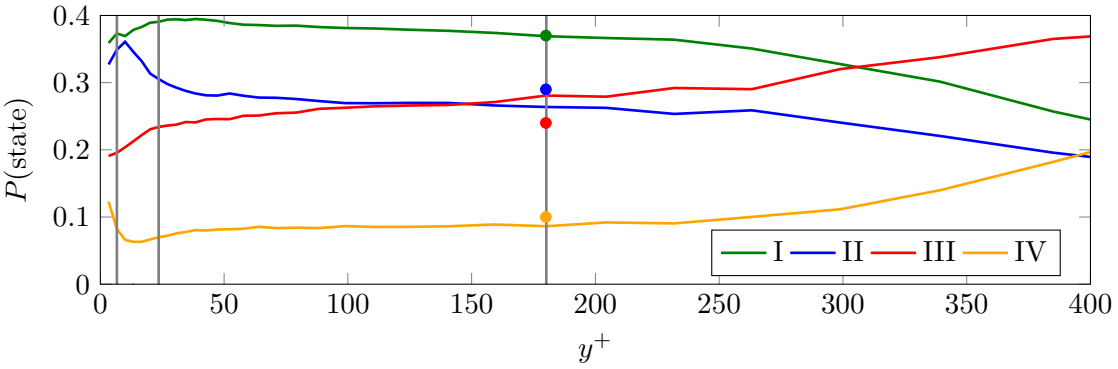

Figure 5.14: Frequency of occurrence P(state) of the respective characteristic states over the wall-normal direction. The vertical grey lines indicate the locations where samples are taken for a more detailed analysis. The coloured dots mark the respective distribution obtained in the far-field of a turbulent jet (Buxton & Ganapathisubramani, 2010).

significantly with the wall-normal location in a turbulent boundary layer. When approaching the wall the tail towards high values of R and low values of Q gets lost and a more oval shape is developed. Further, the extend to higher values of relative Q is reduced in the near-wall region. On the other hand, there is seemingly not significant change of the shape in the logarithmic layer and outer layer of the turbulent boundary layer. And the presumably universal *teardrop* shape is recovered well.

After having seen that the iso-line shapes of the invariants the joint-pdf are not universal in the near-wall region of a boundary layer we reduce the complexity of the QR-plots and integrate the joint-pdf over the area of the respective characteristic types in the QR-space. This leads to the probability P(state) of each characteristic state I, II, III or IV, respectively. In the plot of these probabilities over the distance to the wall (fig. 5.14) we see that even in the outer region there are strong variations of the characteristic distribution of turbulence. So, at least for turbulent boundary layer flows, we can state the the characteristic distribution of turbulence is strongly varying and therefore not universal.

On one hand, the shapes of the joint-pdfs (fig. 5.13) do not show significant changes in the outer regions, but on the other hand, the actual ratios of the characteristic structures (fig. 5.14) reveal that the frequency of occurrence for rotational structures (green, blue) is significantly decreasing compared to pure straining structures (red, orange) when we move towards the outer layer of the boundary layer. This indicates that the actual change of the distribution is happening close to the origin of the QR-space where it is visually less obvious and does not change the overall appearance of the *teardrop* - and let this distribution appear more universal then it actually is. Knowing that, on average, the gradient magnitudes of structures become smaller the closer the are to the origin of the QR-space, this supports what we discussed about the ratios of the principal strains. In the logarithmic layer and the outer layer we find an increasing amount of

structures with little (or no) vorticity (fig. 5.6, c and d) which affects the ratio of the principal strains. The coloured dots in figure (fig. 5.13) indicate the ratio that Buxton & Ganapathisubramani (2010) stated for the far-field of a jet flow which leads to a ratio of $(\lambda_1 : \lambda_2 : \lambda_3) = (2.9 : 1 : -3.9)$ for the principal strains. According to the previous explanation the reduced vortical structures in the present TBL support the direction of change of the principal strain ratio to $(\lambda_1 : \lambda_2 : \lambda_3) = (5.5 : 1 : -6.5)$

In general the relatively smooth changes in the higher layers are contrasted by the strong changes in the near-wall region. Especially the unstable/contracting vortical structures (blue) have a relatively strong near-wall peak. As well, the stable node/saddle structures show a strong increase in their frequency of occurrence right at the wall. The reason for these changes will be discussed in the following chapter (6). Here we discuss the effects the varying distribution of characteristic structures have on the enstrophy production.

The average production conditioned with the respective characteristic states is plotted over the wall-normal distance normalized by the unconditioned mean production (fig. 5.15, a). We find that at no point they match the conditional production of the jet results by Buxton & Ganapathisubramani (2010) that are marked as coloured dots in the plot. This is not very surprising as we have already seen in the previous section that the production is composed in a different way in the TBL then it is in the far-field of the jet flow. Accordingly we find a variation of which characteristic structures contribute how much to the local enstrophy production. In the higher regions above $y^+ \gtrsim 32$ the strongest enstrophy producers are vortices with stretching character which supports the idea that enstrophy production is strongly correlated with vortex stretching. The dominance in the relative production of stretching vortices does become even stronger in the far outer region of the TBL. As well in the region above $y^+ \gtrsim 32$ the relative production of the two pure straining structure types, respectively, is roughly half as strong as the relative production of the stretching vortices. Further, the unstable/contracting vortical structure have a negative mean contribution to the enstrophy production above $y^+ \gtrsim 60$. On average these structures destroy enstrophy at the higher layers that potentially indicates a backscatter mechanism in which the kinetic energy is transferred from smaller scales towards larger scales of motion. Whereas all the relative productions are relatively constant in the logarithmic layer of the TBL, the variation becomes stronger in the near-wall region below $y^+ \lesssim 40 - 50$. We find a relative decrease of the relative production of stretching vortices which comes along with a relative increase of the relative production for purely straining, stable node/saddle structures as well as of unstable/contracting vortical structures. The latter even develop a positive contribution in the near-wall region. However, the strongest increase of relative production is accomplished by pure straining, unstable node/saddle structures. They become and stay the most dominant structures (with respect to relative production) below $y^+ \lesssim 32$. Overall we find that in the near-wall region pure straining structures become stronger producers of enstrophy than rotational structures. This indicates that more enstrophy is produced in the shear layers between the densely packed vortices then by the vortices stretching

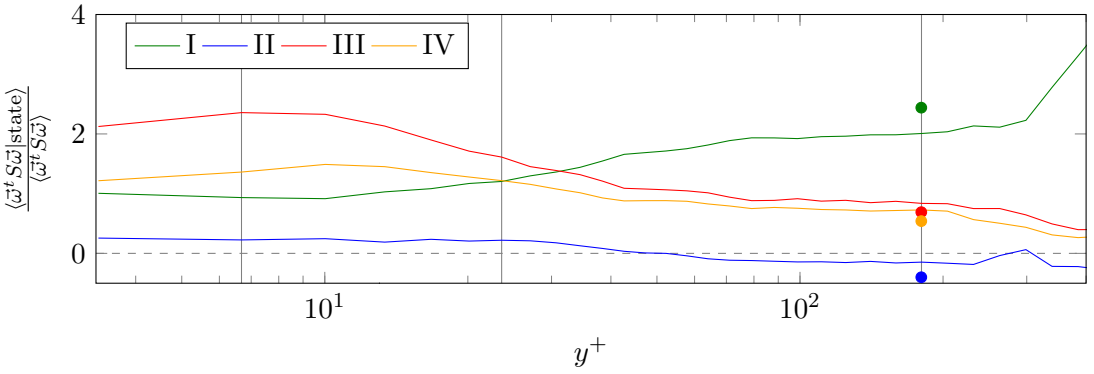

(a) wall-normal development

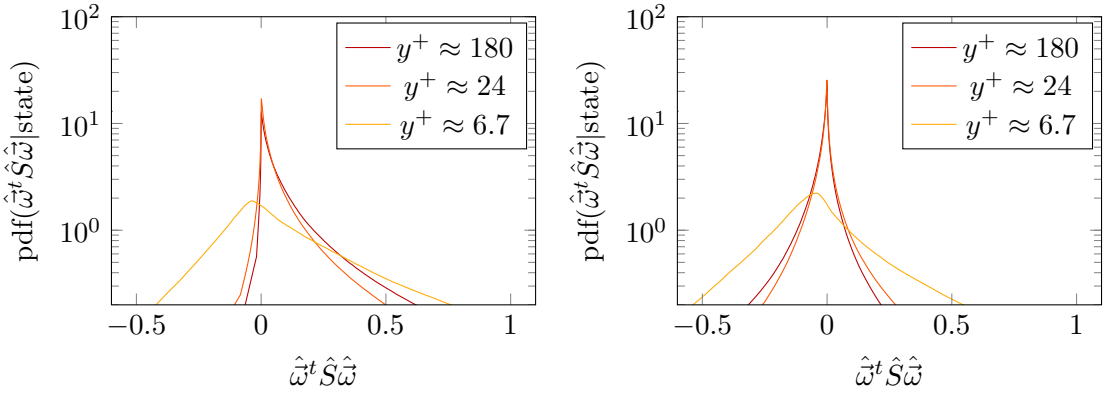

(b) state=I (c) state=II

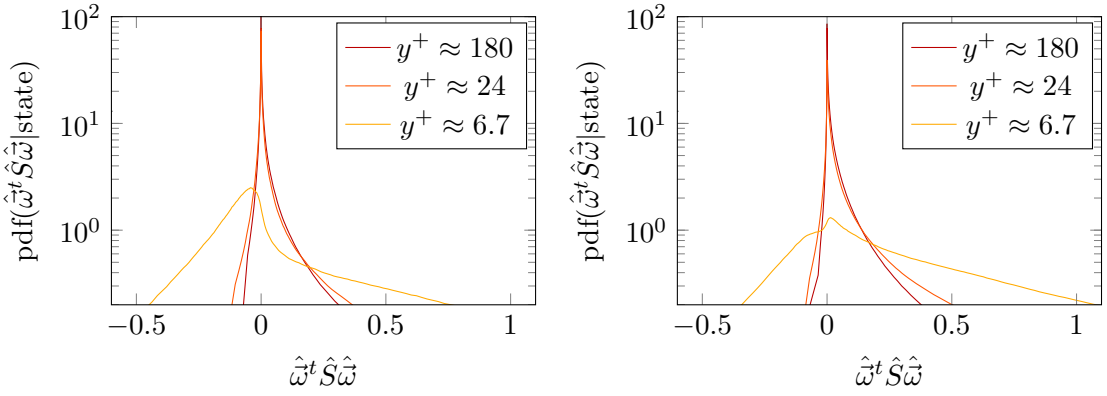

(d) state=IV (e) state=III

Figure 5.15: (a): Conditional average of the relative enstrophy production conditioned with the respective characteristic state plotted over the distance to the wall. The vertical grey lines indicate the locations where samples are taken for a more detailed analysis. The coloured dots mark the respective conditional averages obtained in the far-field of a turbulent jet (Buxton & Ganapathisubramani, 2010). (b-e): Conditional pdfs of the relative enstrophy production conditioned with the respective characteristic state plotted at three different wall-normal locations.

in direction of their axis. This on the other hand supports the previously discussed idea that the strain at the wall mainly acts in the plane normal to the streamwise direction and the stretching of smaller structures by larger structures, as suggested by Leung *et al.* (2012), is suppressed by the wall.

The conditional pdfs at three selected locations (fig. 5.15, b-e) allow more insight in the enstrophy production mechanism. Compared to the unconditional pdfs (fig. 5.3, b) in general for all locations and all characteristic structure types except unstable vortices (II) the negative tails of the pdfs are shortened. For the unstable vortices we find the opposite being true - in this case the positive tails are shortened which results in the low positive or even negative relative production of these structure types. For the selected locations at $y^+ \approx 180$ and $y^+ \approx 24$ the peak of the pdf stays at zero, but the tails vary strongly for the different characteristic types. The stretching vortex topology show the longest tail in positive direction, which supports the idea that the stretching of vortices is likely to coincide with a strong positive enstrophy production. This finally results in the strong dominance of stretching vortices as relative producer of enstrophy in the higher regions. The pdf of the production conditioned with unstable rotational structures is nearly symmetric however, as mentioned before, with a slightly longer tail in the negative direction. This indicates that within this structure type we may find a significant part of structures that destruct enstrophy. This could as well indicate a backscatter mechanism that transfers kinetic energy from small scales of motion towards larger scales of motion. However, still within this structure type, the negative production is balanced by events with a positive production. As we have seen before, this leads to an overall slightly negative production in the higher regions of the boundary layer. The pure straining structures show almost no tails towards the negative side and relatively short tails towards the positive side. This indicates that the majority of events with this structure type shows moderate production rates. For the location $y^+ \approx 6.7$ between the VSL and the buffer layer things do look slightly different. Whereas the enstrophy production pdf conditioned for the stretching vortical structures is nearly unchanged in comparison to the unconditioned pdf, the pdf conditioned for unstable vortical structures develops a nearly symmetric shape. However, unlike at the higher layers we find a slight shift towards the positive production side which leads to the slight positive contribution to the production of these structures. For the pure straining unstable node/saddle structures (III) the peak of the pdf shifts towards zero compared to the unconditional pdfs where it is found being on the negative side. Further, the tail to the negative production side shortens whereas the tail towards the positive side becomes longer. This indicates that we find more extreme events with positive production within this structure type in the near-wall region. This, as well, supports the previously discussed situation at the wall, that the turbulent structures at the wall are densely packed and their strain fields are interacting strongly between each other as well as with the wall. Moreover, for the purely straining stable node/saddle structures (IV) we find the negative tail being unchanged compared to the unconditional pdf, whereas the positive tail recovers its unconditional

length, but shows a dip which leads to lower values of the pdf. This shows that the tendency to positive production is still given, however it seems that it is covered by relatively rare events.

Overall the enstrophy production conditioned with the respective characteristic topologies shows that away from the wall the stretching vortices have the strongest relative production whereas a backscatter mechanism might be covered within the contracting vortical structures. The purely straining structures have a comparably low relative production in the higher layers, but gain strength when approaching the wall. This supports the argument that the dense packing of turbulent structures and their organization at the wall increase the interaction of their strain field with each other as well as with the wall. This feeds the importance of strain regarding the enstrophy production.

The conditional mean development as well as the development of the conditional pdfs of the normalized intermediate strain rate conditioned with the respective characteristic states are plotted in figure (5.16). The mean development shows similar behaviours for all conditions in the entire TBL, except for the far outer layer of the boundary layer where the mean conditioned with the unstable vortical structures increase whereas all others decrease. The mean intermediate strain rate is largest when conditioned with pure straining, unstable node/saddle structures (III) for which it is always positive. However, for the purely straining, stable node/saddle structures (IV) the intermediate strain is always around zero in the mean. For both rotational structure type (I and II) we find the mean intermediate strain rate being approximately half of the mean for characteristic type III in the logarithmic layer. Approaching the wall both are decaying whereas the stable/stretching vortices level out around a zero intermediate strain rate and the unstable/contracting vortices level out around a slightly negative intermediate strain rate below $y^+ \lesssim 10$.

A bit more insight allow the development of the conditional pdfs (5.16, b-e). Overall we find that all structures show a less strict behaviour for the intermediate strain rate in the higher regions and the pdfs are spread. In comparison to this, we find a more defined behaviour in the near-wall region where the pdfs develop relatively strong peaks. This behaviour, in general, agrees with what we have seen in the unconditional pdfs (fig. 5.3). On a closer look the pdf for rotational structures in the outer layer is wider spread and has a significantly lower peak than the pure straining structures. This indicates that vortical structures have more variation in their straining properties whereas the pure straining structures are more defined and show less variation. For structure types I, II and III the pdfs in outer layer are strongly skewed and have their peaks in the positive λ_2-region. Contrasting this the pure straining, stable node/saddle structures (IV) are less skewed and find their peak within the negative λ_2-region. An interpretation of this is yet unclear and it remains just a statement. Approaching the wall all pdfs become less skewed and their peaks move towards zero. However, for structure types I and III the peaks remain shifted slightly towards a positive production. The unstable vortical structures (II) have a peak centered around zero but show a slightly longer tail towards

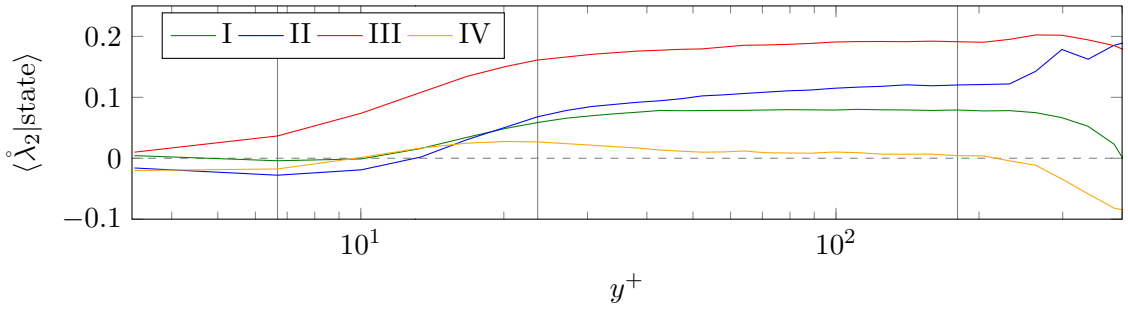

(a) wall-normal development

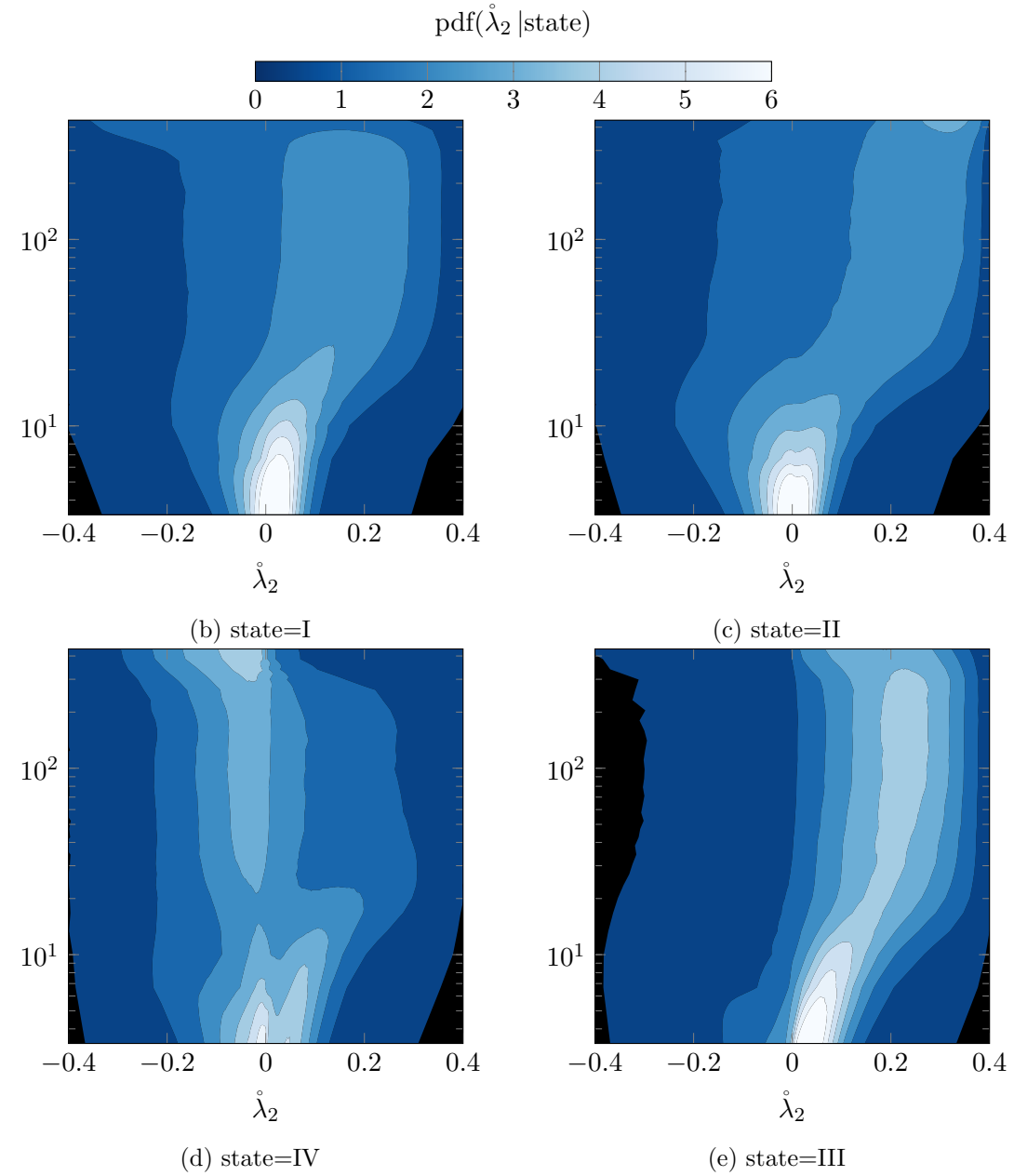

(b) state=I

(c) state=II

(d) state=IV

(e) state=III

Figure 5.16: (a): Conditional averages of the normalized intermediate strain conditioned with the respective characteristic state plotted over the wall-normal location. The vertical grey lines indicate the locations where samples are taken for a more detailed analysis. (b-e): Conditional pdfs of the normalized intermediate strain conditioned with the respective characteristic state plotted for each wall-normal location in one contour plot.

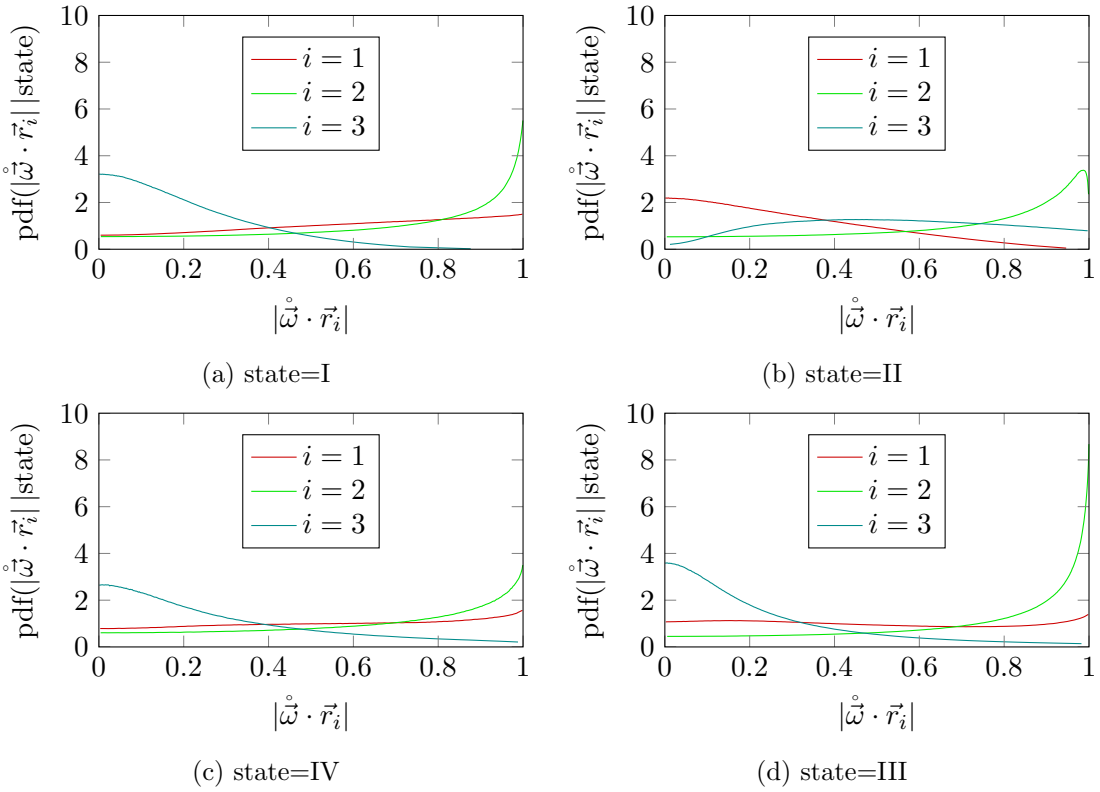

(a) state=I

(b) state=II

(c) state=IV

(d) state=III

Figure 5.17: Conditional pdfs of the alignment between the vorticity vector and the principal strain directions conditioned with the respective characteristic state at a wall-normal location of about $y^+ \approx 180$.

a negative production. The purely straining, stable node/saddle structures develop two peaks in the near-wall region. It is yet unclear how this has to be interpreted, although we believe that the two peaks are caused by high-speed and low-speed events in the TBL that reach down to the wall, respectively. This would suit to what we have discussed in the previous section about the coupling of the velocity gradient magnitude and the intermediate strain rate in the near-wall region (fig. 5.6, b). A high-speed event causes high gradients in the near-wall region and structures are pressed towards the wall such that a strongly straining foot of the structures is developed at the wall. As the joint-pdf of $\|\hat{A}\|_F^2$ and $\mathring{\lambda}_2$ shows, such strong gradients at the wall are likely to develop a positive intermediate strain rate. These structures form the positive branch in the pdf conditioned with characteristic structure type III in figure (5.16, d). The negative branch in the near-wall region represents the low-speed events, that result in relatively low gradients at the wall. On the other hand, these have the tendency to develop a negative intermediate strain rate at the wall as stated by figure (5.6, b). The fact that the positive branch of $\mathring{\lambda}_2$ ends quickly when leaving the wall could be explained by the structures developing a rotational character and leaving characteristic state III much quicker during high-speed events than during low-speed events. However, this cannot be further supported at this stage and therefore remains a hypothesis within the present work.

The remaining piece of the weighting term in the conditioned enstrophy production is the conditioned alignment between vorticity vector and the principal strain directions. The results we found for $y^+ \approx 180$ are shown in figure (5.17). The distributions of the alignments conditioned with the four characteristic states respectively agree qualitatively with the results for the alignment in the far-field of a turbulent jet (Buxton & Ganapathisubramani, 2010). The alignment of the extensive strain looses its overall arbitrary alignment with the vorticity vector. For stable vortices (I) we find both vectors developing a slight tendency to align parallel. Same holds for the stable node/saddle structures (IV). Whereas the unstable node/saddle structures (III) still show an arbitrary alignment of $\vec{\omega}$ and $\vec{r}_1$, we find a relatively strong perpendicular alignment of both for unstable vortical structures (II). The tendency of vorticity and intermediate strain direction to align parallel is given for all structure types. However, the strength of this tendency does vary sightly between the different states. It is more pronounced for state I and III than it is for state II and IV. Moreover, for the unstable contracting vortices we find that the probability is high for both vectors to align nearly parallel, but the pdf drops just before a perfect alignment where $|\mathring{\vec{\omega}} \cdot \vec{r}_2| = 1$. Although, Buxton & Ganapathisubramani (2010) see a level off for the same distribution for nearly parallel alignment, they do not see a drop of the pdf towards a perfect alignment. The pdf of alignment of vorticity with the compressive strain direction shows little variation between the unconditioned and conditioned data for state I, III and IV respectively. For stable vortices we find that the already low value of the distribution for values close to one is decreasing to zero, stating that there are no events where the vorticity vector is parallel to the compressive strain. A similar development can be stated for state III. On the other hand, the unstable/compressing vortices show the strongest change of the distribution of the alignment of vorticity with the compressive strain direction. Here the likely perpendicular alignment that we find for all the other structure types as well as in the unconditioned distribution is not found at all. The pdf approaches zero for $|\mathring{\vec{\omega}} \cdot \vec{r}_3| \to 0$. The pdf for all other values is increased more or less evenly.

The effect of conditioning the alignments with the characteristic states in the buffer layer at $y^+ \approx 24$ is shown in figure (5.18). The trends are similar to what was found for the conditioning at $y^+ \approx 180$, but the unconditioned alignment shows already differences between both wall-normal locations (fig. 5.8). These difference will therefore affect the conditioned averages as well. The tendency to a perpendicular alignment between $\vec{\omega}$ and $\vec{r}_1$ is given in the unconditioned case. This is amplified for characteristic structure type II but it is reduced for the remaining structure types. The tendency of the vorticity vector to align with the intermediate strain direction is strongly increased comparing the unconditioned alignment of $y^+ \approx 24$ to the one of $y^+ \approx 180$. This strong alignment does not show significant changes under the different conditions. It appears to be more likely in the flow at $y^+ \approx 24$ to the one of $y^+ \approx 180$ that vorticity is perpendicular on the extensive strain direction. This as well reflects in the conditioned pdfs of the alignment at $y^+ \approx 24$. Whereas the tendency to align perpendicular is further increased for the

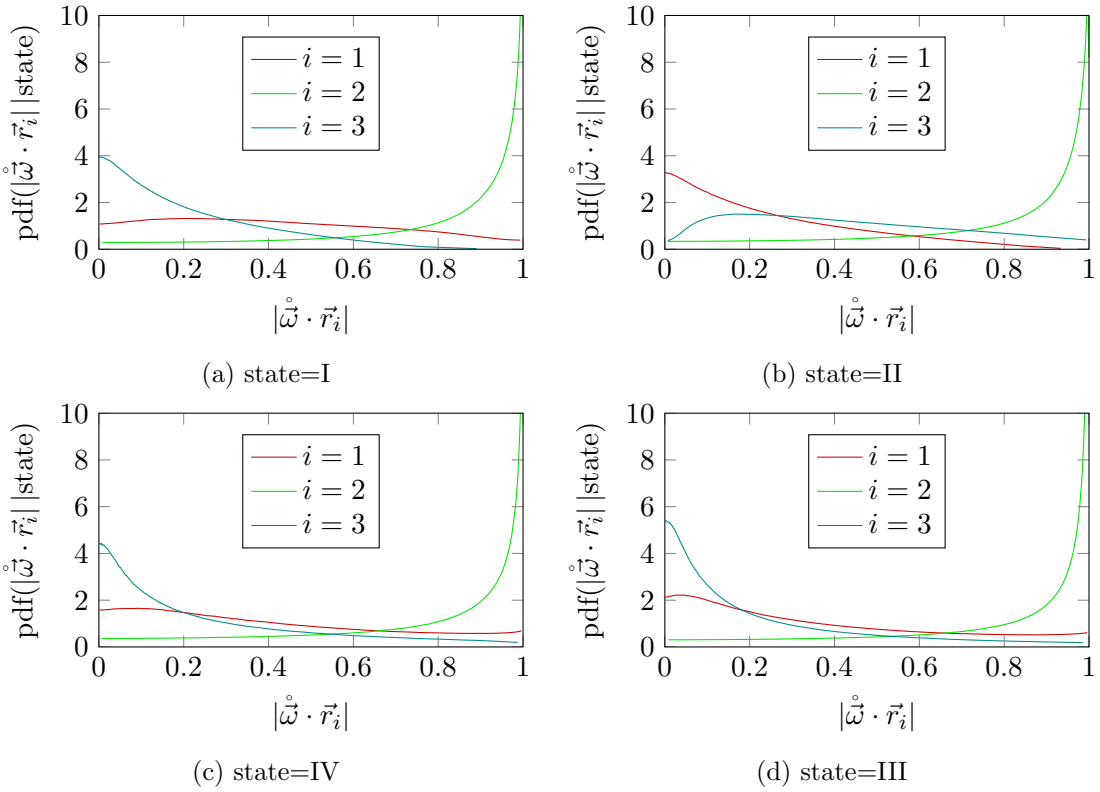

(a) state=I

(b) state=II

(c) state=IV

(d) state=III

Figure 5.18: Conditional pdfs of the alignment between the vorticity vector and the principal strain directions conditioned with the respective characteristic state at a wall-normal location of about $y^+ \approx 24$.

states I, III and IV, we find a decrease of the pdf value for $|\mathring{\vec{\omega}} \cdot \vec{r}_3| \to 0$. This means it is likely for the vorticity vector to be aligned with the compressive strain at a reasonably high angle, however, it is unlikely that both vectors are perpendicular to each other.
Results for the conditional alignment of the vorticity vector with the principal strain directions between the viscous sublayer and the buffer layer are shown in figure (5.19). The unconditional alignments (fig. 5.8) for this location already show extreme situations. The vorticity vector is almost always fully parallel (or nearly parallel) aligned with the intermediate strain direction. Resulting from this we find vorticity nearly perpendicular to the other strain directions most of the time. Conditioning these alignments with the respective characteristic states show no obvious changes in the strong parallel alignment between vorticity and the intermediate strain direction. The full perpendicular alignment of vorticity with the extensive strain direction becomes slightly less likely for the state I, III and IV , but therefore the probability of a nearly perpendicular alignment increase. This leads to a peak of the pdf, not at, but close to zero. For state II the full perpendicular alignment of vorticity with the extensive strain direction becomes even stronger. On the other hand the pdfs of the alignment between vorticity and the compressive strain direction behave the exact opposite way. The probability of a perpendicular alignment is increased for state I, III and IV whereas the pdf conditioned with state II has its peak close to zero, but it decreases at zero.

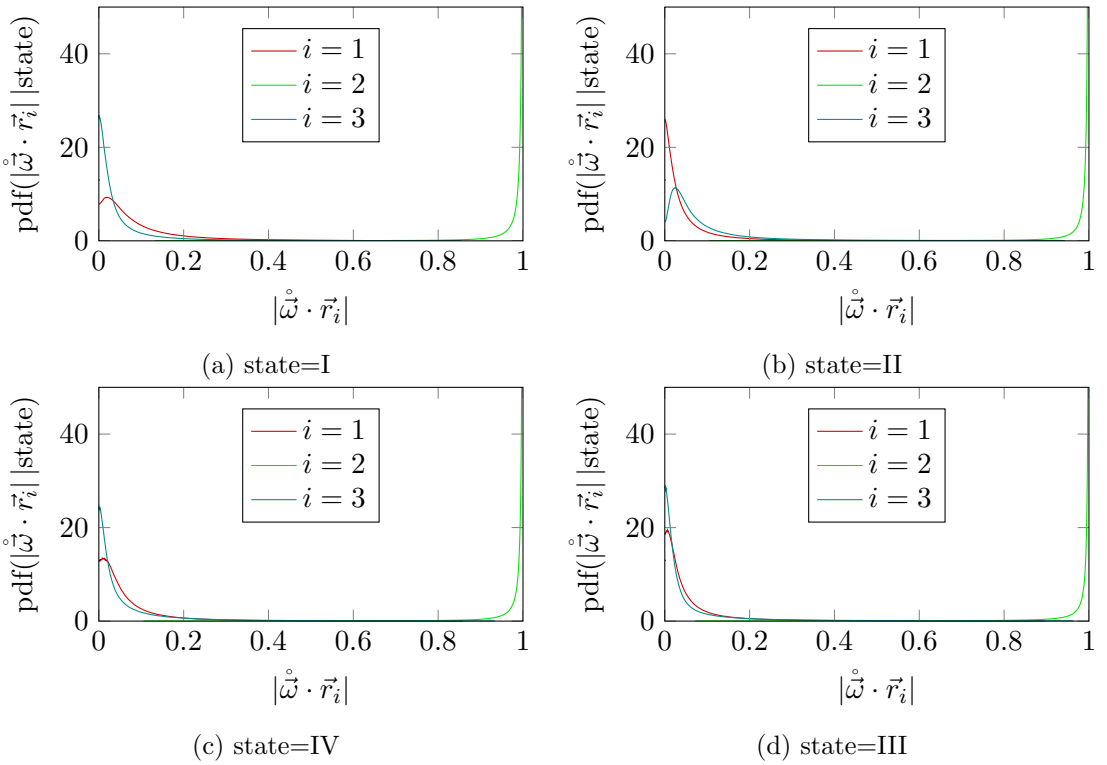

(a) state=I (b) state=II

(c) state=IV (d) state=III

Figure 5.19: Conditional pdfs of the alignment between the vorticity vector and the principal strain directions conditioned with the respective characteristic state at a wall-normal location of about $y^+ \approx 6.7$.

Figure (5.20) summarizes what we have seen and discussed in detail on the previous plots of the alignment-pdfs. The overall development of the unconditioned alignments in wall-normal direction is recovered in the alignments conditioned with the respective characteristic states. We find slight variations in the outer layer of the TBL, but the alignment of vorticity with the different principal strain directions shows almost no variation in the logarithmic layer. When approaching the wall the alignments show strong changes in the way that the vorticity tends to align parallel with the intermediate strain direction and perpendicular with the extensive direction as well as with the compressive direction. This holds for each characteristic state separately as well as in the overall development as discussed in the previous section. The significant difference between the states, however, is that the distributions overall change. Whereas for stable vortices (I) and the pure straining structures (III) and (IV) the alignments are varying slightly compared to the unconditioned alignments, this is different for the unstable vortices (II). For this structure type we find that the alignments of extensive strain and compressive strain are exchanged compared to the other three states. This agrees as well with the results of the far-field of a turbulent jet (Buxton & Ganapathisubramani, 2010). This exchange leads to a higher weight on the compressive strain then we find it for states (I), (III) and (IV). Eventually this leads to a negative enstrophy production for unstable/contracting vortices which might even indicate a backscatter mechanism where kinetic energy is transferred from small scales to large scales of motion. All this seems

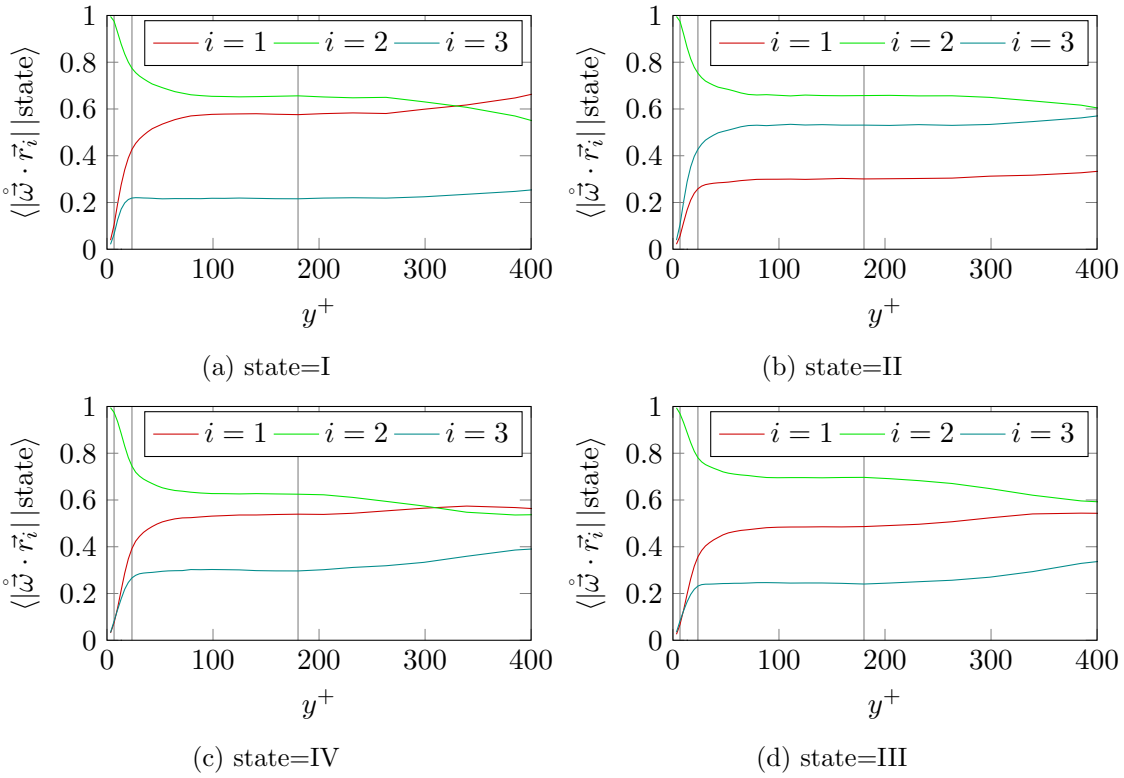

(a) state=I

(b) state=II

(c) state=IV

(d) state=III

Figure 5.20: Conditional averages of the alignment between the vorticity vector and the principal strain directions conditioned with the respective characteristic state plotted over the wall-normal direction.

to hold all the way to the wall, however, the effects that the wall has on the alignment are superimposed and become stronger with decreasing distance to the wall. Eventually the effects of the wall will be strong enough that the exchanged alignment for the different states fades into the background. Just like we scaled the two parts of *vortex stretch model*, introduced by Ashurst *et al.* (1987), with the correlations imposed by the wall to obtain the actual ratio of principal strain rates, it might be well possible to do so in an analogue way with the alignments. The alignments need to be decomposed into a stretching/contracting part and a shearing part. The stretching part might then be independent of the location, but dependent on the characteristic state. Contrasting this, the shearing part can be constructed to be dependent on the correlations that are directed by the flow topologies. However, this remains part of the future work and will not be discussed further at this stage.

5.5 Conclusions

In the light of energy transfer across different scales of motion a turbulent boundary layer at a reasonably high Reynolds number was analysed according to the detailed composition of the enstrophy production. The variation of the overall production as well as

its single parts in wall-normal direction were analysed. This analysis was carried out on the unconditioned turbulence as well as on the turbulence split into flow topologies with specific properties by a characteristic decomposition.

As a first result we found that the probability density function of the enstrophy production has a self-similar shape that scales with the variance $\mathrm{var}(A)^{\frac{3}{2}}$ of the velocity gradient A in the boundary layer above $y^+ \gtrsim 24$. However, the composition of the enstrophy production is changing in this region. Compared to literature of HIT, weak shear layers , etc. (e.g Ashurst *et al.*, 1987; Ganapathisubramani *et al.*, 2008) the ratio of the principal strain, a key property for enstrophy production, becomes more extreme in a sense that the intermediate strain rate reduces its relative contribution. According to Ashurst *et al.* (1987); Hamlington *et al.* (2008); Leung *et al.* (2012) this principal strain is affiliated with the vortex stretching mechanism. Further, in agreement with literature (Ganapathisubramani *et al.*, 2008) we found that for low rotation rate magnitudes the frequency of occurrence for small, or even negative, values of the relative intermediate strain component increases. Our results show that the flow has an increased number of events of low rotation magnitude as well a a decreasing frequency of occurrence of rotational structures towards higher layers. We concluded that this is the reason for the changed principal strain ratios in the region above $y^+ \gtrsim 24$.

The wall has a strong effect on the enstrophy production. Not only the increase strain rate magnitude and rotation rate magnitude scale up the production, as well its composition changes its properties. The probability density function shows a wide spread that does not scale with the velocity gradient variance anymore and indicated the occurrence of relatively extreme production and destruction events. The wall correlates the strain rate magnitude and the rotation rate magnitude. Further it orders turbulence, if we judge from the visual impressions and the principal strain composition. The mean intermediate strain tends to zero and its fluctuations become smaller in the near-wall region. Further, we find streamwise elongated and ordered structures. The vortex stretch models by Ashurst *et al.* (1987) was applied and modified by introducing a weighting ratio of the stretching strain and the shearing strain of the vortical structures. It is believed, but could not be clearly shown, that the correlation of strain rate magnitude and rotation magnitude is coupled with this weighting ratio. Nevertheless, the shearing strain of the near-wall structure becomes the dominant strain of the streamwise elongated structures. This leads to strong strain field of turbulence that is dominant in the plane normal to the streamwise direction. At the same time we see that the straining structures develop to the characteristic structures with the largest relative enstrophy production whereas in the higher layers as well as in literature about the far-field of a jet (Buxton & Ganapathisubramani, 2010) these dominant structures are stretching vortices. This as well supports that the vortex stretching mechanism loses on strength relative to the shearing between the densely packed vortices at the wall. The alignment vorticity with the principal strain directions becomes extreme at the wall. On one hand, this is believed to result from the parallel alignment of the vorticity with the strong

vortex-own strain field as shown for different flows by Ashurst *et al.* (1987); Hamlington *et al.* (2008); Leung *et al.* (2012). But on the other hand, the fact that the vortices are ordered and orientated similarly results in the tendency of their strain fields to coincide. In turn, this implies that a certain alignment of vorticity with the vortex own strain field tends to coincide with a similar alignment of vorticity with the strain field of the neighbouring vortices. This *double* alignment results in the extreme behaviours that occurs close to the wall. We find a strong tendency for full parallel alignment of vorticity with the intermediate strain direction and as well as strong tendency of vorticity to align perpendicular with both remaining strain directions. Due to the streamwise elongated vortices we now know that the weak intermediate strain direction is align parallel with the streamwise direction and the strong extensive and compressive strain directions are perpendicular to the streamwise direction. This finally completes the picture enstrophy production at the wall that is dominated by the 2d strain plane which is normal to the streamwise direction. This wall-forced 2d ordered turbulence becomes a very unstable mechanism due to the loss of one degree of freedom. This as well caused extreme events when structures break out of this arrangement.

Investigations of the characteristic decomposition reveal the the joint probability distribution function of Q and R, often referred to as QR-plot, is not universal. From the QR-plots themselves and from the ratios of the characteristic structure types, obtain by integrating the QR-plot over the respective regions, we find strong changes of the distribution in the near-wall region. These strong changes at the wall are contrasted by graduate but steady changes in the higher layers of the boundary layer. As this is not in the focus of this chapter we just want to state the most interesting features of the development of the characteristic development of turbulence in the TBL. In the near-wall region we find a strong peak in the frequency of occurrence of unstable vortices. In the logarithmic layer as well as in the outer region we find a steady decay of the frequency of occurrence associated with rotational structures.

In terms of enstrophy production conditioned with the respective characteristic states our results in the logarithmic layer agree widely with the results of the far-field of a turbulent jet (Buxton & Ganapathisubramani, 2010). However, the superimposed effects of the wall become dominant below a certain distance to the wall. Before the strong dominance of the wall is present the mean enstrophy production for unstable/contracting vortices is negative and the respective conditional probability density function develops a significant tail in the negative production. Further, we found that the alignment of vorticity with the compressive strain direction, that is associated to the negative principal strain, conditioned with unstable vortices is at a much lower angle that for all other structures types. These results explain the negative mean production for this structure type and suggest the presence of a back scatter mechanism within this characteristic structure type.

In general we suggest that models for the enstrophy production should be composed by three parts. The first two parts are described by Ashurst *et al.* (1987)'s *vortex stretch*

model and cover the stretching mechanism of turbulent structures and the shearing around vortices respectively. We found that this model requires a modification that allows changes of the weighting of the first to parts to the overall result. This weighting is likely to be coupled with the correlation of the strain rate magnitude and the rotation rate magnitude.

Chapter 6

Characterisation of Turbulence in a Flat-Plate Zero Pressure-Gradient Turbulent Boundary Layer

Turbulence has a complex character with many different facets, there are countless different point of views to study its varieties. For over a century scientists have been engaged with improving our understanding of turbulent flows. Great achievements were already made in the past, some of which are outlined in the introduction of this work (1.2), but the general understanding is in many regards still unsatisfactory. A global picture of turbulence describing the cornerstones of the involved mechanisms is still missing. For this reason turbulence models, e.g. those used in LES or RANS, do often have strong limitations. This leads to a variety of specialized turbulence models that are capable of describing the respective flow topology in an appropriate way, but fail for other flow topologies. We do not aim to present a turbulence model in this chapter, nor will the validity of existing models be discussed. The goal of this chapter is to present an overview of turbulence in a turbulent boundary layer flow. Within this overview we want to outline quantities and mechanisms that are crucial for the dynamics in this flow. We will discuss in detail how the energy is distributed spatially as well as across the scales of motion. This overview and discussion in conjunction with the data form a framework for validating models of turbulent boundary layers. Further, the detailed analysis presented can be applied to more complex flow topologies to pinpoint differences and universalities in the turbulent dynamics between flows.

An important role in this discussion play the mechanisms that govern the distribution of energy. The main concern of this work is the turbulent motion which is described by the momentum equations. However, the magnitude of this motion can be describe

by the kinetic energy equation and for many points of this overview it is sufficient to reduce the discussion to the magnitudes of the individual quantities only. Therefore the energy, its redistribution as well as its production and dissipation are studied in detail and from different perspectives.
A wall-bounded flow was picked in the light of the importance for applications. Almost every flow in engineering involves walls and boundary layers form on these. Many of these flows are at high enough Reynolds numbers to develop turbulence in the boundary layer. We choose the relatively simple flow of a compressible flat plate zero pressure-gradient boundary layer to eliminate effects of roughnesses and/or mean pressure gradients, etc. on the turbulence. The here developed fundamental picture of wall-bounded turbulence is hoped to be transferable to more complex flows in the future. Further, the techniques developed in this work will be applied to investigate more complex flows in the future.
Besides Reynolds averaging the current investigations involve the separation of scale by spatially filtering the DNS data. The filter widths used as well as the resulting turbulent properties are outlined in the following section (6.1). In section (6.2) the importance of the different quantities of the flow will be discussed considering the mean energy budgets. For this purpose the energy equation is split into a large scale contribution and a small scale contribution (2.7). Section (6.3) outlines the characteristic decomposition of turbulence which is extensively used in the following section. The structural composition of the turbulent boundary layer is discussed in section (6.4). In that section it is described which flow structures compose a TBL, what their properties are and how they are varying within the flow. Two distinct states of the turbulent flow are shown and merged into the characteristic decomposition for the following: 1) The role of pressure is discussed in section (6.5). Although in the energy budgets pressure appears to be not very dominant, it has a truly dominant role in wall turbulence and it is believed that is is a key quantity for turbulence in general. 2) Section (6.6) discusses dissipation and covers which type of structures dissipate the kinetic energy and how this is varying in the flow and across the scales of motion. 3) The turbulence production is discussed in section (6.7). As representative for the cascading process the production is used to reveal a pseudo backward cascade for a large-scale-small-scale-coupling based on the Favre average as filter operator. On the other hand, for the spatial filtering a distinct real backward cascading process is presented. In section (6.8) the conclusions about the character of turbulence in this turbulent boundary layer are made.

6.1 Location Specification and Filter Characterization

The flow that is used for the investigation is outlined in section (3.3). The data for this chapter is taken in the streamwise range of $Re_\theta \approx 1224 - 1248$ ($Re_\tau \approx 481 - 491$) and the volume is short enough that statistical homogeneity is assumed over its streamwise extent. To avoid confusion about the notation for filtering and averaging we define the

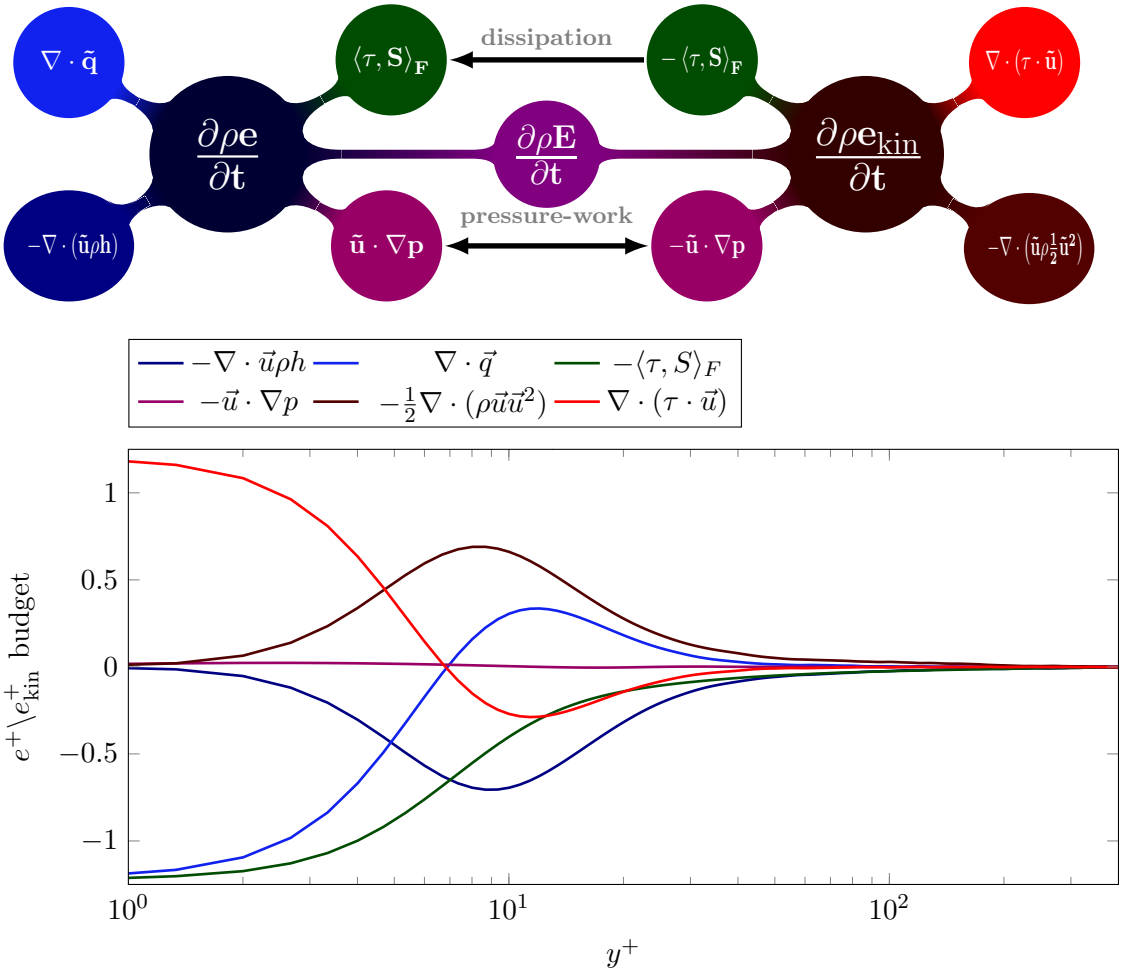

Figure 6.1: Internal and kinetic energy budgets. The image at the top illustrates the governing equations and the plot at the bottom shows the Reynolds averaged terms that govern the energy.

following convention: $\bar{\bullet}$ and $\tilde{\bullet}$ indicate filter operations and Favre filter operations with the filter operator that is specified at the time, respectively. On top of that, all plotted quantities are averaged in time if not specified differently. I.e. a plot labelled as u shows the mean velocity. Also, $\bar{\rho}\frac{1}{2}\tilde{u}\tilde{u}$ denotes the streamwise mean energy component, if the filter operator was specified as Favre operator, but can as well denote the time averaged streamwise large scale energy component if the filter operator is specified as spatial filter. It will get more clear in the following.

A first glance at the mean energy budget that is dissected later in this chapter is shown in figure (6.1). At the top of the figure the schematic description of the equations is outlined and at the bottom of the figure the time averaged terms of these equations are plotted over the wall-normal direction. The same colours are used to draw the links more intuitively. The shades of blue show terms involved in the internal energy budget only, the shades of red show terms involved in the kinetic energy budget only. The

shades of purple coloured terms represent energy transfer due to pressure work and the shades of green coloured terms represent energy transfer due to viscous effects. The first impression of the plot is its nearly symmetric character with respect to the y^+ axis. This indicates that, at least on average, the budgets of both equations are driven by similar mechanisms. At this stage it should be emphasized that the wall temperature is the adiabatic temperature of the freestream. The freestream Mach number is $M_\infty = 0.5$ and therefore the wall is about 5% hotter than the freestream. On the other hand the kinetic energy of the freestream is higher than at the wall, where it is zero. The opposite behaviour of the profiles indicate that in the same way the fluid flow is driven by the freestream flow and the wall, the heat flow is driven by the temperature difference of freestream and wall. It is believed that the valley and peak of the transport terms $-\nabla \cdot (\vec{u}\rho h)$ and $-\nabla \cdot \left(\vec{u}\rho\frac{1}{2}\vec{u}^2\right)$ shown at about $y^+ \approx 9$ respectively are a cooling and an acceleration due to mixing with a laminar freestream. This result will be discussed in more detail in large scale small scale split form. The kinetic energy diffusion $\nabla \cdot (\tau \cdot \vec{u})$ is redistributing kinetic energy due to viscous forces. E.g. the surrounding of a vortex is accelerated by the vortex' rotation due to friction. The same viscous forces are acting at the wall and kinetic energy from the flow is diffused towards the wall. The kinetic energy dissipates into internal energy - a process which is particularly active in the near wall region. The internal energy peaking at the wall is then again diffused into the flow via temperature diffusion $\nabla \cdot \vec{q}$.

This whole process is now split up into contributions of different scales of motion and afterwards further into contribution of different flow structures and flow states. But firstly the filtering operation needs to be outlined. Besides ordinary Favre averaging a spatial filter as described in section (3.2.1) is used. The filter width of the operator cannot be kept constant due to the presence of the wall. However, it was chosen to

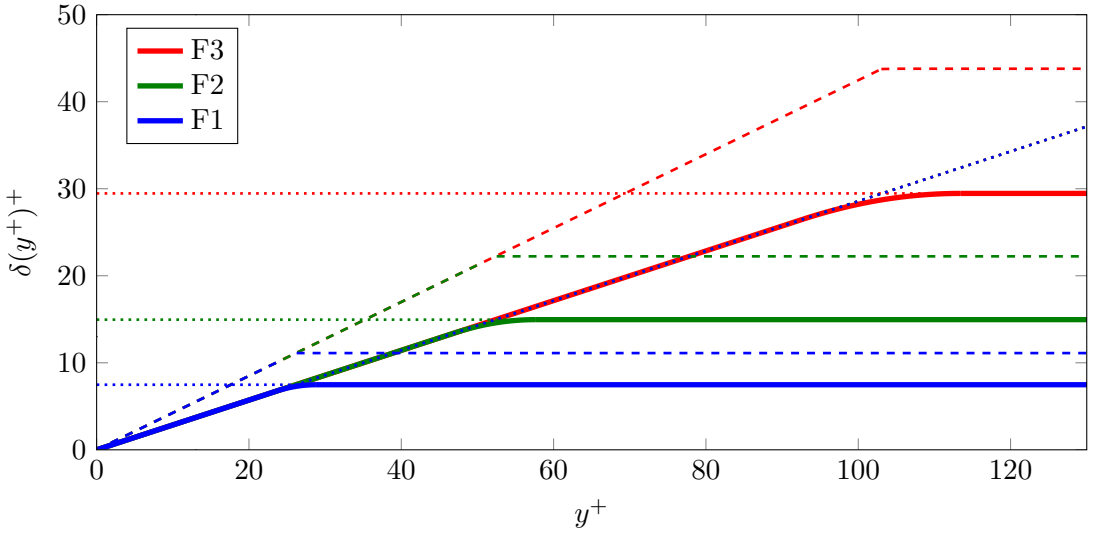

Figure 6.2: Filter widths for the different filters as continuous lines. Dashed lines show the needed halo area width and the dotted lines indicate the filter ramps as well as the freestream filter values.

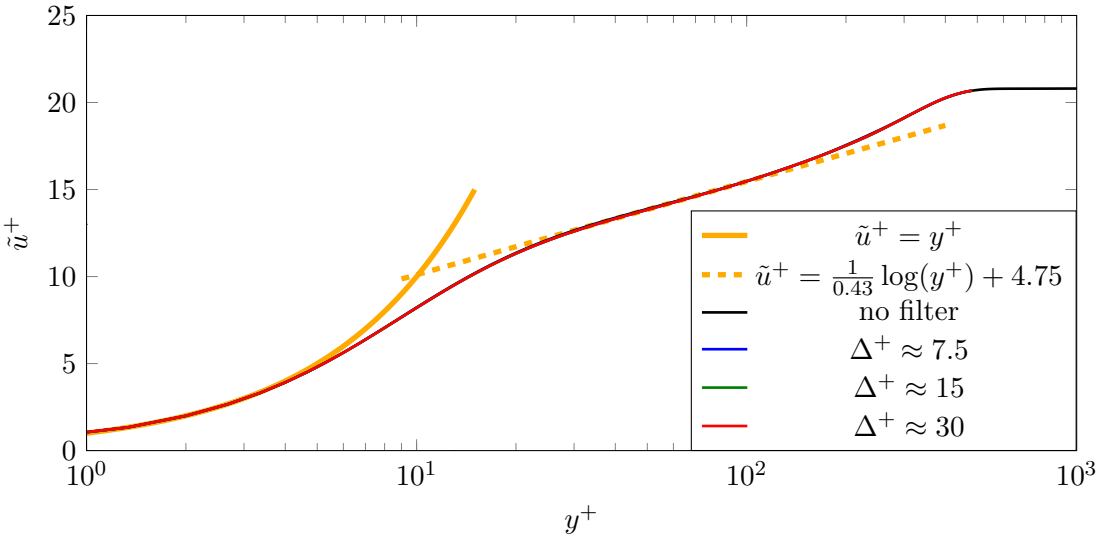

Figure 6.3: Mean streamwise velocity. Raw DNS data is plotted against filtered DNS data for three different filter widths.

have a constant filter width above a certain distance off the wall. Further, the accuracy of the filtered value was decided to be at least 10^{-4} which lead to a choice of $s = 3.5$ for the filter integral parameter (3.10). The actual filter width $\delta(y)$ is then defined by the freestream filter width Δ, the radius of filter halos (defined by $\frac{s\delta(y)}{\sqrt{8\ln(2)}}$) and the distance to the wall. The actual filter width and the needed halo width (dashed lines) are shown in figure (6.2). The filter width function is constant away from the wall and ramps down to zero at the wall. Both pieces (dotted lines) are concatenated via a fourth order polynomial to obtain a one time continuously differentiable filter kernel (continuous line). This is needed to allow continuous derivatives of filtered quantities across the whole domain. However, second order derivatives of filtered quantities will not be smooth at the intersection of constant and ramped filter width. Fortunately, this is only a post-processing issue and just affects the second order derivatives in a local area.

Three different filter widths are chosen for the purpose of this work, which will be referred to as F1, F2 and F3. $\Delta^+ \approx 7.5$ (F1) is the smallest filter width and the width in the freestream is comparable with the thickness of the viscous sublayer. $\Delta^+ \approx 15$ (F2) is the intermediate filter width and its freestream size is comparable with the distance of the wall half into the buffer layer. The largest filter width is $\Delta^+ \approx 30$ (F3). Applying the filter on the DNS data lead to almost no effect on the mean streamwise velocity profile (fig. 6.3). For this plot and for the following we introduce a wall-scaling based on the friction velocity $u_\tau = \sqrt{\frac{\mu_{\text{wall}}}{Re\,\rho_{\text{wall}}}\frac{\partial\tilde{u}}{\partial y}}$ at the particular streamwise location. For the a length l this means $l^+ = l\frac{Re\,\rho_{\text{wall}}u_\tau}{\mu_{\text{wall}}}$ whereas velocities v scale as $v^+ = \frac{v}{u_\tau}$. Energies and velocity products g are scaled as $g^+ = g\frac{1}{u_\tau^2}$ and the terms b of the energy budget are scaled with a density weighted scaling as $b^+ = b\frac{T}{Re\,\rho^2 u_\tau^4}$.

The effects of the filter become obvious considering Favre stresses and kinetic energy spectra. The Favre stresses are plotted in the top part figure (6.4). The plot shows the unfiltered stresses as well as the stresses after filtering the flow field width the three different spatial filter operators. The largest filter effects are found starting from the buffer layer and lasting until the beginning of the outer layer. Close to the wall the filter effects vanish as the filter widths are ramped down to zero. Further, the results of all filters match up to a certain distance from the wall which is another direct result of the ramping of the filter widths. In the log-layer then all filter operators lead to different results. As expected, the filter operator with the smallest filter width has the smallest effect, whereas the F3 filter with the largest filter width has the strongest effect. Moreover, all filters have a stronger absolute effect on the normal stresses $-\sigma_{ii}$ than on the shear stress $-\sigma_{12}$. However, the relative effects on $-\sigma_{11}$ and $-\sigma_{12}$ are equally smaller than the ones on $-\sigma_{22}$ and $-\sigma_{33}$. This is a first indication that$-\sigma_{11}$ and $-\sigma_{12}$ are more large-scale-driven than $-\sigma_{22}$ and $-\sigma_{33}$. The lower part of figure (6.4) shows the scale-wise effect of the filter on the flow field. The spanwise energy spectrum of the spanwise velocity component is shown comparing the unfiltered energy to the energy of the filtered flow field at the different wall-normal locations. The location where the spectra are taken are marked in the plot of the Favre stresses by vertical grey lines. Here as well, the identity of all filter operators is obvious in the near wall region. Further, it can be seen that the filter operators have a relatively small effect on small wave numbers and a steady and smoothly increasing effect towards higher wave numbers. This reflects the character of the Gaussian filter kernel which was chosen for the spatial filter operators.

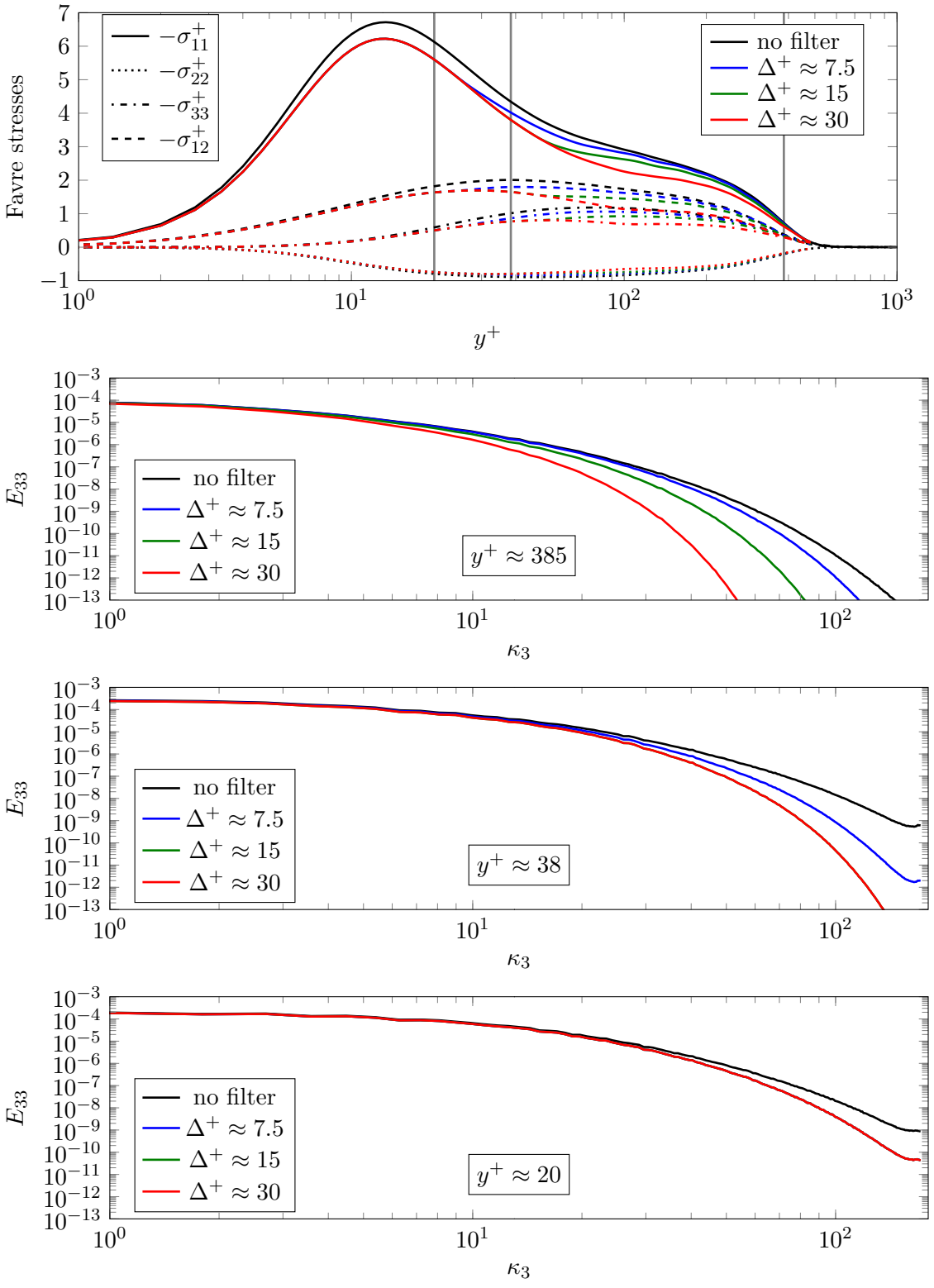

Figure 6.4: Favre stresses and kinetic energy spectra. The plot at the top shows the Favre stresses of the raw DNS data as well as the Favre stresses for the filtered DNS data. The three vertical, grey lines mark the locations where the spectra are taken. The plots below show the spanwise spectra of the spanwise kinetic energy for the same data at three different wall normal locations.

6.2 Mean Energy Budget

In this section the energy budget (fig. 6.1) is split into large-scale and small-scale contributions as explained in detail in section (2.2.2). Besides the three spatial filters that were introduced in the previous section, the Favre averaging is used as temporal filter operator. For two reasons this section is important. Firstly, the split energy budgets highlight the importance of the respective scales for the global energy distribution mechanisms introduced in the previous section. From this point of view it is an introduction to the following characteristic decomposition where certain mechanisms are discussed in detail. Secondly, this section highlights the importance of the respective terms for the flow in the inner region as well as for the outer layer. Further, accurate and detailed data for a compressible turbulent boundary layer flow is provided. This combination constitutes a basis to validate turbulence models for such kind of wall-bounded flows. For this reason it is planned to create a database to make this data publicly available when the results in this chapter are published.

6.2.1 Energy Splitting Based on Favre Averaging

Firstly, the energy budget (fig. 6.1) is split by applying the filter operator defined by the Favre averaging. The Favre averaging is a temporal averaging over an infinite time period. Therefore the filter operator defines the temporal mean of a quantity over this period as large scales part of the quantity, the difference between the unfiltered quantity and the small scale part. Spatially this temporal filter is not distinguishing between different scales and therefore the filter categorizes all spatial structures due to their behaviour in time. This description of the split energy is identical to the one described by the Reynolds averaged Navier-Stokes equations (RANS). Therefore this section, implicitly, is a discussion of what a turbulence model for RANS has to include to capture the correct energy distribution in this turbulent boundary layer flow. The direct influence of the respective terms on the energy distribution over the three different energy types as well as in space is discussed.
Figure (6.6, top) is the visual description of the plots in figures (6.6, bottom) and (6.7). Shades of blue indicate the redistribution terms for the internal energy. Shades of red indicate redistribution terms for the kinetic energy of the mean flow field which is referred to as large scale kinetic energy. Shades of orange indicate the redistribution terms for the averaged kinetic energy of the velocity fluctuations which is referred to as small scale kinetic energy. The remaining terms transfer energy between the different types of energy and are marked with arrows to show the transfer of energy. A detailed description of this form of the energy equations can be found in section (2.2.2). The plots of the respective terms are shown in figure (6.6, bottom) for a section of the outer layer and in figure (6.7) over a logarithmic axis to pronounce the behaviour in the inner layer. We start with the budget for the kinetic energy of the mean velocity e_f. It can be

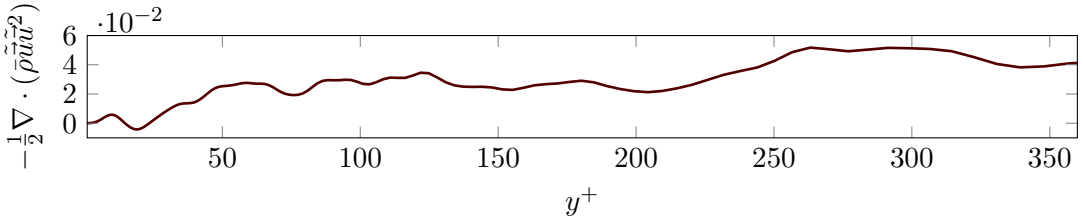

Figure 6.5: Mean transport of kinetic energy.

seen that for the case of mean convection the effect of the overall mean transport of the kinetic energy $\frac{1}{2}\nabla \cdot \left(\rho\vec{u}\vec{u}^2\right)$ (dark red, dashed) is nearly perfectly matched by the turbulent mean diffusion $\nabla \cdot \left(\sigma \cdot \tilde{\vec{u}}\right)$ (pink) in the inner layer. The turbulent mean diffusion, which is a term that couples large scales with small scales, acts as source in the near-wall region and as a sink away from the wall. This suggests that it is representing the turbulent mixing, i.e. turbulent motions that move high momentum fluid from the outer regions towards the wall and at the same time low momentum fluid is lifted from the near-wall region towards the outer layer. The following sections will characterize the structures in more detail. As the turbulent mixing transports energetic fluid from the outer layer to the lower regions, a lag of kinetic energy is created in the outer layer, which is then closed by the large scale kinetic energy transport $\frac{1}{2}\nabla \cdot \left(\bar{\rho}\tilde{\vec{u}}\tilde{\vec{u}}^2\right)$ (dark red). This can be seen in the outer layer plot (fig. 6.6, bottom). In the near-wall region the large scale transport is small compared to the remaining terms, but it gains importance towards the outer region. It is believed to describe the gain of energy that is fed into the turbulent boundary layer from the laminar freestream. We will see in the next section (6.4) that laminar structures from the freestream reach far into the turbulent boundary layer. This then supports the idea that the mean transport term is feeding energy from the freestream into the turbulent boundary layer although the term is acting far into the inner layer (fig. 6.5). The peak of turbulent mixing ($y^+ \approx 9$) is almost coinciding with the global minimum ($y^+ \approx 10$) and the contribution that the turbulence production $\langle\sigma, \bar{S}\rangle_F$ (yellow) has to e_f. The turbulent production acts as a sink for the kinetic energy of the mean flow and is transferring kinetic energy to the turbulent kinetic energy k. This means it covers the transfer of kinetic energy between large scales and small scales. *Large scales* according to Favre averaging, the presently used filter operation, is the mean flow, whereas *small scales* presently refer to the fluctuations around this mean. After the mean transport, the turbulence production has the weakest direct effect on e_f, however, it produces turbulent energy which is the cause for turbulent mixing - a strong mechanism throughout the entire boundary layer as we have just seen. This means its indirect effect is much stronger that its direct effect. The two remaining terms, diffusion of the mean kinetic energy $\nabla \cdot \left(\bar{\tau} \cdot \tilde{\vec{u}}\right)$ (red) and dissipation of the mean kinetic energy $\langle\bar{\tau}, \bar{S}\rangle_F$ (dark green), are viscous large-scale effects. The large scales behave in the same way as their overall counterparts (dashed). The main difference is that the magnitudes are lower than for the total diffusion and dissipation. This is expected as part of the

viscous effects are caused by the small scale motions and therefore they are captured in the equation for k.

Turbulent production is the source of turbulent kinetic energy and its dominant peak is in the near-wall region ($y^+ \approx 10$). However, it can be seen that small scales are produced throughout the entire boundary layer. The turbulent mixing of turbulent kinetic energy $\nabla \cdot \chi$ (light orange), known as turbulent transport, redistributes the turbulent kinetic energy from this peak of production. Its global minimum ($y^+ \approx 12$) nearly coincides with the peak of the production. Besides the small area around the minimum the turbulent transport has a positive contribution to the k-budget. This states that this mechanism is transporting turbulent kinetic energy away from the production peak into the whole boundary layer. Although this term is small compared to other terms it feeds the whole boundary layer with turbulence. Admittedly, turbulent production is the greatest donor of turbulent kinetic energy in most of the boundary layer (except close to the wall), but as turbulent production needs small-scale motion itself ($\sigma \neq 0$) to be active it cannot act without a trigger. This trigger might be turbulent bursts that shoot turbulence for the wall into higher layers. Then turbulence production acts within these turbulent spots. The burst are believed to be covered by the turbulent transport term and are studied from a different perspective in the following (sec. 6.4). The turbulent pressure-work ϑ (light purple) has a small direct effect, but we will see later that pressure has an important role which is not directly obvious from the energy budgets. The transport of turbulent kinetic energy with the mean is small throughout the entire boundary layer. The two remaining terms are turbulent diffusion $\nabla \cdot c_{\tau-u}$ (dark orange) and turbulent dissipation ε (green). Turbulent diffusion acts in the same way as the overall diffusion. It uses friction to transfer turbulent kinetic energy from the energetic region to the wall. Turbulent dissipation then transfers the kinetic energy to internal energy. Turbulent dissipation acts in the whole boundary layer and is the main antagonist to the production. Both will be studied in greater detail in the following sections (6.6,6.7).

The overall dissipation $\langle \tau, S \rangle_F$ (dark green, dashed) acting as source for mean internal energy is decomposed into the dissipation of the mean flow and a turbulent dissipation coming from the turbulent kinetic energy. The dissipation of the mean is the strongly dominant source at the wall and becomes weaker in the buffer layer. At $y^+ \approx 30$ it becomes nearly insignificant compared to the remaining quantities. On the other hand, the turbulent dissipation plays a small role in the viscous sublayer, but gains importance for the overall dissipation within the buffer layer. By the start of the log-layer and within all the remaining boundary layer it is the main contributor to the dissipation, although with relatively minor impact to the internal energy in the outer layer. At this stage it is necessary to emphasize again that the wall conditions for the boundary layer flow impose a constant wall-temperature at approximately 105% of the freestream temperature. Therefore the wall is hotter than the freestream which induces a heat flow away from the wall. Together with the high dissipation at the wall this leads to the

strong heat diffusion at the wall $\nabla \cdot \vec{q}$ (blue) which is heating the buffer layer. Further, it should be noted that the coupling of the mean overall enthalpy transport $\nabla \cdot (\vec{u}\rho h)$ (dark blue, dashed), the mean enthalpy transport with the mean flow $\nabla \cdot \left(\tilde{\vec{u}}\bar{\rho}\tilde{h}\right)$ (dark blue) and the turbulent transport of the enthalpy $\nabla \cdot c_{h-u}$ (light blue) is a nearly perfectly matching with the additive inverse process of what we described as turbulent mixing of kinetic energy of the mean flow. It is believed to be the inverse process. Specifically , this means unlike the imbalance of high kinetic energy in the freestream and no kinetic energy at the wall, that feeds the kinetic turbulent mixing, the process is the other way around in case of internal energy in this particular case. The wall-condition forces the wall to be hotter than the freestream and additionally dissipation is a strong heat source close to the wall. The overall transport of the enthalpy is covered by the turbulent transport of the enthalpy $\nabla \cdot c_{h-u}$ in the near-wall region. It is mainly negative in the viscous sublayer and the buffer layer and then flips sign in the logarithmic layer to remain positive throughout the rest of the boundary layer. This result indicates that $\nabla \cdot c_{h-u}$ covers the turbulent mixing process that brings hot fluid from the wall to cold fluid in the outer layer and vice versa. The mean transport that balances that heat gain in by bringing cold fluid from the freestream into the turbulent boundary layer.

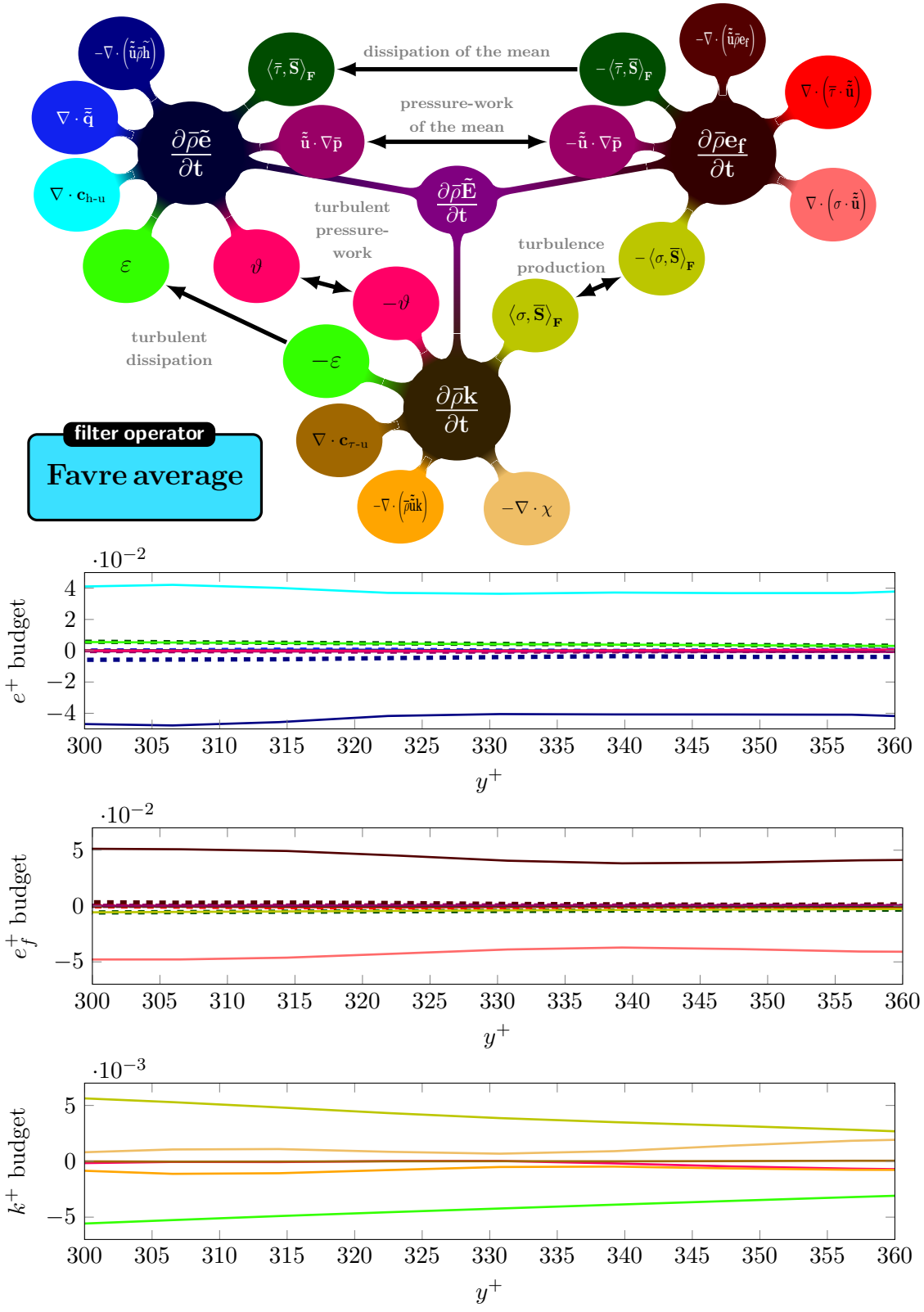

Figure 6.6: Schematic representation of the energy budget decomposed into large scales (LS) and small scales (SS) based on Favre averaging chosen as filter operation.

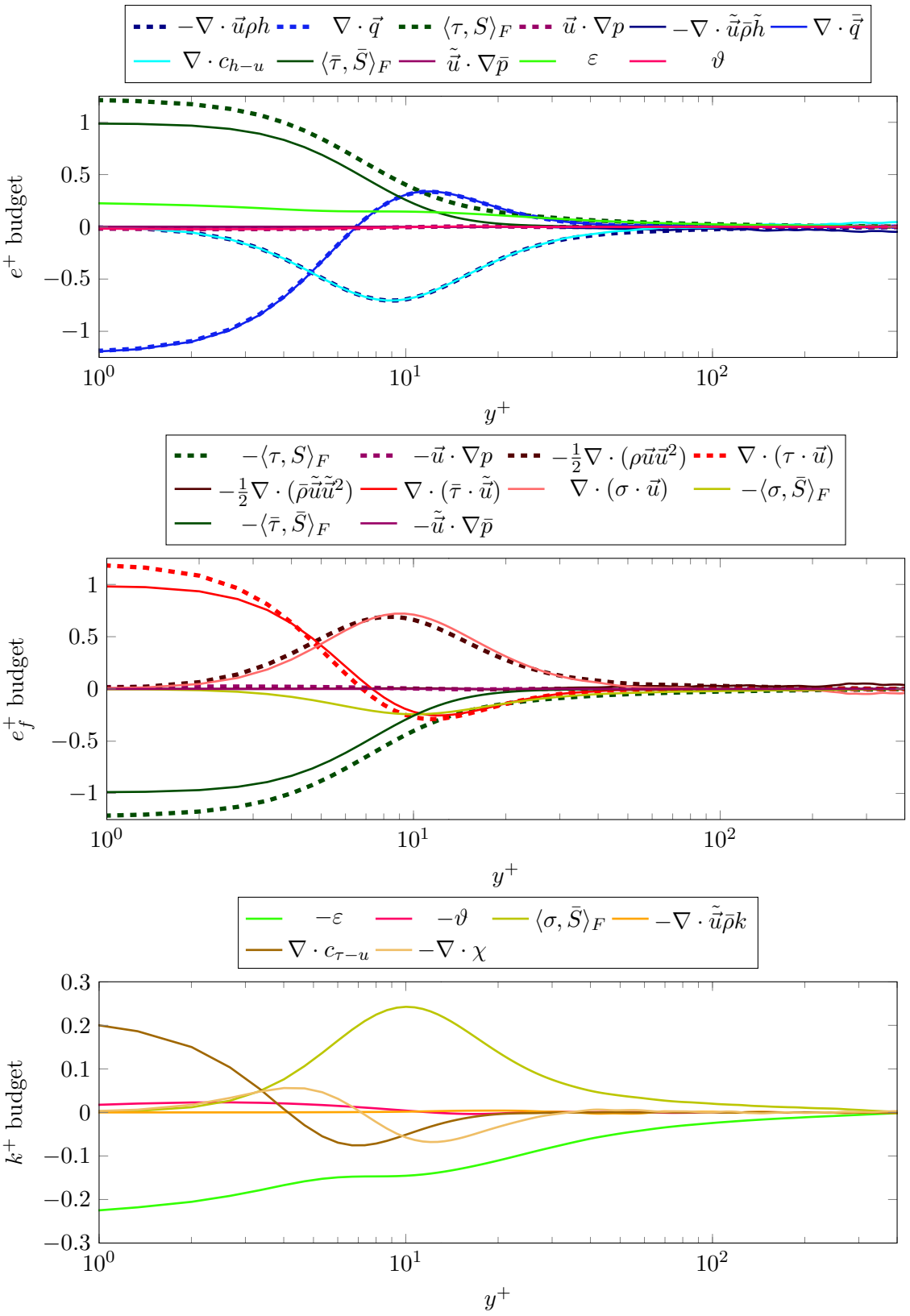

Figure 6.7: Energy budget decomposed into LSs and SSs based on Favre averaging chosen as filter operator. The top plot shows the budget for the LS internal energy. The center plot shows the kinetic energy budget of the LS moments. The bottom plot shows the budget for the averaged SS kinetic energy.

6.2.2 Energy Splitting Based on Spatial Filtering

In this section the flow field is split into large scales and small scales by applying a spatial filter (sec. 3.2.1). Some of the resulting filtered flow quantities were already presented in section (6.1). As mentioned before the filter widths are varying when approaching the wall (fig. 6.2). This leads to two effects that need to be highlighted. Firstly, filter F2 and F3 have the same filter width for $y^+ \lesssim 53$ and further all filters have the same width $y^+ \lesssim 26$. Secondly, the varying filter width implies that the filters are inhomogeneous and in the present case this leads to a filter operation that does not commute with spatial derivatives as discussed in section (2.2.1.1). This, on the other hand, leads to the occurrence of filter residua that describe the effect of the inhomogeneous filter to the energy budgets. This effect is restricted to the area of varying filter width and is therefore not affecting most of the logarithmic layer and the outer layer for any of the filters. Further, the effect is small enough to not affect the large scales, however it appears to have large contributions for the small scale kinetic energy budget. The overall effect of the inhomogeneous filter is still not understood at the current stage which leads to an incomplete interpretation of the small scale behaviour. These gaps in understanding will be pointed out during the discussion (sec. 6.2.3).
The split budgets are stated on three double pages: one double page per filter. The budgets for the smallest filter F1 are shown in figures (6.9,6.10), the budgets resulting from the use of the intermediate filter width F2 are shown in figures (6.11,6.12) and the budgets for the largest filter F3 are shown in figures (6.13,6.14). The respective top figure holds the visual description as well as the plots for the outer layer. The respective second figure from top holds the overall budgets on a logarithmic axis and are emphasizing the near wall region. Shades of blue indicate the redistribution terms for the internal energy. Shades of red indicate redistribution terms for the kinetic energy of the large scale flow field which is referred to as large scale kinetic energy. Shades of orange indicate the redistribution terms for the filtered kinetic energy of the velocity fluctuations which is referred to as small scale kinetic energy. The gray/black terms are filter residua that either redistribute or transfer energy due to inhomogeneous filter operators. The remaining terms transfer energy between the different types of energy and are marked with arrows to show the transfer of energy.
For the large scale kinetic energy e_f the large scales are dominant in the near-wall region. The contributions are one order of magnitude smaller. This is in parts caused by the decreasing filter width for decreasing distance to the wall, which on the other hand reduces the energy of what is defined as small scales by the filter. Figure (6.8, right) magnifies the small scale effects on the large scale kinetic energy in the inner region. It can be seen that the turbulent diffusion $\nabla \cdot \left(\sigma \cdot \tilde{\vec{u}}\right)$ (pink) gains influence whereas the large scale transport $\frac{1}{2}\nabla \cdot \left(\tilde{\vec{u}}\tilde{\rho}\tilde{\vec{u}}^2\right)$ (dark red) loses influence. By contrast, in the outer layer the opposite can be seen. For increasing filter width the affected region in the near-wall region is increasing (fig. 6.8, right) whereas the overall shift of both quantities

is becoming stronger in the outer region (figs. 6.9,6.11,6.13). The interpretation of this effect is yet unclear. Analogue to the case with Favre averaging as filter operator, the described effect is believed to represent the mixing of large scale energy achieved by the small scale movement. The unexplained part is that the effect inverts exactly at the location where the filter width ramp is merged with a constant filter width. This holds for each filter respectively. To understand this behaviour, different processing is needed. Varying the filter width ramp as well as different filter kernels might improve the understanding of the present results. The overall dissipation of the large scale kinetic energy $\langle \tau, S \rangle_F$ (dark green, dashed) is not fully covered by the large scale dissipation $\langle \bar{\tau}, \bar{S} \rangle_F$ (dark green). Before the energy can get dissipated in the large scales a part of the energy is transferred to the small scale kinetic energy via the turbulent production $\langle \sigma, \bar{S} \rangle_F$ (yellow). This effect is present throughout the entire boundary layer. While it has a minor impact on the overall budget in the viscous sublayer and beginning of the buffer-layer, it rapidly gains importance when further increasing the distance to the wall. The shift from large scale dissipation to turbulence production gets more pronounced for larger filter widths, but even for the largest filter width F3 in the logarithmic layer and outer layer the large scale dissipation has a significant contribution to the overall budget. This ratio is expected to vary with Reynolds number.

For every investigated filter width there is no apparent complex mechanism in the logarithmic layer and in the outer layer for the filtered small scale kinetic energy k. Besides a production and turbulent dissipation ε (green) there is no redistribution active, but as expected the production as well as dissipation grow with growing filter width (figs. 6.9,6.11,6.13). The budget for k closer to the wall is similar for all filter widths and below $y^+ \approx 26$ even identical, as defined by the identical filters. The peak of the turbulence production is located between $y^+ \approx 25 - 30$ for all filter widths. The turbulent mixing $\nabla \cdot \chi$ (light orange) then moves turbulent kinetic energy towards the wall as well as further away from the wall. In comparison the mixing process for all spatial filters is, even in relation, weaker that in the case of Favre averaging. The turbulent diffusion $\nabla \cdot c_{\tau-u}$ (dark orange) balances in parts with the filter residuum transfer $\mathbb{T}_R^{e_{\mathrm{kin}}}$ (light gray) which indicates that it is affected by the varying filter widths. Further, sharp peaks can be found in both profiles for all filters. Their locations are coinciding with the end of the ramp that varies the filter width in the near-wall region. The diffusion involves second order derivatives of the flow field, but the filter width function and therefore the resulting filtered quantities are only one time continuously differentiable. This can cause discontinuities in higher order derivatives such as used for diffusion. However, this is a pure post-processing artefact and is restricted to a confined area around the discontinuity itself. The produced and redistributed small scale kinetic energy is finally dissipated into internal energy via the turbulent dissipation. Nevertheless, a detailed interpretation of the behaviour and tasks of the certain term in the k-budget is difficult as the effect of the varying filter width is not clear yet. Therefore the discussion of the near wall k-budget remains incomplete in the present work. For a more detailed

discussion a comparison between different filter kernels is needed. This will allow to distinguish between effects of turbulence and effects that might be caused by the choice of the certain filter.

Analogue to the case of the Favre averaging as filter operator, the mechanisms represented in the e-budget are on average the additive inverse of the mechanisms represented in the e_{kin}-budget. The near-wall budget is almost solely governed by the large scales (according to the presently applied filter). However, taking a closer look to the small scale behaviour (fig. 6.8, left) reveals that the small scale transport of enthalpy $\nabla \cdot c_{h-u}$ (light blue) gains influence whereas the large scale transport $\frac{1}{2}\nabla \cdot \left(\tilde{\vec{u}}\bar{\rho}h\right)$ (dark blue) loses influence on the overall enthalpy transport $\nabla \cdot (\vec{u}\rho h)$ (dark blue, dashed). In the outer layer the opposite can be seen. For increasing filter width the affected region in the near-wall region is increasing, whereas the overall shift of both quantities is becoming stronger in the outer region (figs. 6.9,6.11,6.13). Just like in the case of large scale kinetic energy the interpretation of this effect is yet unclear. Like in the case of using Favre averaging as filter operator, the described effect is believed to represent the mixing of large scale energy achieved by small scale movement. Again the open question is why the effect inverts exactly at the location where the filter width ramp is merged with a constant filter width. This holds for each filter respectively. As the results for the e_{kin}-budget and k-budget have shown, the overall dissipation of the kinetic energy of the mean as source of internal energy is not fully covered by the large scale dissipation and part of it is achieved by the small scale dissipation. This effect is present throughout the entire boundary layer. Whereas it has minor impact on the overall budget in the viscous sublayer and beginning of the buffer-layer, it rapidly gains importance when further increasing the distance to the wall. The shift from large scale dissipation to small scale dissipation gets more pronounced for larger filter widths, but even for the largest filter width F3 in the logarithmic layer and outer layer the large scale dissipation has a significant contribution to the overall budget (fig.6.13). This ratio is expected to vary with Reynolds number.

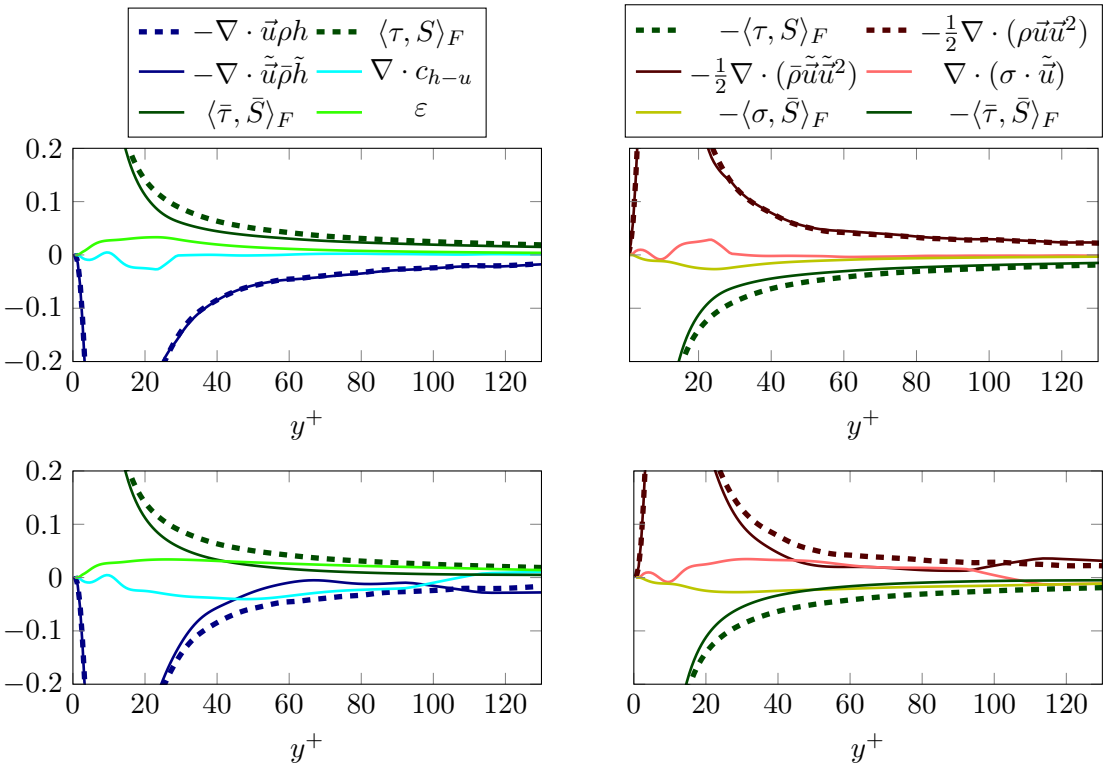

Figure 6.8: Selected terms of the budget for the filtered internal energy (left) and the budget for the kinetic energy of the filtered velocity (right). At the top the results for filter F1 are shown and at the bottom results for filter F3 are shown.

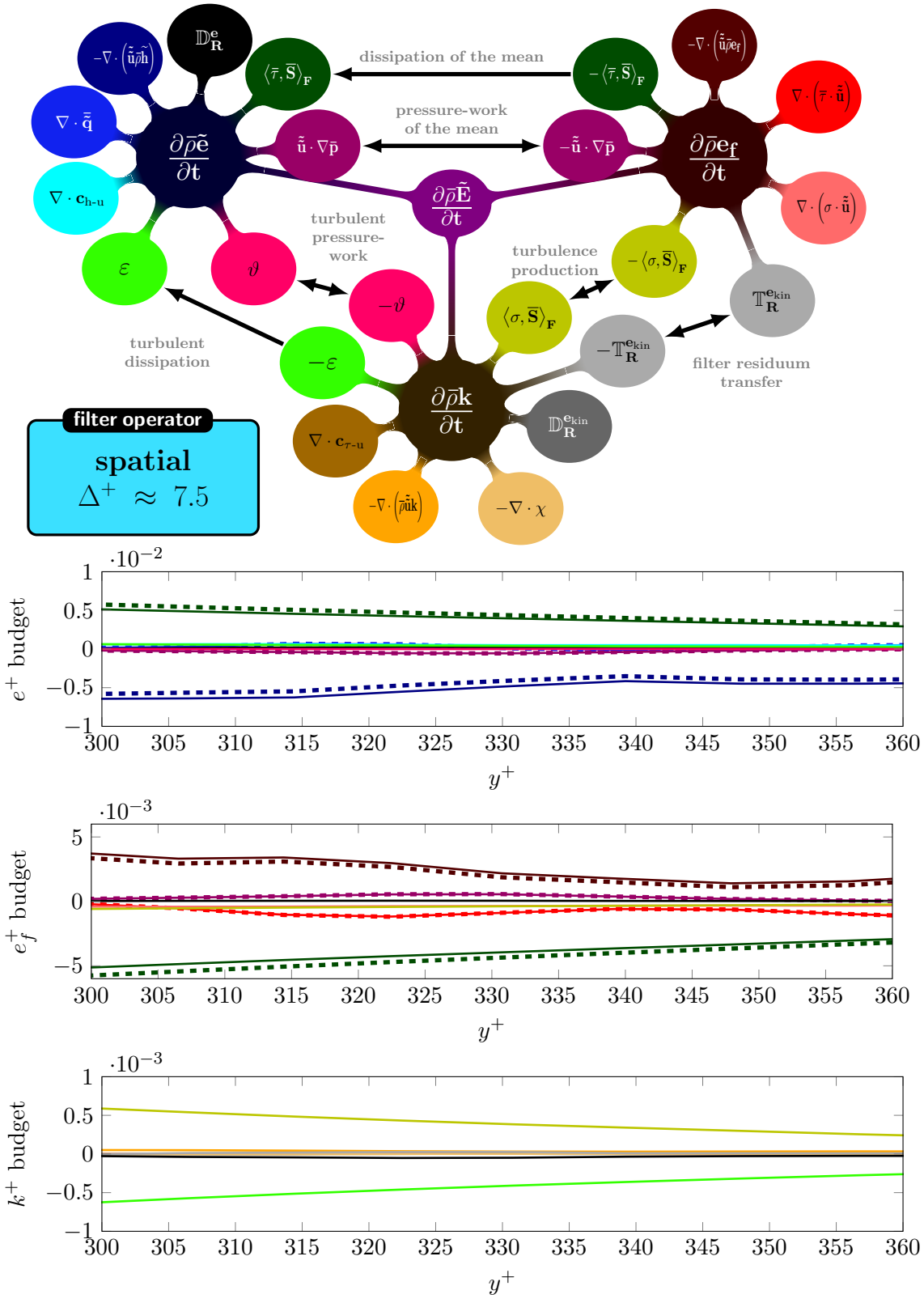

Figure 6.9: Schematic representation of the energy budget decomposed into large scales (LS) and small scales (SS) based on spatial filter F1 chosen as filter operation.

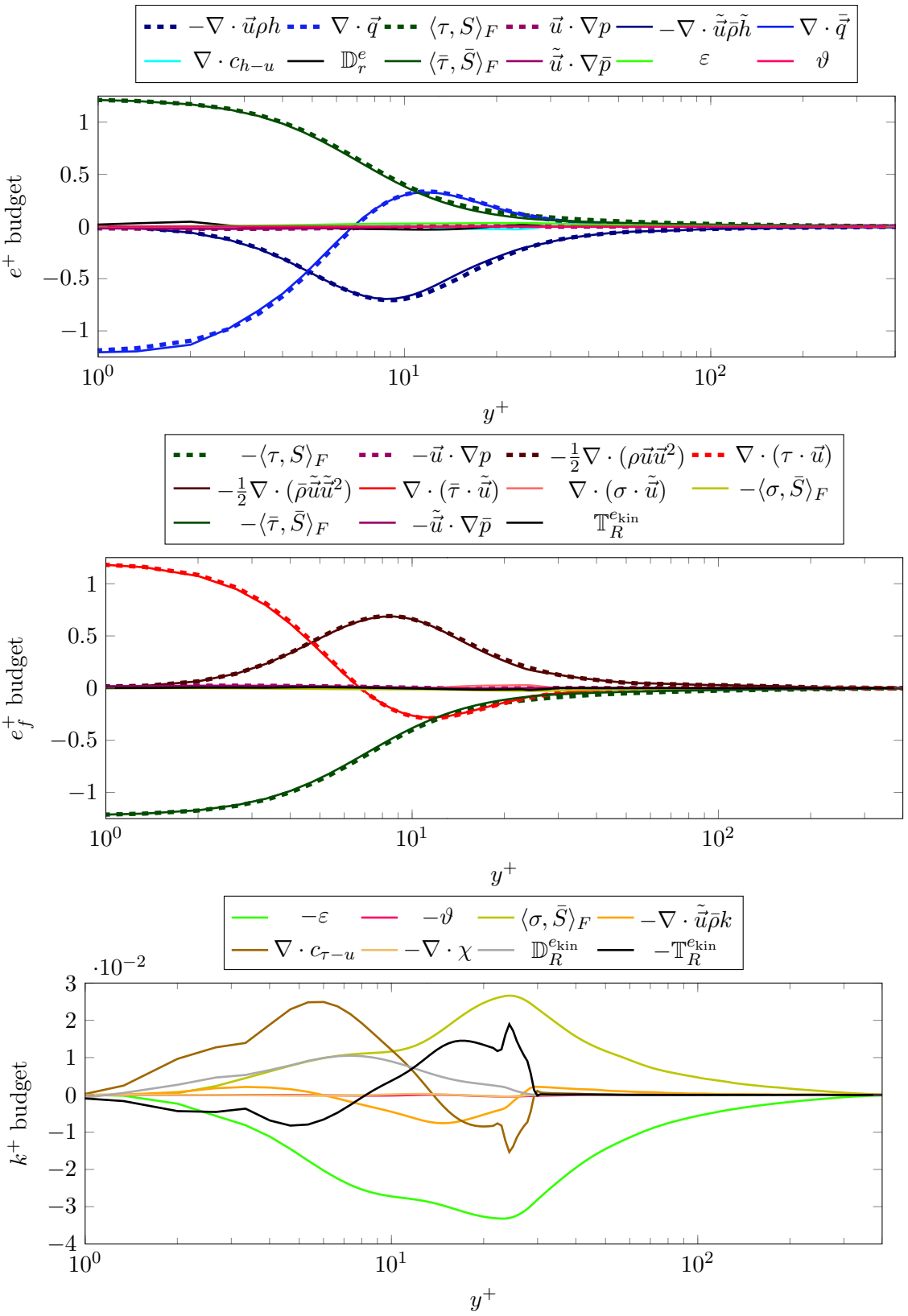

Figure 6.10: Energy budget decomposed into LSs and SSs based on spatial filter F1 chosen as filter operator. The top plot shows the budget for the LS internal energy. The center plot shows the kinetic energy budget of the LS moments. The bottom plot shows the budget for the averaged SS kinetic energy.

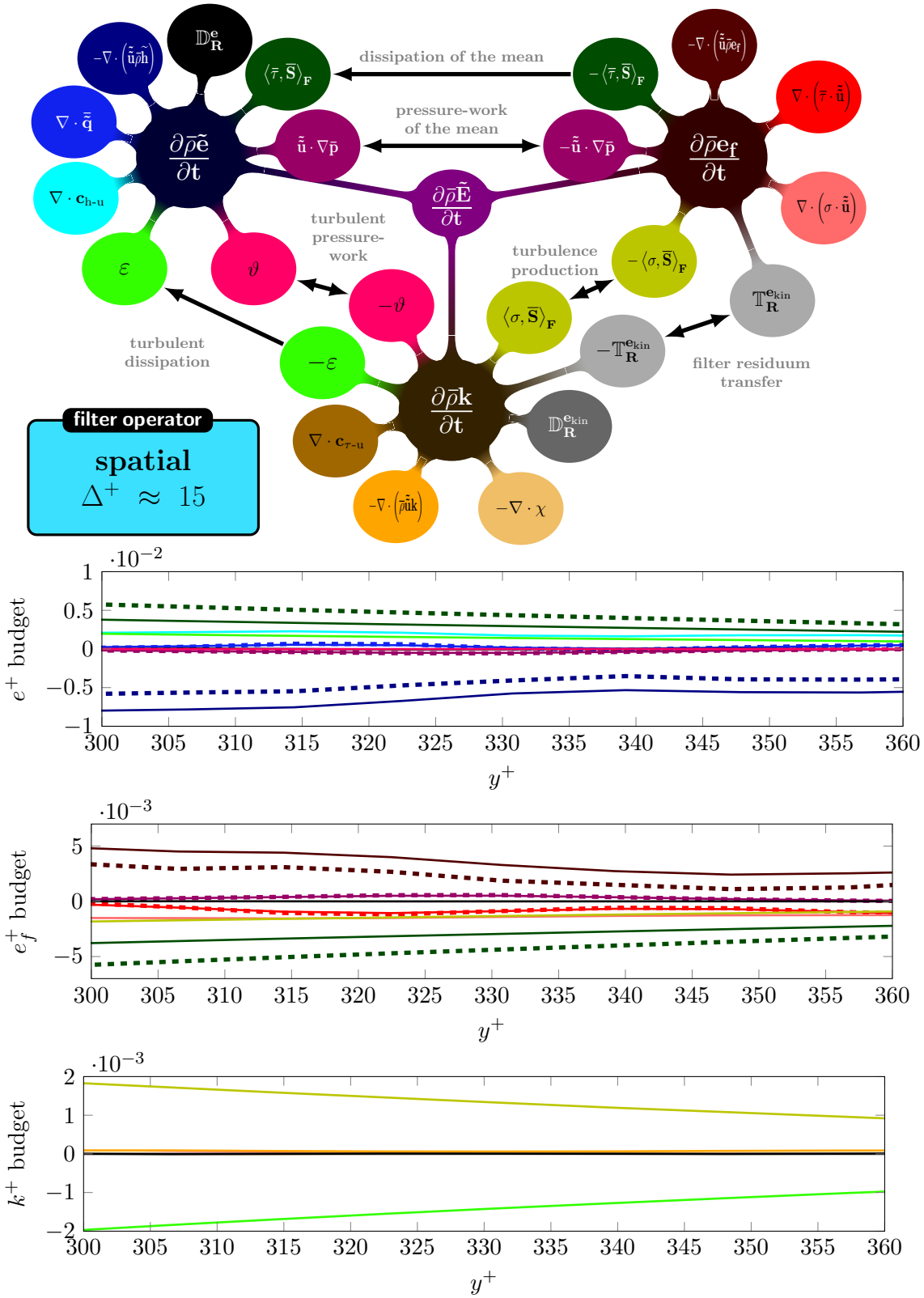

Figure 6.11: Schematic representation of the energy budget decomposed into large scales (LS) and small scales (SS) based on spatial filter F2 chosen as filter operation.

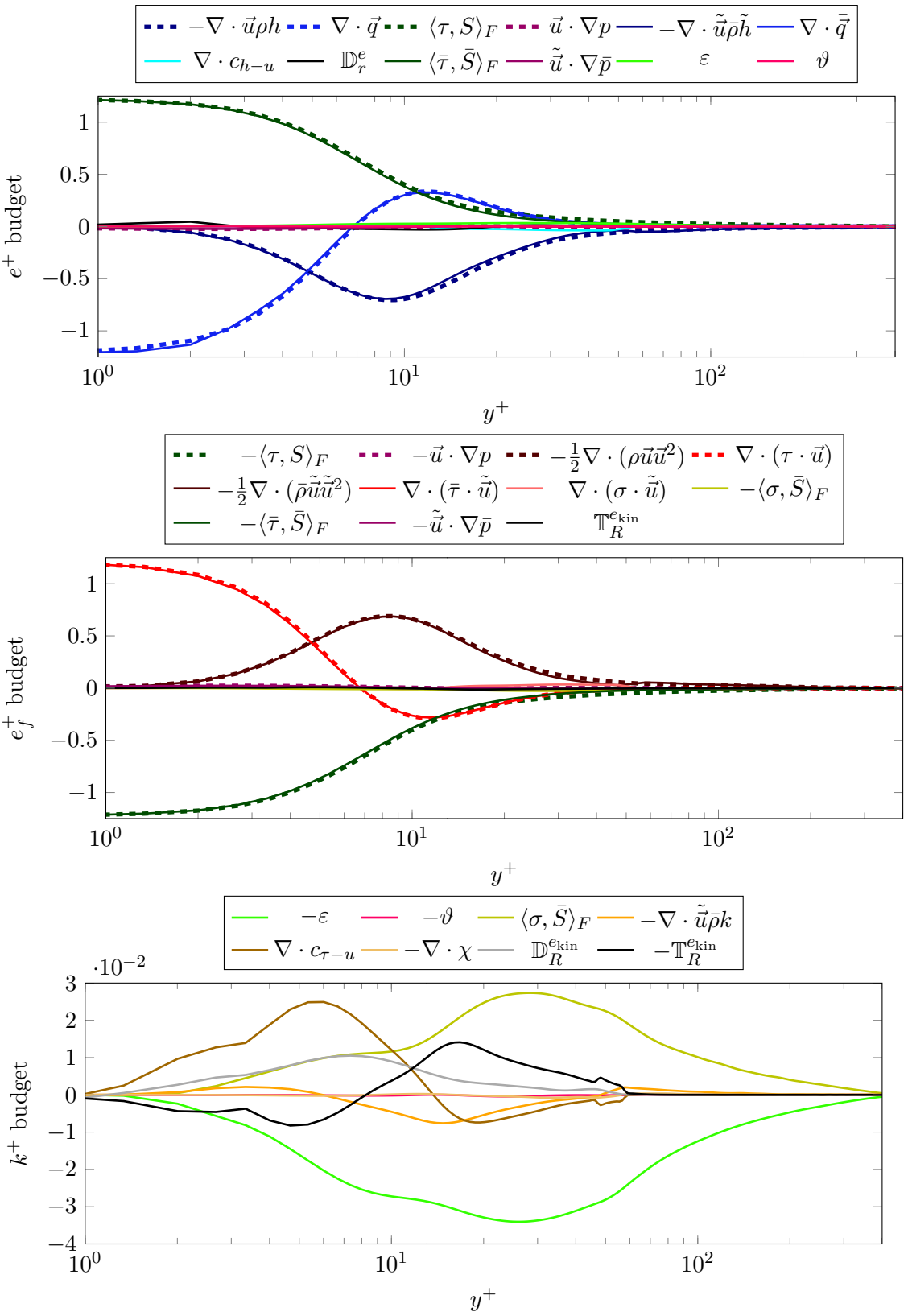

Figure 6.12: Energy budget decomposed into LSs and SSs based on spatial filter F2 chosen as filter operator. The top plot shows the budget for the LS internal energy. The center plot shows the kinetic energy budget of the LS moments. The bottom plot shows the budget for the averaged SS kinetic energy.

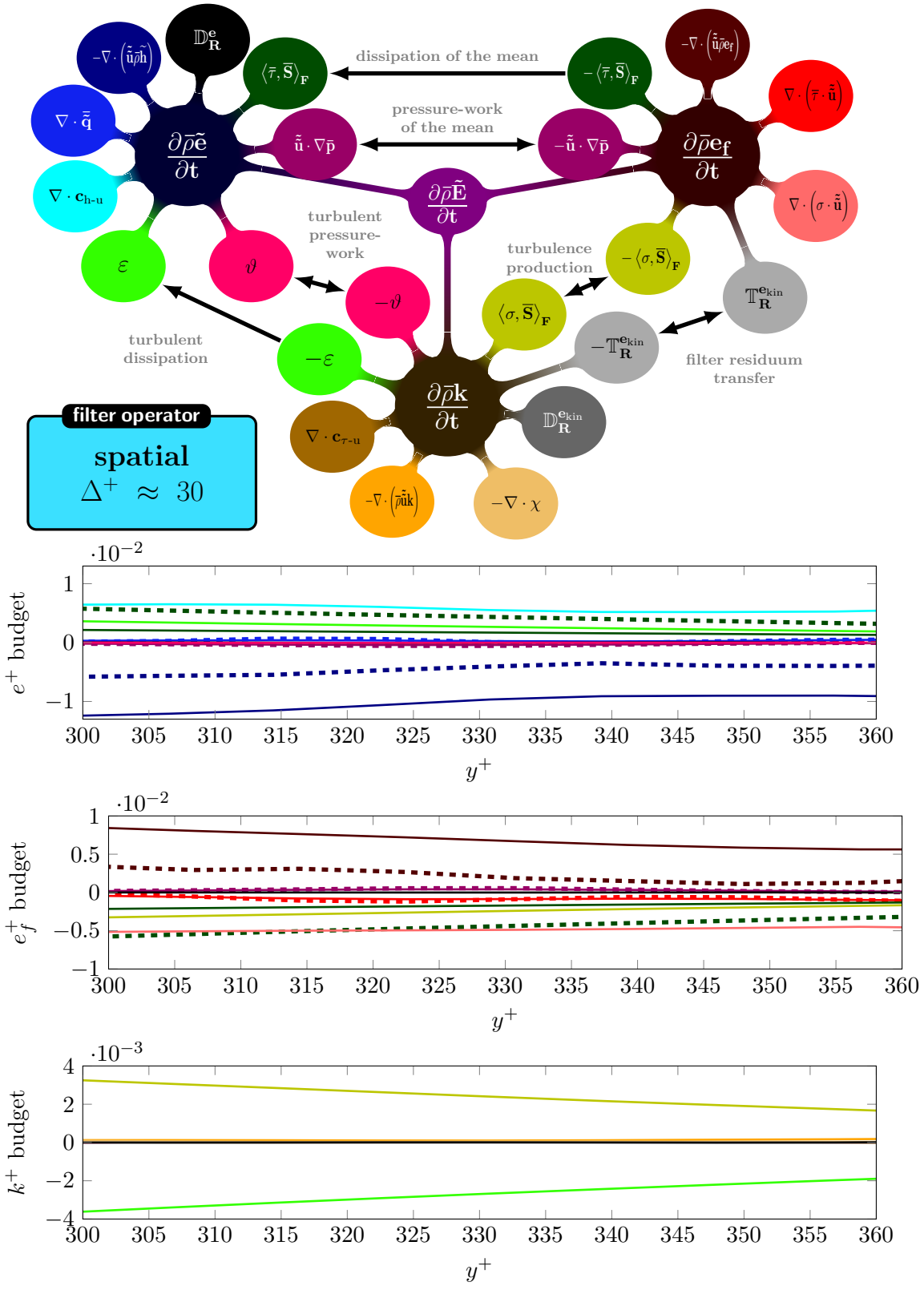

Figure 6.13: Schematic representation of the energy budget decomposed into large scales (LS) and small scales (SS) based on spatial filter F3 chosen as filter operation.

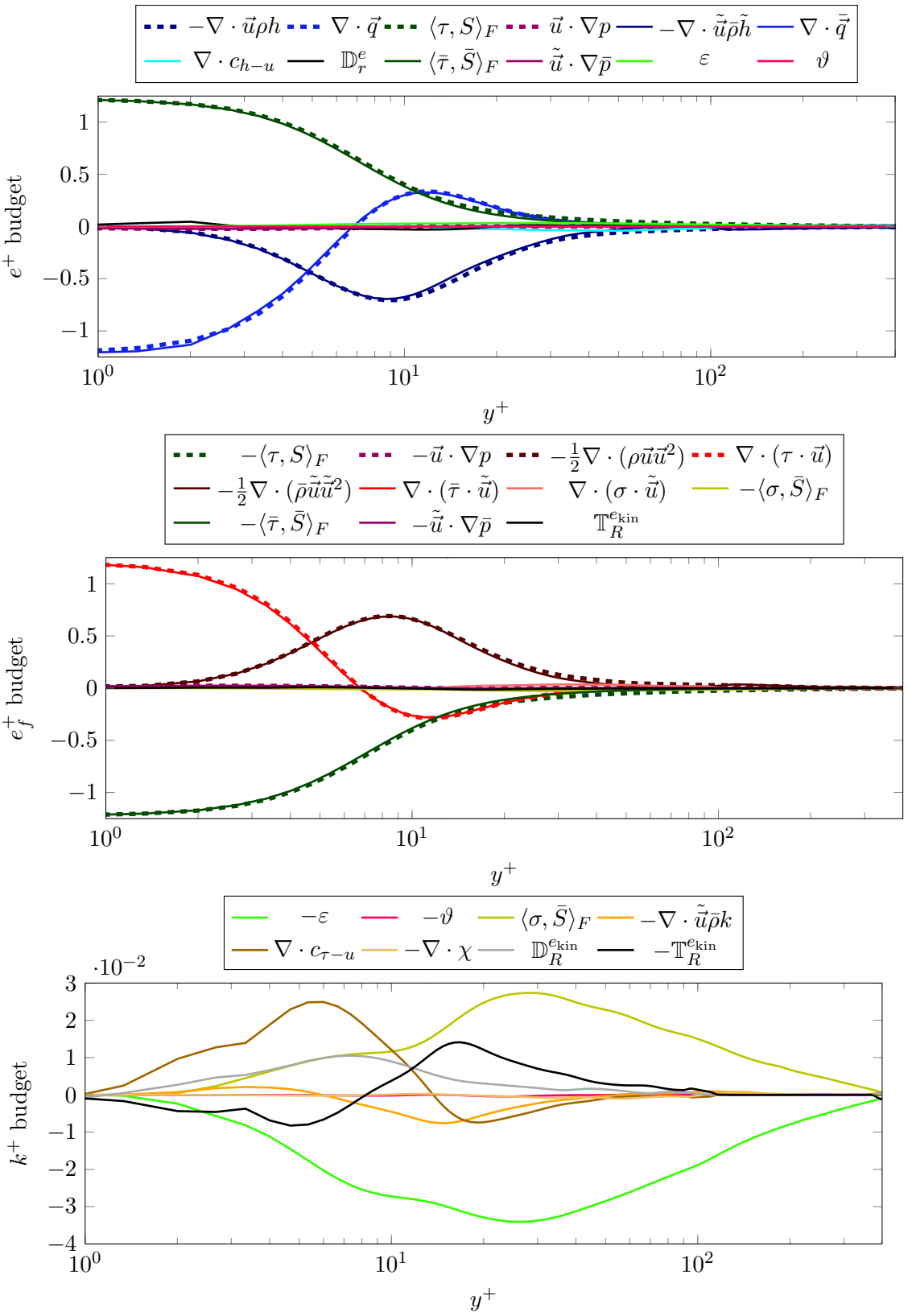

Figure 6.14: Energy budget decomposed into LSs and SSs based on spatial filter F3 chosen as filter operator. The top plot shows the budget for the LS internal energy. The center plot shows the kinetic energy budget of the LS moments. The bottom plot shows the budget for the averaged SS kinetic energy.

6.2.3 Conclusions about Energy Budgets

In this section the energy budgets of a compressible turbulent boundary layer flow at a freestream Mach number of $M_\infty = 0.5$ were discussed at a streamwise location of $Re_\theta \approx 1236$. The Favre averaging as well as spatial filter operations were applied to split the total energy into large scale and small scale components to discuss the respective redistribution mechanisms. This analysis, applied to low Mach number compressible turbulent boundary layer flows, as well as the comparative discussion of Favre averaging and spatial filtering, are novel contributions to the literature on turbulent flows.
Whereas for the Favre average based splitting (FAS) the production of small scales has a strong peak at the beginning of the buffer-layer ($y^+ \approx 10$), the production peak in the spatial filter based splitting (SFS) analysis is less strong and moved further away from the wall ($y^+ \approx 25 - 30$). The turbulence in both cases is diffused towards the wall and mixed in via turbulent transport into the remaining boundary layer. The presence of turbulence in the whole boundary layer then enables production across the entire extent of the boundary layer. The turbulence production drains kinetic energy from the large scale flow which is eventually dissipated into internal energy after undergoing the diffusion and redistribution processes described before. Besides the direct effect that the turbulent production and dissipation have on the large scale kinetic energy and the large scale internal energy, respectively, there is a much stronger secondary effect in case of FAS. The turbulence has a strong mixing effect on the large scale energies. Faster and colder fluid from higher layers is mixed due to turbulent motions with slower and hotter layers close to the wall. In case of SFS this effect is present as well but one order of magnitude weaker that for the FAS. It gains intensity with increasing filter width, but even with a spatial filter width of $\Delta^+ \approx 30$ it is not affecting the near-wall behaviour of the large scales in a significant manner. However, the mixing gains are relatively strong, but believed to be a strictly local contribution for large filters in the logarithmic layer and in the outer layer. The strong difference between FAS and SFS in the turbulent mixing of the large scale energy is an indication that very large scales are the main contributor to this mixing. These structures must exceed at least the size of the largest filter used in SFS analysis - i.e. they need to be larger than 30 plus units. Considering that the turbulent mixing is the largest effect of turbulence on the large scales it is good news for the LES community as the turbulent structures with the most significant impact are large and do therefore not need to be covered by sub-grid-scale models. Further, as stated in section (6.1) the varying effect of the filter on the respective Favre stress components suggests that σ_{11} and σ_{12} find their origin more dominantly in large scale structures compared to the remaining Favre stresses. Together with the large scale character of turbulent mixing it is suggested that the Favre stresses σ_{11} and σ_{12} are coupled with the mixing process. This agrees well with what was discussed in the literature (sec. 3.3.1.1). Then again, for the dissipation it was shown that in the near-wall region most of the energy is dissipated in the large scales. However, for FAS

	FAS	SFS - F1	SFS - F2	SFS - F3
e LS contribution	50%	93%	86%	79%
e SS contribution	50%	7%	14%	21%
e_{kin} LS contribution	49%	94%	88%	82%
e_{kin} SS contribution	51%	6%	12%	18%

Table 6.1: Ratios of large contribution and small scale contribution to the large scale budgets for the different cases.

small-scales take over almost the entire dissipation in the outer layer. On the other hand, SFS show that not only the smallest scales dissipate energy in the outer layer; the large scales contribute significantly - even for the largest filter. The significant (spatial) large scale contribution to the dissipation is believed to be an effect of the relatively low Reynolds number of the flow.

In general the significance of small scales for the large scales can be quantified by splitting the respective equations into pure large scale terms (LS_n) and into mixed terms (SS_n)

$$\frac{\partial f}{\partial t} = \sum \text{LS}_n(y) + \sum \text{SS}_n(y). \tag{6.1}$$

So, for example, the mean transport of the mean enthalpy $\nabla \cdot \left(\tilde{\bar{u}}\bar{\rho}\tilde{h}\right)$ would be pure large scale term whereas the turbulent production $\langle \sigma, \bar{S} \rangle_F$ is a mixed term as it contains σ (small scale) as well as $\bar{S}$ (large scale). The contribution to the respective budget of small scales and large scales can then be quantified by the ratios

$$\text{contribution}_{\text{LS}} := \frac{\int \sum |\text{LS}_n(y)| dy}{\int \sum |\text{LS}_n(y)| + \sum |\text{SS}_n(y)| dy} \tag{6.2}$$

and

$$\text{contribution}_{\text{SS}} := \frac{\int \sum |\text{SS}_n(y)| dy}{\int \sum |\text{LS}_n(y)| + \sum |\text{SS}_n(y)| dy}. \tag{6.3}$$

Calculating this ratio of the large scale budgets for FAS and SFS for all filter widths leads to the results presented in table (6.1). The difference between FAS, that does not distinguish between spatial scales, and SFS is large. Whereas approximately 50% of the large scale flow in the turbulent boundary layer depends on the small scales, the small scales contribute less than 21% to the overall large scale budgets even for the largest filter width in case of SFS.

Finally, it was shown that the splitting of the energy budgets with the spatial filter into large scale and small scale contributions has potential for improvement. The filter has to adapt when approaching the wall, as the filter kernel cannot (or should not) be extended into the wall. Ideally the filter kernel adapts to the wall in the same way turbulent structures adapt to the wall. To obtain a more complete understanding of the spatially small scales close to the wall, a study of the near-wall turbulence with varying filter kernels is suggested.

6.3 Characteristic Decomposition

The overview obtained from the averaged energy budgets presented in the last section does not give a complete picture of the flow and especially not on the structure and character of turbulence in the flow. The averaged budgets are hiding some, potentially important, information about the flow. The average of a quantity can indeed be a misleading quantity. This can be shown using a simple example, visualized in figure (6.15). Take for instance an object (blue circle) that moves at a constant angular velocity on a constant radius around a center. The mean of the location of the object is the center of the circle described by the object's trajectory and marked by a blue dot. It is obvious that the mean location itself is not a state of the objects location at any time - the object never passes this point. One could speak of an *unphysical* mean value. However, it still has a physical meaning but only in a strictly statistical sense. In general, it should be emphasized that the mean budgets that we just discussed are not necessarily describing the physics directly, but they do give an indication about which quantity could have stronger effects and which quantities could have weaker effects.

In this work we study some of the turbulence mechanisms in more detail and we discover quantities for which the pure mean gives a wrong impression of the respective quantity. here, we make use of the critical point analysis introduced in section (1.2.2). This analysis is based on the invariant of the velocity gradient (see sec. 2.3). The effects of compressibility are negligible in the present flow at a freestream Mach number of $M_\infty = 0.5$. The results were compared against a fully compressible analysis, but no significant differences were found. For this reason we map the (P, Q, R) invariant state-space onto the reduced (Q, R) state-space. This does not mean that the flow is considered to be incompressible. The analysis still takes compressibility into account, but the results are not conditioned for values of the first invariant of the velocity gradient $P := \nabla \cdot \vec{u}$. At this stage we will give a brief summary of the critical point analysis,

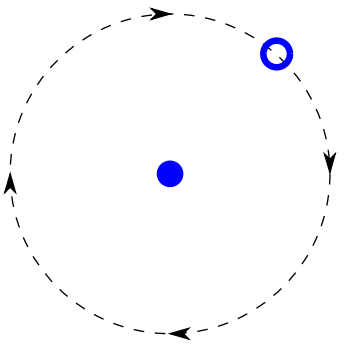

Figure 6.15: The dashed lined indicates the constant circular trajectory of the blue circular object. The blue dot in the center marks the temporal mean of the object's location.

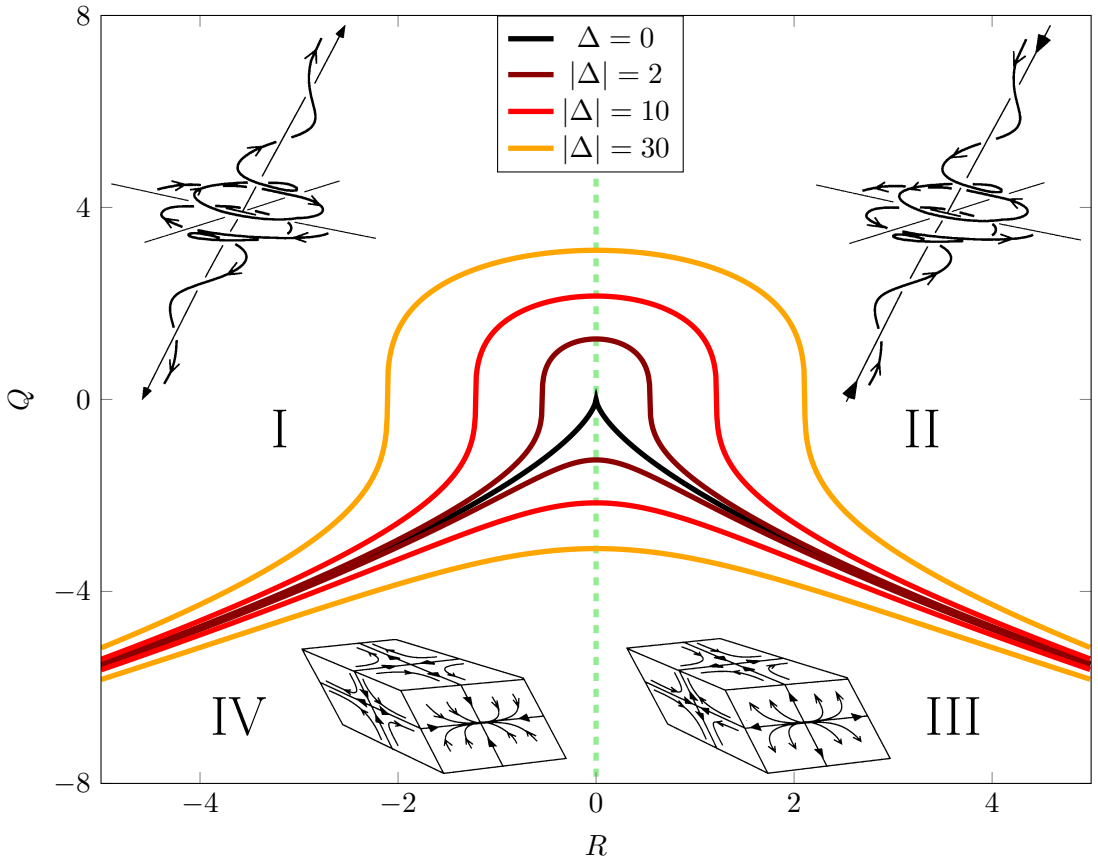

Figure 6.16: Introduction to the invariant space of the velocity gradient.The continuous lines show different values for the discriminant Δ of the velocity gradient and the dashed green line marks $R = 0$. The pictures and numbers show schematically the characteristic structure in the respective area of the QR-space. Subfigures adapted from Ooi *et al.* (1999).

for a more detailed understanding sections (1.2.2) and (2.3) can be reviewed. The QR-state-space, or simply QR-space, is spanned by the second and third invariant, Q and R, of the velocity gradient. From the point of view of a fluid particle located on a structure, it allows to distinguish between four different states of the structure. Figure (6.16) shows the QR-space and the four structure types. The discriminant of the velocity gradient $\Delta = -\frac{1}{4}P^2Q^2 + Q^3 + P^3R + \frac{27}{4}R^2 - \frac{18}{4}PQR$ has an important role in this decomposition. For positive values of $\Delta > 0$ the fluid particle sits on a part of a structure that has a rotational character whereas if $\Delta \leq 0$ the supporting structure is purely straining at the location of the fluid particle. Further, for negative third invariant $R \leq 0$ we find two contracting directions and one stretching direction, whereas if $R > 0$ is positive we find two stretching direction and one contraction direction of the structure at the location of the fluid particle. So four characteristic structure types can be described:

I : vortical structure with stretching character / $\Delta > 0$; $R \leq 0$

II : vortical structure with contracting character / $\Delta > 0$; $R > 0$

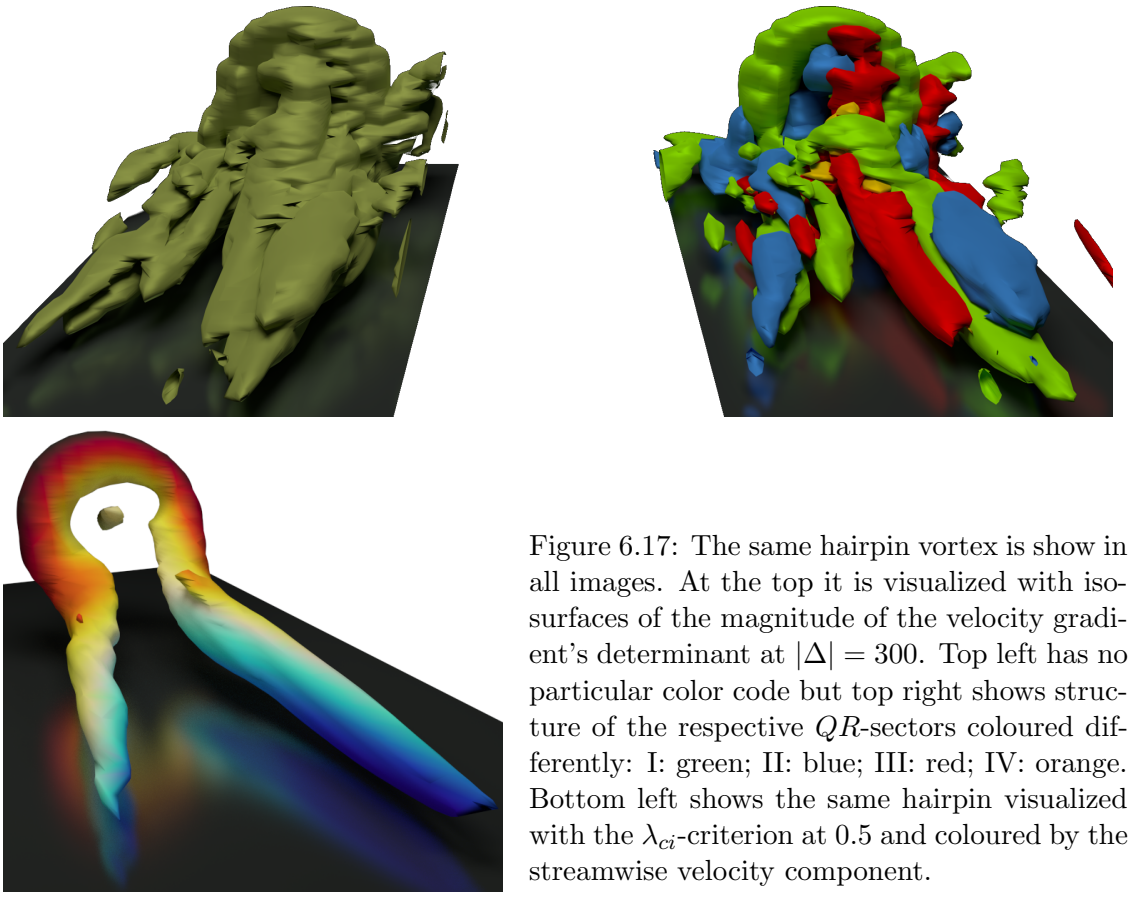

Figure 6.17: The same hairpin vortex is show in all images. At the top it is visualized with iso-surfaces of the magnitude of the velocity gradient's determinant at $|\Delta| = 300$. Top left has no particular color code but top right shows structure of the respective QR-sectors coloured differently: I: green; II: blue; III: red; IV: orange. Bottom left shows the same hairpin visualized with the λ_{ci}-criterion at 0.5 and coloured by the streamwise velocity component.

III : pure straining structure with flattening character / $\Delta \leq 0$; $R > 0$

IV : pure straining structure with elongating character /$\Delta \leq 0$; $R \leq 0$

The result of the characteristic decomposition branching from the critical point analysis is visualized in figure (6.17). The same hairpin structure is show with different visualisation techniques. For the bottom picture the λ_{ci}-criterion was used to create the iso-surface. It is coloured with streamwise velocity from blue (slow) to red (fast). The legs as well as the arc are clearly seen. The top pictures use iso-surfaces based on the magnitude of the discriminant of the velocity gradient. Differently to the λ_{ci}-criterion, this criterion visualized not only rotational structures, but also purely straining structures. This allows for the overall structure (top right) to be decomposed into the respective structure types of the characteristic decomposition. It becomes obvious that a clear distinction of the characteristic structure types is now possible. The decomposition can be used to describe, e.g., which parts of the structure are stretching, which parts are purely straining, etc. This is used extensively in the following and we learn which parts are involved in the cascading process and which are strong contributors to the dissipation etc.

Furthermore, to obtain a better impression of how to interpret the QR-space in terms of scales of motion, figure (6.18) shows a comparison of the discriminant, a meaningful

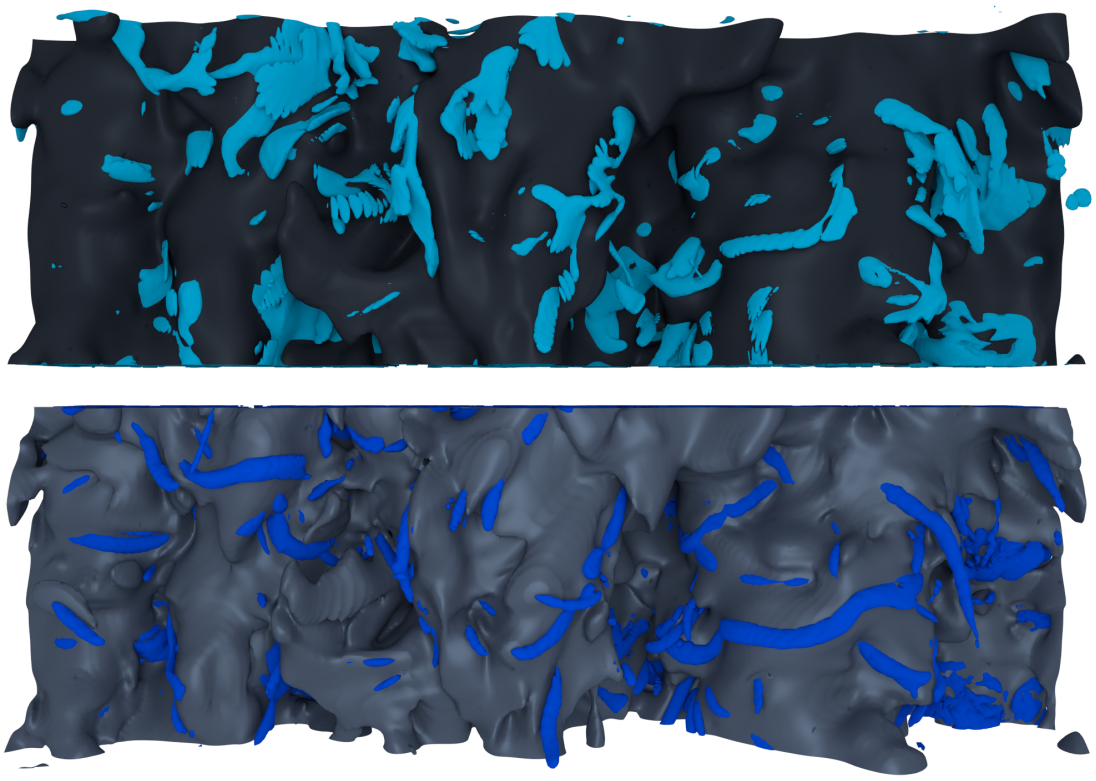

Figure 6.18: Top view onto a section of a boundary layer. Both pictures show the same location at the same instance of time. Flow direction is bottom to top. The top image shows an iso-surface of spatially filtered streamwise velocity at $\tilde{u} = 0.9$ in dark gray. The light blue structures are iso-surfaces of the sub-grid kinetic energy $k = 0.0005$. The filter width is $\Delta^+ \approx 30$. The bottom picture shows the unfiltered flow field. An iso-surface of streamwise velocity at $u = 0.9$ is shown in light gray. The blue structures are iso-surfaces of the absolute value of the velocity gradient discriminant at $|\Delta| = 10$.

quantity in the QR-space, with a scale decomposition via spatial filtering. Both pictures show a snapshot of the same scene in the boundary layer flow. The top image shows results after filtering (F3 filter) whereas the bottom picture shows the raw data. The gray layers are iso-surfaces of filtered and unfiltered streamwise velocity, respectively. The blue structures in the filtered case are iso-surfaces of the sub-grid kinetic energy and the blue structures at the bottom are iso-surfaces of the absolute value of the velocity gradient invariant $|\Delta|$. On a closer look clear similarities of both structures can be found. This means that certain states in the QR-space represent smaller structures and therefore others will represent larger structures. In this particular case structures with a discriminant value of $|\Delta| = 10$ match quite well with the structures of the sub-grid kinetic energy of $k = 0.0005$. As we can see in figure (fig. 6.19) the velocity gradient magnitude is zero at the origin of the QR-space and strictly monotonously increasing with the distance to the origin. A fluid particle with a zero magnitude of the velocity gradient can be seen as in a locally laminar flow regime as the flow field is locally not changing. Further a fluid particle at a location with relatively small velocity gradient

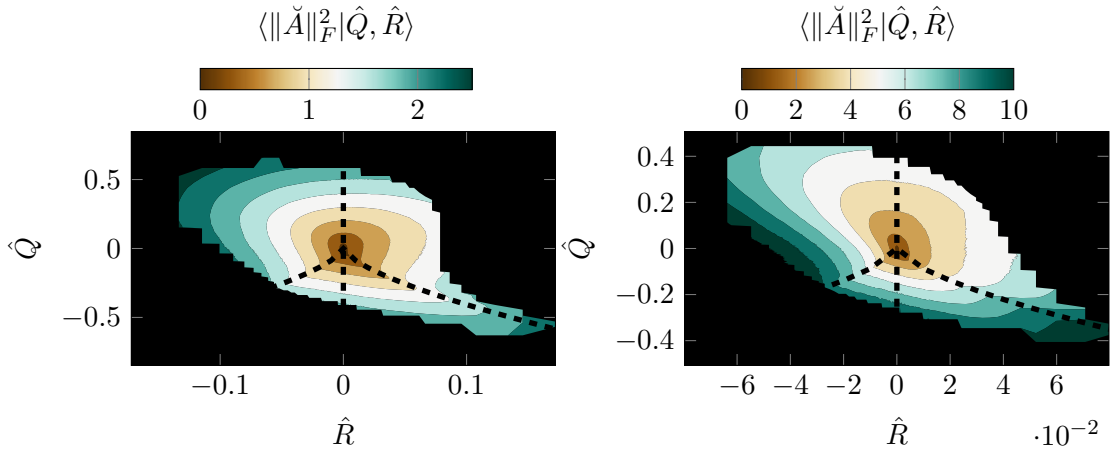

(a) $y^+ \approx 99$ (b) $y^+ \approx 24$

Figure 6.19: Conditional average of the velocity gradient magnitude squared normalized by the ratio of freestream velocity and boundary layer thickness $\breve{A} = A\frac{\delta_{99}}{U_e}$ at two different wall-normal locations.

magnitude could be described to be in a large scale flow regime, whereas a fluid particle at a spot with high velocity gradient magnitude can be seen as in a small scale flow regime as the flow field changes strongly in the surrounding area. This will be further discussed in the following sections.

The characteristic distribution of the turbulence based on the introduced characteristic decomposition can be measured by sampling a joint probability density function (pdf) of Q and R. From these pdfs it can be seen how likely the occurrence of certain states of the QR-space are. The QR-space is closely linked to the velocity gradient itself (sec. 2.4), the spreading of the states reached is therefore linked with the variance of the velocity gradient $A = \nabla \vec{u}$. For this reason we find it appropriate to normalize the invariant by the local variance of the velocity gradient

$$\mathrm{var}(A) := \overline{\langle A - \tilde{A}, A - \tilde{A} \rangle_F}. \tag{6.4}$$

The normalized invariants are the defined as

$$\hat{Q} := \frac{Q}{\mathrm{var}(A)} \tag{6.5}$$

and

$$\hat{R} := \frac{R}{\mathrm{var}(A)^{\frac{3}{2}}}. \tag{6.6}$$

The sampled pdfs are shown in figure (6.20) for six different wall-normal locations. In the previous chapter (5) it was already discussed that these pdf are varying with distance to the wall. Whereas in the outer layer the *teardrop* shape known from homogeneous isotropic turbulence is recovered, the shape of the pdf's iso-lines become more oval

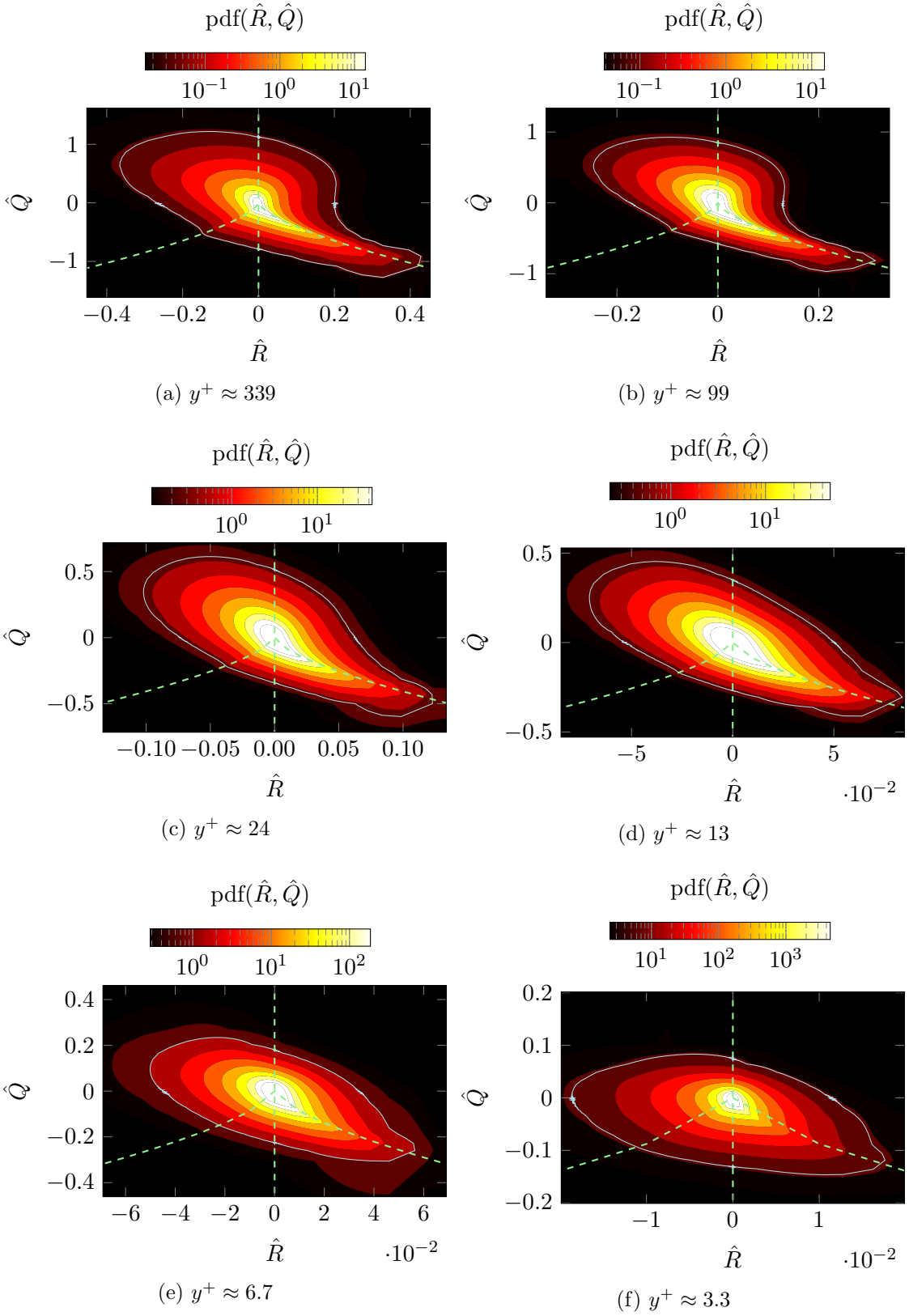

(a) $y^+ \approx 339$ (b) $y^+ \approx 99$

(c) $y^+ \approx 24$ (d) $y^+ \approx 13$

(e) $y^+ \approx 6.7$ (f) $y^+ \approx 3.3$

Figure 6.20: Joint probability density functions for $\hat{Q}$ and $\hat{R}$ at six different wall-normal locations in the boundary layer. The light blue line is the pdf iso-line that is enclosing 95% of all the events.

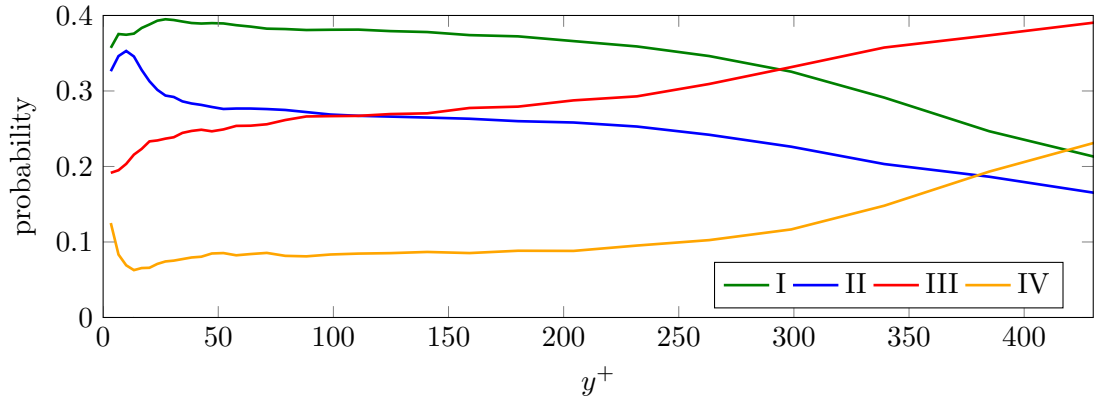

Figure 6.21: Probability of occurrence of the four characteristic structure types I, II, III and IV, plotted over distance to the wall.

shaped and the tilting of the pdf is more and more lost towards the wall. With this development the clearly defined tail of the *teardrop* is lost.
By integrating the pdf over the respective characteristic sectors defined by the critical point analysis, we obtain the probability of a fluid particle being part of a structure of the respective characteristic type. When this is done for every wall-normal location, the development of the characteristic distribution can be plotted over wall-normal direction. In figure (6.21) this development is shown for this turbulent boundary layer. It shows that in the region closer to the wall there is a higher rate of rotational structures (I and II) and a lower rate of pure straining structures. This ratio is changing towards the opposite behaviour when approaching the freestream. So overall it can be stated that the character of turbulence is different in the inner layer compared to the outer layer. Looking at the near-wall region, we find that the probability of occurrence of pure straining structures with elongation character drops in the buffer layer to its global minimum. At the same time the contracting vortical structures show a rapid increase in their probability of occurrence with a peak at a similar location to that of the TKE production. Contracting vortical structures can be vortices that are breaking up. This means that structures could develop from structure type IV to stretching and contracting vortices. This is a hypothesis that will be investigated in more detail in the following.
A logical consequence of the decomposition of turbulence into different structure types is to investigate how these structures contribute to the global picture of turbulence. For this reason we are presenting some key quantities conditionally averaged with the respective QR-states. Due to convergence limitations we have to reduce the QR-space to a subset with a relatively high probability of occurrence. It turned out that the iso-line of the respective pdf that encloses 95% of all the events is a good compromise to separate the significant data from the less accurate data. This iso-line is indicated in the plots in figure (6.20) as light blue line. In other words, 95% of the turbulence at the respective location takes place within the area enclosed by the light blue line. In the following sections, we restrict all conditional statistics to this area and the rest is

blanked out.

6.4 Structural Composition

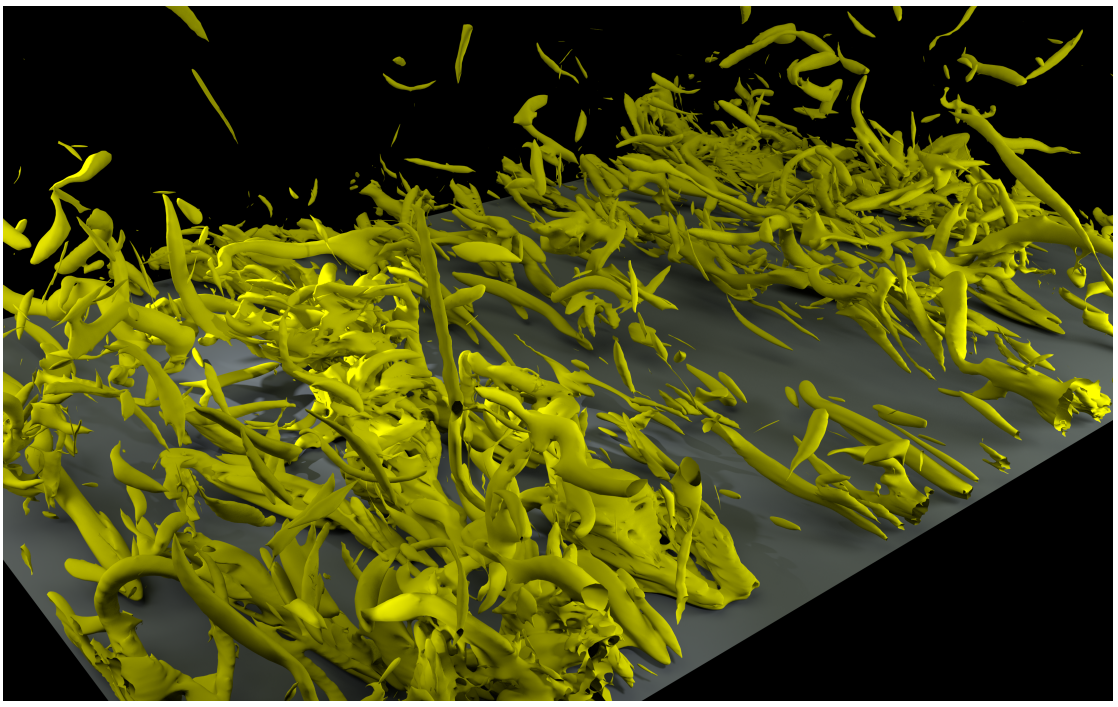

Figure 6.22: Turbulent structures in a boundary layer flow. The wall is coloured in grey, and the turbulent structure in yellow. The flow direction is bottom right to top left and the structures are visualized with iso-surfaces of the velocity gradient discriminant at $\Delta = 100$.

So far the energy budgets as well as the characteristic structure types have been discussed. We have seen that the dynamics in a turbulent boundary layer have various mechanisms, some of which mix the flow and others that lead to the creation of smaller scale structures or dissipate kinetic energy. Further, we know that different characteristic structure types are present in the turbulent boundary layer and that the composition of the different structures in the turbulent flow is varying with the distance to the wall. What is missing to understand the global structure of the flow is how the turbulent structures geometrically compose the boundary layer. An overview of what we discuss in this section is given in figure (6.22). The image shows turbulent structures in a boundary layer visualized with a vortex identification criterion. At first glance the turbulence in this image looks chaotic, but within this section this picture will be cleaned up and logical dynamics in the chaos will be revealed. Already visually two larger structures can be seen in the image. Two structures that are clusters of smaller structures, one of which is in the foreground and starts from the bottom centre and elongates towards the top and tilts slightly towards the left. The second one is in the background and reaches from the mid right towards the top centre. They are both clusters of more compactly packed smaller structures. Whereas the smaller structures are seemingly randomly aligned, the overall clusters are elongated in the stream-wise direction. Further, a gap with a very

little amount of vortical structures is found in-between these two clusters. So in summary we have two large structures that are filled with vortices and an equally large coherent region in-between the clusters that carries almost no vortical structures. This visual impression is quantified in the following.

6.4.1 Laminar versus Turbulent Structures

Firstly, we want to identify a relation between these clusters of turbulent structures and a quantity to identify larger scales of motion. We discussed before (sec. 6.2.3)

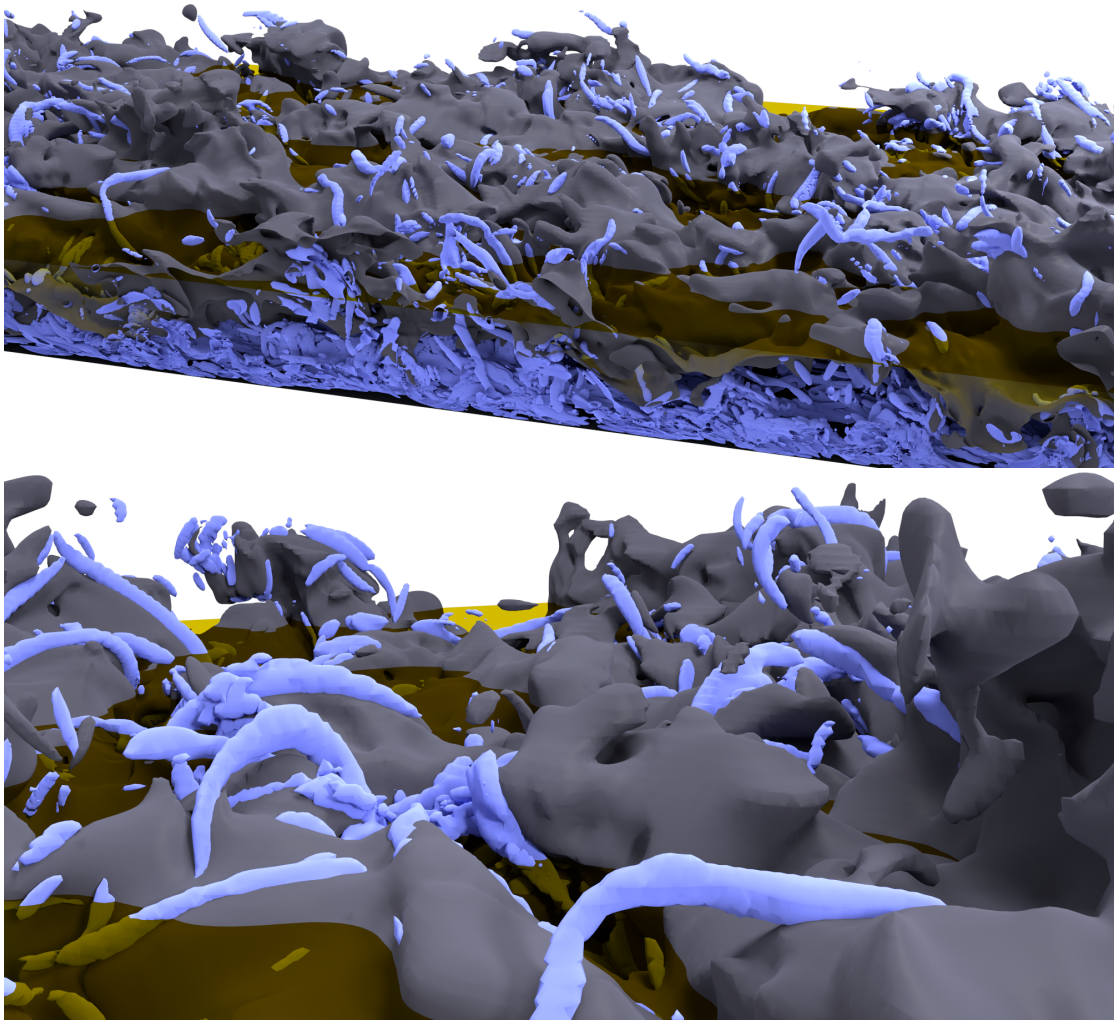

Figure 6.23: An instantaneous snapshot of a TBL is shown from two perspectives. The top shows an overview whereas the bottom is a zoom into the outer layer of the TBL. The wall is shown in dark grey and the flow direction is right to left. The yellow transparent plane shows an iso-surface of the stream-wise mean velocity at $\tilde{u} = 0.85$ and the grey manifold shows an iso-surface of the instantaneous stream-wise velocity at $u = 0.85$. The blue structures are iso-surfaces of the velocity gradient discriminant magnitude at $|\Delta| = 10$.

that the Favre stresses σ_{11} and σ_{12} are covering a relatively high amount of the large scales. A quantity that is involved in both these Favre stresses is the stream-wise velocity component. Therefore we choose u to draw a link between large scales of motion and the clusters of turbulent structures. Figure (6.23) shows turbulent structures and the stream-wise velocity in the same snapshot. The turbulent structures (blue) are shown as iso-surfaces of the velocity gradient discriminant magnitude $|\Delta|$ and form a direct link to the QR-space that we defined in the previous section (6.3). The instantaneous stream-wise velocity component (grey) is shown as iso-surface at $u = 0.85$ and as a reference the Favre averaged stream-wise velocity component is shown as iso-surface at the same level. The latter is shown as a yellow transparent layer. By showing the mean velocity as well as the instantaneous velocity in one plot we can identify regions where the flow field moves faster than the local mean and region where is moves slower. We will describe the regions where the instantaneous u iso-surface is geometrically below the yellow transparent layer, which marks the local mean velocity, as high-speed regions and the areas which are defined by the u iso-surface being geometrically above the yellow transparent layer as low-speed regions. In general we find most of the turbulent structures below the instantaneous iso-surface of u, as many of the structures are in the near-wall region. Spots of turbulent structures at a greater distance to the wall seem to coincide with local low-speed regions. Further, we find some structures on the iso-surface of velocity, but a remarkably small number of structures above the iso-surface of u. This is not directly surprising as the height of the iso-surface is varying with the choice of the value for u and is therefore arbitrary. However, the interesting fact is that even within the high-speed spots, which form sporadically very deep valleys only a very small number of turbulent structures can be found. It seems that the high-speed regions carry a relatively calm flow whereas the low-speed regions carry a relatively turbulent flow. In the previous section (6.3) we mentioned that more calm structures are found around the origin of the QR-space whereas more turbulent structures are found in greater distance to the origin. This property is used to identify the low-speed and high-speed regions in the QR-space. Therefore we sampled conditional averages of the stream-wise velocity component conditioned with the respective QR-state. Hence, for each QR-state we can state the respective mean velocity. Figure (6.24) shows the conditional stream-wise velocity in the QR-space relative to the local overall mean velocity $\tilde{u}$ at two different locations. In the logarithmic layer (a) as well as in the buffer layer (b) it can be seen that close to the origin of the QR-space the stream-wise velocity is relatively high on average whereas at greater distance to the origin the stream-wise velocity is relatively low on average. In other words, the plots allow a fairly obvious distinction between calm high-speed regions and turbulent low-speed regions. This holds for most of the buffer layer, the entire logarithmic layer and the outer layer. Only the viscous sublayer and the lower part of the buffer layer show different behaviour. These results support what we previously discussed about the role of the laminar free stream in the turbulent mixing.

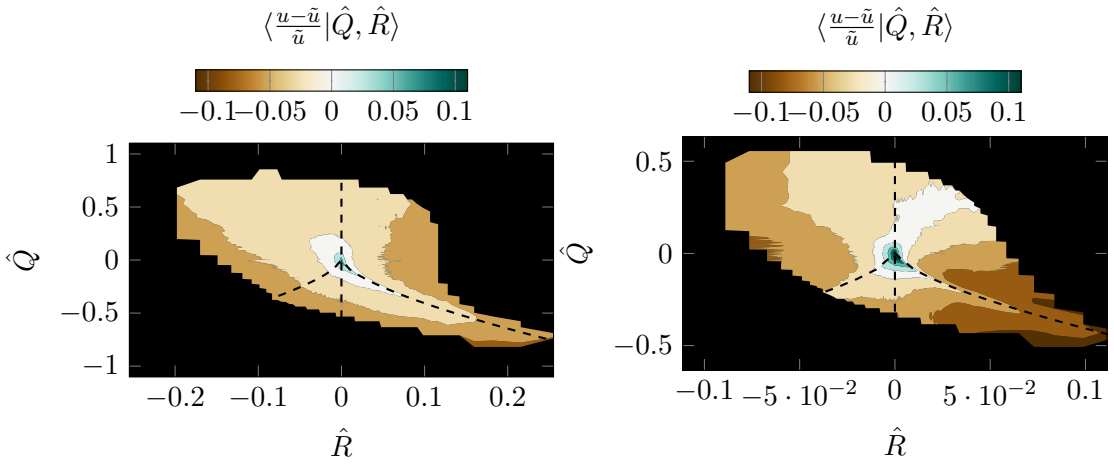

(a) $y^+ \approx 99$ (b) $y^+ \approx 24$

Figure 6.24: Conditional average of the stream-wise velocity component in percentage of the local mean velocity conditioned with the QR-state. The conditional average is shown at two different wall-normal locations.

The fast and calm structures reach from the free stream deep into the turbulent boundary layer and feed it with high momentum fluid. But as figure (6.5) revealed already, the process is not quite reaching the near-wall region. Further, figure (6.24) supports that the turbulent low-speed spots bring low momentum into higher regions. The origin of this lifting of turbulent structures is discussed at the end of this section.
The reflection of the calm high-speed regions in the QR-space allow to refine the characteristic decomposition that was introduced in the previous section. It will be refined specifically to detect the calm high-speed regions as additional state of a characteristic

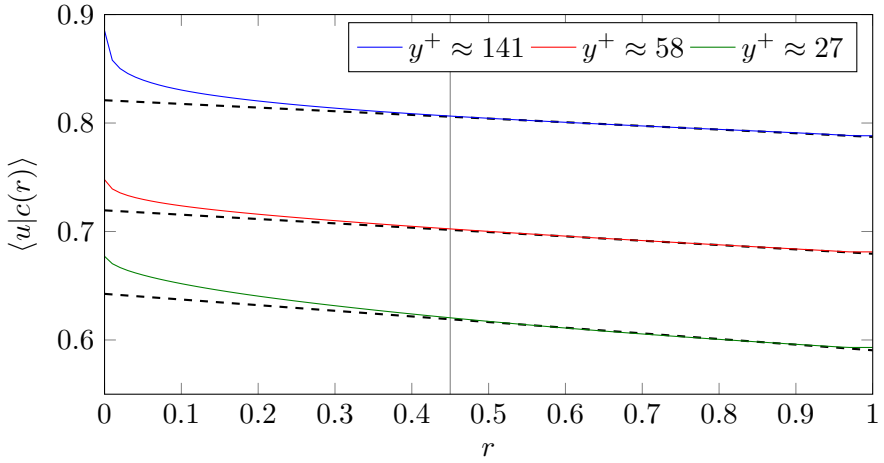

Figure 6.25: Conditional average of the stream-wise velocity component u with the condition (eq. 6.7) at three different wall-normal locations. The dashed lines are straight lines.

structure. The idea is to cut out this additional state as an area around the origin of the QR-space. For this reason we define a condition $c(r)$ that defined as

$$c(r) := \begin{cases} \text{True}: & \text{pdf}(Q,R) \geq p_{\max}(r) \\ \text{False}: & \text{else} \end{cases} \tag{6.7}$$

with

$$p_{\max}(r) := \max! \left\{ p \;\middle|\; \iint_{\text{pdf}(Q,R)>p} \text{pdf}(Q,R) dQ\, dR = r \right\}. \tag{6.8}$$

This condition basically defines the region of the highest values of $\text{pdf}(Q,R)$ that integrate to the probability r. Therefore $p_{\max}(r)$ provides the iso-line of the pdf that encloses the wanted area in the QR-space and $c(r)$ defines a condition that is *True* for all QR-states within this iso-line and *False* for all states outside of the enclosed area. The conditional average of the stream-wise velocity u is shown in figure (6.25) for three different wall-normal locations. The conditional average is plotted over the probability r that indicates the maximum probability $p_{\max}(r)$ of the region that is used to integrate to obtain the conditional average. Besides different magnitudes the average shows similar behaviour for all locations. After an initial relatively strong drop the profiles develop a linear decay with an increase of the ratio. The linear decay starts at about $r \approx 0.45$ which means that the mean velocity is averaged over the most likely 45% of all QR-states. The start of the linear decay is chosen to separate the additional calm state from the remaining characteristic states. This means we split on the basis of a non-linear decay vs. a linear decay of the conditional average $\langle u|c(r)\rangle$ with respect to the probability r. This is based on the assumption that the calm canyons that are entrained into the boundary layer are unstable flow regimes and therefore show stronger changes in the averages when the conditions are changed slightly. The turbulent spots on the other hand are mixed out turbulent clusters and are therefore a stable system that represents averages with small changes when the conditions are changed slightly. An example for the new decomposition is shown in figure (6.26). Further, figure (6.27)

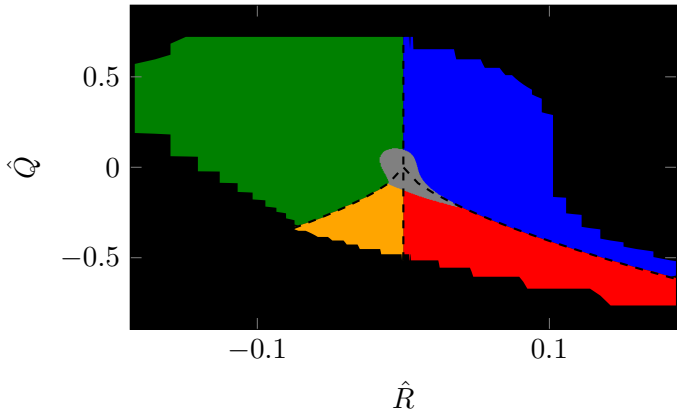

Figure 6.26: Example for characteristic decomposition of the QR-space including the additional calm state. States: calm: grey; I*: green; II*: blue; III*: red and IV*: orange.

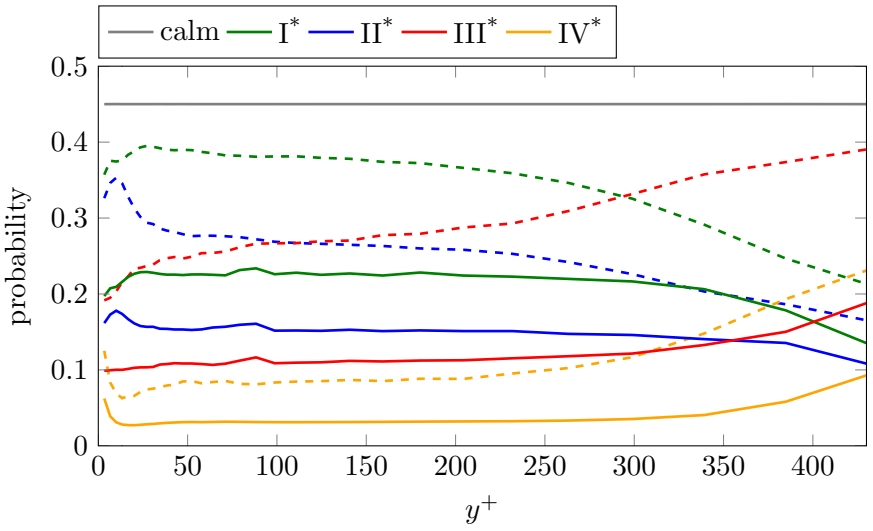

Figure 6.27: Probabilities of the characteristic states. Continuous lines are probabilities for the decomposition including the calm state, whereas the dashed lines are the probabilities for decomposition without the calm state.

shows the probabilities of the newly defined characteristic states and allows to compare them with the original states defined by the critical point analysis. Besides the proportional shift due to the split into an additional state that covers constantly 45% of all states no significant changes can be seen. This means that all original structure types have an equal share in the calm state relative to their respective probability. In other words, if an original state has a probability of 10% then it covers as well about 10% of the calm state.

The newly obtained decomposition is applied to sample the conditional mean velocity profiles for the respective states. Figure (6.28) shows the probability density function of the stream-wise velocity for each wall-normal location in one contour plot. Whereas in the logarithmic layer the pdfs show fairly symmetric shapes, they develop a skewed shape in the buffer layer. However, the skewness changes from a positive skewness in the higher regions of the buffer layer to a negative skewness in the lower buffer layer as well as in the viscous sublayer. The Favre averaged stream-wise velocity is plotted on top of the pdfs as black line. It can be seen that the average does not coincide with the most likely value of u. Besides the skewness this is another indication that the mean is composed of a superposition of different states. This becomes obvious when the mean velocities conditioned with the respective characteristic states are studied. As the conditional averages of u conditioned with the QR-states (fig. 6.24) already suggested is highlighted across the entire turbulent boundary layer in figure (6.28).

In the outer layer and in the outer buffer layer region the calm structures are faster then the turbulent structures. Further, the calm structures seem to follow better the most likely value of the pdfs of u than the actual Favre average does. This is an indication that the calm periods are lasting longer than the turbulent periods. On the other hand,

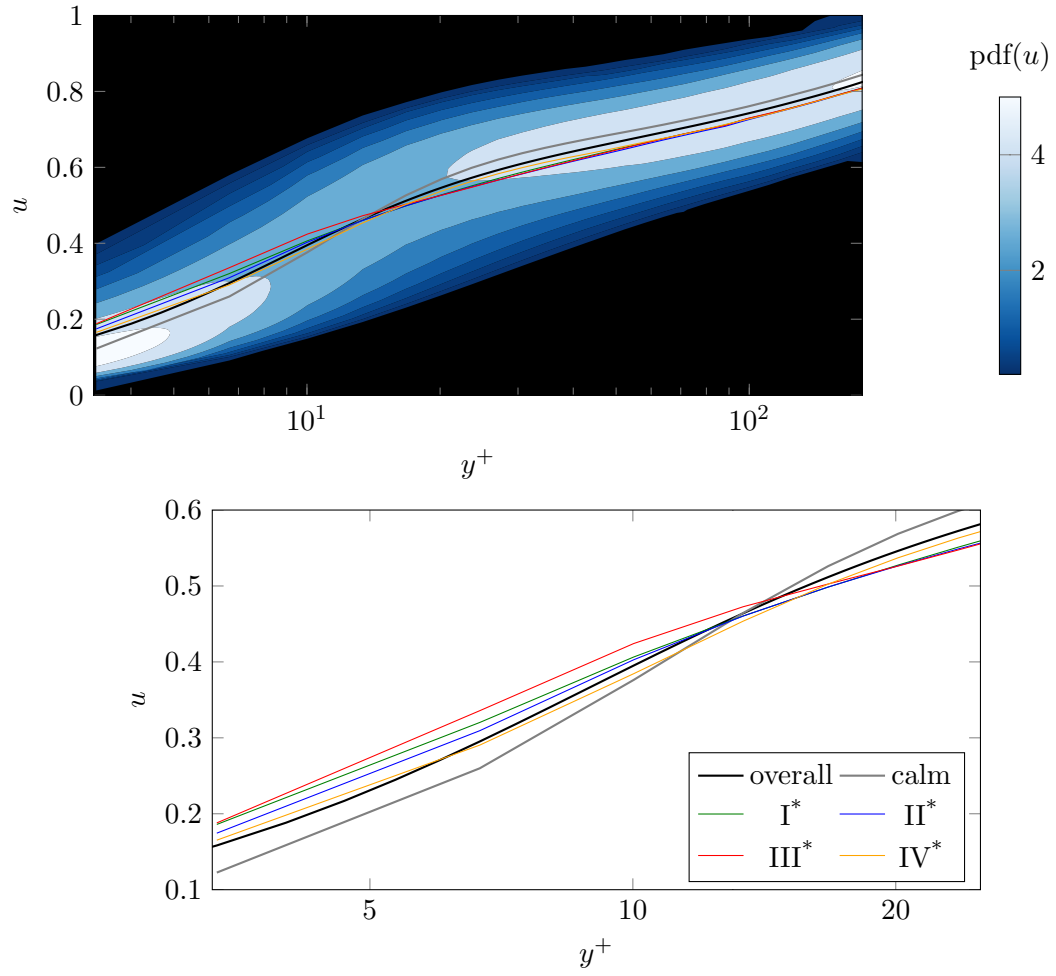

Figure 6.28: Top: Probability density function of stream-wise velocity over wall-normal location. The black line shows the Favre averaged mean, whereas the grey and coloured lines show the conditional averages for the respective states. Bottom: Zoom into the profiles in the near-wall region.

the conditional velocities for all turbulent characteristic states are matching in the logarithmic layer. This sounds plausible as the turbulent spots cover all types of turbulence which are represented by the characteristic states so they all come together as a package (or cluster). When moving towards the wall, the behaviour of the calm structures being faster than the turbulent structures flips at about $y^+ \lesssim 15$ and remains reversed within the viscous sublayer. The interpretation of this fact is yet unclear. Essential for an interpretation of this flip is to understand if the calm-turbulent decomposition of the QR-space is meaningful at such short distance to the wall. If so it might be interpreted in the opposite way, that calm regions lift from the slow viscous sublayer as turbulent structures are suppressed by the wall in that region. But these are speculations that need further investigations.

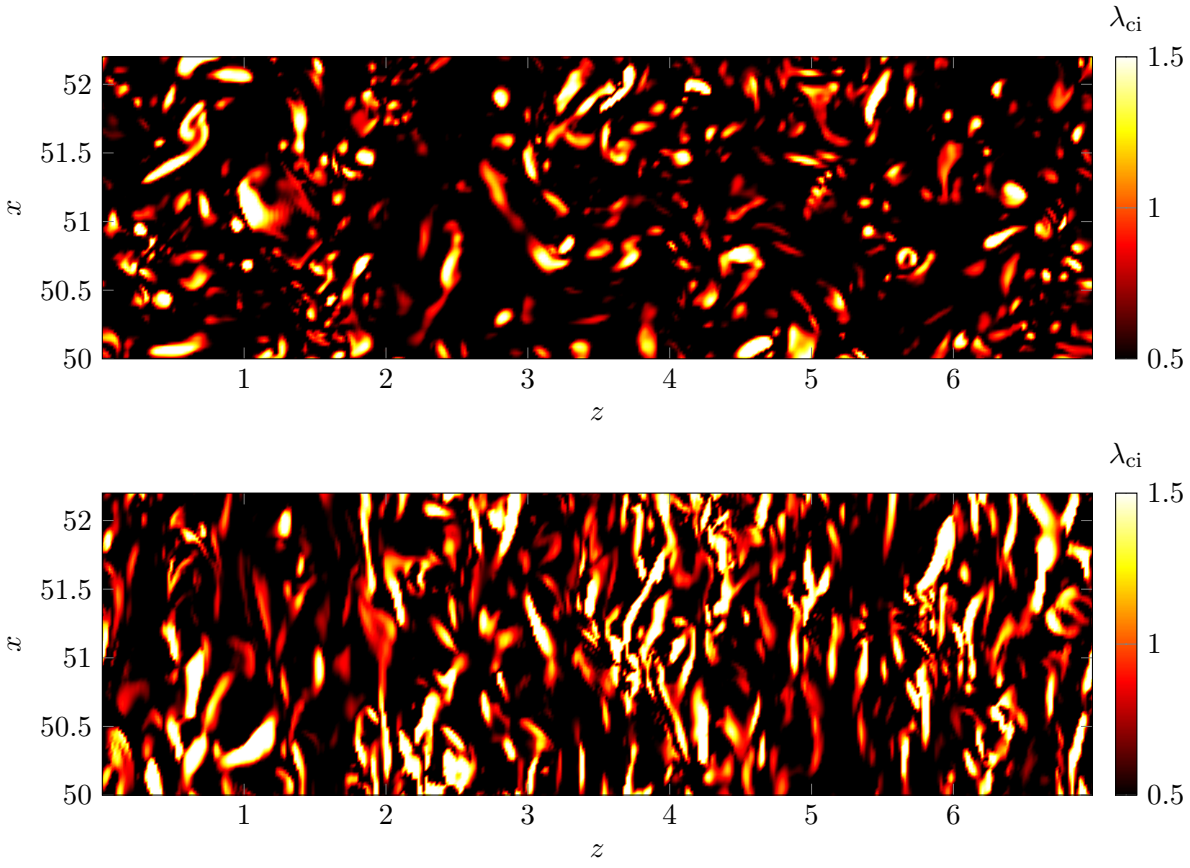

Figure 6.29: Top view onto a boundary layer. The instantaneous snapshots of the λ_{ci}-criterion are taken at the same instance of time at two different heights in the boundary layer. The top is a location within the logarithmic layer ($y^+ \approx 114$) and the bottom shows a location at the lower part of the buffer layer ($y^+ \approx 11$). The flow direction is bottom to top.

6.4.2 Alignment of Structures

Another aspect of the geometrical composition of structures in a turbulent boundary layer is their alignment. The alignment with respect to the wall as well as with respect to each other. The change of this alignment within the boundary layer was already emphasized in the initial description of this turbulent boundary layer case as it is a visually dominant feature of the vortical structures. To highlight the key points again, figure (6.29) shows the top view of slices of a boundary layer at two different heights. In the buffer layer a clear stream-wise alignment has been developed by the vortical structures. Contrasting this, the structures in the logarithmic layer have a seemingly more random alignment. Additionally, the structures in the near-wall region create a more ordered formation that allows much denser packing and the structures are much closer to each other. The alignment is studied in this section, but investigations on the dense packing cannot be made as a non-local quantitative analysis would be needed which has not yet been carried out.

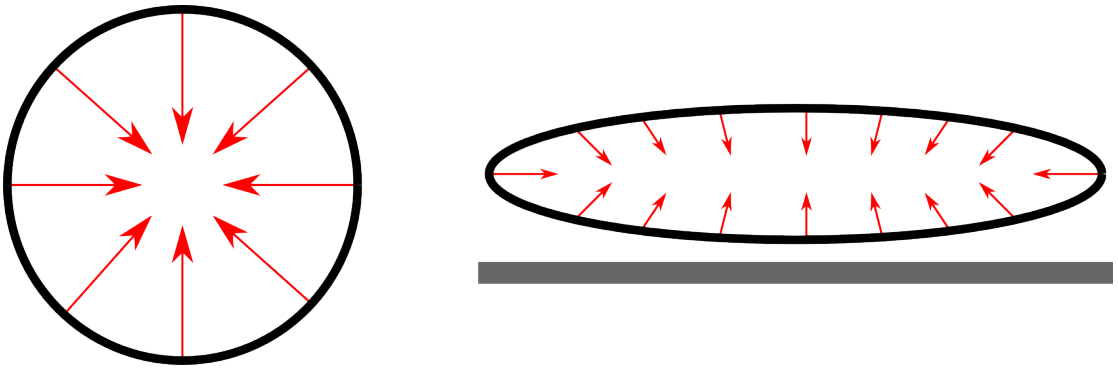

Figure 6.30: Cross sections of schematic vortices. Iso-lines of Q are shown in black and the direction of the gradients ∇Q is shown as red arrows. The left image represents a freely developed vortex whereas the right image shows a vortex squeezed at the wall with the wall shown in grey.

To explain the following analysis, figure (6.36) will help to understand the quantity that is used to investigate the alignment of the vortical structures. Vortex cores, of vortices defined by the Q-criterion, are local maxima of Q itself. Further, the gradient of a quantity always points in the direction of the locally steepest increase of the quantity. For a relatively smooth vortex that means that the gradient of the second invariant ∇Q of the velocity gradient points towards the vortex core. Figure (6.36) shows cross sections

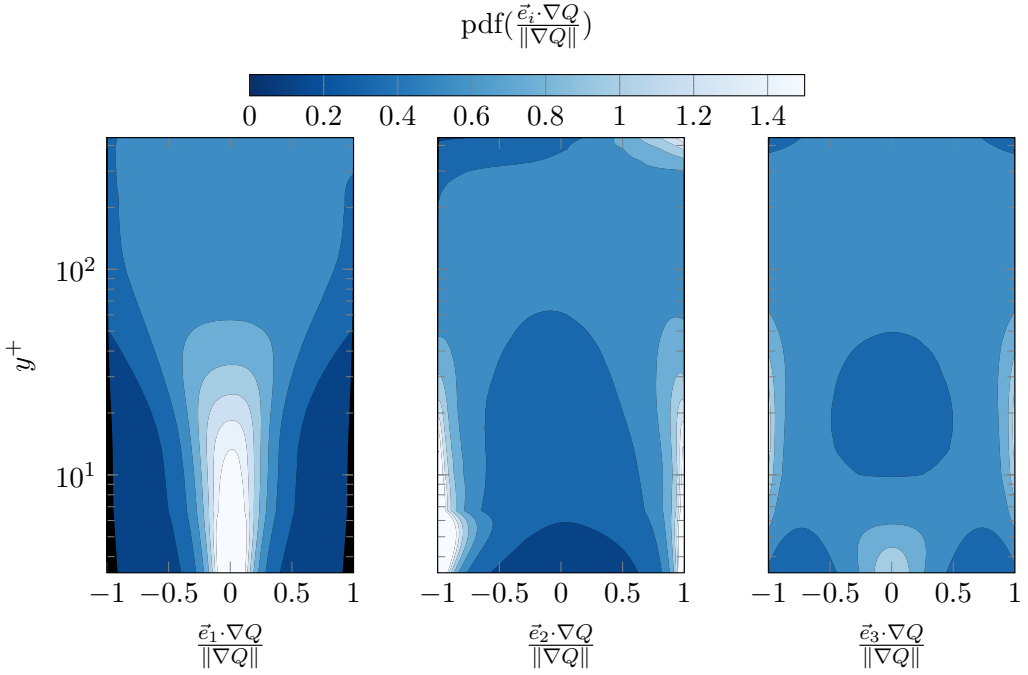

Figure 6.31: The alignments of Q structures with the Cartesian coordinate system is shown via pdfs of the respective alignment for every wall-normal location plotted in one plot, respectively. Left: alignment with the stream-wise direction; centre: alignment with the wall-normal direction; right: alignment with the span wise direction. Black patches indicate the end of the sampling areas.

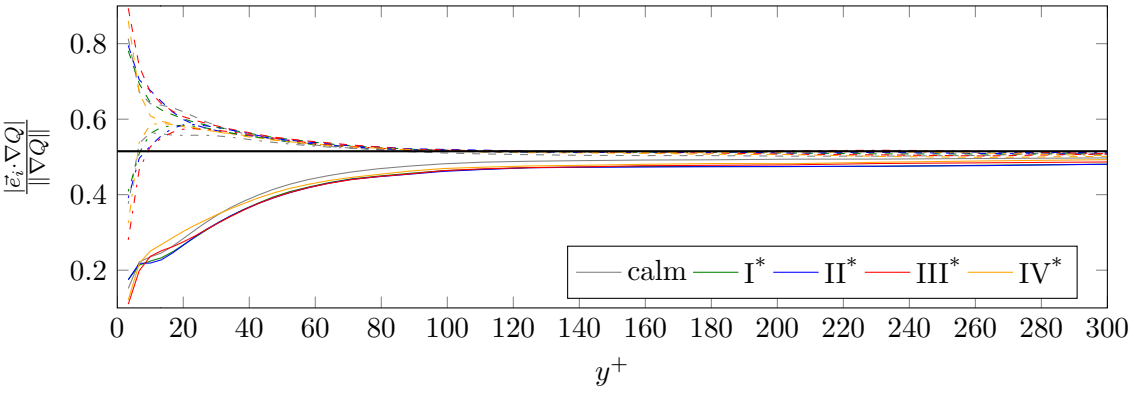

Figure 6.32: The conditional average of the magnitudes of the alignments of ∇Q with the Cartesian coordinate system conditioned with the respective characteristic states. Continuous lines show alignment with the stream-wise direction, the dashed lines show the alignment with the wall-normal direction and the dashed-dotted lines show the alignment with the span-wise direction. Black line indicates mean value for an arbitrarily aligned vector in the three dimensional space.

of idealized vortices. The vortices are elongated along their rotation axis which is the paper-normal direction. On the left it is shown how ∇Q is aligned in a vortex with a perfectly circular cross section. On the right a cross section of a vortex that is squeezed by its proximity to the wall can be seen. Such squeezed vortices were identified when visually studying snapshots of turbulence directly at the wall. Similar constructions are seen as well for some vortices slightly lifted from the wall that developed a footprint on the wall.

Figure (6.31) shows the alignment of the gradient of the second invariant ∇Q with the Cartesian coordinate system. This alignment was sampled as pdfs for every location respectively which are plotted as contour plot over the wall-normal distance. The data shows that the vortical structures are arbitrarily aligned with any direction in the logarithmic layer. This reflects what can be seen in instantaneous snapshots of vortex identification criteria. Moving into the buffer layer a preferred orthogonal alignment of ∇Q with the stream-wise direction $\vec{e}_1$ developed. At the same time the tendency towards a parallel alignment between ∇Q and the wall-normal $\vec{e}_2$ and span-wise $\vec{e}_3$ direction, respectively, grows. This means that the vortex axis develops a preferred parallel alignment with the stream-wise direction. In the viscous sublayer additionally a preferred orthogonal alignment between ∇Q and the span-wise direction is developed. This can be interpreted as the mentioned flattening or at least as the footprint of wall-attached stream-wise aligned structures. It is yet unclear how to interpret the alignments in the very high regions of the outer layer. At these locations the turbulence levels are relatively low and the impact of rare events on the sampled pdfs might be fairly high. Overall it is to say that the quantitative results about the alignment match the visual impression that we got from the turbulent boundary layer. In figure (6.32) the conditional mean alignments are shown for the five characteristic structure types. In this plot the averages

of the absolute value of the alignment are shown as otherwise some of the effects are cancelling out due to symmetries in the pdfs. Overall it can be seen that all structure types behave similar as all structure types show a similar mean orientation across the whole boundary layer. The expected value for an arbitrary alignment is indicated by the black line. The mean value underlines again what we have seen already in the pdfs (fig. 6.31), that the structures in the outer layer are arbitrarily aligned with the coordinate system. A preferred parallel alignment of the rotation axis with the stream-wise direction is developed below $y^+ \approx 120$ and is increasing with decreasing distance to the wall. Consequently the value of $\frac{|\vec{e}_i \cdot \nabla Q|}{\|\nabla Q\|}$ for the other two directions increases in the same way which means at the rotation axis of the structures are less aligned with those directions on average. However, between $y^+ \approx 20 - 30$ the behaviour is changing and $\frac{|\vec{e}_3 \cdot \nabla Q|}{\|\nabla Q\|}$ drops quickly which leads to a nearly full alignment of ∇Q with the wall-normal, direction on average. The following shows that this is due the structures being attached to the wall in this region. This causes the mentioned footprint of structures and/or flattening of the vortical structures at the wall. To discuss this further figure (6.33) shows the span-wise mean value of the stream-wise vorticity component ω_1. The wall is situated at the bottom of this image and the mean flow direction is the positive x-direction. In the upper layers we find random spots of stream-wise vorticity, but no clearly coherent structures can be identified. On the other hand, coherent structures that are attached to the wall are present in the entire plotted section of the image. They all have a thin foot close to the wall that reaches relatively far upstream. Their head then lifts off the wall and reaches into higher layers. Most shown attached structures seem to reach up to a height of about $y^+ \approx 20 - 30$, which coincides with the location where the absolute alignment (fig. 6.32) starts to change significantly.
This leads to a look from another perspective on the near-wall region (fig. 6.34). This

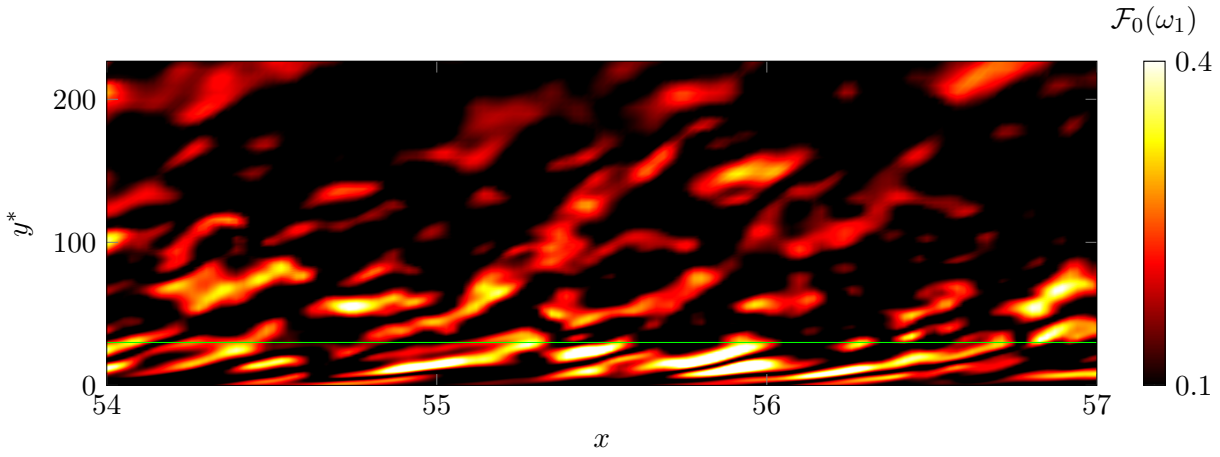

Figure 6.33: Instantaneous snapshot of the span-wise zero-mode (span-wise mean) of the stream-wise vorticity component. Wall is at the bottom and flow direction is x. The green line indicates $y^* = 30$. The scaling for the wall-normal direction y^* corresponds to the usual wall-scaling y^+ at the streamwise center of the plot.

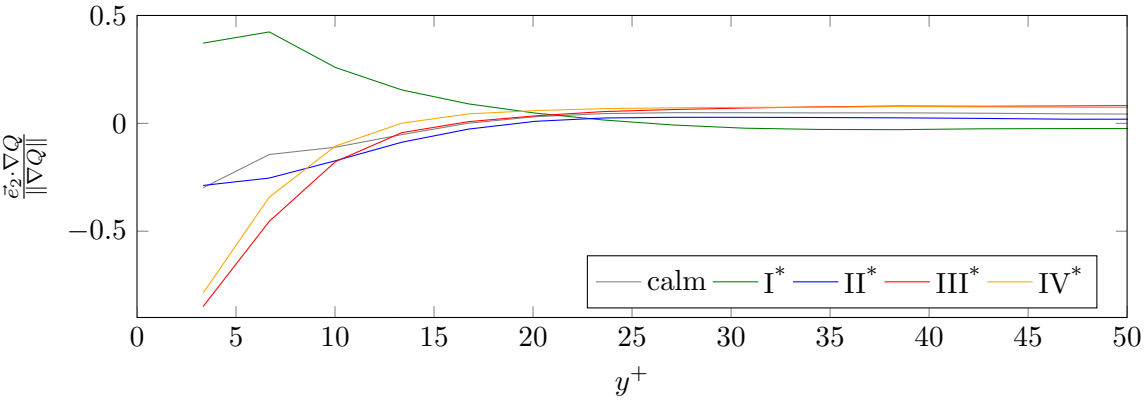

Figure 6.34: Conditional average for the alignment of ∇Q with the wall-normal direction $\vec{e}_2$ conditioned with the 5 characteristic structure types.

figure shows the development of the alignment of ∇Q with the wall-normal direction for the different characteristic structure types in the viscous sublayer and the buffer layer. Unlike for the averages of the absolute values we find differences for different structure types. Whereas for larger distances to the wall all structures are behaving similarly, the development starts to split below $y^+ \approx 20 - 30$. On one hand pure straining structures develop a strongly negative parallel alignment and on the other hand stretching vortical structures develop a positive parallel alignment between ∇Q and $\vec{e}_2$. On a side note, this is believed to show that pure straining structures are preferred to be below the respective measuring location whereas the stretching vortical structures are found preferably above the measuring location where the respective average value is sampled. This means that

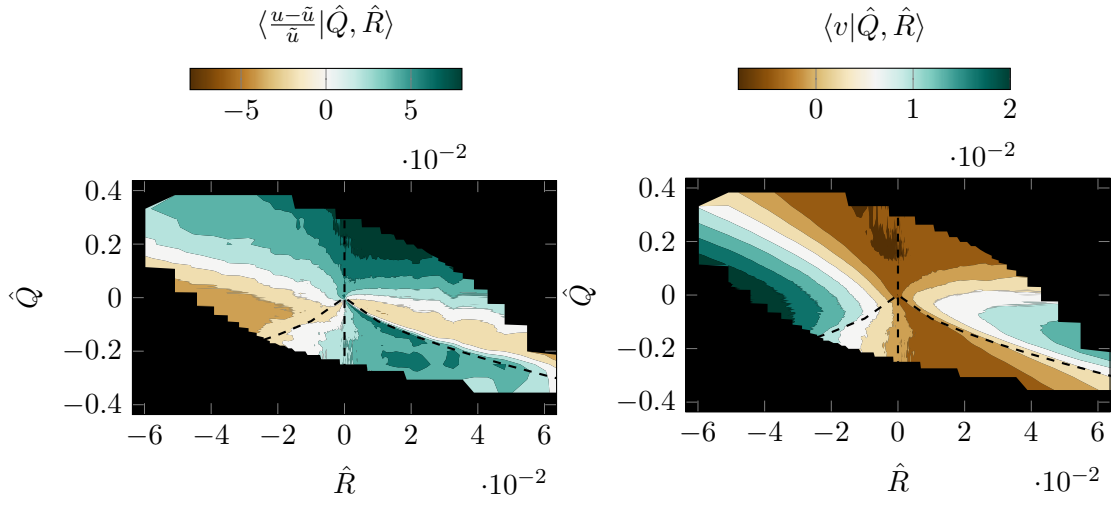

(a) stream-wise velocity

(b) wall-normal velocity

Figure 6.35: Conditional averages of stream-wise and wall-normal velocity at $y^+ \approx 13$, conditioned with the respective QR-states. The stream-wise velocity is shown relative to the overall Favre averaged stream-wise velocity and normalized by the same.

the respective structures have a straining foot on the wall and are lifting as soon as they develop a rotational character. This is the same principle as for the mechanism that forms hairpin structures.

These results suggest another plot is needed to understand the straining and lifting a bit better. In figure (6.35) the stream-wise and wall-normal velocities are shown conditioned with the QR-states. The stream-wise velocity is shown compared to the local stream-wise mean velocity. It can be seen that the pure straining structures in sector III are formed by relatively fast structures that are pushed at the wall as the plot for wall-normal velocity suggests. As soon as the structures become rotational (sector I) they slow down and lift up. This is indicated by a relatively slow stream-wise velocity and a positive wall-normal velocity in sector I respectively. On the other hand we find fast contracting rotational structures that move slightly towards the wall. These are believed to be structures from higher layers being attached or starting to attach to the wall.

6.4.3 Conclusions about the Geometrical Structure of a TBL

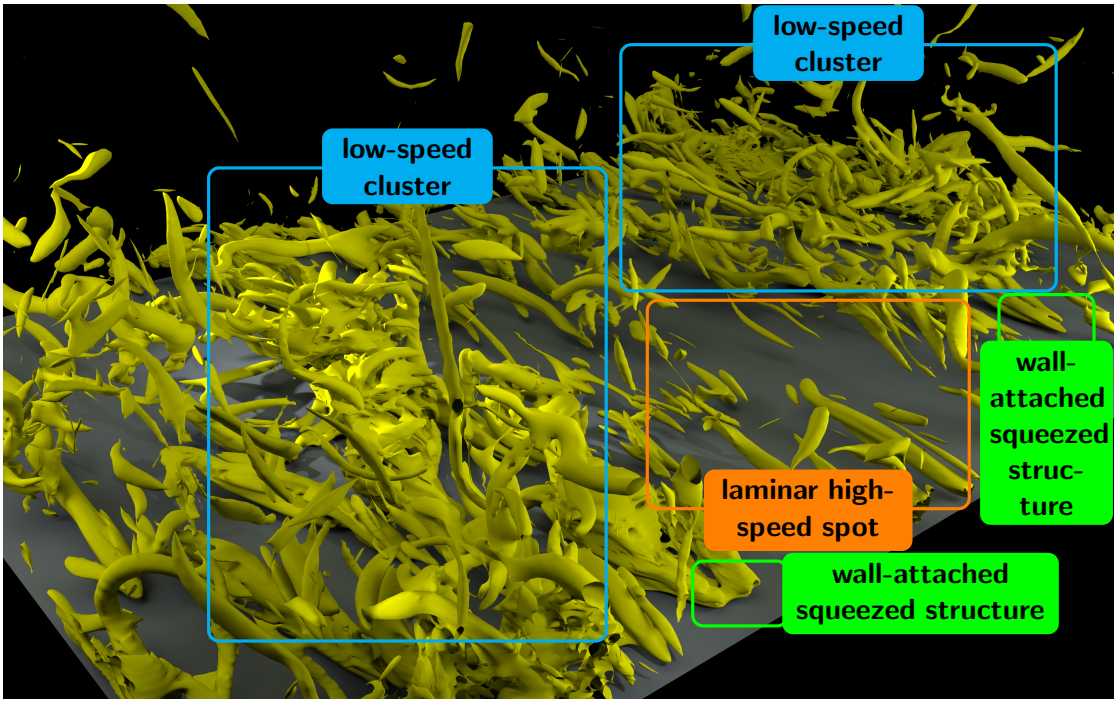

We have seen how turbulent structures start as straining structures at the wall, then begin to rotate and lift towards higher layers. This is a similar, if not the same, mechanism that drives hairpin structures to grow an arc that lifts off the wall. This is most likely not the only mechanism that produces vortical structures in a boundary layer, but certainly one of them. However, it could be the mechanism that triggers the lifting of the low-speed turbulent spots. At least it will contribute to their lifting. While turbulent structures stay in the near-wall region they are mainly aligning in the stream-wise

direction and packed densely as we have seen qualitatively. On the other hand we have identified that turbulence reaches from the wall to higher layers. This happens in relatively slow clusters of single vortical structures. Within these clusters the single vortices are arbitrarily aligned as soon as they reach a large enough distance to the wall. These clusters can reach from the wall up to the outer layer of the turbulent boundary layer. The fluid surrounding these structures is mostly calm and presumably entrained from the free stream. This describes the geometrical structure of calm-turbulent mixing in a flat-plate zero pressure-gradient turbulent boundary layer flow which, as we have seen before (sec. 6.2.3), is the strongest influence that turbulence has on the large-scale flow. In general it is to say that according to alignments as well as velocity distributions the boundary layer could be split into an outer layer above $y^+ \approx 20 - 30$ where we believe to find the laminar free stream entraining into the turbulence boundary layer. In this region the mechanisms stay relatively constant. The other part of the boundary layer is the near-wall region. This region hosts the main production region, and the mechanisms have a much more complex dependency on the distance to the wall.

6.5 Role of Pressure

The previous sections aimed to help understand the structure of the turbulent boundary layer, show how it is composed and which mechanisms are driving the flow to this composition. In this section we have a more detailed look onto local mechanisms that work on turbulent structures. More specifically we discuss how pressure is involved in turbulence and how the wall affects this role of pressure.
To give a general understanding about the role of pressure it helps to consider the inviscid form of the momentum transport equation in Lagrangian form, i.e. we follow a fluid particle

$$\frac{d\rho\vec{u}}{dt} = -\nabla p. \tag{6.9}$$

In this form the similarity of the momentum transport to the equation of motion for a particle becomes obvious. For now we interpret a fluid particle as a particle in motion that is governed by the single external force which is described by the pressure gradient $-\nabla p$. In the next step we develop an understanding for the pressure that governs the movement of the defined particle. Therefore we take the divergence of the incompressible momentum equation. This leaves us with the simple equation that describes the Laplacian of pressure as a function of the second velocity gradient invariant Q

$$-\Delta p = -2Q. \tag{6.10}$$

It is in fact a Poisson equation and if we make a third simplification, that the considered domain is unbounded in $\mathbb{R}^3$, then the general solution for this pressure Poisson equation is

$$p(\vec{x}) = \iiint_{\mathbb{R}^3} -2Q(\vec{y})\frac{1}{4\pi}\frac{1}{\|\vec{x}-\vec{y}\|}d\vec{y}. \tag{6.11}$$

In other words, the pressure is noting else but a convolution of the fundamental solution

Figure 6.36: Cross sections of a schematic vortex. An iso-line of Q is shown as red line and an iso-line of p is shown as blue line. Left: The direction of the gradient ∇Q is shown as red arrows and the direction of the gradient ∇p is shown as blue arrows. Right: The centrifugal force acting on a fluid particle following the iso-lines is shown as red arrows and the force applied by the pressure gradient is shown as blue arrow.

of the Poisson equation with $-2Q$. This means the pressure can be seen as filtered version of Q with the fundamental solution as filter kernel.
We now know from literature (e.g. Chakraborty *et al.*, 2005) and previous discussions in this work about the velocity gradient invariants, that vortices have high values of Q in their core whereas the fluid is swirling around this local maximum of Q. From the simplified pressure-momentum coupling we can see (eq. 6.11) that the vortex core carries a local pressure minimum as well. This pressure minimum is discussed as well in literature (e.g. Jeong & Hussain, 1995). In figure (6.36) the cross section of a schematic vortex is shown via iso-lines of pressure as well as iso-lines of Q. On the left, the direction of the respective gradients is shown. The red arrows show the direction of ∇Q whereas the blue arrows show the direction of ∇p. On the right, we can then see the forces that act in this vortex. Going back to the particle we know that a moving particle does not stay on a circular movement without forces acting on it. Equation (6.9) states that the pressure force (blue) will act against the centrifugal force (red) and therefore keeps the particle on its circular trajectory. With this schematic view of vortices we can discuss two features of the pressure that are important to turbulence. On one hand, the pressure is acting as a reservoir of energy and is the link between internal and kinetic energy during vortex stretching and vortex breakdown (sec. 6.5.1). On the other hand, pressure forces stabilize rotational motions and allow vortices to exist (sec. 6.5.2). Additionally, distinct QR-states are pointed out as main contributor to the pressure fluctuations in the turbulent boundary layer (sec. 6.5.3).

6.5.1 Pressure as Storage of Potential Energy

From the governing equations for the internal energy and the kinetic energy (fig. 2.1) we know that there are two processes that transfer energy from one to the other. One is the dissipation of kinetic energy which is the irreversible transfer from kinetic energy into internal energy due to friction force acting on the fluid in motion. Dissipation is discussed in detail in the next section. Here, we focus on the reversible exchange of kinetic and internal energy - the pressure work $\vec{u} \cdot \nabla p$,

$$\frac{d\rho e}{dt} \underset{\leftarrow}{\overset{\vec{u}\cdot\nabla p}{\rightleftharpoons}} \frac{d\rho e_{\mathrm{kin}}}{dt}. \tag{6.12}$$

The energy budgets (sec. 6.2) have shown that the pressure-work is apparently unimportant for the redistribution of energy in the boundary layer. This was shown for the large scales as well as for the small scales of motion. So why do we discuss this term at this stage? Unlike the terms of dissipation, production or turbulent mixing, the pressure work has a spatially local role and a net contribution of nearly zero in a zero pressure gradient low Mach number turbulent boundary layer. However, for the existence and development of turbulence it plays a significant role. Therefore it is passively involved in all processes driven by turbulence.

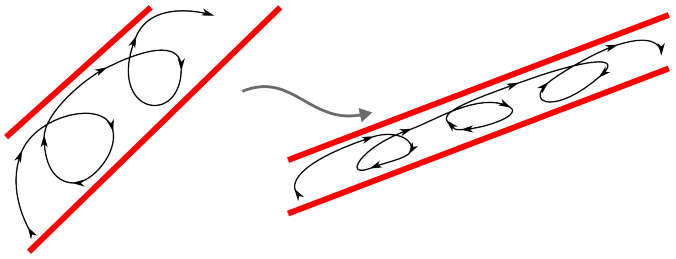

Figure 6.37: Schematic description of vortex stretching. Red lines indicate iso-surfaces of Q and the black lines indicate the motions of the fluid particles.

One of the mechanisms where pressure work is actively involved is vortex stretching combined with vortex destruction. The sketch (fig. 6.37) shows schematically what we mean with vortex stretching. A rotational structure of a given length and width experiences vortex stretching when it elongates along its rotation axis and thins in the other two directions. At the same time the involved fluid particles accelerate. To understand how pressure-work is involved in this, the elongation is not the most important property of this process, but the thinning in combination with the acceleration is. Figure (6.38) shows the conditional averages for the overall as well as the small scale pressure work conditioned with the QR-states and scaled in the same wall-scaling as the budgets shown in section (6.2). We show just the overall contribution as well as the small scale (SFS) contribution of the conditional pressure work as the remaining splittings are nearly identical to what is shown in figure (6.38). The small scale contribution in case of FAS is a simple shift of the overall conditional averages about the mean $-\tilde{\vec{u}} \cdot \nabla \bar{p}$ which is nearly zero in the present flow. The large scales in case of SFS are not showing significant differences to the overall results. Further, the small scales for different filter width are qualitatively the same as (b,d,f), however, the results are scaled down as the energy of the small scales is decreasing with the filter width.
From the definition of the characteristic structure types we know that vortical stretching structures are found in sector I. Focusing on the small scales only (b,d,f) we find negative pressure work in this region. This means that during vortex stretching the pressure work acts favourable for the kinetic energy and transfers energy from internal energy to kinetic energy. In the logarithmic layer (b) we find a mainly neutral contribution from contracting vortices (sector II). But at the intersection of sector II and sector III a sudden increase of pressure work can be found. In this region pressure acts favourable for the internal energy and transfers kinetic energy into internal energy. The region is spreading over the entire sector III and the further we move towards the wall it spreads into the region of contracting vortices.
Figure (6.39) shows a schematic description of our interpretation of what mechanism these plots are revealing. The direction in which the pressure work is transferring energy is defined by the alignment of the velocity vector with the pressure gradient. For a perpendicular alignment we find neutral pressure work, if both vectors are negatively parallel aligned the energy flows from internal energy towards kinetic energy and vice

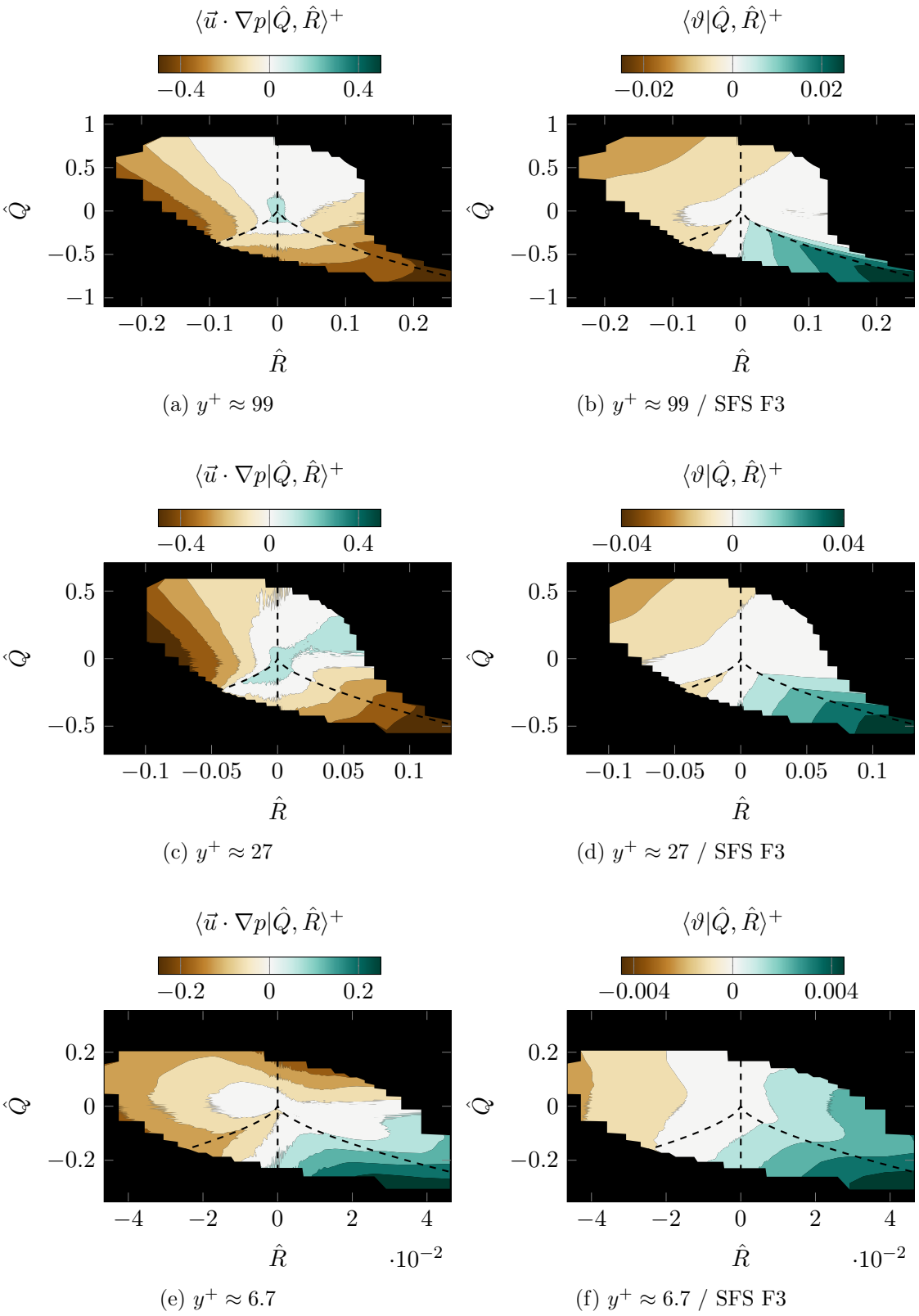

(a) $y^+ \approx 99$

(b) $y^+ \approx 99$ / SFS F3

(c) $y^+ \approx 27$

(d) $y^+ \approx 27$ / SFS F3

(e) $y^+ \approx 6.7$

(f) $y^+ \approx 6.7$ / SFS F3

Figure 6.38: Conditional average of the overall (left) and small scale (right) pressure work ϑ conditioned with the QR-states. The samples are taken at different distances to the wall. The small scales are obtained by spatial filtered based splitting (SFS) for the F3 filter.

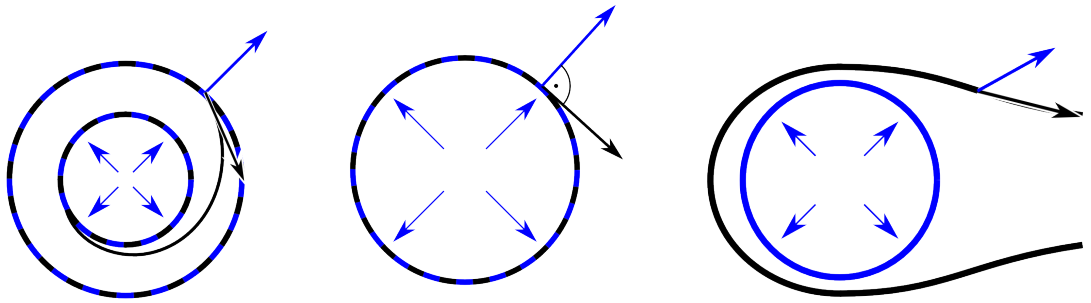

Figure 6.39: Cross sections of schematic structures. Fluid particle trajectories are shown in black and pressure iso-surfaces are shown in blue. The black arrows indicate the direction in which the particle is moving $\vec{u}$. The blue arrows are the direction of the pressure gradient ∇p.

versa if both vectors are positively parallel aligned. Considering a fluid particle in a vortex that is object of a stretching procedure then this particle has to decrease the radius of its circular trajectory. The left image in figure (6.39) shows how such a fluid particle is adjusting its trajectory by moving closer to the vortex core which holds a pressure minimum as explained before. Looking at the alignment of the velocity vector and the pressure gradient in this idealized trajectory alignment, we see that the pressure work will transfer energy from internal energy into kinetic energy. This means that the circular flow is accelerating (kinetic energy increase) which coincides with an increase of Q. As we discussed before, Q is coupled to the pressure via an equation similar to (eq. 6.10) and therefore the pressure in the core is decreasing (internal energy decrease). In this idealized way it is a self sustaining process and the vortex could thin further and further. However, there are many factors that could prevent a vortex from stretching further and further. When a vortex is in a phase where it is not changing its radius, neither the pressure minimum is changing nor is the pressure work contributing anything (fig. 6.39, center). On the other hand, there might be other mechanisms that allow a thickening of vortices with the right pressure redistribution to preserve a neutral pressure work as well. A combination of both is believed to operate in case of QR-states where we find nearly zero contribution of the pressure work. Due to dissipation and interaction with other flow structures or walls the vortices eventually loose kinetic energy which leads to a weakening of the pressure core. If the pressure core becomes too weak or if it gets disturbed in a different way, the vortex is likely to break up along its axis. This scenario is shown in figure (6.39) on the right. It can be seen that as soon as the fluid particles are leaving the core the pressure work is acting favourable for internal energy and the shift due to the vortex stretching is reversed.

The described mechanism is present in the entire boundary layer. However, it seems that in most of the boundary layer the conditioned pressure work can reveal this process just for the SFS pressure work. The left column in figure (6.38) shows the overall contribution of the pressure work conditioned with the respective QR-states. Quantitatively these plots are coinciding with the same plots for the fluctuations around the

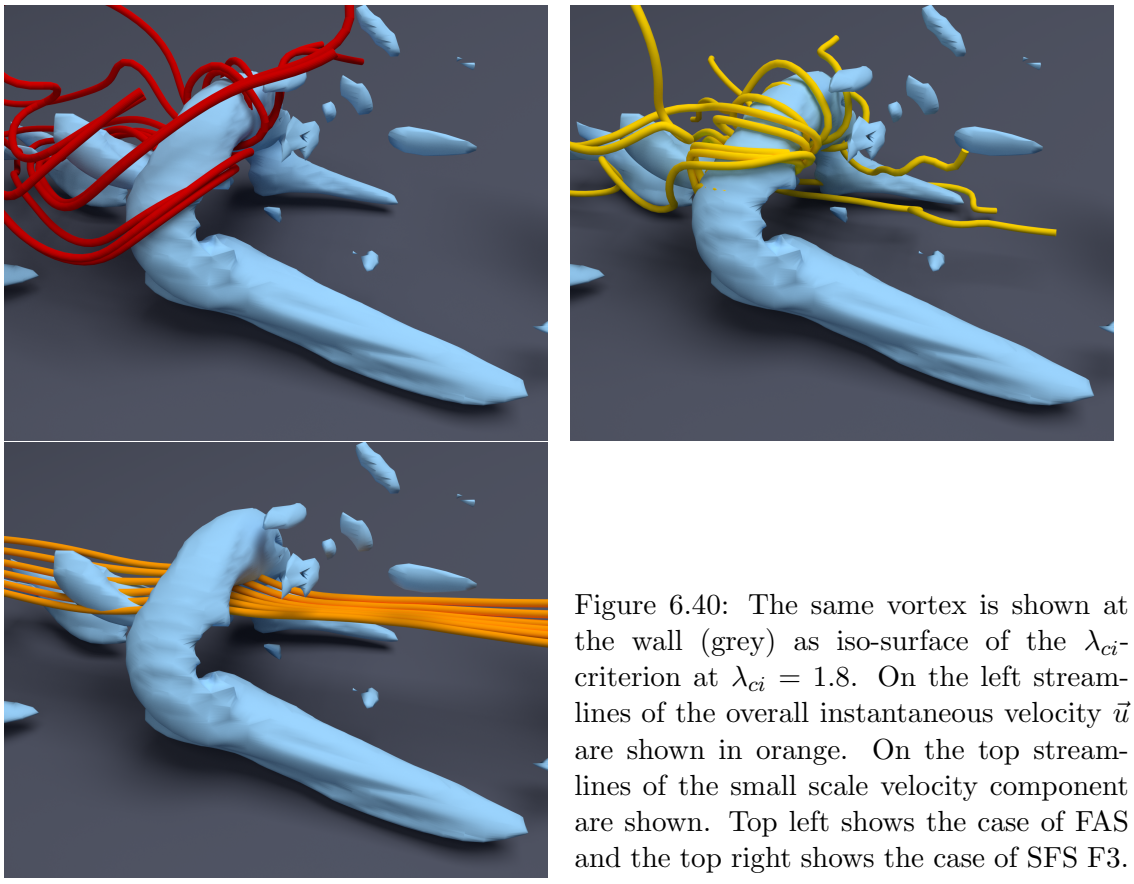

Figure 6.40: The same vortex is shown at the wall (grey) as iso-surface of the λ_{ci}-criterion at $\lambda_{ci} = 1.8$. On the left stream-lines of the overall instantaneous velocity $\vec{u}$ are shown in orange. On the top stream-lines of the small scale velocity component are shown. Top left shows the case of FAS and the top right shows the case of SFS F3.

mean flow contribution. It is not yet possible to doubtlessly describe what the plots are showing. However, the difference to the small scales in case of SFS are believed to be the strong influence of the mean flow and the large scaled temporal fluctuations. Figure (6.40) shows a vortical structure at the wall as well as different stream-lines. It can be seen that the stream-lines for the SFS small scale velocity (yellow) are circulating more or less strictly around the vortical structure - just like we described it in the previous paragraph (fig. 6.39). On the other hand, the stream-lines based on FAS (red) follow the structure to some extent, but by far not as strictly as the SFS ones. Finally, the overall stream-lines (orange) are seemingly not affected by the presence of a vortex. This figure shows that in the case of overall analysis as well as in case of FAS the local velocity vector is strongly affected by the large scale structure, such as e.g. streamwise streaks and/or the mean flow, and not describing the motion of a fluid particle relative to the structure (including its pressure core), which is itself moving with the large scale motion. The results of the overall pressure work nearly recover the effect of the discussed results of SFS in the near-wall region (e). This might be due to the decreased effect of the mean and/or the large streaks in the boundary layer.

As we can see, the pressure is a crucial quantity in the vortex stretching process and related mechanisms. However, some results call for further and deeper analysis to obtain a comprehensive understanding about the role of pressure work.

6.5.2 Pressure as Stabilizer of Vortices

As mentioned before the pressure forces hold the fluid particles on their circular trajectories as they act against the centrifugal forces. Therefore the pressure forces can be seen as stabilizing force for the vortical motions. To study this stabilizing character of pressure in the turbulent boundary layer, the pdf of the alignment of ∇p and ∇Q was sampled for different distances to the wall (fig. 6.41). In the logarithmic layer and in most of the buffer layer a preferred negative parallel alignment can be seen. This, in fact, supports the hypothesis that the pressure forces are working against the centrifugal forces on average. Figure (6.42) shows more quantitatively how this state is pronounced in the logarithmic layer. In the outer layer this preferred parallel alignment is forgotten and the two gradients are more randomly aligned. The reason for this is, just like for the overall alignment in the outer layer (discussed in the previous section), still unclear. It might be caused by the low level of turbulence intensity in this region. However, the preferred negative parallel alignment is stated for the entire logarithmic layer and most of the buffer layer. On the other hand, in the near-wall region below $y^+ < 20$ the preferred parallel alignment is changing towards an orthogonal alignment of ∇p and ∇Q. In the viscous sublayer this preference is strongest. Again, figure (6.42) shows the increased likelihood for the two gradients to align orthogonally in the viscous sublayer. To understand this behaviour better, in figure (6.43) instantaneous snapshots of the boundary layer flow are shown. They show iso-surfaces of positive values of the velocity gradient invariant Q in shades of red and the pressure in shades of blue. The values may change between the different images, but the actual values are not of any importance. The top image shows a scene from the logarithmic layer and outer layer. The two structures in the foreground are in the logarithmic layer whereas the large arc in the background reaches into the outer layer. All mentioned structures show well aligned iso-surfaces for pressure and Q which at the same time indicates that the pressure forces

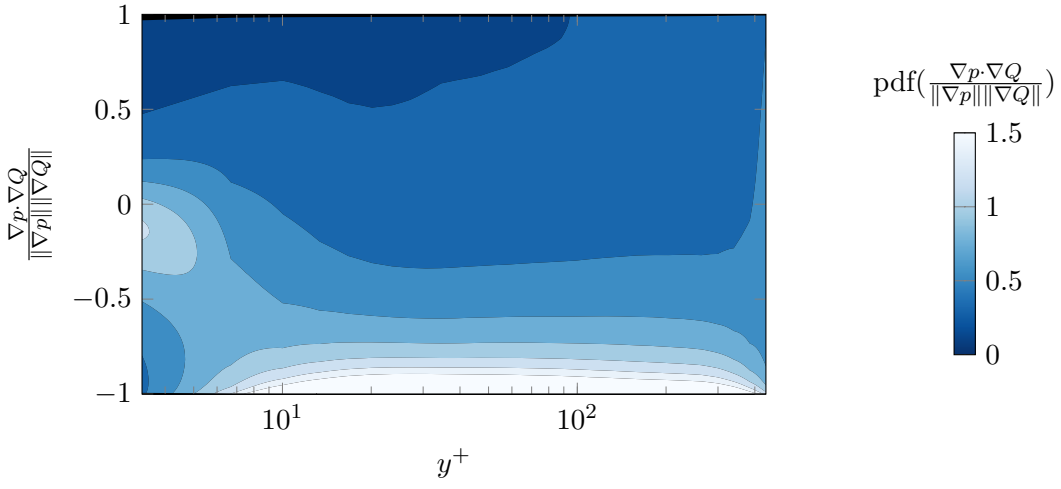

Figure 6.41: Pdfs of the alignment of ∇p and ∇Q for different wall-normal locations.

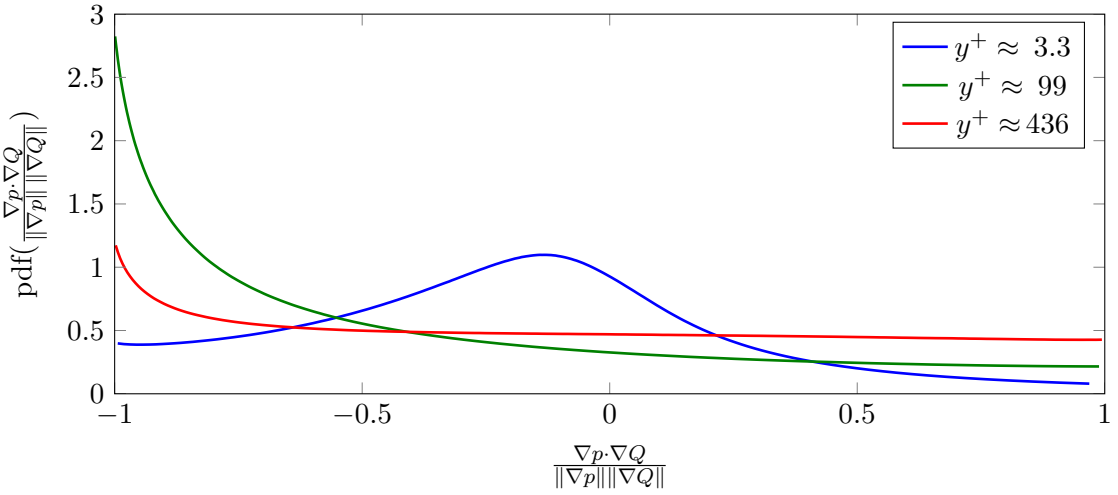

Figure 6.42: Pdfs of the alignment of ∇p and ∇Q at three selected locations.

are aligned with the structure in a stabilizing way. This can be confirmed for the majority of structures that where found in higher layers and not packed in relatively dense clusters. Contrasting that, the structures in the three images beneath visualize a different arrangement between pressure and the velocity gradient invariant. They all show structures relatively close to the wall and the pressure seems to behave differently in this regime. On the left we find a cluster of structures that is very close to the wall. The Q-structures are partly enclosed within the same pressure iso-surface but at other points the pressure planes are cutting through the vortices. At the wall the pressure iso-surfaces develop a foot that is nearly orthogonal to the wall. The image on the right and the image at the bottom show the foot as well as the iso-surface of pressure cutting through the vortices for different scenes and from different perspectives. These images give an idea of what the pdfs show quantitatively.

The mechanism behind this behaviour and possible consequences are described by figure (6.44). As long as the pressure develops a minimum within a rotational structure, the resulting forces are stabilizing the rotational movement of the fluid particles. If rotational structures develop freely then this pressure minimum is created and conserved within the structure. However, this system can be disturbed by the presence of a wall. The pressure iso-surfaces seem to align orthogonally with the wall. This can potentially mis-balance the stabilizing arrangement a vortex needs to survive. Then the iso-surfaces of pressure may misalign with the iso-surfaces of Q. What we have not seen in the data, but what will be investigated in the future is a direct consequence of this. The missing stabilizing character of the forces caused by the pressure minimum in the vortex core causes the centrifugal forces on the fluid particles to take over and the particles will leave their circular trajectories. The structure breaks up on the side where it is attached to the wall. If this is indeed the case, then this would be a suitable explanation for the rotational structures lifting from the wall, which we have seen in the previous section

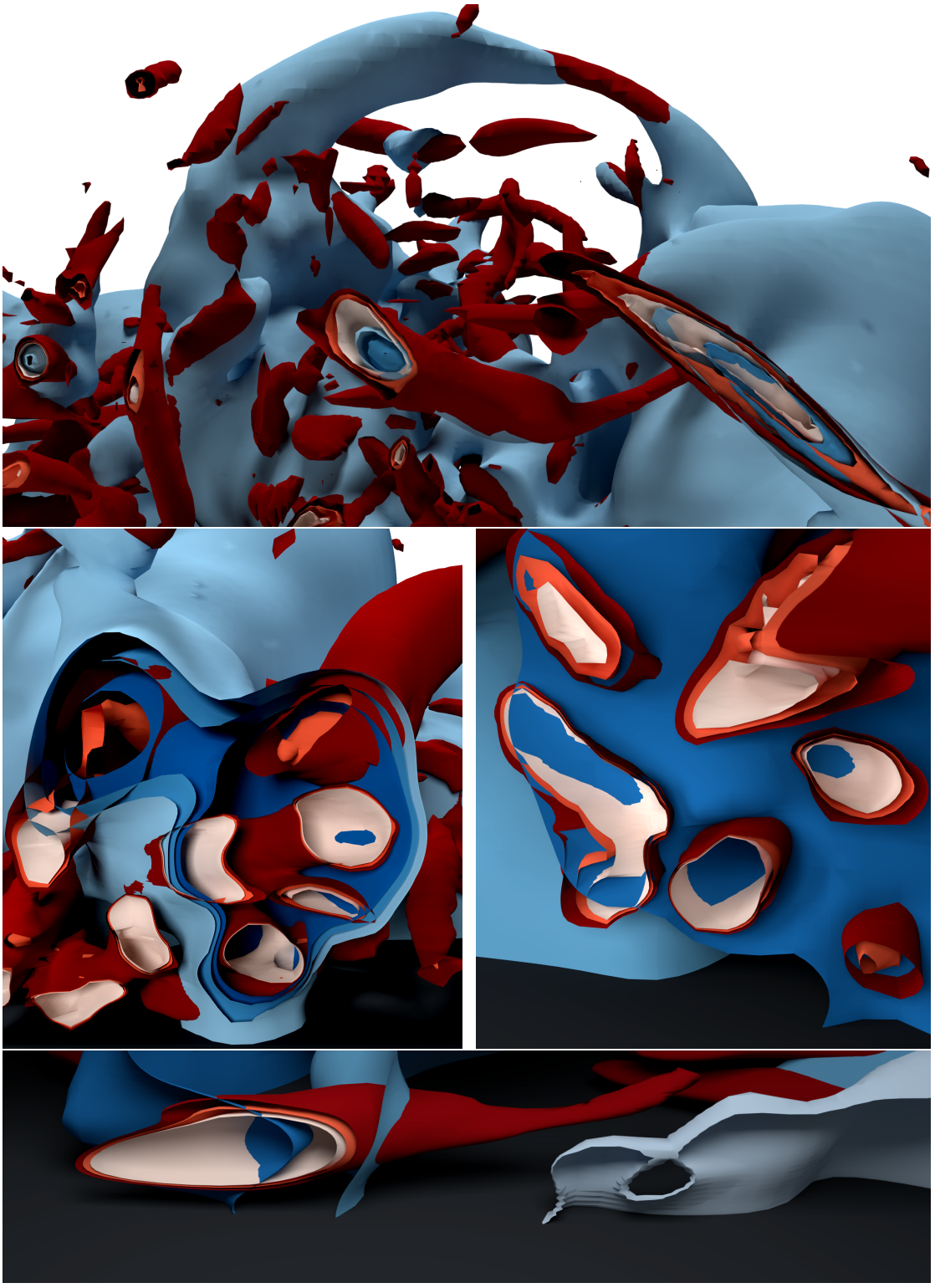

Figure 6.43: The images show iso-surfaces of pressure (shades of blue) and Q (shades of red) in the boundary layer. The top image ($y^+ \approx 115 - 370$) focuses on regions further away from the wall whereas the two images in the middle ($y^+ \approx 0 - 80$) show a region closer to the wall. The image on the bottom ($y^+ \approx 0 - 20$) shows a turbulent structure on the wall. The wall is coloured in dark grey.

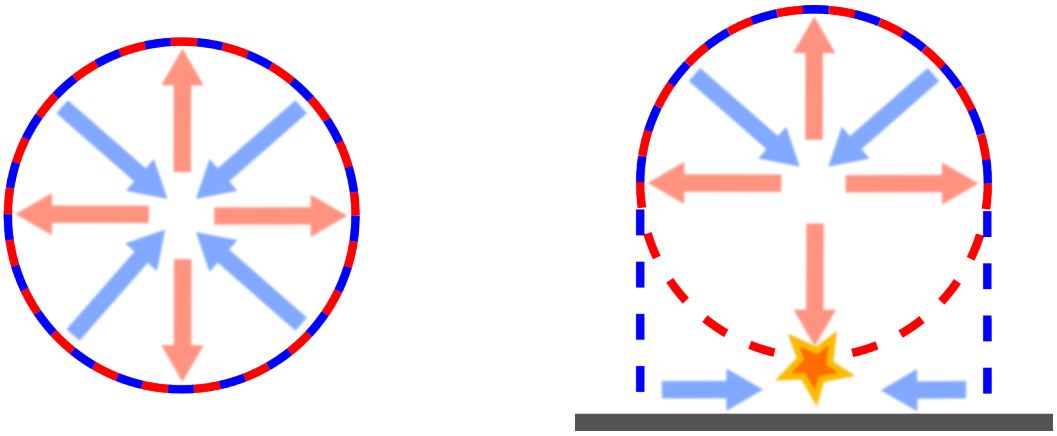

Figure 6.44: Cross sections of a schematic vortex. An iso-line of Q is shown as red dashed line and an iso-line of p is shown as blue dashed line. The centrifugal force acting on a fluid particle following the iso-lines is shown as red arrows and the force applied by the pressure is shown as blue arrows. Left: The vortex is free of any boundary conditions. Right: The vortex' pressure field is affected by the wall. The most unstable location is marked with a spark.

and which is important for the strong mixing effect that turbulence has on the large scale flow.

The effect of the wall destabilizing rotational structures due to attracting their pressure core becomes more obvious when plotting the distribution of the characteristic structure types in this light. Figure (6.45) shows the distribution of characteristic structures according to their frequency of occurrence in the near-wall region. The increase of contracting rotational structures close to the wall is believed to be a direct result of the destabilizing effect of the wall, that we just discussed. This effect has an impact on dissipation as we will see in the next section.

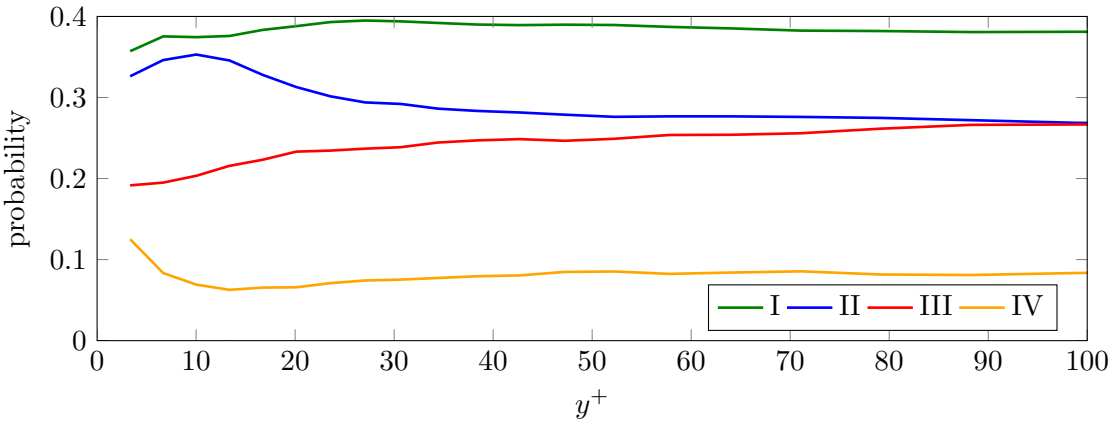

Figure 6.45: Probability of occurrence for the four characteristic structure types I, II, III and IV, plotted over distance to the wall.

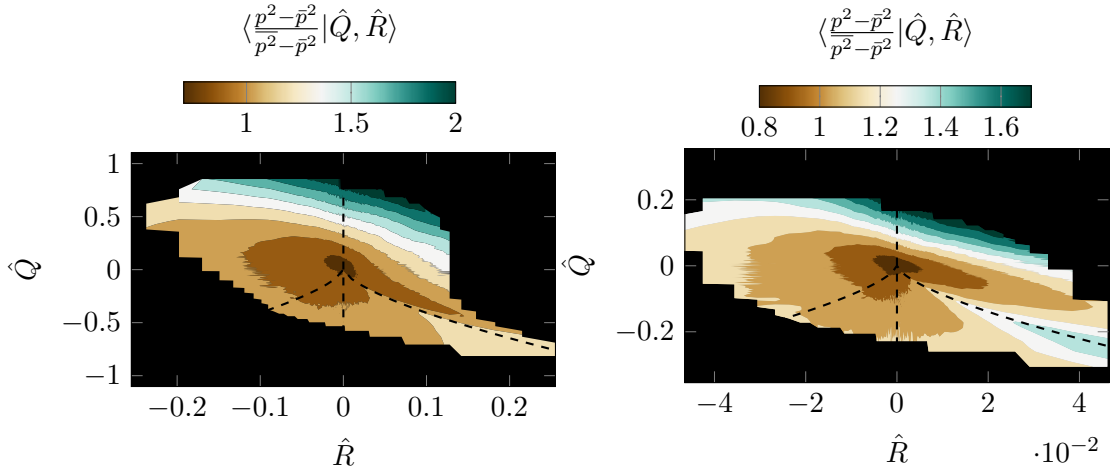

(a) $y^+ \approx 99$ (b) $y^+ \approx 6.7$

Figure 6.46: Normalized pressure fluctuations at two wall-normal locations in the boundary layer, conditioned with the respective QR-states.

6.5.3 Source of Pressure Fluctuations

A process that does not have a strong effect on the turbulence dynamics in a boundary layer, but reflects a potential noise source and might help us to study more about vortex dynamics at a later stage, is the production of pressure fluctuations by vortical structures. Figure (6.46) shows the relative pressure fluctuations conditioned with the respective QR-states. Qualitatively these two plots represent the entire boundary layer. The distribution of the pressure fluctuations is changing in a negligible way. Whereas in most of the QR-space the energy of the pressure fluctuations is relatively balanced and relatively low, we can see a sharp increase for high values of Q in sector I and II. It therefore seems that strong vortices with a stretching character and a contracting character are the main sources for pressure fluctuation. The main events that produce these fluctuations are believed to be the oscillation of strong vortices as well as strongly elongated vortices that snap as they become unstable due to there length-thickness ratio. These interpretations are as yet not supported and need further analysis. However, this is another example for the strong potential of the characteristic decomposition as it allows for this type of analysis.

6.5.4 Conclusions about the Role of Pressure

We have seen that although pressure is not directly influencing the overall energy distribution in this flow, it is a key quantity for the local dynamics of turbulence. Only the stabilizing character of the pressure minima allow vortical structures to exist. Mechanisms that disturb this pressure core can cause an early breakdown of existing vortical

structures. We have seen, that the wall is attracting the pressure core and destabilizes the vortices in the near-wall region. Besides the stabilizing property we found that pressure-work feeds vortices with kinetic energy during vortex stretching, which coincides with an increase of the strength of the structure's pressure core. This kinetic energy is transferred back to internal energy while and after a vortex is being destroyed. So, even if negligible on average, the reversible transfer of kinetic and internal energy is strongly active and of crucial importance for vortex dynamics.

6.6 Dissipation

Dissipation is the irreversible transfer of kinetic energy into internal energy due to viscous friction. In literature dissipation is often reduced to the contribution of the fluctuations with respect to FAS, $\varepsilon = \overline{\langle \tau, S \rangle_F} - \langle \bar{\tau}, \bar{S} \rangle_F$. This is accurate for homogeneous, isotropic turbulence and possibly for flows that are exposed to small mean gradients only. However, for strong shear layers, as we find them, e.g., in turbulent boundary layers, the contribution of the mean dissipation $\langle \bar{\tau}, \bar{S} \rangle_F$ can be locally much stronger than the fluctuation contribution. For this reason we will discuss the total dissipation, $\overline{\langle \tau, S \rangle_F} = \langle \bar{\tau}, \bar{S} \rangle_F + \varepsilon$, in this section.
We split the dissipation into the previously discussed characteristic types (secs. 6.3, 6.4). In this way the properties with respect to dissipation of the certain structures become clear and their contribution to the overall dissipation is discussed. The effect of the wall on this composition of the overall dissipation is discussed as a first step. Next, the dissipation is spatially decomposed into large scales and small scales of motion. This decomposition is then used to discuss how large scales and small scales are coupled with respect to their dissipation.

6.6.1 Characteristic Decomposition of Overall Dissipation

In general the discussion is split into an analysis of a relatively invariant outer region $y^+ \gtrsim 50$ and an analysis of a varying region closer to the wall, $y^+ \lesssim 50$. To obtain an overview about the behaviour of dissipation, figure (6.47) summarizes what we discussed already in section (6.2). Dissipation peaks at the wall. In the surrounding region the large scales with respect to SFS as well as FAS dominate the dissipation over the small scales. This dominance becomes weaker with increasing distance to the wall. In case of FAS the dominance flips at about $y^+ \approx 12 - 13$ and for SFS F3 it flips at $y^+ \approx 40$. Whereas the large-scale dissipation for FAS is essentially zero in the outer layer, there is a shared contribution of large scales and small scales to dissipation in case of SFS in the outer layer. As discussed before (sec. 6.2), the latter property depends on the Reynolds number as well as on the filter width. The dependency of the SFS small scale dissipation on the filter width is illustrated in figure (6.47, c).
Dissipation is discussed conditioned with the respective QR-states (sec. 6.3). The relation between the overall mean and a conditional mean of an arbitrary quantity f and a condition $C = c$ in a discrete sense is given by

$$\langle f \rangle = \sum \langle f | C = c \rangle \, P(C = c). \tag{6.13}$$

In other words, the unconditional mean is the sum of all possible events for the random variable C of the product of conditional average and probability for the respective event.

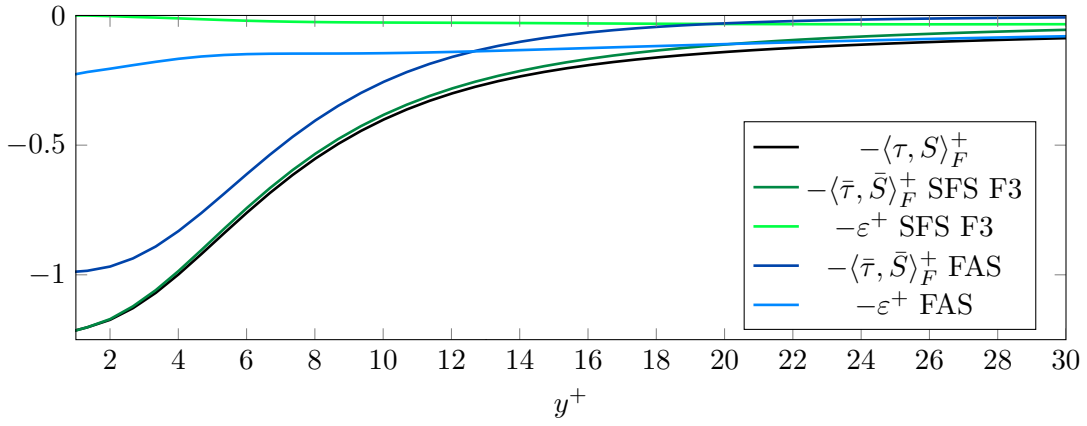

(a) Dissipation in the near-wall region.

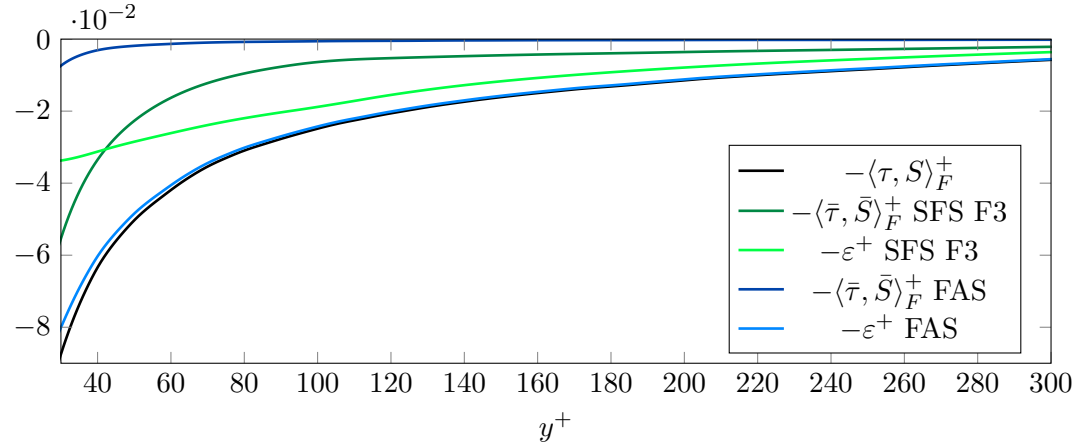

(b) Dissipation in the logarithmic layer and outer layer.

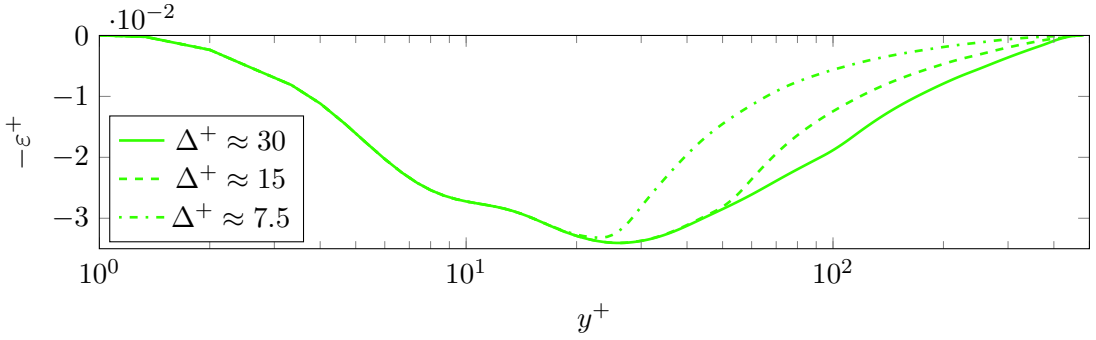

(c) Small scale dissipation in case of SFS.

Figure 6.47: Overall dissipation as well as dissipation split into large-scale and small-scale contributions (top and centre). Small-scale dissipation for different spatial filter widths F1, F2 and F3 at the bottom.

In a continuous form this will read as

$$\langle f \rangle = \int_{\mathbb{R}} \langle f | C = c \rangle \, \mathrm{pdf}_C(c) dc. \tag{6.14}$$

The unconditional mean is the integral over all possible events of the random variable C of the product of conditional average and pdf value for the respective event. For this reason it is always important to have the probabilities and the pdfs in the back of your mind when discussing conditional average with the aim of understanding the contribution of certain states to the unconditional average. In the present case the availability of pdfs of the QR-space (fig. 6.20) are important to interpret the following conditional averages of dissipation conditioned with the respective QR-states (fig. 6.49). The probabilities for the certain characteristic states are shown in figure (6.48). We use the conditional averages in the QR-plane to obtain an overview but then reduce the information to conditional averages conditioned with the four (or five) characteristic states only. This allows a reduction of the amount of information and simplifies the discussion.
Reviewing the probabilities for the characteristic states (fig. 6.48) we find that the additional state of a calm flow topology, introduced before (sec. 6.4), allows us to obtain a relatively homogeneous distribution in the entire outer layer. The role of this additional state in terms of dissipation is discussed in the following. More interestingly, we find a

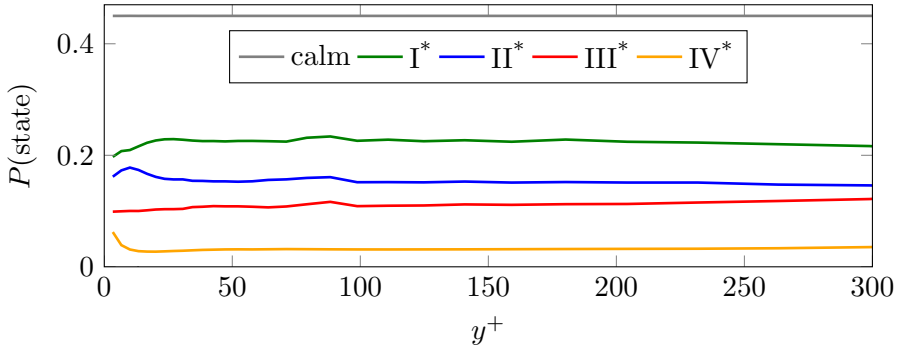

(a) five characteristic states

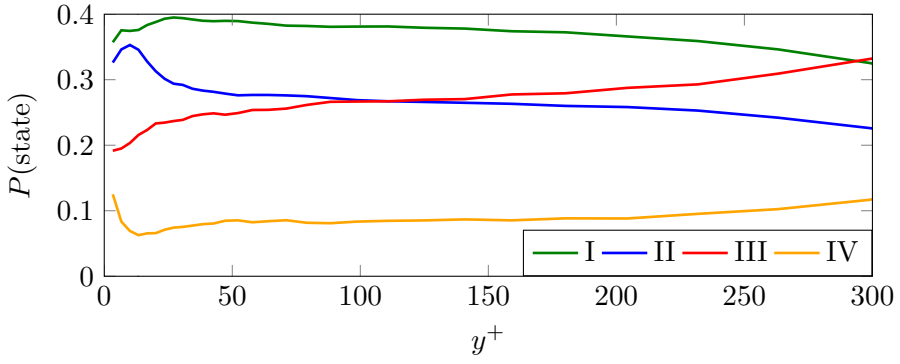

(b) four characteristic states

Figure 6.48: Probabilities of the characteristic states defined in sections (6.3) and (6.4).

strong change of characteristic distribution in the near-wall region. Whereas state III is decreasing gradually closer to the wall, state IV shows a sharp increase at the wall. As discussed in the previous section, the loss of pressure balance at the wall causes a destabilization of vortical structures which results in a strong peak of the probability of state II in the near-wall region. How this affects the dissipation is discussed in the following as well.

Figure (6.49) shows the dissipation conditioned with the respective QR-states. The minimum of dissipation is mostly around the origin of the QR-space. However, the exception is found in the buffer layer. A second minimum is developing within $y^+ \approx 5-20$ and is located in the state of stretching vortical structures. The minimum reaches its strongest point at $y^+ \approx 13$ where it develops to the global minimum for a limited range in wall-distance. Besides this additional minimum, dissipation in general becomes stronger with increasing distances to the origin of the QR-space. Whereas the increase is relatively gradual towards positive values of Q, we find a much stronger change towards negative values of Q. The lowest Q values are at the location where the thin extension of the *teardrop* is developed for the joint-pdf of Q and R in higher layers. The highest values for dissipation are found for low values of Q and high values of R and therefore exactly at the location of the teardrop's thin extension. The conditional averages do not change qualitatively any more above $y^+ \approx 40-50$ and therefore the plot shown at $y^+ \approx 339$ reflects the qualitative distribution in the entire logarithmic layer and in most of the outer layer. As the mentioned additional minimum already suggests, there is a strong variation below $y^+ \approx 30$. In the characteristic section I the high dissipation that is present for low values of Q in higher layers is spreading more into the interior of the characteristic section when approaching the wall. It seems that stretching vortices become more dissipative in the near-wall region. We find slight changes in section II, but the variations are small compared to the remaining sections. When approaching the wall, the thin extension of the *teardrop* towards high values of R and low values of Q are lost and the peak of dissipation at this location is less pronounced and more spread over the entire section III. In section IV we find small changes but no significant trends are seen. All these variations are discussed in the following according to the respective characteristic states.

Integration of the conditional averages over the respective characteristic sections allows to obtain the averages of dissipation conditioned with the respective characteristic states representing the sections. These can then be normalized by the unconditioned dissipation for the respective location to obtain a relative dissipation per characteristic structure. Figure (6.50, left) shows this relative dissipation for the characteristic decomposition with and without the state of calm flow for the region above $y^+ \geq 50$. In general it can be said that the relative dissipation for all structures is relatively constant in the entire plotted region. However, in the outer region ($y^+ \gtrsim 200$) we find small variations. Comparing the two different decompositions, we find the expected effect for the decomposition with the additional calm state. Due to a smooth flow field the relative

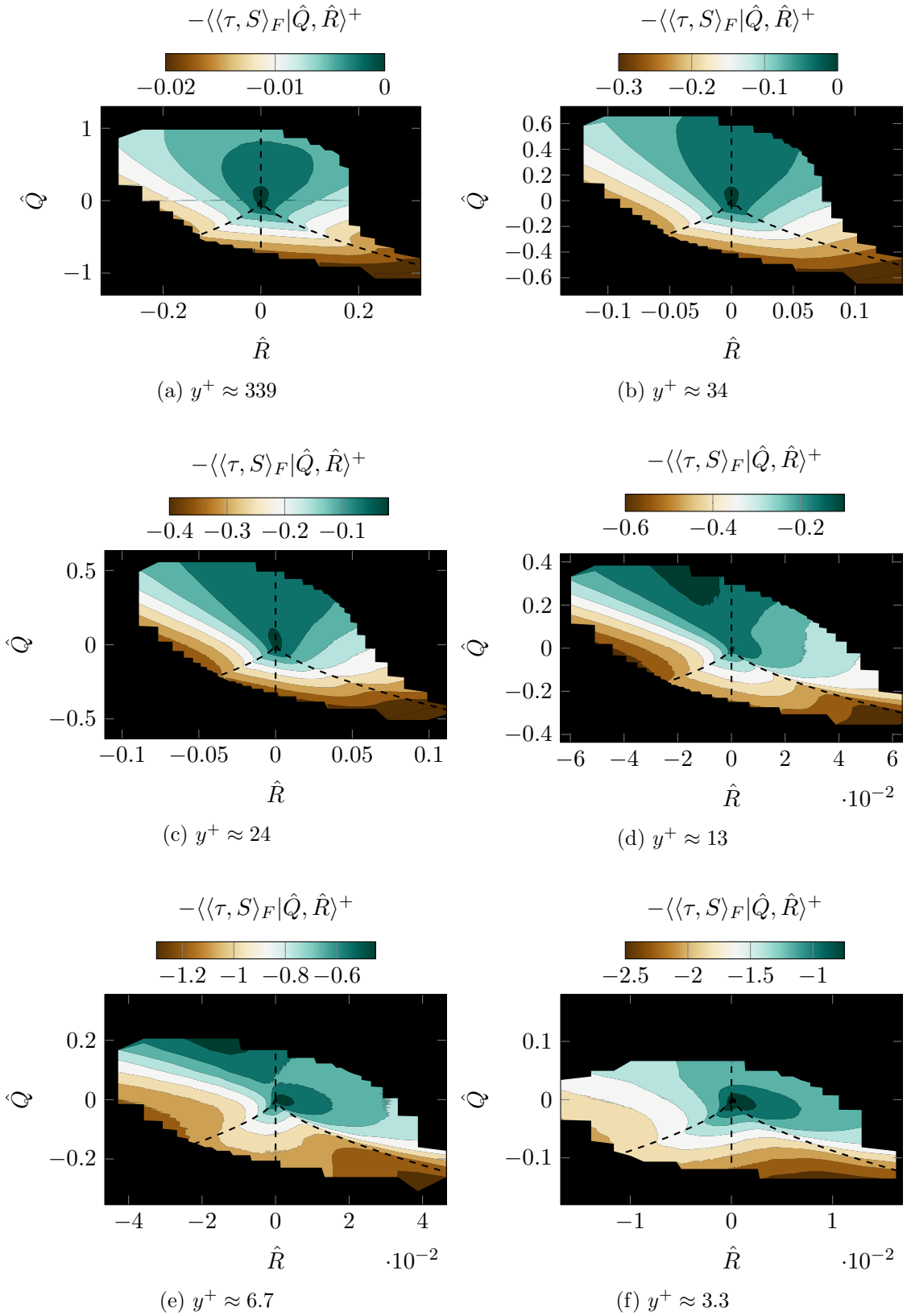

(a) $y^+ \approx 339$ (b) $y^+ \approx 34$

(c) $y^+ \approx 24$ (d) $y^+ \approx 13$

(e) $y^+ \approx 6.7$ (f) $y^+ \approx 3.3$

Figure 6.49: Conditional averages of dissipation at 6 different wall-normal locations conditioned with the respective QR-states.

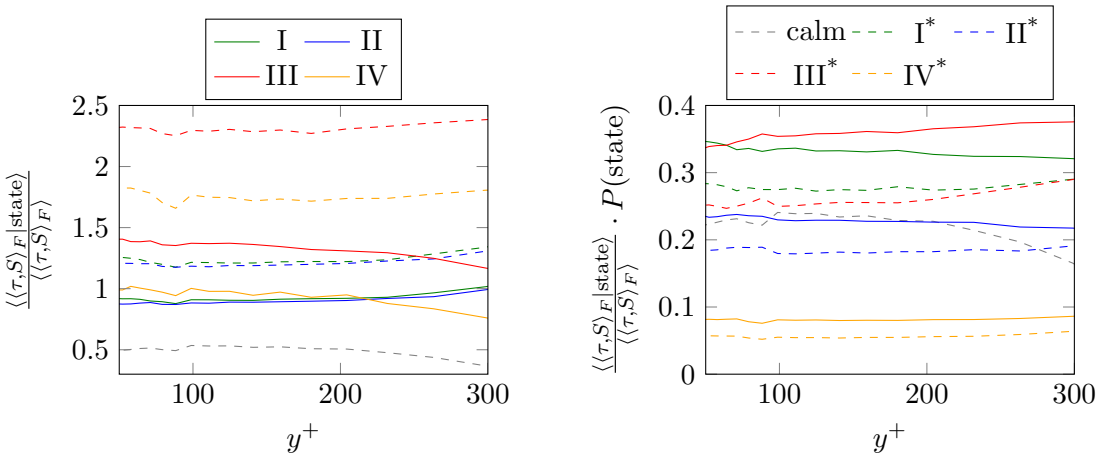

Figure 6.50: Dissipation in the region above $y^+ \geq 50$. Left: Relative, conditional average of dissipation conditioned with the characteristic states defined in sections (6.3) and (6.4) and normalized by the local unconditional average dissipation. Right: Relative contribution of the characteristic states defined in sections (6.3) and (6.4) to the overall dissipation.

dissipation in the calm region is low and it becomes obvious that the turbulent states have a much stronger relative dissipation than the calm spots. Additionally, we find that the pure straining states have opposite trends in the outer region for the different decompositions. The latter is an indication that a refinement of the characteristic decomposition could result in a constant relative dissipation per characteristic structure in the outer region. This is a beneficial fact, that is discussed in the following. The relative contribution of the individual characteristic structures to the overall dissipation is shown for the region above $y^+ \geq 50$ in figure (6.50, right). Considering the characteristic decomposition without the calm structure type (continuous lines), the strongest contribution to the dissipation in the logarithmic layer and the outer layer comes from the pure straining structures with a flattening character (III) as well as from the stretching vortices (I). Contracting vortices (II) have an intermediate contribution to the dissipation and the pure straining structures with elongational character (IV) contribute the least. The latter is mainly due to the low frequency of occurrence of this structure type. Considering the decomposition with the additional calm structure type (dashed lines), we see that a large part of the dissipation is covered by the calm structure. Although their relative dissipation is very low compared to the other structures, they do cover 45% of all events and therefore have a significant contribution to the dissipation in the outer region. In general the other contributions are therefore just scaled down compared to the characteristic decomposition without calm state. However, an additional difference between the two different characteristic decompositions is that the calm structure type covers more dissipation caused by type III structures than caused by type I structures. Therefore their importance flips. The stretching vortices without their calm states are contributing more to the dissipation than the flattening straining structures without their calm parts. Overall it can be stated that although the straining structures with

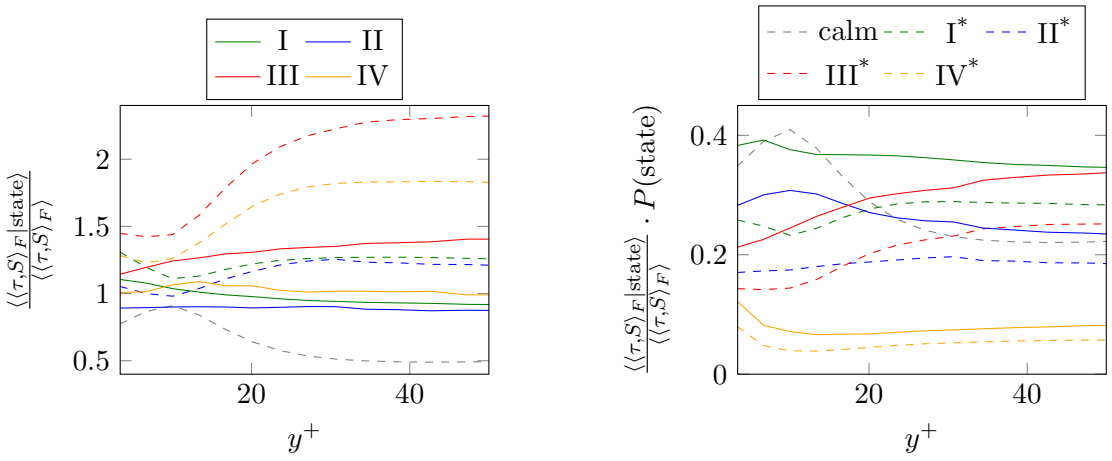

Figure 6.51: Dissipation in the region below $y^+ \leq 50$. Left: Relative, conditional average of dissipation conditioned with the characteristic states defined in sections (6.3) and (6.4) and normalized by the local unconditional average dissipation. Right: Relative contribution of the characteristic states defined in sections (6.3) and (6.4) to the overall dissipation.

flattening character have a much stronger relative dissipation, their dominance, regarding dissipation, over the vortical structures is lost simply due to the high frequency of occurrence of vortical structures.

Figure (6.51) shows the analogue plots, as discussed for the outer regions, for the near wall region. Already at first glance it is obvious that in this region more variation is present. The results for the modified characteristic decomposition including the calm state shows a strongly different behaviour than the original decomposition in the near wall region. Already that the calm state suddenly develops to the strongest contributor to dissipation diverges from the initial idea of this additional state. The state was

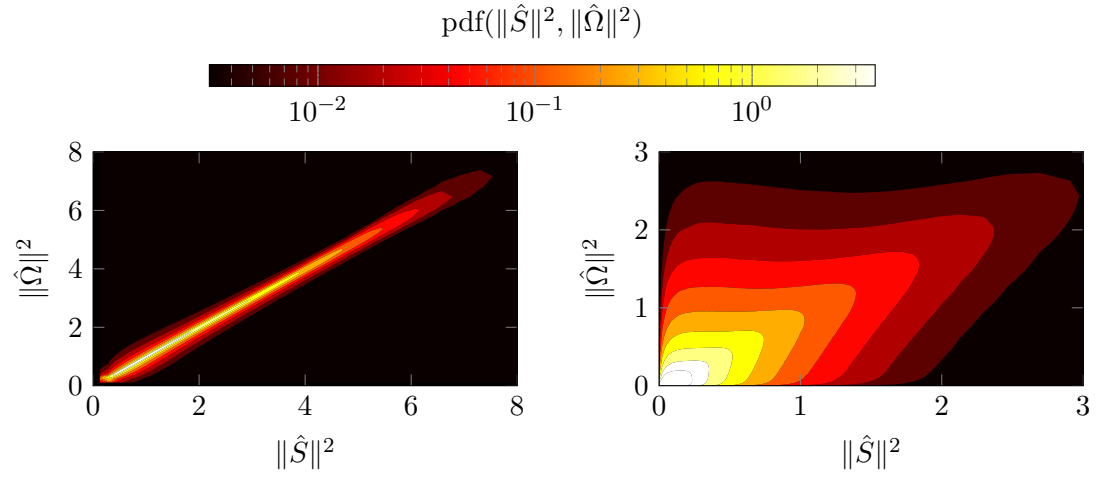

(a) $y^+ \approx 6.7$ (b) $y^+ \approx 34$

Figure 6.52: Joint probability density function of $\|\hat{S}\|^2 = \frac{\|S\|^2}{\|A\|^2}$ and $\|\hat{\Omega}\|^2 = \frac{\|\Omega\|^2}{\|A\|^2}$ at two different wall-normal locations.

introduced as characteristic stated that covers structures with a low velocity gradients magnitude. If, however, the dissipation, and therefore the gradients, of this state becomes strong, that indicates that the definition failed at this point. As mentioned in the previous section the modified characteristic decomposition needs adjustment especially for the use in the near-wall region. In these plots the modified decomposition is plotted for completeness but the discussion focusses on the characteristic decomposition without additional calm state. As the conditional averages in the QR-space (fig. 6.49) already suggested, the relative dissipation of the contracting vortical structures stays relatively constant, i.e. this structure type does not change its dissipative property in the near-wall region. Although showing slight changes the same could be argued for the pure straining structures with elongational character. The variations in this dataset could be caused by the relatively small number of samples (depending on the probabilities shown in figure (6.48)) compared to the remaining structure types. However, this has to be investigated when refining the characteristic decomposition. On the other hand, the stretching vortical structures increase their relative dissipation whereas the pure straining structures with flattening character decrease their relative dissipation. In other words, stretching vortices become as dissipative as the strongest dissipative structure in the decomposition. Together with what we have seen in the previous section (6.4), we understand this as an effect of the alignment of the vortices with the wall together with the much denser packing. This leads to higher straining in the vortical structure and therefore stronger dissipation. To show this from a different perspective figure (6.52) shows the change of the coupling of vorticity from higher regions to the near-wall region. Whereas the coupling of both is fairly loose in the outer layer they are almost fully correlated for high magnitudes in the near-wall region. This means that with high vorticity it comes with high strain - and therefore high relative dissipation. One could argue that this should affect all vortical structures at the same time. However, we discussed in the previous sections that the contracting vortical structures break up due to their pressure cores being affected by the wall. This leads to a lift up of these structures which takes them quickly out of the regions of strong correlation of strain and vorticity. Unlike the slight variations we see for the relative dissipations of the different structures, the contribution of the respective structures to the overall dissipation (fig. 6.51, right) is varying much more strongly. The increase of relative dissipation of stretching vortical structures is barely affecting the contribution of these structures to the overall dissipation. On the other hand the effect of the decreased relative dissipation for pure straining flattening structures is even amplified. Further, we see a sharp increase of the contribution of structure type IV at the wall whereas its relative dissipation remains relatively constant. Similarly the contracting vortical structures have a peak in their contribution to the dissipation in the near-wall region. All of this is a clear effect of the change of characteristic distribution (fig. 6.48) that weights the relative dissipation for the contribution to the overall dissipation.

With this all the previously discussed phenomena (secs. 6.3, 6.4 and 6.5) contributes to

an understanding of the composition of the dissipation. The elongated purely straining footprints of vortical structures at the wall cause an increased probability of structure type IV, which results in an increase of the dissipation contribution of these structures. This does not happen by changing the properties of this characteristic structure type, but much rather by increasing its frequency of occurrence. In general we find densely packed vortical structures in the near-wall region. Together with the wall affecting the pressure-cores of vortical structures causing an increase of contracting vortical structures we find the vortical structures dominating the near-wall dissipation. We see that the main influence on the composition of dissipation comes from the characteristic distribution of turbulent structures. However, the variation of the relative dissipation of the respective structures is not completely negligible as it is not a universal feature in this characteristic decomposition. On the other hand, the relative dissipation is close enough to being constant to justify further investigations to find a characteristic distribution with a potentially universal relative dissipation per structure type. For the understanding and modelling of dissipation and turbulence in general, this would be a great step as the dissipation would be solely governed by the respective distribution for the new characteristic distribution (analogue to figure 6.48). However, this has to be postponed to future work.

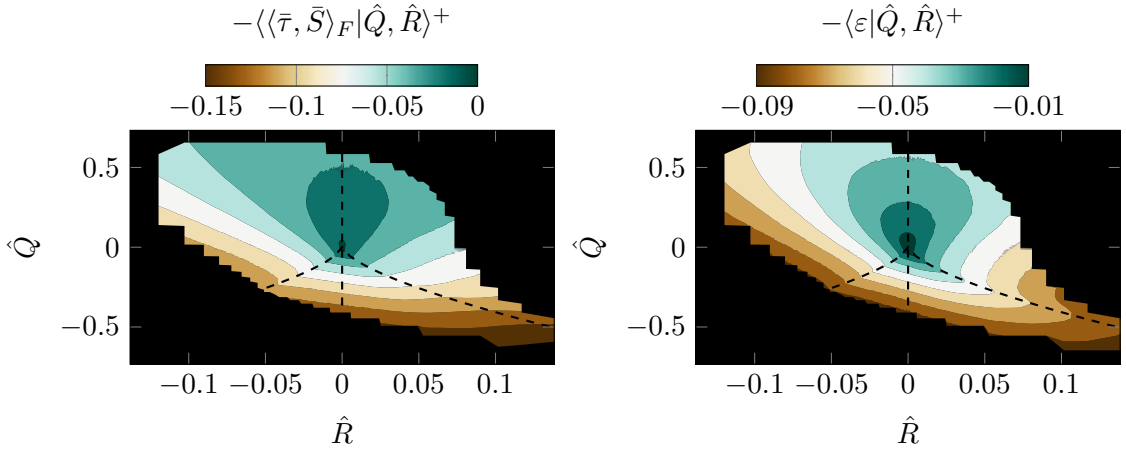

(a) large-scale dissipation

(b) small-scale dissipation

Figure 6.53: Conditional average of large-scale dissipation (left) and small-scale dissipation (right) with respect to SFS F3 ($\Delta^+ \approx 30$) conditioned with the respective QR-states. The data is taken at $y^+ \approx 34$ and therefore qualitatively representative for the logarithmic layer as well as most of the outer layer.

6.6.2 Characteristic Decomposition of Large-Scale vs. Small-Scale Dissipation

This section focuses on the scales split up by the spatial filter with a filter width of $\Delta^+ \approx 30$ (F3). The dissipation for the respective large scales is compared to the dissipation caused by the small scales. Figure (6.53) shows the dissipation of the large scales and small scales, respectively, conditioned with the QR-states. The location for this results is at about $y^+ \approx 34$ and is a qualitative representation of all plots further away from the wall. Just like for the overall dissipation we do not find obvious qualitative changes in the logarithmic layer and in the outer layer. Integrating to the relative contribution of the respective characteristic structures (fig. 6.54), we see that the behaviour of the large scale dissipation agrees in general with the observations that we made about the overall dissipation in the previous section. However, on a closer look we find that the dissipation ratio of rotational structures versus pure straining structures is a bit shifted with the effect that the large scale rotational structures are less dissipative, relative to the pure straining structures, than the unfiltered rotational structures. This shift becomes more obvious within the small scales. Consequently small scale rotational

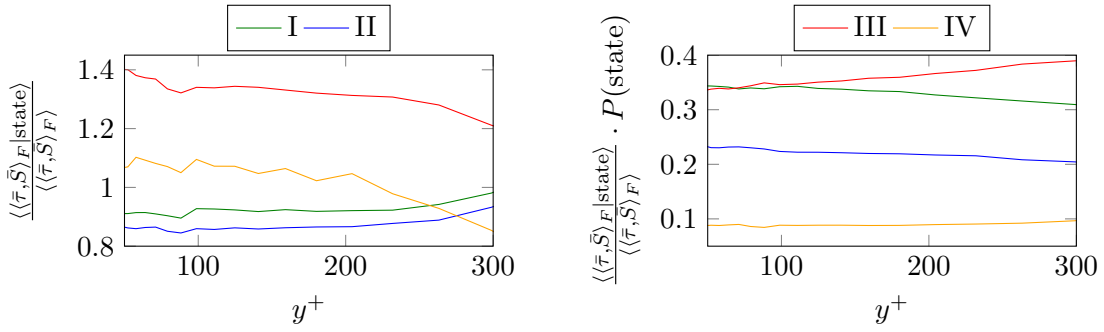

(a) large-scale dissipation

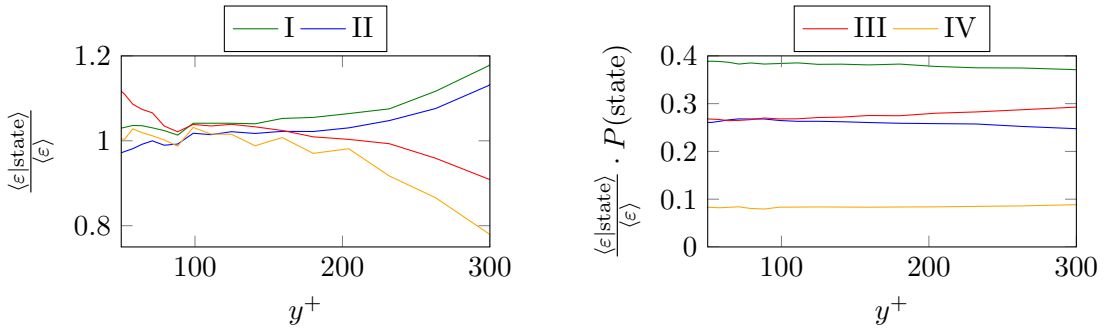

(b) small-scale dissipation

Figure 6.54: Large-scale and small-scale dissipation in the region above $y^+ \geq 50$. Left: Relative, conditional average of dissipation conditioned with the characteristic states defined in sections (6.3) and normalized by the local unconditional average dissipation. Right: Relative contribution of the characteristic states defined in sections (6.3) to the large-scale and small-scale dissipation, respectively.

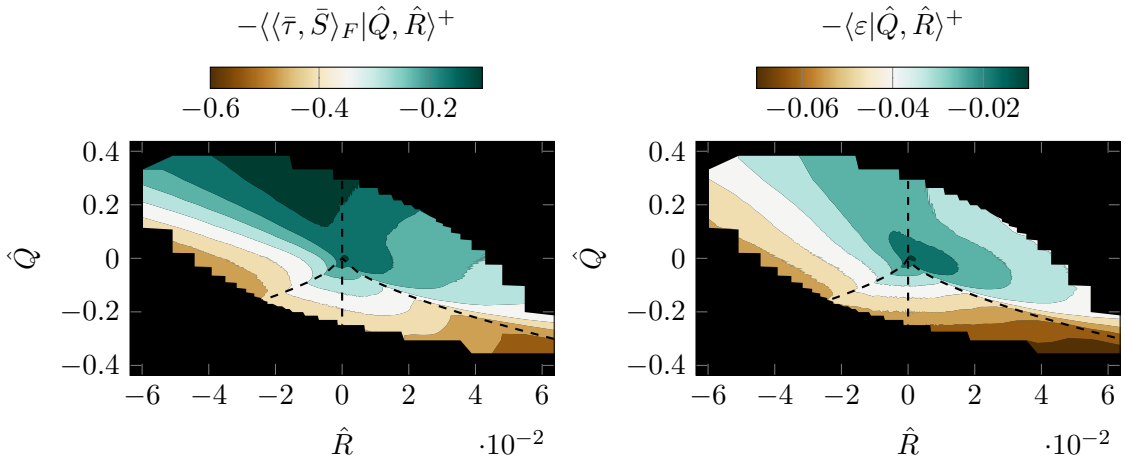

(a) $y^+ \approx 13$; large-scale dissipation

(b) $y^+ \approx 13$; small-scale dissipation

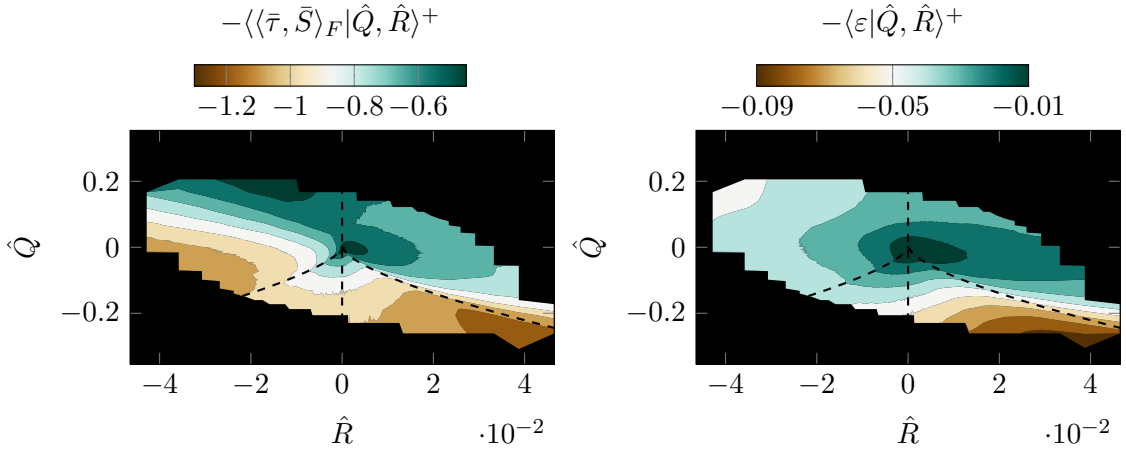

(c) $y^+ \approx 6.7$; large-scale dissipation

(d) $y^+ \approx 6.7$; small-scale dissipation

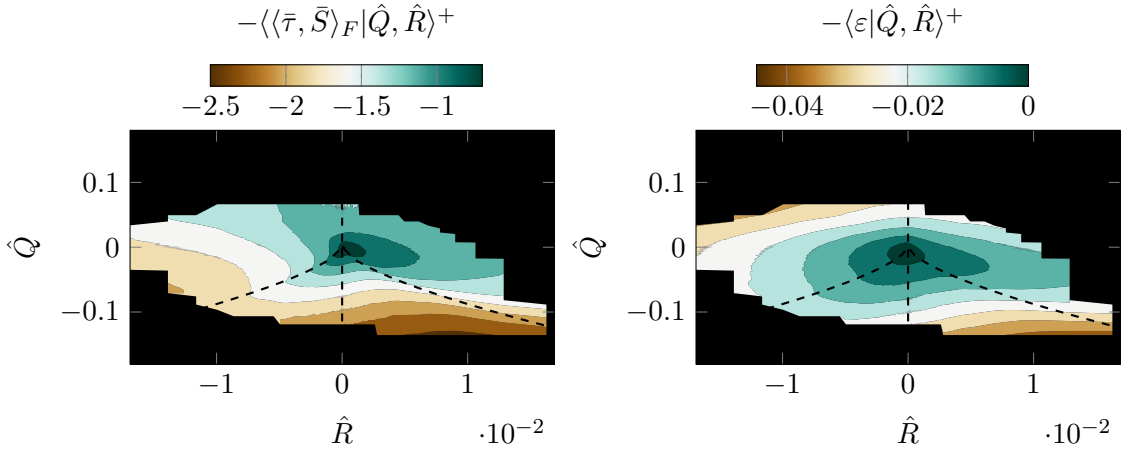

(e) $y^+ \approx 3.4$; large-scale dissipation

(f) $y^+ \approx 3.4$; small-scale dissipation

Figure 6.55: Conditional averages of large-scale dissipation (left) and small-scale dissipation (right) with respect to SFS F3 ($\Delta^+ \approx 30$) conditioned with the respective QR-states. The data is taken at three different locations to describe the near-wall behaviour of dissipation.

structures become more dissipative than the overall rotational structures relative to the pure straining structures. Besides the shift, the small scales follow the same trends as the large scales in terms of dissipation. In principal this would mean that turbulence models for the small scales need to capture the scaling of large scale dissipation versus small scale dissipation only. The distribution of dissipation is given already by the large scale dissipation. However, the Reynolds number in this flow is most likely too low for a general conclusion. A comparison to higher Reynolds number flows is needed to discuss this further. For now we state these results as pure observations.

The near-wall behaviour of dissipation is shown in figure (6.55). Here as well the large scale results are widely agreeing with what was discussed in the previous section about the conditioned unfiltered dissipation (fig. 6.49). Whereas the small scale dissipation shows similarities to the large scales, conditioned with the QR-states, in the higher regions, this changes in the near-wall region. The development of a second minimum within the more turbulent stretching vortices, as we find in the unfiltered case (fig. 6.49)

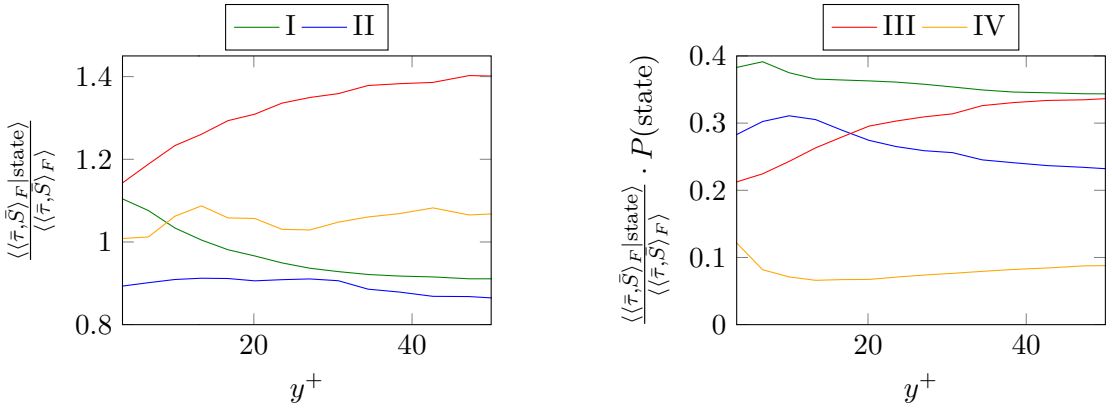

(a) large-scale dissipation

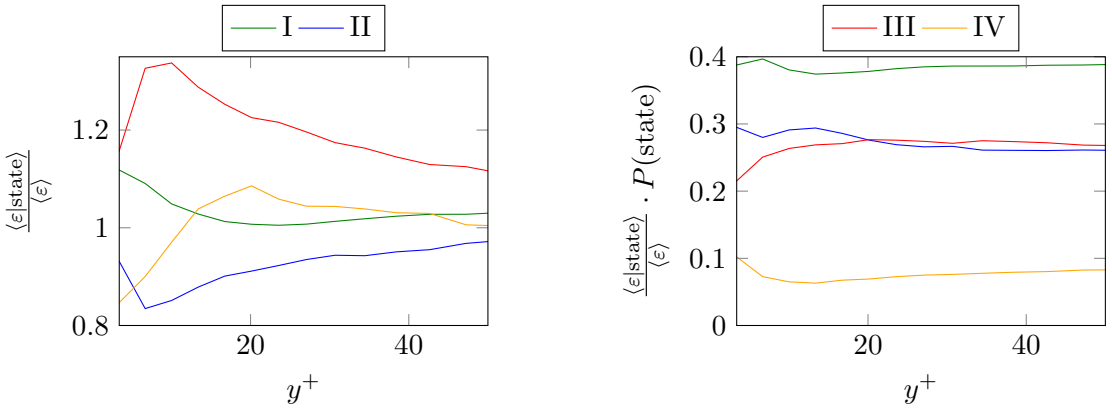

(b) small-scale dissipation

Figure 6.56: Large-scale and small-scale dissipation in the region below $y^+ \leq 50$. Left: Relative, conditional average of dissipation conditioned with the characteristic states defined in sections (6.3) and normalized by the local unconditional average dissipation. Right: Relative contribution of the characteristic states defined in sections (6.3) to the large-scale and small-scale dissipation, respectively.

as well as for the large scales only, is not present for the small scales. In the direct proximity to the wall, the stretching vortices even develop a relative dissipation as strong as the pure straining flattening structures.
Again, integration over the respective characteristic sections leads to the relative dissipation and the relative dissipation contribution per characteristic structure type (fig. 6.56). As for the outer regions a general agreement of the large scale behaviour of dissipation with the overall behaviour can be confirmed. The only difference is the shift of rotational structures versus pure straining structures that is present in large scales and in the opposite way for the small scales. The small scales show significant deviations from the behaviour that is described by the large scales. Due to missing comparison it is not possible to interpret these results at this stage and as for the outer layer they are treated as pure observations. As part of the future work Reynolds number studies as well as comparison of different filter kernels are planned.

6.6.3 Conclusions about the Dissipation of Kinetic Energy

We have seen that a characteristic decomposition allows to obtain relative dissipations per characteristic turbulent structure, that are nearly invariant to variation of the distance to the wall. Therefore the relative dissipation is well described by the frequency of occurrence of the respective characteristic structures. This is a property which finds favour in turbulence modelling as well as in a further analysis of the physics of turbulent structures. However, a refinement of the characteristic decomposition of turbulence is needed.
It has also become clear that in the outer layer, and therefore unaffected by the direct influence of the wall, pure straining structures with flattening character as well as stretching vortices are the dominant dissipators of kinetic energy. Whereas the vortical structures gain importance for the small scale dissipation the balance in the large scale dissipation is almost unchanged compared to the overall dissipation in the outer region. In the near-wall region the effects discussed in previous sections become important. The streamwise elongated, purely straining feet of rotational structures at the wall cause an increase of the probability of structure type IV which directly results in an increase of dissipation caused by these structures. Similarly, the destabilizing effect that the wall has on vortical structures, due to attraction of their pressure-core, results in a peak of the frequency of occurrence of structure type II in the near-wall region. This is another mechanism that contributes to the increased dissipation close to the wall. The last discussed cause of dissipation increase was the more densely packed streamwise elongated rotational structures. The denser packing and the interaction with the wall causes a much stronger linear coupling between rotation rate and strain rate. This results in an increase of dissipation contribution from vortical structures which in general can be seen in the near-wall region.
For the comparison of small scales and large scales no conclusions can be made at this

stage. We have seen indications that there might be a link between large scale dissipation and small scale dissipation, but with the available data and analysis we cannot state any further conclusions about the physical mechanisms responsible. A Reynolds number comparison and, especially for the near-wall region, a comparison of different filter kernels will help to understand the underlying physics better and interpret the results accordingly.

As mentioned a few times, the characteristic decomposition is very helpful, however, not ideal to decompose the structure type and reveal invariant features. The presented results provide a good basis to start developing better and more universal characteristic decompositions. This has to come along with an understanding of how boundary conditions are influencing the respective characteristic decomposition. Although not complete, this section has shown the capabilities of such a decomposition.

6.7 Production

The properties of a turbulent flow discussed in the previous sections are all based on the fact that turbulence is present in the flow. In the dissipation section we studied the destruction of turbulence. In this section we take a closer look at the origin of turbulence. More precisely we discuss the turbulence production term. However, the term *turbulence production* might be misleading as it does not necessarily describe the creation of turbulence. To be exact, turbulence production $\langle \sigma, \bar{S} \rangle_F$ simply describes a part of the cascading process that was described in the introduction (sec. 1.2.1). When we derived the filtered equations (sec. 2.2.2) the role of the origin of the production term as representative for the cascading process became clear. The flow was split into large scales and small scales of motion and equations to govern the respective energies were derived. The energy cascade that, on average, transfers energy from the energy containing range towards smaller and smaller scales down to the dissipation range is therefore interrupted at some point. One part of the cascade is covered by the equation governing the large scales and another part is covered by the equation governing the small scales. The connecting piece that couples large scales to small scales and assembles the separated pieces to the global cascade is the turbulent production. Consequently this production exposes the energy cascade, that is usually covered in the non-linear transport term, at a particular location that is defined by the respective filter operator. This exposed part of the cascade is studied in the following.

To understand which part of the cascade is revealed by the filter operator, the scale decomposition and the turbulent production of the respective processing are shown in figure (6.57). The top two plots show data for the Favre average based splitting (FAS). The FAS method splits the turbulent flow into a temporal mean flow with a Strouhal number of $St = 0$ which represents the large scales and the fluctuations around this mean which represents the small scales. In the upper most plot we show the pre-multiplied energy spectrum $St\, E_{11}$ over Strouhal number. The area (grey) underneath the spectrum represents the streamwise component of the small scale kinetic energy. The transfer of kinetic energy between the mean flow and the fluctuations is then covered by the turbulent production with respect to FAS (fig. 6.57, b). As discussed before (sec. 6.2) the transfer of kinetic energy from the mean flow to the fluctuations around it peaks at around $y^+ \approx 10$, drops quickly towards the wall and gradually towards the freestream. At the wall the turbulent production is zero, but everywhere else we find a non-zero net transfer of kinetic energy from the kinetic energy of the mean flow to kinetic energy of the fluctuations. The bottom two plots in figure (6.57) show the analogue mechanism for the spatial filter based splitting (SFS). The energy spectrum (c) is shown for the pre-multiplied spanwise component of the kinetic energy $\kappa_3\, E_{33}$ over spanwise wavenumber κ_3. The plot shows both, the unfiltered spectrum as well as the spectrum of the data filtered with the largest filter (F3). The large scales' share of the spanwise component of kinetic energy is shown in red. The difference between the overall kinetic energy the

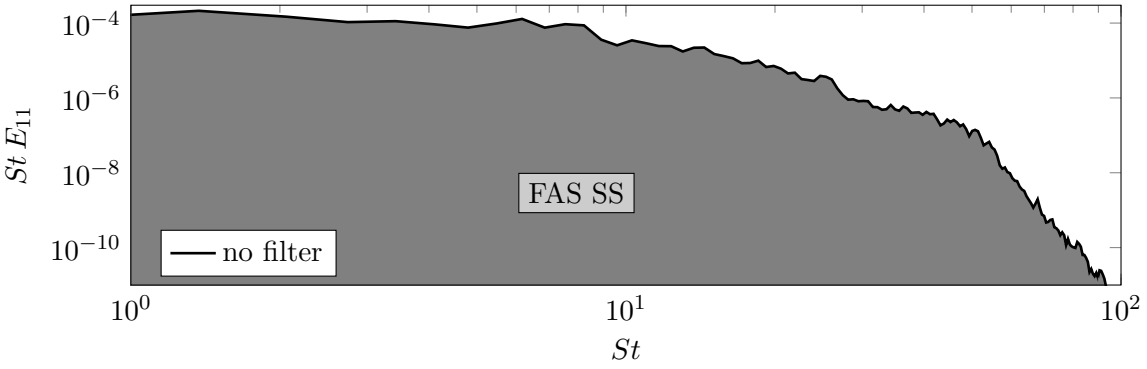

(a) Energy spectrum of stream-wise kinetic energy over Strouhal number $St = \frac{fL}{u_\infty}$.

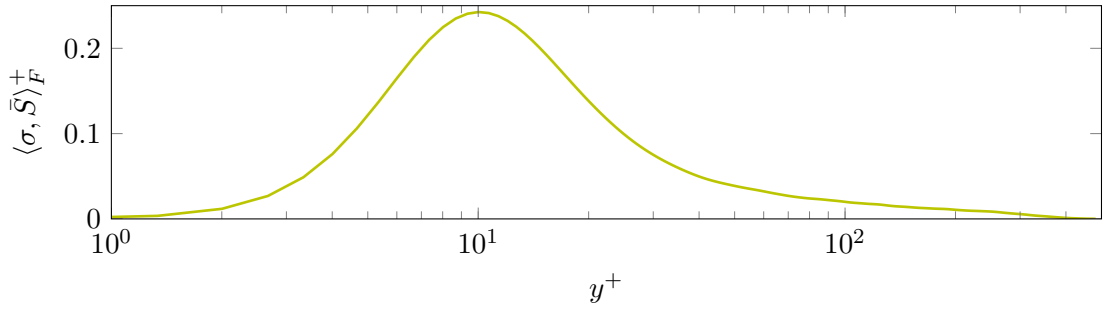

(b) Turbulence production for Favre average based splitting of the energy equation.

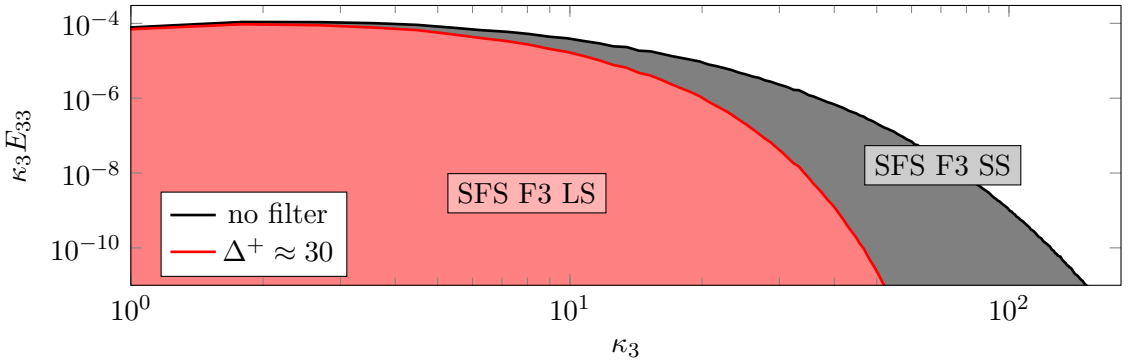

(c) Energy spectrum of spanwise kinetic energy over spanwise wavenumber κ_3.

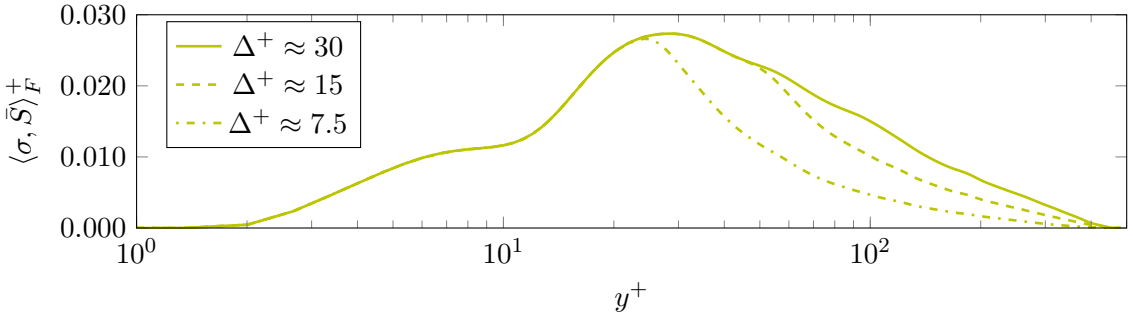

(d) Turbulence production for spatial filter based splitting of the energy equation.

Figure 6.57: Overview over the respective energy distributions and the turbulence productions.

large scale part is the small scales' share of the overall energy (grey). The turbulent production with respect to SFS reveals the part of the energy cascade that handles the transfer of kinetic energy between the red and grey area. The plot at the bottom shows this transfer averaged in time. This, as well, was discussed extensively with the complete budget for the total energy (sec. 6.2). Like the production in case of FAS the net transfer of kinetic energy is always from large scales to small scales of motion. Further, a distinct peak of production can be found between $y^+ \approx 25 - 30$. This peak decays quickly to zero when moving towards the wall and decays slowly towards the freestream. The rate of how fast the production drops towards the freestream strongly depends on the filter width and is more gradual for larger filter width than for smaller ones. In the following we discuss how these net transfers are composed.

6.7.1 Turbulence Production of the Mean-Flow

To analyse which characteristic structure types are taking what roles in the production process we condition the production with the QR-states. In case of FAS this analysis needs to be explained with care. As used in RANS, the energy equations based on Farve average splitting describe the mean and the averaged (!) coupling with the fluctuations around this mean. This implies that for the turbulence production $\langle \sigma, \bar{S} \rangle_F$ only the coupling of the mean quantities σ and $\bar{S}$ are important. In principle the instantaneous behaviour of the analogue of the production is not of direct importance. However, the instantaneous quantities allow to see how the actual mean production is composed. Therefore we define an instantaneous analogue of the Favre stress

$$\sigma^* := -(\rho \vec{u} \otimes \vec{u} - \bar{\rho} \tilde{\vec{u}} \otimes \tilde{\vec{u}}). \tag{6.15}$$

The Reynolds average of this modified Favre stress is simply the classical Favre stress

$$\sigma = \overline{\sigma^*}. \tag{6.16}$$

The same holds for the instantaneous analogue of the production and the classical turbulence production based on FAS

$$\langle \sigma, \bar{S} \rangle_F = \overline{\langle \sigma^*, \bar{S} \rangle_F}. \tag{6.17}$$

This allows to study the instantaneous production events $\langle \sigma^*, \bar{S} \rangle_F$ that compose to the actual production term $\langle \sigma, \bar{S} \rangle_F$. It should be mentioned at this stage that the results about $\langle \sigma^*, \bar{S} \rangle_F$ will appear counter-intuitive. This terms is does not have a direct physical meaning. However, is is applied to explain e.g. the mixing length theory (see Wilcox, 1998). This section will reveal that the interpretation has to be taken with care. Figure (6.58) shows this modified production conditionally averaged with the respective QR-states as conditions. With the previous definition we then obtain the link

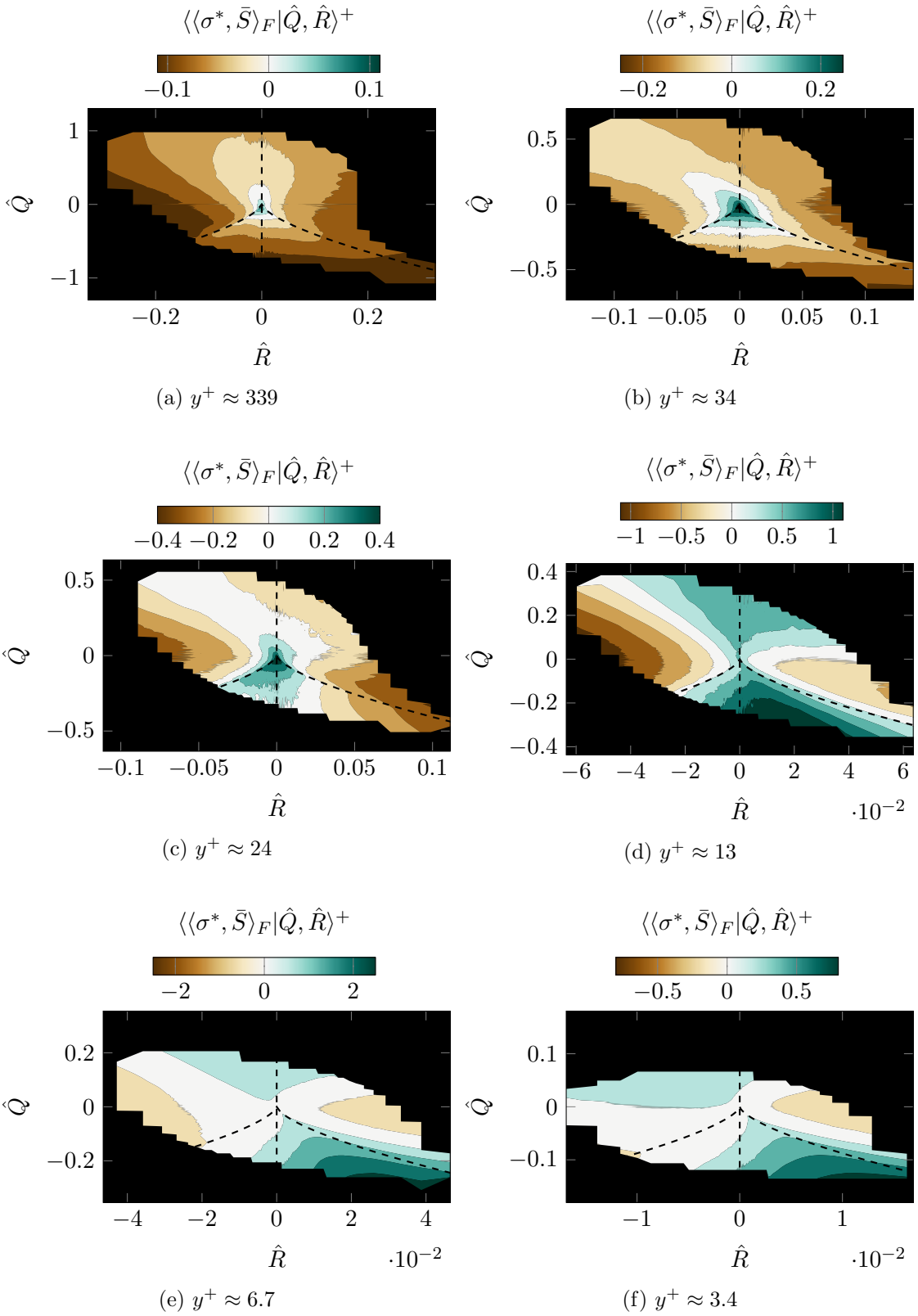

(a) $y^+ \approx 339$ (b) $y^+ \approx 34$

(c) $y^+ \approx 24$ (d) $y^+ \approx 13$

(e) $y^+ \approx 6.7$ (f) $y^+ \approx 3.4$

Figure 6.58: Conditional averages of the modified turbulence production based on FAS at six different wall-normal locations conditioned with the respective QR-states.

between the conditional averages of the modified production and the actual production

$$\langle \sigma, \bar{S} \rangle_F = \iint_{\mathbb{R}^2} \langle \langle \sigma^*, \bar{S} \rangle_F | \hat{Q} = x_2, \hat{R} = x_1 \rangle \, \mathrm{pdf}_{[Q,R]}(x_2, x_1) \, d\vec{x}, \tag{6.18}$$

where $\mathrm{pdf}_{[Q,R]}(x_2, x_1)$ is the joint-pdf of Q and R. Having this in the back of our mind, we can interpret the shown conditional average as a description of how the turbulence production in case of FAS is actually composed. The conditional average at $y^+ \approx 339$ (a) shows an unexpected behaviour for the turbulence production in the outer layer. Whereas we know that the net transfer is from kinetic energy of the mean towards the fluctuations, the plot shows this transfer is strongly active in calm regions of the flow, i.e. around the origin of the QR-space. But contrasting this, a reverse transfer is active for

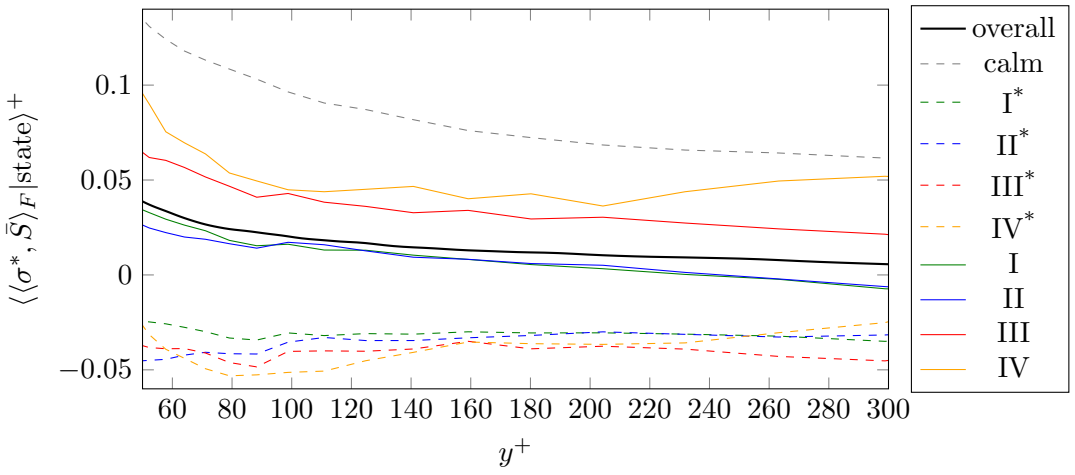

(a) Behaviour in the logarithmic layer and in the outer layer.

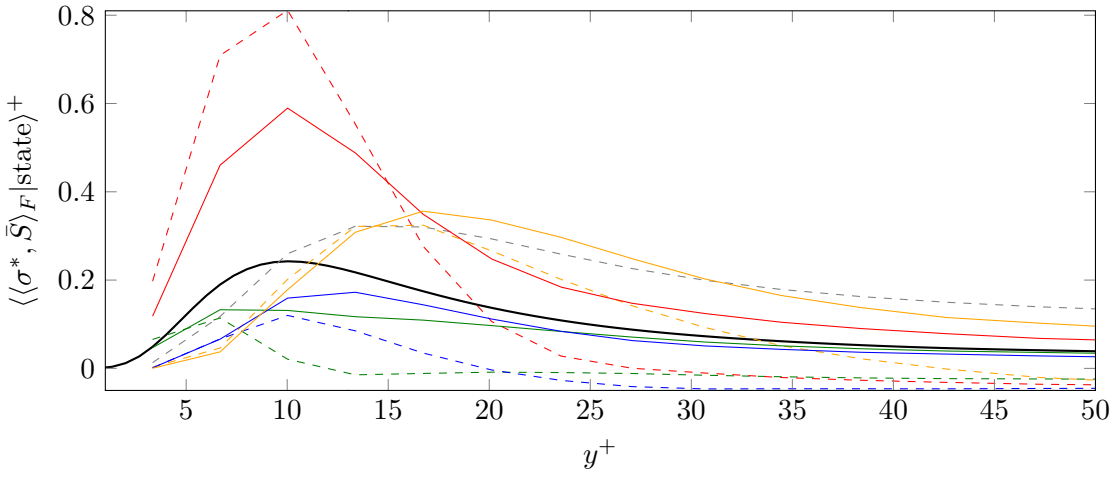

(b) Behaviour in the near-wall region.

Figure 6.59: Conditional average of the turbulence production based on FAS conditioned with the respective characteristic states defined in sections (6.3) (continuous lines) and (6.4) (dashed lines).

the turbulent states further away from the origin of the QR-space. This is an effect that is present from the outer layer until far into the buffer layer but vanishes below $y^+ \approx 20$. In general the plots of the production show a great similarity with what we have seen for the stream-wise velocity component (fig. 6.24) and (fig. 6.35) which indicates that the strong variation of the production is related to the two different states (calm versus turbulent) in the boundary layer, as discussed in section (6.4).

Figure (6.59, a) shows the conditional averages of the modified production integrated over the respective states. Summing up the production of the states weighted with the respective ratios (fig. 6.48) leads to the overall classical view of production (black line). In this plot we want to focus on the characteristic states including the calm state (dashed lines). The characteristic states without calm state (continuous lines) are plotted for completeness as they become more important in the near-wall region. In this plot for the outer region it becomes clear that the actual production in the outer region is a super position of two different events (calm and turbulent) but itself could be described as *unphysical* mean under reference to the characteristic decomposition. Just like in the initial example of the circular movement of an object and its mean location that is no physical state of the object itself (fig. 6.15), here none of the characteristic structures has a production that is close to the overall production. The distribution of production is fairly clear in the outer region. In the near-wall region the behaviour changes (fig. 6.59, b) and as in most of the previous discussions it is unclear how far the additional calm characteristic state is valid when approaching the wall. However, the remaining characteristic states have similar trends for both decompositions which make the interpretation easier. The most important observations are that all states develop a positive production when approaching the wall. Further, the pure straining structures become the relatively strongest producers of kinetic energy of the fluctuations. Looking at the characteristic decomposition without the calm state (continuous lines) we find that the pure straining structures (III and IV) develop a stronger increase of relative production than the rotational structures (I and II) when approaching the wall below $y^+ \approx 40$. The peak for the pure straining structures with elongating character (IV) is at about $y^+ \approx 17$, whereas the other structures have a peak of production between $y^+ \approx 7 - 13$. The largest amplitude is seen for the pure straining structures with flattening character (III).

The interpretation of these results is supported by the schematic description in figure (6.60). It shows the turbulent clusters that were discussed in section (6.4), rising from the wall and forming the turbulent low-speed regions (yellow) surrounded by the calm high-speed region. The vectors $\tilde{\vec{u}}_c$ and $\tilde{\vec{u}}_t$ indicate the conditional mean velocity vectors conditioned for the calm high-speed regions and the lifting low-speed clusters. Whereas the lifting turbulent clusters have a positive wall-normal velocity component on average, the calm high-speed regions entraining into the boundary layer have a negative wall-normal component on average. According to their ratio of frequency of occurrences which is 0.45 : 0.55, for calm versus turbulent, these two conditional mean velocity vectors

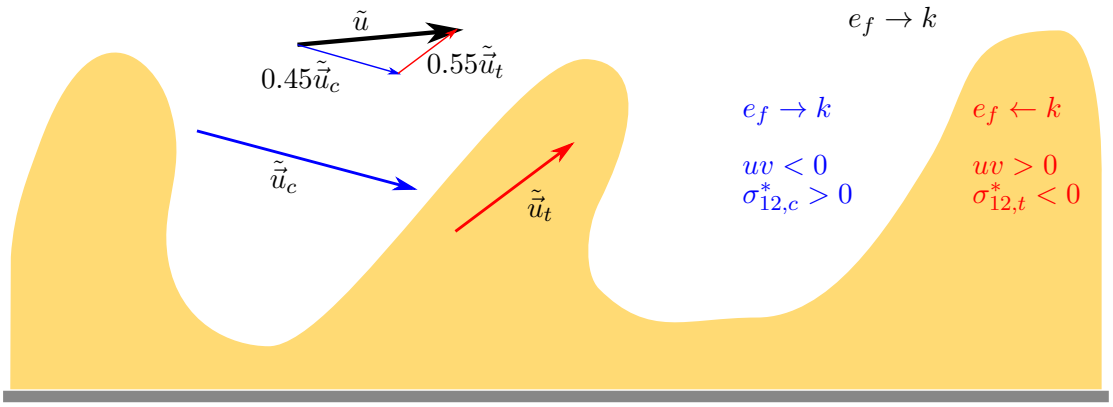

Figure 6.60: Schematic description of the composition of the mean flow as well as the turbulence production in the TBL. Slow, turbulent spots rising from the wall (grey) are shown in yellow. For reference see section (6.4). The illustration shows a cross section looking in the span-wise direction.

contribute to the overall mean velocity vector $\tilde{\vec{u}}$. At this stage it becomes obvious that the overall mean is just a superposition of different states as already discussed in section (6.4). Similarly we can argue for the production. To simplify the whole mechanism we want to focus on the significant quantities and neglect quantities with little impact only. Due to the statistically homogeneous span-wise direction the mean strain rate tensor in this flow has the form

$$\bar{S} = \begin{pmatrix} \frac{\partial \tilde{u}}{\partial x} & \frac{1}{2}\left(\frac{\partial \tilde{u}}{\partial y} + \frac{\partial \tilde{v}}{\partial x}\right) & 0 \\ \frac{1}{2}\left(\frac{\partial \tilde{u}}{\partial y} + \frac{\partial \tilde{v}}{\partial x}\right) & \frac{\partial \tilde{v}}{\partial y} & 0 \\ 0 & 0 & 0 \end{pmatrix}. \tag{6.19}$$

The wall-normal direction in this flow has the most significant variation in the mean quantities, the changes in stream-wise direction are comparably small for most of the boundary layer. Therefore, as a first simplification, we neglect all stream-wise derivatives of mean quantities: $\frac{\partial \tilde{u}}{\partial x} = \frac{\partial \tilde{v}}{\partial x} = 0$. The second and last assumption is that the compressibility effects are small compared to the changes in wall-normal direction which means that we set the trace of the strain rate tensor to zero: $\frac{\partial \tilde{v}}{\partial y} = -\frac{\partial \tilde{u}}{\partial x} = 0$. These assumptions simplify the production to

$$\langle \sigma^*, \bar{S} \rangle_F = \sigma^*_{12} \frac{\partial \tilde{u}}{\partial y}. \tag{6.20}$$

If we now look into a calm high-speed region we find the stream-wise velocity higher than its mean value and additionally we find a negative wall-normal velocity component. This leads to a relatively strong negative shear $uv < 0$ and further to a positive Favre shear stress component $\sigma_{12,c} * 2 > 0$ conditioned for the calm high-speed regions. The wall-normal gradient of the stream-wise mean velocity component is positive $\frac{\partial \tilde{u}}{\partial y} > 0$ and therefore production is positive and seemingly transfers kinetic energy from the mean to the fluctuations. On the other hand, the conditioned mean flow in the turbulent

low-speed regions is directed away from the wall and much slower than the overall mean flow. This leads to a positive shear $uv > 0$ and further to a negative Favre shear stress component $\sigma^2_{12,t} < 0$ conditioned for the turbulent low-speed regions. Putting the pieces together brings us to a negative production and an apparent transfer of kinetic energy from the turbulent fluctuations to the mean flow.

As a summary we find a forward cascade, i.e. kinetic energy from large scales to small scales, in the calm high-speed regions and a backward cascade, i.e. kinetic energy from the small scales to the large scales, in the turbulent low speed regions. This agrees with what the results show in figure (6.59, a). However, the fact that a calm flow region is supposed to produce all of the turbulent kinetic energy in the outer layer, whereas the turbulent regions destroy the turbulent kinetic energy and feeds it back to the mean flow does not sound physically conclusive. Intuitively we would have expected the opposite. The analysis we carried out here reveals a significant fact about the interpretation of physical mechanisms in the sense of FAS. The flow provides two physical states, the fast calm regions and the slow turbulent regions, that behave in different ways. FAS describes the turbulence σ with both states superimposed and couples this superposition to the mean strain rate tensor to obtain a production of small scale kinetic energy. However, if we compare the single physical states rather than their superposition to the mean strain rate tensor, we create a potentially too strong forward cascade in the calm regions and a pseudo backward cascade in the turbulent regions that do not necessarily have a physical meaning.

The same holds in the near-wall region. For example, here the calm high-speed spots develop a strong strain field at the wall. As we have seen before (fig. 6.35), the high-speed fluid $\tilde{u} < u$ presses against the wall ($v < 0$). This happens in form of pure straining structures with flattening character and results in a very high production for these structures (fig. 6.59, b).

However, due to the missing physical interprestation we will not further discuss these results. Nevertheless, the presented results are of importance to understand the meaning of a potentially *unphysical* mean. One has to be aware that a mean does not necessarily represent a single physical state, but a superposition of several states. On the other hand, this is not an issue as long as we are aware of the consequences. Considering for instance the Reynolds average Navier-Stokes (RANS) equation, which are based on FAS. That means RANS as well does not distinguish between the calm high-speed region and the turbulent low-speed regions - it just knows about the mean flow which is the superposition of both states. If we now want to model knowledge that we gained about the physics of turbulence, then these physics have to be translated so that they fit into the superimposed world of RANS. That means, for example, that a region of the flow where the fluid behaves almost laminarly, as for the calm characteristic regions, can indeed be a strong producer of turbulent kinetic energy - although it does not make physical sense.

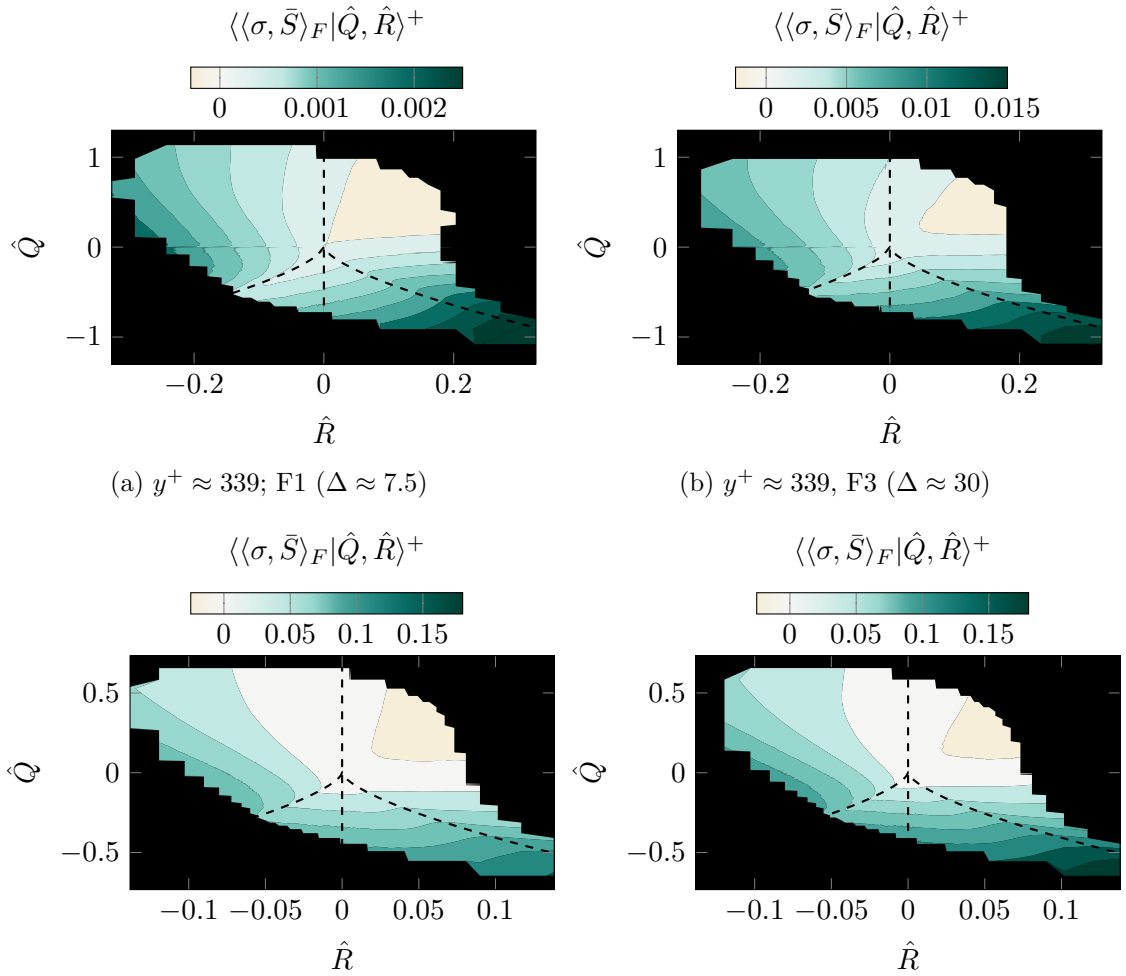

(a) $y^+ \approx 339$; F1 ($\Delta \approx 7.5$)

(b) $y^+ \approx 339$, F3 ($\Delta \approx 30$)

(c) $y^+ \approx 34$, F1 ($\Delta \approx 7.5$)

(d) $y^+ \approx 34$; F3 ($\Delta \approx 30$)

Figure 6.61: Conditional averages of the turbulence production based on SFS at 2 different wall-normal locations and for two different filters (F1 and F3) conditioned with the respective QR-states.

6.7.2 Turbulence Production of the Large Spatial Scales

In case of splitting the flow into large scales and small scales based on spatial filtering, the results are marginally different to the previously discussed case of FAS. Further, in case of SFS the turbulence production is defined purely via spatial operations. This means that we do not have to study a modified production as in the previous section, and the production term can be studied directly. Figure (6.61) shows the conditional averages of the production in the outer region for two different filter operators, conditioned with the respective QR-states. The plots show that the two different filters as well as the two different locations do not have significant qualitative differences. That supports the idea that the characteristic composition of the turbulence production is not changing significantly for the different filters and different locations in the outer region. The strongest production is found in the tail of the *teardrop*, the region where

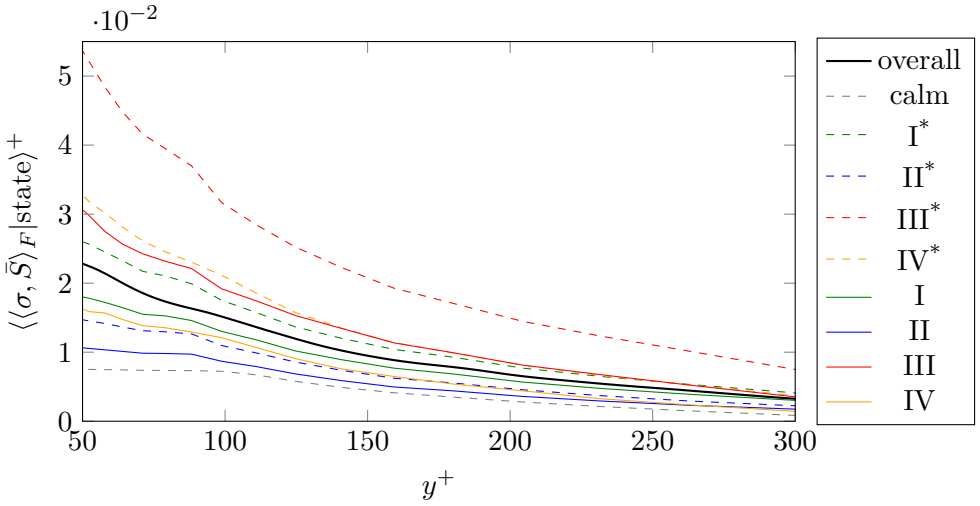

Figure 6.62: Conditional averages of the turbulence production based on SFS F3 conditioned with the respective characteristic states defined in sections (6.3) (continuous lines) and (6.4) (dashed lines).

structures change their character from type II to type III. That means, where contracting rotational structures develop to pure straining structures with flattening character. Towards the pure straining structures with elongating character the production decrease but increases again when we move towards stretching vortices. However, when the vortices become more unstable and move towards the contracting vortical structures, their production decreases steadily. It decreases so much, that for a wide range of QR-states of characteristic type II we find a slightly negative production. This indeed reveals a backwards cascading process within the characteristic structure type of contracting vortices.

Figure (6.62) shows the results of SFS F3 in the outer region, integrated over the respective regions of the characteristic states with and without the calm state. The pure straining structures with flattening character have by far the strongest production and their dominance is even stronger when we consider the characteristic decomposition including the calm state - as suggested for the outer region. The calm state itself has the lowest production throughout. Unlike for the results of the FAS, this behaviour is what we would expect from a flow region that is calm and without strong gradients. Although, they cover the backscatter in the backward cascade, the contracting vortices still have a positive net production due to the strong positive production in the tail of the teardrop. The pure straining structures with elongating character and the stretching vortices show a similar behaviour and form the intermediate structures with respect to turbulence production in case of SFS in the outer region.

The behaviour of production for the near-wall region is shown in figure (6.63). At $y^+ \approx 24$ the distribution looks similar to the outer regions. When we move closer to the wall we can see that initially the backscatter region inflates. By the end of the buffer layer at $y^+ \approx 6.7$ it spreads far into the region of stretching vortices. However, in the viscous sublayer it reduces again to contracting vortices only. In conjunction with that,

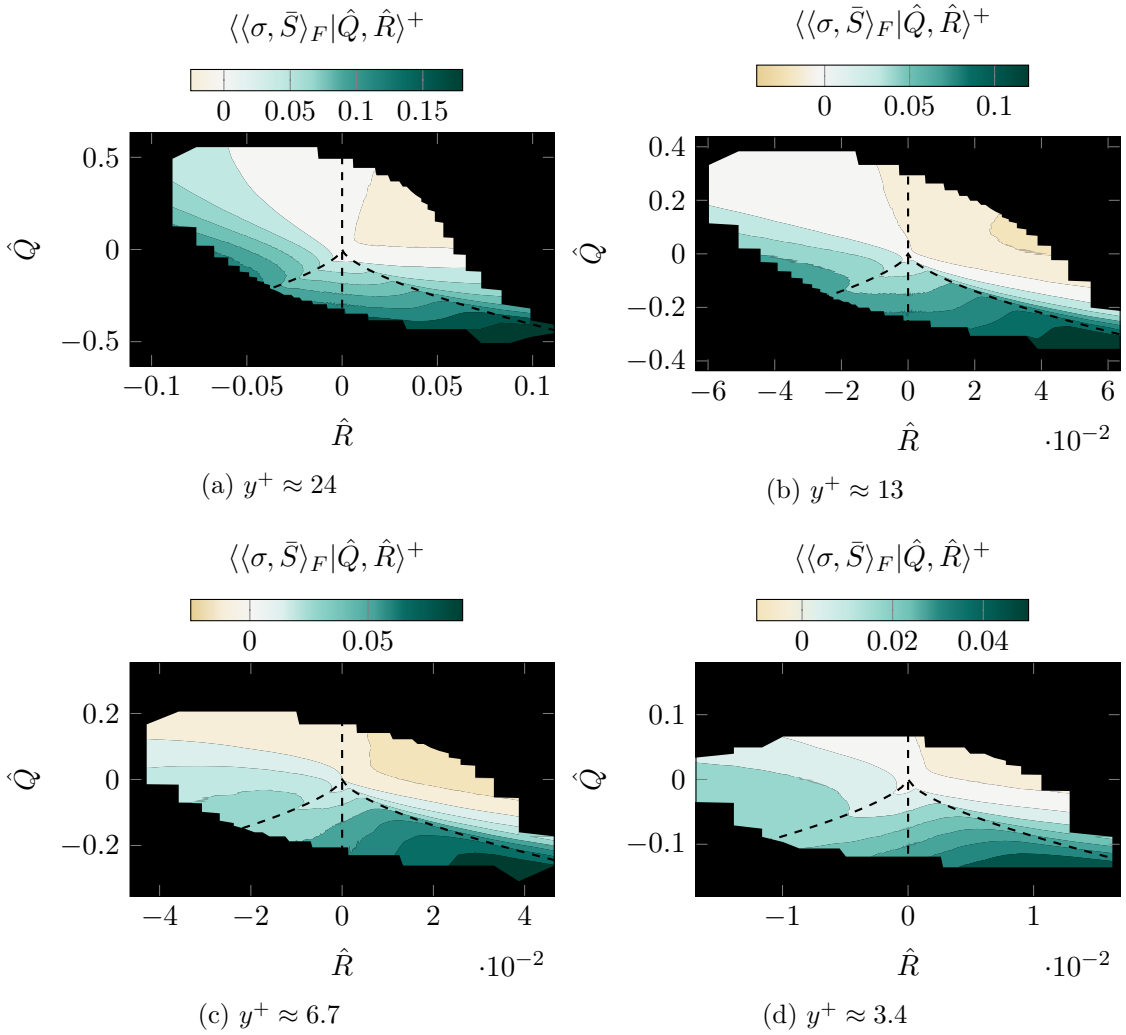

Figure 6.63: Conditional averages of the turbulence production based on SFS F3 ($\Delta \approx 30$) at six different wall-normal locations conditioned with the respective QR-states.

the relative production of the stretching vortices decreases and the relative production for the pure straining structures increases. If the maximum of production was confined in the tail of the teardrop it spreads towards lower values of R when approaching the wall.

Figure (6.64) shows the production for the near-wall region integrated over the respective states of the characteristic structure types. We plotted the results for characteristic decomposition including and excluding the calm state for completeness. However, we reduce the discussion to the characteristic decomposition without the calm state due to the possible misinterpretation of the calm state in the near-wall region as mentioned in previous sections. As the results in figure (6.63) already indicated the outer region dominance of the pure straining structures is amplified closer to the wall. Structure type III remains the relatively strongest producer of small scale kinetic energy, but structure type IV becomes significantly stronger than the stretching vortices below $y^+ \approx 40$. Additionally, the rotational structures show a significant drop of their production rate in

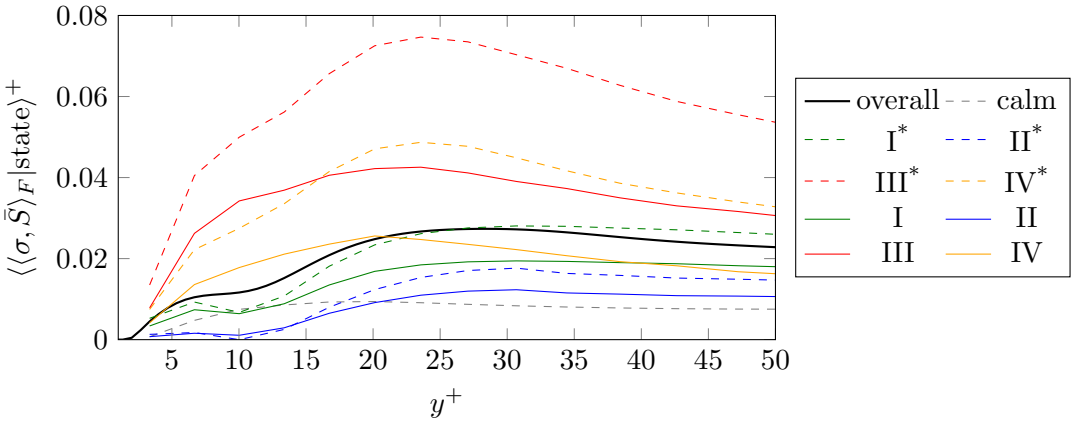

Figure 6.64: Conditional averages of the turbulence production based on SFS F3 conditioned with the respective characteristic states defined in sections (6.3) (continuous lines) and (6.4) (dashed lines).

the near-wall region. Due to the high frequency of occurrence of these structures, this drop causes a flattening of the overall production between $y^+ \approx 8 - 12$ and with that a shift of the production peak to the higher regions of the buffer layer. The drop of the production in the rotational structures is mainly caused by the spreading of the backscatter region that we mentioned before (fig. 6.63).

There are many things yet unclear about the production mechanism, but we can discuss the backwards cascade further. Due to its location in the characteristic region of contracting vortices we can give a suggestion about how this backscatter mechanism might work (fig. 6.65). Vortices during vortex stretching have a positive intermediate strain in the direction of their axis (sec. 4) which causes the vortices to elongate. This is during the phase in which the vortices can be classified by characteristic structure

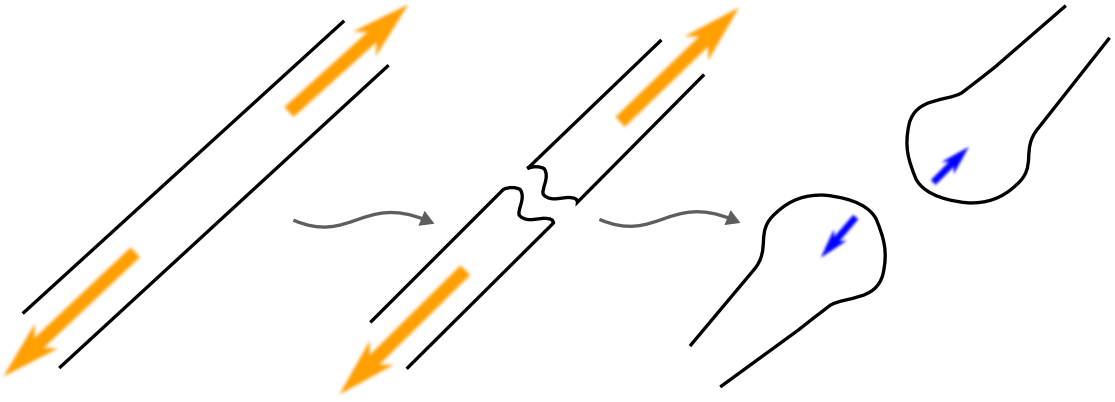

Figure 6.65: Schematic description of the backscatter mechanism: Vortex tube (black) is stretching under tension in the direction of the rotation axis. Tube breaks up. Pressure minimum in vortex core contracts split ends in the axial direction and the vortex forms a bulky shape. Straining forces are marked by yellow arrows and pressure forces are marked by blue arrows.

type I. The vortices will pass a threshold where the stretching process becomes unstable and they will break up locally. The parts of the vortices that break up will be a characteristic type II at this time as this covers unstable/contracting vortices. Once the vortices are split at one location whereas the remaining vortex tubes still exist, the actual backscatter mechanism is active. The vortex cores of the remaining vortices still hold a pressure minimum and attract the fluid at the ends of the vortices that formed due to the breakup. This causes a local increase of diameter of the, still rotating, vortices and therefore a shift of the kinetic energy to a larger scale than for the previously thin vortex. This theory can holds for the outer region, but the cause for the spreading of the backscatter region at the wall remains unclear. The explained scenario, for now, is just a hypothesis that needs to be confirmed. This can be done by a non-local analysis that relates structure shapes to the characteristic decomposition.

6.7.3 Conclusions about Turbulence Production and the Cascading Process of Kinetic Energy

In this section we discussed the origin of turbulence in this turbulent boundary layer flow from two perspectives. In case of FAS it appeared that the calm high-speed flow regions in the boundary layer represent a strong forward cascade that transfers energy from the mean flow to the fluctuations whereas the turbulent low-speed regions represent a backwards cascade that transfers kinetic energy from the fluctuations to the mean flow. However, it turned out that this is a misinterpretation of the results and what we ultimately could show were a too strong forward cascade and a pseudo backward cascade. Due to the fact that the mean of a quantity in general can be a superposition of various physical states but not necessarily representing a single physical state by itself, the analysis carried out has to be studied with care. In the present case we compared a characteristic decomposition of the fluctuations' physical states of turbulence to the non-physically (approximately) unidirectional mean strain. This led to an alignment of these quantities - and further, to a production - that does not describe a physical state. This means that intuitive interpretations might be misleading. As turbulence models for e.g. RANS are based on FAS, we emphasized that it is important to carry out an unphysical-mean-aware-modelling of the physics that we know. This means that we need to interpret the physics in the way that they are understood by the mean flow field. This might then lead to the fact that a calm flow region with small gradients is actually a very strong producer of turbulent kinetic energy simply due to the fact that it is a high-speed region.

In case of SFS we revealed a transfer of kinetic energy from large scales, to small scales mainly for pure straining structures and part of the vortical stretching structures. On the other hand, we identified a backscatter mechanism that transfers kinetic energy from small scales to large scales within the contracting vortical structures. There are possibly two types of forward scale transfer (energy from large scales to small scales).

One would be the *self-transfer*, which is found for elongating pure straining structures and during vortex stretching. It is caused by the thinning of structures and does not need interaction of different structures. This is the weaker of both transfer mechanisms. The stronger mechanism is located in the pure straining structures with flattening character and reaches slightly into the QR-region of the contracting vortical structures. This could be a mechanism that causes new, smaller structures being created in the surrounding shear-layer of larger structures. When approaching the wall this mechanism becomes stronger which supports that in the strong, large shear-layer of the near-wall region the production of turbulence is very active. The backscatter mechanism mainly settled in the QR-region of contracting vortical structures was described as a result of vortical structures breaking up and partially increasing their diameter. Therefore it would be a *self-transfer* and does not involve an interaction between different structures. However, this is as of yet just a hypothesis and needs confirmation with an adapted analysis that relates structure shapes to the characteristic decomposition that we used extensively in this work.

6.8 Conclusions

This chapter is a comprehensive overview and characterisation of the mechanisms that drive turbulence in a fully turbulent flat-plate boundary layer without mean pressure gradient. The global and energetic processes are exposed and discussed as well as some of the relevant couplings that direct the existence and development of certain turbulent structures. The role of the wall was emphasized and the discussion was kept general enough to possibly transfer the theories to general wall-bounded turbulent flows and potentially even further. The detailed analysis was carried out by splitting the flow field into large scales and small scales defined by respective filter operators. In order to interpret the results accurately a set of four different filter operators was applied. The only temporal filter in the set was the Reynolds operator that allowed a splitting into large scales and small scales based on the Favre average decomposition (Favre averaged based splitting, FAS). This way of splitting the flow field is identical to what is applied in the Reynolds averages Navier-Stokes (RANS) equations. Therefore results risen from this splitting method can help to improve turbulence models that are used to close the RANS equations. The remaining three filter operators are purely spatial filter with a Gaussian kernel function. The only parameter that has varied for the filters was the filter width. This was varied in the range from slightly larger than the viscous sublayer (VSL) height up to half the buffer layer height. These filter operators allow a splitting based on the Favre filtered values (spatial filter based splitting, SFS) that are used to decompose the flow field according to structure sizes. This way of splitting the flow field is identical to what is applied in Large-Eddy simulations (LES). The comparison of different filter widths allows conclusions e.g. about how much of the large-scale energy is actually governed by the small-scales of a certain size. Additional to the splitting of the flow field with a spatial or temporal filter operator, a characteristic decomposition was applied on the flow field. This allows to decompose a flow field into distinct structure types with certain characteristics. The aim behind that is to find an appropriate decomposition that defines structures with features that are invariant in the flow. Such universal features provide backbones for solid theory of turbulence and help to improve turbulence models.

One aspect of the flow that was discussed in detail are the processes that create the particular energy distibution in the turbulent boundary layer flow. For the first time this energy distribution was discussed in such a complete form for turbulent boundary layers. Mechanisms like e.g. mean transport and diffusion were classified according to their properties with respect to energy redistribution in the flow. To quantify the impact of turbulence itself on the global boundary layer the ratio of the contribution of large scales and the contribution of small scale on the overall redistribution process was worked out. It became clear that for FAS the contributions of turbulence to the distribution of the energy of the mean flow is about 50%. On the other hand, for SFS the contributions of the small-scales to the energy distribution process of the large scale

energy varied between 6% and 21% for the applied filter operators. At the same time these numbers reflect how high the direct influences of the turbulence models are on the resolved energy in case of RANS and LES, respectively. As expected the direct impact of a turbulence model on the mean flow is much higher for RANS simulations than, even for very coarse, LESs in this particular flow.

Within the different possibilties that turbulence is interacting with the energy distribution on average the mechanism described as *turbulent mixing* is by far the strongest. This mechanism is active from the upper end of the turbulent boundary down until within the buffer layer region and is mainly a spatial large scale feature. For the largest spatial filter width we found a recognizable contribution of the spatial small-scales of motion to the mixing, but this is believed to be a local interaction, whereas the main mixing process is a global event. Turbulent fluid from the near-wall region is bursting out into higher and more calm flow regions. The rising fluid is moving downstream considerably slower than the fluid at the higher layer. Additionally, turbulent structures from the near-wall region are lifted with the fluid so that low-speed clusters of turbulent structures are formed. Inbetween these clusters calm, high-speed fluid from the freestream is entrained into the boundary layer and forms calm, high-speed regions inbetween the turbulent spots. The low-speed clusters and high-speed regions define two states of the boundary layer flow at regions, more or less, above the buffer layer. The characteristics of these large-scale structures are widely agreeing with literature about low-speed streaks and a high-speed streaks. The fact that they are two fairly distinct states contributes strongly to the intermittent character of the turbulent boundary layer flow. Although, a clean split between both states has not yet been defined, an accepatable preliminary definitions has been developed and applied in this chapter.

The internal energy is affected by this mixing process as well. In the present turbulent boundary layer, the wall temperature was chosen to be isothermal at the adiabatic temperature of the freestream. This means that the wall is slightly hotter than the freestream and the negative mean temperature gradient from the wall to the freestream, that occurse due the friction heat produced by the high dissipation at the wall, is promoted. Therefore the turbulent mixing acts in the opposite way on internal energy than it does on the kinetic energy. Hot spots are rising from the wall and bursting into the colder fluid at higher layers. Vice versa cold fluid from the freestream entrains into the warm boundary layer flow.

The wall affects the flow in several diffenent ways. The most obvious ones, that are even present in laminar boundary layers, are that the wall creates a shear layer and potentially a temperature gradient. The temperature gradient in the present case is small enough to have insignificantly small impact on the dynamics of turbulence. The strong shear layer, on the other hand, is the root of the turbulent flow. It drives the strong turbulent production as well as the high dissipation rate in the near-wall region. Further, we have shown that the wall destabilizes vortical structures by interacting with the pressure minimum that develops within a vortex core and balances the centrifugal

forces of the fluid particles in the vortex. The wall attracts this pressure miniumum and pulls it out of the vortex' core. The resulting misbalance of forces is believed to destabilize the vortical motion at the wall-side which causes that they bend and lift towards the far side with respect to the wall. The vortices do not break-up completely and the remaining stable part is lifting and slowing down the fluid at higher locations. This mechanism is similar to the one creating hairpin vortices and is believed to be the trigger for the outbursts of slow turbulent fluid into the higher layers that drive the energetic turbulent mixing.

Whereas in the higher layers we find arbitrary aligned structures, in the near-wall region the rotational structures align their axis with the streamwise direction parallel to the wall. Moreover, the structures are packed very densely in the near-wall region which causes a strong interaction of their surrounding strain field. This and the interaction with the wall itself reflects in a strong coupling of strain rate magnitude and rotation rate magnitude in the near-wall region. This explains the increase of relative dissipation of the stretching vortices close to the wall. Together with the destabalizing effect the wall has on vortices this causes an increase of dissipation for rotational structures which contributes strongly to the high turbulent dissipation at the wall. This is contrasting the conclusion about dissipation in the higher regions. There the strongest relative dissipaters are pure straining structures with flattening character.

The turbulent scale transfer was discussed through the turbulent production which is in the end nothing else but an exposed part of the full cascading process. Which part of the cascade is actually exposed is defined by the respective filter operator. On one hand, we have seen a pseudo backwards cascade and too strong forward cascade in case of FAS. This was found to be a misinterpretation of the analysis process. However, this revealed interpretation issues that might rise when physical mechanisms are supposed to be modeled according to their mean contributions. On the other hand, a physical split of the cascading process in a forward part and a backwards part was found by applying SFS. The analysis revealed two types types of a forward cascading process. The *self-transfer*, which is achieve via vortex stretching by single turbulent structures without much influence of other structures or boundary conditions. This is accompanied by an interaction process in which structures transfer energy through their shear-layers to other structures. These forward processes are contrasted by a backscatter process that acts within the unstable/contracting vortical structures. The clear presence of the backscatter mechanism was shown, but its cause cannot be proven. It is believed to be caused by the thickening of vortical structures after the broke up.

Additional to the stabilizing property of pressure, that was discussed before, we found a second, closely related, role that the pressure has in turbulence. As a reversible energy transfer between kinetic and internal energy is was show that pressure-work utilizes the pressure as temporal donor of energy during vortex dynamics. During vortex stretching the fluid is accelerated around the thinning vortex core. At the same time the local pressure minimum in the vortex core becomes lower and stabilizes the fluid at a higher

angular momentum. During this process, internal energy is transfered to kinetic energy. Once the vortex broke down this energy is transfered back to the internal energy and the pressure minimum vanishes.

A large part of this analysis was supported by the characteristic decomposition of turbulence into structures of different character. This allowed to study which parts of turbulence are involved in certain mechanisms and how much they contribute. For instance this decomposition was the essential tool to reveal the backscatter that is usually superimposed by the much stronger positive part of the turbulence production. Although the decomposition was improved within this chapter it is not ideal yet and will need further adjustments and cross-comparison with different flows. The goal should be to find a more universal decomposition that ultimately decomposes the turbulences into parts that are invariant under the change of flow or flow topology. If the relative contribution of these parts are known then the frequency of occurrence of the respective parts (QR-plot for the present decomposition) will fully describe turbulence. However, this is still quite a big step away.

Chapter 7

Summary and Perspectives for Future Work

This work was embedded in the research project Is fine-scale turbulence universal?. As the name suggests already, the task of this project was the investigation of the potential for universal theories of turbulence. In other words we were concerned to find features of turbulent quantities that are invariant across different flows and different flow topologies. These can then underpin improved and more general turbulence models and form a foundation of a solid theory of turbulent flows. As part of this particular work, we were concerned with numerical simulations of turbulent flows to produce data sets of turbulent flows that were processed and analysed. The achievements along this path are summarized in the following.

7.1 New Developments

1) As part of this particular work, an existing DNS code was extended and improved to be able to produce and capture the data needed for further processing and analysis. To process the large time-resolved datasets of the three different turbulent flows, a post-processing tool was developed. The four cornerstones of the development were scalability, efficiency, modularity and adaptivity. The post-processing tool carries out the processing datasets of several terabytes on HPC clusters, is used by about 10 other academic researchers, processing the data of two different CFD codes, and is soon to be applied to process vector fields of tomographic PIV data.
2) The fully compressible governing equation of the large-scales of flow defined by an arbitrary homogeneous or inhomogeneous filter operator were developed from the compressible Navier-Stokes equations. The small-scale contributions are highlighted and need to be described by a model when the system needs to be closed. The equations can be applied in RANS, URANS, LES, hybrid RANS-LES, DES all with homogeneous

and inhomogeneous filter and averaging operators. However, in this work the equations were applied to analyse the flow data of DNS as a post-processing step. By averaging and filtering the data, we were able to describe the large-scale, small-scale as well as the mixed mechanisms separately.
3) The fully compressible velocity gradient invariant dynamics were derived. They allow the analysis for the characteristic development of turbulence and as a long term goal it is planned to apply them as a turbulence model and merge them into the filtered equations. Although not applied in the present work, this system of equations was applied to analyse the characteristic dynamics in a turbulent boundary layer. The work is about to be published as conference proceedings.

7.2 New Results

7.2.1 Universality of the Velocity Gradient Quantities

In order to investigate universal features of turbulence the different flows were simulated as direct numerical simulation and analysed with the focus on the velocity gradient and related quantities. Therefore different flow regions in a turbulent boundary layer, in a jet flow and in a wake flow were characterised and the universal log-normal distributions of the magnitudes of the velocity gradient, the strain rate tensor and the rotation rate tensor, respectively, were found. Further, a universal mechanism that links the local mean-shear, the correlation of strain rate magnitude and rotation rate magnitude and the alignment of strain rate tensor with the rotation rate tensor, was proposed. The differences in the three flows revealed that the characteristic distribution (QR-plot) is not an universal feature of turbulence.

7.2.2 Enstrophy Production in a TBL

The enstrophy production, an important quantity in the turbulent cascading process, was studied in detail in the turbulent boundary layer flow data. The main focus of the analysis was the variation of enstrophy production normal to the wall. Therefore the enstrophy production was decomposed into strain and rotation magnitude, strain composition and alignment between the vorticity and the strain eigenframe to be analysed for different characteristic structures types separately. This analysis reveals that the wall causes a layer of aligned turbulent structures at the wall. This results in strong shear layers between the structures which eventually leads to extreme events of enstrophy production. The alignments of strain and rotation agree broadly with observations in the strong shear layers in the jet and wake that were discussed before. The strongest producers of enstrophy were found to be vortex stretching. A backscatter mechanism, that was later proven to transfer energy from small-scale motions to large-scale motions,

was already indicated to be caused by unstable vortices. When approaching the wall everything becomes dominated by typical strong shear mechanisms that were discussed before.

7.2.3 Turbulent Mechanisms in a TBL

A turbulent boundary flow (TBL) was simulated via direct numerical simulation and analysed in detail. The processing of the results and the followed discussion provides a detailed overview that allows to obtain a global image of a TBL from several different perspectives. Many of the discussed mechanisms are not restricted to TBLs or at least it is straight forward to apple them to other flow topologies - which is planned for the near future. The investigations were the first detailed and comprehensive analysis of a TBL. Further, it includes the first presentation and discussion of the full, compressible energy budget of a TBL.
By decomposing flow quantities a new perspective on the large streaky structures of flat-plate boundary layers was provided. They have been related with blow-outs of turbulence from the wall together with entrainment of calm fluid from the freestream deep in the boundary layer. This process is described as turbulent mixing and is the strongest global turbulent process that acts on the large scale flow. The consequences for turbulence models caused by the turbulent mixing were discussed in detail.
The energy cascading process, that drives turbulence, was exposed by filter operation and two sorts of positive production mechanisms where found accompanied by a backscatter mechanism with a negative net production. The positive mechanisms were the *self-production* that is basically vortex stretching of a vortex without the interaction with other structures and the *non-self-production* that is cause by the creation and feeding of smaller structures in the strain field surrounding larger structures. This process is for example applied to the flow by the wall itself. The negative production mechanism was found within the unstable/contraction vortical structures. It is believed to be driven by vortices which are subject of a break-up process due to instabilities. These vortices develop bulky ends at the part where they broke up. However, this is just an hypothesis at this stage.
A relatively high concentration of unstable vortical structures was found in the near-wall region. It was shown that the wall has a destabilizing effect on vortices as is attracts the pressure core that balances the forces within the rotational structures. Further, the most dissipative structures where revealed and discussed.

7.2.4 Characteristic Decomposition as a Research Tool

Characteristic decomposition has been proven to be a good analysis tool for turbulent flows. The mechanisms of turbulence are split in a relatively logical way and show trends

towards universal behaviour. However, there is room for improvements. The original decomposition was already well suited to capturing the strongly intermittent turbulence in a turbulent boundary layer. However, there are still unclear parts and open questions that need to be answered. Open questions and problems of the present decomposition were discussed and a path for its further development was suggested.

7.3 Future Work and Suggestions

The extensive analysis that was carried out on the TBL revealed many mechanisms with a great potential to have universal structures. These mechanism should be investigated in different flows. It is planned to analyse high Reynolds number data of a turbulent boundary layer obtain from tomographic particle image velocimetry in the near future. Further, the analysis is planned to be extended to jet data of varying Reynolds number and the recirculation region of the wake flow. This is believed to lead to a more universal image of turbulence. Moreover, it will help to develop and refine the characteristic decomposition further.

Appendix A

Appendix Governing Equations

A.1 Derivation of energy equations

A.1.1 Kinetic energy e_{kin} equation

We obtain the kinetic energy equation by substracting the continuity equation (2.1) premultipied with $\frac{1}{2}\vec{u}^2$ from the momentum equation (2.2) premultipied with $\vec{u}$:

$$\begin{aligned}
&\vec{u}\cdot\left(\frac{\partial\rho\vec{u}}{\partial t}+\nabla\cdot(\rho\vec{u}\otimes\vec{u})+\nabla p-\nabla\cdot\tau\right)-\frac{1}{2}\vec{u}^2\left(\frac{\partial\rho}{\partial t}+\nabla\cdot(\rho\vec{u})\right)\\
=&\vec{u}\cdot\frac{\partial\rho\vec{u}}{\partial t}-\frac{1}{2}\vec{u}^2\frac{\partial\rho}{\partial t}+\vec{u}\cdot\nabla\cdot(\rho\vec{u}\otimes\vec{u})-\frac{1}{2}\vec{u}^2\nabla\cdot(\rho\vec{u})+\vec{u}\cdot\nabla p-\vec{u}\cdot\nabla\cdot\tau\\
=&\frac{\partial\rho\frac{1}{2}\vec{u}^2}{\partial t}+\nabla\cdot(\rho\vec{u}\frac{1}{2}\vec{u}^2)+\vec{u}\cdot\nabla p-\vec{u}\cdot\nabla\cdot\tau\\
=&\frac{\partial\rho e_{\text{kin}}}{\partial t}+\nabla\cdot(\rho\vec{u}e_{\text{kin}})+\vec{u}\cdot\nabla p-\nabla\cdot(\tau\cdot\vec{u})+\langle\tau,\nabla\vec{u}\rangle_F\\
=&0
\end{aligned}\tag{A.1}$$

A.1.2 Internal energy equation

We obtain the equation for internal energy e by substracting the equation for kinetic energy e_{kin} (A.1.1) from the equation of total energy $E=e+e_{\text{kin}}$ (2.3):

$$\begin{aligned}
&\frac{\partial\rho E}{\partial t}+\nabla\cdot(\vec{u}\rho E)+\nabla\cdot(\vec{u}p)-\nabla\cdot(\tau\cdot\vec{u})-\nabla\cdot\vec{q}\\
&-\frac{\partial\rho e_{\text{kin}}}{\partial t}-\nabla\cdot(\vec{u}\rho e_{\text{kin}})-\vec{u}\cdot\nabla p+\nabla\cdot(\tau\cdot\vec{u})-\langle\tau,\nabla\vec{u}\rangle_F\\
=&\frac{\partial\rho(e+e_{\text{kin}})}{\partial t}+\nabla\cdot(\vec{u}\rho(e+e_{\text{kin}}))+\nabla\cdot(\vec{u}p)-\nabla\cdot(\tau\cdot\vec{u})-\nabla\cdot\vec{q}\\
&-\frac{\partial\rho e_{\text{kin}}}{\partial t}-\nabla\cdot(\vec{u}\rho e_{\text{kin}})-\vec{u}\cdot\nabla p+\nabla\cdot(\tau\cdot\vec{u})-\langle\tau,\nabla\vec{u}\rangle_F
\end{aligned}\tag{A.2}$$

Using the definition for enthalpy $\rho h := \rho e + p$ the transport term of the internal energy can be merged with the pressure diffusion to represent an enthalpy transport.

$$\begin{aligned}
&\frac{\partial \rho e}{\partial t} + \frac{\partial \rho e_{\text{kin}}}{\partial t} + \nabla \cdot (\vec{u} \rho h) + \nabla \cdot (\vec{u} \rho e_{\text{kin}}) - \nabla \cdot (\tau \cdot \vec{u}) - \nabla \cdot \vec{q} \\
&- \frac{\partial \rho e_{\text{kin}}}{\partial t} - \nabla \cdot (\vec{u} \rho e_{\text{kin}}) - \vec{u} \cdot \nabla p + \nabla \cdot (\tau \cdot \vec{u}) - \langle \tau, \nabla \vec{u} \rangle_F \\
=&\frac{\partial \rho e}{\partial t} + \nabla \cdot (\vec{u} \rho h) - \vec{u} \cdot \nabla p - \nabla \cdot \vec{q} - \langle \tau, \nabla \vec{u} \rangle_F \\
=&0
\end{aligned} \tag{A.3}$$

A.2 Energy Equation Analysis

A.2.1 Diffusion

$$\begin{aligned}
&\nabla \cdot (\tau \cdot \vec{u}) \\
=&\nabla \cdot \left(2 \frac{\mu}{Re_\infty} S \cdot \vec{u} - \frac{2}{3} \frac{\mu}{Re_\infty} \text{trace}(S) \vec{u} \right) \\
=&\nabla \cdot 2 \frac{\mu}{Re_\infty} \left((S \cdot \vec{u}) - \frac{1}{3} (\text{trace}(S) \vec{u}) \right) \\
=&\nabla \cdot \frac{\mu}{Re_\infty} \left(\vec{u} \cdot \left(\left(\nabla \vec{u} + \nabla \vec{u}^T \right) \right) - \frac{2}{3} \left((\nabla \cdot \vec{u}) \vec{u} \right) \right) \\
=&\nabla \cdot \frac{\mu}{Re_\infty} \left(\vec{u} \cdot (\nabla \vec{u}) + \vec{u} \cdot (\nabla \vec{u})^T - \frac{2}{3} \left((\nabla \cdot \vec{u}) \vec{u} \right) \right) \\
=&\nabla \cdot \frac{\mu}{Re_\infty} \left(\vec{u} \cdot (\nabla \vec{u}) + \frac{1}{2} \nabla \vec{u}^2 - \frac{2}{3} \left((\nabla \cdot \vec{u}) \vec{u} \right) \right) \\
=&\nabla \cdot \frac{\mu}{Re_\infty} \left(\frac{1}{2} \nabla \vec{u}^2 + (\nabla \times \vec{u}) \times \vec{u} + \frac{1}{2} \nabla \vec{u}^2 - \frac{2}{3} \left((\nabla \cdot \vec{u}) \vec{u} \right) \right) \\
=&\nabla \cdot \frac{\mu}{Re_\infty} \left(\nabla \vec{u}^2 + (\nabla \times \vec{u}) \times \vec{u} - \frac{2}{3} \left((\nabla \cdot \vec{u}) \vec{u} \right) \right) \\
=&\nabla \cdot \frac{\mu}{Re_\infty} \left(\nabla \vec{u}^2 + (\nabla \times \vec{u}) \times \vec{u} - \frac{2}{3} \left((\nabla \cdot \vec{u}) \vec{u} \right) \right) \\
=&\nabla \cdot \frac{\mu}{Re_\infty} \nabla \vec{u}^2 + \nabla \cdot \frac{\mu}{Re_\infty} \left((\nabla \times \vec{u}) \times \vec{u} \right) - \nabla \cdot \frac{\mu}{Re_\infty} \frac{2}{3} \left((\nabla \cdot \vec{u}) \vec{u} \right) \\
=&\nabla \cdot \frac{\mu}{Re_\infty} \nabla \vec{u}^2 + \nabla \cdot \frac{\mu}{Re_\infty} (\Omega \cdot \vec{u}) - \nabla \cdot \frac{\mu}{Re_\infty} \frac{2}{3} \left((\nabla \cdot \vec{u}) \vec{u} \right) \\
=&\nabla \cdot \frac{\mu}{Re_\infty} \nabla \vec{u}^2 + \frac{\mu}{Re_\infty} \langle \Omega, \nabla \vec{u} \rangle_F + \vec{u} \cdot \left(\nabla \cdot \frac{\mu}{Re_\infty} \Omega \right) - \nabla \cdot \frac{\mu}{Re_\infty} \frac{2}{3} \left((\nabla \cdot \vec{u}) \vec{u} \right) \\
=&\nabla \cdot \frac{\mu}{Re_\infty} \nabla \vec{u}^2 + \underbrace{\frac{\mu}{Re_\infty} \langle \Omega, \Omega \rangle_F}_{= \|\vec{\omega}\|_F^2} + \underbrace{\frac{\mu}{Re_\infty} \langle \Omega, S \rangle_F}_{= 0 \text{ as } \Omega \text{ skew-sym and } S \text{ sym}} \\
&+ \vec{u} \cdot \left(\nabla \cdot \frac{\mu}{Re_\infty} \Omega \right) - \nabla \cdot \frac{\mu}{Re_\infty} \frac{2}{3} \left((\nabla \cdot \vec{u}) \vec{u} \right)
\end{aligned} \tag{A.4}$$

$$= \nabla \cdot \frac{\mu}{Re_\infty} \nabla \vec{u}^2 + \|\vec{\omega}\|_F^2 + \vec{u} \cdot \left(\nabla \cdot \frac{\mu}{Re_\infty} \Omega \right) - \nabla \cdot \frac{\mu}{Re_\infty} \frac{2}{3} \left((\nabla \cdot \vec{u}) \, \vec{u} \right) \tag{A.5}$$

A.3 Derivation of Filtered Equations

A.3.1 Filtered Continuity

The filtered continuity equation is obtained by filtering the continuity equation (eq. 2.1).

$$\begin{aligned} 0 =& \overline{\frac{\partial \rho}{\partial t} + \nabla \cdot (\rho \vec{u})} \\ =& \frac{\partial \bar{\rho}}{\partial t} + \overline{\nabla \cdot (\rho \vec{u})} \\ =& \frac{\partial \bar{\rho}}{\partial t} + \nabla \cdot \left(\overline{\rho \vec{u}} \right) + [\nabla \cdot (\rho \vec{u})]_R \\ =& \frac{\partial \bar{\rho}}{\partial t} + \nabla \cdot \left(\bar{\rho} \tilde{\vec{u}} \right) + [\nabla \cdot (\rho \vec{u})]_R \end{aligned} \tag{A.6}$$

The filter residuum $[\nabla \cdot (\rho \vec{u})]_R$ is a fracment of a spatially inhomogeneous filter operator (def. 3.2.1).

A.3.2 Filtered Momentum

The filtered momentum equation is obtained by filtering the momentum equation (eq. 2.2).

$$\begin{aligned} 0 =& \overline{\frac{\partial \rho \vec{u}}{\partial t} + \nabla \cdot (\rho \vec{u} \otimes \vec{u}) + \nabla p - \nabla \cdot \tau} \\ =& \overline{\frac{\partial \rho \vec{u}}{\partial t}} + \overline{\nabla \cdot (\rho \vec{u} \otimes \vec{u})} + \overline{\nabla p} - \overline{\nabla \cdot \tau} \\ =& \frac{\partial \overline{\rho \vec{u}}}{\partial t} + \nabla \cdot \left(\overline{\rho \vec{u} \otimes \vec{u}} \right) + \nabla \bar{p} - \nabla \cdot \bar{\tau} + [\nabla \cdot (\rho \vec{u} \otimes \vec{u})]_R + [\nabla p]_R - [\nabla \cdot \tau]_R \\ =& \frac{\partial \bar{\rho} \tilde{\vec{u}}}{\partial t} + \nabla \cdot \left(\overline{\rho \vec{u} \otimes \vec{u}} \right) + \nabla \bar{p} - \nabla \cdot \bar{\tau} + [\nabla \cdot (\rho \vec{u} \otimes \vec{u})]_R + [\nabla p]_R - [\nabla \cdot \tau]_R \end{aligned} \tag{A.7}$$

A.3.3 Filtered Total Energy

The filtered total energy equation is obtained by filtering the total energy equation (eq. 2.3).

$$
\begin{aligned}
0 =& \overline{\frac{\partial \rho E}{\partial t} + \nabla \cdot (\vec{u}\rho E) - \nabla \cdot \vec{q} - \nabla \cdot (\tau \cdot \vec{u}) + \nabla \cdot (\vec{u}p)} \\
=& \overline{\frac{\partial \rho E}{\partial t}} + \overline{\nabla \cdot (\vec{u}\rho E)} - \overline{\nabla \cdot \vec{q}} - \overline{\nabla \cdot (\tau \cdot \vec{u})} + \overline{\nabla \cdot (\vec{u}p)} \\
=& \frac{\partial \bar{\rho}\tilde{E}}{\partial t} + \overline{\nabla \cdot (\vec{u}\rho E)} - \overline{\nabla \cdot \vec{q}} - \overline{\nabla \cdot (\tau \cdot \vec{u})} + \overline{\nabla \cdot (\vec{u}p)} \\
=& \frac{\partial \bar{\rho}\tilde{E}}{\partial t} + \nabla \cdot \left(\overline{\vec{u}\rho E}\right) - \nabla \cdot \bar{\vec{q}} - \nabla \cdot \left(\overline{\tau \cdot \vec{u}}\right) + \nabla \cdot \left(\overline{\vec{u}p}\right) \\
& + [\nabla \cdot (\vec{u}\rho E)]_R - [\nabla \cdot \vec{q}]_R - [\nabla \cdot (\tau \cdot \vec{u})]_R + [\nabla \cdot (\vec{u}p)]_R \\
=& \frac{\partial \bar{\rho}\tilde{E}}{\partial t} + \nabla \cdot \left(\overline{\vec{u}\rho E}\right) - \nabla \cdot \bar{\vec{q}} - \nabla \cdot \left(\overline{\tau \cdot \vec{u}}\right) + \nabla \cdot \left(\overline{\vec{u}p}\right) \\
& + [\nabla \cdot (\vec{u}\rho E)]_R - [\nabla \cdot \vec{q}]_R - [\nabla \cdot (\tau \cdot \vec{u})]_R + [\nabla \cdot (\vec{u}p)]_R
\end{aligned}
\tag{A.8}
$$

A.3.4 Filtered Internal Energy

The filtered internal energy equation is obtained by filtering the internal energy equation (eq. 2.17).

$$
\begin{aligned}
0 =& \overline{\frac{\partial \rho e}{\partial t} + \nabla \cdot (\vec{u}\rho h) - \nabla \cdot \vec{q} - \vec{u} \cdot \nabla p - \langle \tau, \nabla \vec{u} \rangle_F} \\
=& \overline{\frac{\partial \rho e}{\partial t}} + \overline{\nabla \cdot (\vec{u}\rho h)} - \overline{\nabla \cdot \vec{q}} - \overline{\vec{u} \cdot \nabla p} - \overline{\langle \tau, \nabla \vec{u} \rangle_F} \\
=& \frac{\partial \overline{\rho e}}{\partial t} + \nabla \cdot \left(\overline{\vec{u}\rho h}\right) - \nabla \cdot \bar{\vec{q}} - \overline{\vec{u} \cdot \nabla p} - \overline{\langle \tau, \nabla \vec{u} \rangle_F} + [\nabla \cdot (\vec{u}\rho h)]_R - [\nabla \cdot \vec{q}]_R \\
=& \frac{\partial \bar{\rho}\tilde{e}}{\partial t} + \nabla \cdot \left(\overline{\vec{u}\rho h}\right) - \nabla \cdot \bar{\vec{q}} - \overline{\vec{u} \cdot \nabla p} - \overline{\langle \tau, \nabla \vec{u} \rangle_F} + [\nabla \cdot (\vec{u}\rho h)]_R - [\nabla \cdot \vec{q}]_R
\end{aligned}
\tag{A.9}
$$

A.3.5 Filtered Kinetic Energy Equation

The filtered Kinetic energy equation is obtained by filtering the kinetic energy equation (eq. 2.18).

$$\begin{aligned}
0 =& \overline{\frac{\partial \rho \frac{1}{2}\vec{u}^2}{\partial t} + \nabla \cdot \left(\vec{u}\rho\frac{1}{2}\vec{u}^2\right) + \vec{u}\cdot\nabla p - \nabla\cdot(\tau\cdot\vec{u}) + \langle \tau, S\rangle_F} \\
=& \frac{\partial \overline{\rho \frac{1}{2}\vec{u}^2}}{\partial t} + \overline{\nabla \cdot \left(\vec{u}\rho\frac{1}{2}\vec{u}^2\right)} + \overline{\vec{u}\cdot\nabla p} - \overline{\nabla\cdot(\tau\cdot\vec{u})} + \overline{\langle \tau, S\rangle_F} \\
=& \frac{\partial \overline{\rho \frac{1}{2}\vec{u}^2}}{\partial t} + \nabla \cdot \left(\overline{\vec{u}\rho\frac{1}{2}\vec{u}^2}\right) + \overline{\vec{u}\cdot\nabla p} - \nabla\cdot\left(\overline{\tau\cdot\vec{u}}\right) + \overline{\langle \tau, S\rangle_F} \\
&+ \left[\nabla \cdot \left(\vec{u}\rho\frac{1}{2}\vec{u}^2\right)\right]_R - [\nabla\cdot(\tau\cdot\vec{u})]_R \\
=& \frac{\partial \frac{1}{2}\overline{\rho\vec{u}^2}}{\partial t} + \nabla \cdot \left(\tilde{\vec{u}}\frac{1}{2}\overline{\rho\vec{u}^2}\right) + \overline{\vec{u}\cdot\nabla p} - \nabla\cdot\left(\overline{\tau\cdot\vec{u}}\right) + \overline{\langle \tau, S\rangle_F} \\
&+ \nabla\cdot\left(\frac{1}{2}\overline{\rho\vec{u}\vec{u}^2} + \bar{\rho}\tilde{\vec{u}}\frac{1}{2}\overline{\rho\vec{u}^2}\right) + \left[\nabla \cdot \left(\vec{u}\rho\frac{1}{2}\vec{u}^2\right)\right]_R - [\nabla\cdot(\tau\cdot\vec{u})]_R
\end{aligned} \tag{A.10}$$

A.3.6 Kinetic Energy Equation of the Filtered Velocity

The kinetic energy equation of the filtered velocity is obtained multiplying $\tilde{\vec{u}}$ to the filtered momentum equation (eq. A.7) and subtracting $\frac{1}{2}\tilde{\vec{u}}^2$ multiplied to the filtered continuity equation (eq. A.6).

$$\text{Transport-Eq}(\bar{\rho}\frac{1}{2}\tilde{\vec{u}}^2) = \tilde{\vec{u}}\cdot\text{Transport-Eq}(\bar{\rho}\tilde{\vec{u}}) - \frac{1}{2}\tilde{\vec{u}}^2\text{Transport-Eq}(\bar{\rho}) \tag{A.11}$$

This leads to the following equation.

$$\begin{aligned}
0 =& \tilde{\vec{u}}\cdot\left(\frac{\partial\bar{\rho}\tilde{\vec{u}}}{\partial t} + \overline{\nabla\cdot(\rho\vec{u}\otimes\vec{u})} + \overline{\nabla p} - \overline{\nabla\cdot\tau}\right) - \frac{1}{2}\tilde{\vec{u}}^2\left(\frac{\partial\bar{\rho}}{\partial t} + \overline{\nabla\cdot(\rho\vec{u})}\right) \\
=& \tilde{\vec{u}}\cdot\frac{\partial\bar{\rho}\tilde{\vec{u}}}{\partial t} - \frac{1}{2}\tilde{\vec{u}}^2\frac{\partial\bar{\rho}}{\partial t} + \tilde{\vec{u}}\cdot\left(\overline{\nabla\cdot(\rho\vec{u}\otimes\vec{u})}\right) - \frac{1}{2}\tilde{\vec{u}}^2\overline{\nabla\cdot(\rho\vec{u})} + \tilde{\vec{u}}\cdot\overline{\nabla p} - \tilde{\vec{u}}\cdot\left(\overline{\nabla\cdot\tau}\right) \\
=& \frac{\partial\bar{\rho}\frac{1}{2}\tilde{\vec{u}}^2}{\partial t} + \tilde{\vec{u}}\cdot\left(\overline{\nabla\cdot(\rho\vec{u}\otimes\vec{u})}\right) - \frac{1}{2}\tilde{\vec{u}}^2\overline{\nabla\cdot(\rho\vec{u})} + \tilde{\vec{u}}\cdot\overline{\nabla p} - \tilde{\vec{u}}\cdot\left(\overline{\nabla\cdot\tau}\right) \\
=& \frac{\partial\bar{\rho}\frac{1}{2}\tilde{\vec{u}}^2}{\partial t} + \tilde{\vec{u}}\cdot\left(\nabla\cdot\left(\overline{\rho\vec{u}\otimes\vec{u}}\right)\right) - \frac{1}{2}\tilde{\vec{u}}^2\nabla\cdot\left(\bar{\rho}\tilde{\vec{u}}\right) + \tilde{\vec{u}}\cdot\nabla\bar{p} - \tilde{\vec{u}}\cdot(\nabla\cdot\bar{\tau}) \\
&+ \tilde{\vec{u}}\cdot[\nabla\cdot(\rho\vec{u}\otimes\vec{u})]_R - \frac{1}{2}\tilde{\vec{u}}^2[\nabla\cdot(\rho\vec{u})]_R + \tilde{\vec{u}}\cdot[\nabla p]_R - \tilde{\vec{u}}\cdot[\nabla\cdot\tau]_R
\end{aligned} \tag{A.12}$$

For the transport term we use the following identity:

$$\begin{aligned}
\nabla\cdot\left(\frac{1}{2}\overline{\rho\vec{u}\otimes\vec{u}}\cdot\tilde{\vec{u}}\right) =& \frac{1}{2}\tilde{\vec{u}}\cdot\left(\nabla\cdot\left(\overline{\rho\vec{u}\otimes\vec{u}}\right)\right) + \frac{1}{2}\left\langle\overline{\rho\vec{u}\otimes\vec{u}},\nabla\tilde{\vec{u}}\right\rangle_F \\
=& \frac{1}{2}\tilde{\vec{u}}\cdot\left(\nabla\cdot\left(\overline{\rho\vec{u}\otimes\vec{u}}\right)\right) + \underbrace{\frac{1}{2}\left\langle\bar{\rho}\tilde{\vec{u}}\otimes\tilde{\vec{u}},\nabla\tilde{\vec{u}}\right\rangle_F}_{=\frac{1}{2}\tilde{\vec{u}}\cdot\left(\nabla\cdot\left(\bar{\rho}\tilde{\vec{u}}\otimes\tilde{\vec{u}}\right)\right)-\frac{1}{2}\tilde{\vec{u}}^2\nabla\cdot\bar{\rho}\tilde{\vec{u}}} \\
&+ \frac{1}{2}\left\langle\overline{\rho\vec{u}\otimes\vec{u}},\nabla\tilde{\vec{u}}\right\rangle_F - \frac{1}{2}\left\langle\bar{\rho}\tilde{\vec{u}}\otimes\tilde{\vec{u}},\nabla\tilde{\vec{u}}\right\rangle_F \\
=& \frac{1}{2}\tilde{\vec{u}}\cdot\left(\nabla\cdot\left(\overline{\rho\vec{u}\otimes\vec{u}}\right)\right) - \frac{1}{2}\tilde{\vec{u}}^2\nabla\cdot\bar{\rho}\tilde{\vec{u}} + \underbrace{\frac{1}{2}\tilde{\vec{u}}\cdot\left(\nabla\cdot\left(\bar{\rho}\tilde{\vec{u}}\otimes\tilde{\vec{u}}\right)\right)}_{=\frac{1}{2}\tilde{\vec{u}}\cdot\left(\nabla\cdot\left(\overline{\rho\vec{u}\otimes\vec{u}}\right)\right)+\frac{1}{2}\tilde{\vec{u}}\cdot\left(\nabla\cdot\left(\bar{\rho}\tilde{\vec{u}}\otimes\tilde{\vec{u}}\right)\right)-\frac{1}{2}\tilde{\vec{u}}\cdot\left(\nabla\cdot\left(\overline{\rho\vec{u}\otimes\vec{u}}\right)\right)} \\
&+ \frac{1}{2}\left\langle\overline{\rho\vec{u}\otimes\vec{u}}-\bar{\rho}\tilde{\vec{u}}\otimes\tilde{\vec{u}},\nabla\tilde{\vec{u}}\right\rangle_F \\
=& \tilde{\vec{u}}\cdot\left(\nabla\cdot\left(\overline{\rho\vec{u}\otimes\vec{u}}\right)\right) - \frac{1}{2}\tilde{\vec{u}}^2\nabla\cdot\bar{\rho}\tilde{\vec{u}} \\
&- \frac{1}{2}\tilde{\vec{u}}\cdot\left(\nabla\cdot\left(\overline{\rho\vec{u}\otimes\vec{u}}-\bar{\rho}\tilde{\vec{u}}\otimes\tilde{\vec{u}}\right)\right) + \frac{1}{2}\left\langle\overline{\rho\vec{u}\otimes\vec{u}}-\bar{\rho}\tilde{\vec{u}}\otimes\tilde{\vec{u}},\nabla\tilde{\vec{u}}\right\rangle_F \\
=& \tilde{\vec{u}}\cdot\left(\nabla\cdot\left(\overline{\rho\vec{u}\otimes\vec{u}}\right)\right) - \frac{1}{2}\tilde{\vec{u}}^2\nabla\cdot\bar{\rho}\tilde{\vec{u}} \\
&- \frac{1}{2}\nabla\cdot\left(\left(\overline{\rho\vec{u}\otimes\vec{u}}-\bar{\rho}\tilde{\vec{u}}\otimes\tilde{\vec{u}}\right)\cdot\tilde{\vec{u}}\right) + \left\langle\overline{\rho\vec{u}\otimes\vec{u}}-\bar{\rho}\tilde{\vec{u}}\otimes\tilde{\vec{u}},\nabla\tilde{\vec{u}}\right\rangle_F
\end{aligned} \tag{A.13}$$

Substituding the identity (eq. A.13) into equation (eq. A.12) results in

$$\begin{aligned}
\frac{\partial\bar{\rho}\frac{1}{2}\tilde{\vec{u}}^2}{\partial t} + \nabla\cdot\left(\frac{1}{2}\overline{\rho\vec{u}\otimes\vec{u}}\cdot\tilde{\vec{u}}\right) - \frac{1}{2}\nabla\cdot\left(\sigma\cdot\tilde{\vec{u}}\right) + \left\langle\sigma,\nabla\tilde{\vec{u}}\right\rangle_F = & -\tilde{\vec{u}}\cdot(\nabla\bar{p}) + \tilde{\vec{u}}\cdot(\nabla\cdot\bar{\tau}) \\
& - \tilde{\vec{u}}\cdot[\nabla\cdot(\rho\vec{u}\otimes\vec{u})]_R + \frac{1}{2}\tilde{\vec{u}}^2[\nabla\cdot(\rho\vec{u})]_R - \tilde{\vec{u}}\cdot[\nabla p]_R + \tilde{\vec{u}}\cdot[\nabla\cdot\tau]_R.
\end{aligned} \tag{A.14}$$

Further modification on the non-linear term and substituding the definition for the residual stress σ (def. 2.40) leads to the following form

$$\begin{aligned}
&\frac{\partial\bar{\rho}\frac{1}{2}\tilde{\vec{u}}^2}{\partial t} + \nabla\cdot\underbrace{\left(\frac{1}{2}\left(\bar{\rho}\tilde{\vec{u}}\otimes\tilde{\vec{u}}\right)\cdot\tilde{\vec{u}}\right)}_{=\tilde{\vec{u}}\frac{1}{2}\bar{\rho}\tilde{\vec{u}}^2} + \nabla\cdot\left(\frac{1}{2}\underbrace{\left(\overline{\rho\vec{u}\otimes\vec{u}}-\bar{\rho}\tilde{\vec{u}}\otimes\tilde{\vec{u}}\right)}_{=-\sigma}\cdot\tilde{\vec{u}}\right) - \frac{1}{2}\nabla\cdot\left(\sigma\cdot\tilde{\vec{u}}\right) + \left\langle\sigma,\nabla\tilde{\vec{u}}\right\rangle_F = \\
&- \tilde{\vec{u}}\cdot(\nabla\bar{p}) + \tilde{\vec{u}}\cdot(\nabla\cdot\bar{\tau}) - \tilde{\vec{u}}\cdot[\nabla\cdot(\rho\vec{u}\otimes\vec{u})]_R + \frac{1}{2}\tilde{\vec{u}}^2[\nabla\cdot(\rho\vec{u})]_R - \tilde{\vec{u}}\cdot[\nabla p]_R + \tilde{\vec{u}}\cdot[\nabla\cdot\tau]_R
\end{aligned} \tag{A.15}$$

which is equivalent to

$$\begin{aligned}
\frac{\partial\bar{\rho}\frac{1}{2}\tilde{\vec{u}}^2}{\partial t} + \nabla\cdot\left(\tilde{\vec{u}}\frac{1}{2}\bar{\rho}\tilde{\vec{u}}^2\right) = & \nabla\cdot\left(\sigma\cdot\tilde{\vec{u}}\right) - \left\langle\sigma,\nabla\tilde{\vec{u}}\right\rangle_F - \tilde{\vec{u}}\cdot(\nabla\bar{p}) + \tilde{\vec{u}}\cdot(\nabla\cdot\bar{\tau}) \\
& - \tilde{\vec{u}}\cdot[\nabla\cdot(\rho\vec{u}\otimes\vec{u})]_R + \frac{1}{2}\tilde{\vec{u}}^2[\nabla\cdot(\rho\vec{u})]_R - \tilde{\vec{u}}\cdot[\nabla p]_R + \tilde{\vec{u}}\cdot[\nabla\cdot\tau]_R.
\end{aligned} \tag{A.16}$$

Applying the chainrule to diffusion term leads to the form

$$\frac{\partial \bar{\rho}\frac{1}{2}\tilde{\vec{u}}^2}{\partial t} + \nabla \cdot \left(\tilde{\vec{u}} \frac{1}{2} \bar{\rho} \tilde{\vec{u}}^2 \right) = \nabla \cdot \left(\sigma \cdot \tilde{\vec{u}} \right) - \left\langle \sigma, \nabla \tilde{\vec{u}} \right\rangle_F - \tilde{\vec{u}} \cdot (\nabla \bar{p}) + \nabla \cdot \left(\bar{\tau} \cdot \tilde{\vec{u}} \right) - \langle \bar{\tau}, S \rangle_F$$
$$- \tilde{\vec{u}} \cdot [\nabla \cdot (\rho \vec{u} \otimes \vec{u})]_R + \frac{1}{2} \tilde{\vec{u}}^2 [\nabla \cdot (\rho \vec{u})]_R - \tilde{\vec{u}} \cdot [\nabla p]_R + \tilde{\vec{u}} \cdot [\nabla \cdot \tau]_R. \quad \text{(A.17)}$$

Appendix B

Coordinate System Transformations

B.1 Coordinate systems

After modelling a physical problem in the abstract mathematical way we obtain a system of partial differential equations (eq. 2.9) that needs to be fullfilled in a space-time-domain Ω_T. To get to a well-defined problem initial and boundary conditions are essential. Inital conditions are defined on the closure of the spatial domain $\overline{\Omega}$ at time $t = t_0$ whereas the boundary conditions need to be fullfilled at all times on the boundary of the domain $\partial\Omega_T$. To facilitate further processes it can be helpful to change the reference coordinate system. Therefore we consider four different reference coordinate systems. The systems and their relation to the Cartesian coordinate systems will be outlined in the following.

B.2 Derivatives

B.2.1 General Transformation

$$\begin{aligned} x &= x(\xi, \eta, \zeta) \\ y &= y(\xi, \eta, \zeta) \\ z &= z(\xi, \eta, \zeta) \end{aligned} \tag{B.1}$$

and

$$\begin{aligned} \xi &= \xi(x, y, z) \\ \eta &= \eta(x, y, z) \\ \zeta &= \zeta(x, y, z) \end{aligned} \tag{B.2}$$

try

$$\begin{aligned}\frac{\partial}{\partial x} &= \frac{\partial \xi}{\partial x}\frac{\partial}{\partial \xi} + \frac{\partial \eta}{\partial x}\frac{\partial}{\partial \eta} + \frac{\partial \zeta}{\partial x}\frac{\partial}{\partial \zeta} \\ \frac{\partial}{\partial y} &= \frac{\partial \xi}{\partial y}\frac{\partial}{\partial \xi} + \frac{\partial \eta}{\partial y}\frac{\partial}{\partial \eta} + \frac{\partial \zeta}{\partial y}\frac{\partial}{\partial \zeta} \\ \frac{\partial}{\partial z} &= \frac{\partial \xi}{\partial z}\frac{\partial}{\partial \xi} + \frac{\partial \eta}{\partial z}\frac{\partial}{\partial \eta} + \frac{\partial \zeta}{\partial z}\frac{\partial}{\partial \zeta}\end{aligned} \tag{B.3}$$

Red terms are usually not available for grids...
so do

$$\begin{aligned}\frac{\partial}{\partial \xi} &= \frac{\partial x}{\partial \xi}\frac{\partial}{\partial x} + \frac{\partial y}{\partial \xi}\frac{\partial}{\partial y} + \frac{\partial z}{\partial \xi}\frac{\partial}{\partial z} \\ \frac{\partial}{\partial \eta} &= \frac{\partial x}{\partial \eta}\frac{\partial}{\partial x} + \frac{\partial y}{\partial \eta}\frac{\partial}{\partial y} + \frac{\partial z}{\partial \eta}\frac{\partial}{\partial z} \\ \frac{\partial}{\partial \zeta} &= \frac{\partial x}{\partial \zeta}\frac{\partial}{\partial x} + \frac{\partial y}{\partial \zeta}\frac{\partial}{\partial y} + \frac{\partial z}{\partial \zeta}\frac{\partial}{\partial z}\end{aligned} \tag{B.4}$$

And solve this linear system for $\frac{\partial}{\partial x}, \frac{\partial}{\partial y}$ and $\frac{\partial}{\partial z}$...
This results in:...

B.2.2 Cylindrical Coordinate System

The cylindrical coordinate system (x, r, θ) is obtained via transformation of the second and third dimension of the Cartesian coordinate system (x, y, z) to polar coordinates. The first dimension is mapped by the identity function, thus

$$\begin{aligned}x &= x \\ r &= \sqrt{y^2 + z^2} \\ \theta &= \operatorname{atan2}(y, z)\end{aligned} \tag{B.5}$$

where

$$\operatorname{atan2}(z, y) = \begin{cases} \arctan\left(\frac{y}{z}\right) & z > 0 \\ \arctan\left(\frac{y}{z}\right) + \pi & y \geq 0, z < 0 \\ \arctan\left(\frac{y}{z}\right) - \pi & y < 0, z < 0 \\ +\frac{\pi}{2} & y > 0, z = 0 \\ -\frac{\pi}{2} & y < 0, z = 0 \\ \text{undefined} & y = 0, z = 0. \end{cases} \tag{B.6}$$

The inverse mapping from cylindrical coordinates to Cartesian coordinates then reads as follows

$$\begin{aligned}x &= x \\ y &= r\sin(\theta) \\ z &= r\cos(\theta).\end{aligned} \tag{B.7}$$

These relations lead to the coupling of derivatives in both coordinate systems. For the derivatives in the orthogonal coordinate system (ξ, η, ζ)

$$\begin{aligned}\frac{\partial}{\partial x} &= \frac{\partial}{\partial x} \\ \frac{\partial}{\partial r} &= \frac{\partial y}{\partial r}\frac{\partial}{\partial y} + \frac{\partial z}{\partial r}\frac{\partial}{\partial z} \\ \frac{\partial}{\partial \theta} &= \frac{\partial y}{\partial \theta}\frac{\partial}{\partial y} + \frac{\partial z}{\partial \theta}\frac{\partial}{\partial z}\end{aligned} \tag{B.8}$$

holds. From eq. B.7

$$\begin{aligned}\frac{\partial y}{\partial r} &= \sin(\theta) \\ \frac{\partial z}{\partial r} &= \cos(\theta) \\ \frac{\partial y}{\partial \theta} &= r\cos(\theta) \\ \frac{\partial z}{\partial \theta} &= -r\sin(\theta)\end{aligned} \tag{B.9}$$

can be derived. Using this in eq. B.8 leads to

$$\begin{aligned}\frac{\partial}{\partial x} &= \frac{\partial}{\partial x} \\ \frac{\partial}{\partial r} &= \sin(\theta)\frac{\partial}{\partial y} + \cos(\theta)\frac{\partial}{\partial z} \\ \frac{\partial}{\partial \theta} &= r\cos(\theta)\frac{\partial}{\partial y} - r\sin(\theta)\frac{\partial}{\partial z}\end{aligned} \tag{B.10}$$

The second and third equation of eq.B.10 define a system of linear equation that can be solved for $\frac{\partial}{\partial y}$ and $\frac{\partial}{\partial z}$. With the solution the derivatives in the reference coordinate system can be expressed as

$$\begin{aligned}\frac{\partial}{\partial x} &= \frac{\partial}{\partial x} \\ \frac{\partial}{\partial y} &= \frac{1}{J}\frac{\partial z}{\partial \theta}\frac{\partial}{\partial r} - \frac{1}{J}\frac{\partial z}{\partial r}\frac{\partial}{\partial \theta} \\ \frac{\partial}{\partial z} &= \frac{1}{J}\frac{\partial y}{\partial \theta}\frac{\partial}{\partial r} - \frac{1}{J}\frac{\partial y}{\partial r}\frac{\partial}{\partial \theta}.\end{aligned} \tag{B.11}$$

J is the Jacobian which is here defined as

$$J = \begin{vmatrix}\frac{\partial y}{\partial r} & \frac{\partial y}{\partial \theta} \\ \frac{\partial z}{\partial r} & \frac{\partial z}{\partial \theta}\end{vmatrix} = \begin{vmatrix}\sin(\theta) & r\cos(\theta) \\ \cos(\theta) & -r\sin(\theta)\end{vmatrix} = -r \tag{B.12}$$

Therefore

$$\begin{aligned}\frac{\partial}{\partial x} &= \frac{\partial}{\partial x} \\ \frac{\partial}{\partial y} &= \sin(\theta)\frac{\partial}{\partial r} + \frac{1}{r}\cos(\theta)\frac{\partial}{\partial \theta} \\ \frac{\partial}{\partial z} &= \cos(\theta)\frac{\partial}{\partial r} - \frac{1}{r}\sin(\theta)\frac{\partial}{\partial \theta}.\end{aligned} \tag{B.13}$$

The time-derivatives are not effected by this transformation.

B.2.3 Orthogonal Coordinate System

The orthogonal coordinate system (ξ, η, ζ) is obtained via pure streching from an abitrary reference coordinate system (x, y, z). It is called 'orthogonal' as the axes of the system are orthogonal in the reference system. The mapping form reference coordinates to orthogonal coodinates is defined as

$$\begin{aligned} \xi &= \xi(x) \\ \eta &= \eta(y) \\ \zeta &= \zeta(z), \end{aligned} \tag{B.14}$$

where $\xi(x), \eta(y), \zeta(z)$ are abitrary bijective differentiable functions. Further restrictions may be applied later. The inverse mapping from orthogonal coordinates to Cartesian coordinates then reads as follows

$$\begin{aligned} x &= x(\xi) \\ y &= y(\eta) \\ z &= z(\zeta). \end{aligned} \tag{B.15}$$

So each direction of the new coordinate system is depending on one direction of the cartesian coordinate system only and vice versa. These relations lead to the coupling of derivatives in both coordinate systems. For the derivatives in the orthogonal coordinate system (ξ, η, ζ)

$$\begin{aligned} \frac{\partial}{\partial \xi} &= \frac{\partial x}{\partial \xi}\frac{\partial}{\partial x} \\ \frac{\partial}{\partial \eta} &= \frac{\partial y}{\partial \eta}\frac{\partial}{\partial y} \\ \frac{\partial}{\partial \zeta} &= \frac{\partial z}{\partial \zeta}\frac{\partial}{\partial z} \end{aligned} \tag{B.16}$$

holds. Solving these equations for the derivatives in Cartesian coordinates leads to

$$\begin{aligned} \frac{\partial}{\partial x} &= \frac{1}{\frac{\partial x}{\partial \xi}}\frac{\partial}{\partial \xi} \\ \frac{\partial}{\partial y} &= \frac{1}{\frac{\partial y}{\partial \eta}}\frac{\partial}{\partial \eta} \\ \frac{\partial}{\partial z} &= \frac{1}{\frac{\partial z}{\partial \zeta}}\frac{\partial}{\partial \zeta}. \end{aligned} \tag{B.17}$$

The time-derivatives are not affected by this transformation.

B.2.4 Semi-Generalized Coordinate System

The semi-generalized coordinate (ξ, η, ζ) is obtained by using generalized coordinates for the first end second dimension and using streching only for the third dimension of an abitrary reference coordinate system (x, y, z). The mapping between both coordinate system is described by

$$\begin{aligned} \xi &= \xi(x, y) \\ \eta &= \eta(x, y) \\ \zeta &= \zeta(z) \end{aligned} \tag{B.18}$$

were $(\xi(x, y), \eta(x, y))$ and $\zeta(z)$ are abitrary bijective differentiable functions. Further restrictions maybe applied later. The inverse mapping from the semi-generalized coordinate system back to the reference system can be stated as

$$\begin{aligned} x &= x(\xi, \eta) \\ y &= y(\xi, \eta) \\ z &= z(\zeta). \end{aligned} \tag{B.19}$$

So the third direction of the new coordinate system is depending on third direction of the reference coordinate system only and vice versa. In contrast to that the first and second dimension of one coordinate system are depending in the first two dimension of the other system respectively. These relations define the coupling of derivatives in both coordinate systems. By applying the chainrule one can obtain that for the derivatives in the semi-generalized coordinate system (ξ, η, ζ)

$$\begin{aligned} \frac{\partial}{\partial \xi} &= \frac{\partial x}{\partial \xi}\frac{\partial}{\partial x} + \frac{\partial y}{\partial \xi}\frac{\partial}{\partial y} \\ \frac{\partial}{\partial \eta} &= \frac{\partial x}{\partial \eta}\frac{\partial}{\partial x} + \frac{\partial y}{\partial \eta}\frac{\partial}{\partial y} \\ \frac{\partial}{\partial \zeta} &= \frac{\partial z}{\partial \zeta}\frac{\partial}{\partial z} \end{aligned} \tag{B.20}$$

holds. Solving this system for the derivatives in the reference systems leads to

$$\begin{aligned} \frac{\partial}{\partial x} &= \frac{1}{J}\frac{\partial y}{\partial \eta}\frac{\partial}{\partial \xi} - \frac{1}{J}\frac{\partial y}{\partial \xi}\frac{\partial}{\partial \eta} \\ \frac{\partial}{\partial y} &= -\frac{1}{J}\frac{\partial x}{\partial \eta}\frac{\partial}{\partial \xi} + \frac{1}{J}\frac{\partial x}{\partial \xi}\frac{\partial}{\partial \eta} \\ \frac{\partial}{\partial z} &= \frac{1}{\frac{\partial z}{\partial \zeta}}\frac{\partial}{\partial \zeta} \end{aligned} \tag{B.21}$$

J is the jacobian which is here defined as

$$J = \begin{vmatrix} \frac{\partial x}{\partial \xi} & \frac{\partial y}{\partial \xi} \\ \frac{\partial x}{\partial \eta} & \frac{\partial y}{\partial \eta} \end{vmatrix} = \frac{\partial x}{\partial \xi}\frac{\partial y}{\partial \eta} - \frac{\partial x}{\partial \eta}\frac{\partial y}{\partial \xi} \tag{B.22}$$

The time-derivatives are not effected by this transformation.

B.2.5 Orthogonal Cylindrical Coordinate System

The orthogonal cylindrical coordinate system (ξ, η, ζ) is obtained by combining an orthogonal coordinate system with a cylindrical coordinate system. The mapping from the reference coordinates to the new coordinate system is defined as

$$\begin{aligned} \xi &\overset{B.14}{=} \xi(x) \\ \eta &\overset{B.14}{=} \eta(r) \overset{B.5}{=} \eta(\sqrt{y^2+z^2}) \\ \zeta &\overset{B.14}{=} \zeta(\theta) \overset{B.5}{=} \zeta(\operatorname{atan2}(z,y)) \end{aligned} \tag{B.23}$$

were $\xi(x), \eta(r), \zeta(\theta)$ are abitrary bijective differentiable functions. Further restrictions may be applied later. The inverse mapping from orthogonal cylindrical coordinates to Cartesian coordinates then reads as follows

$$\begin{aligned} x &\overset{B.9}{=} x(\xi) \\ y &\overset{B.9}{=} r\sin(\theta) \overset{B.15}{=} r(\eta)\sin(\theta(\zeta)) \\ z &\overset{B.9}{=} r\cos(\theta) \overset{B.15}{=} r(\eta)\cos(\theta(\zeta)). \end{aligned} \tag{B.24}$$

So each direction of the new coordinate system is depending on one direction of the cartesian coordinate system only and vice versa. These relations lead to the coupling of derivatives in both coordinate systems. For the derivatives in the orthogonal coordinate system (ξ, η, ζ)

$$\begin{aligned} \frac{\partial}{\partial\xi} &\overset{B.16}{=} \frac{\partial x}{\partial\xi}\frac{\partial}{\partial x} \\ \frac{\partial}{\partial\eta} &\overset{B.16}{=} \frac{\partial r}{\partial\eta}\frac{\partial}{\partial r} \overset{B.10}{=} \frac{\partial r}{\partial\eta}\sin(\theta)\frac{\partial}{\partial y} + \frac{\partial r}{\partial\eta}\cos(\theta)\frac{\partial}{\partial z} \\ \frac{\partial}{\partial\zeta} &\overset{B.16}{=} \frac{\partial\theta}{\partial\zeta}\frac{\partial}{\partial\theta} \overset{B.10}{=} \frac{\partial\theta}{\partial\zeta}r\cos(\theta)\frac{\partial}{\partial y} - \frac{\partial\theta}{\partial\zeta}r\sin(\theta)\frac{\partial}{\partial z} \end{aligned} \tag{B.25}$$

holds. Solving these equations for the derivatives in cartesian coordinates leads to

$$\begin{aligned} \frac{\partial}{\partial x} &\overset{B.17}{=} \frac{\partial}{\partial x} \\ \frac{\partial}{\partial y} &\overset{B.13}{=} \sin(\theta)\frac{\partial}{\partial r} + \frac{1}{r}\cos(\theta)\frac{\partial}{\partial\theta} \overset{B.17}{=} \sin(\theta)\frac{1}{\frac{\partial r}{\partial\eta}}\frac{\partial}{\partial\eta} + \frac{1}{r}\cos(\theta)\frac{1}{\frac{\partial\theta}{\partial\zeta}}\frac{\partial}{\partial\zeta} \\ \frac{\partial}{\partial z} &\overset{B.13}{=} \cos(\theta)\frac{\partial}{\partial r} - \frac{1}{r}\sin(\theta)\frac{\partial}{\partial\theta} \overset{B.17}{=} \cos(\theta)\frac{1}{\frac{\partial r}{\partial\eta}}\frac{\partial}{\partial\eta} - \frac{1}{r}\sin(\theta)\frac{1}{\frac{\partial\theta}{\partial\zeta}}\frac{\partial}{\partial\zeta}. \end{aligned} \tag{B.26}$$

The time-derivatives are not effected by this transformation.

B.2.6 Semi-Generalized Cylintrical Coordinate System

The orthogonal coordinate system (ξ, η, ζ) is obtained via pure streching from the cartesian coordinate system (x, y, z). The mapping form cartesian coordinates to orthogonal coodinates is defined as

$$\begin{aligned} \xi &= \xi(x, r) \overset{B.5}{=} \xi(x, \sqrt{y^2 + z^2}) \\ \eta &= \eta(x, r) \overset{B.5}{=} \eta(x, \sqrt{y^2 + z^2}) \\ \zeta &= \zeta(\theta) \overset{B.5}{=} \zeta(\text{atan2}(z, y)) \end{aligned} \tag{B.27}$$

were $(\xi(x), \eta(y), \zeta(z))$ are abitrary bijective differentiable functions. Further restrictions maybe applied later. The inverse mapping from orthogonal coordinates to cartesian coordinates then reads as follows

$$\begin{aligned} x &= x(\xi, r(\eta, \zeta)) = x(\xi, \sqrt{\eta^2 + \zeta^2}) \\ y &= y(\xi, r(\eta, \zeta)) = y(\xi, \sqrt{\eta^2 + \zeta^2}) \\ z &= z(r(\eta, \zeta), \theta(\eta, \zeta)) = z(\sqrt{\eta^2 + \zeta^2}, \text{atan2}(\eta, \zeta)). \end{aligned} \tag{B.28}$$

So each direction of the new coordinate system is depending on one direction of the cartesian coordinate system only and vice versa. These relations define lead to the coupling of derivatives in both coordinate systems. For the derivatives in the orthogonal coordinate system (ξ, η, ζ)

$$\begin{aligned} \frac{\partial}{\partial \xi} &= ... \\ \frac{\partial}{\partial \eta} &= ... \\ \frac{\partial}{\partial \zeta} &= ... \end{aligned} \tag{B.29}$$

holds. Solving these equations for the derivatives in cartesian coordinates leads to

$$\begin{aligned} \frac{\partial}{\partial x} &= ... \\ \frac{\partial}{\partial y} &= ... \\ \frac{\partial}{\partial z} &= ... \end{aligned} \tag{B.30}$$

The time-derivatives are not effected by this transformation.

B.2.7 Generalized Coordinate System

$$J = \begin{vmatrix} \frac{\partial x}{\partial \xi} & \frac{\partial x}{\partial \eta} & \frac{\partial x}{\partial \zeta} \\ \frac{\partial y}{\partial \xi} & \frac{\partial y}{\partial \eta} & \frac{\partial y}{\partial \zeta} \\ \frac{\partial z}{\partial \xi} & \frac{\partial z}{\partial \eta} & \frac{\partial z}{\partial \zeta} \end{vmatrix} \tag{B.31}$$

$$
\begin{aligned}
\frac{\partial}{\partial x} &= \frac{1}{J}\left(\frac{\partial y}{\partial \eta}\frac{\partial z}{\partial \zeta}\frac{\partial}{\partial \xi} - \frac{\partial y}{\partial \zeta}\frac{\partial z}{\partial \eta}\frac{\partial}{\partial \xi} + \frac{\partial y}{\partial \zeta}\frac{\partial z}{\partial \xi}\frac{\partial}{\partial \eta} - \frac{\partial y}{\partial \xi}\frac{\partial z}{\partial \zeta}\frac{\partial}{\partial \eta} + \frac{\partial y}{\partial \xi}\frac{\partial z}{\partial \eta}\frac{\partial}{\partial \zeta} - \frac{\partial y}{\partial \eta}\frac{\partial z}{\partial \xi}\frac{\partial}{\partial \zeta}\right) \\
\frac{\partial}{\partial y} &= -\frac{1}{J}\left(\frac{\partial x}{\partial \eta}\frac{\partial z}{\partial \zeta}\frac{\partial}{\partial \xi} - \frac{\partial x}{\partial \zeta}\frac{\partial z}{\partial \eta}\frac{\partial}{\partial \xi} + \frac{\partial x}{\partial \zeta}\frac{\partial z}{\partial \xi}\frac{\partial}{\partial \eta} - \frac{\partial x}{\partial \xi}\frac{\partial z}{\partial \zeta}\frac{\partial}{\partial \eta} + \frac{\partial x}{\partial \xi}\frac{\partial z}{\partial \eta}\frac{\partial}{\partial \zeta} - \frac{\partial x}{\partial \eta}\frac{\partial z}{\partial \xi}\frac{\partial}{\partial \zeta}\right) \\
\frac{\partial}{\partial z} &= \frac{1}{J}\left(\frac{\partial x}{\partial \eta}\frac{\partial y}{\partial \zeta}\frac{\partial}{\partial \xi} - \frac{\partial x}{\partial \zeta}\frac{\partial y}{\partial \eta}\frac{\partial}{\partial \xi} + \frac{\partial x}{\partial \zeta}\frac{\partial y}{\partial \xi}\frac{\partial}{\partial \eta} - \frac{\partial x}{\partial \xi}\frac{\partial y}{\partial \zeta}\frac{\partial}{\partial \eta} + \frac{\partial x}{\partial \xi}\frac{\partial y}{\partial \eta}\frac{\partial}{\partial \zeta} - \frac{\partial x}{\partial \eta}\frac{\partial y}{\partial \xi}\frac{\partial}{\partial \zeta}\right)
\end{aligned}
\tag{B.32}
$$

$$
\begin{aligned}
\frac{\partial}{\partial x} &= \frac{1}{J}\left(\underbrace{\left(\frac{\partial y}{\partial \eta}\frac{\partial z}{\partial \zeta} - \frac{\partial y}{\partial \zeta}\frac{\partial z}{\partial \eta}\right)}_{:=J_{x\xi}}\frac{\partial}{\partial \xi} + \underbrace{\left(\frac{\partial y}{\partial \zeta}\frac{\partial z}{\partial \xi} - \frac{\partial y}{\partial \xi}\frac{\partial z}{\partial \zeta}\right)}_{:=J_{x\eta}}\frac{\partial}{\partial \eta} + \underbrace{\left(\frac{\partial y}{\partial \xi}\frac{\partial z}{\partial \eta} - \frac{\partial y}{\partial \eta}\frac{\partial z}{\partial \xi}\right)}_{:=J_{x\zeta}}\frac{\partial}{\partial \zeta}\right) \\
\frac{\partial}{\partial y} &= \frac{1}{J}\left(\underbrace{\left(\frac{\partial x}{\partial \zeta}\frac{\partial z}{\partial \eta} - \frac{\partial x}{\partial \eta}\frac{\partial z}{\partial \zeta}\right)}_{:=J_{y\xi}}\frac{\partial}{\partial \xi} + \underbrace{\left(\frac{\partial x}{\partial \xi}\frac{\partial z}{\partial \zeta} + \frac{\partial x}{\partial \zeta}\frac{\partial z}{\partial \xi}\right)}_{:=J_{y\eta}}\frac{\partial}{\partial \eta} + \underbrace{\left(\frac{\partial x}{\partial \eta}\frac{\partial z}{\partial \xi} + \frac{\partial x}{\partial \xi}\frac{\partial z}{\partial \eta}\right)}_{:=J_{y\zeta}}\frac{\partial}{\partial \zeta}\right) \\
\frac{\partial}{\partial z} &= \frac{1}{J}\left(\underbrace{\left(\frac{\partial x}{\partial \eta}\frac{\partial y}{\partial \zeta} - \frac{\partial x}{\partial \zeta}\frac{\partial y}{\partial \eta}\right)}_{:=J_{z\xi}}\frac{\partial}{\partial \xi} + \underbrace{\left(\frac{\partial x}{\partial \zeta}\frac{\partial y}{\partial \xi} - \frac{\partial x}{\partial \xi}\frac{\partial y}{\partial \zeta}\right)}_{:=J_{z\eta}}\frac{\partial}{\partial \eta} + \underbrace{\left(\frac{\partial x}{\partial \xi}\frac{\partial y}{\partial \eta} - \frac{\partial x}{\partial \eta}\frac{\partial y}{\partial \xi}\right)}_{:=J_{z\zeta}}\frac{\partial}{\partial \zeta}\right)
\end{aligned}
\tag{B.33}
$$

Bibliography

A., Favre 1965 Équations des gaz turbulents compressibles I.- Formes générales. *Journal de Mécanique* **4**, 361–390.

Adrian, R J 2007 Hairpin vortex organization in wall turbulence. *Phys. Fluids* **19**, 41301.

del Alamo, J C & Jiménez, J 2006 Linear energy amplification in turbulent channels. *J. Fluid Mech.* **559**, 205–213.

Anderson, J D 2005 Ludwig Prandtl's Boundary Layer. *Physics Today* **58**, 42–48.

Ashurst, W T, Kerstein, A R, Kerr, R M & Gibson, C H 1987 Alignment of vorticity and scalar gradient with strain rate in simulated Navier-Stokes turbulence. *Phys. Fluids* **30**, 2343–2353.

Batchelor, G. K. 1959 *The Theory of Homogeneous Turbulence*. Cambridge University Press, Cambridge, UK.

Betchov, R. 1975 Numerical simulation of isotropic turbulence. *Physics of Fluids* **18** (10), 1230.

Blackburn, Hugh M., Mansour, Nagi N. & Cantwell, Brian J. 1996 Topology of fine-scale motions in turbulent channel flow. *Journal of Fluid Mechanics* **310** (-1), 269.

Brasseur, James G & Yeung, P K 1991 Large and small-scale coupling in homogeneous turbulence: Analysis of the Navier-Stokes equation in the asymptotic limit. In *Eigth Symposium on Turbulent Shear Flows*.

Buxton, O. R. H. & Ganapathisubramani, B. 2010 Amplification of enstrophy in the far field of an axisymmetric turbulent jet. *Journal of Fluid Mechanics* **651**, 483.

Buxton, O. R. H., Laizet, S. & Ganapathisubramani, B. 2011 The interaction between strain-rate and rotation in shear flow turbulence from inertial range to dissipative length scales. *Physics of Fluids* **23** (6), 061704.

Cantwell, Brian J 1992 Exact solution of a restricted Euler equation for the velocity gradient tensor. *Physics of Fluids A: Fluid Dynamics* **4** (4), 782.

Carlier, J & Stanislas, M 2005 Experimental study of eddy structures in a turbulent boundary layer using particle image velocimetry. *J. Fluid Mech.* **535**, 143–188.

Carpenter, M H, Nordström, J & Gottlieb, D 1999 A Stable and Conservative Interface Treatment of Arbitrary Spatial Accuracy. *J. Comp. Phys.* **148** (2), 341–365.

Chakraborty, Pinaki, Balachandar, S. & Adrian, Ronald J. 2005 On the relationships between local vortex identification schemes. *Journal of Fluid Mechanics* **535** (2005), 189–214.

Chen, J. H., Chong, M. S., Soria, J., Sondergaard, R., Perry, A. E., Rogers, M., Moser, R. & Cantwell, B. J. 1990 A study of the topology of dissipating motions in direct simulations of time-developing compressible and incompressible mixing layers. In *Summer Program, Center for Turbulence Research*, pp. 139–161.

Chen, Shiyi, Doolen, Gary, Herring, Jackson R, Kraichnan, Robert H & Orszag, Steven A 1993 Far-dissipation range of turbulence. *Physical Review Letters* (70), 3051–3054.

Chong, M S, Perry, a. E & Cantwell, B J 1990 A general classification of three-dimensional flow fields. *Physics of Fluids A: Fluid Dynamics* **2** (5), 765.

Chong, M. S., Soria, J., Perry, a. E., Chacin, J., Cantwell, B. J. & Na, Y. 1998 Turbulence structures of wall-bounded shear flows found using DNS data. *Journal of Fluid Mechanics* **357**, 225–247.

Chorin, A J 1994 *Vorticity and Turbulence*. Springer-Verlag.

De Graaff, D P & Eaton, J K 2000 Reynolds number scaling of the flat-plate turbulent boundary layer. *J. Fluid Mech.* **422**, 319–346.

del Álamo, J.C. and Jimenéz, J. 2003 Scaling of the energy spectra of turbulent channels. *Phys. Fluids* **15**, L41—-L44.

Doering, C R & D.Gibbon, J, ed. 2004 *Applied Analysis of the Navier-Stokes Equations*. Cambridge University Press, Cambridge.

Elsinga, G E & Marusic, I 2010 Evolution and lifetimes of flow topology in a turbulent boundary layer. *Physics of Fluids* **22** (1), 15102.

Foias, C, Manley, O & Sirovich, L 1990 Empirical and Stokes eigenfunctions and the far-dissipation turbulent spectrum. *Phys. Fluids A* (2), 464–467.

Frigo, Matteo & Johnson, Steven G 2005 The Design and Implementation of {FFTW3}. *Proceedings of the IEEE* **93** (2), 216–231.

Frisch, Uriel 1995 *Turbulence: The Legacy of A.N. Kolmogorov*. Cambridge University Press.

Ganapathisubramani, B., Hutchins, N., Monty, J. P., Chung, D. & Marusic, I. 2012 Amplitude and frequency modulation in wall turbulence. *Journal of Fluid Mechanics* pp. 1–31.

Ganapathisubramani, B., Lakshminarasimhan, K. & Clemens, N. T. 2008 Investigation of three-dimensional structure of fine scales in a turbulent jet by using cinematographic stereoscopic particle image velocimetry. *Journal of Fluid Mechanics* **598**, 141–175.

Ganapathisubramani, B, Longmire, E & Marusic, I 2003 Characteristics of vortex packets in turbulent boundary layers. *J. Fluid Mech.* **478**, 35–46.

Ganapathisubramani, B. 2007 Statistical properties of streamwise velocity in a supersonic turbulent boundary layer. *Phys. Fluids* **19**, 098108–[4pp].

Guala, M, Hommema, S E & Adrian, R J 2006 Large-Scale and very large-scale motions in turbulent pipe flow. *J. Fluid Mech.* **554**, 521–542.

Hamlington, Peter E, Schumacher, Joerg & Dahm, Werner J A 2008 Local and Nonlocal Strain Rate Fields and Vorticity Alignment in Turbulent Flows pp. 1–9.

Herpin, S 2010 Study on the influence of the Reynolds number on the organization of wall-bounded turbulence. PhD thesis, Mech. Eng.,Ecole Cent. Lille, France.

Horn, Roger A & Johnson, Charles R, ed. 2006 *Matrix Analysis*. Cambridge University Press, Cambridge.

Hoyas, S & Jiménez, J 2006 Scaling of the velocity fluctuations in turbulent channels up to Re= 2003. *Physics of Fluids* **18**, 11702.

Hutchins, N, J.P., Monty, Ganapathisubramani, B, Ng, H C H & Marusic 2011 Three-dimensional conditional structure of a high-Reynolds-number turbulent boundary layer. *J. Fluid Mech.* **673**, 255–285.

Hutchins, N & Marusic, I 2007*a* Evidence of very long meandering features in the logarithmic region of turbulent boundary layers. *J. Fluid Mech.* **579**, 1–28.

Hutchins, N & Marusic, I 2007*b* Large-scale influences in the near-wall turbulence. *Philisophical Transaction of the Royal Society* **365**, 647–664.

Jain, Raj & Chlamtac, Imrich 1985 The P2 algorithm for dynamic calculation of quantiles and histograms without storing observations. *Communications of the ACM* **28** (10), 1076–1085.

Jeong, Jinhee & Hussain, Fazle 1995 On the identification of a vortex. *Journal of Fluid Mechanics* **285** (-1), 69.

Jiménez, J, del Álamo, J C & Flores, O 1999 The large-scale dynamics of near-wall turbulence. *J. Fluid Mech.* **505**, 179.

Jimenez, J, Hoyas, S, Simens, M P & Mizuno, Y 2010 Turbulent boundary layers and channels at moderate Reynolds numbers. *J. Fluid Mech.* **657**, 335–360.

Jiménéz, J. 2012 Cascades in Wall-Bounded Turbulence. *Annual Review of Fluid Mechanics* **44**, 27–45.

Johnstone, R & Coleman, G N 2012 The turbulent Ekman boundary layer over an infinite wind-turbine array. *Journal of Wind Engineering and Industrial Aerodynamics* **100**, 46–57.

Kailasnath, P, Migdal, A, Sreenivasan, KR, Yakhot, A & Zubair, L. 1992 The Kolmogorov 4/5-ths lawand the odd-order moments of velocity differences in turbulence. *Tech. Rep.*. Yale University Department of Mechanical Engineering.

Kennedy, C A, Carpenter, M H & Lewis, R M 2000 Low-storage, explicit {R}unge–{K}utta schemes for the compressible {N}avier–{S}tokes equations. *Applied Numerical Mathematics* **35**, 177–219.

Kennedy, C A & Gruber, Andrea 2008 Reduced aliasing formulations of the convective terms within the {N}avier–{S}tokes equations for a compressible fluid. *J. Comp. Phys.* **227**, 1676–1700.

Kerr, Robert M 1990 Velocity, scalar and transfer spectra in numerical turbulence. *Journal of Fluid Mechanics* **211**, 309–332.

Kerr, Robert M, Domaradzki, J Andrzej & Barbier, Gilles 1996 Small-scale properties of nonlinear interactions and subgrid-scale energy transfer in isotropic turbulence. *Physics of Fluids* **8** (1), 197.

Kholmyansky, M., Tsinober, a. & Yorish, S. 2001 Velocity derivatives in the atmospheric surface layer at Re?? = 104. *Physics of Fluids* **13** (1), 311–314.

Kim, H T, Kline, S J & Reynolds, W C 1971 The production of turbulence near a smooth wall in a turbulent boundary layer. *J. Fluid Mech.* **50**, 133–166.

Kim, J W 2007 Optimised boundary compact finit difference schemes for computational aeroacoustics. *J. Comp. Phys.* **225**, 995–1019.

Kim, J W & Lee, D J 1996 Optimized compact difference schemes with maximum resolution. *AIAA J.* **34** (5), 887.

Kim, J W & Lee, D J 2000 Generalized Characteristic Boundary Conditions for Computational Aeroacoustics. *AIAA J.* **38** (11), 2040–2049.

Kim, J W & Lee, D J 2003 Characteristic Interface Conditions for Multiblock High-Order Computation on Singular Structured Grid. *AIAA Journal* **41** (12), 2341–2348.

Kim, J W & Sandberg, R D 2011 Efficient Parallel Computing with Compact Finite Difference Schemes. *under review in Computer and Fluids* .

Kim, K C & Adrian, R J 1999 Very large-scale motion in the outer layer. *Phys. Fluids* **11**, 417–422.

Klein, M, Sadiki, A & Janicka, J 2003 A digital filter based generation of inflow data for spatially developing direct numerical or large eddy simulations. *J. Comp. Phys.* **186** (2), 652–665.

Kline, S J, Reynolds, W C, Schraub, F A & Runstadler, P W 1967 Structure of turbulent boundary layers. *J. Fluid Mech.* **30**, 741–773.

Kolmogorov, A N 1941 The Local Structure of Turbulence in Incompressible Viscous Fluid for Very Large Reynolds Numbers. *Doklady Akademii Nauk SSSR* **30** (4).

Leung, T., Swaminathan, N. & Davidson, P. a. 2012 Geometry and interaction of structures in homogeneous isotropic turbulence. *Journal of Fluid Mechanics* **710**, 453–481.

Lund, Thomas S. & Rogers, Michael M. 1994 An improved measure of strain state probability in turbulent flows. *Physics of Fluids* **6** (5), 1838–1847.

Lund, T S, Wu, X & Squires, K D 1998 Generation of Turbulent Inflow Data for Spatially-Developing Boundary Layer Simulations. *J. Comp. Phys.* **140** (2), 233–258.

Lüthi, Beat, Tsinober, Arkady & Kinzelbach, Wolfgang 2005 Lagrangian measurement of vorticity dynamics in turbulent flow. *Journal of Fluid Mechanics* **528**, 87–118.

Martin, Jesus, Ooi, Andrew, Chong, M S & Soria, Julio 1998 Dynamics of the velocity gradient tensor invariants in isotropic turbulence. *Physics of Fluids* **10** (9), 2336.

Marusic, I, McKeon, B J, Monkewitz, P A, Nagib, H M & Sreenivasan, K R 2010 Wall-bounded turbulent flows at high Reynolds numbers: Recent advances and key issues. *Fluid of Physics* **22**, 65103–65124.

Mathis, R, Hutchins, N & Marusic, I 2009 Large-scale amplitude modulation of the small-scale structuresin turbulent boundary layers. *J. Fluid Mech.* **628**, 311–337.

Meneveau, Charles 2011 Lagrangian Dynamics and Models of the Velocity Gradient Tensor in Turbulent Flows. *Annual Review of Fluid Mechanics* **43** (1), 219–245.

Monin, A.S. & Yaglom, A.M. 1975 *Statistical Fluid Mechanics: Mechanics of Turbulence (Vol. 2)*. MIT Press.

Monkewitz, P A, Chauhan, K A & Nagib, H M 2007 Self-contained high-Reynolds-number asymptotics for zero-pressure-gradient turbulent boundary layers. *Phys. Fluids* **19**, 115101.

Monty, J P, Hutchins, N, NG, H C H, Marusic, I & Chong, M S 2009 A comparison of turbulent pipe, channel and boundary layer flows. *J. Fluid Mech.* **632**, 431–442.

Mullin, John a. & Dahm, Werner J a. 2006 Dual-plane stereo particle image velocimetry measurements of velocity gradient tensor fields in turbulent shear flow. I. Accuracy assessments. *Physics of Fluids* **18** (3), 35101.

Novikov, E.A. 1971 Intermittency and scale similarity in the structure of a turbulent flow. *Prikl. Mat. Mec* **35**, 266–277.

Oboukhov, A M 1962 Some specific features of atmospheric tubulence ". *Journal of Fluid Mechanics* **13**, 77–81.

Ooi, Andrew, Martin, Jesus, Soriam, Julio & Chong, M S 1999 A study of the evolution and characteristics of the invariants of the velocity-gradient tensor in isotropic turbulence. *Journal of Fluid Mechanics* **381**, 141–174.

Österlund, J M, Johansson, A V, Nagib, H M & Hites, M H 2000 A note on the overlap region in turbulent boundary layers. *Phys. Fluids* **12**, 1–4.

Pai, Shih-I & Luo, Shijun, ed. 1991 *Theoretical and Computational Dynamics of a compressible flow*. Van Nostrand Reinhold and Science Press, Beijing.

Peers, E, Xhang, X & Kim, J W 2009 Patched Characteristic Interface Conditions for High-Order Aeroacoustic Computation. *AIAA Paper 2009-3112* (12), 2341–2348.

Perry, A E & Chong, M S 1987 A DESCRIPTION OF EDDYING MOTIONS AND FLOW PATTERNS USING CRITICAL-POINT CONCEPTS. *Annual Review of Fluid Mechanics* **19**, 125–155.

Perry, a. E. & Chong, M. S. 1994 Topology of flow patterns in vortex motions and turbulence. *Applied Scientific Research* **53** (3-4), 357–374.

Poinsot, T J & Lele, S K 1992 Boundary Conditions for Direct Simulations of Compressible Viscous Flows. *J. Comp. Phys.* **101** (1), 104–129.

Pope, S B, ed. 2000 *Turbulent Flows*. Cambridge University Press, Cambridge.

Reynolds, O 1895 On the dynamical theory of incompressible viscous fluids and the determination of the criterion. *Philosophical Transactions of the Royal Society of London, Series A* **186**, 123.

Richardson, L F 1925 *Weather Prediction by Numerical Process*. Cambridge University Press, Cambridge.

Robinson, S K 1991 Coherent motions in the turbulent boundary layer. *Annual Review of Fluid Mechanics* **23**, 601–639.

Saddoughi, Seyed G & Veeravalli, Srinivas V 1994 Local isotropy in turbulent boundary layers at high Reynolds number. *Journal of Fluid Mechanics* **268**, 333–372.

Sanada, T. 1992 Comment on the dissipation-range spectrum in turbulent flows. *Phys. Fluids A* (4), 1086–1087.

Sandberg, R.D. 2012*a* Numerical investigation of turbulent supersonic axisymmetric wakes pp. 488–520.

Sandberg, R D 2009 Generalized cylindrical coordinates for characteristic boundary conditions and characteristic interface conditions. AFM 09/02. University of Southampton.

Sandberg, R D 2011 An axis treatment for flow equations in cylindrical coordinates based on parity conditions. *Computers and Fluids* **49**, 166–172.

Sandberg, Richard D. 2012*b* Numerical investigation of turbulent axisymmetric wakes. *Journal of Fluid Mechanics* **702**, 488–520.

Sandberg, R D & Sandham, N D 2006 Nonreflecting zonal characteristic boundary condition for direct numerical simulation of aerodynamic sound. *AIAA J.* **44** (2), 402–405.

Sandberg, Richard D., Sandham, Neil D. & Suponitsky, V 2012 DNS of compressible pipe flow exiting into a coflow. *International Journal of Heat and Fluid Flow* **35**, 33–44.

Schlatter, P, Li, Q, Brethouwer, G, Johansson, A V & Henningson, D S 2010 Simulations of spatially evolving turbulent boundary layers up to Re_θ=4300. *International Journal of Heat and Fluid Flow* **31**, 251–261.

Schlatter, Philipp & Örlü, Ramis 2010 Assessment of direct numerical simulation data of turbulent boundary layers. *Journal of Fluid Mechanics* **659**, 116–126.

Schlatter, P, Örlü, R, Li, Q, Brethouwer, G, Fransson, J H M, Johansson, A V, Alfredsson, P H & Henningson, D S 2009 Turbulent boundary layers up to Re_θ= 2500 studied through simulation and experiment. *Phys. Fluids* **21**, 1–4.

Schlatter, P & Örlü, R. 2010 Assessment of direct numerical simulation data of turbulent boundary layers. *J. Fluid Mech.* **659**, 116–126.

Schlichting, Hermann 1979 *Boundary Layer Theory*, 7th edn. McGraw-Hill.

Sillero, J 2011 Direct simulation of a zero-pressure-gradient turbulent boundary layer up to Re_θ=6650. *Journal of Physics: Concerence Series* **318**, 1–7.

Sirovich, Lawrence, Smith, Leslie & Yakhot, Victor 1994 Energy spectrum of homogeneous and isotropic turbulence in far dissipation range. *Phys. Fluids A* **72** (3), 344–347.

Soria, Julio, Sondergaard, R., Cantwell, Brian J., Chong, M. S. & Perry, a. E. 1994 A study of the fine-scale motions of incompressible time-developing mixing layers. *Physics of Fluids* **6** (1994), 871.

Spalart, P R 1988 Direct simulation of a turbulent boundary layer up to Re_{θ}=1410. *J. Fluid Mech.* **187**, 61–98.

Sreenivasan, K R & Antonia, R a. 1997 the Phenomenology of Small-Scale Turbulence. *Annual Review of Fluid Mechanics* **29** (1), 435–472.

Taylor, Geoffrey Ingram 1935 Statistical Theory of Turbulence. In *Proceedings of the Royal Society of London*, p. 421.

Taylor, G I 1938 Production and Dissipation of Vorticity in a Turbulent Fluid. *Proceedings of the Royal Society A: Mathematical, Physical and Engineering Sciences* **164** (916), 15–23.

Tennekes, H & Lumley, J 1972 *A First Course in Turbulence*. MIT Press.

Thompson, K W 1987 Time Dependent Boundary Conditions for Hyperbolic Systems. *J. Comp. Phys.* **68**, 1–24.

Thompson, K W 1990 Time Dependent Boundary Conditions for Hyperbolic Systems, II. *J. Comp. Phys.* **89**, 439–461.

Tomkins, C D & Adrian, R J 2003 Spanwise structure and scale growth in turbulent boundary layers. *J. Fluid Mech.* **490**, 37–74.

Touber, E & Sandham, N D 2009 Large-eddy simulation of low-frequency unsteadiness in a turbulent shock-induced separation bubble. *Theor. Comp. Fluid Dyn.* **23** (2), 79–107.

Townsend, A A 1961 Equilibrium layers and wall turbulence. *J. Fluid Mech.* **11**, 97–120.

Townsend, A A 1976 *The Structure of Turbulent Shear Flow*. Cambridge University Press, Cambridge.

Tsinober, a. 2000 Vortex stretching versus production of strain/dissipation.

Tsinober, a., Kit, E. & Dracos, T. 1992 Experimental investigation of the field of velocity gradients in turbulent flows. *Journal of Fluid Mechanics* **242** (-1), 169.

Vainshtein, S.I. & Sreenivasan, K. R. 1994 Kolmogorovs 4/5th law and intermittency in turbulence. *Physical Review Letters* .

Van Dyke, M 1982 *An Album of Fluid Motion*. The Parabolic Press.

Vasilyev, Ov, Lund, Ts & Moin, Parviz 1998 A general class of commutative filters for LES in complex geometries. *Journal of Computational Physics* **146** (1), 82–104.

Vieillefosse, P 1982 Local interaction between vorticity and shear in a perfect incompressible fluid. *Le Journal de Physique* **43**, 836–842.

Vieillefosse, P 1984 Internal motion of a small element of fluid in an inviscid flow. *Physica A: Statistical Mechanics and its Applications* **125** (1), 150–162.

Vincent, A & Meneguzzi, M 1994 The dynamics of vorticity tubes in homogeneous turbulence. *J. Fluid Mech.* **258**, 245–254.

Wilcox, D C 1998 *Turbulence Modeling for CFD*, 2nd edn. DCW Industries.

Wu, X & Moin, P 2009 Direct numerical simulation of turbulence in a nominal zero-pressure-gradient flat-plate boundary layer. *J. Fluid Mech.* **630**, 5–41.

Wu, Y & Christensen, K T 2005 Population trends of spanwise vortices in wall turbulence. *J. Fluid Mech.* **568**, 55–76.

Xie, Z T & Castro, I P 2008 Efficient generation of inflow conditions for large-eddy simulation of street-scale flows. *Flow, Turbulence and Combustion* **81** (3), 449–470.

Zubair, L. 1993 Studies in turbulence using wavelet transforms for data compression and scale separation. PhD thesis, Yale University, New Haven, CT.